EFFECTS OF THE BUILT-IN CONSTRUCTION GRADIENT AND ENVIRONMENTAL CONDITIONS ON JOINTED PLAIN CONCRETE PAVEMENTS

by

Rania Elias Asbahan

B.E. in Civil Engineering, American University of Beirut, 1999

M.E. in Civil Engineering, American University of Beirut, 2001

Submitted to the Graduate Faculty of

The Swanson School of Engineering in partial fulfillment

of the requirements for the degree of

Doctor of Philosophy

University of Pittsburgh

2009

UNIVERSITY OF PITTSBURGH

SWANSON SCHOOL OF ENGINEERING

This dissertation was presented

by

Rania Elias Asbahan

It was defended on

May 29, 2009

and approved by

Amir Koubaa, PhD, Assistant Professor and Academic Coordinator,
Department of Civil and Environmental Engineering

Jeen-Shang Lin, PhD, Associate Professor,
Department of Civil and Environmental Engineering

Patrick Smolinski, PhD, Associate Professor,
Department of Mechanical Engineering and Materials Science;
Associate Faculty, Department of Bioengineering

Luis E. Vallejo, PhD, Professor,
Department of Civil and Environmental Engineering

Dissertation Director: Julie M. Vandenbossche, PhD, Assistant Professor,
Department of Civil and Environmental Engineering

EFFECTS OF THE BUILT-IN CONSTRUCTION GRADIENT AND ENVIRONMENTAL CONDITIONS ON JOINTED PLAIN CONCRETE PAVEMENTS

Rania Elias Asbahan, PhD

University of Pittsburgh, 2009

Slab curvature, which represents the response of concrete pavement to environmental loads, influences the location and magnitude of critical slab stresses and affects long-term pavement performance. The purpose of this study was to measure the changes in temperature and moisture profiles in a newly constructed concrete pavement, to determine the deformed shape of the slabs and the resulting stress and identify the relative contributions of built-in and transient environmental effects over time. To do this, an instrumented jointed plain concrete pavement (JPCP) was monitored over a two-year period.

The built-in construction gradient is a major factor contributing to slab curvature and stress. Therefore, first, static strain and pressure gage data used to establish the built-in gradient and zero stress temperature.

Slab curvature was predicted using measurements of temperature and moisture conditions in the slab and computed using static strain and pavement surface profile measurements. It was found that the additional restraint provided by the dowel and tie bars does not appear to significantly reduce slab curvature resulting from daily temperature fluctuations or from reversible drying shrinkage. It does have a substantial effect on reducing slab curvature due to long-term drying shrinkage. It was also found that the slab curvature is predominantly curled upward (99 percent of the time), resulting in top-down fatigue cracking, while it is traditionally assumed that fatigue cracking in concrete pavements initiates at the bottom.

Finite element models were developed to study the effect of various environmental conditions and slab restraints on the development of stress in the slabs. The models were validated based on measured strain data. It was found that the effect of moisture has the most significant effect on stress in the slabs. The measured curvature in the restrained slab (tie and dowel bars) is over 50 percent lower when compared to the unrestrained (no tie or dowel bars) slab. This reduction in deformation resulted in a critical stress that was 20 to 22 percent larger for the restrained slab compared to the unrestrained slab.

TABLE OF CONTENTS

LIST OF TABLES

LIST OF FIGURES

ACKNOWLEDGEMENTS

I would first like to express my thanks to my advisor, Dr. Julie Vandenbossche, for her inspiration, valuable technical guidance and support throughout the phases of this research. I feel privileged to have been mentored by Dr. Vandenbossche for the last four years, and will forever be grateful to her. I would like to express my sincere appreciation to Dr. Amir Koubaa who highly encouraged me to pursue this path and provided great insight and advice on academic issues and other general life matters.

I would also like to thank Dr. Luis Vallejo, Dr. Patrick Smolinski and Dr. Jeen-Shang Lin for serving on my doctoral committee and for taking valuable time out of their schedules to review my dissertation. I am very grateful to Dr. Rachmadian Wulandana for the long hours and the valuable feedback he provided on the finite element problems. I am also very grateful for the graduate and undergraduate students who assisted with the field work and data analysis for this project. Their hard work is greatly appreciated. Special thanks to my colleague Ms. Jennifer McCracken who was present along my side throughout this whole endeavor.

The financial support provided by the Pennsylvania Department of Transportation and the Federal Highway Administration is also acknowledged, along with their assistance in performing the field work pertaining to this research.

Last but not least, I would like to thank my family, friends and coworkers for standing by me in stressful times. I could not have done this without their constant encouragement. Special thanks to my husband, Haitham, for his support and understanding throughout this time-consuming process.

This dissertation is dedicated to Robert Saliba, a great teacher and a wonderful person, who inspired me to be where I am today and to my grandmother Linda Khoury, who is the source of my strength.

1.0 INTRODUCTION

1.1 BACKGROUND

The current design procedure adopted for the design and rehabilitation of pavement structures is an empirical approach based on performance equations developed at the American Association of State Highway Officials Road Test (AASHO) conducted near Ottawa, Illinois, in the late 1950's. Since the time of the AASHO Road Test, there have been many significant changes in trucks and truck volumes, materials, construction, rehabilitation and design needs. With time, it became clear that modifications to the design procedure were needed to account for such changes. Based on this, the development of a new design guide was initiated.

The new design procedure incorporates mechanistic-based models and performance predictions models that are calibrated using a database reflecting current paving materials and traffic conditions. In this mechanistic-empirical design approach, the following factors are taken into account throughout the entire design life: impact of climate and aging on material properties, variations in traffic loadings, and ocations of critical stresses in the pavement and subgrade layers due to both traffic loads and climatic factors.

The damage caused by the critical stresses is accumulated monthly over the design period and the total accumulated damage is then related to specific pavement distresses.

Factors influencing the development of stress in concrete pavements include:

1. the variation in temperature and moisture conditions throughout the depth of the slab,
2. the temperature and moisture condition present at the time the concrete sets,
3. conditions restraining the movement of the slab,
4. concrete material properties, and
5. magnitude and locations of vehicle loads.

This study will address the first three factors, which are briefly explained in this section. The variation in temperature and moisture conditions throughout the depth of the slab causes the concrete to expand and/or contract at different rates throughout its depth, thus causing curvature in the slab. Curvature due to temperature is referred to as curling and curvature due to moisture is referred to as warping. The magnitude of curling and warping that develops varies both diurnally and seasonally. The temperature and moisture conditions that are present at the time of set constitute what is referred to as the built-in construction gradient. At the time the concrete sets, the slab remains flat since the concrete is still in a plastic state and has not yet developed sufficient stiffness. This implies that, at any point in time, when the temperature and moisture profile is of the same magnitude as that corresponding to the built-in construction gradient, the slab is flat with zero stress. When the slab is in a zero gradient condition, it deforms. This built-in gradient has proven to be an important factor in estimating stress in concrete pavements, especially when adopting the new mechanistic-empirical pavement design approach. However, a methodology to accurately determine the built-in construction gradient of concrete pavements is not available.

Along with evaluating the effects of the environmental conditions (temperature and moisture) on stresses in the slab, this study also characterizes the effects of different slab restraints on stress. Restraining the slab movement caused by thermal or moisture changes contributes to the development of stress in concrete pavement. Other than the slab self-weight, discussed in the previous paragraphs, other factors are known to reduce slab movements. These include friction at the slab/base interface and restraints along the transverse and longitudinal joints and will be considered in this work.

1.2 RESEARCH OBJECTIVES

This research has two main objectives: the first is to establish a method for determining the built-in construction gradient of a jointed plain concrete pavement. The second objective is to examine the effects of seasonal variations in the temperature and moisture throughout the slab depth on the development of stress in the slab and examine the effects of different slab restraining conditions on slab deformation and stress.

1.3 GENERAL RESEARCH APPROACH

To achieve the first objective, two approaches will be followed and compared. The concrete set time needs to be determined so that o the time when the development of stress and strain within the concrete is initiated. The first approach involves analyzing data collected from strain gages placed at different locations and depths in the concrete and using the measured strain to identifying the time when the concrete starts experiencing a constant change in strain with a constant change in temperature. The second approach involves analyzing data collected from pressure cells placed at different locations along the interface between the slab and the base layer and using the measured pressure to identifying the time when the concrete starts experiencing a constant change in pressure with a constant change in temperature. The results of these two methods are evaluated to establish the built-in construction gradient of the pavement. Conclusions are drawn regarding the applicability of both methods to restrained and unrestrained slabs. The new design guide, referred to as the Mechanistic-Empirical Pavement Design Guide (MEPDG), will be used to evaluate the effect of the built-in construction gradient on the performance of the concrete pavement.

To achieve the second objective, the pavement structure will be modeled using a two dimensional finite element program to study the effects of the presence of different temperature and moisture gradients on stress inside the slab. The model will be calibrated using static strains measured in the field. This will provide a better understanding of the response of restrained and unrestrained concrete slabs to environmental loads. In addition, the MEPDG will be used to predict the seasonal environmental changes in the concrete slab. The predicted variations in concrete temperature and moisture conditions will be compared to those measured on the field.

1.4 SIGNIFICANCE OF THE RESEARCH

Several studies have shown that the built-in construction gradient is an important factor in estimating stresses in concrete pavements, especially when adopting the new design guide. When using the MEPDG, the default input value for the temperature difference across the slab depth based on the construction gradient is equal to -10˚F from top to bottom of the slab. The

design guide recommends not modifying this value unless more precise data is available. This value was obtained based on an analysis conducted using the fatigue damage algorithm and the field cracking from over 500 observations. The value of -10˚F was selected to result in the lowest error between measured and predicted cracking. However, the actual built-in construction gradient covers a wide range of values and varies with several factors including type of base, type of curing, concrete mix and material properties and climatic conditions at the time of construction.

Researchers have been using a wide variety of methods to estimate the built-in construction gradient. Most of these methods are based on analyzing surface movements of the slab with respect to changes in temperature gradients along the slab depth. These analyses usually involve the use of prediction models to estimate slab curvatures for different temperature gradients and the selection of the gradient that results in the least error between predicted and measured curvatures. As such, there is a need to establish a methodology for the characterization of the built-in construction gradient in jointed plain concrete pavements.

The MEPDG incorporates mechanistic-based models and performance predictions models that are calibrated using a database reflecting current paving materials and traffic conditions. Studies have been and are currently being carried out to study the effects of environmental conditions on the performance of concrete pavements. Most of these studies involve the analysis of field data collected from instrumented concrete pavements constructed in several states around the country. These studies show that the performance of concrete pavements is significantly affected by several factors including temperature changes, moisture changes, built-in gradients, concrete drying shrinkage, along with other factors. More research is still required in this area to develop a better understanding of the behavior of concrete slabs under the effects of environmental loading. As a result, this research is being conducted based on data collected in the state of Pennsylvania to evaluate the effects of seasonal variations in the temperature and moisture throughout the slab depth on the development of stress in the slab and examine the effects of different slab restraining conditions on slab deformation and stress.

1.5 STRUCTURE OF THE DISSERTATION

The structure of this dissertation is as follows: Chapter 2 includes a literature review of the factors associated with the development of stresses in concrete pavements. Chapter 3 is a description of the instrumented pavement section constructed in the field. Chapter 4 establishes a method for the determination of the built-in construction gradient in the concrete slab based on the two approaches described earlier. Chapter 5 is an analysis of the temperature and moisture conditions in the concrete; it includes evaluation of the conditions measured on site and those predicted by available models. Chapter 6 combines the results of surface profile testing and static strain measurements to evaluate the drying shrinkage of the concrete; in addition, it includes a comparison of the strains measured on site to those predicted by available models. Chapter 7 details the finite element modeling of the pavement structure and the analysis of the stress generated in the concrete due to the different inputs determined in the preceding chapters. Chapter 8 presents the summary and conclusions of this study and recommendations for future research.

2.0 LITERATURE REVIEW

This chapter presents the review of available literature regarding the development of stress in concrete pavements. It starts out with presenting the historical approach to the design of concrete pavements, followed by a detailed description of the behavior of concrete slabs under environmental loading conditions. Factors influencing curvature of the slabs are also discussed. The methods for estimating stresses in concrete pavements due to the environmental loading conditions are also presented; these include the closed form solutions and the finite element methods. The last section of this chapter briefly presents previous research carried out regarding the response of concrete pavements to environmental loads.

2.1 HISTORICAL REVIEW OF CONCRETE PAVEMENT DESIGN APPROACHES

A jointed plain concrete pavement (JPCP) is composed of unreinforced concrete slabs constructed adjacent to each other. Tie bars and dowel bars may be placed along the interface between adjacent slabs, as shown in Figure 2.1 showing the basic components of a JPCP. The slabs are placed on a base or subbase material, which may consist of unstabilized granular material or stabilized material. The subbase or base material is placed on the existing soil, which is referred to as the subgrade. Several factors including environmental conditions, material properties, layer thicknesses and traffic loading conditions affect the development of distresses in JPCP.

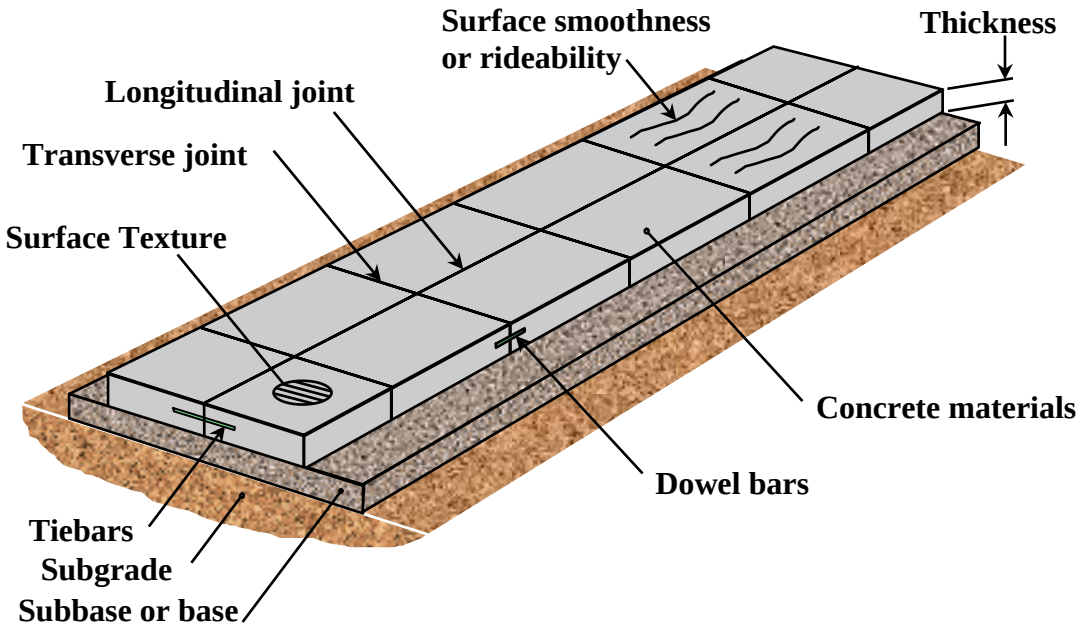

Figure 2.1. Basic components of a jointed plain concrete pavement.

Currently, the *Guide for Design of Pavement Structures* is the primary document adopted for the design and rehabilitation of pavement structures. The first edition of the guide was published in an interim form in 1972 based on limited empirical performance equations developed at the American Association of State Highway Officials Road Test (AASHO) conducted near Ottawa, Illinois, in the late 1950's. In 1986, a revised edition was issued incorporating refinements in materials input parameters and the addition of a section on rehabilitation of pavements. In 1993, a further refined edition was released incorporating changes to the overlay design procedure and accompanying appendices (AASHTO 1993).

Regression prediction equations were developed empirically from field observations at the AASHO Road Test. The 1993 Guide predicts the amount of traffic that can be sustained by a pavement before deteriorating to some selected terminal level of serviceability. The level of serviceability represents the functional performance of the pavement which is characterized by the quality of the ride as evaluated by the user. The input parameters that influence the design include: 28-day concrete modulus of elasticity and modulus of rupture, modulus of subgrade reaction, total cumulative 18-kip equivalent single axle loads (ESAL) at the end of the design period, and slab thickness (AASHTO 1993).

Several limitations are identified in this design procedure. The AASHO Road Test used a specific set of pavement materials and one roadbed soil in one single environment. Traffic was accumulated on each test section by operating vehicles with identical axle loads and axle configurations as opposed to mixed traffic. Field testing was performed for two years and results were extrapolated to 10- or 20-year design periods (AASHTO 1993).

Since the time of the AASHO Road Test, there have been many significant changes in trucks and truck volumes, materials, construction practices, rehabilitation and design needs. With time, it was clear that modifications to the design procedure were needed to account for such changes. Based on this, the development of the *2004 Guide for Design of New and Rehabilitated Pavement Structures* was initiated. The new guide incorporates mechanistic-based models and performance predictions models that are calibrated using a database reflecting current paving materials and traffic conditions (ARA 2004). The new guide was scheduled to be put before the American Association of State Highway and Transportation Officials (AASHTO) for vote in the spring of 2007.

The new design procedure incorporates the impact of climate and aging on material properties in an iterative (biweekly, monthly) manner throughout the entire design life. Hourly, monthly, and annual variations in traffic loadings are also studied with respect to variations of material and climate properties. Three components are involved in the overall structural modeling of the pavement. First, structural response models are used to compute critical stresses at critical locations in the pavement and subgrade layers due to both traffic loads and climatic factors (temperature and moisture). Then, damage models are used to accumulate damage, month by month, over the design period. Finally, transfer functions are used to relate the accumulated damage to specific distresses (ARA 2004). The structural response model, damage model and transfer functions used in the new design guide are briefly explained in the following paragraphs.

The structural model used for rigid pavement analysis in the new guide is ISLAB2000, a two dimensional finite element program developed by Khazanovich et al. (2000). The incremental design procedure adopted in the new guide requires hundreds of thousands of stress and deflection calculations to compute monthly damage for the different loads, load positions, and equivalent temperature differences over a design period of many years. To perform the

required large number of computations in a rapid manner, rapid solution neural networks (NN) were developed based on the critical stresses and deflections determined using the ISLAB2000 model (ARA 2004).

The damage model is an incremental model based on Miner's damage hypothesis (1945). The damage due to the different combinations of wheel loads and prevailing environmental conditions is accumulated over the entire design period of the pavement. The damage is estimated as a ratio of the applied to the allowable number of load applications at specific conditions representing the pavement age, month of the year (to account for base and subgrade material properties), traffic (axle type and load level), existing temperature gradient inside the slab and the location of the traffic load. Damage models considered in the design guide for JPCP are transverse cracking and faulting across transverse joints (ARA 2004).

The transfer functions were developed primarily using field distress data in the Long Term Pavement Performance (LTPP) database. This database is populated with a large number of pavement structures located around the country that were subjected to a broad range of traffic and environmental loading conditions. The development of the transfer functions constitutes the main empirical part of this design procedure (ARA 2004).

The complex models and design concepts are incorporated into a user-friendly software package (ARA 2004). As a result, the new design guide is composed of two types of analyses (mechanistic and empirical) and is therefore referred to as the Mechanistic-Empirical Pavement Design Guide (MEPDG).

2.2 SLAB CURLING AND WARPING

Environmental conditions affecting the curvature of a concrete slab can be attributed to changes in temperature and moisture conditions inside the slab. Curvature due to variations in slab temperature is referred to as curling of the slab and curvature due to variations in slab moisture conditions is referred to as warping of the slab. As the result of upward and downward slab curvature, critical tensile stresses occur at different locations, as shown in Figure 2.2. The slab on the left side of the figure represents a situation when the environmental conditions are causing the lower part of the slab to expand more than the top part of the slab. This is referred to as a

negative gradient and causes the slab to curve upwards. Support is lost near the ends of the slab, and hence, the self weight of the slab exerts tensile stresses near the top of the PCC. Similarly, the slab on the right side of the figure represents a situation when the environmental conditions are causing the top part of the slab to expand more than the lower part of the slab. This is referred to as a positive gradient and causes the slab to curve downwards. In this case, support is lost near the center of the slab and the self weight of the slab exerts tensile stresses near the bottom of the slab (Jeong and Zollinger 2005; Huang 2004; Yu et al. 1998).

Figure 2.2. Locations of critical stresses due to slab curling and warping (Wells et al. 2005).

In addition, vehicular loads also induce stresses in concrete pavements. Depending on the curvature of the slab at the time of loading, the critical location of the load varies, as shown in Figure 2.3. In the presence of a positive gradient, the slab curvature is downwards (shown in the first part of the figure) and critical cracking is expected to initiate from the bottom, at midslab. Vehicular loading at midslab constitutes the critical loading condition. Similarly, in the presence of a negative gradient, the slab curves upwards (shown in the lower part of the figure) and critical cracking is expected to initiate from the top, at midslab. In this case, vehicular loading at the slab edges constitutes the critical loading condition (ARA 2004). When using the MEPDG, traffic loads are automatically applied at different locations on the slab surface to identify the critical locations that result in the generation of the peak stresses, when combined with the different environmental conditions of the slab.

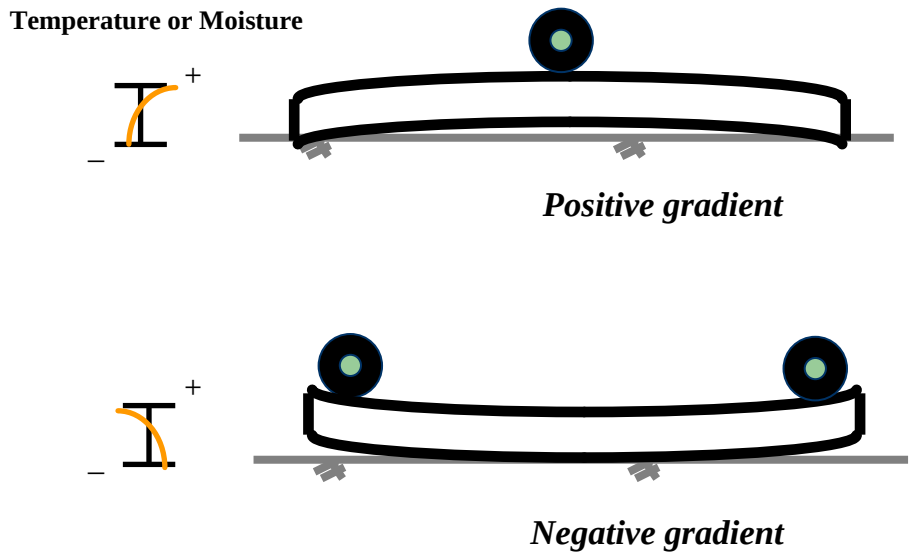

Figure 2.3. Critical loading conditions due to the combined effect of environmental and vehicular loads (Wells et al. 2005).

2.3 FACTORS AFFECTING CURLING AND WARPING

Curling and warping of the slab are mostly due to variations of the slab temperature and moisture conditions, respectively. These variations cause the development of temperature and moisture gradients through the slab that vary daily and seasonally. Temperature and moisture conditions at the time of construction cause gradients that affect the long-term behavior of the slab; these are generally referred to as built-in construction gradients.

Other factors influencing the amounts of curling and warping include concrete material properties such as the coefficient of thermal expansion, drying shrinkage, creep and elastic modulus of the concrete.

Restraining the slab movement caused by thermal or moisture changes also contributes to the development of stresses in concrete pavements. Several factors are known to reduce slab movements; these include: the slab self-weight, friction at the slab/base interface and restraints along the transverse and longitudinal joints.

The above-mentioned factors influencing curling and warping of concrete pavements are discussed in this section.

2.3.1 Temperature gradient through the slab

A temperature gradient develops in the slab when the PCC temperature at the top of the slab is different than the temperature at the bottom of the slab. Temperature gradients throughout the pavement structure are affected by both seasonal and daily environmental conditions. The top of the pavement is mostly affected by daily environmental changes while the bottom varies more seasonally (Wells et al. 2006). A positive gradient is defined as when the temperature at the top of a slab is higher than at the bottom, resulting in downward curvature; this case is predominant during the daytime. In contrast, a negative gradient occurs when the temperature at the bottom of the slab is greater than the top, resulting in upward slab curvature; this case is predominant during the nighttime. Temperature gradients are affected by ambient environmental conditions such as air temperature, solar radiation, cloud cover and precipitation (Rao and Roesler 2005).

Positive gradients force the edges and corners of the pavement downwards thereby increasing support in these locations and decreasing the support at the center of the slab. Negative gradients force the corners and edges of the pavement upwards and the center of the pavement downwards, thereby reducing support at the corners while increasing it at midpanel (Jeong and Zollinger 2005; Huang 2004; Yu et al. 1998).

Temperature gradients are calculated by dividing the difference between the measured temperatures at the top and the bottom of the concrete pavement by the distance between them, thus providing a linear relationship. However, several field studies have shown that the temperature distribution throughout the depth of the slab is primarily nonlinear in nature (Armaghani et al. 1987; Yu et al. 1998). The nonlinearity in the temperature distribution through a concrete slab was theoretically predicted by Thomlinson (1940) and was subsequently proven by experimental data presented by numerous investigators (Mirambell 1990; Dempsey 1969; Jansen 1988).

To account for nonlinear temperature gradients in concrete slabs, Janssen and Snyder (2000) presented a method for estimating the moment produced by a nonlinear temperature profile about the bottom of the slab. The temperature moment can be calculated using Equation 2-1. Figure 2.4 provides a graphical representation of the temperature moment parameter.

$$TM_o = -0.25\sum_{i=1}^{n}\left[(t_i + t_{i+1})(d_i^2 - d_{i+1}^2) - 2(d_1^2 - d_n^2)T_{wave}\right] \quad \text{(Equation 2-1)}$$

Where: TM_o = Temperature moment

t_i = Temperature at location i

d_i = Depth at location i

T_{wave} = Weighted average temperature, given by Equation 2-2.

$$T_{wave} = \sum_{i=1}^{n}\left[\frac{(0.5)(t_i - t_{i+1})(d_i + d_{i+1})}{(d_1 - d_n)}\right] \quad \text{(Equation 2-2)}$$

The temperature moment can be converted into an equivalent linear gradient by determining the linear gradient that produces the same magnitude of temperature moment as the measured surface profile, by using Equation 2-3.

$$ELG = -\frac{12(TMo)}{h^3} \quad \text{(Equation 2-3)}$$

Where: ELG = Equivalent linear gradient

h = Slab thickness

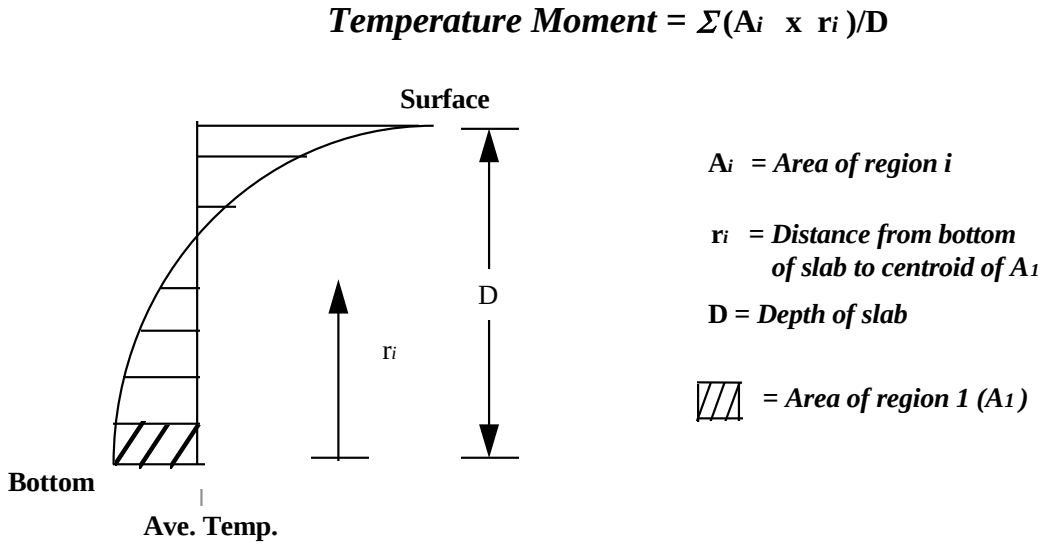

Figure 2.4. Graphical representation of the temperature moment parameter (Wells et al. 2005).

As can be noticed from the previous equation, a positive linear gradient will produce a negative temperature moment and a negative linear gradient will produce a positive temperature moment. The temperature moment parameter can be used to analyze daily and seasonal variations in temperature gradients and has been used by researchers (Janssen and Snyder 2000; Rao et al. 2001).

Other researchers have proposed representing the nonlinear temperature profile along the slab depth by a quadratic equation or a third degree polynomial (Choubane and Tia 1992; Zhang et al. 2003). Based on a regression analysis of the measured temperatures along the slab depth, regression coefficients are obtained from the nonlinear profile that best fits the measured data. The regression coefficients are then used to estimate an equivalent temperature difference across the slab depth. This equivalent temperature difference produces the same curvature as that caused by a linear temperature gradient used in the solutions developed by Westergaard and Bradbury (Mohamed and Hansen 1997; Jeong and Zollinger 2005). The solutions developed by Westergaard (1926) and Bradbury (1938) are detailed in section 2.4 of this chapter. The equivalent linear temperature gradients developed using this approach are then used to estimate stresses in the concrete slabs due to the nonlinear temperature profiles.

The method proposed by Mohamed and Hansen (1997) requires estimating the equivalent linear temperature gradients by using the regression coefficients from the fitting of a polynomial through the measured temperature profiles. The method proposed by Janssen and Snyder (2000) assumes a linear relationship between the temperature measurements and directly uses the temperature moment to estimate the equivalent linear gradient. The difference between both methods is minimal since the temperature measurements in the slab are closely spaced in the nonlinear regions. The method proposed by Janssen and Snyder (2000) will be used in this study to characterize the daily and seasonal temperature profiles.

Slab deformation due to the presence of nonlinear temperature profiles across the slab depth can be separated into three components. The three components represent the uniform, linear and nonlinear portions of the temperature profiles. Uniform temperature change causes uniform contraction and expansion along the slab depth. Linear temperature change causes bending of the slab. And nonlinear temperature change is simply what remains after subtracting the uniform and linear components from the total temperature. Researchers have established these three components based on the basic assumption of the classical theory of plates that the

cross section of the plate remains plane after bending. This theory implies that the plate can either expand or contract along its axial direction or bend with its cross-section remaining plane (Zhang et al. 2003; Choubane and Tia 1992; Siddique et al. 2005). A more thorough look at the behavior of slabs subjected to temperature loading is presented in section 2.4 of this chapter.

2.3.2 Moisture gradient through the slab

Similarly to temperature gradients, moisture gradients develop in the slab when the concrete moisture levels at the top of the slab are different than those at the bottom of the slab. A positive moisture gradient is when the moisture at the top of a slab is higher than at the bottom, resulting in downward curvature. In contrast, a negative gradient occurs when the moisture at the bottom of the slab is greater than the top, resulting in upward slab curvature.

In general, moisture gradients are due to the drying shrinkage of the concrete at the slab surface which may be accompanied by concrete expansion at the bottom of the slab due to high moisture levels. As a result, moisture gradients usually contribute to the development of upward warping of the slab (Eisenmann and Leykauf 1990). Moisture gradients are affected by the concrete drying shrinkage, pavement drainage conditions and atmospheric climatic conditions such as relative humidity, rainfall and snow. Concrete drying shrinkage is a function of the degree of saturation of the cement paste; as the degree of saturation increases, shrinkage decreases (Mindess et al. 2003). Aggregates restrain deformations of the concrete due to drying shrinkage. The larger the volumetric aggregate content of the concrete, the larger the amount of restraint and the smaller the amount of shrinkage (Powers 1959).

The distribution of moisture in the concrete can be determined by placing sensors designed to measure relative humidity levels inside the concrete. Different types of sensors exist and have been successfully used by researchers in the past. In some field studies, psychometers (Janssen 1987), digital capacitive sensors (Grasley et al. 2003) and dew point sensors (Jeong and Zollinger 2005) were used to monitor moisture level changes inside concrete slabs. In some laboratory tests, dew point meters (Yang 1999) and humidity probes (McCarter et al. 2001) were used to monitor moisture level changes inside concrete specimens. These different types of

sensors and probes operate in different methods, but the end result is a relative humidity measurement. The newer methods result in more accurate results and allow more frequent readings (Grasley and Lange 2002).

In the study by Janssen (1987), pavement moisture contents were determined by field moisture measurements, laboratory measurements and computer simulation to determine a typical pavement moisture distribution. Field measurements included placing psychometers at different depths inside 8-inch thick concrete slabs constructed in Illinois to record relative humidity levels. These levels were then used in estimating the degree of saturation of the concrete, based on laboratory calibrations. The results showed that the moisture content varies in the top two inches of the concrete surface and does not vary much at deeper levels. Laboratory measurements involved casting of concrete cylinders, placing them on a crushed-stone base saturated at the bottom surface, subjecting them to freeze-thaw cycles, breaking the cylinders into 2-inch thick pieces and drying them to determine moisture contents at different levels. The results showed that the moisture content does not vary much along the depth. A computer developed for simulating the movement of moisture through soils was used to simulate the movement of water in the concrete. The pavement structure was modeled with different initial saturation levels for a period of three months. It was found that surface drying does not extend very far into the concrete and this was attributed to the very low permeability of the concrete. Based on the three methods, a typical pavement moisture distribution was developed for an 8-inch thick pavement in a moderate climate subject to freeze-thaw cycling, and is shown in Figure 2.5. This causes shrinkage that is nonlinear throughout the slab thickness and affects concrete pavement in a manner similar to a nonlinear temperature distribution. Based on field measurements of moisture levels in concrete slabs, it was found that drying shrinkage occurs down to a shallow depth of two inches, while the deeper part of the slab remains at relative humidity levels higher than 80 percent. The bottom portion of the slab remains saturated (Janssen 1987).

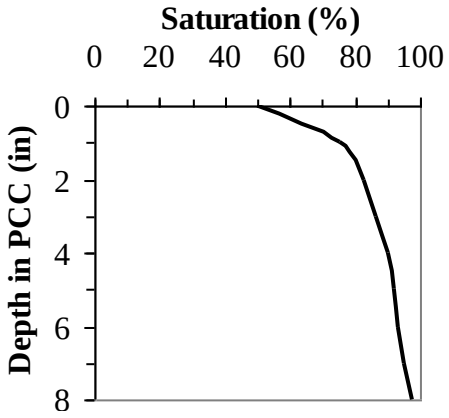

Figure 2.5. Typical moisture profile in an 8-inch concrete slab, reproduced based on data from Janssen (1987).

Subsequently, studies were conducted by Eisenmann and Leykauf (1990) to evaluate the amount of slab curling caused by surface shrinkage. In these studies, a simplified method for calculating the upward deflection due to the presence of a moisture gradient along the slab depth is presented. The slab is modeled as a beam supported by a rigid base, the moisture gradient is represented by a linear temperature gradient causing an equivalent moment in the beam section and the surface shrinkage extends to a depth of 1.6 inches. Upward deflections calculated by this method were found to be in good agreement with those measured during field tests conducted at Munich Technical University. In addition, it was found that the warping caused by surface shrinkage can be greatly reduced by increasing the slab thickness and is influenced by the restraining conditions along the slab edges. The presence of dowel bars and tied shoulders cause a decrease in the amount of warping.

The linear temperature gradient causing an equivalent moment in the beam section due to the presence of a moisture gradient is given by Equation 2-4 (Eisenmann and Leykauf 1990). This equation is for upward warping due to a negative moisture gradient.

$$\Delta t = \frac{6\, t\, \varepsilon_s \left(h - t\right)}{\alpha\, h^3} \qquad \text{(Equation 2-4)}$$

Where: Δt = Linear temperature gradient, ˚F/in

ε_s = Surface shrinkage

h = PCC slab thickness, inches

t = Depth of the shrinkage zone, varies between 1.5 and 2 inches

α = PCC coefficient of thermal expansion, /˚F

The new design guide uses this same concept of representing the moisture gradient through the slab by an equivalent temperature difference along the slab depth. However, since the new design procedure incorporates the impact of climate and aging on material properties throughout the entire design life, moisture warping needs to be adjusted monthly based on atmospheric relative humidity. The effects of monthly variation in moisture warping are expressed in terms of equivalent temperature difference and are added to the equivalent linear temperature difference during stress calculations (ARA 2004). Equation 2-5 presents the equivalent temperature difference representing deviations in moisture warping from the annual average adjusted based on atmospheric relative humidity.

$$ETG_{Shi} = \frac{3(\varphi . \varepsilon_{su})(S_{hi} - S_{h\,ave})h_S\left(\frac{h}{2} - \frac{h_S}{3}\right)}{\alpha\, h^2 .100} \qquad \text{(Equation 2-5)}$$

Where: ETG_{Shi} = Temperature difference equivalent of the deviation of moisture warping in month i from the annual average, ˚F

φ = Reversible shrinkage factor, fraction of total shrinkage. A value of 0.5 is recommended for use unless more accurate information is available

ε_{su} = Ultimate shrinkage based on PCC mix properties, x 10^6

S_{hi} = Relative humidity factor for month i:

$S_{hi} = 1.1\ RH_a$ for $RH_a < 30\ \%$

$S_{hi} = 1.4 - 0.01\ RH_a$ for $30\ \% < RH_a < 80\ \%$

$S_{hi} = 3.0 - 0.03\ RH_a$ for $RH_a \geq 80\ \%$

RH_a = Ambient average relative humidity, percent

$S_{h\,ave}$ = Annual average relative humidity factor. Annual average of S_{hi}

h_s = Depth of shrinkage zone, typically 2 inches

h = PCC slab thickness, inches

α = PCC coefficient of thermal expansion, /˚F

The previous equation is based on the ultimate shrinkage of the concrete, which requires time to fully develop. To estimate the temperature difference equivalent of the deviation of moisture warping at any time from placement, Equation 2-6 was developed and is presented in the new design guide (ARA 2004).

$$ETG_{Sht} = \left(\frac{Age}{n + Age} \right) ETG_{Shi} \qquad \text{(Equation 2-6)}$$

Where: ETG_{Sht} = ETG_{Shi} at any time t days from PCC placement, °F

Age = PCC age, days since placement

n = time to develop 50% of ultimate shrinkage strain, days

During stress calculations, the equivalent temperature difference corresponding to the actual moisture difference can be added to the equivalent linear temperature difference (ARA 2004).

2.3.3 Built-in construction gradient

Concrete set time represents the time when the concrete reaches a solid state, and when the development of stresses and strains within the concrete is initiated (Ruiz et al. 2001). The climatic conditions at the time of set greatly affect curling and warping of the slab. A built-in construction gradient is defined as the gradient due to temperature and moisture that is present in the slab when it sets (Wells et al. 2006; Yu and Khazanovich 2001).

If paving is carried out in conditions when the top of the slab is exposed to higher temperatures than the bottom of the slab, the built-in gradient is positive, and if the top of the slab is exposed to lower temperatures, the built-in gradient is negative. The larger the difference between the top and bottom of the slab, the larger the gradient. At the time the concrete sets, the slab remains flat since the concrete is still in its plastic state and has not yet developed sufficient stiffness (Wells et al. 2006). This implies that, at any point in time, when the gradients in the slab are at the same magnitude as that corresponding to the built-in construction gradient, the slab is flat. When the slab is in a zero gradient condition, it curls instead of remaining flat. The curling is upward if the built-in gradient is positive and downward if it is negative (Eisenmann and Leykauf 1990).

Researchers have been using a wide variety of methods to estimate the effective built-in temperature difference. The effective built-in temperature difference is equivalent to the effective linear temperature gradient built-in during construction. It is attributed to the effects of temperature, moisture and shrinkage during construction and creep recovered over time (Rao and Roesler 2005). Section 2.5.2 of this chapter presents in detail different methods used by researchers to determine the built-in construction gradients in concrete pavements. A summary of the results reached by these researchers is presented in the following paragraph.

Byrum (2000) observed equivalent linear temperature gradients ranging between -8 and 10˚F/in, based on analysis of high speed profile data for curvatures of 7.9-in thick jointed plain concrete slabs. Yu et al (1998) concluded that a built-in gradient of -1.74˚F/in gave a good match between measured and calculated curling values for 11.5-in thick slabs in Colorado. Rao et al. (2001) estimated built-in gradients ranging between -2.6 and -3.8˚F/in for 13.8-in thick doweled slabs in Arizona, 40 days after construction. This study includes an analysis of surface profiles measured in the transverse, longitudinal and diagonal directions and comparing these values to surface profiles predicted by the two-dimensional finite element program ISLAB2000. Beckemeyer et al. (2002) found the built-in gradient to be -1.25˚F/in for slabs evaluated that were constructed on open-graded granular bases and -1˚F/in for slabs constructed on asphalt-treated permeable bases in Pennsylvania. This study was based on a comparison between measured slab curling and that predicted using ISLAB2000. As can be noticed, the construction gradient that is built-in in concrete slabs covers a wide range of values and varies with several factors including type of base, concrete mix and material properties and climatic conditions at the time of construction.

The built-in construction gradient has proved to be an important factor in estimating stresses in concrete pavements, especially when adopting the MEPDG (Hansen et al. 2006; Wells et al. 2006; Yu et al. 1998). When using the MEPDG, the default input value for the temperature difference across the slab depth based on the construction gradient is equal to -10˚F from top to bottom of the slab. This value was obtained based on an analysis conducted using the fatigue damage algorithm and the field cracking from over 500 observations. The value of -10˚F was selected to result in the lowest error between measured and predicted cracking. The actual value is dependent on factors such as shrinkage of the PCC mix, actual temperature gradients at the time of placement and inadequate curing. The design guide recommends not

modifying this value unless more precise data is available (ARA 2004). Chapter 4 of this document details the elaborate methodology developed to determine the construction gradient as accurately as possible and shows the importance of this parameter in the predicted performance of a concrete pavement structure. Selecting an inappropriate construction gradient value in the MEPDG could result in excessively under-designed or over-designed cross-sections.

2.3.4 Concrete material properties

Concrete material properties are a major factor influencing curling and warping of concrete slabs. These include the coefficient of thermal expansion, drying shrinkage, creep and elastic modulus of the concrete. Their influence is discussed herein.

2.3.4.1 Coefficient of thermal expansion

The coefficient of thermal expansion (CTE) of concrete reflects the change in strain as a function of a change in temperature. The CTE is mainly a function of the type of aggregates used in the concrete mixture. Concrete with a larger coefficient of thermal expansion will tend to expand more when subjected to the same temperature changes. This implies that for the same temperature gradient, the curvature of the slab would be larger if the CTE was larger. In addition, when the thermal coefficient of expansion of the concrete and the underlying layer are drastically different, the amount of strain that each layer tends to gain is also drastically different. This implies that large frictional stresses are generated between the two layers.

2.3.4.2 Drying shrinkage

Concrete drying shrinkage represents the reduction in concrete volume due to loss of water. Shrinkage of concrete has two components: reversible and irreversible portions. The irreversible shrinkage of the concrete is responsible for permanent warping of the slab, while the reversible portion varies with the seasonal climatic conditions and causes seasonal moisture warping (Hansen et al. 2006; Janssen 1987; Rao et al. 2001; Suprenant 2002). During dry seasons, as the surface of the slab dries, there is a reduction in the volume of the concrete, while, at the bottom

of the slab which is still highly saturated, less shrinkage occurs. This leads to the development of moisture gradients and warping of the slab. The main parameter affecting the amount of early age drying shrinkage is the type of curing applied to the slab (Rao and Roesler 2005).

2.3.4.3 Creep

A part of the permanent curling can be recovered due to reversible drying shrinkage and creep, which is a gradual decrease of strain in time. The magnitude of creep is a function of the PCC mixture design and restraint conditions. These restraint conditions include the type of connection to the adjacent slabs, and slab self-weight (Rao and Roesler 2005; Schmidt 2000; Rao et al. 2001).

2.3.4.4 Elastic modulus

The elastic modulus of concrete represents the rate of changes of stress with changes in strain. The larger the elastic modulus, the larger the stresses that are generated in the concrete for a constant increase in strain.

2.3.5 Slab restraining conditions

Restraining the slab movement caused by thermal or moisture changes contributes to the development of stresses in concrete pavements. Other than the slab self-weight, which was discussed previously, several other factors are known to reduce slab movements. These include: friction at the slab/base interface and restraints along the transverse and longitudinal joints.

2.3.5.1 Friction at the slab/base interface

As concrete is subjected to changes in temperature, it expands or contracts. However, the underlying base layer restrains the movement, thus developing frictional stress in the concrete at the interface, with the largest stress at midpanel and lowest towards the edges. The magnitude of the frictional stress in the concrete is a direct function of the unit weight of the concrete, the length of the slab and the average coefficient of friction between the slab and base layers (Huang 2004). The coefficient of friction between the two layers depends on the type of base material.

A concrete slab constructed on a highly permeable base results in the infiltration of the concrete between the relatively large voids in the base. This results in a higher frictional coefficient and hence higher stresses.

2.3.5.2 Restraint along the transverse and longitudinal joints

Poor load transfer efficiency (LTE) across transverse joints is a major contributor to joint faulting. The LTE represents the ability of the joint to efficiently transfer loads from one slab to the next. The LTE across a joint is mostly a function of aggregate interlock, the presence of dowel bars and, to a lesser extent, the type of base (ARA 2004).

Tie bars are usually placed along longitudinal joints to keep the joints tight and prevent the infiltration of water into the pavement structure. Keeping the joints tight allows the load to be transferred from one slab to the other through the action of aggregate interlock (Huang 2004). The aggregate interlock factor is a function of the size, strength, durability and angularity of the aggregates used in the PCC mix along with the crack width (Kelleher and Larson 1989). The load is transferred across the joint in a shear mode mechanism and does not largely influence curling and warping (Wells 2005). Load transfer due to aggregate interlock has been found to be lower compared to that caused by the presence of dowel bars (Ioannides and Hammons 1996).

The presence of dowel bars across transverse joints is by far the component that has the largest effect on the overall load transfer efficiency. Dowels are not intended to act as reinforcement of the slabs; they act to minimize joint faulting. Slab curvature is restrained by the dowel bars. This causes a redistribution of stresses in the slab, especially in the areas surrounding the bars (Wells 2005). Other studies have also investigated the effect of dowel bars on curling and warping stresses in concrete slabs. William and Shoukry (2001, 2003) carried out three dimensional finite element modeling of doweled JPCP which revealed that dowels restrict the slab from free contraction, reduce slab deflections along the transverse joint and affect the curling-induced stresses, especially in the regions surrounding the dowels. Davids (2000) used finite element modeling to show that the presence of dowel bars increase stresses within the panel and affect the performance life of the pavement. In a study carried out by Vandenbossche (2003), it was shown that the curvature of doweled slabs is less affected by variations in slab temperature and moisture conditions compared to the curvature of undoweled slabs.

2.4 STRESS DUE TO CURLING AND WARPING

Upward and downward slab curvature due to curling and warping affects the magnitude and location of stress inside the slab. In the case of an upward slab curvature, tensile stresses are exerted at the top of the slab and compressive at the bottom of the slab. In the case of a downward curvature, tensile stresses are exerted at the bottom of the slab and compressive at the top of the slab. To determine the magnitude of the resulting stresses generated in the concrete slabs, closed form solutions were developed in the 1920's to solve for the stresses due to linear temperature differences across the slab depth (Westergaard 1926; Westergaard 1927; Bradbury 1938). Road tests conducted in the 1930's showed that profiles along the slab depth are nonlinear in nature (Teller and Sutherland 1936) and new theoretical methods to characterize the nonlinearity in the temperature distribution were developed (Thomlinson 1940; Bergstrom 1950). Instrumental methods to validate these theoretical models were then proposed by numerous researchers by measuring temperatures at different points along the slab depth (Thompson et al. 1987; Richardson and Armaghani 1987; Armaghani et al. 1987; Yu et al. 1998). This necessitated revisiting the methods for evaluating stresses in the concrete slabs due to nonlinear temperature profiles and resulted in the development of more updated closed form solutions (Harik et al. 1994; Mohamed and Hansen 1997). The installation of moisture sensors in the concrete lead to a more accurate depiction of the moisture profiles that develop throughout the depth of the slab. Studies have revealed that the moisture varies in the top 50 mm of the slab while remaining at high saturation levels in the deeper portion of the slab, irrespective of the overall slab depth (Eisenmann and Leykauf 1990; Janssen 1987; Grasley and Lange 2004; Wells et al. 2006). In the 1990's and 2000's, the stress equations were further refined to consider the effects of moisture differences across the slab depth on stress in the slab (Grasley and Lange 2004; ARA 2004). Nowadays, the analysis of stress in concrete pavements by the use of finite element method tools has become popular as it allows the analysis of more complex pavement structures than the conventional closed form solutions. Nowadays, the analysis of stress in concrete pavements by the use of finite element tools has become popular as it allows the analysis of more complex pavement structures than the conventional closed form solutions (Khazanovich et al. 2000; Shoukry 2000; Rao et al. 2001; William and Shoukry 2001; Heath et al. 2003).

The culmination of the research just described has made it possible to take a more realistic approach to pavement design. The above-mentioned methods for the determination of stresses in concrete pavements due to temperature and moisture temperature differences are presented in this section.

2.4.1 Curling stress due to linear temperature gradients

One theory to estimate the curling stresses due to linear temperature gradients suggests modeling the slab as a plate on a Winkler foundation. A Winkler foundation is represented by a series of springs attached to the plate. As the slab is subjected to different temperatures causing it to curl up or down, the springs are either in tension or compression, depending on their location with respect to the center of the slab.

Westergaard (1926) developed equations for determining the curling stresses in concrete pavements based on the plate theory (Huang 2004). Based on the assumption that the temperature distribution is linear throughout the depth of the slab, the total stress due to slab curling can be calculated for the case of an infinite plate by using Equation 2-7.

$$\sigma_0 = \frac{E\ \alpha\ \Delta T}{2\left(1-\nu\right)} \qquad \text{(Equation 2-7)}$$

Where: σ_0 = stress at the slab center

E = modulus of elasticity of the slab

α = coefficient of thermal expansion of the concrete

ΔT = temperature difference of the slab top from bottom

ν = Poisson's ratio

To estimate stresses in a finite slab, a correction factor was introduced by Westergaard (1927) and the equations for determining the stresses in the x and y directions were updated and are given in Equations 2-8 and 2-9. Based on this analysis, Bradbury (1938) developed charts for determining factors for correcting the stresses to take into account the length of the slab in the x and y directions. These factors are based on the ratios L_x / ℓ and L_y / ℓ, where ℓ is the radius of relative stiffness, given by Equation 2-10. The correction factor increases as the ratio L / ℓ increases, and reaches a value of 1.0 as L / ℓ reaches infinity. This implies that as the slab size increases, the stresses due to curling also increase.

$$\sigma_x = \frac{E\ \alpha\ \Delta T}{2\left(1-\nu^2\right)}\left(C_x + \nu\ C_y\right) \qquad \text{(Equation 2-8)}$$

$$\sigma_y = \frac{E\ \alpha\ \Delta T}{2\left(1-\nu^2\right)}\left(C_y + \nu\ C_x\right) \qquad \text{(Equation 2-9)}$$

Where: σ_x = longitudinal stress in the direction of the longitudinal centerline

σ_y = transverse stress in the direction of the transverse centerline

C_x = correction factor for the length of the slab in the x direction

C_y = correction factor for the length of the slab in the y direction

$$\ell = \sqrt[4]{\frac{E\ h^3}{12\left(1-\nu^2\right)k}} \qquad \text{(Equation 2-10)}$$

Where: h = slab thickness

k = modulus of subgrade reaction

2.4.2 Curling stress due to nonlinear temperature gradients

The Westergaard and Bradbury models have shown that stresses due to temperature differences can be as high as those caused by traffic loads. The equations estimating curling stresses are based on an assumption of linear temperature distribution throughout the depth of the slab (Mohamed and Hansen 1997). However, as previously mentioned in section 2.3.1, several studies have shown that the temperature distribution throughout the depth of the slab is primarily nonlinear in nature based on field measurements in Illinois (Thompson et al. 1987), Florida (Richardson and Armaghani 1987; Armaghani et al. 1987) and Kansas (Yu et al. 1998).

Armaghani et al. (1987) and Choubane and Tia (1992) analyzed numerous field test data obtained by Florida Department of Transportation personnel and concluded that a quadratic function can often adequately describe in situ temperature distributions. They stated that replacing an actual distribution by a linear approximation determined based on the temperatures at the top and bottom of the slab leads to the overestimation of maximum stresses for daytime conditions. This also leads to the underestimation of maximum stresses in the slab for nighttime conditions. The same conclusion was also reached independently by Mirambell (1990).

To account for the effect of nonlinearity in the temperature distribution on curling stresses, methods based on numerical analysis were developed by Hariq et al. (1994) and a closed-form solution technique is presented by Mohamed and Hansen (1997).

The technique developed by Mohamed and Hansen (1997) is discussed herein. The analysis method involves two steps. First, by assuming that the internal stresses within the slab cross-section satisfy the internal equilibrium conditions and continuity of the strain field, an equation for estimating the self-equilibrated stresses within a cross-section due to internal restraint was developed. These stresses are independent of slab dimensions and boundary conditions. Then, the existing closed form solutions developed by Westergaard and Bradbury are used in conjunction with the equations developed for self-equilibrated stresses to obtain the equivalent linear temperature gradient. Using this parameter, the stresses due to external restraining conditions (such as self-weight of the slab and subgrade reaction) are calculated. The total internal stresses due to nonlinear gradients are obtained by the superposition principle. This method of analysis was applied to two field cases and results were compared to stresses calculated by the Westergaard and Bradbury methods. The results indicated that the assumption of linear temperature gradients does not accurately portray the curling stresses and underestimated tensile stresses in the concrete, especially during nighttime and early morning hours.

The equivalent linear temperature gradient represents the temperature difference between the top and bottom of the slab that produces the same curvature as used by Westergaard and Bardbury in their linear gradient solution. The equivalent linear temperature gradient is as given by Equation 2-3. The equivalent linear temperature gradient is calculated based on the temperature profile throughout the concrete slab and simplifies the calculation of stresses due to nonlinear temperature or moisture profiles to a calculation of stresses due to linear profiles (Mohamed and Hansen 1997).

2.4.3 Curling and warping stress due to nonlinear temperature and moisture gradients

In the current approach for designing concrete pavements, stresses due to temperature and moisture related curling and warping are not directly considered. However, in the new mechanistic design approach, the effects of variations in temperature and moisture conditions on stresses in concrete pavements are taken into account (ARA 2004).

In the MEPDG, the Westergaard equation for the maximum stress at the slab center due to slab curling is modified to include the effects of both curling and warping, and is given by Equation 2-11. Rapid solution neural networks (NN) were developed based on the critical stresses and deflections determined using the ISLAB2000 model to perform the required large number of computations in a rapid manner.

$$\sigma_0 = \frac{E\ \Delta\varepsilon_{tot}}{2\left(1-\nu\right)} \qquad \text{(Equation 2-11)}$$

Where: $\Delta\varepsilon_{tot}$ = unrestrained curling and warping strain, given by Equation 2-12

$$\Delta\varepsilon_{tot} = \alpha\ \Delta T_{eqv} + \varepsilon_{\infty}\Delta\left(1-rh^3\right)_{eqv} \qquad \text{(Equation 2-12)}$$

Where: ΔT_{eqv} = equivalent temperature difference

ε_{∞} = ultimate shrinkage of the concrete

$\Delta\left(1-rh^3\right)_{eqv}$ = relative humidity differences between the pavement surface and bottom based on formulations given by Mohamed and Hansen (1987)

rh = relative humidity

2.4.4 Curling and warping stress based on finite element modeling

The Westergaard equations provide simplified solutions to estimate stresses due to the combined effects of temperature gradients and corner, edge and/or interior wheel loading conditions. Nowadays, the analysis of stresses in concrete pavements by the use of finite element tools has become popular. The use of finite element has the advantage of allowing the user to analyze pavements structures consisting of multiple layers, and allows modeling of separation between the layers. Linear and nonlinear temperature differences across the concrete slabs can also be modeled successfully to estimate stresses in the concrete slabs (Rao et al. 2001).

Two dimensional and three dimensional finite element modeling tools are available for engineers to analyze the response of complex pavement systems to linear or nonlinear temperature differences across the concrete slabs. The MEPDG uses rapid solution neural networks (NN) that were developed based on the critical stresses and deflections determined using the ISLAB2000 model. The program ISLAB2000 is a two dimensional finite element program developed by Khazanovich et al. (2000). This program is a user-friendly program that is frequently used in the pavement community. The modeling assumptions inherent to this program are representative of those used in the majority of the other finite element pavement analysis programs frequently used. The slab is modeled as a medium-thick plate and the pavement structure is modeled as an equivalent two-layer system. ISLAB2000 is also capable of analyzing the presence of linear and nonlinear temperature differences along the slab depths.

2.5 PREVIOUS RESEARCH ON THE RESPONSE OF CONCRETE PAVEMENTS TO ENVIRONMENTAL LOADS

This section presents previous research carried out on the response of concrete pavements to environmental loads. It includes the following three sub-sections: studies evaluating the effects of environmental conditions on the performance of concrete pavements, efforts made to characterize the built-in construction gradient in concrete pavements and studies involving modeling concrete pavements using finite element tools.

2.5.1 Effect of environmental conditions on concrete pavement performance

Recent studies evaluating the effects of variations in environmental conditions on the performance of jointed plain concrete pavements are presented in this section.

A concrete slab was constructed in Texas to study the effects of temperature, moisture and creep on the curling and warping behavior of jointed plain concrete pavements under different curing conditions. Details of this test section are included in Jeong and Zollinger (2004). The initial and final setting times of the slabs were determined based on penetration

resistance testing and using the maturity concept. The set times were found to correlate well with the initiation point of slab curling and warping, as determined from deflectometers placed along the slab depth. Slabs cured by the use of an insulation mat developed less shrinkage than slabs cured using a curing compound. The study found that drying shrinkage created a higher level of tensile strain in the top of the slab which increases the upward movement of the slab while creep strain caused a shift in the strain cycle with respect to time. The study also found that the shrinkage significantly affects long-term warping behavior of the slab. This research was taken a further step and Jeong and Zollinger (2005) describe a more detailed analysis of daily and seasonal variations of strains in the slabs. This more recent study showed that both the top and the bottom parts of the slab experienced compressive and tensile strains on a daily basis, due to daily cycles of slab curling and warping. Drying shrinkage increased upward movement of the slab creating a higher level of tensile strains in the top of the slab and lower in the bottom.

In 2005, Ahmed et al. conducted a study with the main purpose of validating the predictions made by the EICM with field-measured temperature and moisture profiles and calibrate the results to reflect conditions for the New Jersey area. It was intended to use the calibrated EICM to predict pavement moisture and temperature conditions and associated pavement performance for different pavements in the New Jersey area. This effort was not successful and the study concluded that the EICM could not be used in its present form to account for seasonal adjustments on pavement sections within New Jersey. The study also suggested that adjustments need to be made to the EICM or a new model needs to be developed to reflect the environmental conditions in New Jersey. It should be noted that 21 of the 24 pavement sections analyzed in this study were flexible structures, two were rigid and one was composite.

Zaghloul et al. (2006) conducted a study to evaluate the impact of the EICM on the performance of pavements in New Jersey. This study investigates the impacts of environmental and traffic conditions on the predictions of the new mechanistic-empirical design guide. It includes limited calibration of the MEPDG performance models based on the performance of one flexible pavement structure in the LTPP database. The calibrated models were then used to assess the response of the pavement structure based on climatic data from the 8 closest weather stations. The study concluded that the MEPDG is highly sensitive to predictions of the weather

data and to interactions between traffic and environmental components. The study recommends that further studies be made to evaluate the impacts of the various components on the MEPDG predictions.

Wells et al. (2006) carried out a study evaluating the effects of environmental loads on strains in a jointed plain concrete pavement. The study included analysis of strain data collected immediately after paving and throughout the first ten months after construction of a jointed plain concrete pavement in Murrysville, Pennsylvania. The same pavement structure is the object of analysis in this research. The study helped to characterize thermal and moisture-related deformation that occurs in the concrete slab shortly after paving and during the ten months following construction. The study concluded that the magnitude of the strains decrease with increasing slab depth, indicating that the bond between the slab and the base layer is sufficient to restrain deformation of the slab. Also, the strains were negative all year long and at all depths, indicating that the slabs are in a state of contraction. The average strain was highest in magnitude in the winter, followed by the fall, and the lowest was during the spring and summer seasons. In addition, moisture-related shrinkage is lowest at midpanel and highest along the lane/shoulder joint; it varied as a function of the concrete surface area that is exposed to the ambient air. Moisture-related shrinkage decreases as precipitation events become more frequent.

2.5.2 Characterization of the built-in construction gradient

The effect of the climatic conditions at the time of paving on the magnitude of the built-in construction gradient is acknowledged by researchers. Several studies have taken on the charge of characterizing the built-in construction gradient by the use of different methods. These are presented in detail in this section.

Yu et al. (1998) conducted a study analyzing the responses of concrete pavements to temperature and wheel loads, based on data measured from instrumented slabs. The instrumentation consisted of dial gauges at the slab corners and edges, surface-mounted strain gages along the slab edges and wheel path and thermocouples placed at five different depths. The test slabs were constructed in the westbound driving lanes of I-70 in Colorado near the Kansas-Colorado border. An analysis of the slab curling as a function of the measured temperature differences across the slab depth was carried out by using the two-dimensional finite

element program, ILSL2. The study revealed that the use of a built-in temperature gradient of -20˚F gave the best results in matching the predicted 11.5-in thick slab curling to the measured curling. This is equivalent to a built-in gradient of -1.74˚F/in. The study concluded that the presence of built-in curling affects the development of critical stresses in concrete slabs.

The study by Beckemeyer et al. (2002) discusses the determination of the amount of built-in curling in a jointed plain concrete pavement in Pennsylvania. A total of 6 test sites are involved in this analysis. Temperatures were monitored in the slabs and curling movements were measured for periods of 48 hours for each of the test sites. The pavement sections were analyzed using the finite element program, ISLAB2000. The measured temperatures were used to estimate the surface deflections and compare them to those measured. A series of analyses were made by modifying the built-in curling and obtain the results that best match the measured curling. The built-in curling was found to be -1.25˚F/in for slabs constructed on open-graded granular bases and -1.00˚F/in for slabs constructed on asphalt-treated permeable bases. This indicates that the slabs placed on open graded base have a larger amount of built-in curling and are more likely to develop top-down cracking.

An instrumented concrete pavement section was constructed in California under desert conditions. Fast-setting hydraulic cement was used and both doweled and undoweled slabs were constructed during the daytime. The slab was modeled using the finite element modeling program ISLAB2000 and estimated deflections were compared to measured slab deflections to determine if any effective built-in curl was present in the slabs. Details of this study are provided in Rao and Roesler (2005). Measured slab deflections were obtained for loaded and unloaded slabs. Results provided an estimate of the minimum amount of built-in gradient in the slabs. The largest built-in gradient was found to correspond to the slabs with the least restraint (no dowel bars or tied concrete shoulders) and was estimated to be between 4 and 7˚F/in while the gradient for slabs with higher restraints was found to be between 0 and -3.7˚F/in. In addition, the study found that dowel bars reduced the built-in gradient by restraining the slabs from lifting off the base layer and that higher gradients were estimated for the slab edges and corners compared to the midslab. The study also concluded that the built-in gradient could not be accurately predicted based on measured deflections at locations where the slab was in contact with the base.

Wells et al. (2006) carried out a study quantifying the built-in construction gradients and early age slab deformation caused by environmental loads in a jointed plain concrete pavement. The study included analysis of surface deflection data, temperature data and strain data collected immediately after paving and throughout the first week after construction of a jointed plain concrete pavement in Murrysville, Pennsylvania. The same pavement structure is the object of analysis in this research. The built-in construction gradient was identified as that corresponding to the time of set of concrete based on the rate of variation of strain with temperature changes. The strain measurements were those measured at midpanel at the top of one of the doweled slabs. The equivalent linear temperature gradient built-in at the time of construction was found to be equal to 0.55˚F/in. The study also analyzed the variation in slab curvatures due to variations in ambient temperature and relative humidity conditions and found that the response of doweled and undoweled slabs is different under the same conditions. Curvature of the undoweled slabs was 7 percent larger than curvature of the doweled slabs, for the same temperature moments in the slabs. The surface profiles also showed that the doweled slabs exhibited less movement over the whole length of the slabs, compared to the undoweled slabs. In addition, the edges of the undoweled slabs became completely unsupported at certain times.

Hansen et al. (2006) studied the effects of paving conditions on built-in curling and pavement performance. Sensors were placed to monitor temperatures in two pavement sections constructed in the summer and fall conditions in Michigan. The relationship between set time and curing temperature was determined by testing mortar specimens in the lab. The final set times were determined by converting field pavement temperatures to a reference temperature, using the maturity concept. And, the corresponding temperature differences along the slab depths were determined from the temperature profiles along the slabs at the time of set. According to this study, the summertime construction results in an unfavorable upward slab shape that leads to loss of support along the slab edges. The fall construction is more favorable in maintaining permanent slab-base contact during daily temperature changes. The built-in temperature gradients were found to be 0.5˚F/in and -0.08˚F/in for summer and fall constructions.

2.5.3 Finite element modeling

Finite element modeling tools are used to analyze the response of complex pavement systems to linear or nonlinear temperature and/or moisture differences across concrete slabs. Studies involving three dimensional finite element modeling of concrete slabs for the purpose of evaluating their performance are presented in this section.

Shoukry and William (2003) developed a three-dimensional finite element model to investigate the applicability of Westergaard's curling stress equations to doweled jointed concrete pavements. The basic feature of this model is the detailed modeling of the dowel bars and their interface with the concrete using three dimensional solid brick elements. The use of a very fine mesh for the concrete and circular dowel bars permitted the application of nonlinear thermal gradients through the slab thickness. The modeled road section includes two full slabs and the base and subgrade layers were widened on each side of the slab. A 0.4-in wide gap was assumed between the slabs to allow for slab expansion and contraction. Sliding interfaces with frictional contact were assumed between the concrete and the subgrade and between each dowel and the surrounding concrete. The concrete and dowel bar materials were represented using a thermo-elastic-plastic model whose material constants were assumed to remain constant with temperature variations. The subgrade and base materials were represented using elastic material models. The study showed that, overall, the stresses estimated from the finite element model were in agreement with the stresses estimated based on the Westergaard equations, with minor differences attributed to the simplifying assumptions made by Westergaard to obtain closed form solutions. However, the stresses estimated in the longitudinal directions were found to be quite different than those estimated by the closed form equations. This same observation was found by experimental results carried out by Iwama (1964) and Nishizawa et al. (1998). The study proposes a modified equation to estimate stresses in the longitudinal direction. It was concluded that the model is suitable for the prediction of curling stresses and that the Westergaard equations provide an adequate method for estimating stresses due to slab curling. The stresses due to the uniform temperature changes need to be added to those estimated from the Westergaard equations to obtain the total stresses due to temperature changes.

The study by Shoukry et al. (2003) deals with characterizing the effects of nonlinear temperature gradients on dowel jointed concrete slabs. An instrumented test section in West Virginia is used for the collection of temperature and strain data from the field. The pavement was modeled using the three dimensional finite element model developed by the authors and described in Shoukry and William (2003). The study concluded that, based on measured and predicted strain data, nonlinearity of temperature gradients along the slab depth has a major effect on stresses along the doweled transverse joints, and minimal effect on the stresses at midslab. Curling of the slabs causes bending of the dowel bars which restrains the movement of the slabs along the transverse joints. The study also emphasizes the importance of modeling nonlinear temperature profiles without breaking them down into uniform and gradient components.

In 2004, Shoukry et al. carried out a study to validate the three dimensional model developed in their previous study based on field data. Field data from an instrumented pavement test section in West Virginia was used for this purpose. The instrumentation included placement of thermocouples and strain gages at different locations in the slabs and embedding vibrating wire gages in the dowel bars. The model predicts the response of jointed concrete pavements to temperature variations. This study presents a method to validate the response of three-dimensional finite element models of dowel jointed plain concrete pavements based on field-measured data. Although the measured strains include the effects of construction curling, shrinkage and moisture changes that are not accounted for in the model, their influence can be significantly reduced by considering the change in strain that occurs over a short period of time. The measured and predicted strains were found to be in agreement within reasonable limits.

In 2005, Siddique et al. used ANSYS, a finite element program, to model a jointed plain concrete pavement section in Kansas. The modeled road section includes two lanes and one shoulder on either side. Because of the symmetry in the longitudinal direction, half of two slabs on either side of a transverse joint were used as the model geometry. The dowels were modeled as three dimensional solid brick elements. The interaction between the concrete and steel dowels was modeled as contact problem. The curling of the slabs due to temperature loading was predicted by the model and compared to curling measurements made on the field. The study concluded that the in situ curling of concrete slabs can be estimated from a properly built finite element model.

3.0 INSTRUMENTED PAVEMENT SECTION

To achieve the set objectives of this research study, the results obtained from laboratory and field testing and the data collected from an instrumented section of a jointed plain concrete pavement structure will be used. A heavily instrumented pavement section was constructed in Murrysville, Pennsylvania in August 2004. The instrumentation includes sensors collecting environmental data, static strain data and dynamic strain data. A construction report was written that describes the details of the construction of the test section, along with the early-age material properties and early-age pavement response characteristics (Wells et al. 2005). More recently, two more reports were issued describing the one-year material properties and the one- and three-year pavement response characteristics (Asbahan et al. 2006; McCracken et al. 2008). These reports can be referred to for additional details not included here.

This chapter presents an overview of the instrumented pavement section and details that are relevant to the proper analysis of the pavement. It includes a description of the project location, design and construction details, instrumentation details, paving details and general material characteristics.

3.1 PROJECT LOCATION

The instrumented pavement section was constructed along a 3.4-mile highway section of U.S. Route 22 (SR22). The section runs through the municipality of Murrysville in Westmoreland and Allegheny counties and is located approximately 20 miles east of Pittsburgh, as shown in Figure 3.1. The test section consists of 14 Portland cement concrete (PCC) slabs in the westbound truck lane. More details regarding the project location and site description are provided in Wells et al. (2005).

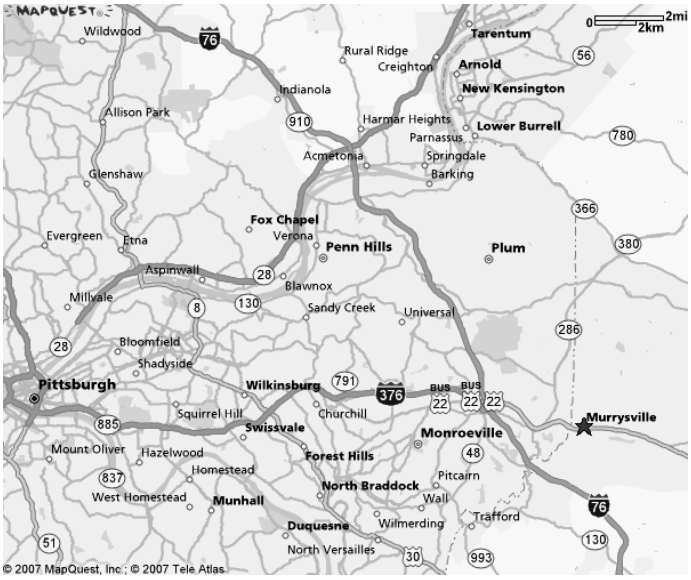

Figure 3.1. Project location with respect to Pittsburgh (www.mapquest.com, March 2007).

3.2 DESIGN AND CONSTRUCTION DETAILS

The design and construction details that are needed for proper modeling of the pavement include the traffic details, geometric characteristics and details of the pavement structure. The design and construction details are presented in this section; more details are included in the construction report (Wells et al. 2005).

3.2.1 Traffic details

The roadway is a four-lane urban major arterial divided by a concrete median. At the time of design in June 2002, the two-way average daily traffic (ADT) volume was 26,950 vehicles with 5 percent being truck traffic. The projected ADT at the end of the design life in 2022 is 36,780 vehicles. This indicates that the growth rate is linear and varies at a rate of 1.8 percent per year. The design hourly volume in June 2002 was 3,678 vehicles with a directional split of 60 percent in the predominate direction of travel. The posted speed limit is 35 miles per hour, with several traffic signals and business entrances occurring along the roadway (Wells et al. 2005).

3.2.2 Geometric characteristics

The pavement is a JPCP with 15-ft transverse joints and 12-ft wide lanes. The concrete medians vary in width from 14.4 ft to 2.0 ft with concrete mountable curbs. The roadway section is crowned with a 2.0 percent transverse slope and a 2.4 percent longitudinal slope, and contains 2.6-ft wide concrete curb-and-gutter shoulders (Wells et al. 2005).

3.2.3 Pavement structure

The pavement structure is composed of a 12-inch thick PCC layer placed over a 4-inch thick asphalt treated permeable base. The subbase material consists of slag material and is 5-inches thick. Originally, the pavement was to be constructed directly on the subgrade but the poor soil conditions required the removal of 24 inches of the subgrade material and backfilling using a gap-graded soil and aggregate mixture (Wells et al. 2005). The layers making up the pavement structure are presented in Figure 3.2.

Two types of slabs were constructed: unrestrained and restrained. For the case of the restrained slabs, No. 5 epoxy-coated tie bars were placed every 2.5 ft along both the lane/shoulder and centerline joints and 1.5-in epoxy-coated dowel bars were spaced every 12 inches along the transverse joints. For the case of the unrestrained slabs, no bars were placed along the joints (Wells et al. 2005).

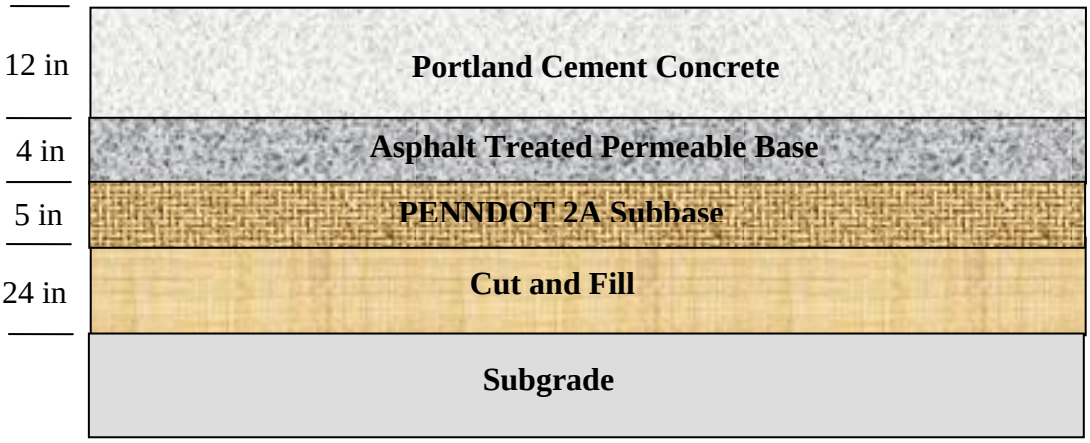

Figure 3.2. Design thicknesses of the pavement layers (Wells et al. 2005).

3.3 INSTRUMENTATION DETAILS

Sensors monitoring environmental and static strain and pressure were embedded in the pavement structure during construction. In this section, the details pertaining to the types and locations of the sensors are presented. More details concerning the development of the instrumentation plan, the selection, testing and installation of the sensors and data acquisition systems are provided in the construction report for the test section (Wells et al. 2005).

The environmental and static sensors were embedded in two sets of slabs, each set consisting of three slabs. The sets are referred to as Cell 3 and Cell 4. Environmental sensors are only placed in the slabs of Cell 4. Static sensors are located in Cells 3 and 4 and are of the same type, quantity, depth and location. The main difference between the slabs of Cells 3 and 4 is that Cell 3 consists of slabs unrestrained by dowel and tie bars and Cell 4 consists of slabs restrained by dowel and tie bars. A non-instrumented transition panel, referred to as Slab Z, acts to isolate the unrestrained slabs of Cell 3 from the restrained slabs of Cell 4 (Wells et al. 2005). The layout of the test section is shown in Figure 3.3. A summary of the type and quantities of the environmental and static sensors installed in Cells 3 and 4 is presented in Table 3.1.

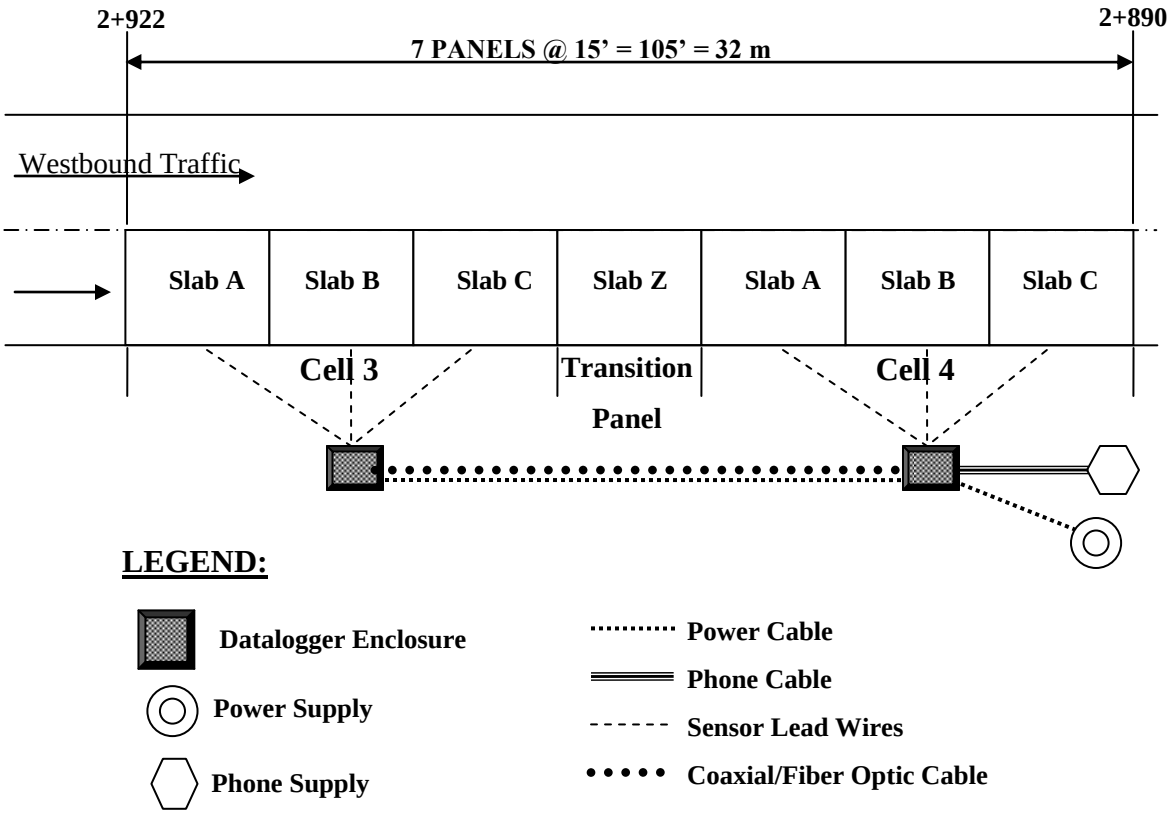

Figure 3.3. Layout of the test section.

Table 3.1. Summary of sensors installed in Cells 3 and 4 (Wells et al. 2005).

Sensor Type	Sensor Name	Qty.	Measurement	Cell
Environmental	Thermocouple	60	Temperature	4
Environmental	Moisture Sensor	24	Relative Humidity	4
Environmental	Time Domain Reflectometer	16	Moisture Content	4
Static Load	Vibrating Wire Strain Gage	156	Static Strain	3, 4
Static Load	Static Pressure Cell	8	Static Pressure	3, 4

Each cell has its own specific set of datalogging equipment that collects data form the sensors in the cell. The dataloggers for each cell are housed within protective enclosures that were constructed directly adjacent to the instrumented panels and approximately twelve inches away from the edge of the curb. Electricity is provided for each of these enclosures and phone service is provided for the enclosures for Cells 3 and 4. Data from the environmental and static sensors in Cells 3 and 4 are collected automatically. The sensors are wired to multiplexors, which are wired to dataloggers. The dataloggers in Cells 3 and 4 automatically retrieve data every 15 minutes. Once per day, the data collected on the dataloggers is sent via telephone modems to a computer database located at the University of Pittsburgh. The data from each datalogger is then appended to the end of the existing data files. This data communication process is repeated daily and backed-up weekly (Wells et al. 2005).

The performance of each sensor was tested at the University of Pittsburgh's Pavement Mechanics and Materials Lab (PMML) prior to installation, to ensure that the manufacturer specifications were met. The sensors installed in Cells 3 and 4 monitor variations in ambient temperature and moisture conditions, variations in temperature and moisture conditions along the pavement structure, variations in static strain in the concrete slab and variations in static pressure along the slab/base interface. Photos showing the installation of the sensors involved in this study are provided in Figure 3.4. The type, location and depth of the environmental and static sensors involved in this study are detailed in the following sub-sections.

3.3.1 Weather station

An on-site weather station was installed to monitor and record variations in air temperature, relative humidity and wind speed. The weather station is linked to the automated data collection system in Cell 4, whereby data is recorded every 15 minutes and saved daily in the database on a computer at the University of Pittsburgh (Wells et al. 2005).

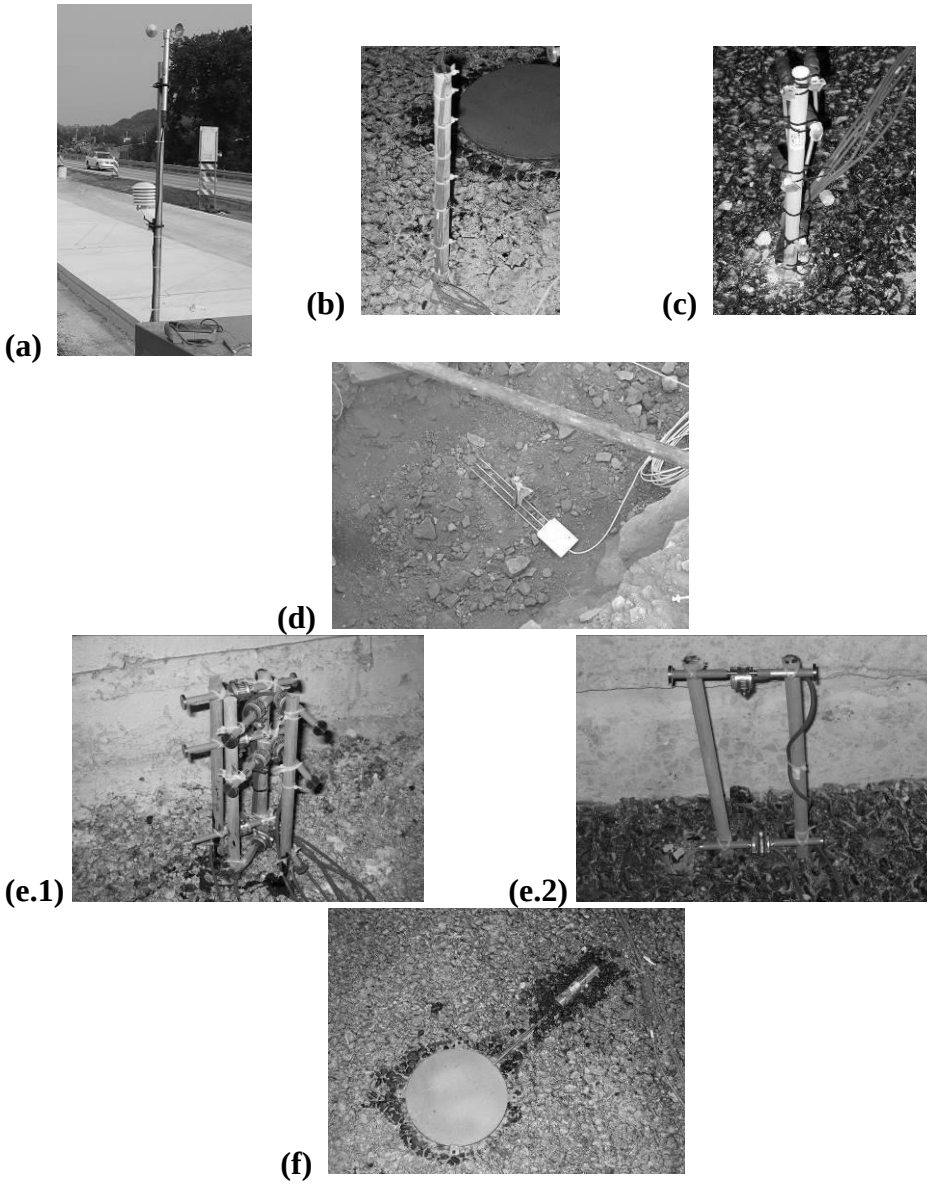

Figure 3.4. Installation of environmental and static sensors: (a) onsite weather station; (b) thermocouples; (c) moisture sensors in the concrete; (d) time domain reflectometers in the granular layers; (e) vibrating wire strain gages in the concrete: (e.1) corner installation and (e.2) edge installation; (f) static pressure cells (Wells et al. 2005).

3.3.2 Temperature sensors in the pavement structure

Type T thermocouple wire from Omega Engineering was used for making the thermocouples. When a junction is formed between the two metals forming the wire (copper and constantan), a unique voltage is produced. Since this voltage is approximately linear with temperature, a relationship can be established. Prior to installation, the ends of the thermocouple wire were spliced and soldered, creating a junction at the end of the wire (Wells et al. 2005). A total of 60 thermocouples were installed at four locations in Cell 4, as follows:

- Two locations in the corners of Slabs Z and C, and
- Two locations at midpanel of Slabs B and C.

Locations of the thermocouples are shown in Figure 3.5. At each location, fifteen sensors were placed: seven in the Portland cement concrete slab, two in the asphalt treated permeable base, two in the 2A-subbase, three in the fill material and one in the subgrade. Temperature readings are automatically taken at 15-minute intervals. The approximate depths at which they were placed are indicated in Figure 3.6.

The construction report took on the task of validating the measurements made by the four thermocouple trees. It was found that the temperature measurements recorded by the thermocouple trees placed at similar locations were similar (Wells et al. 2005). As a result, the midpanel tree of Slab B and the corner tree of Slab Z will be used in this study.

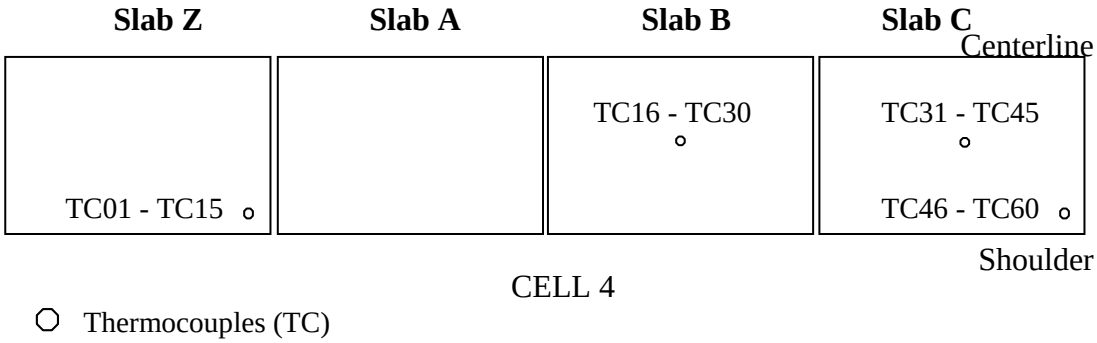

Figure 3.5. Location of temperature sensors in Cell 4 (Wells et al. 2005).

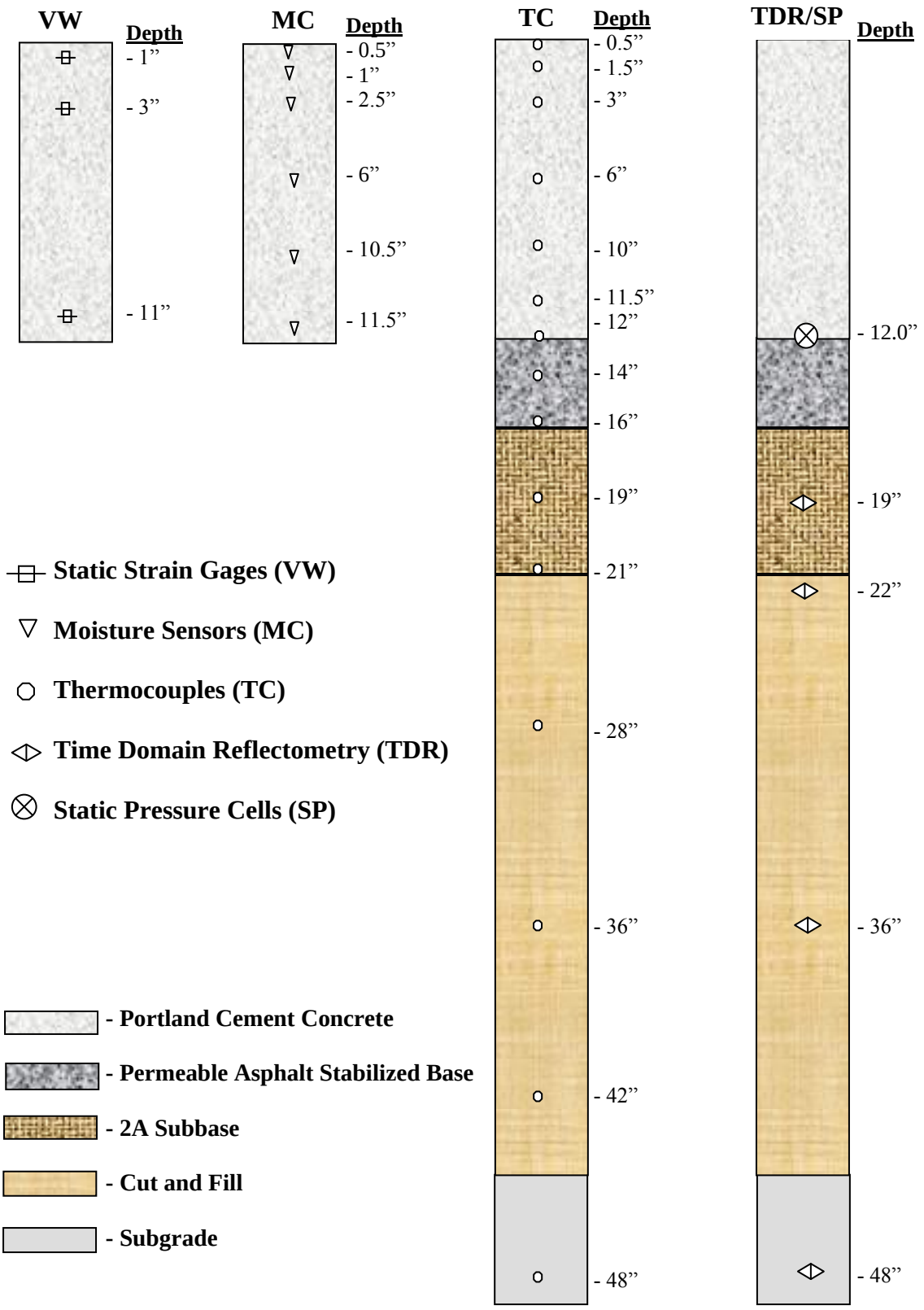

Figure 3.6. Depth of environmental sensors in Cell 4 and static sensors in Cells 3 and 4.

3.3.3 Moisture sensors in the concrete slab

Sensirion SHT75 relative humidity and temperature sensors were installed at various depths in the PCC layer to capture the variation in moisture levels within the slab. The sensor uses a capacitive polymer sensing element to measure relative humidity and a band gap temperature sensor to measure temperature (Wells et al. 2005). A total of twenty four moisture sensors were installed at the slab corners and at midslab within Cell 4, as shown in Figure 3.7. At each location, six sensors were placed along the slab depth, as indicated in Figure 3.6. Concrete moisture readings are taken at 10- to 15-minute intervals. However, the data collection system is not automatically linked to the main database and gaps in the data collection are often present. In addition, of the twenty four sensors placed inside the concrete, quality moisture data was only collected from twelve. Of the twelve sensors recording moisture, four sensors are actually along the same tree at the midpanel location and four are along the same tree at the edge location.

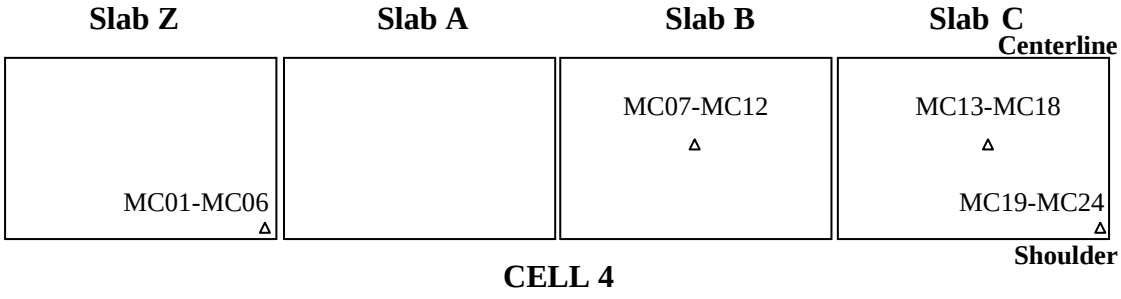

Figure 3.7. Location of concrete moisture sensors in Cell 4 (Wells et al. 2005).

3.3.4 Moisture sensors in the granular layers

A Time Domain Reflectometry (TDR) system from Campbell Scientific was used to monitor moisture content and frost depth within the subbase and subgrade. An electromagnetic pulse is generated across the probe, the level of impedance across the probe will be unique depending on

the dielectric constant of the soil. Since the dielectric constant of the soil varies with the amount of water present, volumetric moisture content can be inferred from the reflected pulse attenuation (Wells et al. 2005). Sixteen CS605L wave guide probes were placed at various depths in the wheelpath and along the longitudinal slab edge of Cell 4, as shown in Figure 3.8. At each location, four TDR probes were placed: one in the 2A-subbase, two in the fill material and one in the subgrade at the depths indicated in Figure 3.6. TDR readings are automatically taken at 15-minute intervals.

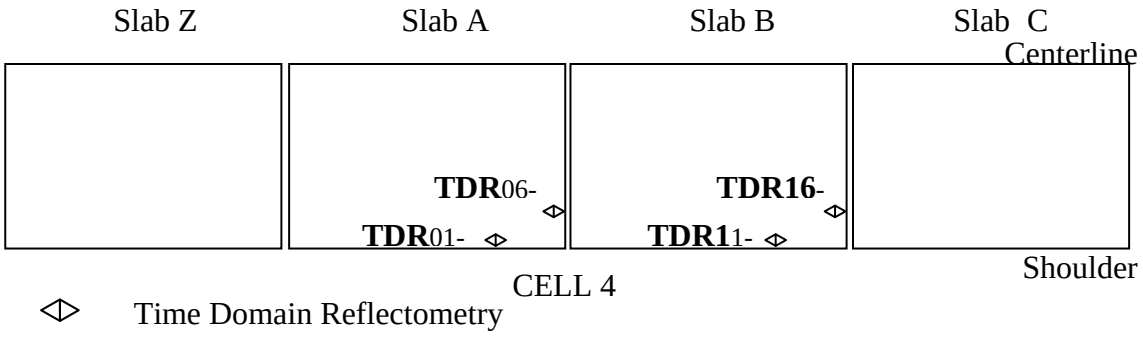

Figure 3.8. Location of moisture sensors in the granular layers in Cell 4 (Wells et al. 2005).

3.3.5 Static strain sensors

Geokon Model 4200 vibrating wire (VW) concrete embedment strain gages were used. The gages operate on the vibrating wire principle. A steel cable is tensioned between two metal end blocks. When the gage is embedded in concrete and concrete deformations take place, these end blocks move relative to one another. The movement of these end blocks influences the degree of tension in the steel cable. This tension in the cable is quantified by an electromagnetic coil, which measures the cable's resonant frequency of vibration upon being plucked. The sensor is also equipped with a thermistor to allow for corrections for the effect of temperature (Wells et al. 2005).

VW strain gages were installed at various depths in the PCC layer at four critical slab locations: the corners, midpanel and the transverse and longitudinal edges. The corner VW strain gages were configured in a rosette formation in order to capture strains in the longitudinal, diagonal, and transverse directions. The corresponding edge gages were oriented in the same direction of the adjacent joint and the midpanel gages were oriented longitudinally (Wells et al. 2005). The corner and edge configurations of the static strain gages are shown in Figure 3.4. A total of 156 VW strain gages were installed at 60 locations in Cells 3 and 4, as shown in Figure 3.9. Three VW gages were placed at each corner location, and two were placed at each edge and midpanel location. Depths at which the gages were placed are provided in Figure 3.6. VW strain readings are automatically taken at 15-minute intervals.

3.3.6 Static pressure cells

Pressure induced by the PCC slabs on the base layer are measured using Geokon 4800 Earth Pressure Cells. The pressure cells consist of two 9-inch diameter stainless steel plates welded together around their periphery and separated by a narrow gap filled with hydraulic fluid. External pressures cause the two plates to come closer together thus exerting an equal pressure on the internal fluid. The fluid filled cavity is connected to a vibrating wire transducer that converts the fluid pressure into an electric signal transmitted to the datalogger. The resonant frequency of vibration is read by an electromagnetic coil (Wells et al. 2005).

The pressure cells are positioned at the interface between the asphalt treated permeable base layer and the concrete layer at locations of critical static stresses: at both midpanel and at the corners. Pressure values at these locations would indicate the magnitude of the pressure being exerted on the base layers by the PCC due to curling and warping. A total of eight pressure cells were installed at the slab corners and at midslab in Cells 3 and 4, as shown in Figure 3.9. The depth at which the pressure cells were placed is provided in Figure 3.6. Pressure readings are automatically taken at 15-minute intervals.

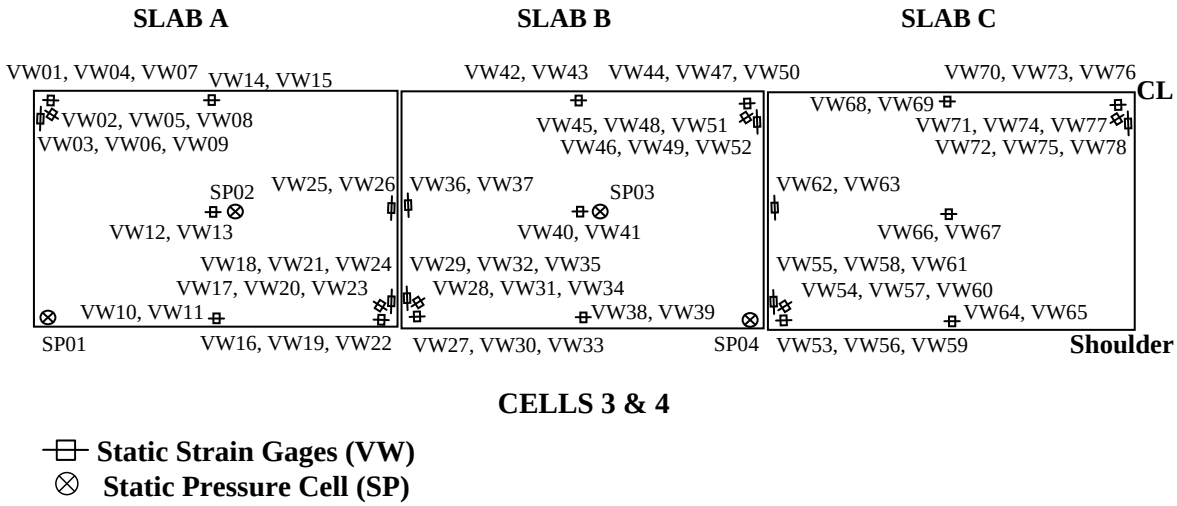

Figure 3.9. Location of static strain gages and static pressure cells in Cells 3 and 4 (Minor variations in the numbering of the sensors exist between sensors in Cells 3 and 4).

3.4 PAVING

The previous section presented the details of the different types of sensors placed in the instrumented test section. This section summarizes the activities carried out at the time of construction of the roadway.

Paving of the test section took place on the morning of August 16, 2004 beginning at approximately 6:15 AM and ending at approximately 7:00 AM. The time of paving of each slab was determined based on data collected from the thermocouples embedded in the slabs. As the concrete is placed at the sensor locations, a sudden rise in temperature is recorded. Based on this, the time of paving of each section of slab was determined and is graphically shown in Figure 3.10. During paving, great care was taken to protect the sensors located throughout the slab from damage associated with the paving equipment. Prior to the passing of the paver, fresh concrete was mounded around each sensor installation by hand and then consolidated using a flexible shaft. Only the westbound lane (test section) was paved on August 16; the eastbound lane had already been constructed at an earlier date and the curb and gutter were constructed and tied to the westbound lane at a later date (Wells et al. 2005).

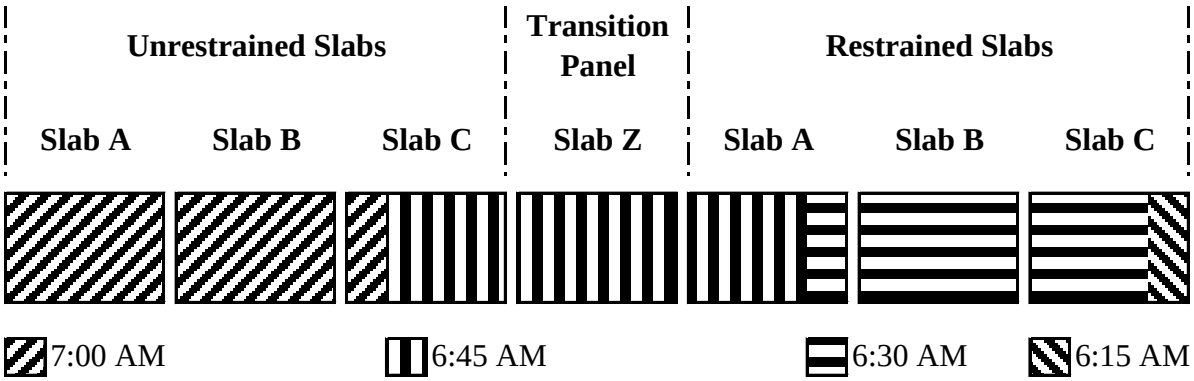

Figure 3.10. Time of paving of the slabs on August 16, 2004.

Approximately one hour following paving, transverse tinning was performed, and a single coat of liquid curing compound was applied to the surface. Sawing of the joints was carried out to a depth of one third the slab thickness, starting at approximately 5:00 PM that evening, 10.75 hours after paving. Cracking of the joints was observed approximately 17 to 19 hours after paving (Wells et al. 2005).

3.5 GENERAL MATERIAL PROPERTIES

In analyzing and designing concrete pavements, the properties of all the components constituting the pavement structure highly influence the performance. As previously mentioned in section 3.2.3, the pavement structure consists of the exiting subgrade, the fill material, the 2A-subbase material, the asphalt treated permeable base layer and the concrete layer. In this section, a general description of the materials used is provided. The more detailed material characteristics needed to properly analyze the pavement structure are presented in subsequent chapters. Additional details regarding the properties of each of these materials and the methods through which they were obtained are included in Wells et al. (2005) and Asbahan et al. (2006).

3.5.1 Unstabilized materials

This first subsection presents the general properties of the unstabilized materials, which include the natural subgrade, the backfill material and the subbase material.

Prior to construction, a subsurface investigation was carried out for the project site. It included the execution of nineteen borings along the proposed alignment of the roadway. The depths to the water table and bedrock were identified based on the results of the geotechnical investigation. In some of the borings, rock layers and water tables were not detected. On average, the depth to either a layer of bedrock or a water table was found to be at least 10 ft (Wells et al. 2005).

The geotechnical investigation indicated that the existing subgrade can be classified as an A-6 material based on the AASHTO classification system, which constitutes a fair to poor subgrade material. As a result, in accordance with PENNDOT construction specifications, it was recommended to cut 2 feet of the existing material and fill with more suitable material. The excavated area was backfilled using a gap-graded soil and aggregate mixture, containing a significant amount of 206 rock, which included large sandstone with diameters as large as 22 inches (Wells et al. 2005).

The subbase was the placed on top of the backfill material. The subbase consisted of slag material meeting the gradation requirements of the PENNDOT Class 2A material specifications, listed in PENNDOT Publication 408 (Wells et al. 2005).

3.5.2 Asphalt treated permeable base

The base layer is an asphalt treated permeable material. The asphalt treated permeable base layer (ATPB) was composed of coarse aggregate conforming to PENNDOT A57 specifications, fine aggregate conforming to PENNDOT B3 specifications and PG 64-22 binder (Wells et al. 2005). The proportions of the mixture are provided in Table 3.2.

Table 3.2. Mixture design of the ATPB (Wells et al. 2005).

Material Type	Material Specification	Proportion of Total Mixture	Bulk Specific Gravity	Absorption
Coarse Aggregate	PENNDOT A57	87.8 %	2.661	0.44 %
Fine Aggregate	PENNDOT B3	9.7 %	2.631	0.89 %
Binder	PG 64-22	2.5 %	1.030	-

3.5.3 Portland cement concrete

The concrete used for paving was mixed at a portable plant located approximately five miles east of the project site in Export, Pennsylvania and was delivered to the site via front-discharge mixer trucks. The cementitious materials included Type I cement as well as ground granulated blast furnace slag. The coarse aggregate consisted primarily of limestone. Air entrainment and water reducing admixtures were also used (Wells et al. 2005). A summary of the mixture design can be found in Table 3.3.

Table 3.3. Concrete mixture design used in the construction (Wells et al. 2005).

Material	Specific Gravity	Absorption	Batch Weight (per yd^3)
Type I Cement	3.15	n/a	382 lbs
Ground Granulated Blast Furnace Slag	2.89	n/a	206 lbs
Fine Aggregate (PENNDOT Spec. Type A)	2.61	1.15 %	1248 lbs
Coarse Aggregate (AASHTO No. 57)	2.68	0.5 %	1881 lbs
Air Entrainment – Catexol 360	n/a	n/a	5.7 oz
Water Reducer – Catexol 100N		n/a	17 oz
Water Content	1	n/a	286 lbs

The design water-to-cement (w/c) ratio was 0.36. However, the actual w/c ratio of the field mixture was determined based on a series of microwave water content tests. The tests exhibited a wide range of variability and the measured w/c ratio was on average equal to 0.44. The reasons behind the difference between the design and the measured w/c are not clear. Although the measured w/c ratio was significantly lower than the design w/c ratio, the results from the strength tests on the hardened concrete samples indicated that sufficient strength development occurred in the concrete (Wells et al. 2005).

The slump and entrained air content of the concrete mix were measured in the field during construction. The slump was determined to be 2 inches by following the standard test method for slump of hydraulic cement concrete, ASTM C143. The entrained air content was determined to be 6 percent ± 1.5 percent by adopting the standard test method for air content of freshly mixed concrete by the pressure method, ASTM C231 (Wells et al. 2005).

Relevant material properties needed for the analysis of the performance of the concrete pavement using the MEPDG include unit weight, Poisson's ratio, coefficient of thermal expansion, drying shrinkage, flexural strength, compressive strength and elastic modulus. The properties of the hardened concrete were determined for the concrete at different ages. Beams and cylinders were cast on-site while the test sections were being paved. These specimens were tested for different properties at concrete ages of 1, 3, 7, 28 and 365 days. Also, cores were pulled from the pavement and were subjected to testing at ages of 28 and 365 days. The results of the early-age testing are provided in detail in the construction report (Wells et al. 2005) and the results of the one-year tests are provided in detail in the one-year report (Asbahan et al. 2006).

4.0 ESTABLISHING A METHOD TO QUANTIFY THE BUILT-IN CONSTRUCTION GRADIENT FOR A JOINTED PLAIN CONCRETE PAVEMENT

The temperature and moisture inside the concrete at the time of set result in the development of a built-in construction gradient inside the slab. A built-in construction gradient is defined as the gradient due to temperature and moisture that is present in the slab when it sets (Wells et al. 2006; Yu and Khazanovich 2001; Rao and Roesler 2005). The magnitude of the built-in construction gradient influences slab curling and warping and thus affects the development of stress and strain within the concrete at later ages.

Researchers have been using a wide variety of methods to estimate the built-in construction gradient. Most of these methods are based on analyzing the deformation of the surface of the slab with respect to changes in temperature gradients along the slab depth. These analyses usually involve the use of prediction models to estimate slab curvature for different temperature gradients and the selection of the gradient that results in the least error between predicted and measured curvatures. The built-in construction gradient estimated by these different methods was found to cover a wide range of values and varies with several factors including type of base, type of curing, concrete mixture design, material properties and climatic conditions at the time of construction (Byrum 2000; Yu et al. 1998; Rao et al. 2001; Beckemeyer et al. 2002). However, a standard methodology to accurately determine the built-in construction gradient of concrete pavements is not available.

The built-in construction gradient has proven to be an important factor in estimating stress in concrete pavements, especially when adopting the new mechanistic-empirical pavement design approach (Hansen et al. 2006; Wells et al. 2006; Yu et al. 1998). Since the new design approach takes into account the effect of climatic conditions on the performance of the pavement, selecting a non-representative construction gradient value in the MEPDG could result in excessively under-designed or over-designed pavement structures. The first objective of this

research is to establish a methodology for determining the built-in construction gradient of a jointed plain concrete pavement and evaluate its effect on the performance of the pavement. This chapter details the methodology adopted to determine the built-in construction gradient in the slabs as accurately as possible. The analysis involves studying the early-age behavior of two types of slabs: restrained slabs and unrestrained slabs. For this purpose, two approaches for determining the concrete set time are followed and compared.

The first approach involves analyzing data collected from strain gages embedded at different locations and depths in the concrete slabs. The strain data is analyzed for the first 42 hours after placement to identify the time when the concrete starts experiencing strain corresponding to changes in temperature. The second approach involves analyzing data collected from static pressure cells embedded at different locations along the interface between the concrete slab and the base layer. The pressure cell data is analyzed for the first 42 hours after placement to identify the time when the base layer starts experiencing uniform changes in pressure corresponding to changes in temperature gradients within the slab. The results of these two methods are analyzed and compared to determine the time of set. Once the set time is determined, data from the thermocouples embedded in the concrete slabs is used to estimate the corresponding built-in construction gradient.

The first section of this chapter presents the temperature and moisture conditions in the slab during the first 24 hours after placement of the concrete. The second section describes the set time and corresponding built-in construction gradient determined based on the early-age vibrating wire data in the restrained and unrestrained slabs. Next, the set time and built-in construction gradient determined based on the early-age pressure cell data in the restrained and unrestrained slabs are discussed. After that, a comparison between the set times and built-in construction gradients determined based on the different methods is presented. Finally, the last section summarizes the results and conclusions made regarding the determination of the built-in construction gradient for the jointed plain concrete slabs.

4.1 EARLY-AGE CONCRETE TEMPERATURE AND MOISTURE

The built-in construction gradient is a function of the temperature and moisture conditions at the time of set. Before quantifying this parameter, the variation in the temperature and moisture conditions in the slab during the first 24 hours is examined and presented in this section, along with the corresponding temperature and moisture gradients.

4.1.1 Early-age concrete temperature

The variation of temperature within the concrete slab was monitored using thermocouples embedded at seven different depths throughout the 12.7-inch thick concrete slab. The slab temperatures measured in the field during the first 24 hours after paving are shown in Figure 4.1 based on the thermocouples located at midpanel of restrained Slab B. The concrete temperature increases from 70˚F to 110˚F during the first 12 hours, after which it decreases. The increase in temperature is due to the hydration of the cement and the increase in the ambient temperature and the decrease is a function of the decrease in ambient temperature during the evening and nighttime hours.

To account for nonlinear temperature gradients in the slab, Janssen and Snyder (2000) presented a method for estimating the moment produced by a nonlinear temperature profile about the bottom of the slab. This was previously presented in Chapter 2. The equivalent linear temperature gradient can be estimated based on the variation in the temperatures along the slab depth, using Equation 2-3. The variation in the equivalent linear temperature gradient during the first 24 hours after paving is presented in Figure 4.2. The figure shows that the equivalent linear temperature gradient fluctuates between 0 and 1.1˚F/in during the first 12 hours and then decreases to -1.25˚F/in during the subsequent 12 hours. This is equivalent to a temperature difference of -15.7˚F to +13.8˚F between the top and bottom of the 12.7-in thick slab. A negative temperature difference indicates upward slab curvature and a positive difference indicates downward slab curvature when moisture gradients are not present. The range of temperature differences indicates that an appropriate selection of the built-in temperature gradient is necessary to differentiate between situations when the slab is curved upwards and downwards when exposed to different ambient temperature conditions.

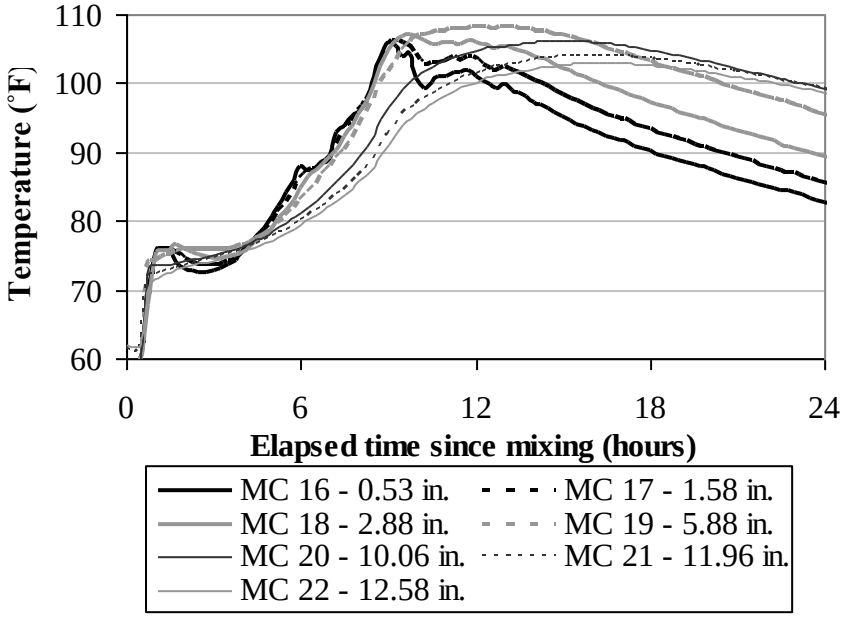

Figure 4.1. Early-age concrete temperature variation at midpanel of the restrained slab.

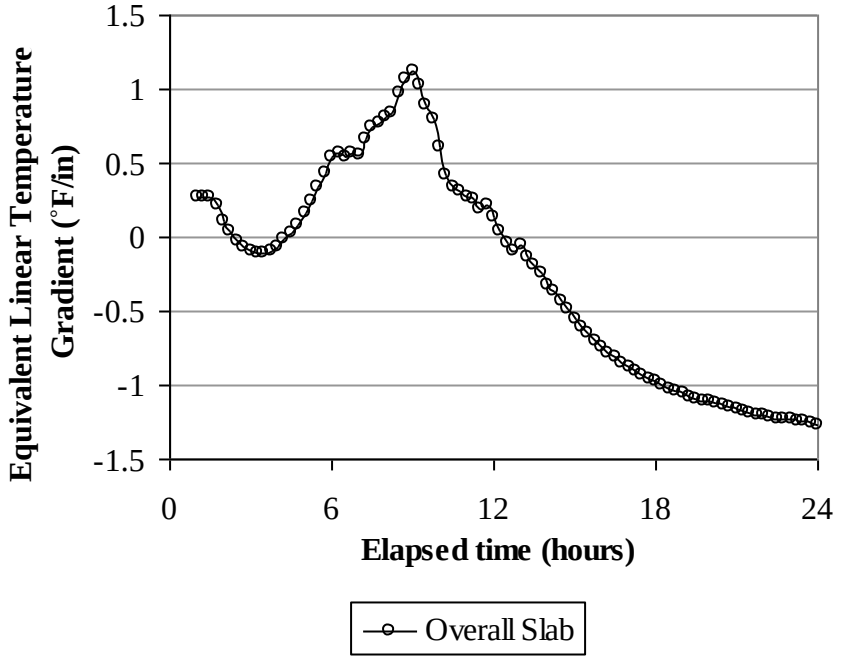

Figure 4.2. Early-age variation in equivalent linear temperature gradient in the concrete slab.

4.1.2 Early-age concrete moisture

The moisture in the slab was monitored using relative humidity sensors embedded at four different depths throughout the 12.7-inch slab. Unfortunately, moisture data during the first 24 hours after paving is not available. When the concrete is first placed, it is in a liquid state, which may be represented by a moisture level of 100 percent across the whole slab. The concrete moisture levels measured during the first week after paving are available and are presented in Figure 4.3, based on relative humidity sensors located at midpanel of the restrained slabs. The concrete moisture varies between 92 and 96 percent in the top two inches of the slab, between 93 and 94 percent at mid-depth, and remains constant at 96 percent in the bottom portion of the slab.

The measured concrete moisture profile representing the conditions during the second day after paving is presented in Figure 4.4. The concrete moisture content varies between 94 and 96 percent along the slab depth, indicating that the concrete moisture drops from a level of 100 percent to an average of 94 to 96 percent during the first 24 hours after paving. This also indicates that the change in relative humidity is relatively small throughout the depth of the slab. The sensors measure relative humidity within an accuracy of 1.8 percent. However, the moisture sensors are not all that accurate at these high relative humidity levels, and it can therefore be assumed that the slab is saturated throughout.

Comparing the contributions of the temperature and moisture to the built-in construction gradient, the effect of temperature is much more significant than the effect of moisture. The temperature gradient during the first 24 hours after paving varies between -1.25˚F/in and 1.1˚F/in and the corresponding range of temperature difference across the slab depth is -15.7˚F to +13.8˚F. While the moisture gradient remains at zero during the first 24 hours after construction. It can be concluded that the effect of moisture does not contribute to the overall built-in gradient. As a result, the built-in construction gradient will be estimated solely based on the temperature conditions in the slab.

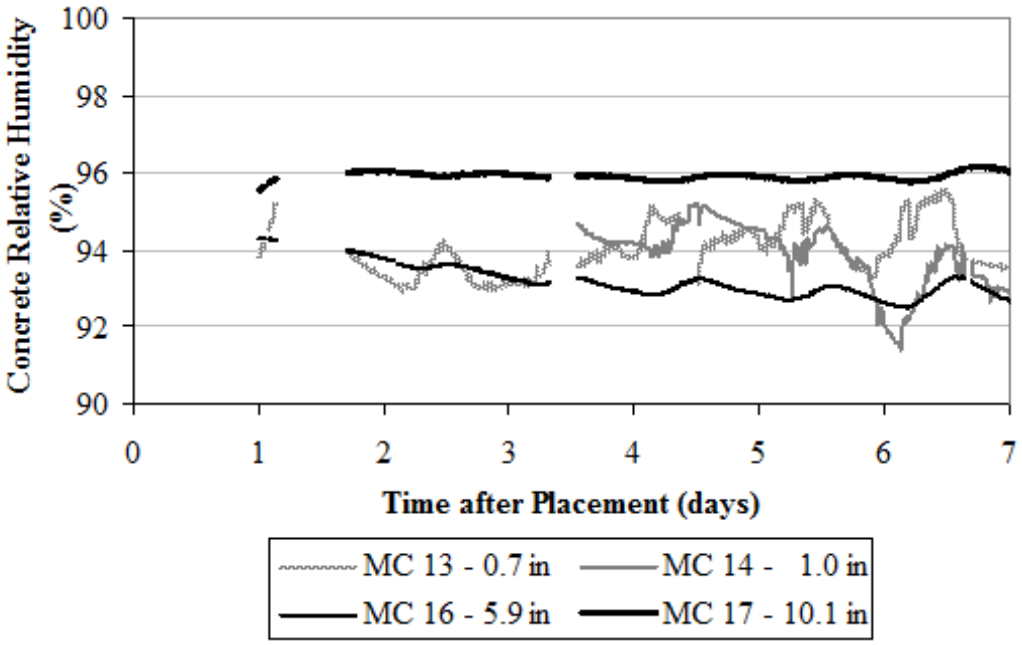

Figure 4.3. Early-age concrete moisture variation at midpanel of the restrained slab.

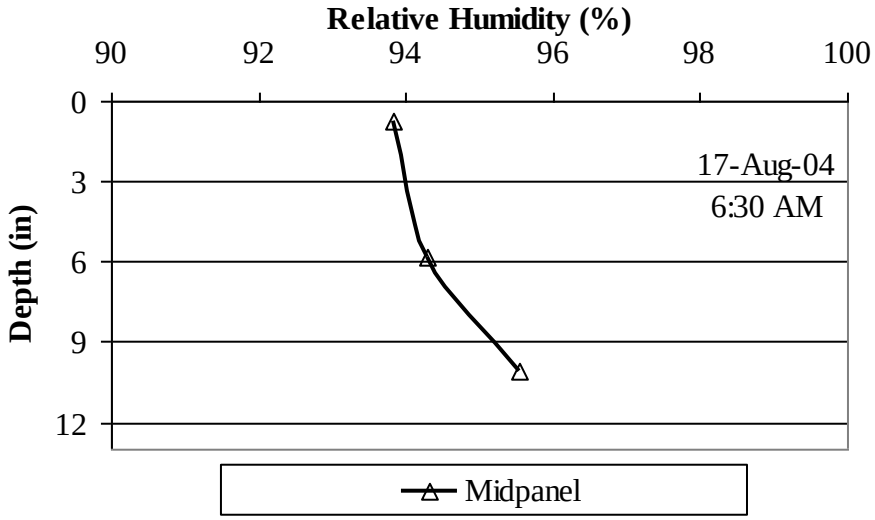

Figure 4.4. Early-age concrete moisture profile at midpanel in the restrained slab.

4.2 EARLY-AGE STRAIN WITHIN THE JPCP SLABS

When the concrete is placed, it is in a plastic state. As it loses workability, it transitions from a plastic to a solid state, when the concrete starts developing its mechanical properties. The set time defines the point at which concrete starts gaining strength. In the plastic state, the concrete can experience large changes in temperatures with little to no change in strain. At the set time, the concrete experiences movements that accompany changes in temperature and strain measurements can be recorded. The variation of the degree of set with the transition of concrete from plastic to solid states is illustrated in Figure 4.5, which is based on a similar illustration in the manual for the High Performance Paving (HIPERPAV) software. The set time is a material property which is not affected by slab restraints, however, the time at which the zero stress gradient is established might be a function of restraint.

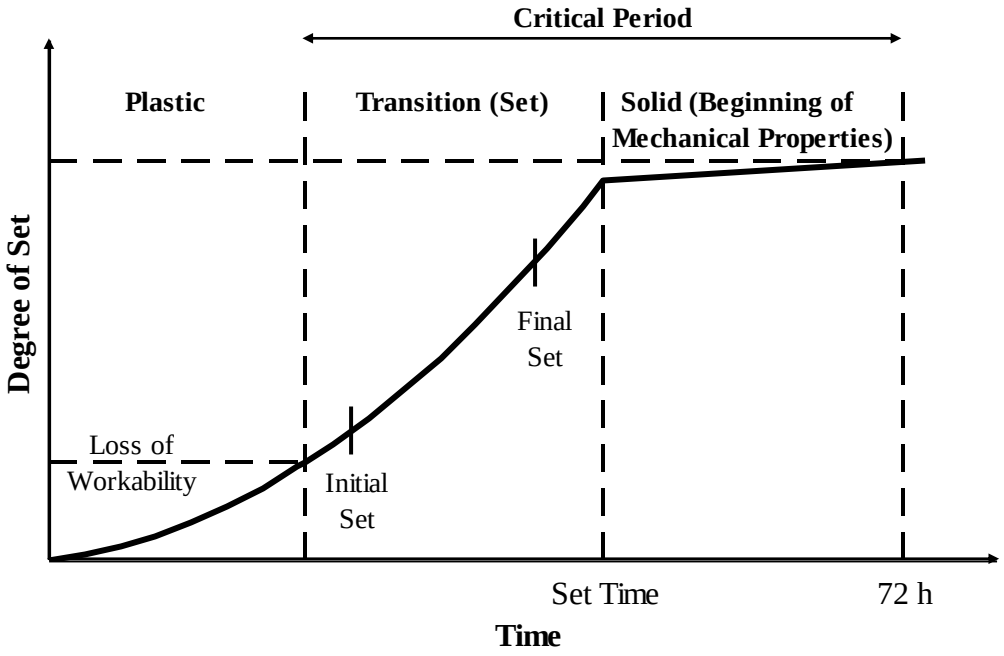

Figure 4.5. Definition of set time in terms of the concrete degree of set.

Data was collected from the vibrating wire gages embedded in the concrete slabs at different locations and depths. The variation in measured strain with respect to temperature change during the first 42 hours after placement is used to identify the concrete set time. The set time is selected as that corresponding to the time when expansion/contraction is measured with changes in temperature. The analysis of the early-age variation in strain with respect to temperature included all the vibrating wire sensors of the restrained and unrestrained slabs. The general trends observed are presented in this section, along with some of the figures that were used. The remaining figures showing the early-age data from all the sensors of the restrained and unrestrained slabs are included in Appendix A. As a result of the analysis of the early-age variation in strain measurements, the set time is established. Finally, the built-in temperature gradient corresponding to the time of set is estimated. A general overview of the static strain gage used is presented first.

4.2.1 Static strain gage

A total of 156 VW strain gages were installed at 60 locations in the unrestrained and restrained slabs at four critical slab locations: the corners, midpanels and along the transverse and longitudinal edges. VW gages were placed at three different depths within the slab for each corner location, and two different depths at each edge and midpanel location. Strain readings are automatically taken at 15-minute intervals (Wells et al. 2005). A plan showing the locations of the strain gages and a cross-section showing their depths were previously presented in Figure 3.9 and Figure 3.6.

The raw strain reading represents the slab deformation due to the effects of temperature change, moisture change, shrinkage and creep. The strain reading is also affected by factors that restrain the movement of the slab. As a result, the strain measurements based on the sensors embedded in the restrained and unrestrained slabs are expected to be different. The raw strain reading is first corrected for the effect of temperature on the steel wire in the gage and then converted into total strain, which reflects the total deformation measured in the slab (Wells et al. 2005). The correction is accounted for by using Equation 4-1 to calculate the total strain experienced by the concrete. In this chapter, the strain measurements are zeroed based on the time the concrete was placed and will be used to determine the set time of the concrete.

$$\varepsilon_{total} = (R_1 - R_0)B + (T_1 - T_0)\alpha_s \qquad \text{(Equation 4-1)}$$

where: ε_{total} = Total strain in the concrete

R_0 = Raw strain at time 0 (concrete set time)

R_1 = Raw strain at time 1

T_0 = Temperature at time 0 (initial concrete set)

T_1 = Temperature at time 1

α_s = Thermal coefficient of expansion of steel in strain gage = 6.78 με/°F

B = Batch calibration factor (provided by the manufacturer)

4.2.2 Restrained slabs

The variation of the measured strain with respect to temperature changes during the first 42 hours after placement is used to identify the concrete set time. The set time is selected as that corresponding to the time when expansion/contraction is measured with changes in temperature. The early-age variation in the total strain for the midpanel sensors oriented in the longitudinal direction and located at the top and bottom of the restrained Slab B are illustrated in Figure 4.6 and Figure 4.7. Based on these figures, the set times were found to correspond to 2:46 PM for the top of the slab and 4:01 PM for the bottom of the slab. These times are then zeroed to the time when concrete mixing was initiated, which is discussed in the following paragraph.

The concrete was mixed at a portable plant located approximately five miles east of the project site in Export, Pennsylvania and was delivered to the site via front-discharge trucks. The time from when the water hits the cement in the batching process to the time the concrete truck pulls away to head to the job site, including the time for mixing and loading the truck, was estimated at eight minutes. The travel time needed to reach the job site was estimated at twelve minutes. Once on the site, the time for testing of the concrete was estimated at fifteen minutes. And, the time to place the concrete on the grade was estimated at ten minutes. In total, an additional 45 minutes are accounted for between the time water hits the concrete and the time the thermocouples begin recording temperatures. The maturity accumulated in the 45 minutes preceding concrete placement is assumed to be equal to the maturity accumulated in the first 45 minutes following placement.

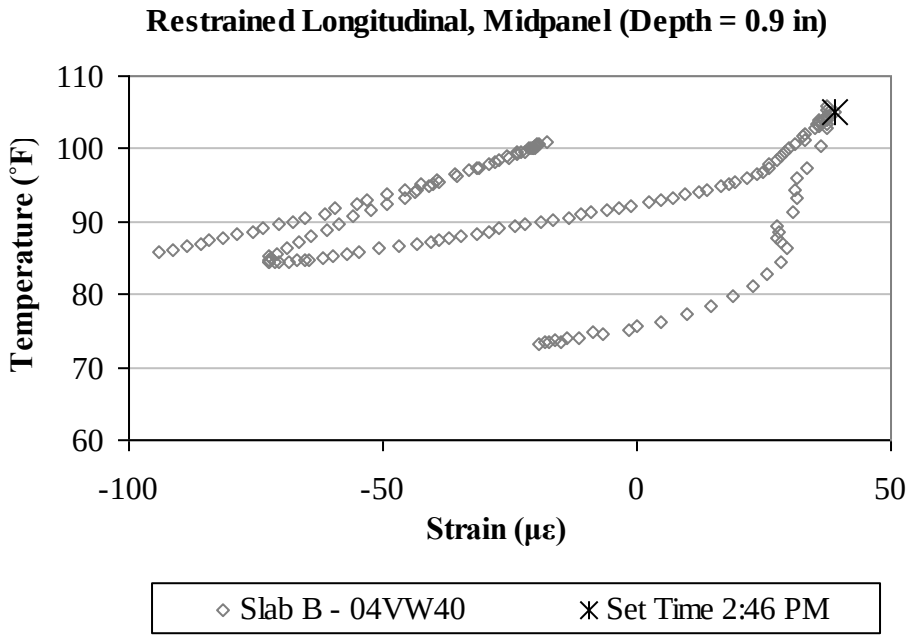

Figure 4.6. Early-age variation in the total strain with temperature, in the longitudinal direction, for the top sensor located at midpanel of restrained Slab B.

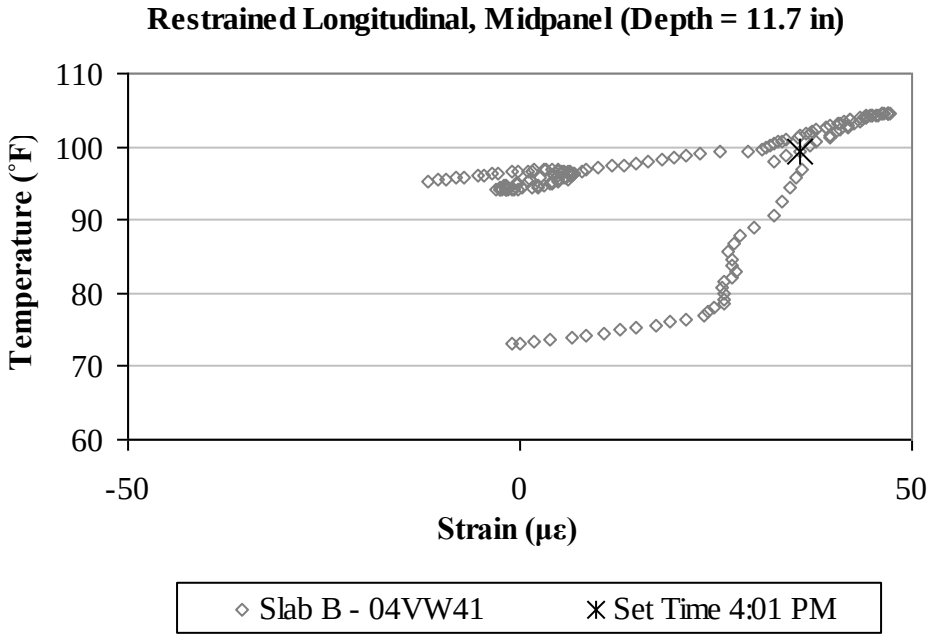

Figure 4.7. Early-age variation in the total strain with temperature, in the longitudinal direction, for the bottom sensor located at midpanel of restrained Slab B.

According to the thermistor readings, the concrete was placed at 6:31 AM at the midpanel of restrained Slab B. Accordingly, the concrete set times for the midpanel of restrained Slab B are found to correspond to elapsed times of 8.25 hours (top of slab) and 9.5 hours (bottom of slab) after mixing.

A similar procedure was followed to determine the concrete set times for every sensor at every depth and location within restrained Slabs A, B and C. The figures illustrating the early-age variations of total strain with temperature are included in Appendix A. Based on the early-age variation in the strain data, the set times are presented in Figure 4.8 and Table 4.1 for the restrained slabs.

Restrained Slabs

Slab A			Slab B			Slab C		
10.5 ± 0.25 (T)	10.5 (T)			9.75 (T)	10.33 ± 0.52 (T)		10.75 (T)	10.92 ± 0.29 (T)
10.5 ± 0.0 (M)	10.5 (B)			10.25 (B)	10.33 ± 0.52 (M)		10.75 (B)	10.88 ± 0.18 (M)
10.83 ± 0.38 (B)					10.38 ± 0.18 (B)			11.5 ± 0.71 (B)
	10.75 (T)	11.25 (T)	11.25 (T)	9 (T)		11.25 (T)	11.5 (T)	
	10.75 (B)	11.25 (B)	11.75 (B)	10.25 (B)		12.25 (B)	11.5 (B)	
		10.33 ± 0.16 (T)	10.5 ± 0.25 (T)			10.58 ± 1.01 (T)		
	10.5 (T)	10.13 ± 0.53 (M)	10.5 ± 0.25 (M)	9.5 (T)		10.25 ± 0.5 (M)	9.75 (T)	
	11 (B)	11.17 ± 0.52 (B)	10.75 ± 0.25 (B)	10 (B)		10.67 ± 0.8 (B)	9.75 (B)	

T: Top of slab; M: Middepth; B: Bottom of slab

Figure 4.8. Set times in the restrained slabs.

Table 4.1. Concrete set time based on early-age vibrating wire data for restrained slabs.

Location	Direction[1]	Depth	Concrete Set Time[2,3] (hours)			
			Slab A	Slab B	Slab C	Average
Corner; Centerline	L	Top	10.5	10.75	11.25	10.83
		Middepth	10.5	10.75	--	10.63
		Bottom	10.5	--	--	10.50
	D	Top	10.75	10.5	10.75	10.67
		Middepth	--	10.5	11	10.75
		Bottom	10.75	10.5	12	11.08
	T	Top	10.25	9.75	10.75	10.25
		Middepth	10.5	9.75	10.75	10.33
		Bottom	11.25	10.25	11	10.83
Edge; Centerline	L	Top	10.5	9.75	10.75	10.33
		Bottom	10.5	10.25	10.75	10.50
Midpanel	L	Top	10.75	9	11.5	10.42
		Bottom	10.75	10.25	11.5	10.83
Edge; Lane/Shoulder	L	Top	10.5	9.5	9.75	9.92
		Bottom	11	10	9.75	10.25
Transverse Joint	T	Top	11.25	11.25	11.25	11.25
		Bottom	11.25	11.75	12.25	11.75
Corner; Lane/Shoulder	L	Top	10.25	10.5	11.5	10.75
		Middepth	9.75	10.5	10.25	10.17
		Bottom	11	11	11	11.00
	D	Top	10.25	10.75	9.5	10.17
		Middepth	--	10.75	9.75	10.25
		Bottom	10.75	10.75	9.75	10.42
	T	Top	10.5	10.25	10.75	10.50
		Middepth	10.5	10.25	10.75	10.50
		Bottom	11.75	10.5	11.25	11.17

[1] L: Longitudinal direction; D: Diagonal direction; T: Transverse direction
[2] Set time is zeroed to the concrete mixing time (45 minutes prior to placement)
[3] Dashed lines indicate that VW data is not available or cannot be interpreted

The results indicate that the average concrete set time varies between 9 and 12.25 hours after mixing, with an overall average of 10.62 hours. At each location, the set times estimated based on the sensors located at the top, middepth and bottom of the slab are similar. The largest difference between top and bottom of the slab was recorded at the midpanel of restrained Slab B and amounts to 1.25 hours. To further illustrate this point, the average set times at the top, middepth and bottom of the slab were calculated based on the data collected from the sensors in all the slabs, and are compared to each other in Figure 4.9. The figure shows that the set times of the top, middle and bottom portions of the slabs are within 4 percent of each other. Moreover, the concrete set times estimated at the different locations within the slabs are within 18 percent of each other and do not show any specific pattern of variation. This implies that the slab restraining conditions do not significantly affect the concrete set time. However, the slab restraining conditions are expected to affect the built-in stresses within the slabs.

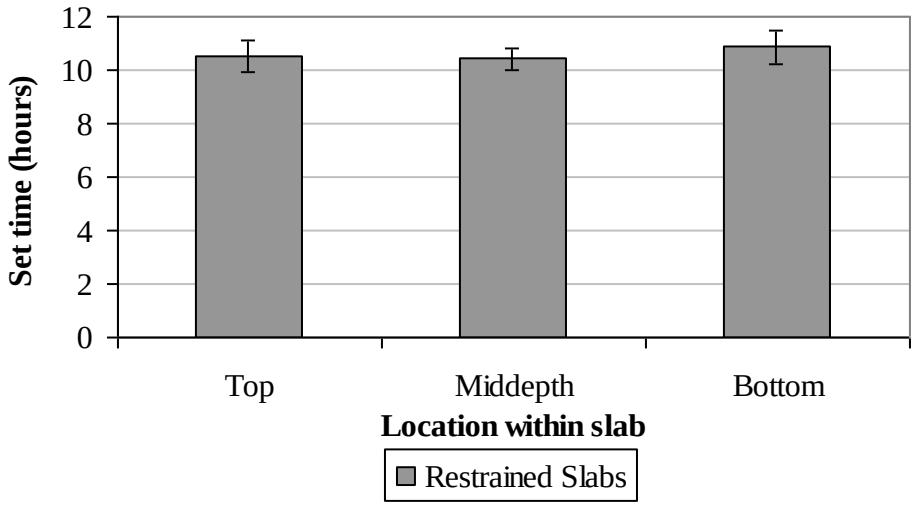

Figure 4.9. Variation in average concrete set time with depth, for restrained slabs.

Since the strength, and therefore stiffness, of the concrete is a function of maturity, the stiffness of the concrete at different locations in the slab can be assessed by using the maturity concept. Additional stiffness needed by the concrete to overcome the restraint can be quantified by evaluating the difference in the concrete maturity at the time of set. For this purpose, the

maturity of the concrete at different locations and depths was estimated for the time of set at each location. The maturity concept assumes that the strength of a particular concrete mixture is a function of the maturity of that concrete, regardless of the time-temperature combinations leading to that maturity. Since concrete strength is a function of time and temperature, different combinations of time and temperature can be used to determine the maturity of the concrete. Concrete maturity represents the area under the temperature versus time graph, with reference to a datum temperature, and can be estimated by using the Nurse-Saul expression provided in Equation 4-2 (Mindess et al. 2003).

$$Maturity\ Function = M(t) = \sum (T_a - T_0)\Delta t \qquad \text{(Equation 4-2)}$$

Where: M(t) = Temperature-time factor at age t (degree-hours)

Δt = Time interval

T_a = Average concrete temperature during the time interval Δt

T_0 = Datum temperature below which there is no strength gain, assumed to be 14˚F.

The temperatures recorded by the vibrating wire gages were used in calculating the maturity. The maturity corresponding to the time of set for each gage is presented in Table 4.2 and illustrated in Figure 4.10. The maturity at the time of set indicates that the maturity at the top, middle and bottom portions of the slab are within 20 percent of each other, which does not constitute a significant difference for concrete maturity. In Figure 4.10, CL refers to Centerline and L/S refers to Lane/Shoulder.

Table 4.2. Concrete maturity corresponding to the estimated set times for restrained slabs.

Location	Direction[1]	Depth	Maturity at Concrete Set (°F-hour)			
			Slab A	Slab B	Slab C	Average
Corner; Centerline	L	Top	754	794	844	797
		Middepth	761	795	--	778
		Bottom	725	--	--	725
	D	Top	788	774	800	787
		Middepth	--	775	808	792
		Bottom	757	738	860	785
	T	Top	752	706	795	751
		Middepth	767	707	791	755
		Bottom	804	721	778	768
Edge; Centerline	L	Top	736	671	746	718
		Bottom	705	682	717	701
Midpanel	L	Top	780	641	886	769
		Bottom	739	718	837	764
Edge; Lane/Shoulder	L	Top	736	663	666	689
		Bottom	756	679	669	701
Transverse Joint	T	Top	830	823	817	823
		Bottom	793	832	864	830
Corner; Lane/Shoulder	L	Top	732	761	841	778
		Middepth	687	764	739	730
		Bottom	779	772	766	772
	D	Top	729	786	671	729
		Middepth	--	784	690	737
		Bottom	732	741	662	712
	T	Top	756	742	781	760
		Middepth	747	742	776	755
		Bottom	816	728	777	774

[1] L: Longitudinal direction; D: Diagonal direction; T: Transverse direction

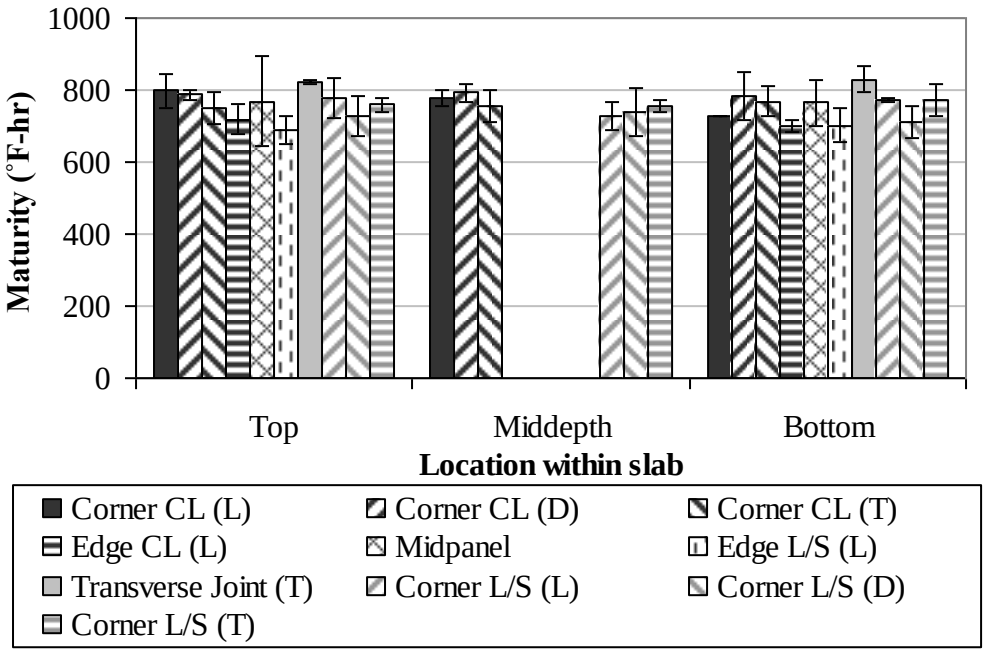

Figure 4.10. Average maturity at time of set for restrained slabs.

The variation in the concrete maturity at the time of set along the slab depth is further examined in Figure 4.11. The figure presents the maturity versus a normalized depth parameter. The normalized depth parameter is calculated by dividing the depth of the sensor by the slab thickness at the location of the sensor. This parameter is introduced to take into account the variability of the slab thickness during construction and provides a non-dimensional value that can be used to compare maturities for sensors located at varying depths with respect to the slab thickness. The figure confirms that, at the time of set, the maturity is not affected by the depth within the slab.

Moreover, Figure 4.12 presents the maturity at the time of set as a function of the type of restraint. The investigated restraints considered include: presence of tie bars, presence of dowel bars, presence of an adjacent slab, and friction along the slab/base interface. The figure is based on data from the corner sensors at the centerline joint and the lane/shoulder joint. According to the figure, the maturity at the time of set established using the VW gages is similar throughout the restrained slabs.

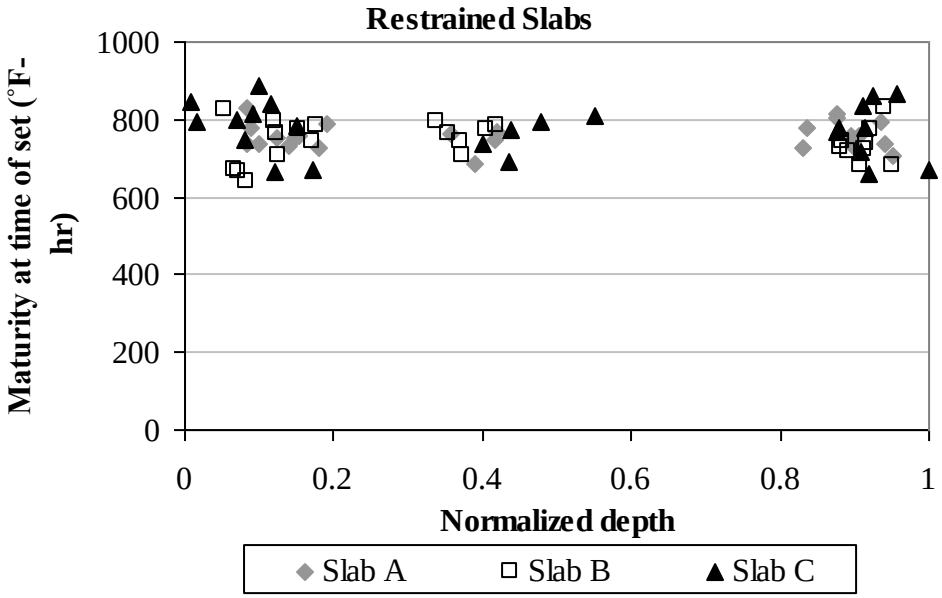

Figure 4.11. Maturity at time of set with respect to sensor depth for restrained slabs.

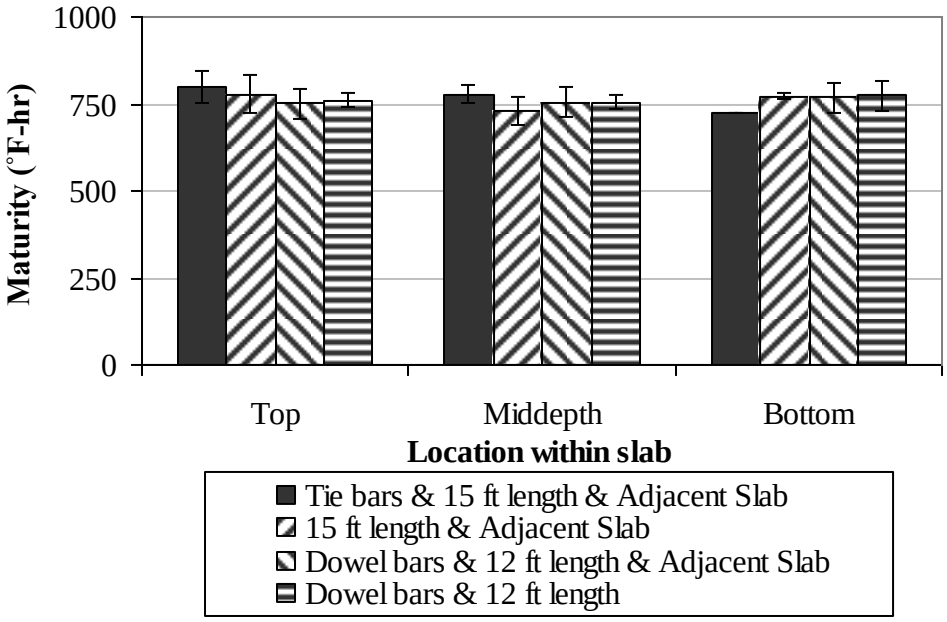

Figure 4.12. Effect of restraining conditions on maturity at set time for restrained slabs.

4.2.3 Unrestrained slabs

Similarly to what was carried out for the restrained slabs, the variation in the measured strain with respect to temperature changes during the first 42 hours after placement is used to identify the concrete set time for the unrestrained slabs. The concrete set time is selected as that corresponding to the time when expansion/contraction is measured with changes in temperature. The early-age variation in the total strain for the midpanel sensors oriented in the longitudinal direction and located at the top and bottom of the unrestrained Slab B are illustrated in Figure 4.13 and Figure 4.14. Based on these figures, the set times were found to correspond to 5:15 PM for the top of the slab and 4:30 PM for the bottom of the slab. These times are then zeroed to the time when concrete mixing was initiated, which is assumed to be 45 minutes prior to concrete placement, as previously explained in section 4.2.2. According to the thermistor readings, the concrete was placed at 7:00 AM at the midpanel of unrestrained Slab B. The concrete set times for the midpanel of unrestrained Slab B are found to correspond to elapsed times of 10.25 hours (top of slab) and 9.5 hours (bottom of slab) after mixing.

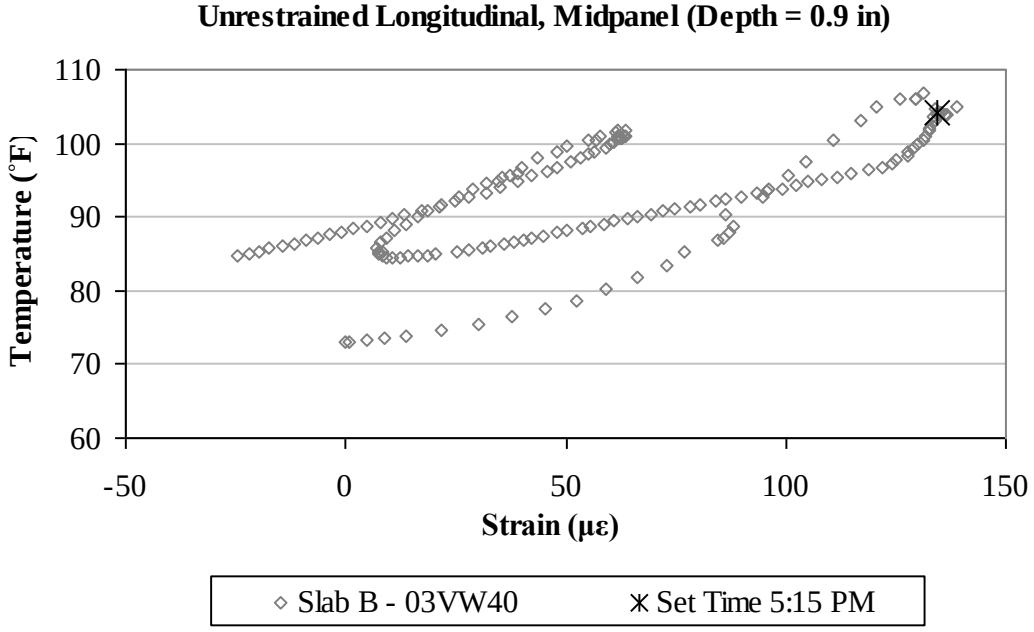

Figure 4.13. Early-age variation in the total strain with temperature, in the longitudinal direction, for the top sensor located at midpanel in unrestrained Slab B.

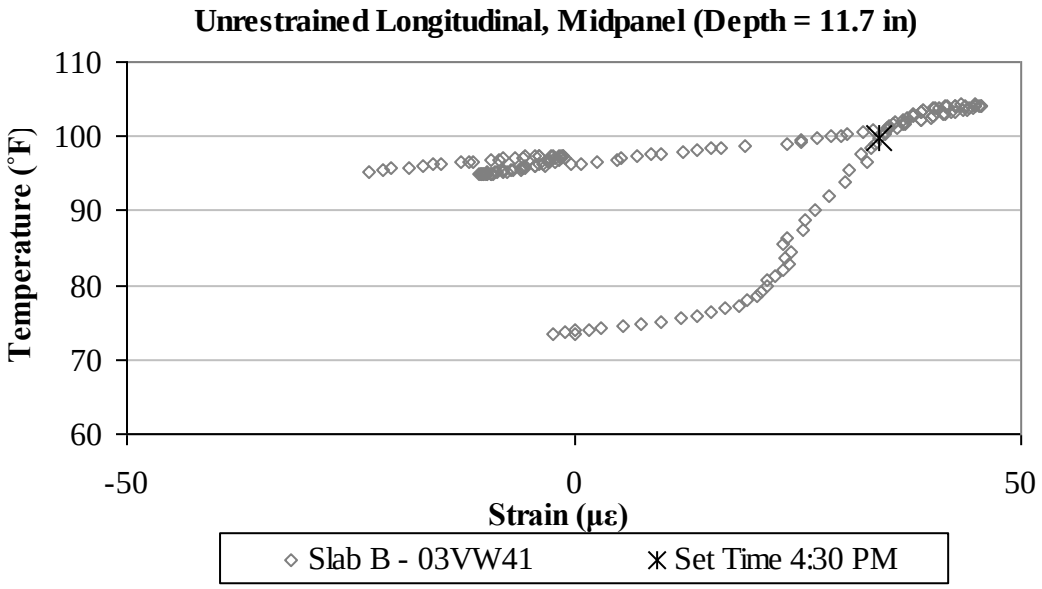

Figure 4.14. Early-age variation in the total strain with temperature, in the longitudinal direction, for the bottom sensor located at midpanel in unrestrained Slab B.

A similar procedure was followed to determine the concrete set time for every sensor at every depth and location within unrestrained Slabs A, B and C. The figures illustrating the early-age variations of total strain with temperature are included in Appendix A. The set times established based on the early-age variation in the strain data are presented in Table 4.3 and Figure 4.15 for the unrestrained slabs.

Unrestrained Slabs

Slab A			Slab B			Slab C	
9.92 ± 0.14 (T)	10 (T)			10 (T)	9.92 ± 0.14 (T)	10.5 (T)	10.83 ± 0.29 (T)
10.13 ± 0.18 (M)	10 (B)			10.25 (B)	10.17 ± 0.14 (M)	9.75 (B)	10.63 ± 0.18 (M)
10.67 ± 0.76 (B)					10.63 ± 0.18 (B)		11.25 ± 0.90 (B)
	10 (T)	9.75 (T)	10 (T)	11 (T)		10.75 (T)	10.5 (T)
	10.75 (B)	10.75 (B)	11.5 (B)	10.25 (B)		10.75 (B)	11.75 (B)
		9.83 ± 0.29 (T)	9.50 ± 0.0 (T)			9.58 ± 0.14 (T)	
	10 (T)	10.13 ± 0.18 (M)	10.0 ± 0.43 (M)	11.75 (T)		9.58 ± 0.52 (M)	10.5 (T)
	9.5 (B)	10.67 ± 0.76 (B)	10.42 ± 0.14 (B)	12 (B)		10.17 ± 0.14 (B)	N/A (B)

T: Top of slab; M: Middepth; B: Bottom of slab

Figure 4.15. Set times in the unrestrained slabs.

Table 4.3. Concrete set time based on early-age vibrating wire data for unrestrained slabs.

Location	Direction[1]	Depth	Concrete Set Time[2,3] (hours)			
			Slab A	Slab B	Slab C	Average
Corner; Centerline	L	Top	10	10	10.5	10.17
		Middepth	10.25	10	10.5	10.25
		Bottom	11.5	--	10.5	11.00
	D	Top	9.75	9.75	11	10.17
		Middepth	10	10.25	10.75	10.33
		Bottom	10.5	10.75	11	10.75
	T	Top	10	10	11	10.33
		Middepth	--	10.25	--	10.25
		Bottom	10	10.5	12.25	10.92
Edge; Centerline	L	Top	10	10	10.5	10.17
		Bottom	10	10.25	9.75	10.00
Midpanel	L	Top	10	11	10.5	10.50
		Bottom	10.75	10.25	11.75	10.92
Edge; Lane/Shoulder	L	Top	10	11.75	10.5	10.75
		Bottom	9.5	12	--	10.75
Transverse Joint	T	Top	9.75	10	10.75	10.17
		Bottom	10.75	11.5	10.75	11.00
Corner; Lane/Shoulder	L	Top	9.5	9.5	9.75	9.58
		Middepth	10.25	9.5	9	9.58
		Bottom	10.5	10.5	10.25	10.42
	D	Top	10	9.5	9.5	9.67
		Middepth	--	10.25	9.75	10.00
		Bottom	10	10.25	10	10.08
	T	Top	10	9.5	9.5	9.67
		Middepth	10	10.25	10	10.08
		Bottom	11.5	10.5	10.25	10.75

[1] L: Longitudinal direction; D: Diagonal direction; T: Transverse direction
[2] Set time is zeroed to the concrete mixing time (45 minutes prior to placement)
[3] Dashed lines indicate that VW data is not available or cannot be interpreted

The results indicate that the average concrete set time varies between 9.5 and 12 hours after mixing, with an overall average of 10 hours. At each location, the set times estimated based on the sensors located at the top, middepth and bottom of the slab are similar. The largest difference between top and bottom of the slab was recorded at the midpanel of unrestrained Slab C and amounts to 1.25 hours. To further illustrate this point, the average set times at the top, middepth and bottom of the slab were calculated based on the data collected from the sensors in all the slabs, and are compared to each other in Figure 4.16. The figure shows that the set times for the top, middle and bottom portions of the slabs are within 6 percent of each other. Moreover, the concrete set times estimated at the different locations within the slabs are within 26 percent of each other and do not show any specific pattern in variation.

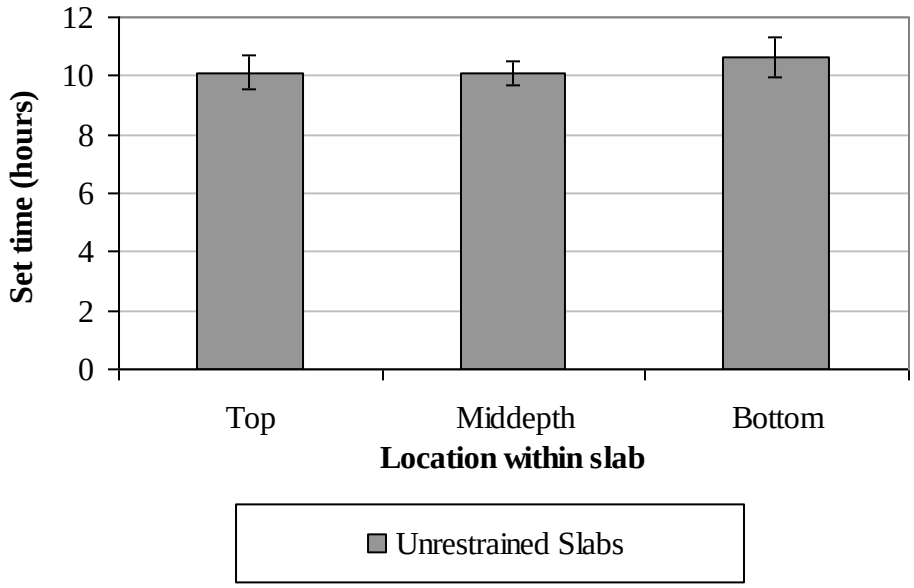

Figure 4.16. Variation in average concrete set time with depth, for unrestrained slabs.

Similarly to the analysis carried out for the restrained slabs, the maturity of the concrete at different locations and depths were estimated for the time of set at each location. The procedure described in section 4.2.2 was adopted and the temperatures recorded by the vibrating wire gages were used in calculating the maturity. The maturity corresponding to the set time of

each gage is presented in Table 4.4 and illustrated in Figure 4.17. The maturity at the set time indicates that the maturity at the top, middle and bottom portions of the slab are not significantly different, within 19 percent of each other. This confirms the previous observation that the concrete uniformly sets within the same time period, irrespective of the slab restraining conditions.

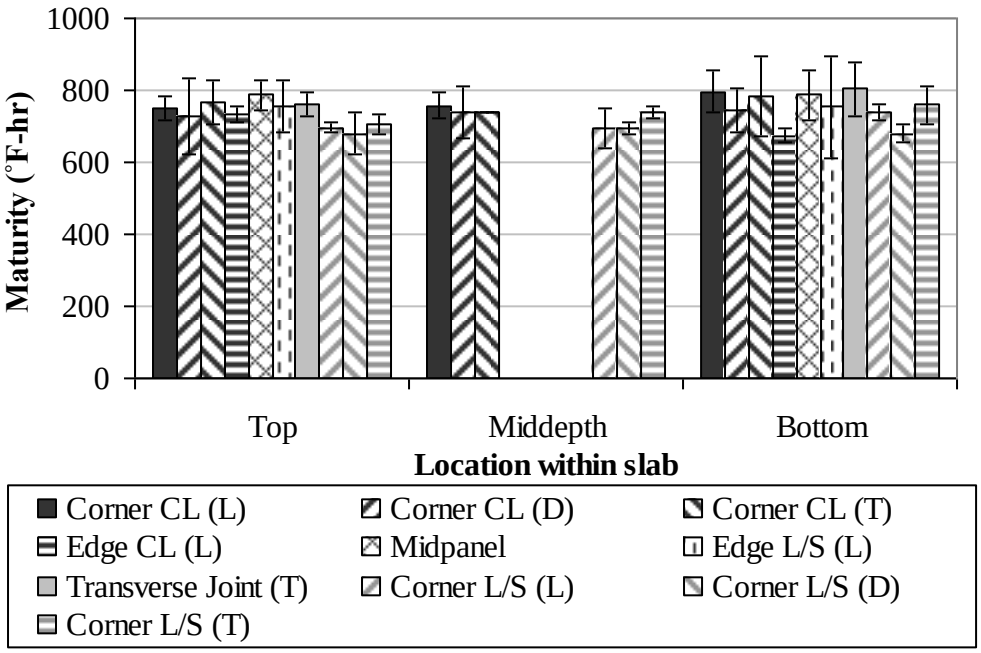

Figure 4.17. Average maturity at time of set for unrestrained slabs.

Table 4.4. Concrete maturity corresponding to the estimated set times for unrestrained slabs.

Location	Direction[1]	Depth	Maturity at Concrete Set (°F-hour)			
			Slab A	Slab B	Slab C	Average
Corner; Centerline	L	Top	745	720	786	750
		Middepth	764	717	789	757
		Bottom	837	--	753	795
	D	Top	722	623	834	726
		Middepth	743	667	811	740
		Bottom	749	682	800	744
	T	Top	748	720	835	768
		Middepth	--	738	--	738
		Bottom	709	732	912	784
Edge; Centerline	L	Top	--	715	746	731
		Bottom	670	694	657	674
Midpanel	L	Top	746	832	782	787
		Bottom	779	724	861	788
Edge; Lane/Shoulder	L	Top	718	841	714	757
		Bottom	654	854	--	754
Transverse Joint	T	Top	736	754	801	764
		Bottom	777	887	747	804
Corner; Lane/Shoulder	L	Top	687	687	712	695
		Middepth	750	692	639	694
		Bottom	745	756	713	738
	D	Top	732	617	689	679
		Middepth	--	685	708	697
		Bottom	692	650	699	680
	T	Top	736	691	690	706
		Middepth	729	760	728	739
		Bottom	816	745	716	759

[1] L: Longitudinal direction; D: Diagonal direction; T: Transverse direction

The variation of the concrete maturity at the time of set along the slab depth is examined in Figure 4.18. The figure presents the maturity at the time of set versus the normalized depth. As previously explained in section 4.2.2, the normalized depth parameter is calculated by dividing the depth of the sensor by the slab thickness at the location of the sensor. The figure confirms that, at the time of set, the maturity is not affected by the depth within the slab.

Moreover, Figure 4.19 presents the maturity at the set time as a function of the type of restraint affecting the strain recorded by the sensors. The investigated restraints include: presence of an adjacent slab, and friction along the slab/base interface. The figure is based on data from the corner sensors at the centerline joint and the lane/shoulder joint. According to the figure, the maturity at set time is not affected by the slab restraining conditions.

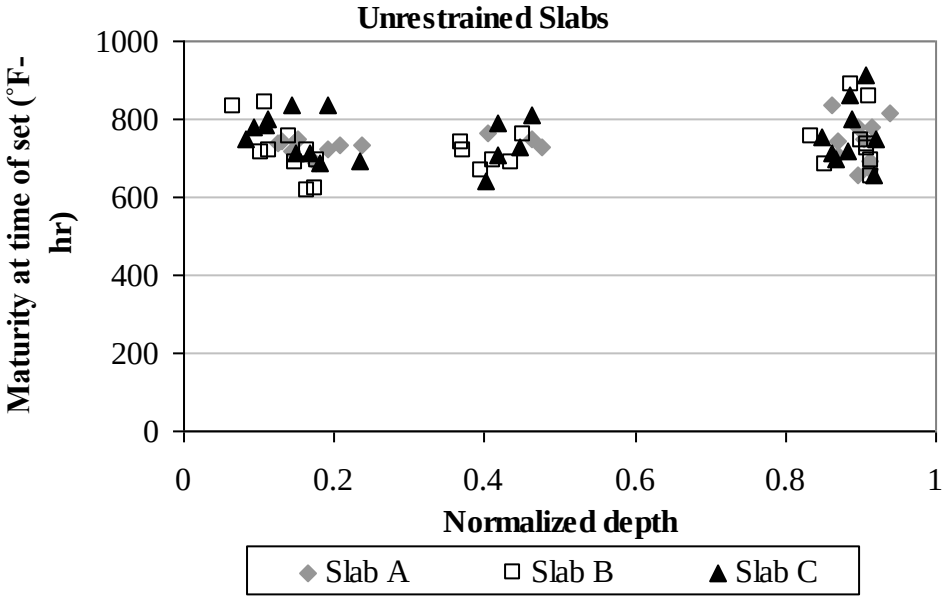

Figure 4.18. Maturity at time of set with respect to sensor depth for unrestrained slabs.

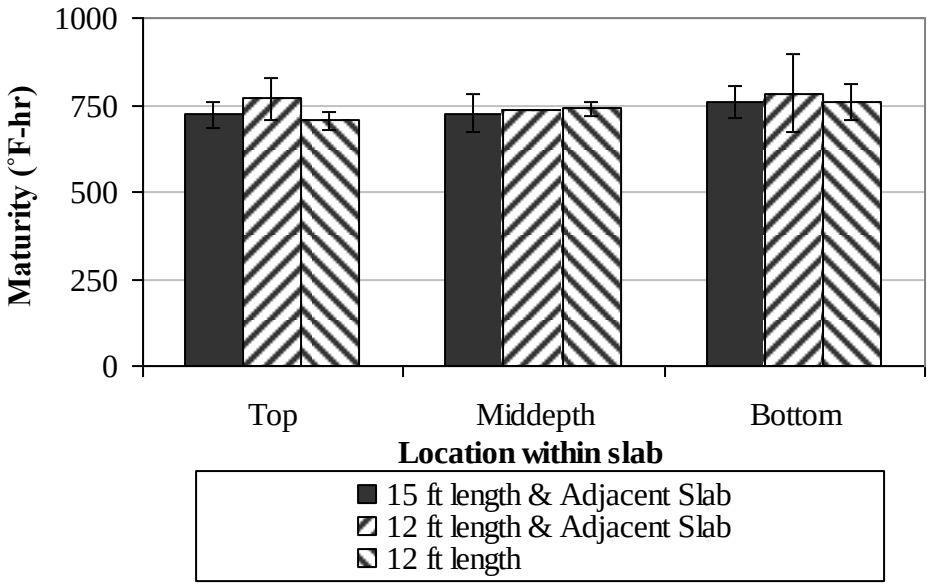

Figure 4.19. Effect of restraining conditions on maturity at set time for unrestrained slabs.

4.2.4 Comparison between restrained and unrestrained slabs

The concrete set time is similar for both restrained and unrestrained slabs, irrespective of the sensor location within the slab and the slab restraining conditions. Figure 4.20 presents the variation in the concrete maturity at the time of set with the normalized slab depths for both types of slabs. The figure confirms the previous statements that the concrete set time is similar across the slab depth. The figure also shows that the maturity at set time is not affected by the slab restraining conditions.

Moreover, Figure 4.21 compares the maturity at the set time depending on the type of restraint affecting the movements recorded by the sensors in the restrained and unrestrained slabs. The figure is based on data from the corner sensors at the centerline joint and the lane/shoulder joint. The figure confirms the previous observations that the slab restraining conditions do not affect the set time of the concrete. The maturity values are within 16 percent of each other.

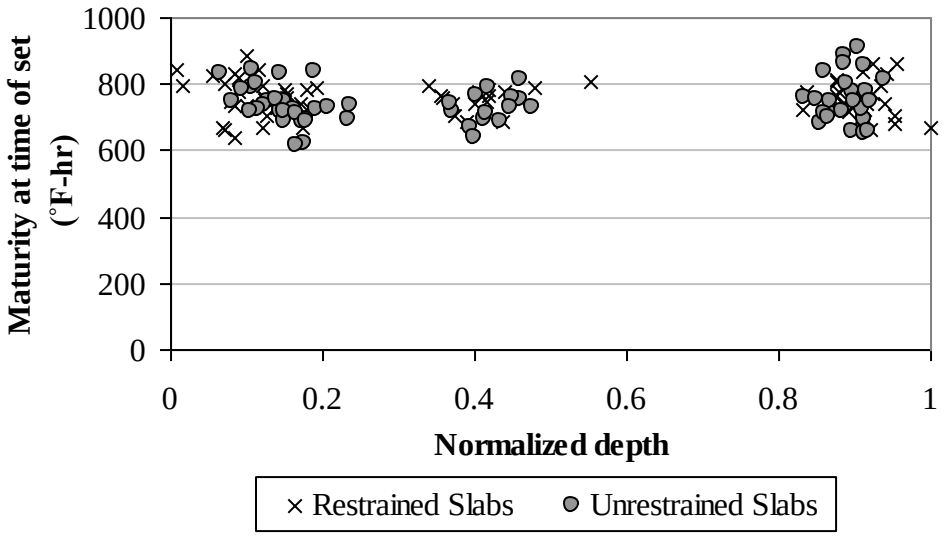

Figure 4.20. Maturity at set time with respect to depth for restrained and unrestrained slabs.

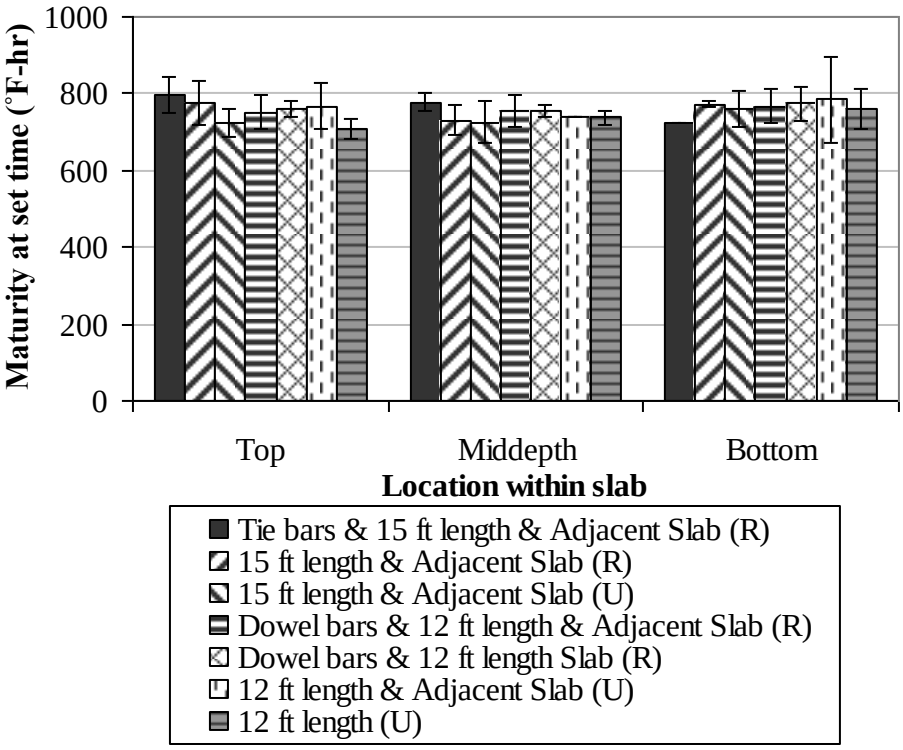

Figure 4.21. Effect of restraining conditions on maturity at set time for restrained and unrestrained slabs.

4.2.5 Built-in temperature gradient based on concrete strain measurements

As determined in sections 4.2.2 and 4.2.3, the set time of the restrained slabs takes place between 2:46 PM and 6:01 PM on the day of construction, and the set time of the unrestrained slabs takes place between 3:15 PM and 6:15 PM on the day of construction. During these time periods, the concrete temperature conditions and the corresponding equivalent linear temperature gradients vary significantly, as presented in section 4.1.1. The temperature profiles corresponding to the upper and lower limits of the time ranges are presented in Figure 4.22. The corresponding equivalent linear temperature gradients are presented in Figure 4.23 for the restrained and unrestrained slabs. The temperature gradients vary between 1.12 and 0.05˚F/in for the case of the restrained slabs, and between 0.90 and 0.14˚F/in for the case of the unrestrained slabs. This constitutes a relatively large range of temperature gradients.

Previous research studying the behavior of JPCP slabs in response to temperature and moisture changes has shown that the response of the slabs is controlled by the temperature and moisture conditions at midpanels, and not at the edges (Vandenbossche 2003). As a result, the temperature conditions at midpanel will be considered in establishing the built-in construction gradient. Moreover, relaxation of the concrete at the slab surface might affect the time of set. Therefore, it would be logical to use the data based on the sensors located at the bottom portion of the slab. In this case, the midpanel gradients (sensors at bottom of slab) vary between 0.19 and 0.42˚F/in for the restrained slabs, with an average of 0.31˚F/in. For the unrestrained slabs, the midpanel gradients (sensors at bottom of slab) vary between 0.21 and 0.42˚F/in for the restrained slabs, with an average of 0.31˚F/in. As a result, the built-in temperature gradient is 0.31˚F/in, for both restrained and unrestrained slabs. This built-in gradient is equivalent to a 3.9˚F temperature difference across the slab depth.

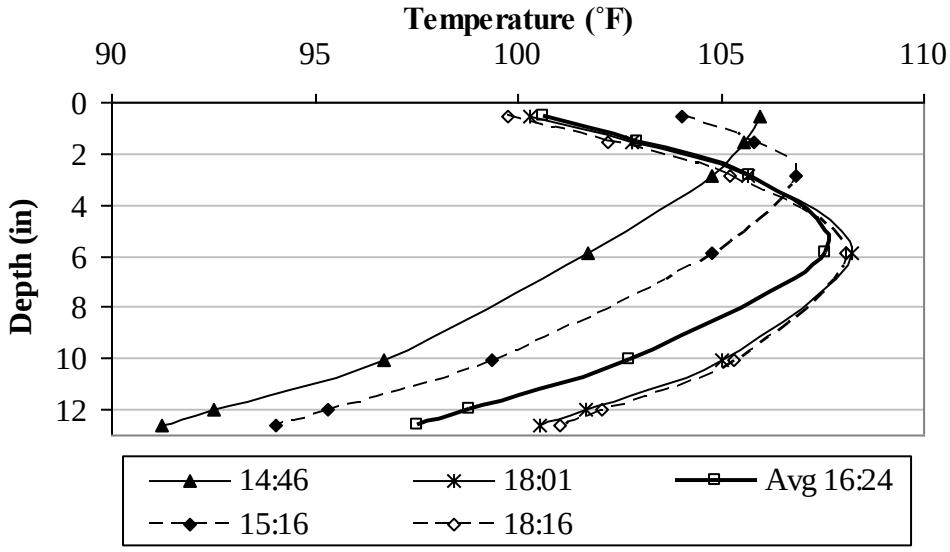

Figure 4.22. Range of temperature profiles at the set time of the restrained and unrestrained slabs based on VW data.

Restrained Slabs

Slab A			Slab B			Slab C		
0.36 ± 0.06 (T)	0.34 (T)			0.80 (T)	0.48 ± 0.27 (T)		0.31 (T)	0.29 ± 0.03 (T)
0.34 ± 0.0 (M)	0.34 (B)			0.42 (B)	0.48 ± 0.27 (M)		0.31 (B)	0.29 ± 0.03 (M)
0.30 ± 0.04 (B)					0.38 ± 0.05 (B)			0.20 ± 0.10 (B)
	0.31 (T)	0.26 (T)	0.26 (T)	1.12 (T)		0.26 (T)	0.19 (T)	
	0.31 (B)	0.26 (B)	0.21 (B)	0.42 (B)		0.05 (B)	0.19 (B)	
		0.39 ± 0.04 (T)	0.36 ± 0.06 (T)			0.47 ± 0.38 (T)		
	0.34 (T)	0.57 ± 0.32 (M)	0.36 ± 0.06 (M)	0.90 (T)		0.51 ± 0.26 (M)	0.80 (T)	
	0.27 (B)	0.26 ± 0.05 (B)	0.31 ± 0.04 (B)	0.60 (B)		0.44 ± 0.31 (B)	0.80 (B)	

T: Top of slab; M: Middepth; B: Bottom of slab

Unrestrained Slabs

Slab A			Slab B			Slab C		
0.67 ± 0.11 (T)	0.60 (T)			0.60 (T)	0.67 ± 0.11 (T)		0.34 (T)	0.29 ± 0.04 (T)
0.51 ± 0.13 (M)	0.60 (B)			0.42 (B)	0.48 ± 0.11 (M)		0.80 (B)	0.33 ± 0.02 (M)
0.38 ± 0.21 (B)					0.33 ± 0.02 (B)			0.22 ± 0.15 (B)
	0.60 (T)	0.80 (T)	0.60 (T)	0.27 (T)		0.31 (T)	0.34 (T)	
	0.31 (B)	0.31 (B)	0.19 (B)	0.42 (B)		0.31 (B)	0.21 (B)	
		0.70 ± 0.17 (T)	0.90 ± 0.0 (T)			0.86 ± 0.06 (T)		
	0.60 (T)	0.51 ± 0.13 (M)	0.58 ± 0.28 (M)	0.21 (T)		0.84 ± 0.26 (M)	0.34 (T)	
	0.90 (B)	0.38 ± 0.21 (B)	0.37 ± 0.04 (B)	0.14 (B)		0.48 ± 0.11 (B)	N/A (B)	

T: Top of slab; M: Middepth; B: Bottom of slab

Figure 4.23. Gradients at set time in restrained and unrestrained slabs.

4.3 EARLY-AGE PRESSURE ALONG THE SLAB/BASE INTERFACE

Static pressure cells were placed at the interface between the JPCP slabs and the asphalt treated permeable base layer. Pressure values at midpanel and corner locations would indicate the change in pressure exerted on the base layers by the PCC due to curling and warping. Once the concrete sets to the point that it has achieved sufficient stiffness, the pressure exerted by the slabs on the base is expected to vary along uniform rates. At the slab corner, the pressure is expected to increase with increasing concrete temperature gradients and at midpanel, the pressure is expected to decrease with increasing concrete temperature gradients. Before the concrete sets, the pressure exerted on the base layer is not expected to vary along a uniform rate. Data was collected from the static pressure cells and the variation in the measured pressure with respect to changes in the concrete temperature gradients during the first 42 hours after placement are used to identify the slab set time. The set time of the slabs is selected as that corresponding to the time when uniform changes in pressure are measured with changes in temperature gradients.

The analysis of the early-age variation in pressure with respect to temperature gradients included all the pressure cells in the restrained and unrestrained slabs. The general trends observed are presented in sections 4.3.2 and 4.3.3. As a result of the analysis of the early-age variation in pressure measurements, the set time of the slabs is determined. Finally, the built-in temperature gradient corresponding to the set time is estimated in section 4.3.4. A general overview of the static pressure cells is presented first.

4.3.1 Static pressure cell

Pressure induced by the PCC slabs on the base layer is measured using Geokon 4800 Earth Pressure Cells. These cells, also referred to as static pressure cells, were placed at the interface between the JPCP slabs and the asphalt treated permeable base layer at the midpanel and corner locations in two restrained and two unrestrained slabs. A total of eight pressure cells were installed at eight locations at the interface between the slabs and the base layer. Pressure readings are automatically recorded at 15-minute intervals (Wells et al. 2005). A plan showing the locations of the static pressure cells and a cross-section showing their depths were previously presented in Figure 3.9 and Figure 3.6.

Temperature changes cause the internal fluid to expand at a different rate than the surrounding material. The pressure readings are automatically corrected for the effect of temperature on the vibrating wires in the pressure cells (Geokon 2006). This is done internally by the datalogger based on Equation 4-3, provided by the manufacturer. The calibration factor and the thermal factor are provided by the manufacturer for every pressure cell.

$$P_{corrected} = (R_0 - R_1)C + (T_1 - T_0)K \qquad \text{(Equation 4-3)}$$

where: $P_{corrected}$ = Thermally corrected pressure

R_0 = Initial reading

R_1 = Current reading

C = Calibration factor (provided by the manufacturer)

T_1 = Current temperature

T_0 = Initial temperature

K = Thermal factor (provided by the manufacturer)

The pressure measurements are zeroed based on the pressure recorded prior to loading of the cells (or placement of the concrete). The variation of the pressure measurements during the first 48 hours after placement of the concrete are presented in Figure 4.24 for the restrained slabs and Figure 4.25 for the unrestrained slabs. Both figures show that during the first couple of hours, the pressure increases with increasing time at all locations. This reflects the time needed by the pressure cell to adjust to the weight of the concrete that had just been placed. After approximately 10 hours, the pressure along the corners decreases while the pressure at midpanel increases. The concrete temperatures and resulting gradients affect the recorded pressures. When subjected to positive temperature gradients, the slab curls downward, resulting in a decreased pressure level at midpanel and increased pressure level at the slab edge. The situation is reversed when the temperature gradients are negative. Approximately ten hours after construction, the temperature variations are uniform along the slab depth and a negative temperature gradient is present (representative of the nighttime condition). The negative gradient causes the slab to curl upwards; this accounts for the decrease in pressure at the slab edge and the increase in pressure at midpanel.

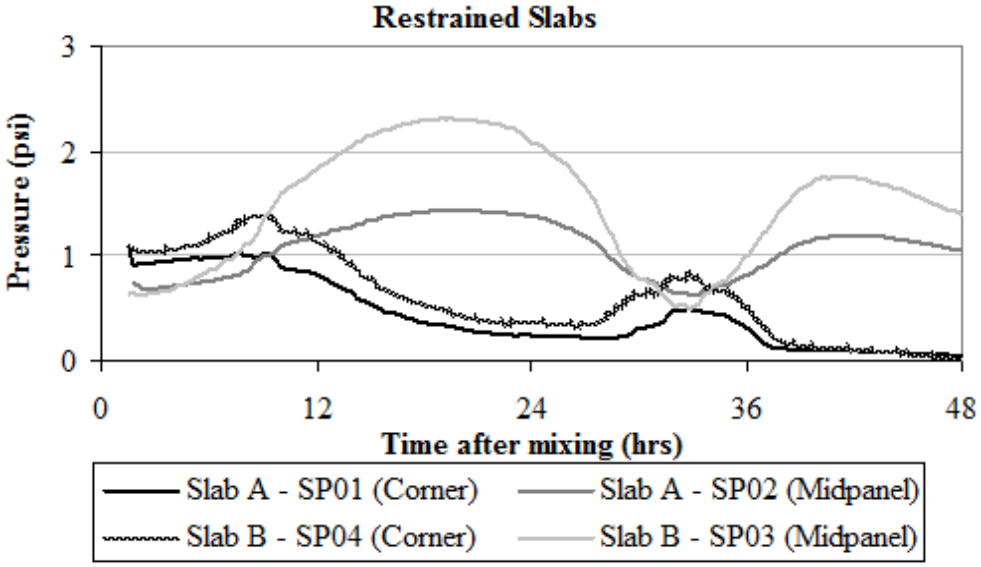

Figure 4.24. Early-age variation in pressure with time for the restrained slabs.

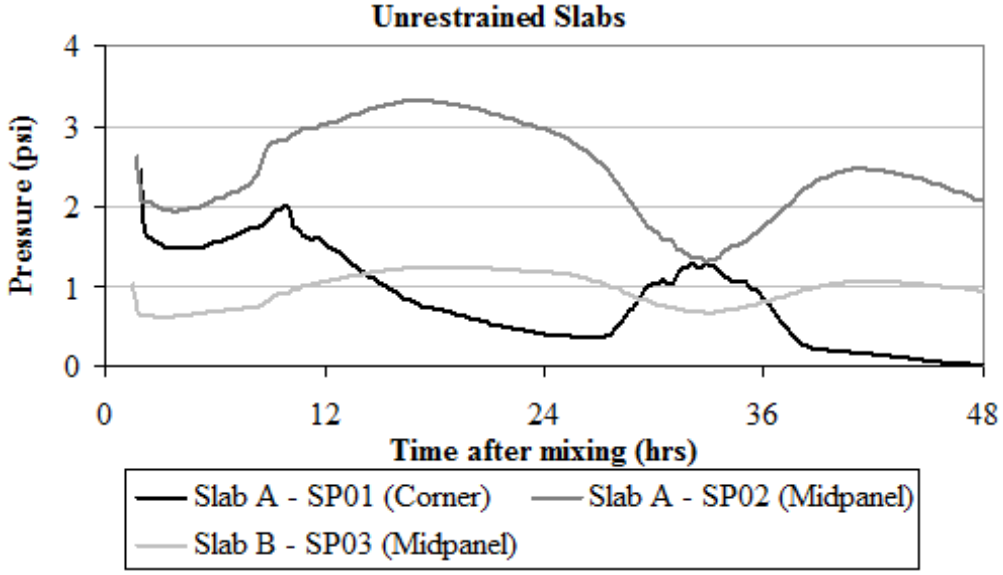

Figure 4.25. Early-age variation in pressure with time for the unrestrained slabs.

4.3.2 Restrained slabs

Having established that the pressure at the slab/base interface is affected by temperature variations, the pressure readings at an early age can be used to estimate the set time of the overall slab. As the concrete temperature increases due to hydration, and as long as the concrete is still in its plastic state, pressure measurements do not vary uniformly with temperature. As the concrete sets, the pressure measurements become a function of the temperature gradients in the concrete. The point in time when pressure measurements are uniform with changes in temperature gradients is considered representative of the slab set time at the corresponding locations.

The variation in pressure measurements with changes in the temperature gradient is plotted for the four pressure cells in the restrained Slab A and Slab B, and is presented in Figure 4.26 to Figure 4.29. According to the figures, the set time for the restrained slab takes place between 3:46 PM and 4:01 PM. These times are zeroed to the time when concrete mixing was initiated, which was assumed to be 45 minutes prior to concrete placement. Concrete placement was initiated at 6:46 AM for restrained Slab A and at 6:31 AM for restrained Slab B. This indicates that the restrained slabs set after an elapsed time of 9.25 hours after placement of the concrete, or 10 hours after mixing of the concrete.

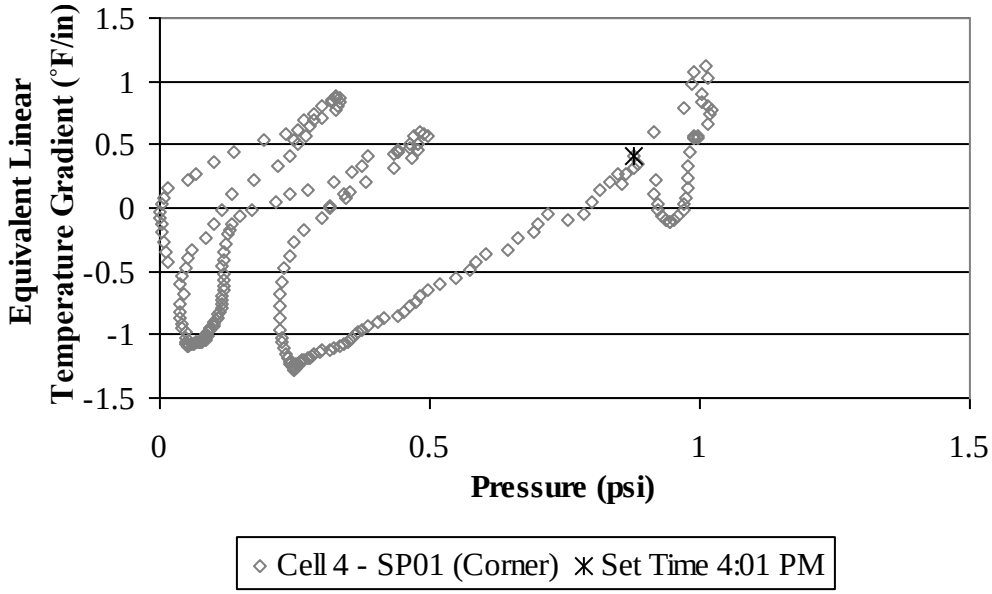

Figure 4.26. Early-age variation in pressure with changes in the temperature gradient for the corner of restrained Slab A.

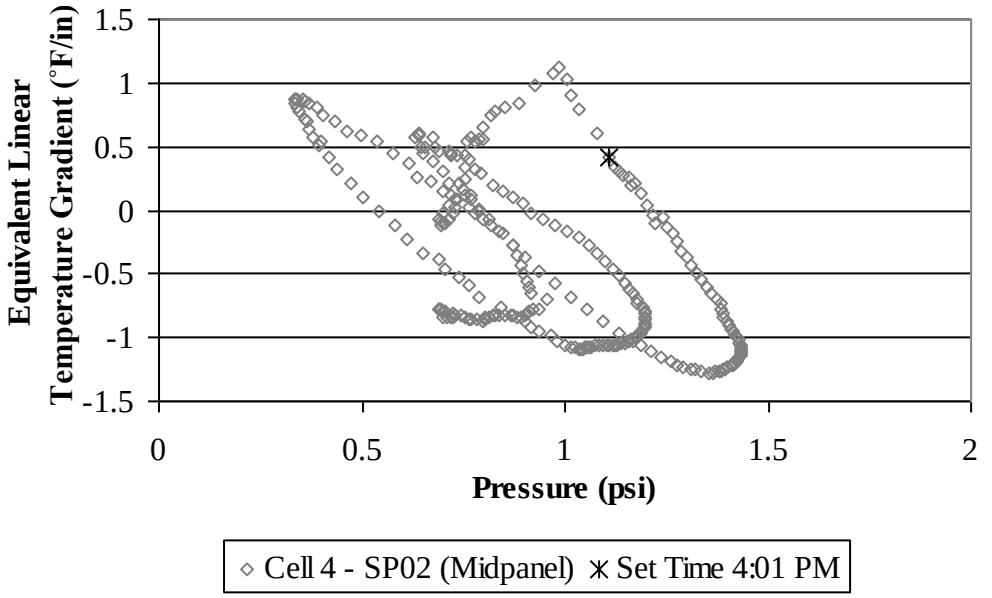

Figure 4.27. Early-age variation in pressure with changes in the temperature gradient for the midpanel of restrained Slab A.

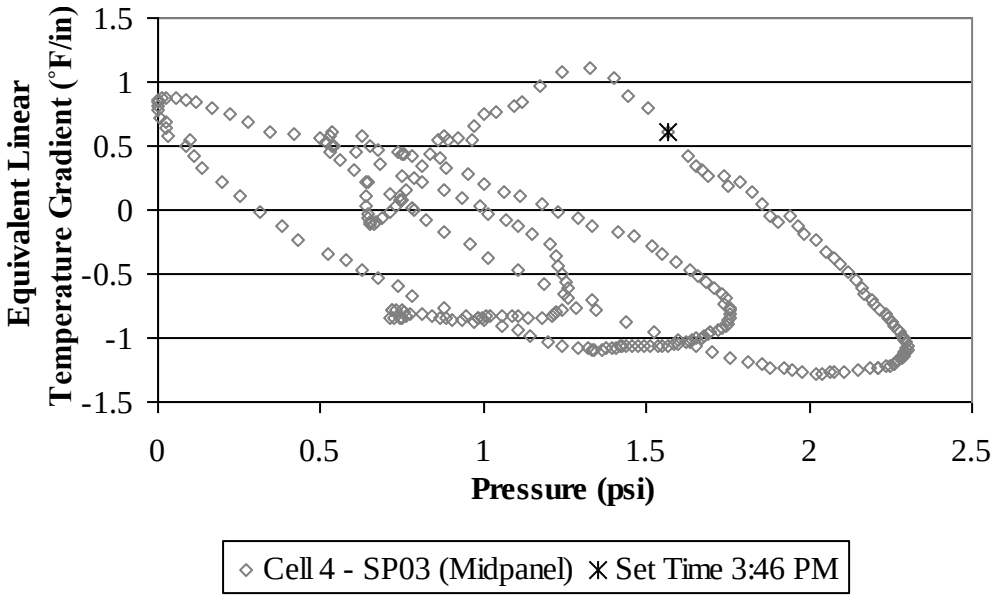

Figure 4.28. Early-age variation in pressure with changes in the temperature gradient for the midpanel of restrained Slab B.

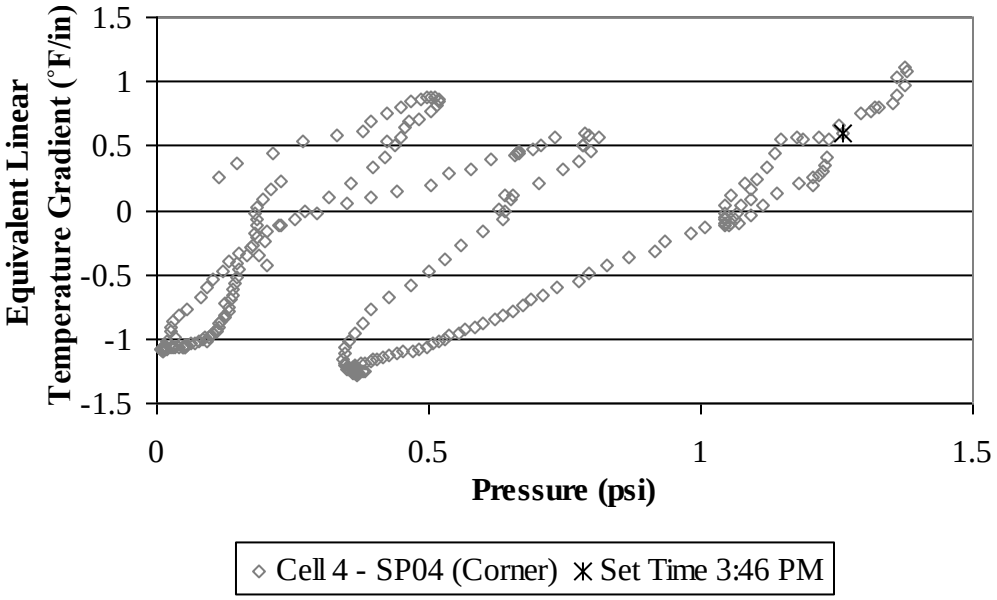

Figure 4.29. Early-age variation in pressure with changes in the temperature gradient for the corner of restrained Slab B.

4.3.3 Unrestrained slabs

Similarly to the procedure carried out for the restrained slabs, the early-age variation in the pressure measurements in the unrestrained slabs is also examined. Unfortunately, the pressure cell located at the corner of Slab B was not recording valid data since construction. The variation in pressure measurements with temperature gradient is plotted for the three remaining pressure cells in the unrestrained Slab A and Slab B, and is presented in Figure 4.30 to Figure 4.32. According to the figures, the time of set of the unrestrained slabs takes place at 4:00 PM. The set time is zeroed to the time when concrete mixing was initiated, which is estimated to be 45 minutes prior to concrete placement, as previously explained. Concrete placement was initiated at 7:00 AM for unrestrained Slabs A and B. This indicates that the unrestrained slabs set after an elapsed time of 9 hours after placement of the concrete or 9.75 hours after mixing of the concrete.

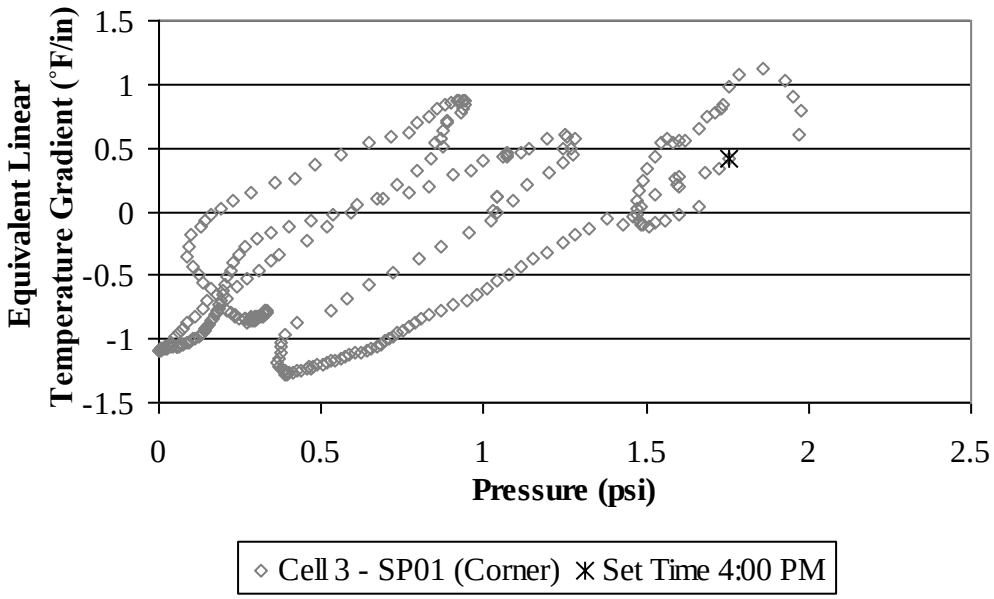

Figure 4.30. Early-age variation in pressure with changes in the temperature gradient for the corner of unrestrained Slab A.

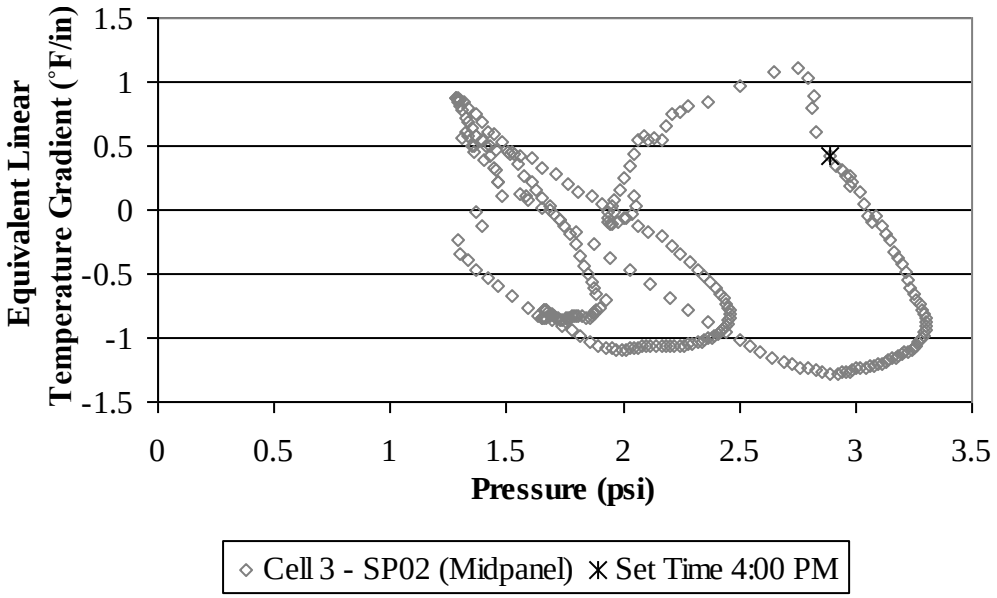

Figure 4.31. Early-age variation in pressure with changes in the temperature gradient for the midpanel of unrestrained Slab A.

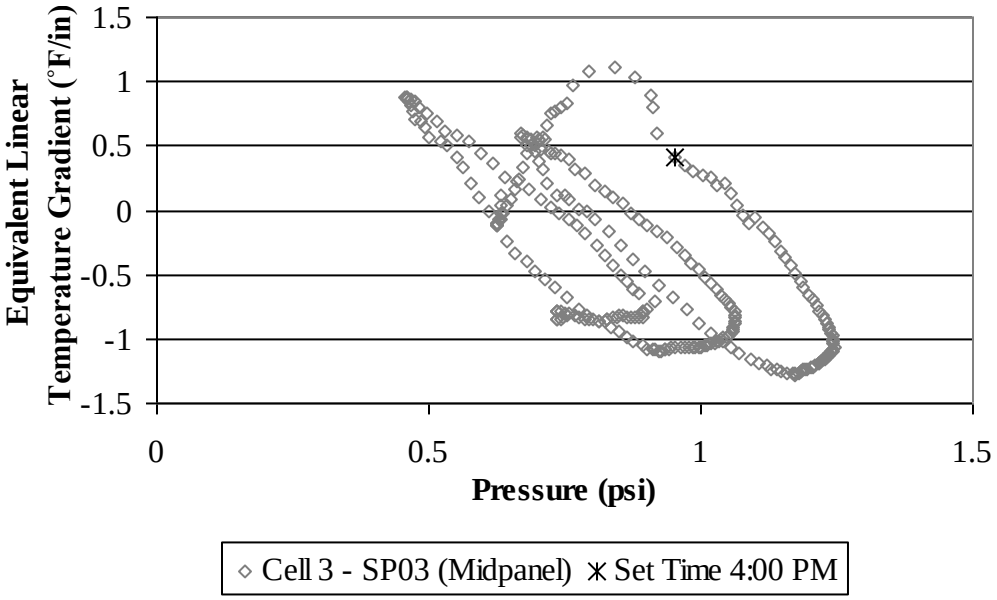

Figure 4.32. Early-age variation in pressure with changes in the temperature gradient for the midpanel of unrestrained Slab B.

4.3.4 Built-in temperature gradient based on pressure measurements

The set time of the restrained slabs takes place between 3:46 PM and 4:01 PM, and the set time of the unrestrained slabs takes place at approximately 4:00 PM. The temperature profiles do not vary much during this time period, as shown in Figure 4.33. The corresponding equivalent linear temperature gradients vary between 0.60 and 0.42˚F/in. The difference in gradients during these times is not significant, and it can be concluded that the built-in temperature gradient based on the pressure cell data is, on average, 0.51˚F/in for the restrained slabs and 0.42˚F/in for the unrestrained slabs. These gradients are equivalent to a 6.4˚F temperature difference across the restrained slab depth and 5.3˚F temperature difference across the unrestrained slab depth.

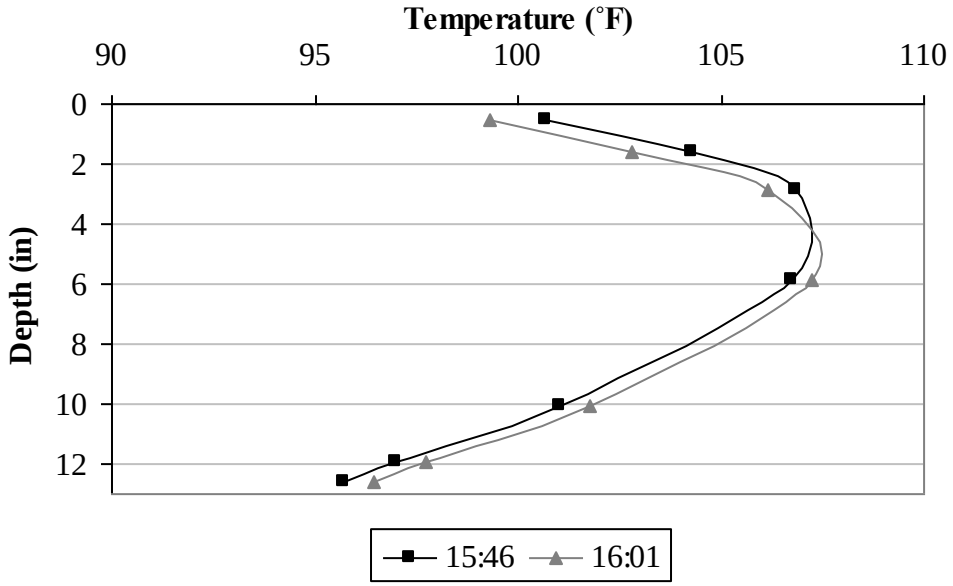

Figure 4.33. Temperature profiles of the restrained and unrestrained slabs at set time based on pressure measurements.

4.4 BUILT-IN CONSTRUCTION GRADIENT

Static strain and pressure data were analyzed during the first 42 hours after construction of the pavement to estimate the set time and the corresponding built-in temperature gradient in the restrained and unrestrained slabs. The results of the two methods are compared and summarized in this section, and the appropriate built-in construction gradient in the JPCP slabs is established.

4.4.1 Set time and corresponding built-in temperature gradient

The set time, built-in temperature gradient, and slab weighted average temperature based on the vibrating wire data and the pressure measurements are summarized in Table 4.5. The set times determined based on the static strain data are longer than those determined based on the static pressure data. The time of set based on the static pressure data takes place approximately 0.83 to 1.17 hours (50 to 90 minutes) after that determined based on the static strain data. The corresponding weighted average slab temperature based on both methods is similar, as is the equivalent linear temperature gradient.

Table 4.5. Set time, built-in temperature gradient and weighted average temperature based on the two methods.

Method	Set Time (hours)[1]	Weighted Average Temperature (˚F)[2]	Equivalent Linear Temperature Gradient (˚F/in)[2]	Type of Slab[3]
Static Strain Measurements	10.83	104.3	0.31	R
	10.92	104.4	0.31	UR
Static Pressure Measurements	10.0	103.6	0.51	R
	9.75	103.6	0.42	UR

[1] After mixing of the concrete
[2] Based on thermocouples located at slab midpanel
[3] R: Restrained; UR: Unrestrained

There are several advantages and disadvantages associated with the procedures followed for determining the set times based on the two methods. The differences are discussed in this section for the purpose of establishing the most suitable method for selecting the time of set and the corresponding built-in temperature gradient for the restrained and unrestrained slabs.

The determination of the set time based on the variation in strain with temperature reflects the time when the concrete starts experiencing movement. Even though this may not reflect the exact time when the concrete sets, the point when the slab starts experiencing deformation reflects the actual time when it actually has sufficient stiffness so that stress will not creep out. This method eliminates the need for going through a determination of the set time using an analysis of the slab surface deformations and the use of prediction models to correlate back to the time when deformation starts taking place.

When carrying out the analysis of the early-age variation in pressure measurements, the following disadvantage is noted. The graphs showing the variations in pressure along the slab/base interface with temperature gradients all showed a slight increase in pressure during the first couple of hours. There is not an explanation for this increase in pressure. After this point, the relationship between pressure and the measured temperature gradient follows the anticipated trends (increased pressure at midpanel and decreased pressure at slab corners with negative temperature gradients in the slabs, and vice versa).

Based on the above, it can be concluded that the time when concrete starts experiencing deformation, as determined based on the static strain sensors, is the most appropriate time to use in establishing the built-in temperature gradient in the slab. Although, the difference between the two methods is not substantially different. Therefore, the corresponding built-in temperature gradient is found to be 0.31˚F/in for the restrained and unrestrained slabs.

4.4.2 Built-in moisture gradient

As previously mentioned in section 4.1.2, it can be assumed that the slab is saturated throughout at the time of set. The equivalent gradient due to moisture will therefore not be included in the determination of the overall built-in construction gradient. However, the moisture profile at the time of set will be used in subsequent sections to evaluate the effect of shrinkage and creep on slab curvature.

4.5 SUMMARY AND CONCLUSIONS

In this chapter, two methods were followed to estimate the set time and the corresponding built-in construction gradient in the slabs. The first method consisted of analyzing the strain measurements in the concrete slabs, and the second method consisted of analyzing the pressure measurements exerted by the slabs on the underlying base layer.

A comparison between the results of the two methods and an analysis of the advantages and disadvantages associated with each method revealed that the time when the concrete starts experiencing deformation, as determined based on the static strain sensors, is the most appropriate time to use in establishing the built-in gradient in the slab. Accordingly, the corresponding built-in temperature gradient is found to be 0.31˚F/in and the weighted average slab temperature is found to be 104.3˚F for the restrained and unrestrained slabs. Moreover, the effect of moisture is neglected in the determination of the overall built-in construction gradient but will be used in subsequent sections to evaluate the effect of shrinkage and creep on slab curvature.

5.0 TEMPERATURE AND MOISTURE CONDITIONS

Daily and seasonal variations in temperature and moisture conditions cause the development of temperature and moisture gradients in the concrete slab. These gradients cause slab curling and warping and upward or downward curvature depending on whether the gradients are negative or positive. However, concrete slabs are not fully free to move and therefore, restraint in slab movement caused by thermal or moisture changes contributes to the development of stresses in concrete pavements. As a result, temperature and moisture gradients affect the long-term performance of concrete pavements.

As previously stated in Chapter 1, the second objective of this research is to examine the effects of seasonal variations in temperature and moisture throughout the slab depth on stress in the slab and to examine the effects of different slab restraining conditions on the slab deformation and stress.

This chapter discusses the daily and seasonal variations in the environmental conditions affecting the performance of the concrete pavement during the first two years after construction of the pavement. This chapter is subdivided into four major sections. The first and second sections present the variation in the temperature and moisture conditions in the pavement system. In the third section, the Enhanced Integrated Climatic Model (EICM) embedded in the new MEPDG is used to evaluate the seasonal changes in the temperature and moisture conditions in the pavement structure and the predicted conditions are compared to the temperature and moisture conditions measured in the field. The last section summarizes the results of the work carried out in this chapter.

5.1 TEMPERATURE MEASUREMENTS IN THE PAVEMENT STRUCTURE

The influence of ambient conditions on pavement temperature is examined in this section. An analysis of the temperature measurements in the concrete slab and underlying layers during the first two years after construction is presented in this section.

5.1.1 Temperature measurements within the concrete slab

The effect of seasonal and daily environmental conditions on temperature measurements within the concrete is examined in this section. The average slab temperature will affect the stress state in the slab as a function of the set temperature. It will also dictate the restraint provided at the undoweled joints since the average slab temperature will influence the crack width at the joint.

The weighted average temperature of the concrete slab follows the same seasonal trends as the ambient temperature, as shown in Figure 5.1. This figure presents the weighted average temperature based on the thermocouple data collected at midpanel during the first two years after construction of the pavement. The highest weighted average temperature reached 105˚F and was recorded in August 2004, shortly after construction and is due to hydration of the concrete. Other than this peak high temperature, the highest weighted average temperature reached 98˚F and was recorded in August 2006 and the lowest weighted average temperature reached 15˚F and was recorded in January 2005. The temperatures recorded by the thermocouples located at the slab edge showed the same weighted average temperature and similar seasonal trends.

During the first two years after construction, the minimum weighted average temperature at midpanel varied between 15°F and 74°F and the maximum weighted average temperature varied between 44°F and 104°F, confirming that the concrete slab experiences large fluctuations in temperature throughout the year. The maximum and minimum monthly ambient and concrete temperatures are both plotted in Figure 5.2. The ambient temperature covers a wider range of values than the concrete temperature.

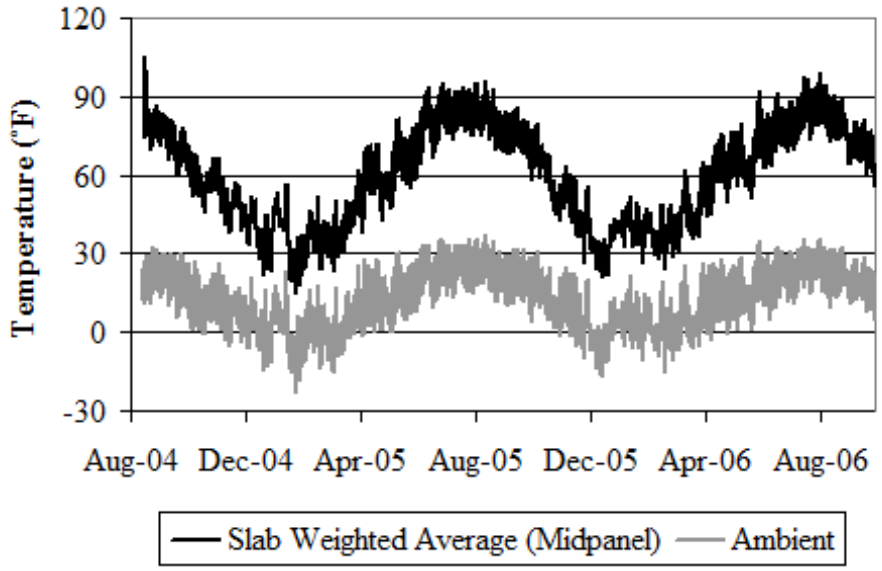

Figure 5.1. Weighted average concrete temperature at slab midpanel during the first two years after construction.

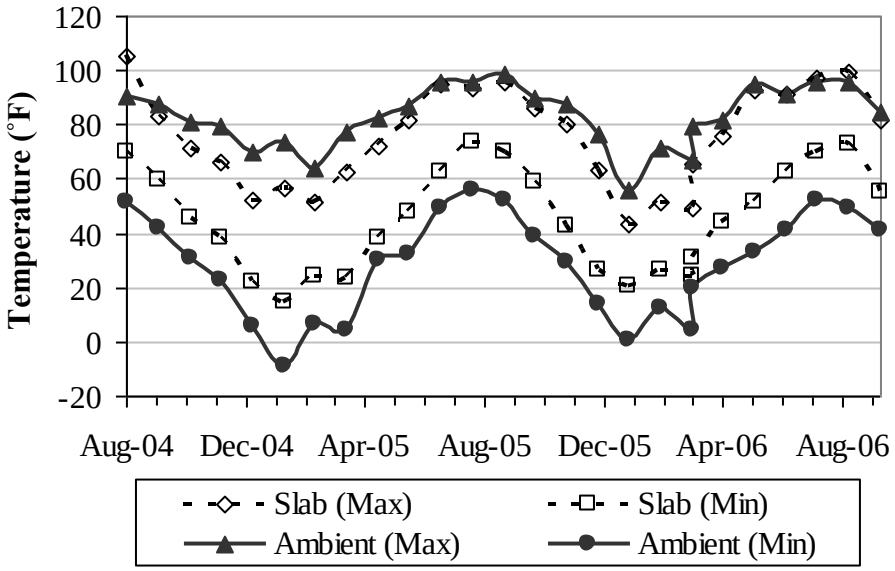

Figure 5.2. Monthly maximum and minimum ambient temperature and weighted average concrete temperature.

The equivalent linear temperature gradients corresponding to the midpanel temperature profiles were calculated based on the equations presented in section 2.3.1. Table 5.1 summarizes the monthly maximum positive and negative equivalent linear temperature gradients within the slab during the first two years after construction, using the temperatures measured at midpanel. The equivalent linear temperature gradient varies between -1.39°F/in and 2.47°F/in throughout the two years. The range of temperature gradient is largest during the spring and summer and smallest during the winter. The time of the day when no gradient is present changes depending on the ambient conditions. In addition, the duration of time when the concrete slab is subjected to a positive temperature gradient is different depending on the climatic conditions. A positive gradient is present for a duration of approximately twelve hours per day during the summer and spring (noon to midnight), a duration of approximately nine hours per day during the fall (10:00 AM to 7:00 PM), and a duration of approximately six hours per day during the winter (noon to 6:00 PM).

Table 5.1. Monthly maximum positive and negative equivalent linear temperature gradients.

Season	Month	Max. Equivalent Linear Temp. Gradient (°F/in)		Month	Max. Equivalent Linear Temp. Gradient (°F/in)	
		Positive	Negative		Positive	Negative
Summer	Aug-04[1]	1.40	-1.28	---	---	---
	Sep-04	1.59	-1.08	---	---	---
Fall	Oct-04	1.48	-1.14	Oct-05	1.62	-1.08
	Nov-04	1.29	-1.06	Nov-05	1.45	-1.21
	Dec-04	1.19	-1.35	Dec-05	1.06	-1.15
Winter	Jan-05	1.13	-1.39	Jan-06	1.47	-1.04
	Feb-05	1.74	-1.09	Feb-06	1.67	-1.29
	Mar-05	2.13	-1.16	Mar-06	2.22	-1.07
Spring	Apr-05	2.42	-1.15	Apr-06	2.11	-1.15
	May-05	2.33	-1.00	May-06	2.47	-1.23
	Jun-05	2.35	-0.99	Jun-06	2.23	-1.17
Summer	Jul-05	2.02	-0.97	Jul-06	2.16	-1.08
	Aug-05	1.99	-1.12	Aug-06	1.98	-1.25
	Sep-05	1.78	-1.28	Sep-06	1.78	-0.97

Notes:
[1] The test section was constructed on August 16, 2004.

5.1.2 Temperature measurements within the underlying layers

This section presents the temperature measurements within the underlying layers throughout the first two years after construction. Determination of temperature in the underlying layers is necessary to characterize the temperature variation in the overall pavement structure and provides insight into the stiffness and support of the underlying layers. As previously discussed, the pavement structure consists of concrete placed on an asphalt treated permeable base (ATPB), which is placed on a granular layer. The variations of temperatures in the ATPB layer are presented first.

The stiffness of the ATPB is largely a function of the temperature of the ATPB throughout the year. Figure 5.3 shows the variation in the temperature in the ATPB during the first two years after construction of the pavement. The mid-depth temperature of the ATPB follows the same trend as the ambient climatic temperature. The ATPB temperature ranged between 29˚F and 92˚F with an average of 39˚F during the winter, 53˚F during the fall, 68˚F during the spring and 78˚F during the summer.

The coldest temperatures were recorded during the periods of December 16 to 29, 2004, January 25 to February 6, 2005 and December 14 to 22, 2005. During these periods, the thermocouples embedded in the ATPB recorded a temperature at or below freezing. This indicates that, during these periods, the ATPB was frozen down to a depth of 14 inches below the pavement surface.

The temperature variations in the layers beneath the base during the first two years after construction of the pavement are shown in Figure 5.4 for the thermocouples located at midpanel. The coldest temperature was recorded during the period between January 25 and February 6, 2005. During that period, the thermocouples within the 2A-subbase recorded temperatures at or close to freezing, implying that the pavement structure was frozen down to a depth of 21 inches. Therefore, the frost depth for this pavement structure in the winter can be estimated to be 21 inches or 1.75 feet.

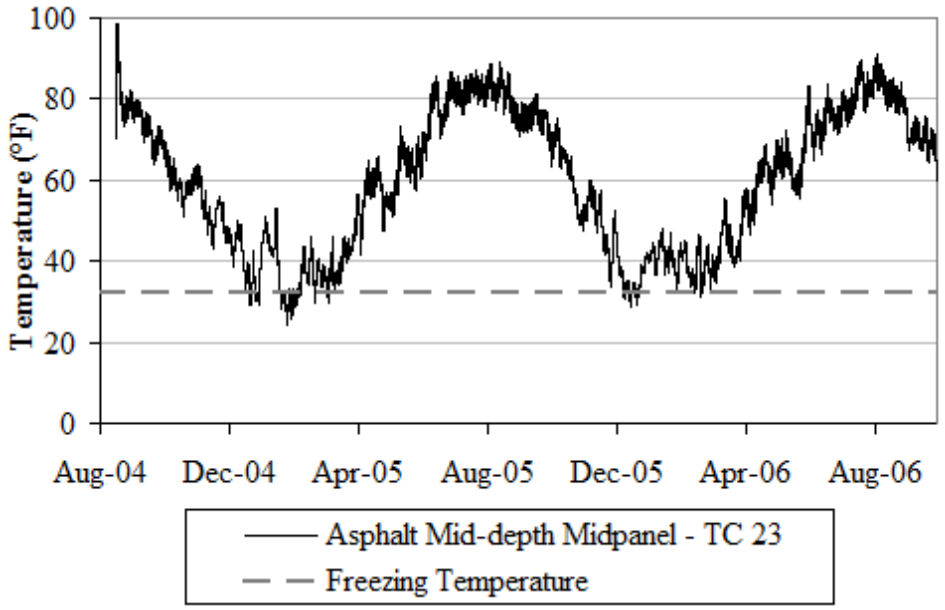

Figure 5.3. ATPB temperature at mid-depth during the first two years after construction.

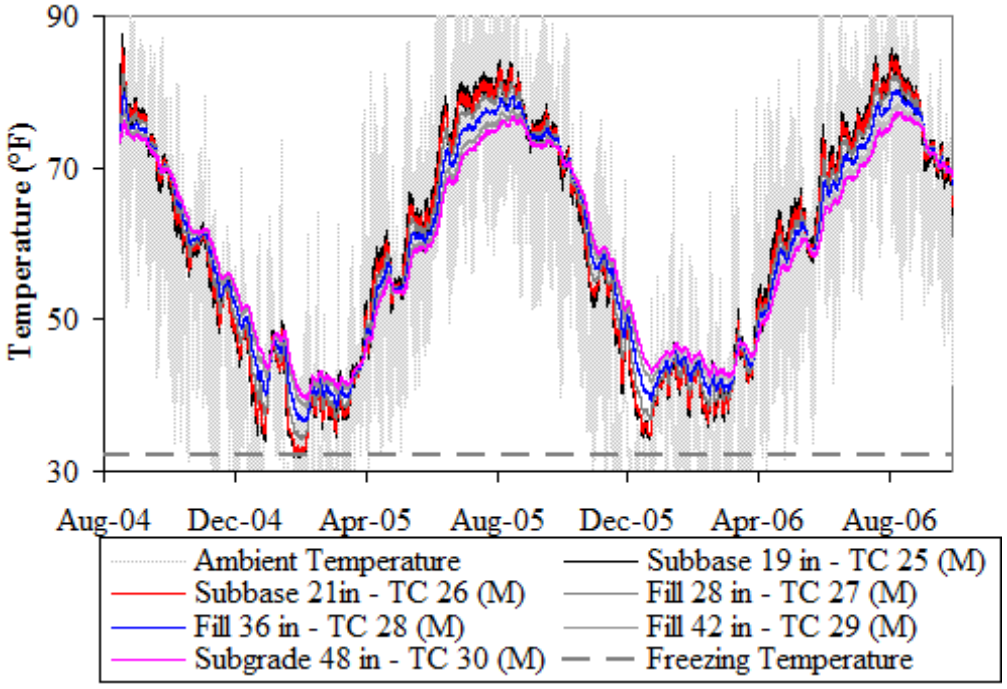

Figure 5.4. Subbase and subgrade temperature during the first two years after construction.

5.1.3 Summary

The weighted average temperature within the pavement structure indicated that the pavement experiences large fluctuations in temperature throughout the year. Both seasonal and daily climatic cycles affect the pavement temperature. Irrespective of the season, the slab is subjected to alternating cycles of negative and positive temperature gradients on a daily basis. The equivalent linear temperature gradients vary between -1.39°F/in and 2.47°F/in throughout the two years after construction. In addition, the midpanel exhibited more variation in temperature than the slab edge.

The frost depth for this pavement structure is 21 inches or 1.75 feet and lasts for approximately two weeks during the winter.

5.2 MOISTURE MEASUREMENTS IN THE PAVEMENT STRUCTURE

As previously discussed, moisture in the pavement structure is another major factor that is known to affect pavement performance. An analysis of the moisture measurements in the concrete slab and underlying layers during the first two years after construction of the pavement is presented in this section.

5.2.1 Moisture measurements within the concrete slab

The variation in moisture content within the concrete follows seasonal trends, as shown in Figure 5.5 and Figure 5.6. These figures present the concrete moisture content based on data collected from the midpanel and edge of the slab during the first two years after construction. The figures show that there are some gaps in the collected data, which are due to communication problems encountered with the data acquisition system.

At both locations, the moisture content increases with increasing slab depth. This is consistent with the conclusions arrived at by Eisenmann and Leykauf (1990) and Janssen (1987) stating that concrete moisture levels vary in the top two inches of a concrete slab and remain

relatively constant at higher levels in deeper portions of the slab. At midpanel and the slab edge, the moisture content of the concrete stabilized three to four weeks after construction and remained relatively constant throughout the remainder of the fall season. The moisture content stabilized to an average value of 80 percent relative humidity in the top two inches, 95 percent at mid-depth and 100 percent in the bottom half of the slab. The moisture content in the upper two inches reached a minimum during the winter, and increased thereafter reaching a maximum during the spring. The moisture content followed the same seasonal trends for the first two years after construction; however, the measured relative humidity during the second year was lower than the first year. This indicates that the moisture content is decreasing with time.

At midpanel, only two sensors were operational during the two-year period. At a depth of 0.7 inch, the moisture content varied between 73 and 81 percent during the first year and between 57 and 65 percent during the second year. At a depth of 1.0 inch, the moisture content varied between 87 and 93 percent during the first year and between 63 and 74 percent during the second year.

As Figure 5.6 shows, moisture content at the slab edge is higher than at midpanel. At this location, four sensors are operational; however, two of the sensors at the bottom of the slab recorded moisture levels higher than 100 percent for the majority of the time. This may be due to possible condensation along the sensor tips. Moisture levels higher than 100 percent are not realistic although the trends recorded by the sensors are consistent with the general observations that moisture levels increase with increasing slab depth. As a result, moisture levels that are higher than 100 percent are assumed to be equal to 100 percent. Throughout the two-year period, the moisture content varied between 90 and 100 percent during the first year and between 82 and 91 percent during the second year at a depth of 1.6 inches, between 93 and 100 percent during the first year and between 84 and 95 percent during the second year at a depth of 6.6 inches. Below 10.5 inches, the moisture content is at 100 percent.

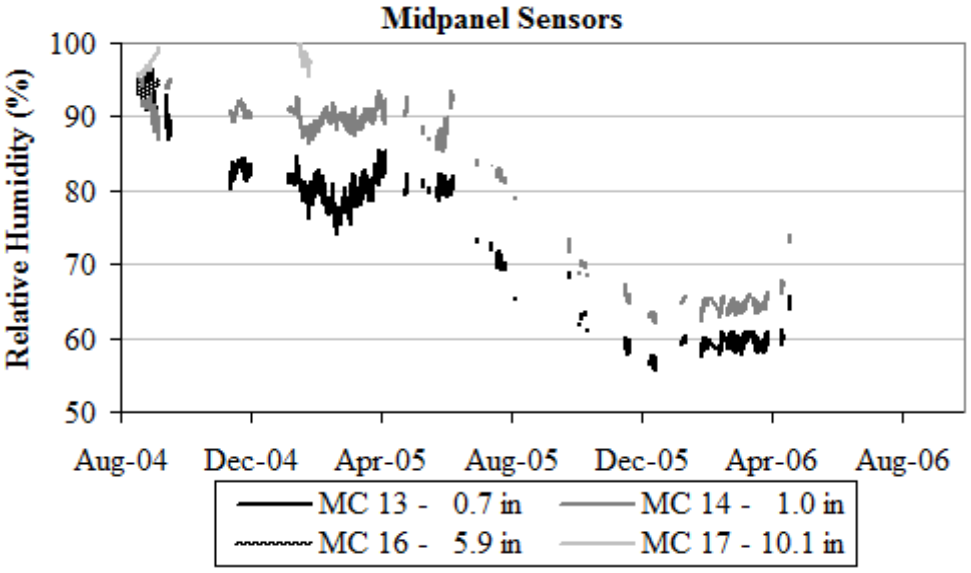

Figure 5.5. Concrete moisture content at midpanel during the first two years after construction.

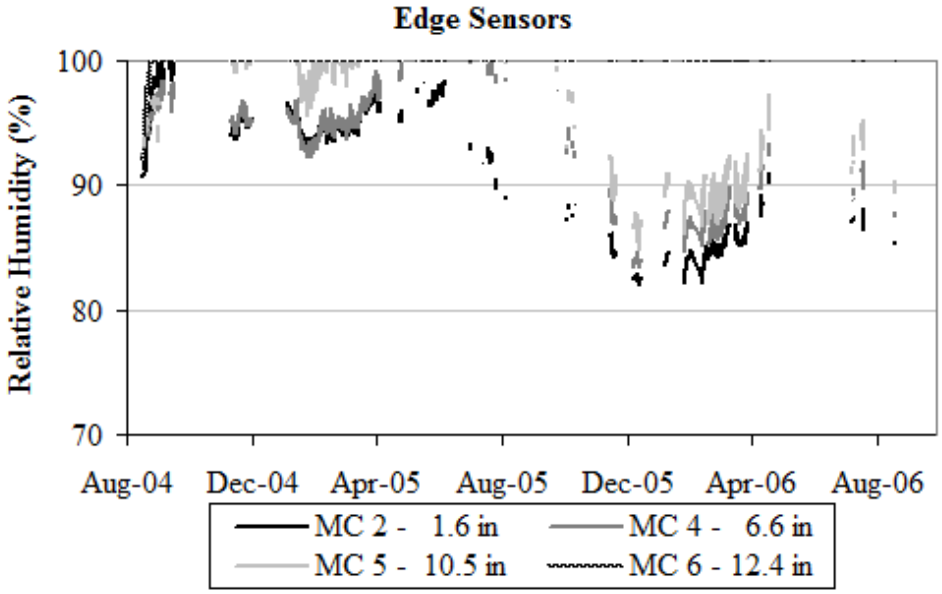

Figure 5.6. Concrete moisture content at slab edge during the first two years after construction.

The effect of the variations in ambient relative humidity and the frequency of occurrence of precipitation events on moisture measurements within the concrete is examined. In this analysis, the moisture content measured within the top two inches of the slab was considered, since the moisture content at deeper portions of the slab were not affected by changes in ambient climatic conditions.

During the first two years after construction, the ambient relative humidity ranged between 20 and 100 percent, with an average range of 60 to 80 percent. The minimum and maximum concrete moisture content was compared to the ambient relative humidity and is presented in Figure 5.7. The figure shows that the concrete moisture content in the top two inches of the slab is not highly affected by variations in the ambient relative humidity.

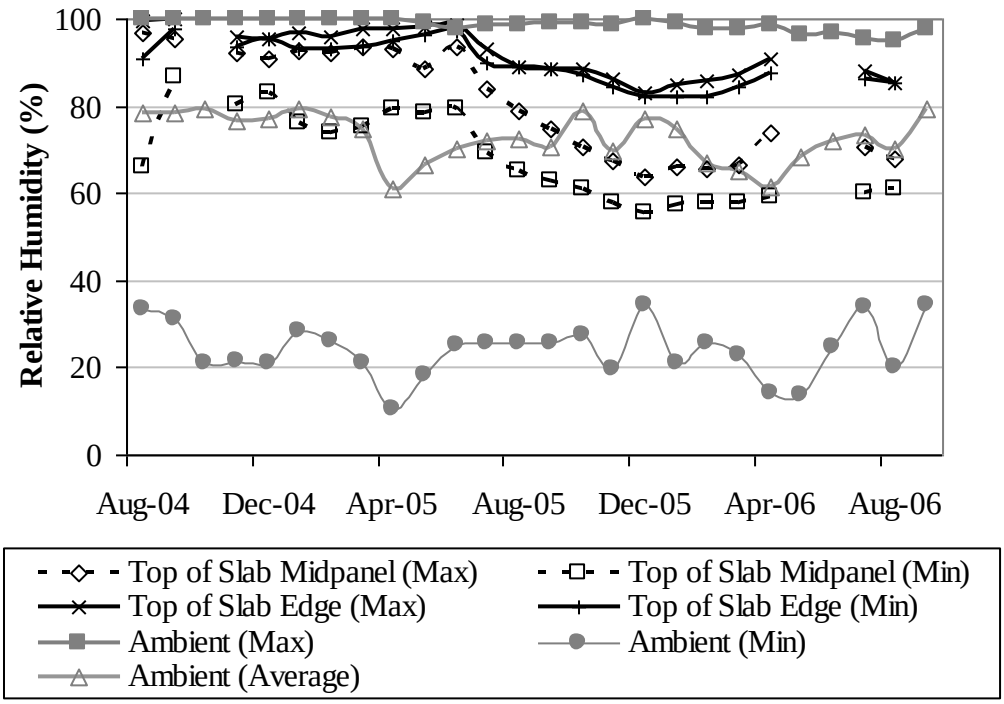

Figure 5.7. Monthly maximum and minimum concrete moisture content at midpanel and slab edge in comparison to ambient relative humidity.

The onsite weather station does not provide precipitation readings, therefore daily and hourly precipitation recorded by the weather station located at the Allegheny County Airport (ACA) are used to represent the field conditions. ACA was selected because it is the weather station closest to the project site, located approximately 25.7 miles from the project site. The precipitation data from other weather stations was also analyzed and compared to the ACA data; this will be presented in detail in section 5.3.3. The precipitation data is obtained from the website maintained by the National Oceanic & Atmospheric Administration Satellite and Information Service and the National Climatic Data Center (www.ncdc.noaa.gov). During the first two years after construction, the seasonal average rainfall precipitation varied between 2.7 and 3.6 inches per month. The highest precipitation was recorded during the summer and the lowest during the fall. The frequency of occurrence of rain events does not vary much throughout the two-year period. During the summer, a monthly average of 12 days with rain events was recorded compared to a monthly average of 14 days with rain events during the remaining seasons. The minimum and maximum concrete moisture content was compared to the monthly precipitation and the frequency of occurrence of rain events in Figure 5.8 and Figure 5.9. The moisture content in the upper portion of the slab increases during the spring and summer seasons. The graphs do not show a clear relationship between monthly precipitation or frequency of rain events and the moisture content in the upper portion of the slab. This may be due to the high relative humidity in the slab.

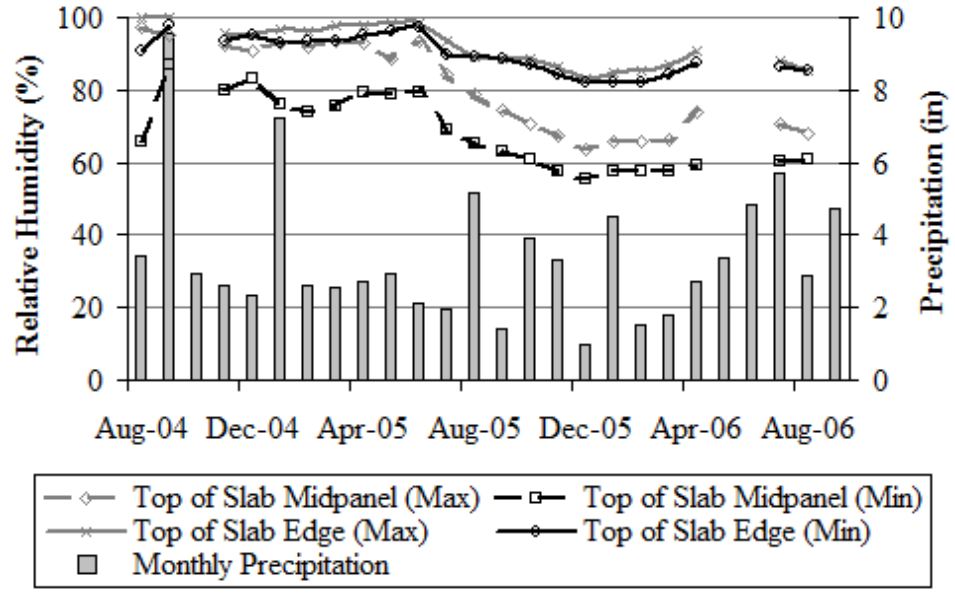

Figure 5.8. Monthly maximum and minimum concrete relative humidity at midpanel and slab edge in comparison to precipitation.

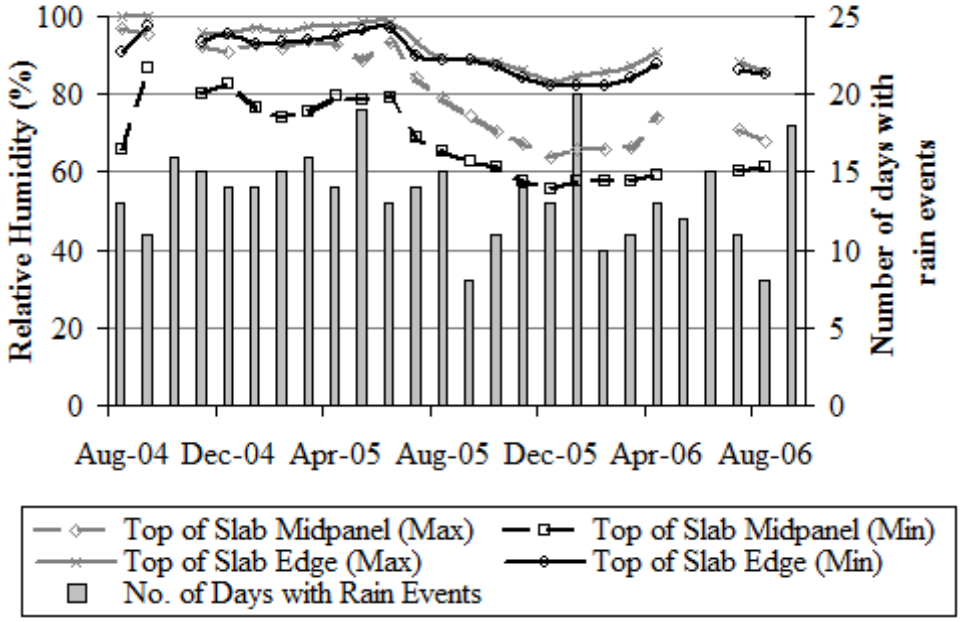

Figure 5.9. Monthly maximum and minimum concrete relative humidity at midpanel and slab edge in comparison to frequency of occurrence of daily rain events.

Based on Figure 5.5 and Figure 5.6, the relative humidity in the top two inches of the concrete slab varies seasonally. However, a comparison between concrete relative humidity and the ambient climatic conditions showed no correlation (see Figure 5.8 and Figure 5.9). Therefore, seasonal variations in concrete moisture content will be investigated to explore a possible correlation between the concrete moisture content and climatic conditions. Since the effect of rainfall on concrete moisture is not instantaneous, an analysis was performed while considering a time period of ten days. Profiles showing the variation in relative humidity across the slab depth at different times of the day and during different seasons are presented next.

Profiles showing the relative humidity at three-hour intervals two days after construction are presented in Figure 5.10 and Figure 5.11, at midpanel and slab edge. The profiles representing the midpanel are closer together than those at slab edge; however, the variations at any depth and location are within 2 percent of each other. This implies that daily variations are insignificant and that a profile at any time of the day can be selected as representative of the whole day.

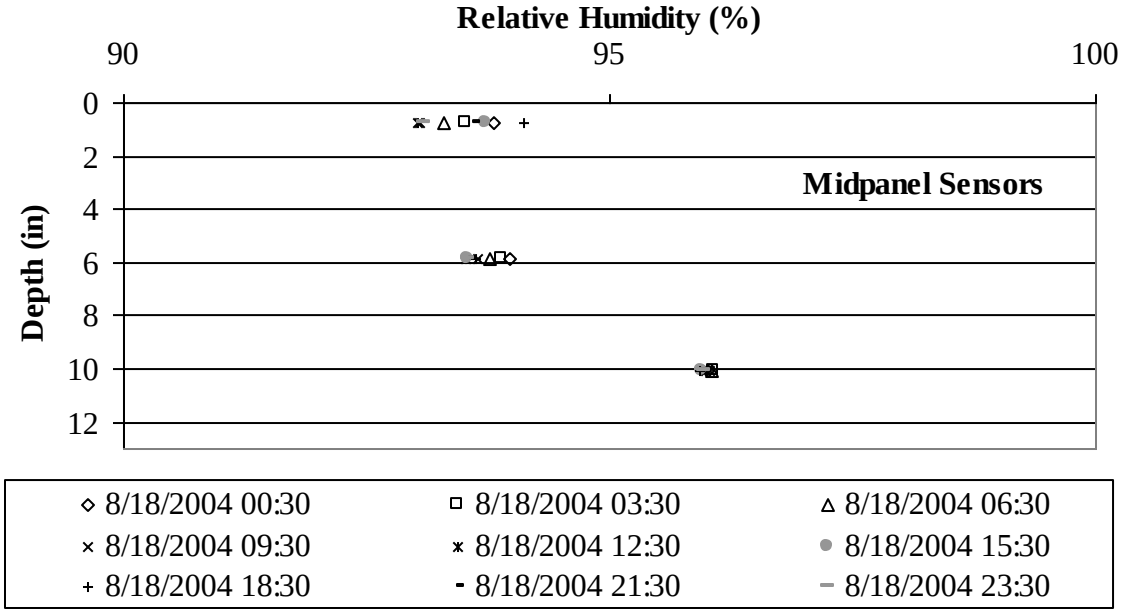

Figure 5.10. Midpanel concrete relative humidity at three-hour intervals two days after construction.

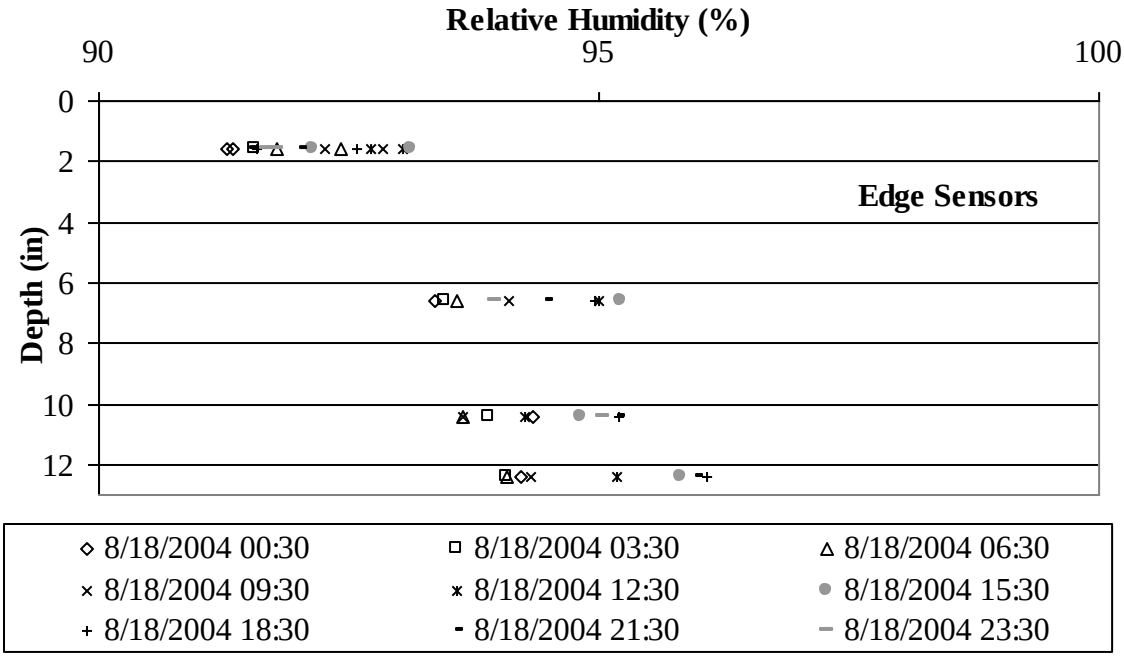

Figure 5.11. Edge concrete relative humidity at three-hour intervals two days after construction.

Figure 5.12 and Figure 5.13 show the daily relative humidity at midpanel and slab edge for a ten-day period during the summer 2004 season, shortly after construction. The vertical dashed lines in the figures represent points in time when rain events of total rainfall exceeding 0.1 inch occurred. At both locations, the relative humidity is relatively constant, with slight variations in the top portion of the slab. In the top portion of the slab, the relative humidity reached 90 to 95 percent at midpanel and 95 to 99 at the slab edge.

Concrete relative humidity profiles representing each day were plotted to compare the moisture variation during the different seasons. The relative humidity profiles representing the midpanel and slab edge relative humidity for the summer 2004 season (starting on August 16, 2004) are provided in Figure 5.14 and Figure 5.15. At midpanel, the concrete relative humidity varied between 87 and 96 percent at the slab top, between 93 and 95 percent at mid-depth, and between 95 and 99 percent at the slab bottom. At the slab edge, the concrete relative humidity varied between 90 and 99 percent at the slab top, between 92 and 97 percent at mid-depth, and between 92 and 100 percent at the slab bottom.

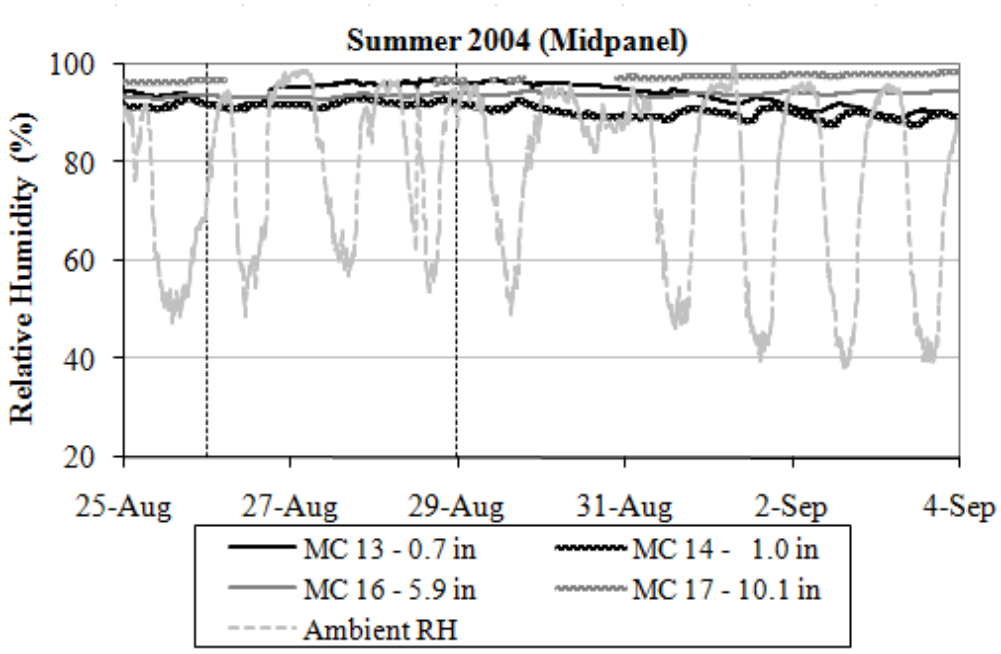

Figure 5.12. Midpanel concrete relative humidity for a ten-day period representing the summer of 2004.

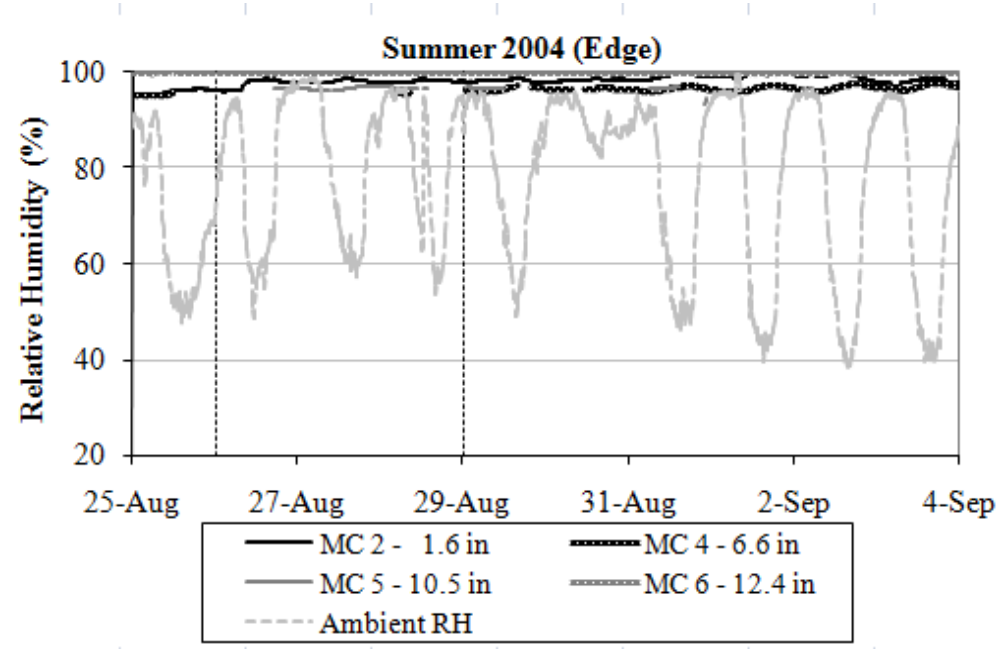

Figure 5.13. Edge concrete relative humidity for a ten-day period representing the summer of 2004.

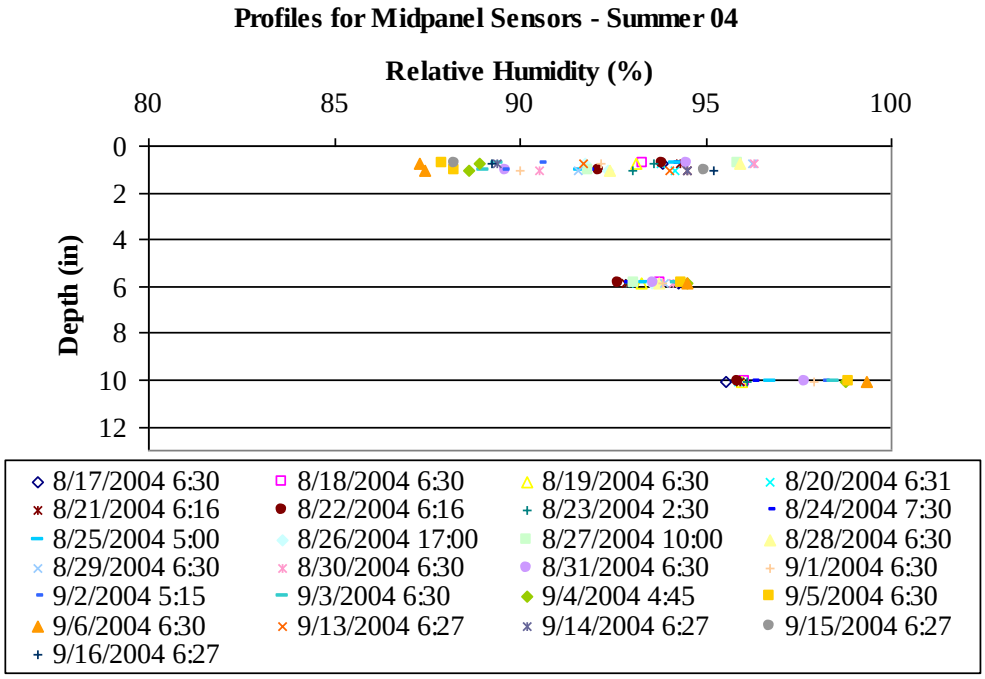

Figure 5.14. Midpanel concrete relative humidity at one-day intervals during the summer of 2004.

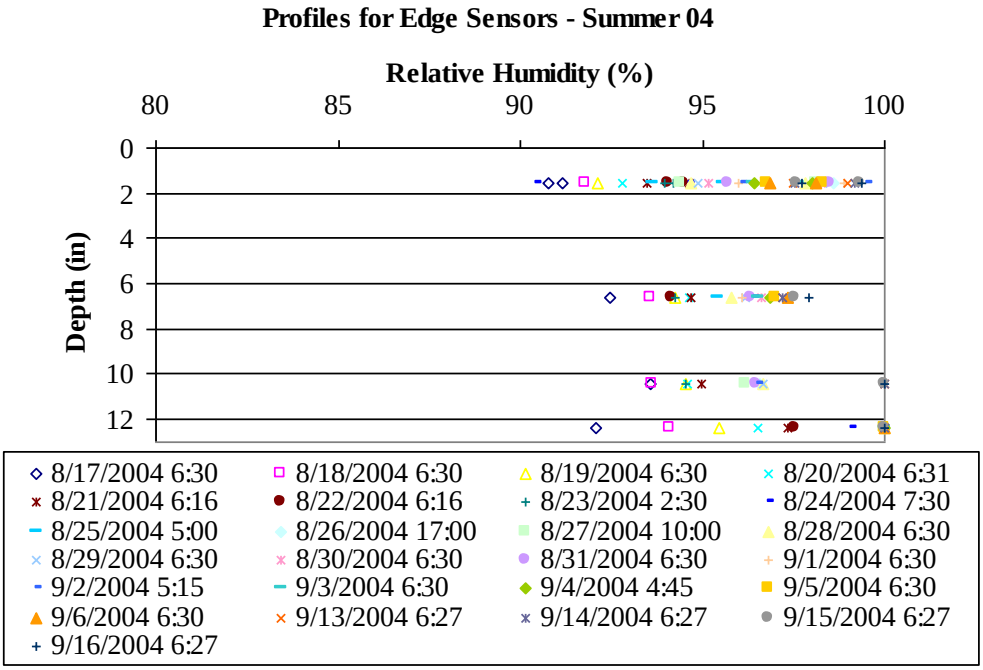

Figure 5.15. Edge concrete relative humidity at one-day intervals during the summer of 2004.

Figure 5.16 and Figure 5.17 present the daily concrete relative humidity at midpanel and slab edge for a ten-day period representing the fall of 2004, a couple of months after construction. The midpanel sensors show variations between 80 and 92 percent, which is a relatively large difference considering that the difference in depth between the two sensors is only 0.3 inch. There is no indication of malfunction or erroneous readings on either of the two sensors, and therefore, both will be used as representative of the moisture at midpanel. These readings further confirm that moisture content can vary significantly in the top two inches of the slab. At the slab edge, relative humidity is approximately 92 percent at the top of slab, 94 percent at mid-depth, and it is saturated at the bottom.

Similar trends were observed for the remaining seasons. The relative humidity of the concrete in the slab increases slightly after precipitation events with the increase being more pronounced at the top of the slab and not substantially affected at mid-depth. Relative humidity also increases with increasing depth at both midpanel and slab edge, with a higher rate of variation in the top half of the slab compared to the bottom half.

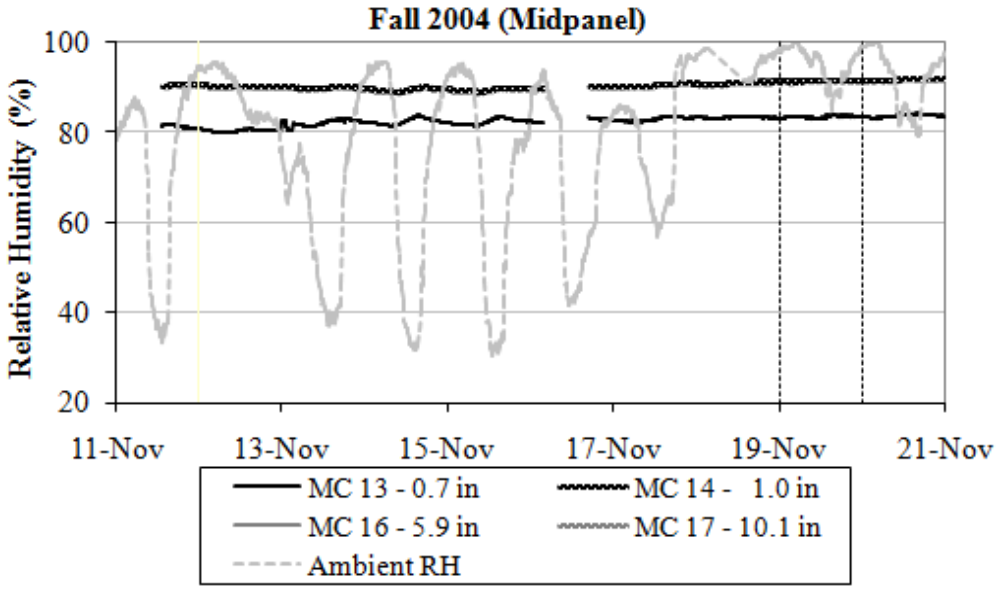

Figure 5.16. Midpanel concrete relative humidity for a ten-day period representing the fall of 2004.

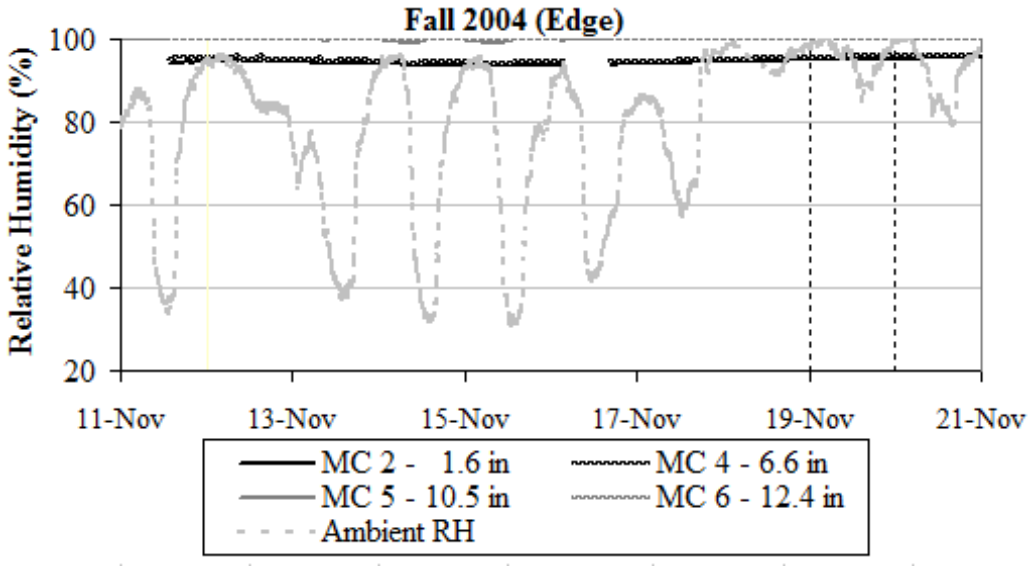

Figure 5.17. Edge concrete relative humidity for a ten-day period representing the fall of 2004.

The trends observed for the second year after paving are similar to those observed for the first year. Figures showing the daily moisture levels at midpanel and slab edge for ten-day periods representing the remaining seasons (fall 2005, winter 2006, spring 2006 and summer 2006) are included in the three-year report (McCracken et al. 2008). The average concrete moisture content was calculated for every climatic season during the two years following the construction of the pavement. The averages of the data recorded by the midpanel and edge sensors are presented Figure 5.18 and Figure 5.19. The figures show that the concrete relative humidity increases with increasing slab depth. The rate of increase is higher in the top portion of the slab (at midpanel) compared to the bottom portion of the slab (at the slab edge). The relative humidity in the concrete is higher along the edge of the slab than at midpanel, which is justified by the proximity to the joints. The relative humidity measured during the second year after construction is lower than that recorded during the first year after construction. This is observed at both midpanel and slab edge. At the bottom of the slab, the concrete relative humidity is at 100 percent throughout the two years and is not affected by variations in seasonal climatic conditions. There is a clear seasonal trend in the upper portion of the slab with the relative humidity increasing during the spring and summer and decreasing during the fall and winter. This occurs at midpanel and the edge.

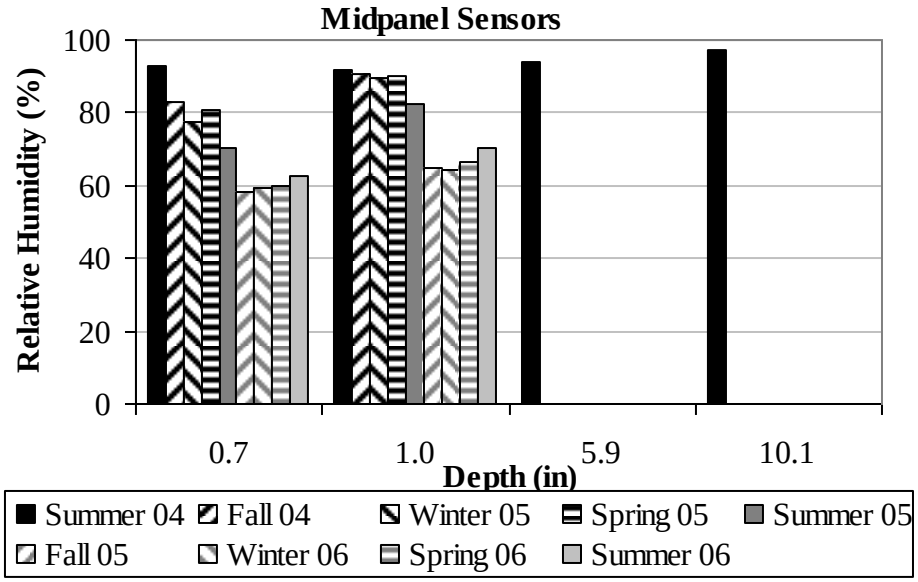

Figure 5.18. Seasonal average midpanel concrete relative humidity.

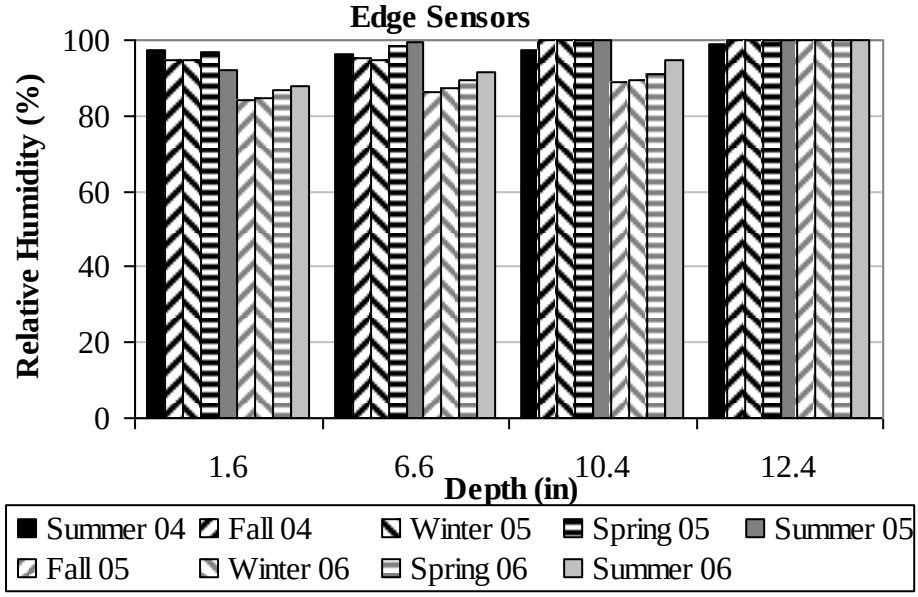

Figure 5.19. Seasonal average edge concrete relative humidity.

5.2.2 Moisture measurements within the granular layers

An analysis of the data collected from the TDR system showed that the probes installed in this project are not appropriate in soils where conductivity is higher than 0.14 Siemens/m. According to the data collected, the soil conductivity reaches levels higher than 0.14 Siemens/m during the spring and summer. These levels of soil conductivity were not anticipated at the time of selection and installation of the TDR probes (Asbahan et al. 2006; McCracken et al. 2008). As a result, the TDR system does not allow for a proper analysis of moisture content in the granular layers.

The volumetric moisture content of the granular layers corresponding to full saturation can be estimated using available literature based on the material properties. The procedure is detailed in section 5.3.2 of this chapter and the volumetric moisture contents corresponding to 100 percent saturation are 27 percent for the subbase, 28 percent for the fill, and 19 percent for the subgrade. During the two-year period, the volumetric moisture content measured by the TDRs varied between 5 and 90 percent for the different layers. This indicates that the granular layers are in wet to saturated conditions during most of the two-year period and they are below saturation during the period extending between March and October of the year 2005, representing the spring and summer seasons.

5.2.3 Summary

The concrete moisture content shows the same seasonal trends irrespective of the location of the sensor (edge or midslab) in the concrete slab. The concrete moisture content reaches minimum values during the winter and maximum values during the spring. The seasonal trends are similar for both years after construction. However, the moisture content during the second year is lower than those measured during the first year and the moisture content measured at the slab edge is higher than that at midpanel.

At midpanel, the relative humidity in the top two inches of the slab varies between 73 and 93 percent during the first year and between 57 and 74 percent during the second year. At the slab edge, the concrete the relative humidity in the top two inches of the slab varied between 90 and 100 percent during the first year and between 82 and 91 percent during the second year. At

mid-depth, the relative humidity varied between 93 and 100 percent during the first year and between 84 and 95 percent during the second year and at the bottom of the slab, the relative humidity is at 100 percent during the two-year period.

Daily variations in concrete relative humidity are insignificant; however, the concrete relative humidity in the top two inches of the slab varies seasonally, and increases during the spring thaw periods. The moisture content is not affected by variations in the ambient relative humidity. The frequency of occurrence of rain events does not vary much throughout the two years and therefore does not directly affect the concrete moisture levels in the top portion of the slab.

The TDR probes installed in the granular layers do not provide consistent readings and do not allow for a proper analysis of moisture content. However, based on the available data, it can be concluded that the granular layers are in wet to saturated conditions during most of the two-year period.

5.3 TEMPERATURE AND MOISTURE PREDICTIONS IN THE PAVEMENT STRUCTURE

Models have been developed by researchers to estimate the variation in temperature and moisture in the pavement structure based on changes in ambient climatic conditions. The most recent modeling tool incorporating the effects of ambient conditions on the pavement material properties and on the infiltration through the pavement structure has been embedded in the new MEPDG and is referred to as the Enhanced Integrated Climatic Model (EICM) (ARA 2004).

The seasonal variations in ambient climatic conditions and the accompanying temperature and moisture measurements in the pavement structure were presented in the three previous sections of this chapter. In this section, the pavement structure will be modeled using the EICM to estimate the temperature and moisture conditions in the pavement structure. Climatic data from the onsite weather station and from other weather stations close to the site will be used as inputs. The predicted conditions will then be compared to those measured in the field to validate the EICM predictions. First, a general overview of the EICM is presented. This is followed by the characterization of the pavement materials and a brief summary of the data

collected by the climatic weather stations close to the site. Finally, the predicted temperature and moisture conditions inside the pavement structure are compared to those measured in the field.

5.3.1 General overview

The new MEPDG uses the EICM as a climatic modeling tool to account for changes in temperature and moisture conditions inside the pavement structure. The EICM simulates changes in the moisture, temperature and material properties (as a function of the temperature and moisture conditions) of the pavement and subgrade materials as the ambient climatic conditions fluctuate over the design life of the pavement. The EICM is a combination of three separate models that evaluate the effects of heat and moisture flow in a one-dimensional direction through the pavement structure (ARA 2004). The three models composing the EICM are:

- The Climatic-Materials-Structural Model developed at the University of Illinois (Dempsey et al., 1985).
- The CRREL Frost Heave and Thaw Settlement Model developed at the United States Army Cold Regions Research and Engineering Laboratory (Guymon, et al., 1986).
- The Infiltration and Drainage Model developed at Texas A&M University (Lytton et al., 1990).

The EICM predicts temperature, resilient modulus adjustment factors, pore water pressure, water content, frost and thaw depth, frost heave, and drainage throughout the entire pavement structure. The climatic conditions over the pavement life are based on a climatic database containing hourly data from 800 weather stations from across the United States. The climatic database is obtained from the National Climatic Data Center (NCDC) and is included with the EICM. The ambient climatic conditions include sunshine, rainfall, wind speed, temperature, and relative humidity. The latest version of the EICM is fully embedded in the MEPDG and performs all calculations internally (ARA 2004). The results obtained from the EICM analysis include the following:

- a set of adjustment factors for unbound material layers that account for the effects of environmental parameters and conditions such as moisture content changes, freezing, thawing, and recovery from thawing,
- in-situ temperatures at the midpoints of each bound layer,
- temperature profiles within the asphalt and concrete layers (at eleven evenly spaced points through the thickness of the concrete) for every hour, and
- average monthly moisture contents for each layer in the pavement structure.

The output from the EICM is used by the structural response models and performance prediction models of the MEPDG to evaluate the performance of the trial design pavement over the design life. When the MEPDG uses the damage accumulation model, the design analysis period is divided into monthly time increments to analyze the proposed pavement structure. Each month is then subdivided into two-hour periods to establish the temperature profiles in the slab. For each time increment, the equivalent linear temperature difference through the concrete slab is accounted for in increments of 2°F for both positive (daytime) and negative (nighttime) top-to-bottom temperature differences. In addition, all other factors that affect pavement response and damage are held constant within each time increment; they include: concrete strength and modulus, base modulus, subgrade modulus and joint load transfer across transverse and longitudinal joints. For each time increment, critical stresses, strains and deflections are determined along with damage accumulated during that time increment.

5.3.2 Material characteristics

The characteristics of the pavement materials influence the performance of the pavement due to their effects on the load-carrying capacity of the pavement structure. These characteristics include the susceptibility of the materials to moisture and freeze-thaw, drainabiltiy of the materials and infiltration potential. The load-carrying capacity of the pavement is affected by changes in the resilient modulus of the pavement materials. These are dependent on the variations in temperature of the materials and variations in moisture content in the underlying granular layers. Soil properties affecting variations in water content include gradation, Atterberg limits and suction parameters. The relationship between soil suction and soil moisture content

can be defined by establishing representative soil-water characteristic curves (SWCC) for the different layers constituting the pavement. The SWCC allows the prediction of changes in volume and shear strength of soil with changes in moisture content (Larson and Dempsey 1997; ARA 2004). In this section, the relevant characteristics of the existing subgrade, fill material, subbase material, asphalt treated permeable base and concrete are presented. More details regarding the properties of each of these materials and the methods through which the properties were obtained are included in the construction report (Wells et al. 2005).

Prior to construction, a subsurface investigation was carried out for the project site. The investigation included the execution of nineteen borings along the proposed alignment of the roadway. The results indicated that the existing subgrade can be classified as an A-6 material based on the AASHTO classification system, which constitutes a fair to poor subgrade material. The gradation of the existing subgrade material was obtained from a sieve analysis of samples obtained from the field and is presented in Figure 5.20. According to the AASHTO Soil Classification System, A-6 material can have a plasticity index of up to 11. As a result, in accordance with PennDOT construction specifications, it was recommended to subcut two feet of the existing material and fill with more suitable material. The excavated area was backfilled using a gap-graded soil and aggregate mixture, containing a significant amount of 206 rock, which included large stone with diameters as large as 22 inches (Wells et al. 2005).

Since no additional data is available regarding the fill material, it is assumed that it possesses the same characteristics as the PennDOT Class 2A subbase material, except for the gradation. Assuming the fill has the same plasticity characteristics as the subbase material and a smaller amount of fines, it can be classified as an A-1 material based on the AASHTO soil classification system. Such a material possesses the gradation properties presented in Table 5.2. The gradation of the fill material was plotted based on the assumed values and is presented in Figure 5.20 along with that of the subgrade.

The subbase consists of slag material meeting the gradation requirements of the PennDOT Class 2A material specifications, listed in PennDOT Publication 408 (Wells et al. 2005). The upper and lower limits of the gradation requirements of the specifications are also shown in Figure 5.20. Based on the AASHTO soil classification system, this material satisfies

the gradation requirements of type A-1, A-2 or A-3 material. However, assuming that the major constituent material in it is non-plastic silty or clayey gravel and sand, it can be classified as A-2 material. Such material can have a plasticity index of 10.

In addition, the depth to the water table and to bedrock were identified based on the results of the geotechnical investigation. In some of the borings, rock layers and water tables were not detected. On average, the depth to either a layer of bedrock or a water table was found to be at least 10 ft (Wells et al. 2005).

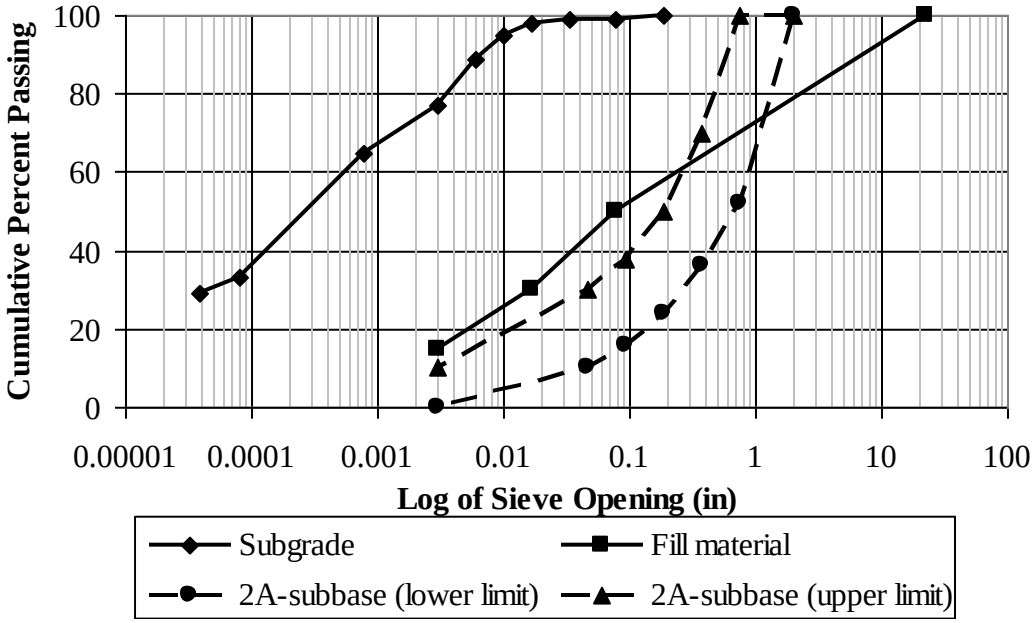

Figure 5.20. Gradations of the existing subgrade, fill and subbase materials.

Table 5.2. Assumed properties of the fill material based on AASHTO A-1 material classification.

Material property	Range of Values
Percent passing No. 200 sieve	Maximum 15 %
Percent passing No. 40 sieve	Maximum 30 %
Percent passing No. 10 sieve	Maximum 50 %
Liquid Limit	N/A
Plasticity Index	Maximum 6

The asphalt treated permeable base layer is composed of a coarse aggregate conforming to PennDOT A57 specifications, a fine aggregate conforming to PennDOT B3 specifications and a PG 64-22 binder (Wells et al. 2005). The proportions of the mixture are provided in section 3.5 and the gradation of the open-graded aggregate is provided in Figure 5.21.

Thermal properties that control the heat flow through the pavement system include the surface shortwave absorptivity, thermal conductivity and heat or thermal capacity. The surface shortwave absorptivity correlates to the amount of energy that is absorbed by the pavement surface. Lighter and more reflective surfaces tend to have lower absorptivity levels. The thermal conductivity refers to the quantity of heat that flows normally across a surface of unit area per unit time and per unit of temperature gradient. This parameter varies when water content is high. The heat capacity reflects the actual amount of heat energy necessary to change the temperature of a unit mass by one degree. The thermal properties can be determined by laboratory testing. When laboratory data is not available, the properties are determined based on typical values available in the literature (ARA 2004). For this project, the thermal properties were determined based on typical values for the granular and stabilized materials making up the pavement structure and are presented in Table 5.3.

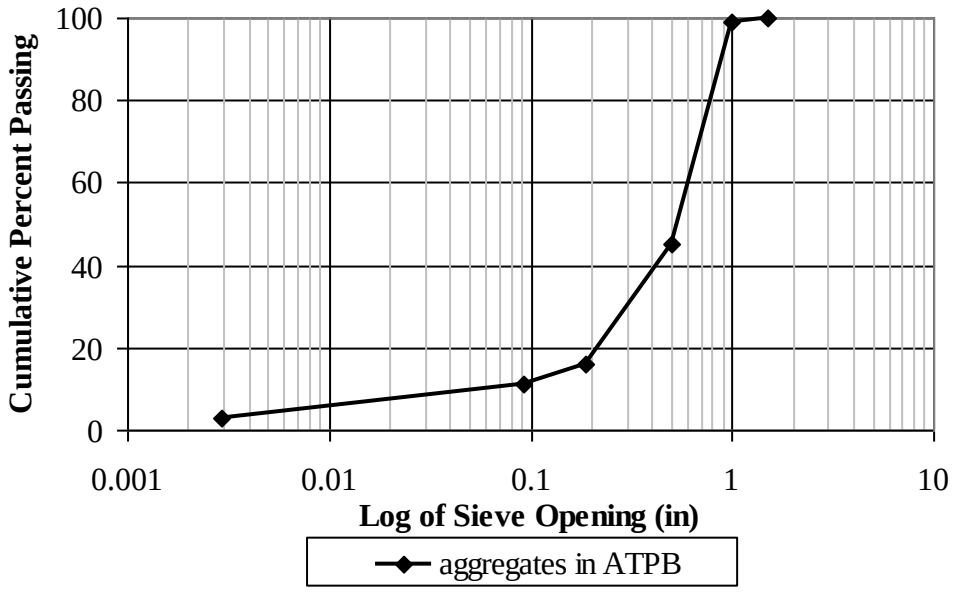

Figure 5.21. Gradation of the open-graded aggregates used in the ATPB.

Table 5.3. Thermal properties of the pavement materials.

	Surface Shortwave Absorptivity	Thermal conductivity, Btu/(ft)(hr)(˚F)	Heat capacity, Btu/(lb)(˚F)
Concrete	0.85	1.25	0.28
ATPB	---	0.62	0.31
Subbase	---	0.20	0.18
Fill	---	0.30	0.18
Subgrade	---	0.18	0.18

The material properties are used to establish soil-water characteristic curves (SWCC) representative of the different layers constituting the pavement structure. The SWCC is the variation of water storage capacity within the macro- and micro- pores of a soil, with respect to suction (Larson and Dempsey 1997; ARA 2004). The parameters of interest in the determination of the mass-volume parameters include the specific gravity, G_s, the maximum dry density, γ_{dmax}, and the optimum gravimetric moisture content, w_{opt}. These parameters are determined for the pavement materials and they are presented in the following paragraphs.

The specific gravity can be determined by laboratory testing. When laboratory testing was not conducted, the specific gravity can be estimated based on the amount of fines and plasticity of the material. The relationship described by Equation 5-1 is provided in the MEPDG documentation for the estimation of the specific gravity of unbound materials.

$$G_s = 0.041(P_{200}.PI)^{0.29} + 2.65 \qquad \text{(Equation 5-1)}$$

where: P_{200} = Percentage of material passing the No. 200 sieve

PI = Plasticity index

The optimum gravimetric water content and the maximum dry unit weight of soils can also be determined based on the gradation and plasticity of the material. The relationships adopted by the MEPDG are presented herein. The first step involves estimating the optimum saturation level, S_{opt}, and the optimum gravimetric moisture content, w_{opt}, as shown in Equation 5-2 to Equation 5-4.

$$S_{opt} = 6.752\left(P_{200}.PI\right)^{0.147} + 78 \qquad \text{(Equation 5-2)}$$

$$w_{opt} = 1.3\left(P_{200}.PI\right)^{0.73} + 11 \quad \text{if} \quad P_{200.}.PI > 0 \qquad \text{(Equation 5-3)}$$

$$w_{opt(T99)} = 8.6425\left(D_{60}\right)^{-0.1038} \quad \text{if} \quad P_{200.}.PI = 0 \qquad \text{(Equation 5-4)}$$

If layer is not a base course: $w_{opt} = w_{opt\,(T99)}$

If layer is a base course: $w_{opt} = w_{opt\,(T99)} - \Delta w_{opt}$

Where: $\Delta w_{opt} = 0.0156\left[w_{opt\,(T99)}\right]^2 - 0.1465 w_{opt\,(T99)} + 0.9$

D_{60} = effective grain size corresponding to 60% passing by weight

This is followed by an estimation of the maximum dry unit weight of the material, γ_{dmax}, based on the maximum dry unit weight of the compacted material, $\gamma_{dmax\ compacted}$, as shown in Equation 5-5. Depending on the level of compaction of layer, the maximum dry unit weight of the layer is estimated, as shown in Equation 5-6a and 5-6b.

$$\gamma_{d\ \max\ comp} = \frac{G_s \gamma_{water}}{1 + \dfrac{w_{opt} G_s}{S_{opt}}} \qquad \text{(Equation 5-5)}$$

$$\gamma_{d\ \max} = \gamma_{d\ \max\ comp} \quad \text{If layer is a compacted material} \qquad \text{(Equation 5-6a)}$$

$$\gamma_{d\ \max} = 0.90\gamma_{d\ \max\ comp} \quad \text{If layer is a natural in-situ material} \qquad \text{(Equation 5-6b)}$$

The material properties determined based on the previous equations are then used to estimate the optimum saturation level, S_{opt}, the optimum volumetric moisture content, θ_{opt}, and the volumetric moisture content at saturation level, θ_{sat}. These parameters are calculated internally in the EICM using Equations 5-7 to 5-9.

$$\theta_{opt} = \frac{w_{opt} \gamma_{d\ \max}}{\gamma_{water}} \qquad \text{(Equation 5-7)}$$

$$S_{opt} = \frac{\theta_{opt}}{1 - \dfrac{\gamma_{d\ \max}}{\gamma_{water} G_s}} \qquad \text{(Equation 5-8)}$$

$$\theta_{sat} = \frac{\theta_{opt}}{S_{opt}}$$ (Equation 5-9)

In addition, the saturated hydraulic conductivity, k_{sat}, is needed to determine the transient moisture profiles in compacted unbound materials and to compute their drainage characteristics. The saturated hydraulic conductivity can be estimated based on the particle size distribution, as presented in Equations 5-10a and 5-10b. The conductivities calculated using these equations are given in units of ft/hr.

If $0 \le P_{200.}.PI < 1$ and $D_{60} < 0.75\ in$:

$$k_{sat} = 118.11x10^{\left[-1.1275(\log D_{60}+2)^2+7.2816(\log D_{60}+2)-11.2891\right]}$$ (Equation 5-10a)

If $0 \le P_{200.}.PI < 1$ and $D_{60} > 0.75\ in$, set $D_{60} = 0.75\ in$ and use Equation 5-10a

If $P_{200.}.PI \ge 1$, $k_{sat} = 118.11x10^{\left[0.0004(P_{200}PI)^2-0.0929(P_{200}PI)-6.56\right]}$ (Equation 5-10b)

The SWCC defines the relationship between water content and suction for a given soil (ARA 2004; Fredlund et al. 1995). The most accurate method of determining the parameters required to develop the SWCC is to carry out testing to obtain direct measurements of suction and volumetric water content, in addition to testing for the characterization of the specific gravity and maximum dry unit weights of the material. In cases when such tests are not carried out, the parameters required to develop the SWCC may be estimated by using correlations with gradation properties of the material. The correlations are obtained by non-linear regression analyses and are provided in the MEPDG. The relationships providing the four parameters needed to develop the SWCC are presented in Equations 5-11 to 5-14.

If $P_{200.}.PI > 0$:

$$a_f = \frac{0.00364\left(P_{200}.PI\right)^{3.35} + 4\left(P_{200}.PI\right) + 11}{6.895}\text{, psi}$$ (Equation 5-11a)

$$\frac{b_f}{c_f} = -2.313\left(P_{200}.PI\right)^{0.14} + 5$$ (Equation 5-12a)

$$c_f = 0.0514\left(P_{200}.PI\right)^{0.465} + 0.5$$ (Equation 5-13a)

$$\frac{h_r}{a_f} = 32.44e^{0.0186(P_{200}.PI)}$$ (Equation 5-14a)

If $P_{200.}.PI = 0$:

$$a_f = \frac{0.8627(D_{60})^{-0.751}}{6.895}, \text{ psi}$$ (Equation 5-11b)

$$\bar{b}_f = 7.5$$ (Equation 5-12b)

$$c_f = 0.1772\ln(D_{60}) + 0.7734$$ (Equation 5-13b)

$$\frac{h_r}{a_f} = \frac{1}{D_{60} + 9.7e^{-4}}$$ (Equation 5-14b)

where: a_f, b_f, and c_f are the SWCC model parameters, and

h_r = suction, psi

Based on the SWCC model parameters estimated in the previous step, the relationship proposed by Fredlund and Xing (1994) can be used to estimate pairs of suction and corresponding volumetric water contents, shown in Equations 5-15 and 5-16. The EICM automatically generates the SWCC based on the four parameters presented in the previous paragraph.

$$\theta_w = C(h)\left[\frac{\theta_{sat}}{\left[\ln\left[EXP(1) + \left(\frac{h}{a_f}\right)^{b_f}\right]\right]^{c_f}}\right]$$ (Equation 5-15)

$$C(h) = \left[1 - \frac{\ln\left(1 + \frac{h}{h_r}\right)}{\ln\left(1 + \frac{1.45x10^5}{h_r}\right)}\right]$$ (Equation 5-16)

The pavement structure was modeled using the EICM. The material properties used as inputs to the model included gradations and plasticity indices. The EICM internally calculates the corresponding mass-volume parameters and the Fredlund and Xing parameters. The mass-volume parameters and saturated hydraulic conductivities were estimated internally by the EICM for the subbase, fill and subgrade material, and are provided in Table 5.4, in addition to the Fredlund and Xing parameters. Using the parameters presented in the table, the SWCC were established for the subbase, fill and subgrade materials, and are presented in Figure 5.22. Based on the figure, the SWCC curves are quite similar for both the subbase and the fill materials.

Table 5.4. Mass-volume parameters and Fredlund and Xing parameters for the granular materials.

	Subbase	**Fill**	**Subgrade**
P_{200} (%)	5	7.5	77
PI	10	6	11
G_s	2.70	2.70	2.70
w_{opt} (%)	7.5	17.0	16.2
γ_{dmax} (lb/ft^3)	127.5	108.8	110.4
θ_{opt} (%)	15.3	29.6	28.7
S_{opt} (%)	62.7	83.7	83.1
θ_{sat} (%)	24.4	35.4	34.5
k_{sat} (ft/hr)	0.083	3.1	8.3×10^{-5}
a_f (psi)	3.96	5.81	102.6
b_f	1.96	1.56	0.72
c_f	0.796	0.779	0.254
h_r (psi)	200	190	500

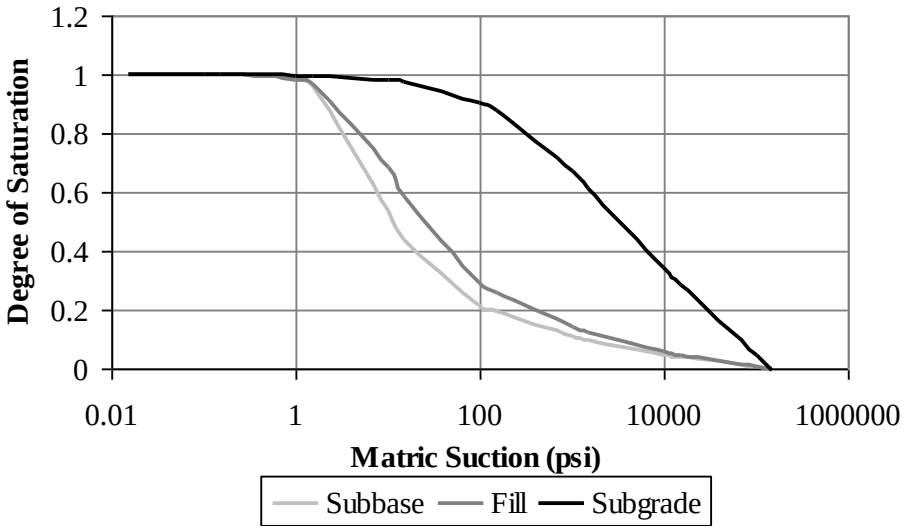

Figure 5.22. Soil-water characteristic curves for the subbase, fill and subgrade layers.

5.3.3 Climatic databases

The effect of the climatic data on the prediction made by the EICM will be evaluated using climatic data from different weather stations. Data collected from the onsite weather station will be used as an input in the EICM to predict the temperature and moisture conditions in the pavement structure. In addition, the climatic data collected from each of the five weather stations closest to the site will be used as the climatic inputs and the predicted conditions will be compared to those measured. The locations of the selected weather stations are presented in Figure 5.23 and listed in Table 5.5. The table also includes the proximity of the weather stations to the site and the number of available data for each station. An additional analysis will be made using the weather data triangulated from the three closest weather stations and another using the weather data interpolated between the five stations. In total, eight runs of the EICM using different climatic data will be analyzed. The weather data triangulated from the three closest weather stations will be based on the data from the stations located in Pittsburgh, Allegheny and Wheeling, and will be referred to as P-A-W. The weather data interpolated from the five stations will include data from the stations located in Meadville and Dubois along with the previous three P-A-W weather stations, and will be referred to as INT.

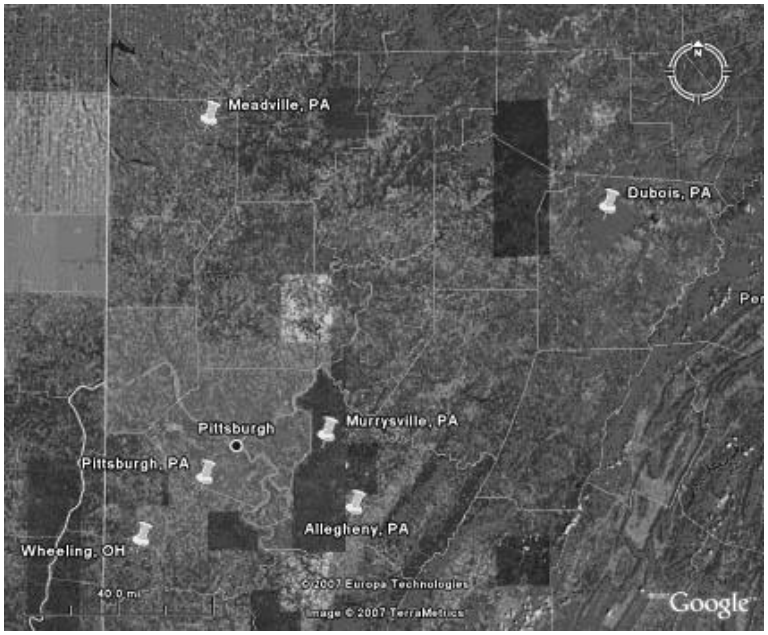

Figure 5.23. Locations of the weather stations with respect to the site (www.earth.google.com).

Table 5.5. Weather stations used in the analysis.

	Latitude (degrees)	Longitude (degrees)	Elevation (ft)	Distance from site (miles)	Available data (months)
Murrysville (onsite)	40.43 N	79.66 W	935	--	32
Pittsburgh International Airport	40.30 N	80.14 W	1175	19.3	116
Allegheny County Airport	40.21 N	79.55 W	1281	25.7	85
Wheeling Ohio County Airport	40.11 N	80.39 W	1225	50.2	95
Port Meadville Airport	41.38 N	80.13 W	1406	64.3	104
Du Bois-Jefferson County Airport	41.11 N	78.54 W	1807	65.8	68

A comparison of the climatic data collected by the different weather stations is presented in this section. The air temperature, rainfall, wind speed, sunshine and relative humidity are compared. The onsite weather station monitors ambient temperature, relative humidity, and wind speed at 15-minute intervals. The remaining climatic databases include data collected at 1-hour intervals. Therefore, the data collected from the onsite weather station was reduced to 1-hour intervals and used in the analysis presented in this section. The climatic data available from the onsite weather station covers a period of 32 months from August 16, 2004 to April 12, 2007, and the data available from the remaining weather stations covers a period of 5.7 to 9.7 years, as indicated in Table 5.5.

A summary of the measured hourly air temperature is presented in Figure 5.24. The boxes in the figure represent the range of temperatures extending between the average plus one standard deviation and the average minus one standard deviation. The lines extending from the boxes represent the overall range of temperatures extending between the minimum and maximum values. The air temperature is in the range -9˚F to 98˚F and the averages are close to each other while varying between 47˚F and 52˚F.

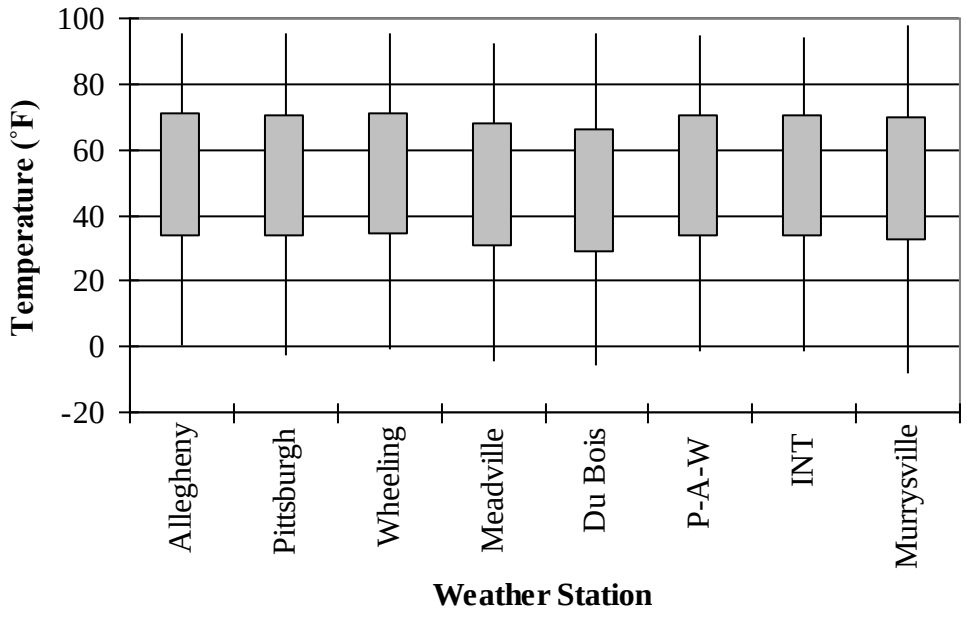

Figure 5.24. Measured hourly air temperature for the different weather stations.

A summary of the measured rainfall is presented in Figure 5.25 and Figure 5.26. The Meadville station recorded the lowest average yearly rainfall (34.9 inches), which is on average 8 percent lower than the average rainfall recorded by the remaining stations. The remaining stations recorded a similar average rainfall; the average yearly rainfall varied between 37 and 40.8 inches, with a standard deviation of 5.6 to 15.1 inches. The maximum hourly rainfall reached 6 inches for the Allegheny and Pittsburgh stations, which are the two closest stations to the site. This was a single event recorded during the hurricane Ivan in September of 2004. Excluding this event, the maximum hourly rainfall varied between 3 and 4 inches for all the weather stations.

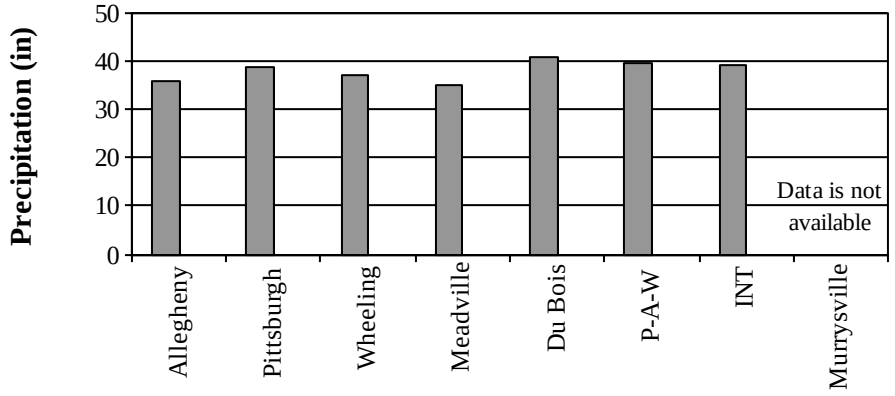

Average	35.6	38.5	37.0	34.9	40.8	39.3	39.2	Data is not available
Standard deviation	15.1	6.1	7.2	6.9	10.2	5.6	5.6	

Figure 5.25. Average measured yearly rainfall for the different weather stations.

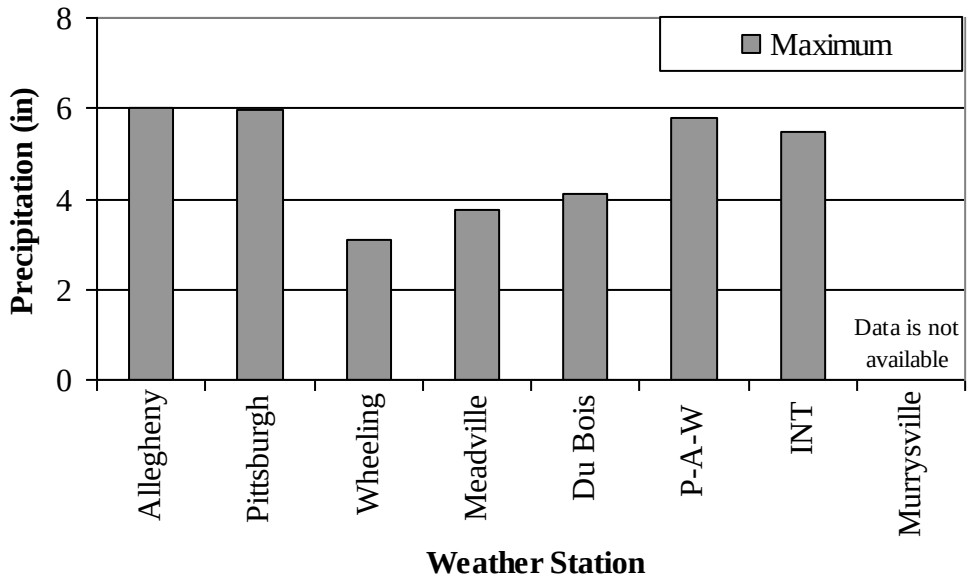

Figure 5.26. Maximum measured hourly rainfall for the different weather stations.

A summary of the average and maximum measured wind speed is presented in Figure 5.27 and Figure 5.28. The average hourly wind speed recorded by all the weather stations varied between 6 and 7 mph, with the exception of the onsite station which recorded an average hourly wind speed of 3 mph. This indicates that the wind speed at the site is more than two times less than that recorded at the remaining stations. The maximum wind speed is largest for the Allegheny station at 38 mph and lowest for the onsite station at 22 mph.

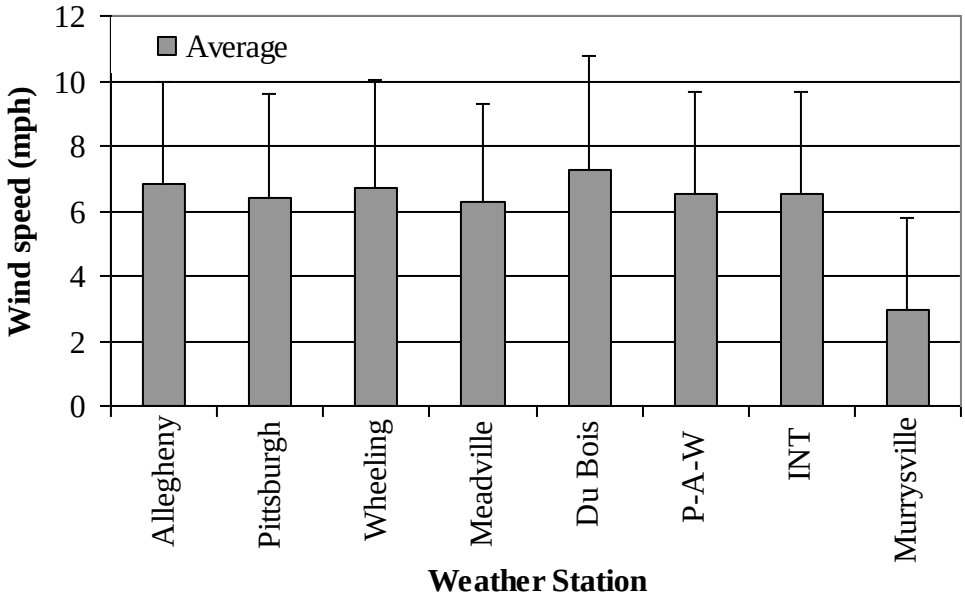

Figure 5.27. Average measured hourly wind speed for the different weather stations.

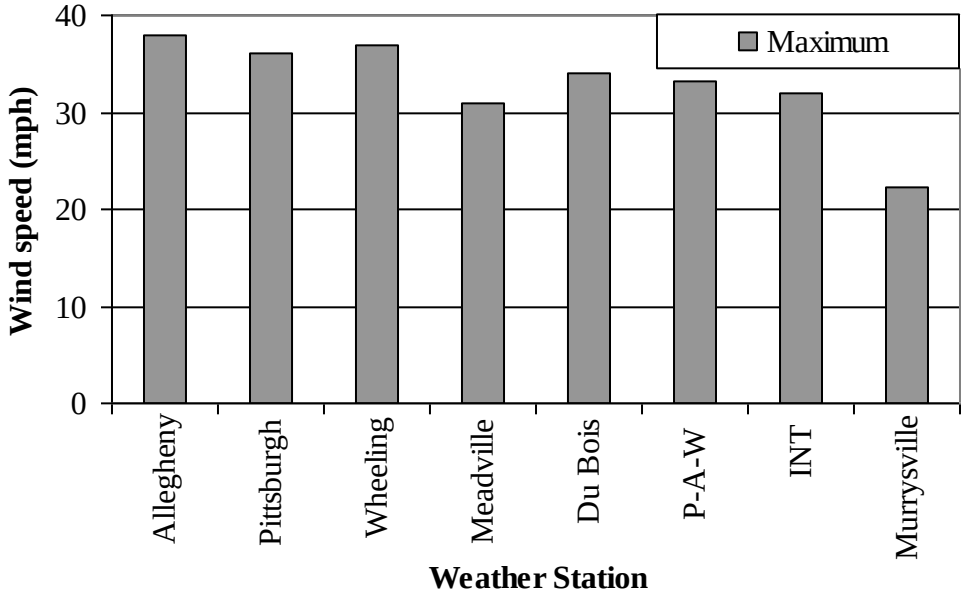

Figure 5.28. Maximum measured hourly wind speed for the different weather stations.

A summary of the average measured hourly percent sunshine is presented in Figure 5.29. The average percent sunshine varies between 30 percent for the Pittsburgh station and 54 percent for the Wheeling station.

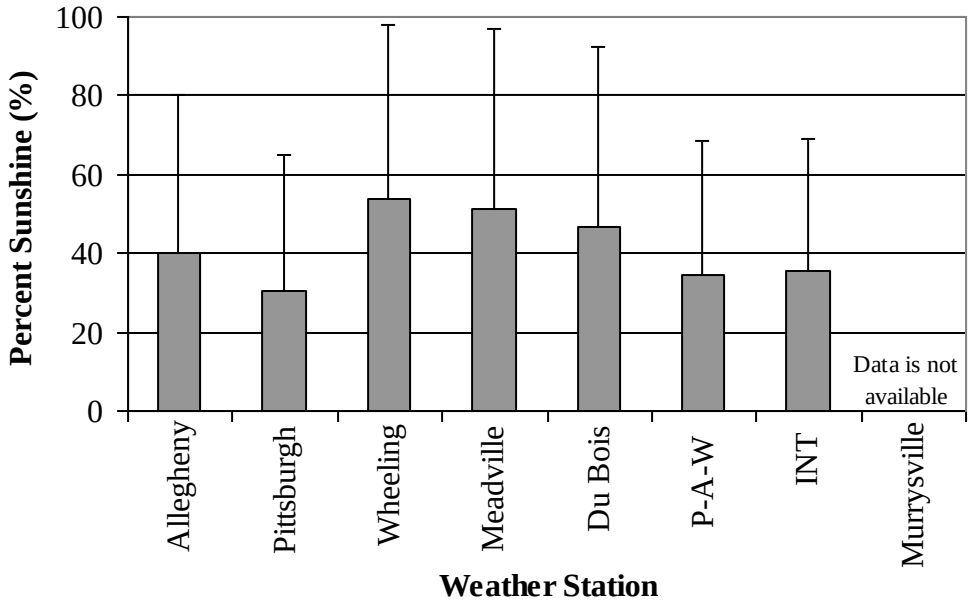

Figure 5.29. Summary of average measured hourly percent sunshine for the different weather stations.

A summary of the measured hourly ambient relative humidity is presented in Figure 5.30. The minimum ambient relative humidity varies between 61 and 70 percent for all the stations. The average relative humidity is similar for all the stations and varies between 71 and 76 percent.

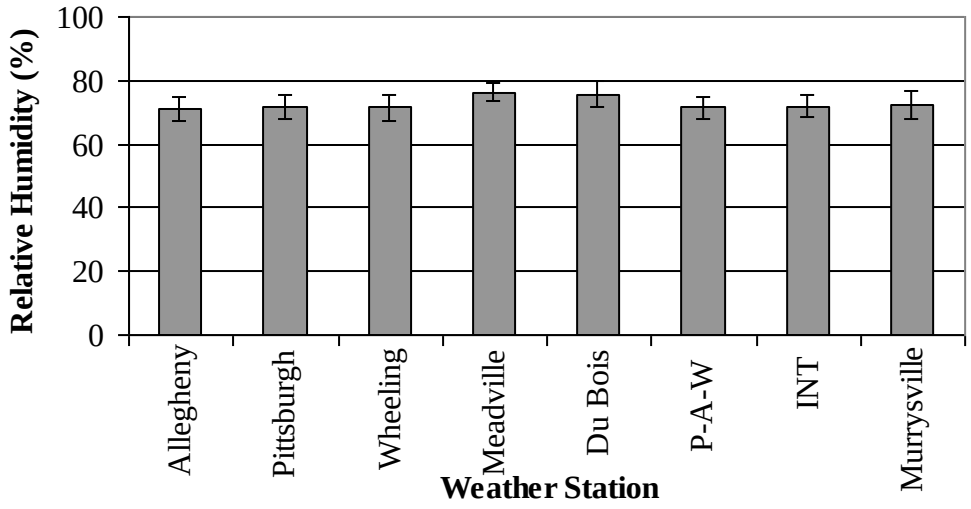

Figure 5.30. Average measured hourly ambient relative humidity for the different weather stations.

Since the onsite weather station does not include data for the percent sunshine or precipitation, and since the data collected by the two closest weather stations (Pittsburgh and Allegheny) are similar, the percent sunshine and precipitation data from the Pittsburgh station was used as representative of the conditions on the site and was appended to the remaining data collected onsite. The updated onsite weather station is used in the prediction of the temperature and moisture conditions in the pavement structure and the pavement performance, using the EICM and the MEPDG. The results are presented in the following sections.

5.3.4 Temperature predictions within the concrete slabs

In the previous section, the data collected by the six weather stations was presented and compared to each other. The EICM was used to predict the temperature and moisture conditions based on each of these weather stations and based on climatic data interpolated from the individual stations. The EICM predicts the temperature conditions within the concrete at eleven evenly spaced locations within the slab. In this section, the predicted concrete temperatures during the first two years after construction of the pavement are presented and compared to those measured.

The monthly averages of the predicted and measured weighted (as a function of depth) average concrete temperature during the first two years after construction are compared in Figure 5.31. The predicted and measured temperatures follow the same seasonal trends. The temperatures predicted by the different weather stations are close to each other and close to those measured.

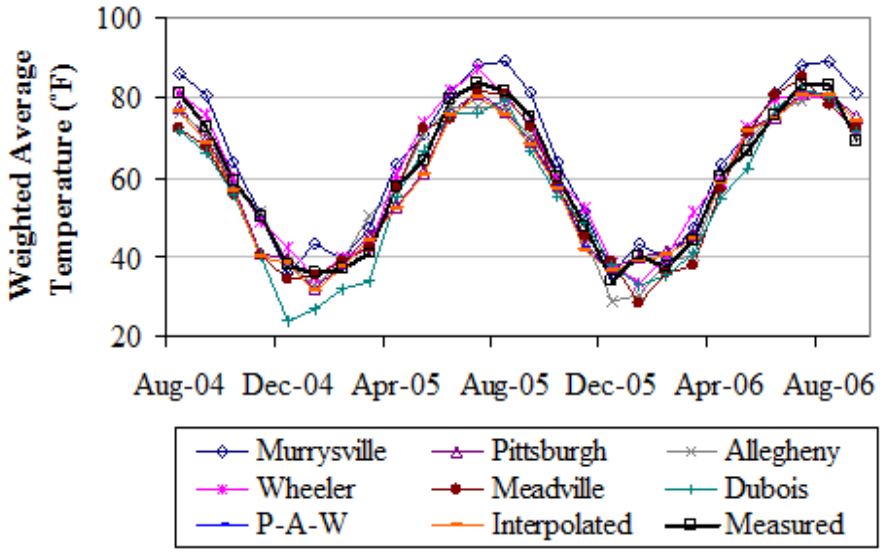

Figure 5.31. Monthly weighted average for the predicted and measured temperature.

The seasonal variation in the predicted temperature is presented in Figure 5.32. The figure presents the seasonal average and standard deviation of the weighted average for the predicted temperature. The predicted temperature using the Murrysville (onsite) weather station is the highest compared to those predicted using the remaining weather stations. This may be due to the fact that the data available based on the onsite station (32 months) is small compared to the remaining stations (68 to 116 months). The weighted average for the predicted temperature based on the different climatic databases is within 10 percent of the weighted average for the measured temperature.

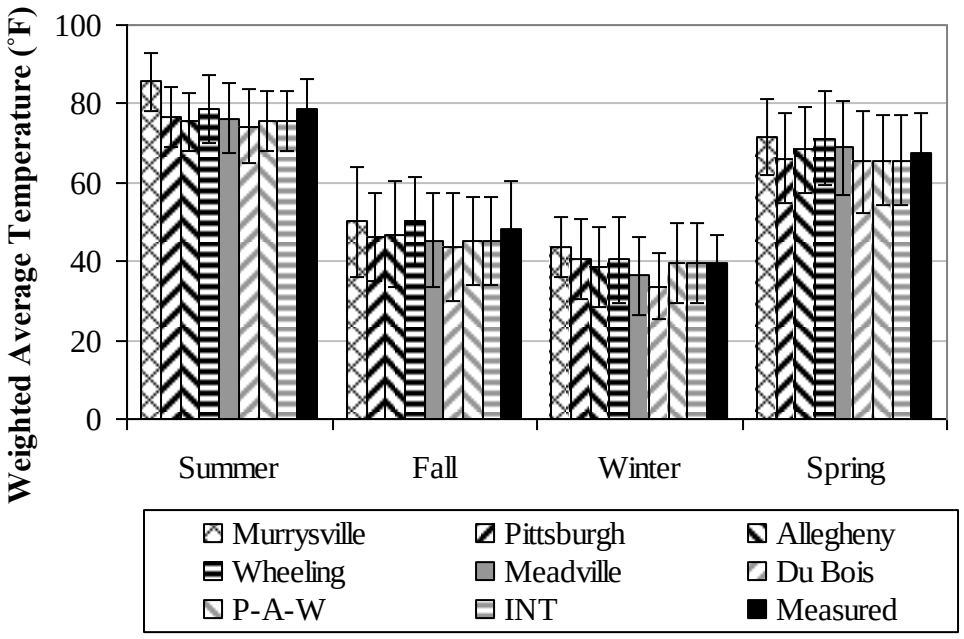

Figure 5.32. Weighted average of the predicted and measured seasonal temperature.

The accuracy of the climatic model in predicting the weighted average concrete temperature is evaluated using statistical analysis. First, the weighted average for the predicted temperature is plotted versus the weighted average for the measured temperature, as shown in Figure 5.33. This figure shows the data predicted based on data from the Pittsburgh weather station. The correlation coefficient (R^2) between predicted and measured for the Pittsburgh station was equal to 0.89, indicating that the climatic model explains 89 percent of the total variability in temperature predictions for the 18,526 data points. This number of data points corresponds to data predicted at 1-hour intervals for a two-year period. This same procedure was carried out for the data predicted based on the eight climatic data files. A summary of the correlation coefficients determined for each prediction case is presented in Table 5.6. The correlation coefficient varies between 86 and 94 percent, indicating that the climatic model is accurately predicting concrete temperatures. The highest correlation coefficient was that corresponding to the use of the Murrysville onsite weather station. This indicates that the slab temperature predicted using the climatic data from the different climatic databases is accurately predicting the slab temperature.

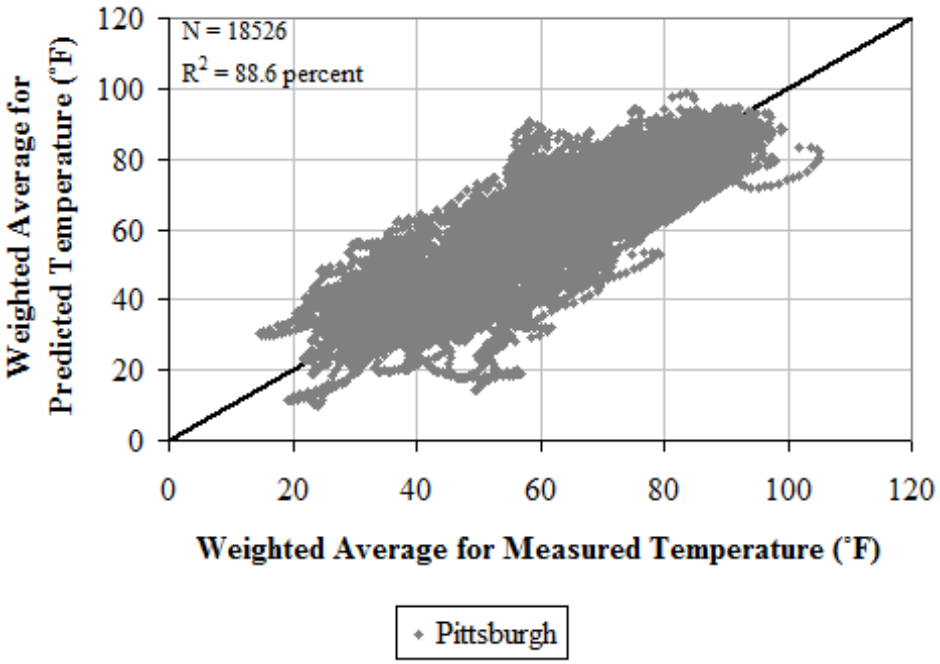

Figure 5.33. Weighted average for predicted versus measured temperature (Pittsburgh station).

Table 5.6. Statistical analysis of weighted average for predicted and measured concrete temperature.

Weather Station	R^2 (%)	N
Murrysville	94	18,526
Pittsburgh	89	18,526
Allegheny	89	18,526
Wheeling	86	18,526
Meadville	87	18,526
Bu Bois	88	18,526
P-A-W	89	18,526
INT	89	18,526

In addition, the scatter around the one-to-one line in Figure 5.33 is an indication of the residual error involved in the temperature prediction. If there are more data points above or below this line, this might indicate a bias in the prediction. The residuals representing the difference between the weighted average for the predicted and measured temperatures were plotted against the weighted average for the measured temperature, and are presented in Figure 5.27, which corresponds to the predictions based on the Pittsburgh station. The figure shows a horizontal band with no abnormalities or trends, implying that the data used in the analysis is independent. This was also carried out for the data predicted by the eight climatic data files and the results were similar.

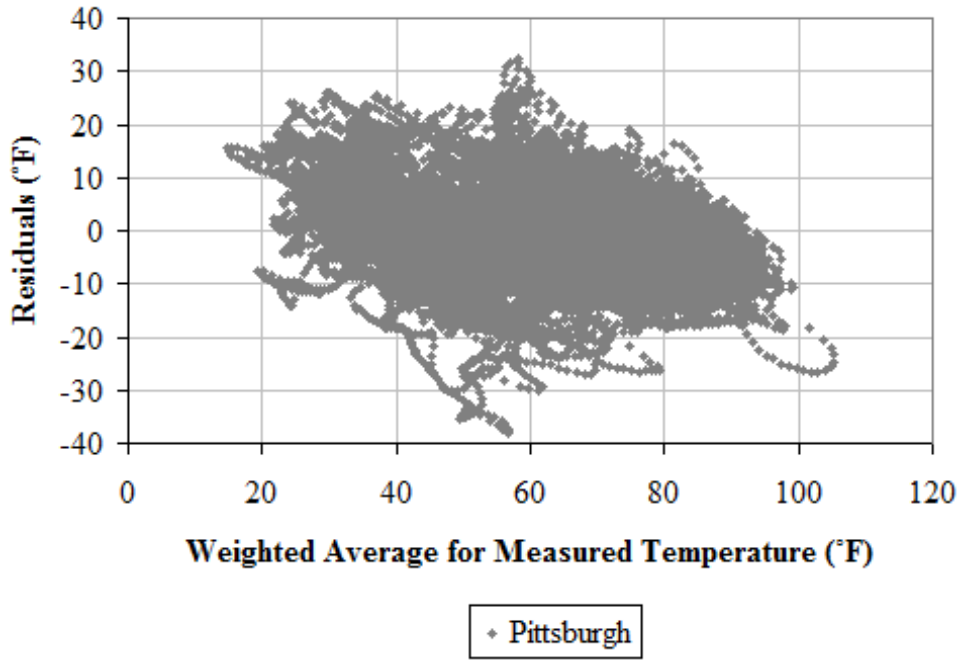

Figure 5.34. Residual weighted average for predicted temperature versus weighted average for measured temperature (Pittsburgh station).

Having established that the weighted average concrete temperature for predicted temperature is similar to that for the measured temperature, another aspect of the predicted temperature also needs to be examined. The temperature predicted along the slab depth

influences the temperature gradient within the slab. Therefore, the equivalent linear temperature gradient based on the predicted temperature is compared to the gradient based on the measured temperature.

The seasonal variation in the equivalent linear temperature gradient calculated using the predicted and measured temperatures is presented in Figure 5.35 to Figure 5.37. The figures show the maximum positive, the maximum negative and the average equivalent linear temperature gradient. According to Figure 5.35, the maximum positive gradient based on the predicted temperature is higher than that based on the measured temperature for all the seasons, with the exception of the predicted temperature using the onsite weather station for the spring season. This indicates that the predicted temperature over-estimates the maximum positive temperature gradient in the slab. Similarly, the predicted temperature over-estimates the maximum negative temperature gradient in the slab, as shown in Figure 5.36. Moreover, the average temperature gradient is positive in the spring and summer and negative in the fall and winter, as shown in Figure 5.37. The predicted temperatures are at eleven evenly spaced locations within the slab, while the measured temperatures are at seven locations (three sensors in the top, one in the middle and three in the bottom of the slab). This difference in the location of the temperature reading explains the difference in the magnitude of the gradients. The over-estimation of the predicted maximum positive and negative gradient would result in over-estimation of the damage caused by these gradients. As a result, the predicted performance of the pavement would be underestimated when compared to the actual performance.

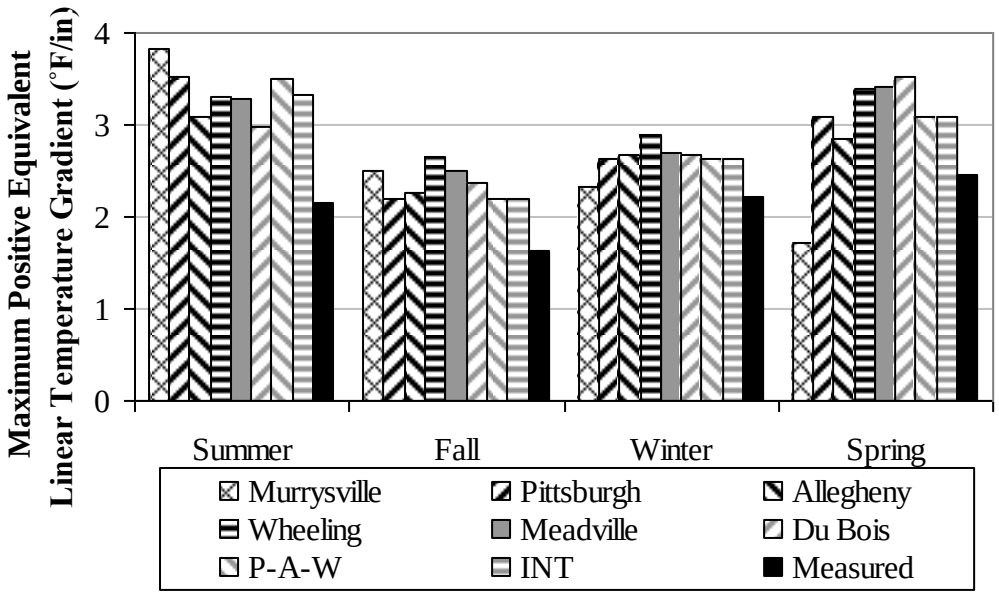

Figure 5.35. Seasonal maximum positive equivalent linear temperature gradient based on the temperature predicted at 1-hour intervals and the temperature measured at 15-minute intervals.

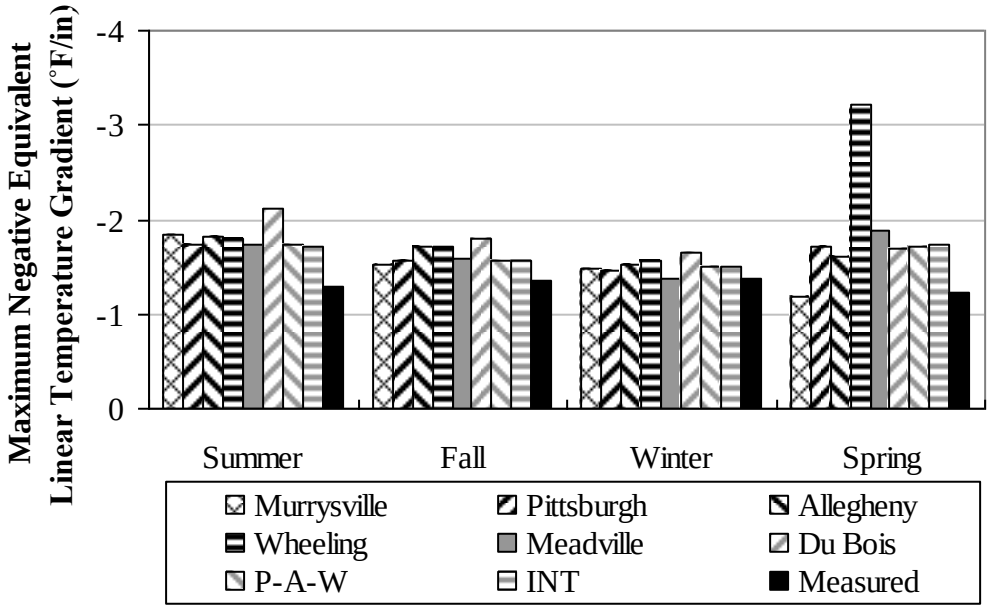

Figure 5.36. Seasonal maximum negative equivalent linear temperature gradient based on the temperature predicted at 1-hour intervals and the temperature measured at 15-minute intervals.

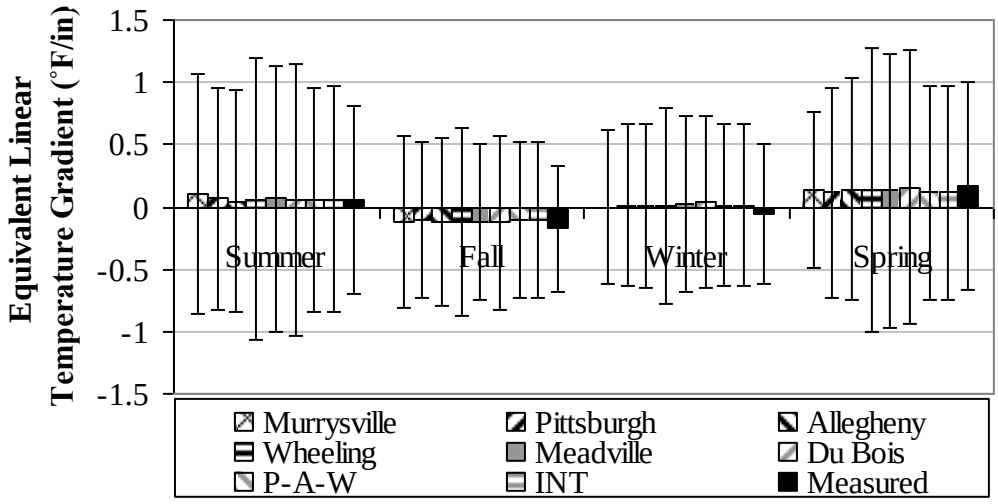

Figure 5.37. Seasonal average equivalent linear temperature gradient based on the temperature predicted at 1-hour intervals and the temperature measured at 15-minute intervals.

For every season, the range of the average gradient based on the predicted temperature is compared to that based on the measured temperature. The range represents the average predicted using the different climatic databases. The average gradient based on the predicted temperature varies between -0.13˚F/in and 0.15˚F/in, and the average gradient based on the measured temperature varies between -0.17˚F/in and 0.17˚F/in. With the exception of the winter, the gradient based on the predicted temperature overestimates the gradient based on the measured temperature by an average of 23 to 34 percent. This indicates that the predicted performance of the pavement will take into account that the slab is subjected to temperature gradients that are larger than what would actually be measured. Therefore, the predicted design life of the slab is expected to be smaller than the actual service life; resulting in a conservative pavement design.

Similar to the statistical analysis carried out for the weighted average temperature, the accuracy of the climatic model in estimating the equivalent linear temperature gradient was also evaluated. The correlation coefficient between the gradient based on the predicted and measured temperature is determined and presented in Table 5.7. The correlation coefficient varies between 62 and 66 percent, indicating that the climatic model is accurately predicting the temperature gradient. Similar to the observation made regarding the weighted average temperature, the prediction made based on the Murrysville station resulted in the highest correlation coefficient.

Table 5.7. Statistical analysis of predicted and measured equivalent linear temperature gradient.

Weather Station	R^2 (%)	N
Murrysville	66	18,526
Pittsburgh	62	18,526
Allegheny	64	18,526
Wheeling	62	18,526
Meadville	63	18,526
Bu Bois	63	18,526
P-A-W	62	18,526
INT	62	18,526

In summary, the weighted average temperature and the equivalent linear temperature gradient over the two-year period are compared in Figure 5.38 and Figure 5.39. In these figures, the box represents the range of values between the average plus one standard deviation and the average minus one standard deviation. The lines extending from the box represent the overall range of values showing the minimum and maximum value. The weighted average temperature predicted by the different weather stations are similar to each other and to those measured. With the exception of the peak negative gradient predicted based on the Wheeling weather station, the equivalent linear gradient based on the predicted and measured temperatures are also similar.

The predicted and measured seasonal variation in temperature along the depth of the concrete slab was calculated for the four climatic seasons based on the data collected during the first two years after construction. The average temperature profile for the summer season is presented in Figure 5.40. The temperature predicted based on the climatic data of the station located at Wheeling is closest to those measured. Unexpectedly, the average temperature predicted based on the climatic data from the onsite weather station is substantially larger than the measured values. The predicted temperatures based on the climatic data from the remaining other weather stations are close to each other. The average predicted and measured temperature gradients for the summer season are similar, and vary between 0.05 and 0.06˚F/in for all the climatic data files used in the analysis, except for the onsite weather data, which gave an average gradient of 0.10˚F/in.

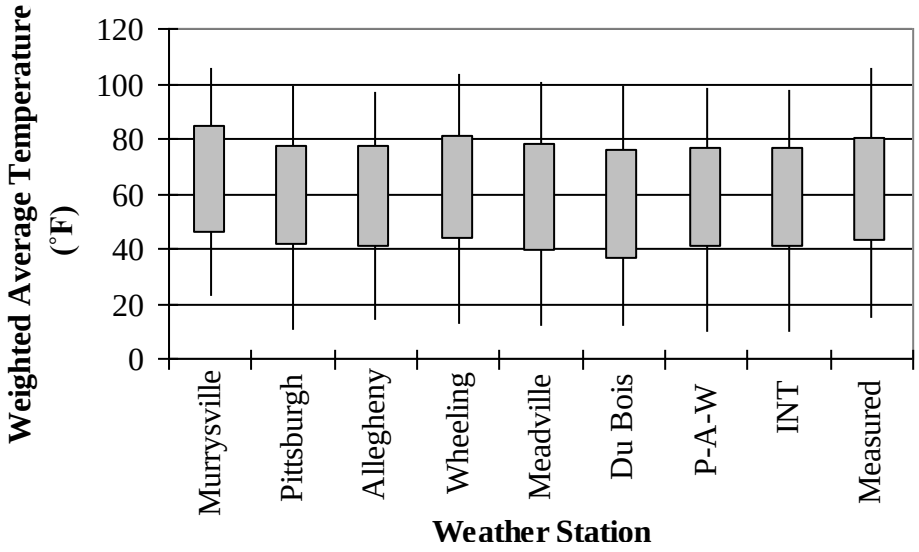

Figure 5.38. Weighted average for predicted and measured temperatures over the two-year period.

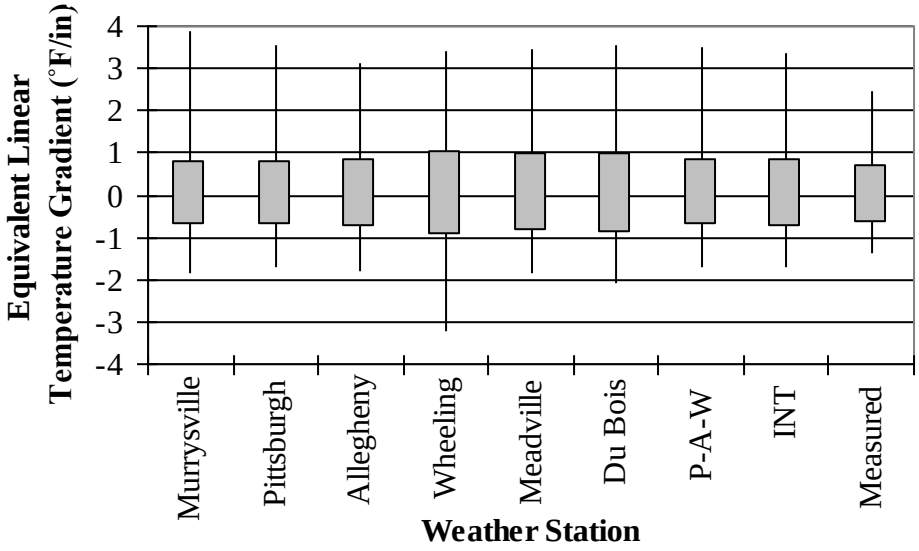

Figure 5.39. Equivalent linear gradient for predicted and measured temperatures over the two-year period.

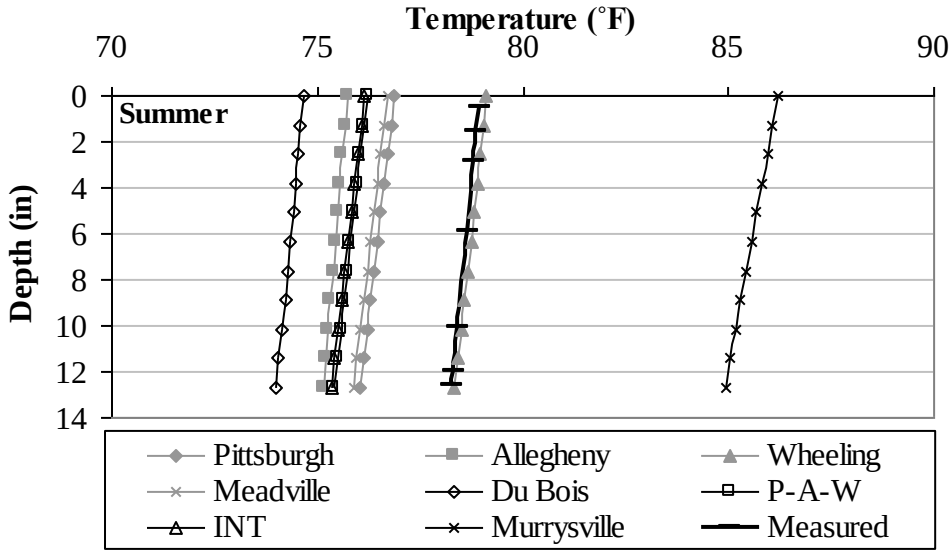

Figure 5.40. Average predicted and measured concrete temperature profiles during the summer.

The average temperature profile for the fall is presented in Figure 5.41. All of the predicted temperatures were within a couple of degrees of the measured temperatures except the temperatures predicted using data from the DuBois weather station. The average predicted temperature gradient varies between -0.10 and -0.13˚F/in for all the climatic data files used in the analysis. The average measured gradient is -0.17˚F/in.

The average temperature profiles for the winter are presented in Figure 5.42. Most of the predicted temperature profiles are within a few degrees of the measured temperature profile. The exception is the temperature profile generated using climatic data from the Meadville and DuBois weather stations. These temperature profiles are significantly different from the measured temperature profile. These two weather stations are also located the furthest distance from the test section. The average predicted temperature gradient varies between 0.00 and 0.05˚F/in for all the climatic data files used in the analysis. The average measured gradient is -0.06˚F/in. There is not a significant difference between any of these gradients.

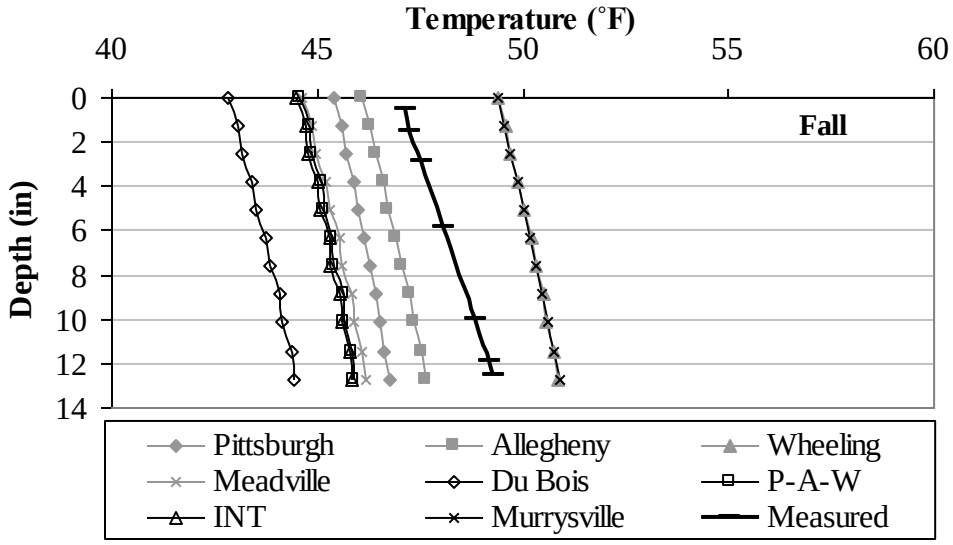

Figure 5.41. Average predicted and measured concrete temperature profiles during the fall.

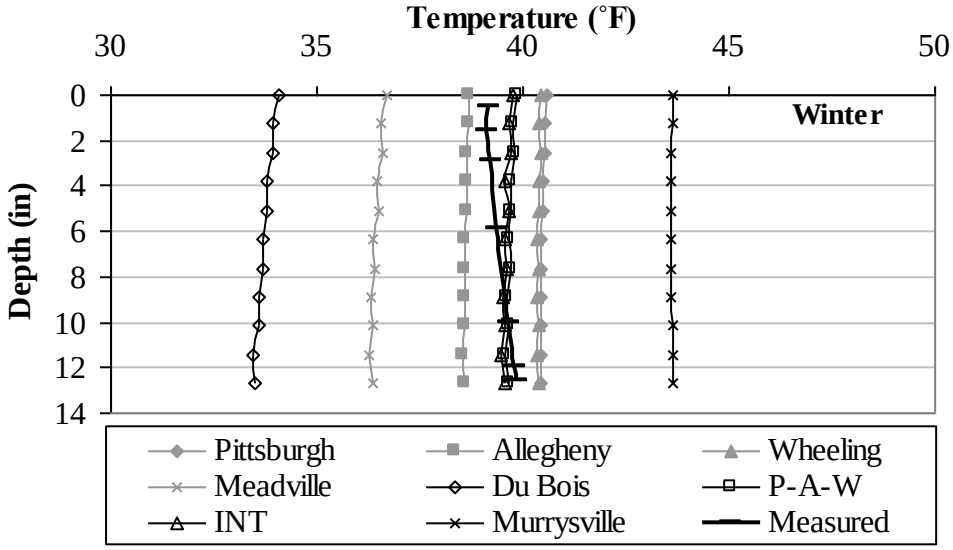

Figure 5.42. Average predicted and measured concrete temperature profiles during the winter.

The average temperature profiles for the spring are presented in Figure 5.43. All predicted temperature profiles are within a couple of degrees of the measured temperature profile. The average predicted temperature gradient varies between 0.11 and 0.15˚F/in for all the climatic data files used in the analysis. The gradient for the measured average temperature profile was 0.17˚F/in, which is very close to the predicted values.

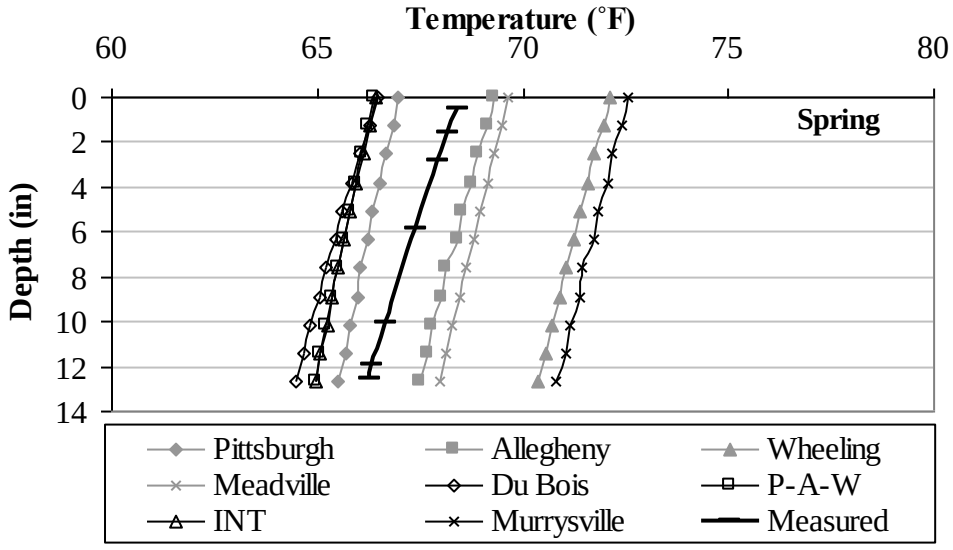

Figure 5.43. Average predicted and measured concrete temperature profiles during the spring.

In general, the temperature generated using climatic data from weather stations close to the site (within 50 miles) predicted the average temperatures within a couple of degrees. The predicted average gradients were also very close to the measured average gradient. It is surprising that the average temperature profiles predicted using the onsite weather station are so different from the measured values. The reason for this is not clear.

5.3.5 Temperature predictions within the underlying layers

In addition to predicting temperatures in the concrete slab, the EICM also predicts temperatures within the layers beneath the slab. In relatively thick layers, the layer is subdivided into thinner layers and the temperatures are predicted at mid-depth of the layer. In thin layers, the temperatures are simply predicted at mid-depth. The 24-inch fill was automatically subdivided into four equal layers 6-inch thick, and the top 24 inches of the subgrade is treated as a separate layer. In this section, the predicted temperatures in the stabilized and granular layers during the first two years after construction of the pavement are presented and compared to those measured.

Starting with the 4-inch ATPB layer, the temperature was predicted at mid-depth of the layer. The thermocouples measuring temperature in this layer are located at approximate depths of 14 and 16 inches from the top of the pavement, which corresponds to the mid-depth of the ATPB and the bottom of the ATPB. The predicted and measured average seasonal temperatures are presented in Figure 5.44. The average temperatures predicted based on the climatic data from the Murrysville (onsite) station are the highest, followed by those based on the Wheeling station. Overall, the predicted temperatures are similar to the measured temperatures.

Moving to the 5-inch subbase, the temperatures were also predicted at mid-depth. The thermocouples measuring temperature in this layer were located at approximate depths of 19 and 21 inches from the top of the pavement, which correspond to middepth and the bottom of the subbase. The predicted and measured average seasonal temperatures are presented in Figure 5.45. The average temperature predicted based on the climatic data from the Murrysville (onsite) station is the highest.

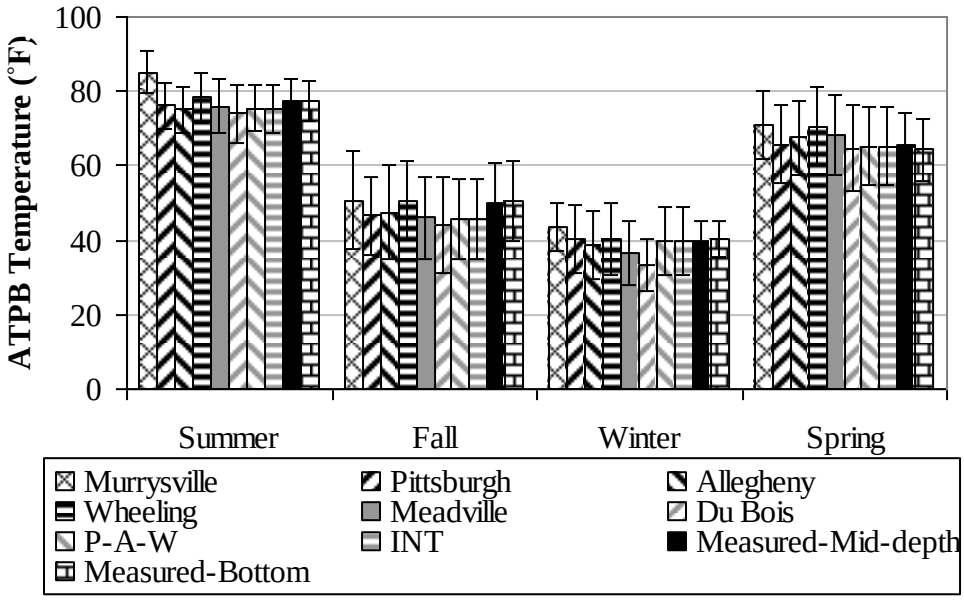

Figure 5.44. Average seasonal predicted and measured temperatures at mid-depth of the ATPB.

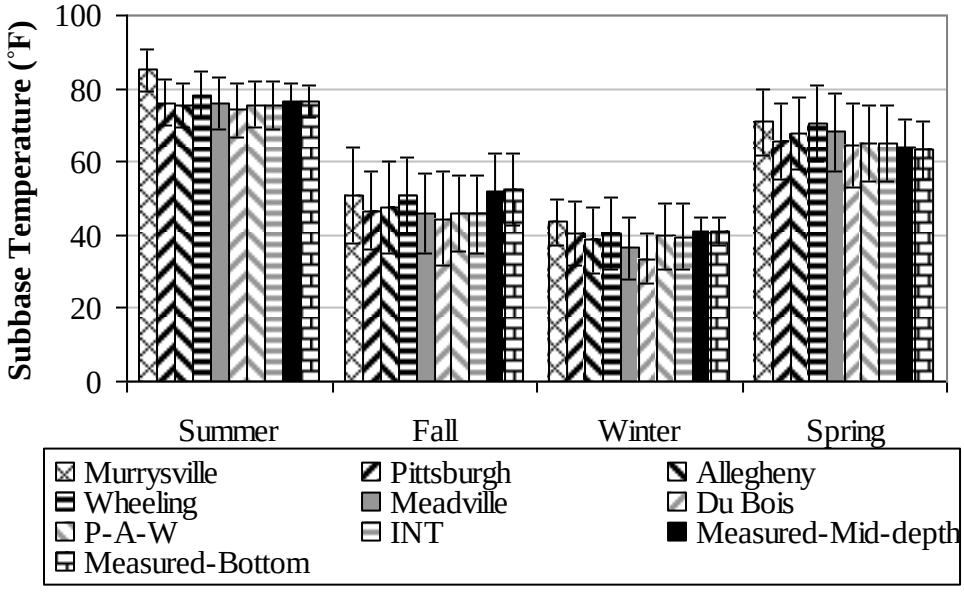

Figure 5.45. Average seasonal predicted and measured temperatures at mid-depth of the subbase.

Going deeper into the pavement structure, the fill layer was automatically subdivided into four sublayers, 6 inches in thickness. The temperatures were predicted at mid-depth for each sublayer. The thermocouples measuring temperatures in this layer were located at approximate depths of 28, 36 and 42 inches from the top of the pavement, which correspond to depths of 7, 15 and 21 inches from the top of the fill layer, or 1 inch in the second sublayer, 3 inches in the third sublayer and 3 inches in the fourth sublayer. The seasonal trends of the predicted temperatures were similar in the four sublayers. To minimize repetition, only the predicted and measured average seasonal temperatures for the second sublayer are presented in Figure 5.46. The average temperature predicted based on the climatic data from the Murrysville (onsite) station is the highest, followed by that based on the Wheeling station. Overall, the predicted temperatures are similar to those measured.

The subgrade layer was automatically subdivided into two sublayers. The first sublayer is 24 inches thick and the second consists of the remaining of the modeled thickness. The temperatures were predicted at mid-depth of each sublayer. The thermocouples measuring temperatures in this layer are located at an approximate depth of 48 inches from the top of the pavement, which corresponds to a depth of 3 inches from the top of the subgrade layer. The seasonal trends of the predicted temperature are similar in the two sublayers. To minimize repetition, only the predicted and measured average seasonal temperatures for the first sublayer are presented in Figure 5.47. The average temperature predicted based on the climatic data from the Murrysville (onsite) station is the highest, followed by that based on the Wheeling station. Overall, the predicted temperatures are similar to those measured.

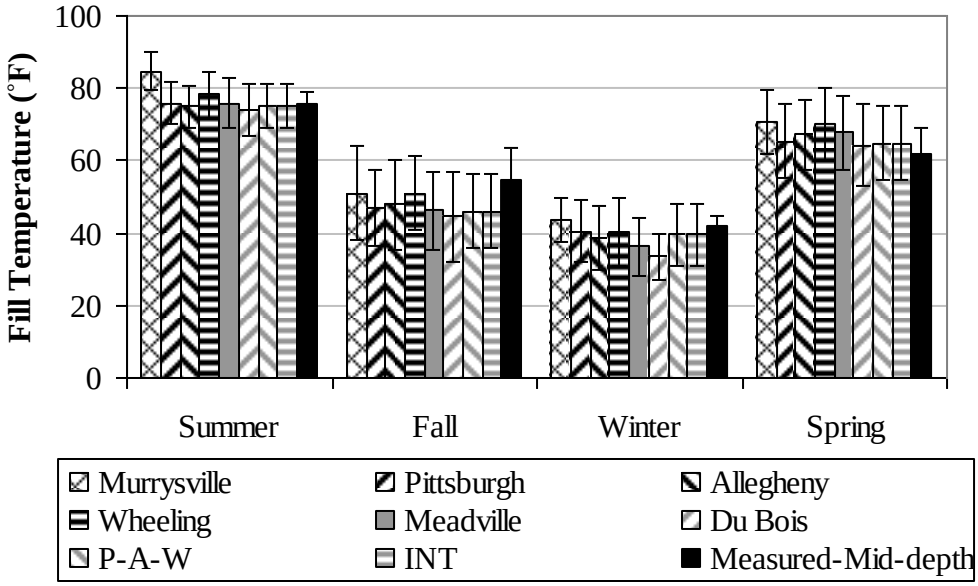

Figure 5.46. Average seasonal predicted and measured fill temperatures at a fill depth of 6 to12 inches.

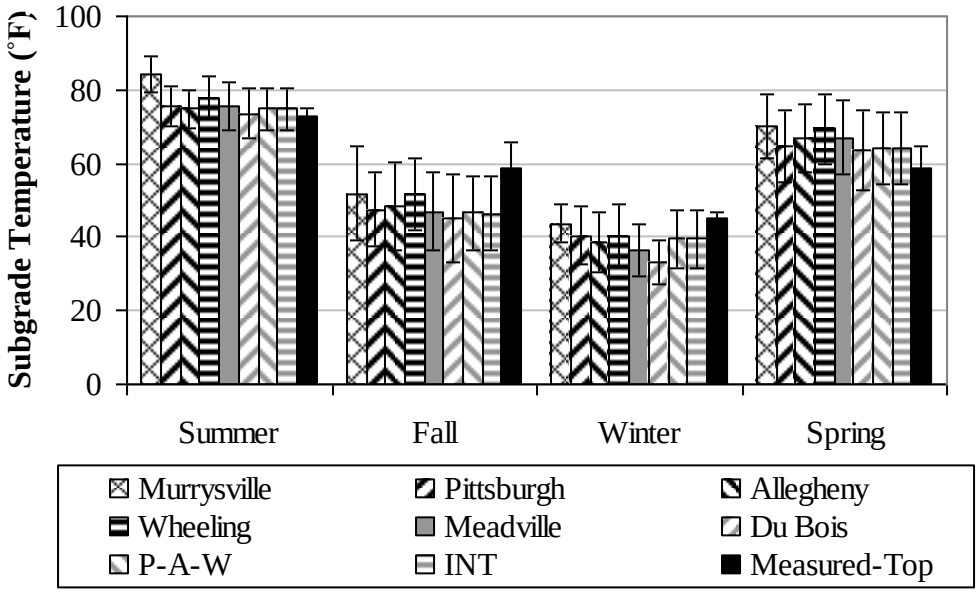

Figure 5.47. Average seasonal predicted and measured subgrade temperatures at a subgrade depth of 0 to 24 inches.

Similar to the statistical analysis carried out for slab temperature in section 5.3.4, the accuracy of the climatic model in predicting the temperature of the underlying layers was also evaluated. The correlation coefficient between the predicted and measured temperature is determined and presented in Table 5.8. The correlation coefficient varies between 85 and 95 percent, indicating that the climatic model is accurately predicting the temperature of the underlying layers. The highest correlation coefficient was that corresponding to the use of the Murrysville onsite weather station, which is consistent with the observations made for the slab temperature predictions.

Table 5.8. Statistical analysis of predicted and measured temperature in the underlying layers.

Weather Station	N	R^2 for the underlying layers (%)			
		ATPB	Subbase	Fill	Subgrade
Murrysville	18,526	95	95	95	90
Pittsburgh	18,526	91	91	90	86
Allegheny	18,526	91	91	91	87
Wheeling	18,526	89	89	89	85
Meadville	18,526	90	90	90	86
Bu Bois	18,526	91	91	91	88
P-A-W	18,526	91	91	91	86
INT	18,526	91	91	91	86

The predicted and measured seasonal variation in temperature along the depth of the layers underlying the concrete slab was calculated for the four climatic seasons based on the data for the two years. The average profiles for the summer season are presented in Figure 5.48. Based on the figure, the predicted temperature profiles are different from the measured profile. The average temperature predicted based on the climatic data from the onsite weather station shows the most significant difference from the measured temperature. The predicted temperatures based on the remaining climatic data files are close to each other.

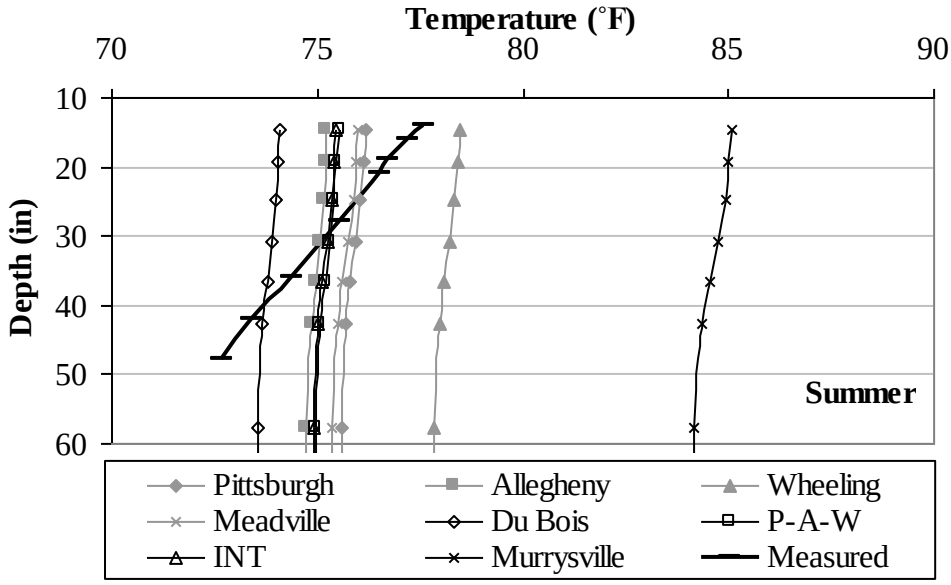

Figure 5.48. Average seasonal temperature profiles within the underlying layers during the summer.

The average profiles for the fall season are presented in Figure 5.49. Based on the figure, the predicted temperature profiles are different from the measured profile. The predicted temperature profiles are similar to the measured values in the upper potion of the pavement structure during the fall but substantially different in the lower layers. The might be attributed to the fact the material properties of the layers were estimated primarily based on estimations using the particle distribution and the plasticity characteristics.

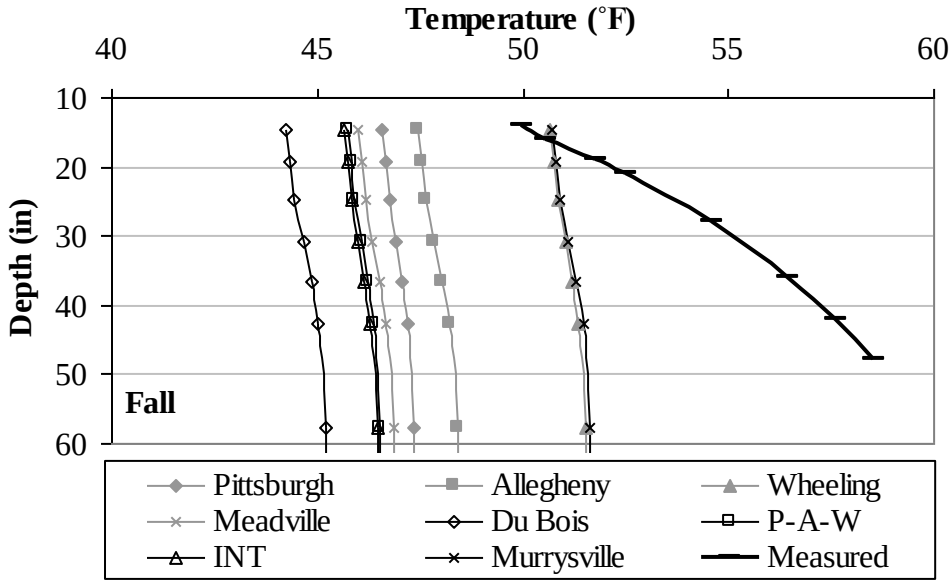

Figure 5.49. Average seasonal temperature profiles within the underlying layers during the fall.

The average profiles for the winter season are presented in Figure 5.50. The predicted temperature profiles are similar to the measured temperature profiles except when the weather stations furthest from the test section (Meadville and DuBois) are used for the temperature predictions. As with the fall season, the predicted temperatures in the lower portion of the structure tend to underestimate the measured temperature during the winter.

The average profiles for the spring season are presented in Figure 5.51. Unlike during the winter and fall seasons, the predicted temperatures tend to over estimate the measured temperature by about 10˚F during the spring. The onsite weather station drastically overestimates the measured temperature.

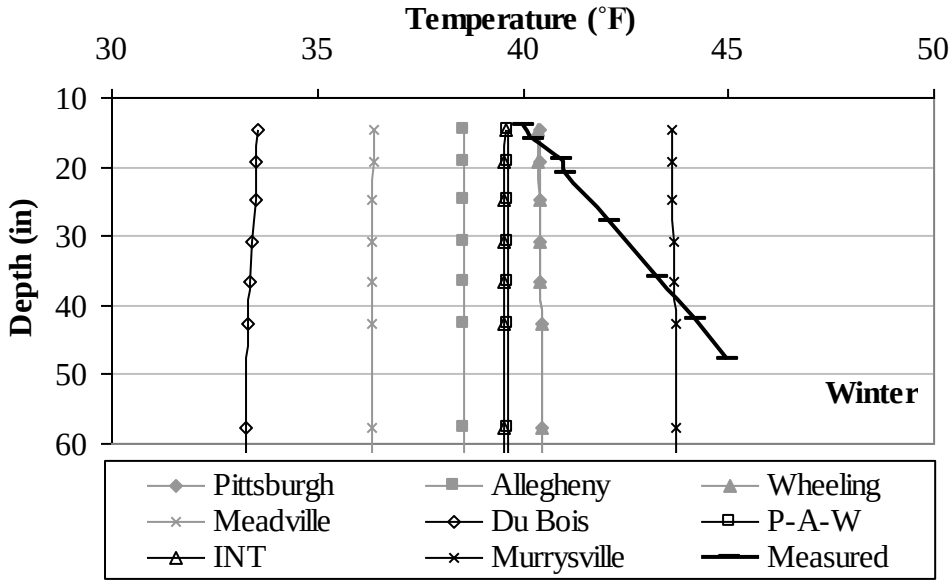

Figure 5.50. Average seasonal temperature profiles within the underlying layers during the winter.

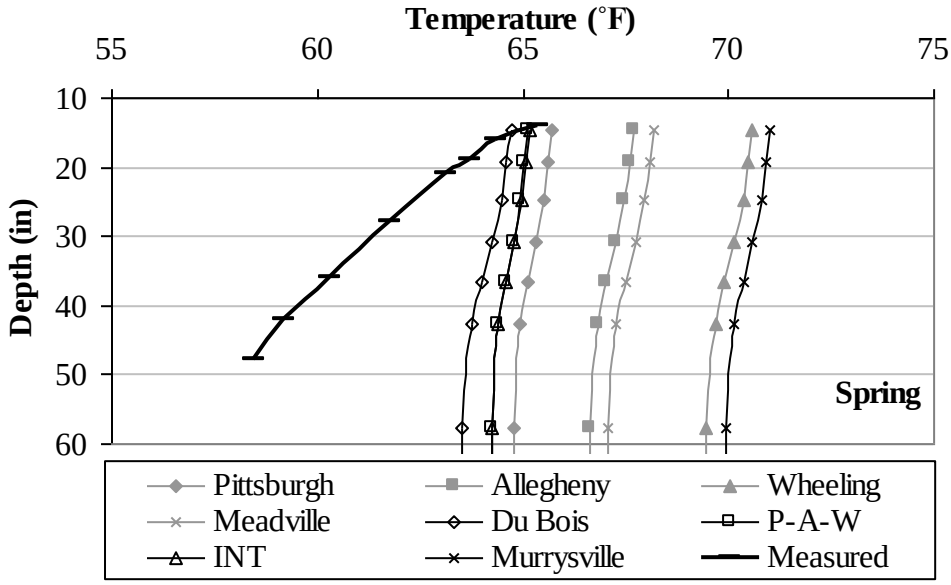

Figure 5.51. Average seasonal temperature profiles within the underlying layers during the spring.

In summary, it can be concluded that the temperatures predicted in the underlying layers are representative of the measured conditions. The largest influence in the temperature of the underlying layers on the pavement response is when the granular layers are frozen. Fortunately, the frost depth is shallow and the lower layers do not freeze and therefore errors in the temperature are not very influential. It has been shown that the weather stations greater than 50 miles away from the test section did not predict temperature as well as the stations that are closer to the site. If the Meadville climatic data was used to predict temperature during the winter season, the underlying layers might appear frozen when they actually are not. Table 5.9 summarizes the average number of freeze-thaw cycles recorded for each of the climatic databases. With the exception of the onsite weather station, the average annual number of freeze-thaw cycles varies between 45 and 54 days for the remaining climatic databases. In section 5.3.7, the effect of these differences in temperature on pavement performance will be evaluated to confirm the theory that these differences in temperature predictions are not significant on pavement design for this project. These errors between predicted and measured temperatures might have an impact on pavement designs for different locations when the temperatures are closer to freezing.

Table 5.9. Average annual number of freeze-thaw cycles for the climatic databases.

Weather Station	Average Annual No. of Freeze-Thaw Cycles
Murrysville	70
Pittsburgh	53
Allegheny	45
Wheeling	49
Meadville	48
Bu Bois	54
P-A-W	60
INT	59

5.3.6 Moisture predictions within the granular layers

In addition to predicting temperatures, the EICM also predicts the moisture content within the granular layers; it does not predict moisture content in the concrete or in stabilized layers. This is because the change in moisture content for the bound layer will not impact the stiffness of that layer. Similarly to the temperature predictions in granular layers, thick layers are subdivided into thinner sublayers and the moisture contents are predicted at mid-depth of the layer. In thin layers, the moisture content is simply predicted at mid-depth. The 24-inch fill layer was automatically subdivided into four layers each of which are 6 inches thick. The top 24 inches of the subgrade layer was treated as a separate layer. In this section, the predicted moisture content in the granular layers during the first two years after construction of the pavement are presented and compared to measured moisture content.

The volumetric water content (VWC) predicted based on the climatic data from the Pittsburgh weather station is presented in Figure 5.52 for the first two years after construction of the pavement. The moisture content did not vary much throughout the two-year period but clearly indicates a sharp decrease during the first winter season. This decrease in VWC is attributed to the freezing of the underlying layers during that period. The VWC increases with depth. During the two-year period, the subbase is at a moisture content of 0.1 or 10 percent, the fill at a moisture content of 20 to 25 percent, and the subgrade at a moisture content of 34 to 35 percent. The same trends were obtained based on the climatic data from the remaining weather stations, with the exception of the predictions based on the onsite station. The predicted moisture content based on the onsite weather station showed a constant moisture content during the two-year period. According to the material characteristics, the volumetric moisture content corresponding to 100 percent saturation are equal to 27 percent for the subbase, 28 percent for the fill, and 19 percent for the subgrade (McCracken et al. 2008). Based on the predicted moisture levels, the fill layer is close to saturation and the subgrade layer is fully saturated during the two-year period, irrespective of the climatic season.

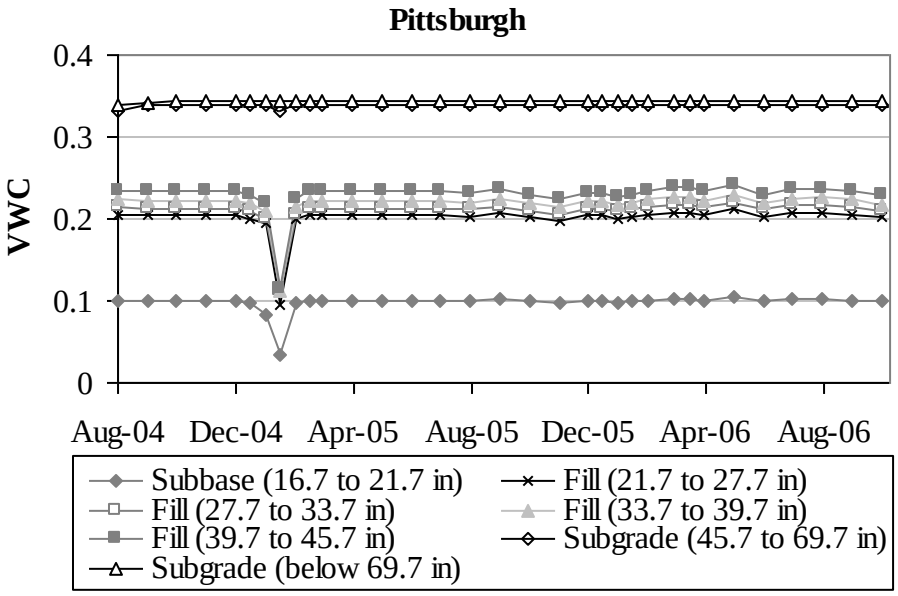

Figure 5.52. Predicted volumetric water content within the granular layers based on climatic data from the Pittsburgh station.

The predicted moisture content based on the climatic data from the different weather stations are compared to each other for the case of the subbase layer, and are presented in Figure 5.53. Data from the onsite weather station shows the lowest predicted moisture content and data from the DuBois weather station results in the highest moisture content. These observations are consistent in all the layers. This difference is not significant.

A comparison between the predicted and measured VWC in the granular layers is not possible due to the absence of valid moisture readings from the TDR system, as previously mentioned in section 5.2.2.

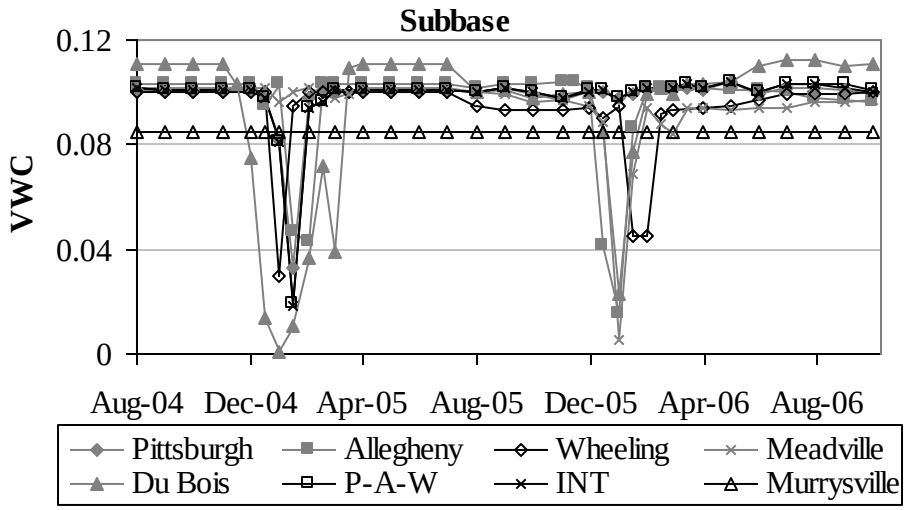

Figure 5.53. Predicted VWC within the subbase.

5.3.7 Pavement performance

It was found in section 5.3.4 that the concrete temperature and average gradient generated using climatic data from weather stations close to the site (within 50 miles) predicted the measured average temperatures and measured average gradient within a couple of degrees. It was also found in section 5.3.5 that the temperatures predicted in the underlying layers are not representative of the measured conditions. In addition, according to section 5.3.6, the moisture content in the granular layers generated using the climatic data was similar for all the weather stations from weather stations close to the site. The predicted moisture content was not compared to the measured due to the lack of valid measured moisture content. In this section, the MEPDG is used to evaluate the effect of the differences in temperature on pavement performance.

To evaluate the performance of a JPCP, the MEPDG predicts slab cracking and faulting over the pavement design life. The restrained slabs were analyzed over a 20-year design life at a 90 percent reliability level. The results are summarized in Table 5.10. The predicted slab cracking and faulting is the same for all the climatic files. The results confirm that the differences in temperature predictions are not significant on pavement design for this project.

Table 5.10. Pavement performance based on MEPDG.

Climatic File	Faulting (inches)	Percent Slabs Cracked (%)
Allegheny	0.031	3.8
Pittsburgh	0.030	3.8
Wheeling	0.033	3.8
Meadville	0.033	3.8
Du Bois	0.031	3.8
P-A-W	0.029	3.8
Interpolated	0.029	3.8
Murrysville (onsite)	0.029	3.8

5.3.8 Summary

The temperature and moisture conditions inside the pavement structure were predicted based on ambient climatic data from the onsite weather station and five of the closest weather stations to the site.

The predicted slab temperatures are close to those measured. The correlation coefficients between the predicted and measured concrete weighted average temperatures were higher than 86 percent, indicating excellent correlation between both variables. The correlation coefficients between the predicted and measured concrete equivalent linear temperature gradients were higher than 62 percent, indicating an acceptable level of correlation between both variables. In addition, the predicted temperature in the asphalt and granular layers were also close to those measured.

The predicted moisture content in the granular layers does not vary much throughout the seasons and significantly decreases when the pavement structure is subjected to a very low temperature that reaches the freezing point of water in the structure. A comparison between the predicted and measured moisture contents could not be properly carried out since the measured moisture content could not be interpreted.

The difference between the measured and predicted temperature and moisture profiles throughout the pavement structure does not significantly affect the pavement performance predicted using the MEPDG.

5.4 SUMMARY AND CONCLUSIONS

In the top two inches of the slab, the concrete relative humidity reaches a minimum value during the winter and maximum value during the spring, and is not affected by variations in the ambient relative humidity. In the deeper portion of the slab, the concrete moisture content remains relatively constant throughout the two-year period. The seasonal trends are similar for both years after construction; however, the moisture content during the second year is lower than the moisture content measured during the first year. During the first year after paving, the average moisture content was 80 percent in the top 2 inches, 90 percent at mid-depth and 100 percent at the bottom of the slab. During the second year, the average moisture content was 60 percent in the top 2 inches, 80 percent at mid-depth and 100 percent at the bottom of the slab.

As for the moisture content measurements within the granular layers, it was found that the TDR probes installed in the granular layers do not provide consistent readings and do not allow for a proper analysis of the data.

The EICM embedded in the MEPDG was used to predict temperature and moisture inside the pavement structure. The analysis was based on ambient climatic data from the onsite weather station and five of the closest stations to the site. The predicted temperature in the concrete and the underlying stabilized and granular layers are close to those measured. The predicted moisture content in the granular layers does not vary much throughout the seasons. A comparison between the predicted and measured moisture contents could not be properly carried out since the measured moisture content could not be interpreted. The difference between the measured and predicted temperature and moisture profiles throughout the pavement structure did not affect the predicted pavement performance based on the MEPDG.

6.0 SLAB SURFACE CURVATURE

The environmental loads to which the pavement is subjected were presented in the previous chapter, and the response of the pavement structure to these loads is discussed in this chapter. The pavement response is characterized in terms of the seasonal variation in the strain measured in the concrete and the measured surface profiles during the first two years after construction. Moreover, the static strain measurements and the measured surface profiles will be used to estimate the slab curvature. A comparison of the curvatures from both sets of data will help quantify the effect of warping as a result of drying shrinkage.

This chapter consists of five major sections. First, the thermal and moisture strains will be quantified based on the measured temperature and moisture data. Then, the seasonal variation of the strain measured in the restrained and unrestrained slabs will be discussed. In the third section, the seasonal variation of the measured surface profile is presented. The fourth section deals with evaluating the effect of slab moisture on the drying shrinkage of the concrete, based on the slab curvature estimated from the strain data, the surface profile measurements and the calculated thermal and moisture-induced strains. Finally, the last section summarizes the results and conclusions made regarding the work carried out in this chapter.

6.1 QUANTIFICATION OF THERMAL AND MOISTURE STRAINS

In this section, the effects of temperature and moisture on the behavior of the slab are further examined. A quantification of the thermal and moisture strain at the surface of the slab based on the measured temperature and moisture distribution throughout the depth of the slab is carried out. The adopted methodology is similar to the methodology followed at Texas A&M University to assess the effects of temperature and moisture conditions in the concrete slab on

the behavior of a jointed plain concrete pavement (Jeong and Zollinger 2005). Strain and curvature of the slab were determined based on the measured concrete temperature and moisture conditions inside the slab. The equivalent linear temperature and humidity differences throughout the depth of the slab were used to estimate the temperature-induced and moisture-induced strain and vertical displacement. The study revealed the behavior of the slab is highly affected by drying shrinkage and creep strain.

In this section, the methodology behind the quantification of the thermal and moisture strain is presented first, followed by a detailed analysis of the estimated thermal and moisture strains and the resulting slab curvature. Then, the strain and curvature estimated in this section are compared to the measured strain (presented in section 6.2.2). Finally the findings of this section are summarized.

6.1.1 Background

The difference in temperature and moisture conditions between the top and bottom portion of the slab can be represented by the equivalent linear temperature difference coefficient and the equivalent linear humidity difference coefficient. These coefficients are determined based on a regression analysis of the profiles of temperature difference and relative humidity difference. A third degree polynomial is assumed to represent the difference profile through the slab. This approach was based on a similar approach suggested by Mohamed and Hansen (1997) to determine the linear temperature and humidity differences through the slab using the actual temperature and humidity differences. Equations 6-1 and 6-2 show the method to estimate the equivalent linear temperature difference, ΔT_{eq}, by fitting a third degree polynomial to the temperature difference along the slab depth (Jeong and Zollinger 2005).

$$\Delta T = A + Bz + Cz^2 + Dz^3 \qquad \text{(Equation 6-1)}$$

$$\Delta T_{eq} = -12\left(\frac{Bh}{12} + \frac{Dh^3}{80}\right) \qquad \text{(Equation 6-2)}$$

Where: z = coordinate defined as zero at middepth of the slab, where upward is negative and downward is positive,

A, B, C, D are regression coefficients, and

h = thickness of the concrete slab.

Similarly, Equations 6-3 and 6-4 show the method to estimate the equivalent linear humidity difference coefficient, $\Delta\left[1-(RH/100)^3\right]_{eq}$, by fitting a third degree polynomial to the humidity difference coefficients from measured relative humidity values along the slab depth.

$$\Delta\left[1-\left(\frac{RH}{100}\right)^3\right]=A+Bz+Cz^2+Dz^3 \qquad \text{(Equation 6-3)}$$

$$\Delta\left[1-\left(\frac{RH}{100}\right)^3\right]_{eq}=-12\left(\frac{Bh}{12}+\frac{Dh^3}{80}\right) \qquad \text{(Equation 6-4)}$$

The thermal and moisture strain (due to gradients) at the slab surface can be estimated based on the equivalent linear temperature difference, equivalent linear humidity difference coefficient, coefficient of thermal expansion and ultimate shrinkage strain (Jeong and Zollinger 2005). The relationships are provided in Equations 6-5 and 6-6.

$$\varepsilon_{TG}=\alpha_T\Delta T_{eq} \qquad \text{(Equation 6-5)}$$

$$\varepsilon_M=-\varepsilon_\infty\Delta\left[1-\left(\frac{RH}{100}\right)^3\right]_{eq} \qquad \text{(Equation 6-6)}$$

Where: ε_{TG} = thermal strain due to temperature gradient,

ε_M = moisture strain,

α_T = coefficient of thermal expansion of the concrete,

ε_ω = ultimate shrinkage strain,

ΔT_{eq} = equivalent linear temperature difference, and

$\Delta\left[1-\left(\frac{RH}{100}\right)^3\right]_{eq}$ = equivalent linear humidity difference coefficient.

Moreover, the strain due to uniform temperature changes across the slab depth, ε_{TU}, is estimated using Equation 6-7. This equation does not represent an actual measured thermal strain and assumes that the coefficient of expansion of the material (the concrete) is the same as that of the structure (the slab), without taking into account the effect of the restraints (the boundary conditions).

$$\varepsilon_{TU}=(T_1-T_0)\alpha_T \qquad \text{(Equation 6-7)}$$

The total strain, ε_{Tot}, at the slab surface due to the effects of temperature and moisture can be estimated based on the relationship in Equation 6-8.

$$\varepsilon_{Tot} = \varepsilon_{TG} + \varepsilon_{TU} + \varepsilon_{M} = \alpha_T \Delta T_{eq} + \alpha_T (T_1 - T_0) - \varepsilon_\infty \Delta \left[1 - \left(\frac{RH}{100} \right)^3 \right]_{eq} \qquad \text{(Equation 6-8)}$$

The thermal and moisture strains were estimated using the previous equations and the results are presented in the following sections 6.1.2 and 6.1.3.

6.1.2 Thermal strain

The variation in the temperature difference coefficient and the resulting thermal strain are presented in this section, for the two-year period following construction. The variation in temperature difference at different depths of the slab was calculated by using the midpanel sensors TC16 to TC22. The top sensor is located at a depth of 0.5 inch and the bottom sensor is located at a depth of 12.6 inches below the surface. According to the survey performed at the time of construction, the thickness of the slab at the location of these thermocouples is 12.7 inches.

The temperature data collected over a period of two years after construction is used to estimate the temperature difference along the slab depth. For every measurement, a third degree polynomial was fit through the measured temperature data to estimate the regression coefficients A, B, C and D. Profiles of the temperature differences were calculated based on the regression coefficients. The measured temperature and the profile of the calculated temperature difference are plotted with respect to slab depth at slab ages of 7 days, 1 year and 2 years, shown in Figure 6.1, Figure 6.2 and Figure 6.3, respectively. The figures show that the profiles are not linear. During the nighttime (10:00 PM to 6:00 AM), the temperatures at the bottom of the slab are highest.

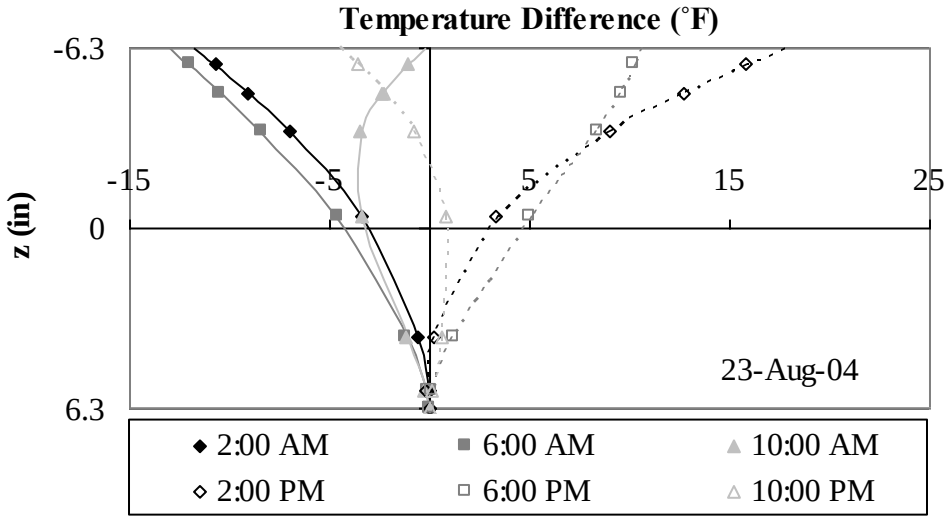

Figure 6.1. Temperature difference profiles on August 23, 2004 (Slab age of 7 days).

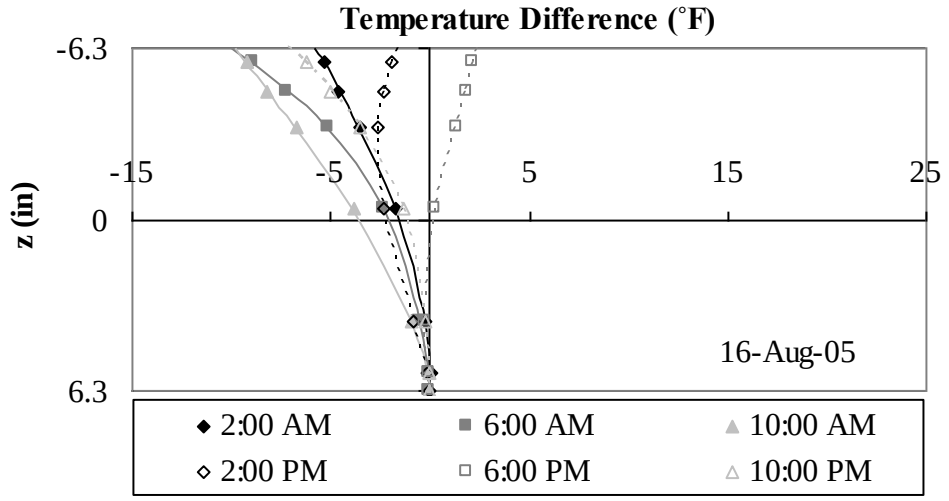

Figure 6.2. Temperature difference profiles on August 16, 2005 (Slab age of 1 year).

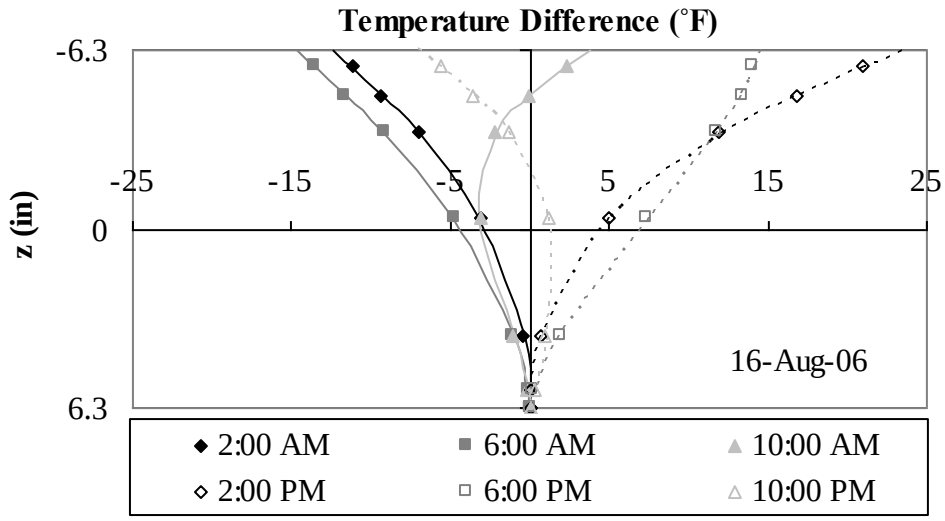

Figure 6.3. Temperature difference profiles on August 16, 2006 (Slab age of 2 years).

The regression coefficients obtained from the third degree polynomial fitting the temperature difference profiles were used in Equation 6-2 to estimate the equivalent linear temperature difference over the two-year period. Figure 6.4 presents a summary of the range and average value of the equivalent linear temperature difference during the two years after construction. The boxes represent the monthly averages plus or minus one standard deviation and the line represents the range of maximum and minimum values. The equivalent linear temperature difference across the slab covers the widest range during the summer and the smallest range during the winter. This confirms the previous findings of section 5.1 that the range of measured temperature gradients is largest during the spring and summer and smallest during the winter.

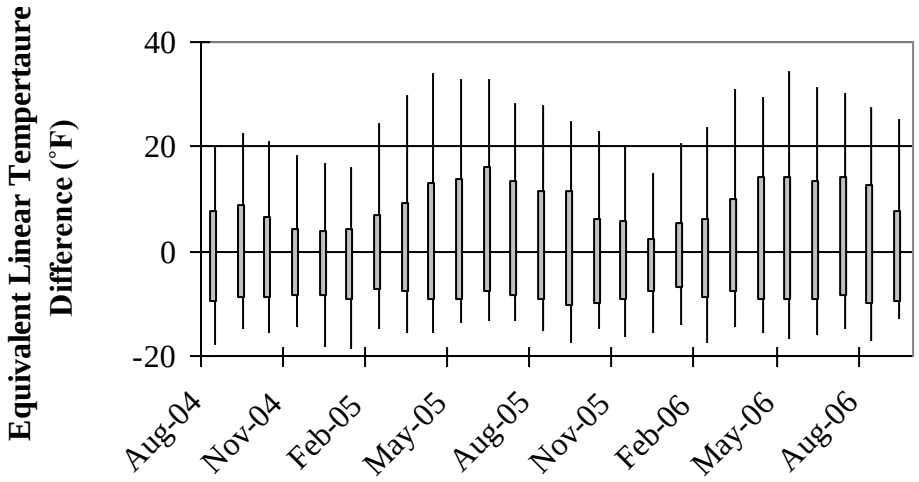

Figure 6.4. Equivalent linear temperature difference during the first two years after construction.

The equivalent linear temperature difference represents the difference between the temperature at the top and bottom of the slab. Therefore, the temperature at the slab surface is estimated based on the equivalent linear temperature difference and the temperature at the bottom of the slab. The predicted temperature at the slab surface and the temperature measured at the bottom of the slab are used to plot the equivalent linear temperature profile along the slab depth. The temperature profiles are presented for a 24-hour period two years after construction. In calculating the temperature at the top and bottom of the slab using the estimated temperature difference along the slab depth, it is assumed that the temperature at mid-depth of the slab ($z = 0$) is equal to the weighted average temperature. Figure 6.5 presents a comparison between the following parameters:

1.) measured temperature profile (points),

2.) the profile fitted by the regression analysis (solid lines),

3.) the equivalent linear temperature difference across the slab determined based on the equations in this section (dashed lines), and

4.) the temperature calculated based on the equivalent linear temperature gradient using the temperature moment concept introduced by Janssen and Snyder (2000) and presented in section 2.3.1 (solid bold lines).

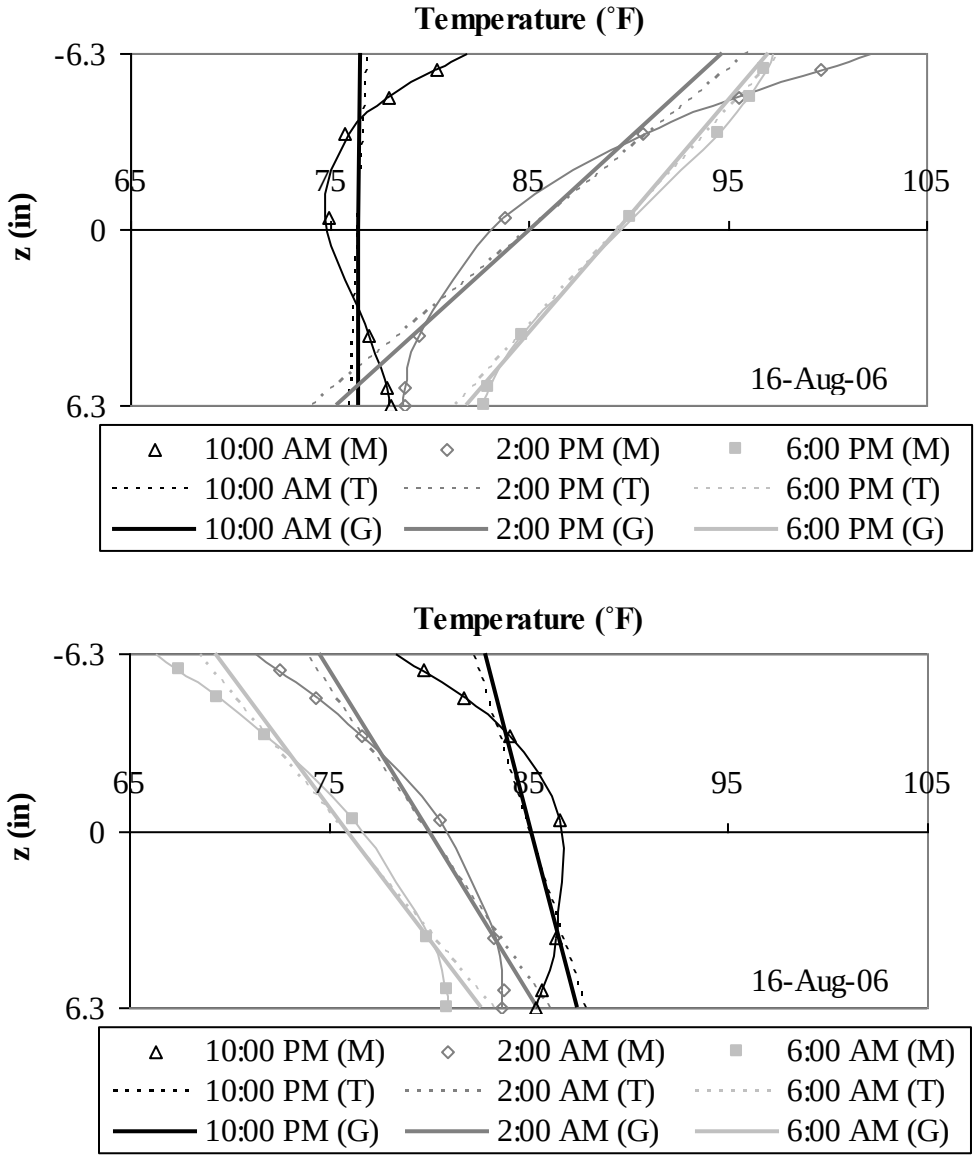

Note: M: Measured; T: Based on the equivalent linear temperature difference

G: Based on the temperature moment concept

Figure 6.5. Comparison between the measured temperature profile and the profile calculated based on different methods for August 16, 2006 (2 years after construction).

Figure 6.5 shows that the equivalent linear temperature difference provides comparable results to the temperature moment concept proposed by Janssen and Snyder (2000). The reason behind the slight differences shown in the figure is explained in the next paragraph.

The temperature difference method calculates the temperature difference between the temperature at any depth within the slab and the temperature at the bottom of the slab. The thermocouple located at the bottom of the slab is at a depth of 12.6 inches, while the slab thickness at that same location is 12.7 inches. Using the temperature difference method, without extrapolating to estimate the temperature at the bottom of the slab, is introducing a small amount of error in estimating the temperature gradient across the slab. However, the amount of error introduced is not significant and does not affect the overall temperature difference across the slab, as shown in Figure 6.6. Therefore, the temperature difference calculated based on the equivalent linear temperature gradient (using the temperature moment concept) will be used to estimate the temperature-induced strain at the slab surface.

To estimate the temperature-induced strain at the surface of the slab using Equations 6-5 or 6-7, the coefficient of thermal expansion is required. The coefficient of thermal expansion of the paving concrete was measured in the laboratory and found to be 5.9 x 10^{-6} in/in/°F (Wells et al. 2005). The strain is zeroed based on the strain due to the built-in temperature gradient at the time of set of the concrete. The built-in equivalent linear temperature gradient was estimated to be 0.31°F/in, in Chapter 4. The corresponding strain is estimated using Equation 6-5 and is presented in the following:

$$\varepsilon_T = \alpha_T \Delta T_{eq} = \left(5.9 \times 10^{-6}\right)(0.31)(12.7) = 23\ microstrain$$

This indicates that the strain due to the temperature gradient at the time of set is equivalent to 11.5 microstrain at the top of the slab and -11.5 microstrain at the bottom.

Figure 6.7 presents the variation of the calculated thermal strain over the two-year period after construction of the pavement. According to the equation used, the thermal strain is linearly proportional to the concrete coefficient of thermal expansion and the equivalent linear temperature difference. Therefore, it is expected that the calculated thermal strain exhibits trends that are similar to those of the equivalent linear temperature differences. The thermal strain fluctuates daily and seasonally during the two years, with the largest fluctuations during the summer and the smallest during the winter. During the two-year period, the calculated thermal strain due to temperature gradients fluctuates between -120 microstrain and 150 microstrain.

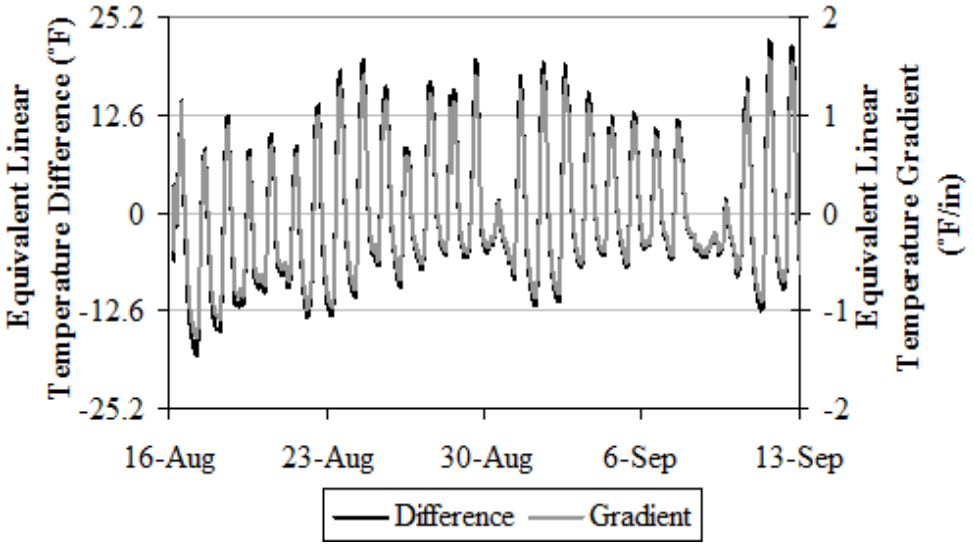

Figure 6.6. Equivalent linear temperature difference and equivalent linear temperature gradient, for the first month after construction.

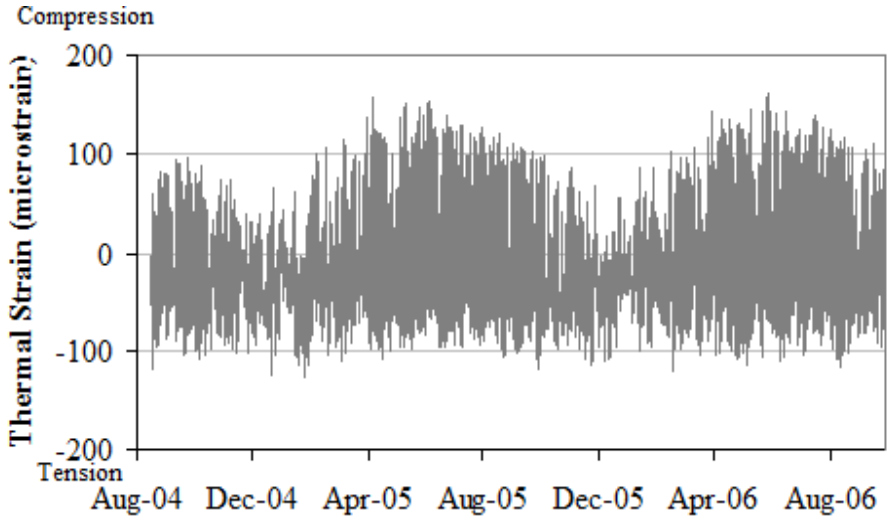

Figure 6.7. Thermal strain due to temperature gradient at slab surface, for the two-year period after construction.

The slab is subjected to positive and negative temperature gradients on a daily basis, as shown in Figure 6.8 for the first month after paving. The daily cycles of variation in the temperature difference across the slab depth showed that the maximum positive difference occurs during the afternoon hours and the maximum negative difference occurs during the early morning hours.

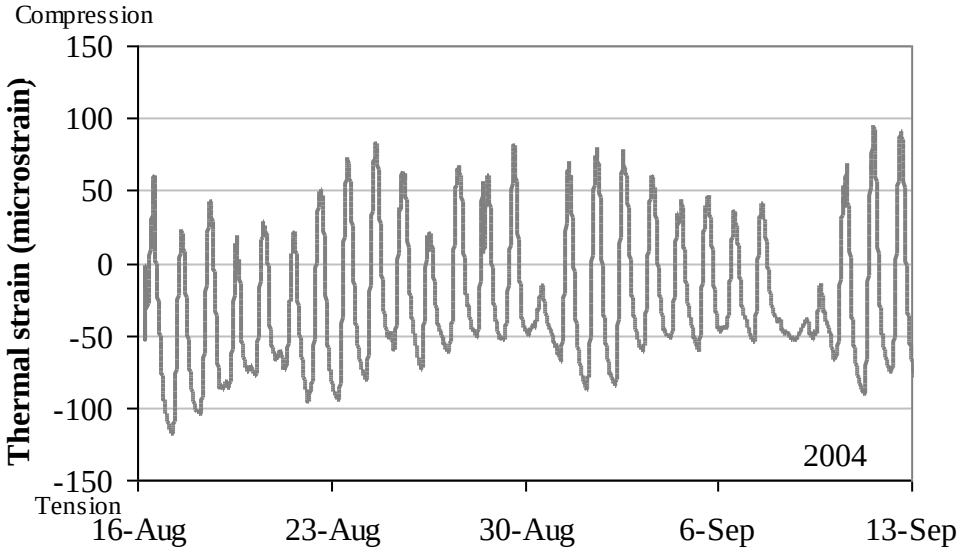

Figure 6.8. Thermal strain due to temperature gradient at slab surface, for the first month after paving.

As previously discussed in Chapter 2, the deformation of the slab due to temperature is due to three components representing the uniform, linear and nonlinear portions of the temperature profiles. Equation 6-5, which is used in this section to calculate the thermal strain, takes into account the linear and nonlinear components that cause bending of the slab, without taking into account the uniform temperature change that causes uniform contraction and expansion along the slab depth. The uniform thermal strain, presented in Equation 6-7, was calculated based on the uniform temperature changes across the slab. The uniform temperature-induced strain is similar for both restrained and unrestrained slabs and therefore unaffected by the restraining conditions of the slab. A comparison between the thermal strain due to the

temperature gradient and the thermal strain due to uniform temperature change is presented in Figure 6.9. The uniform thermal strain presented in this figure corresponds to the temperature data from the static strain sensor located at the slab surface in the midpanel location. As expected, the figure shows that the thermal strain due to the temperature gradient, calculated earlier in this section, fluctuates between positive and negative values on a daily basis, while the uniform strain is negative throughout the two-year period and exhibits seasonal fluctuations.

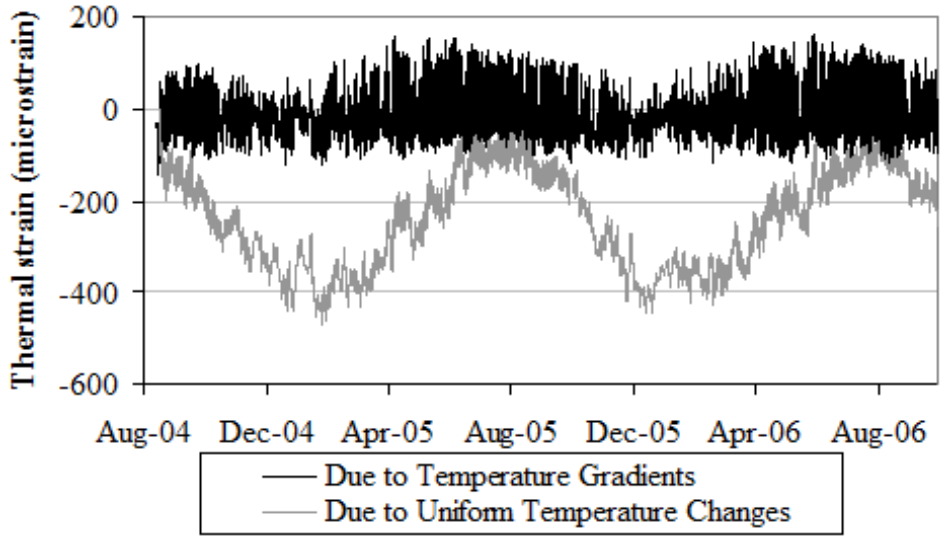

Figure 6.9. Thermal strains due to temperature gradient and to uniform temperature change.

Figure 6.10, presenting the frequency of occurrence of equivalent linear gradients during the two-year period, shows that the equivalent linear gradient is less than the built-in gradient of 0.31˚F/in for approximately 86 percent of the time. This confirms that the slab is typically curled upward during the two-year period. As a result, the average thermal strain due to the temperature gradient is negative throughout the two-year period.

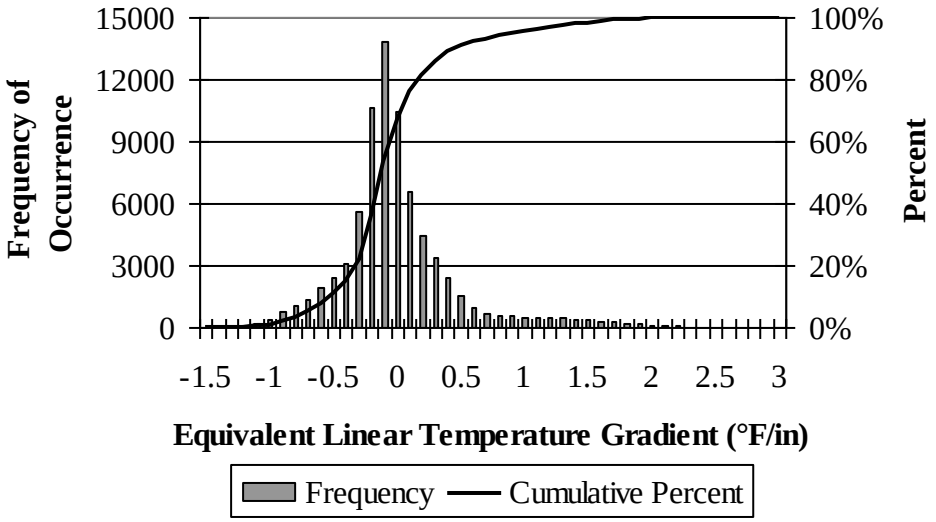

Figure 6.10. Frequency of occurrence of equivalent linear gradients.

The movement of the slab attributed to uniform temperature changes also varies seasonally but remains negative throughout the two-year period, as presented in Figure 6.11. The strain is largest in magnitude during the fall and winter and smallest in magnitude during the spring and summer. This is due to the fact that the concrete slabs are subjected to the coldest temperatures during the fall and winter and the highest during the spring and summer, which causes the slabs to contract the most during the colder seasons and the least during the warmer seasons. It is interesting to note that the strain due to the uniform temperature changes and the strain due to the temperature gradient act in the same manner and cause the total strain to be higher than that due to the sole effect of the uniform temperature change. On average, the magnitude of the strain due to the temperature gradient constitutes 13 percent of the magnitude of the strain due to uniform temperature changes during the summer, 11 percent during the fall, 7 percent during the winter and 5 percent during the spring.

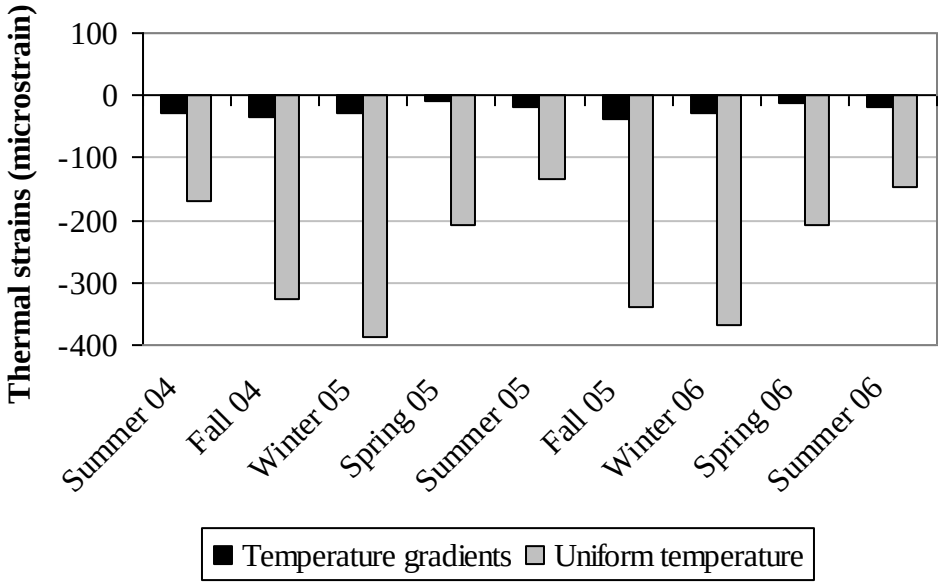

Figure 6.11. Seasonal variation of thermal strain at the slab surface.

6.1.3 Moisture-induced strain

The surface moisture strain can be estimated based on the difference in the concrete relative humidity throughout the slab. The variation in the relative humidity difference coefficient and the resulting moisture-induced strain are presented in this section, for the two-year period following construction. The variation in relative humidity difference at different depths of the slab was calculated by using the relative humidity measurements from the midpanel sensors MC13 to MC17. However, since only two of the sensors remained operational after a couple of weeks after construction, the humidity difference coefficients calculated using theses sensors yielded unrealistic results due to insufficient data. As a result, the edge sensors MC2 to MC6 were used in calculating the humidity difference coefficients. The top sensor is located at a depth of 1.6 inches and the bottom sensor is located at a depth of 12.4 inches below the surface. According to the survey performed at the time of construction, the thickness of the slab at the location of these moisture sensors is 13.4 inches.

The relative humidity data collected over a period of two years after construction is used to estimate the humidity difference coefficient along the slab depth. The relative humidity at the bottom of the slab is needed to estimate the humidity difference coefficient at different depths. Based on previous studies, it has been shown that the relative humidity at the bottom of the slab does not vary much during the pavement lifetime and remains at relatively high levels indicating saturation (ARA 2004; Eisenmann 1990). According to the relative humidity data collected over the two years, sensor MC6 recorded relative humidity levels between 81 and 100 percent at a depth of 12.4 inches in the slab (Figure 5.6). Based on this, a relative humidity level of 100 percent at the bottom of the slab is assumed in this section.

For every set of relative humidity measurements taken throughout the depth of the slab, a third degree polynomial was fit through the measured data to estimate the regression coefficients A, B, C and D. Profiles of the relative humidity difference were calculated based on the regression coefficients. The calculated humidity differences and the profiles of the fitted polynomials are plotted with respect to slab depth at slab ages of 7 days, 1 year and 2 years, shown in Figure 6.12, Figure 6.13 and Figure 6.14. The figures show that the profiles are not linear and that the humidity difference coefficient at the top of the slab varies at a higher rate than at the bottom of the slab. Profiles with missing data points are excluded from the analysis and not used to estimate the moisture-related strain.

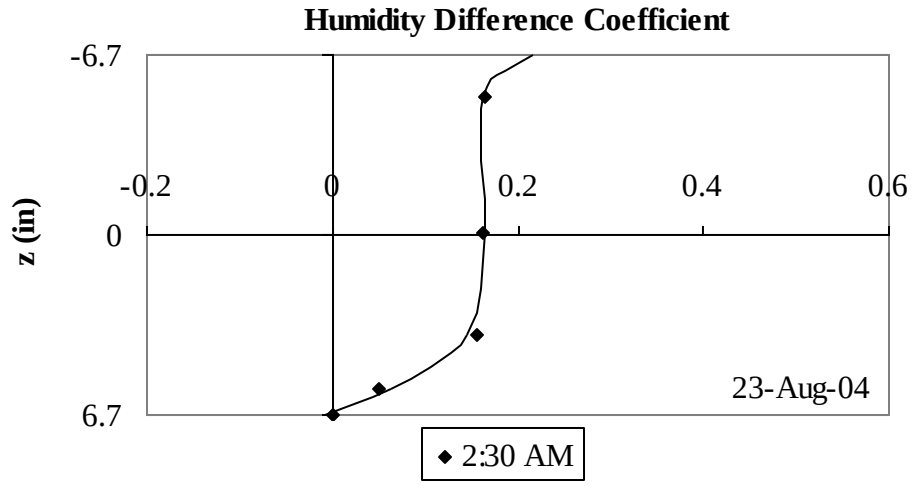

Figure 6.12. Profile of humidity difference coefficient on August 23, 2004 (7 days after construction).

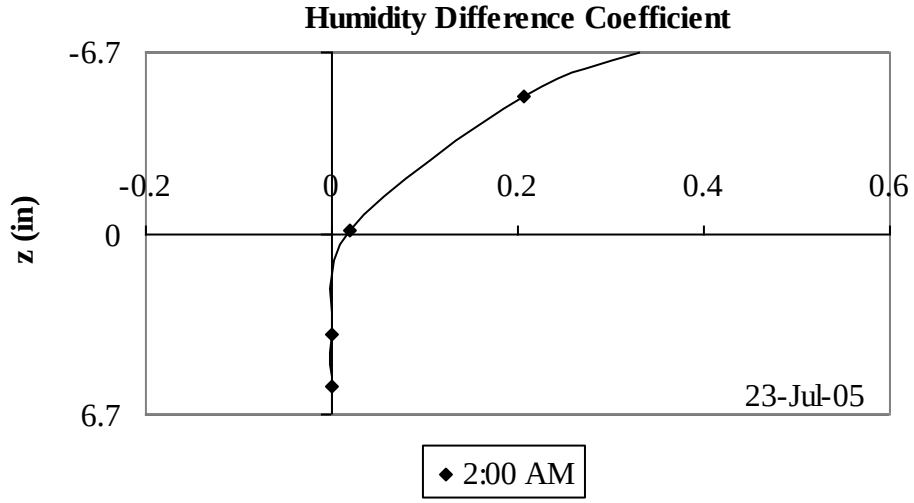

Figure 6.13. Profile of humidity difference coefficient on July 23, 2005 (1 year after construction).

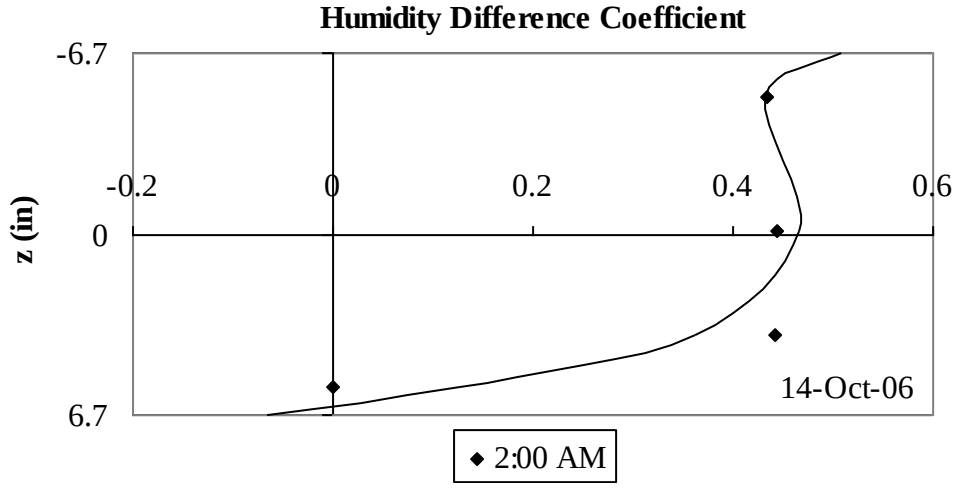

Figure 6.14. Profile of humidity difference coefficient on October 14, 2006 (2 years after construction).

The regression coefficients obtained from the third degree polynomial fitting the humidity difference coefficient profiles were used in Equation 6-4 to estimate the equivalent linear humidity difference coefficient over the two-year period, as presented in Figure 6.15. The gaps in the figure are due to the lack of the relative humidity data. According to the figure, the equivalent humidity difference coefficient fluctuates seasonally and is larger during the second year after construction compared to the first year. During the first winter, the coefficient increases and reaches a value of 0.23 towards the beginning of the spring, when it decreases until reaching 0.15 in the beginning of the summer. During the second year, the coefficient is highest during the fall at 0.40 and lowest during the spring at 0.30. Also, the fluctuations in the second year are less than those observed during the first year. Excluding the first week after construction, the relative humidity coefficient varies between 0.15 and 0.40 during the two-year period.

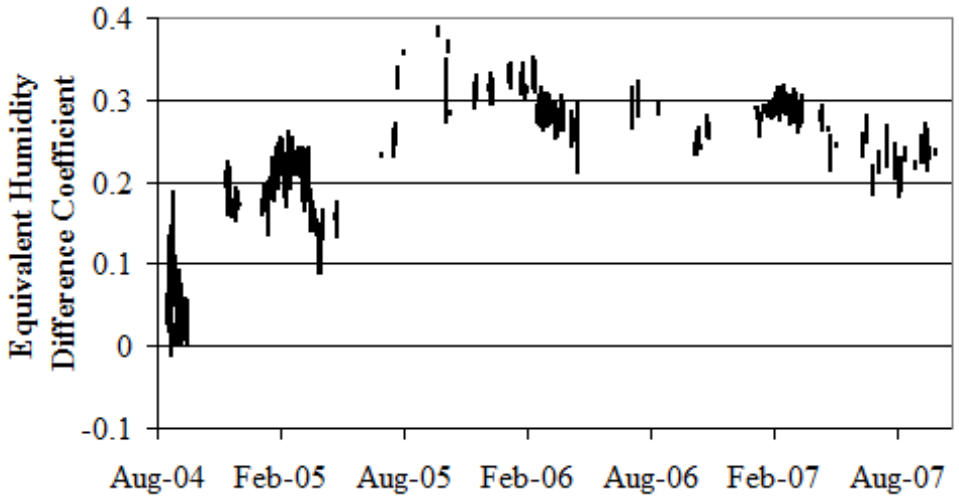

Figure 6.15. Variation of the equivalent linear humidity difference coefficient during the three years after construction.

The equations provided in this section do not predict the relative humidity in the slab but can provide an estimate of the relative humidity at the top of the slab. The equivalent linear humidity difference coefficient represents the difference between the humidity difference coefficient at the top and bottom of the slab. Therefore, the humidity difference coefficient at the slab surface can be estimated based on the equivalent linear temperature difference and the humidity difference coefficient at the bottom of the slab. Since the humidity level at the bottom of the slab is assumed to be 100 percent, the coefficient at the bottom of the slab is calculated as 0. This implies that the coefficient at the top of the slab is equal to the equivalent linear coefficient. Based on this, the humidity levels at the top of the slab that would provide the equivalent linear difference can be calculated. The minimum and maximum coefficient values of 0.15 and 0.40 correspond to relative humidity values of 95 and 84 percent at the slab surface, respectively. These relative humidity levels are consistent with those recorded by the concrete moisture sensors at the slab edge (refer to section 5.2.1).

To estimate the moisture-induced strain at the surface of the slab using Equation 6-6, the ultimate drying shrinkage is required. The concrete ultimate shrinkage strain was estimated from lab testing on three concrete beams cast from the field mix at the time of paving and monitoring the length and mass change in the specimens over a period of 250 days and 1 year (Wells et al. 2005; Asbahan et al. 2006). From these studies, the drying shrinkage of the concrete stabilized at an average of 945 microstrain. The strain is zeroed based on the strain due to the built-in moisture conditions. At set time, the slab was fully saturated, as discussed in section 4.1.2, and therefore, the strain due to the built-in moisture conditions is taken as zero.

Figure 6.16 presents the variation of the calculated moisture-related strain over the two-year period after construction. According to the equation used, the moisture-related strain is linearly proportional to the concrete drying shrinkage and the equivalent linear humidity difference coefficient. Therefore, it is expected that the calculated moisture-related strain exhibits trends that are similar to those of the equivalent linear humidity difference coefficient. The moisture-induced strain fluctuates seasonally, but remains negative during the three-year period, indicating that the moisture conditions cause the slab surface to curl upward (slab in compression) irrespective of the seasons. This is consistent with the expected slab behavior due

to the moisture conditions, since the moisture conditions only fluctuate seasonally in the top two inches of concrete and remain at a level of 100 percent in the bottom half of the slab (Eisenman 1990; ARA 2004). This negative moisture gradient is expected to cause upward curvature.

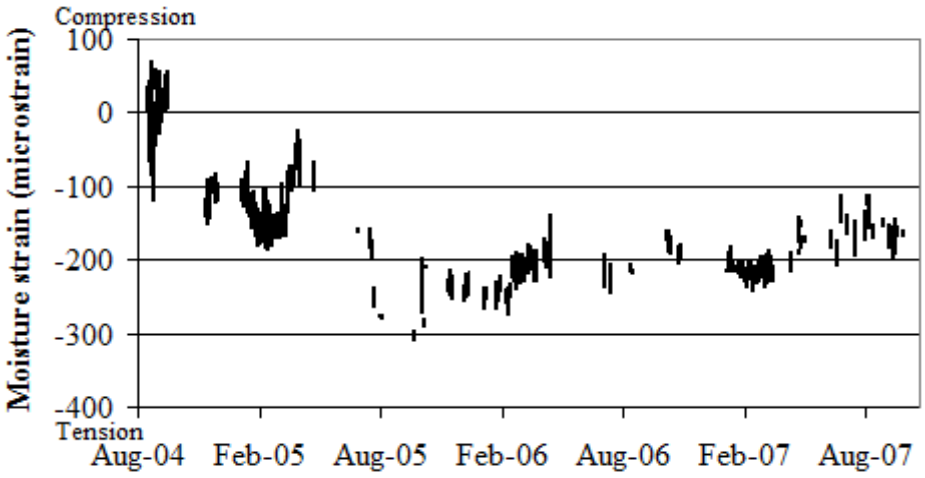

Figure 6.16. Calculated moisture-related strain at slab surface for the three-year period.

With the exception of the first couple of weeks after construction, the strain varies between -180 and -30 microstrain during the first year after construction. During the second and third years, the strain estimated using the moisture measurements varies between -300 and -110 microstrain. The magnitude of the calculated moisture-related strain is highest in the fall and lowest in the spring. This is consistent with the observations made in section 6.2.2 regarding the seasonal variations of the measured strain due to moisture and other factors. During the spring, the higher amount of precipitation causes the slab to expand, which is exhibited by a decrease in the slab contraction, and thus the lower magnitude of the strain. Moreover, the moisture-related strain during the second year significantly increased in magnitude when compared to the calculated strain for the first year after paving. The average strain for the fall season doubled in magnitude, increased by 50 percent for the winter, increased by six times for the spring, and increased by 25 percent for the summer between the first and second year after paving.

6.1.4 Equivalent temperature difference due to concrete moisture gradient

The equivalent temperature difference due to the presence of a moisture gradient in the concrete slab was estimated using two approaches. The first approach makes use of the moisture measurements within the slab and the second method makes use of the ambient relative humidity measurements. The results are presented and discussed in this section.

The first approach to estimate the equivalent temperature difference due to the presence of a moisture gradient in the concrete slabs is based on the moisture strain calculated in the previous section. As previously stated in section 2.4, the Westergaard equation for the maximum stress at the slab center due to slab curling is given by Equation 2-12, which includes the effects of both curling and warping (ARA 2004; Mohamed and Hansen 1987). Rearranging the terms of that equation, the strain caused by a moisture gradient across the slab depth can be converted into an equivalent temperature gradient across the slab by equating the strain caused by moisture to a strain caused by a fictitious temperature difference. As a result, the following Equation 6-9 is generated.

$$\Delta T_{eqv} = \frac{-\varepsilon_{\infty}\Delta\left[1-(RH/100)^3\right]_{eq}}{\alpha_T} \qquad \text{(Equation 6-9)}$$

Where: ΔT_{eqv} = equivalent linear temperature difference,

ε_{∞} = ultimate shrinkage strain,

α_T = coefficient of thermal expansion of the concrete, and

$\Delta\left[1-\left(\frac{RH}{100}\right)^3\right]_{eq}$ = equivalent linear humidity difference coefficient.

Using Equation 6-9, the temperature difference equivalent to the presence of a moisture gradient is calculated and is presented in Figure 6.17 for the first three years following construction. Figure 6.17 shows that the equivalent linear temperature difference varies between -31˚F and -5˚F during the first year after construction (excluding the first couple of weeks after paving) and between -45˚F and -20˚F during the following two years.

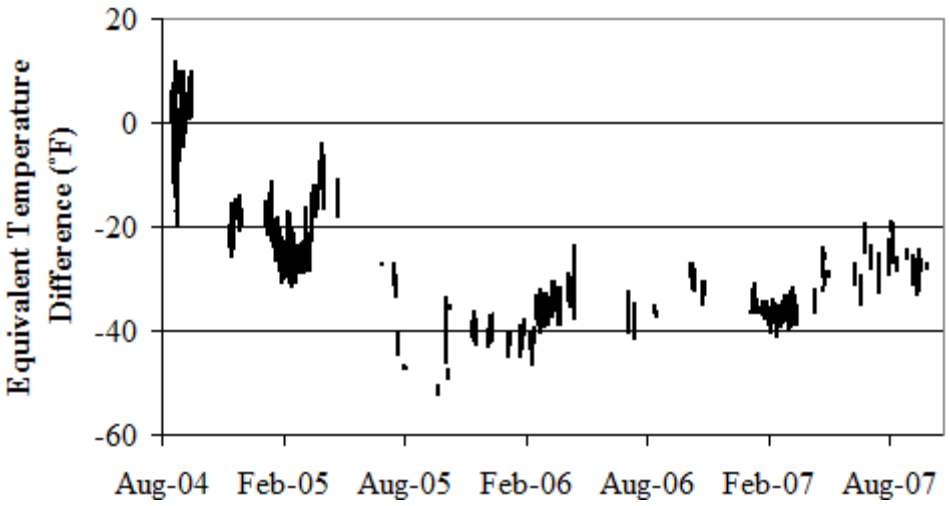

Figure 6.17. Equivalent temperature difference due to moisture based on moisture measurements.

The equivalent linear temperature difference is then used to determine the temperature gradient, and the corresponding equivalent linear temperature gradients are presented in Figure 6.18. The corresponding equivalent linear temperature gradient varies between -2.4˚F/in and -0.4˚F/in during the first year after construction (excluding the first couple of weeks after paving) and between -4.0˚F/in and -1.5˚F/in during the second and third years after construction.

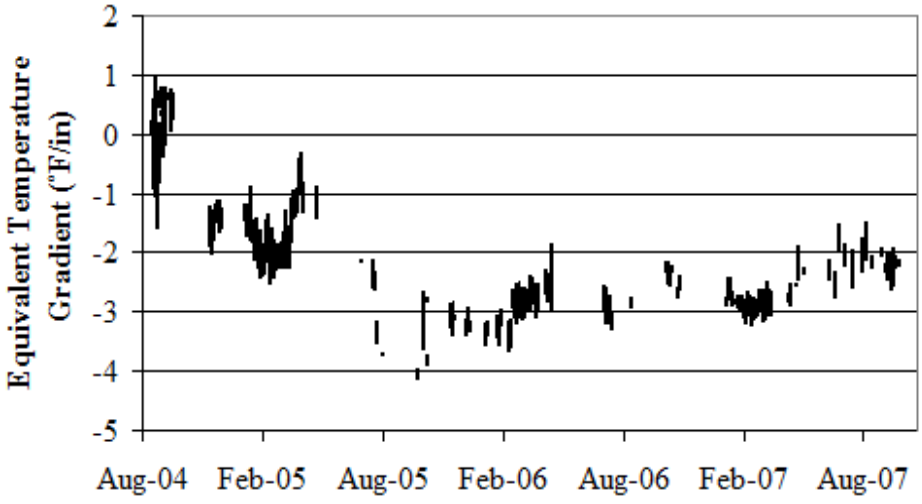

Figure 6.18. Equivalent linear temperature gradient due to moisture based on moisture measurements.

The second approach to estimate the equivalent temperature difference due to the presence of a moisture gradient in the concrete slabs is based on the ambient relative humidity measurements. The most recent method for estimating the equivalent temperature gradient due to the effect of moisture is adopted by the MEPDG. It was developed based on Equation 2-4 (Eisenmann and Leykauf 1990), and was previously presented in Equation 2-5 (see section 2.3). Moisture warping is calculated based on the assumption that concrete moisture varies in the top 2 inches of the slab, depending on the ambient relative humidity, and the concrete moisture in the deeper portion of the slab remains constant at a saturation level of 85 percent or higher (ARA 2004; Janssen 1987). This was verified by the concrete moisture measurements during the two years after construction, which were presented in section 5.2.

This method calculates the equivalent temperature difference representing slab warping due to moisture, based on relative changes in monthly atmospheric relative humidity with respect to the annual average atmospheric relative humidity. This method represents the warping due to a negative moisture gradient, i.e., a positive temperature difference indicates a negative gradient and an upward curvature while a negative temperature difference indicates a positive gradient and a downward curvature.

This method requires several parameters characterizing the concrete material properties. The concrete material parameters were determined by laboratory testing and are presented in detail in technical reports (Wells et al. 2005; Asbahan et al. 2006). The relevant concrete material properties needed to estimate the equivalent temperature gradient are listed in Table 6.1.

Table 6.1. Concrete material parameters needed for the estimation of the equivalent temperature gradient due to concrete moisture.

Concrete Parameter	**Value**
Surface shrinkage, ε_s	945 με
PCC slab thickness, h (at the location of the moisture sensors)	13.4 inches
Depth of the shrinkage zone, t	2 inches
PCC coefficient of thermal expansion, α	5.9×10^{-6} /˚F
Reversible shrinkage factor, φ	0.5 (assumed)
Time to develop 50 percent of the ultimate shrinkage	8 days

The use of this equation also requires parameters characterizing the effects of the ambient relative humidity conditions on the concrete. The ambient relative humidity conditions were measured using the on-site weather station and the average monthly ambient relative humidity are summarized in Table 6.2. The relative humidity factors corresponding to the average monthly ambient relative humidity were calculated based on the ambient relative humidity, RH_a, and are also listed in Table 6.2.

Using Equation 2-5, the material properties provided in Table 6.1 and the relative humidity factors determined in Table 6.2, the moisture gradient is converted into an equivalent linear temperature gradient and the corresponding temperature difference across the top 2 inches of the slab, ETG_{Shi}, is calculated and presented in Table 6.3, for the first two years after construction. The equivalent temperature gradient representing the combined effect of the moisture gradient in upper 2 inches and the drying shrinkage that has occurred over time is represented by ETG_{Sht}. The temperature difference equivalent to moisture warping during the two-year period is also illustrated in Figure 6.19.

Since the concrete moisture at the bottom portion of the slab is higher than at the top portion, the moisture gradient is expected to be negative throughout the year resulting in an upward slab curvature due to warping. However, the calculations presented in Table 6.3 and Figure 6.19 indicate that the equivalent temperature difference fluctuates between positive and negative values throughout the two-year period. This is explained by the method of calculation of the equivalent temperature difference, which estimates the temperature difference in the top 2 inches of the slab with respect to the annual average ambient relative humidity, while maintaining an 85 percent saturation level in the deeper portion of the slab (ARA 2004).

Table 6.2. Average monthly ambient relative humidity and relative humidity factors.

Month	Monthly Average Ambient Relative Humidity, Rh_a (%)	Relative Humidity Factor for Month i, S_{hi} (1)	Annual Average RH_a (%)	Annual Average Relative Humidity Factor, $S_{h\ ave}$ (2)
Aug-04	79	0.613	--	0.661
Sep-04	78	0.615	74	0.661
Oct-04	79	0.605		
Nov-04	76	0.636		
Dec-04	77	0.629		
Jan-05	80	0.605		
Feb-05	78	0.623		
Mar-05	75	0.652		
Apr-05	61	0.789		
May-05	67	0.733		
Jun-05	70	0.697		
Jul-05	72	0.680		
Aug-05	73	0.674		
Sep-05	71	0.694	71	0.692
Oct-05	79	0.609		
Nov-05	70	0.702		
Dec-05	77	0.628		
Jan-06	75	0.650		
Feb-06	67	0.731		
Mar-06	65	0.750		
Apr-06	61	0.787		
May-06	68	0.718		
Jun-06	72	0.678		
Jul-06	74	0.664		
Aug-06	70	0.697		
Sep-06	79	0.605	--	0.692

Notes: (1) Equation 2-5: $S_{hi} = 1.4 - 0.01\ RH_a$ for $30\ \% < RH_a < 80\ \%$

(2) $S_{h.ave}$ = Annual average of S_{hi}

Table 6.3. Equivalent temperature difference due to the presence of a moisture gradient calculated based on Eisenmann and Leykauf (1990).

Month	ETG_{Shi} (1,4) (˚F)	Age (days)	Time Factor, St (2)	ETG_{Sht} (3,4) (˚F)
Aug-04	-0.775	15	0.65	-0.506
Sep-04	-0.744	45	0.85	-0.631
Oct-04	-0.903	76	0.90	-0.817
Nov-04	-0.415	106	0.93	-0.386
Dec-04	-0.529	137	0.94	-0.499
Jan-05	-0.912	168	0.95	-0.871
Feb-05	-0.624	196	0.96	-0.599
Mar-05	-0.156	227	0.97	-0.151
Apr-05	2.057	257	0.97	1.995
May-05	1.149	288	0.97	1.118
Jun-05	0.571	318	0.98	0.557
Jul-05	0.301	349	0.98	0.295
Aug-05	0.204	380	0.98	0.200
Sep-05	0.019	410	0.98	0.018
Oct-05	-1.344	441	0.98	-1.320
Nov-05	0.149	471	0.98	0.147
Dec-05	-1.041	502	0.98	-1.025
Jan-06	-0.682	533	0.99	-0.672
Feb-06	0.628	561	0.99	0.620
Mar-06	0.934	592	0.99	0.922
Apr-06	1.529	622	0.99	1.510
May-06	0.419	653	0.99	0.413
Jun-06	-0.231	683	0.99	-0.228
Jul-06	-0.460	714	0.99	-0.455
Aug-06	0.080	745	0.99	0.079
Sep-06	-1.405	775	0.99	-1.390

Notes: (1) ETG_{Shi} = Temperature difference equivalent of the deviation of moisture warping in month i from the annual average, Equation 2-5: $ETG_{Shi} = \frac{3(\varphi \cdot \varepsilon_{su})(S_{hi} - S_{h\,ave})h_S\left(\frac{h}{2} - \frac{h_S}{3}\right)}{\alpha\, h^2}$

(2) St is a time factor to account for the time to develop full shrinkage, Equation 2-6: $\left(\frac{Age}{n + Age}\right)$

(3) ETG_{Sht} = ETG_{Shi} at any time t days from PCC placement

(4) Negative values indicate downward curvature and positive values indicate upward curvature

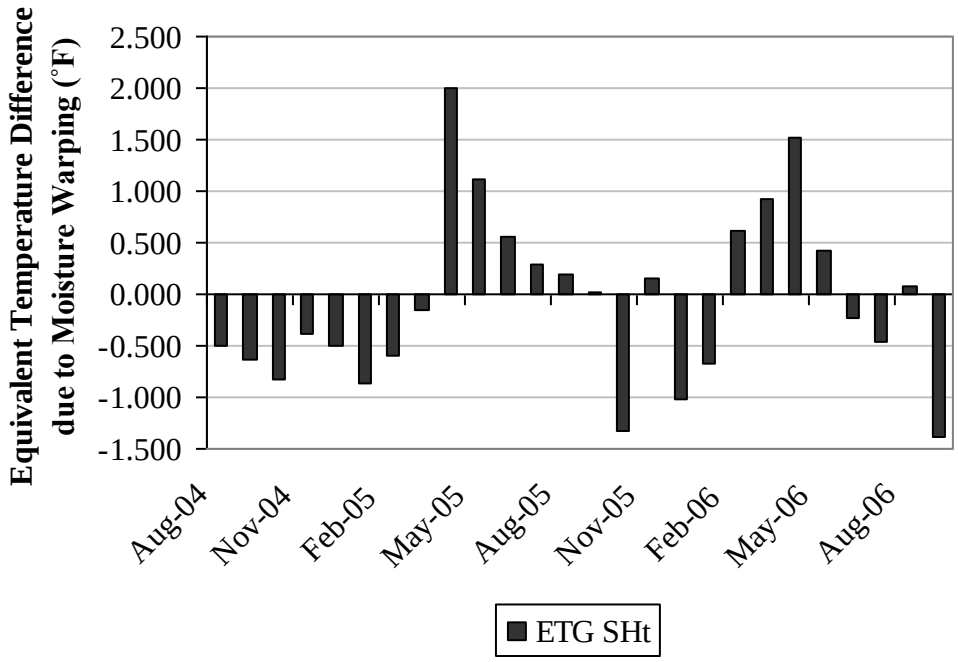

Figure 6.19. Temperature difference equivalent to moisture warping based on the ambient relative humidity measurements.

The equivalent temperature difference starts out with small negative values of -0.15˚F to -0.87˚F shortly after construction and during the first couple of months after paving. The ambient relative humidity during these months varies between 75 and 78 percent, which is close to the average annual relative humidity during the first year after construction (74 percent). As a result, slab movement due to the moisture gradient is minimal during this time period. During the spring of 2005, the ambient relative humidity significantly decreases to 61 percent, and is accompanied by an increase in the temperature difference due to slab warping of -2˚F, which represents a more negative gradient. During the second year after paving, the annual average relative humidity is 71 percent. During the months when the ambient relative humidity is lower than 71 percent, an equivalent positive temperature difference is calculated and during the months when the ambient relative humidity is higher than 71 percent, an equivalent negative temperature difference is calculated. During the two-year period, the gradient corresponding to the equivalent temperature difference varies between -0.10˚F/in and 0.15˚F/in.

The equivalent temperature differences based on the two approaches are significantly different, as compared in Figure 6.20. There is a significant difference between the two methods. The equivalent temperature gradient obtained based on the concrete moisture measurements is considered to be more representative of the moisture conditions inside the concrete. Therefore, the temperature difference based on the concrete moisture measurements will be used in quantifying the effect of moisture on the slab throughout this study.

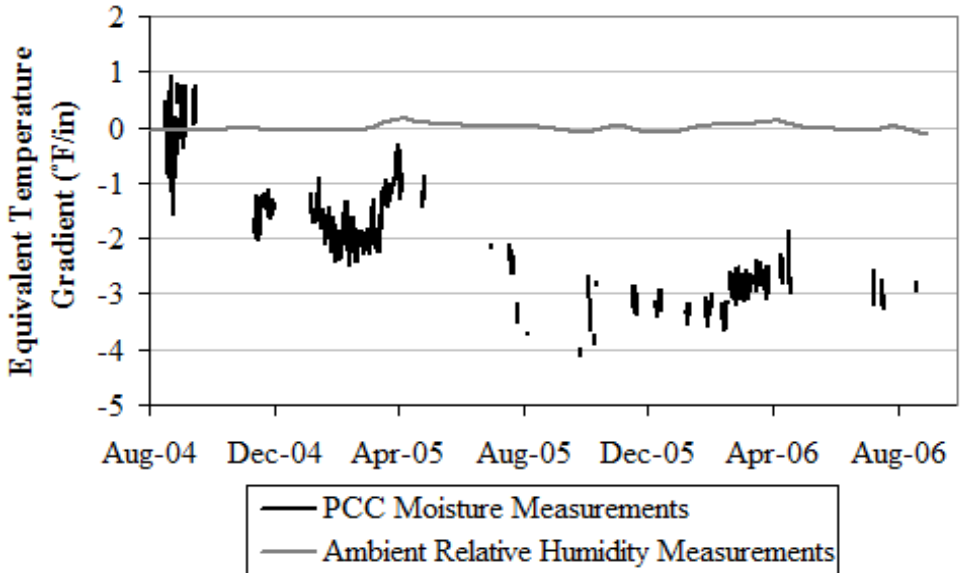

Figure 6.20. Equivalent temperature difference based on the concrete moisture measurements and the ambient relative humidity measurements.

6.1.5 Slab curvature

As the slab is subjected to a given set of moisture and temperature gradients, slab strains vary through the thickness of the concrete, causing the slab to curl/warp either upward or downward, depending upon whether the net gradient is negative or positive. The difference in strain at the top and bottom of the slab can be used to compute the slab curvature using Equation 6-10. This equation was derived using the following assumptions (Mohamed and Hansen 1997): (a) the slab is elastic, homogenous and isotropic, with temperature-independent material properties; (b) plane

sections remain plane after bending; (c) stresses and strains in the vertical direction are zero; (d) the deflection of the slab is small compared to the slab dimensions; and (e) temperature or shrinkage strains vary in the vertical direction only.

$$\rho = -\frac{\varepsilon_t - \varepsilon_b}{D(1 + \varepsilon_t + \varepsilon_b)} \qquad \text{(Equation 6-10)}$$

Where: ρ = Slab curvature (positive values indicate upward curvature), in units of 1/ft

ε_t = Calculated strain at the top of the slab at the time of interest

ε_b = Calculated strain at the bottom of the slab at the time of interest

D = Distance between the top and bottom of the slab where strain is calculated, ft.

Equation 6-10 was used to calculate the curvature based on the thermal and moisture-induced strains presented in sections 6.1.2 and 6.1.3. The distance between the top and bottom of the slab where strain is calculated was 12.7 inches for the thermal strain and 12.65 inches in the case of moisture-induced strain.

Slab curvatures computed based on the calculated thermal and moisture strains are presented in Figure 6.21. It is important to note that these calculated curvatures do not consider the factors that restrain slab deformation; therefore, they overestimate the actual slab curvature. The curvature due solely to the calculated thermal strain fluctuates between positive and negative values throughout the two-year period, with a relatively small range of curvatures during the winter and a larger range of curvatures during the summer. This indicates that the daily fluctuations in the temperature gradient cause the slab to curl upward and downward during all seasons at this site, and that the range of movement is smallest during the winter. The curvature due to the calculated moisture-induced strain is mostly positive, indicating that the moisture gradient produced upward warping throughout the two-year period. Soon after construction, the magnitude of the moisture-induced curvature becomes larger than the magnitude of the thermal-induced curvature. Therefore, the net effect is that the curvature of the slabs is predominantly upward by the summer following construction. This condition would contribute to top-down fatigue cracking (rather than the bottom-up fatigue cracking that is traditionally assumed for JPCP).

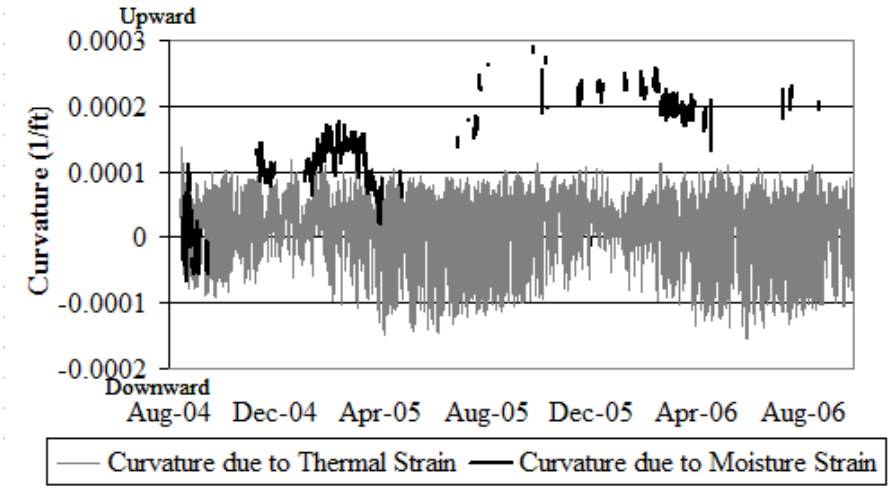

Figure 6.21. Slab curvature based on the calculated thermal and moisture-induced strain.

The slab curvature calculated in this section will be compared to the slab curvature calculated based on the static strain measurements and the surface profile testing, and will be presented in section 6.4.

6.1.6 Summary

The thermal strain fluctuates daily and seasonally during the two years following construction, with the largest fluctuation occurring during the summer and the lowest during the winter. During the two-year period, the thermal strain due solely to the temperature gradients fluctuated between -120 and 150 microstrain. The daily cycles of variation in the temperature differences across the slab depth showed that the maximum positive difference occurs during the afternoon hours and the maximum negative difference occurs during the early morning hours. The strain due to the uniform temperature changes and the strain due to the temperature gradient act in the same manner and cause the total strain to be higher than that due to the sole effect of the uniform temperature change. On average, the magnitude of the strain due to the temperature gradient constitutes 13 percent of the magnitude of the strain due to uniform temperature changes during the summer, 11 percent during the fall, 7 percent during the winter and 5 percent during the spring.

Based on the temperature measurements, the average temperature gradient is smaller than the built-in temperature gradient throughout the whole year, indicating that the slab is curled upward. As a result, the average thermal strain due to the temperature gradient is negative throughout the two-year period.

The moisture-related strain fluctuates seasonally, but remains negative during the two-year period, indicating that the moisture conditions cause the slab surface to curl upward (slab in compression) irrespective of the season. This is consistent with the expected slab behavior due to the moisture conditions, since the moisture conditions only fluctuate seasonally in the top 2 inches of concrete and the bottom portion of the slab remains at a level of 100 percent relative humidity. The magnitude of the calculated moisture-related strain is highest in the fall and lowest in the spring. During the spring, the higher amount of precipitation causes the slabs to expand, which is exhibited by a decrease in the slab contraction, resulting in strains of lower magnitude. Moreover, the moisture-related strain that developed during the second year significantly increased in magnitude when compared to the calculated strain for the first year after paving. This is due to the observed decrease in relative humidity levels in the top 2 inches of the slab in the second year, when compared to the first year.

The moisture strain was used to calculate the equivalent temperature difference due to the presence of a moisture gradient in the concrete slabs. During the two-year period, the gradient corresponding to the equivalent temperature difference varies between -4.0˚F/in and -0.4˚F/in. This will be used in quantifying the effect of moisture on the slabs in the development of the finite element models (Chapter 7).

6.2 CONCRETE STRAIN MEASUREMENTS

Static strain gages were installed at different locations and depths within the slab. The strain gages measure slab deformations caused by temperature and moisture changes. Stress will not develop if the slab is free to deform; it is when this deformation is restrained that stress develops. The deformation is restrained primarily by the friction between the bottom of the slab and the

base, the presence of dowel and tie bars, and the weight of the slab itself. These factors affect the strain measurements. All strain measurements comparisons made in this section are based on an average of the values from three replicated restrained and unrestrained slabs.

This section deals with analyzing the slab movements under varying temperature and moisture conditions during the first two years after construction of the pavement. The effects of the different slab restraint conditions on slab movements are also analyzed. The investigated slab restraint conditions include depth within the slab and the presence of dowel bars or tie bars along the joints. In addition, slab curvature will also be estimated based on the strain measurements at the slab corners. Finally, a summary of the findings of this section is also included.

6.2.1 Background

The raw strain reading represents the slab deformation due to the effects of temperature and moisture changes in the concrete and concrete creep. The raw reading also includes the effect of temperature on the steel wire inside the gage. The raw strain reading is first corrected for the effect of temperature on the steel wire within the gage and then converted into a total strain reading, which reflects the total deformations measured in the slab. The correction is accounted for by using Equation 4-1 to calculate the total strain experienced by the concrete. The strain measurements are zeroed based on the time of set of the concrete. The set times corresponding to each sensor were presented in Chapter 4.

The total strain calculated using Equation 4-1 is then separated into strain due to temperature effects and strain due to other remaining factors including moisture, creep, and slab restraining conditions. Strain due to temperature gradients was estimated using Equation 6-5; strain due to uniform temperature change was estimated using Equation 6-7 and strain due to other components is estimated by subtracting the thermal strain from the total strain, as shown in Equation 6-11.

$$\varepsilon_{other} = \varepsilon_{total} - \varepsilon_{thermal} \qquad \text{(Equation 6-11)}$$

Where: $\varepsilon_{thermal}$ = Thermal strain in the concrete

ε_{other} = Strain in the concrete due to all factors that are not temperature related

α_c = Thermal coefficient of expansion of the concrete = 5.67 με/°F

6.2.2 Static strain measurements within the concrete slabs

This section examines the effects of seasonal variations in temperature and moisture conditions on the development of strain at different locations and depths within the slabs. The effects of slab restraints on strain development are also analyzed.

6.2.2.1 Environmental conditions

This section investigates the effects of environmental factors on strain development at different locations and depths within the slab. The environmental factors include variations in seasonal temperature and moisture conditions, freezing of the underlying layers and joint locking.

Figure 6.22 and Figure 6.23 provide a comparison between the total strain, the uniform temperature-induced strain, and the strain due to moisture, creep and other factors. The total strain presented in these two figures is measured in the longitudinal direction, at the top of the restrained and unrestrained midpanels. The strain is negative throughout the first two years after construction, for both the restrained and unrestrained slabs, indicating that the slabs are in a state of contraction. The variation in strain follows seasonal trends. The total and the uniform temperature-induced strain increases in magnitude until reaching a maximum in the winter, after which strain decreases throughout the spring and reaches a minimum value in the summer. Decreasing temperature causes the concrete to contract and increasing temperature causes the concrete to expand. Therefore, it is expected that the lower temperature observed during the winter season would induce the largest amount of contraction in the slab, while the smallest contraction is observed in the summer. This is observed in both the restrained and unrestrained slabs.

As previously mentioned in the previous section, the strain due to moisture and other factors was calculated by subtracting the strain due to uniform temperature changes and the strain due to temperature gradients from the total measured strain (Equation 6-11). The strain due to moisture and other factors does not vary much throughout the different seasons, while the temperature-induced strain exhibits a larger amount of fluctuation. This is due to the fact that the temperature conditions inside the concrete fluctuate greatly during the different climatic seasons, as previously shown in Chapter 5, while the concrete moisture conditions do not vary substantially throughout the year.

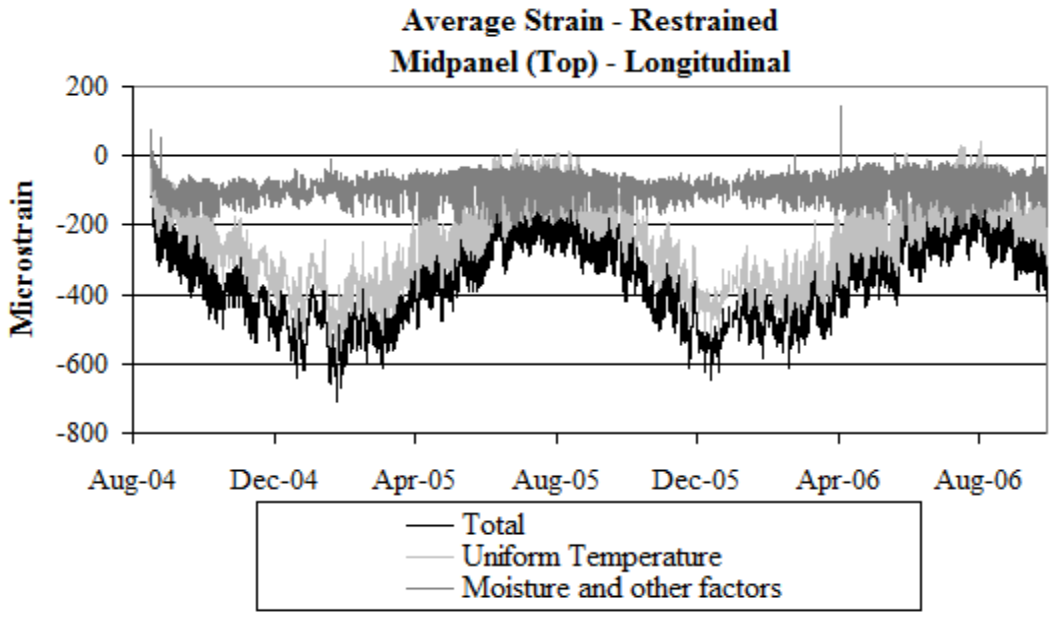

Figure 6.22. Strain in the longitudinal direction at midpanel at the top of the restrained slabs.

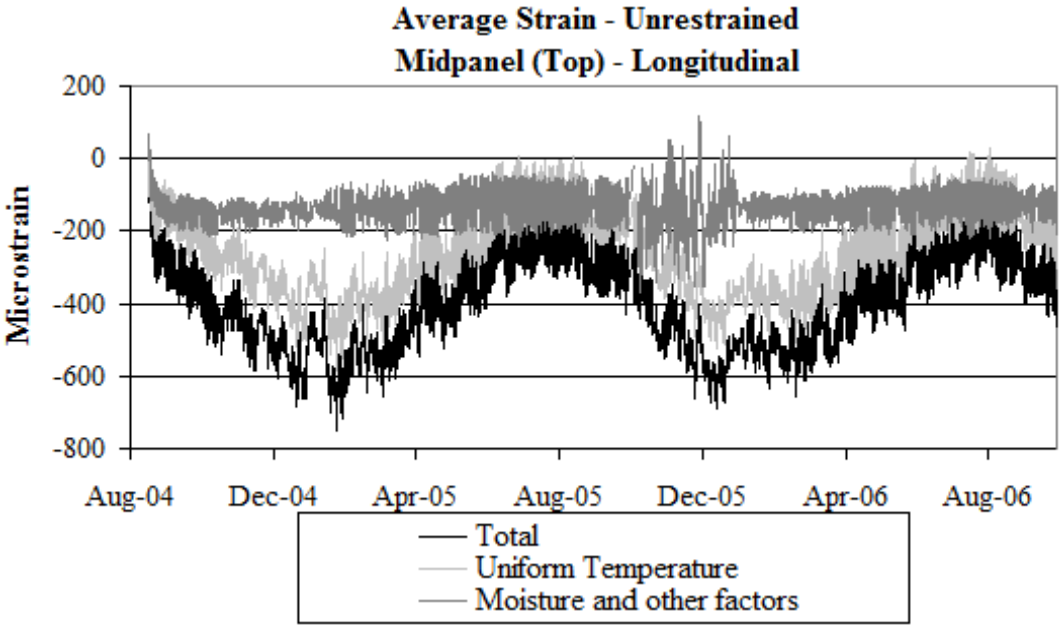

Figure 6.23. Strain in the longitudinal direction at midpanel at the top of the unrestrained slabs.

The seasonal contribution of both components to the total strain was compared to each other and is presented in Figure 6.24, for strain in the longitudinal direction, at the top of restrained and unrestrained slabs and at midpanel. For the restrained slabs, the uniform temperature-induced strain varies between -145 microstrain during the summer and -378 microstrain during the winter. The smaller strain during the summer is expected, since during the summer, the higher temperature contributes to expansion in the slab, which is exhibited by a decrease in the contraction of the slab. The contribution of the temperature-induced strain is lowest during the summer, constituting 61 percent of the total strain and highest during the winter, constituting 79 percent of the total strain.

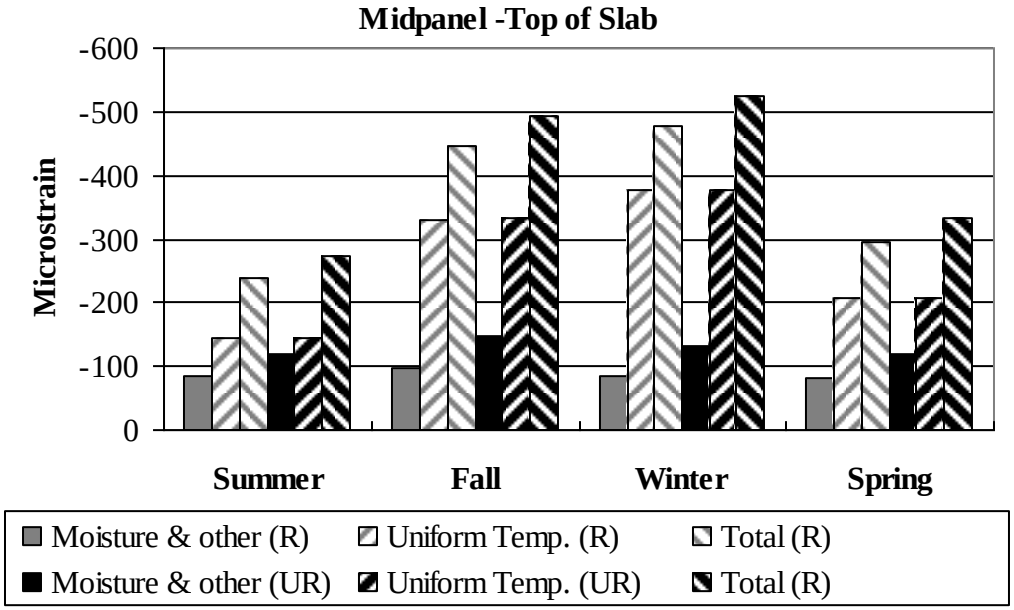

Figure 6.24. Seasonal contributions of the various components to the development of total strain in the longitudinal direction at midpanel at the top of the restrained and unrestrained slabs.

For the restrained slabs, the strain due to moisture and other factors varies between -82 microstrain during the spring and -96 microstrain during the fall, on average. The smaller strain during the spring is expected, since during the spring, the higher amount of precipitation causes the slab to expand (as discussed in Chapter 5), which is exhibited by a decrease in the slab

contraction. The contribution of the moisture-induced strain is lowest during the winter, constituting 18 percent of the total strain for the restrained slab, and highest during the summer, constituting 35 percent of the total strain. The magnitude of the temperature-induced strain is much higher than the magnitude of the strain due to other factors (including moisture). As a result, the variation of temperature conditions is the dominant factor in contributing to the development of total strain in the concrete slab.

Similarly, the same trends were observed for the strain at midpanel of the unrestrained slab. The temperature-induced strain varies between -146 microstrain during the summer and -378 microstrain during the winter, indicating that the higher temperature during the summer contributes to expansion of the slab. The contribution of the temperature-induced strain is lowest during the summer, constituting 53 percent of the total strain and highest during the winter, constituting 72 percent of the total strain. The strain due to moisture and other factors varies between -120 microstrain during the spring and -146 microstrain during the fall, indicating that the higher amount of precipitation during the spring contributes to expansion of the slab. The contribution of the moisture-induced strain is lowest during the winter, constituting 25 percent of the total strain and highest during the summer, constituting 43 percent of the total strain. These seasonal changes in the relative humidity in the slab were discussed in Chapter 5. The variation in temperature conditions is the dominant factor in contributing to the development of total strain in the concrete slab. However, for the case of the restrained slab, the magnitude of the strain due to moisture and other factors is 32 percent smaller than that for the unrestrained slab, indicating that the slab restraints cause a 32 percent decrease in strain.

Similar trends regarding the seasonal contribution of temperature, moisture and other factors to total concrete strain were also observed based on strain measured at different locations and depths within the restrained and unrestrained slabs. A full set of figures showing the variation in strain with time during the two-year period after construction of the pavement is included in Appendix B.

The influence of temperature variations in the underlying layers is examined in this paragraph. For example, subjecting the asphalt treated base layer to very low temperatures causes an increase in the stiffness of the ATPB. This implies that the bond between the slab and the base will provide an additional restraint on the slab. In such a case, the strain in the concrete is expected to be lower as a result of this increased restraint.

The coldest temperatures were recorded during the period between January 25 and February 6, 2005 (see section 5.1). During that period, the thermocouples within the subbase recorded temperatures at or close to the freezing temperature, implying that the resilient modulus of the ATPB layer was higher than usual. During this period, the total strain and the temperature-induced strain decrease in magnitude, as shown in Figure 6.22 and Figure 6.23. This confirms that a stiffer ATPB layer poses an additional restraint on the concrete slab and causes a decrease in strain.

For the top of the slab, the average total strain during the frozen period is -445 microstrain for the restrained slab and -490 microstrain for the unrestrained slab. These are 9 percent lower than the average for the winter season. The average uniform temperature-induced strain is -345 microstrain for the restrained slab and -344 microstrain for the unrestrained slab, which are 11 percent lower than the average for the winter season. The average strain due to moisture and other factors is -100 microstrain for the restrained slab and -145 microstrain for the unrestrained slab, which are similar to the average for the winter season. The strain at the bottom of the slab also decreases by the same percentages with respect to the average strain measured during the winter season.

The strain due to moisture and other factors is compared to the moisture-related strain calculated based on the concrete moisture measurements, which was presented in section 6.1.3. The comparison is presented in Figure 6.25 for the strain due to moisture and other factors estimated based on the static strain data at the slab surface at the midpanel location. The figure shows that the strain measured in the restrained slab is, on average, 33 percent smaller in magnitude than the strain measured in the unrestrained slab. The figure also shows that the calculated moisture-related strain is close in magnitude to the measured strain (due to moisture and slab restraining conditions), during the first two years after construction.

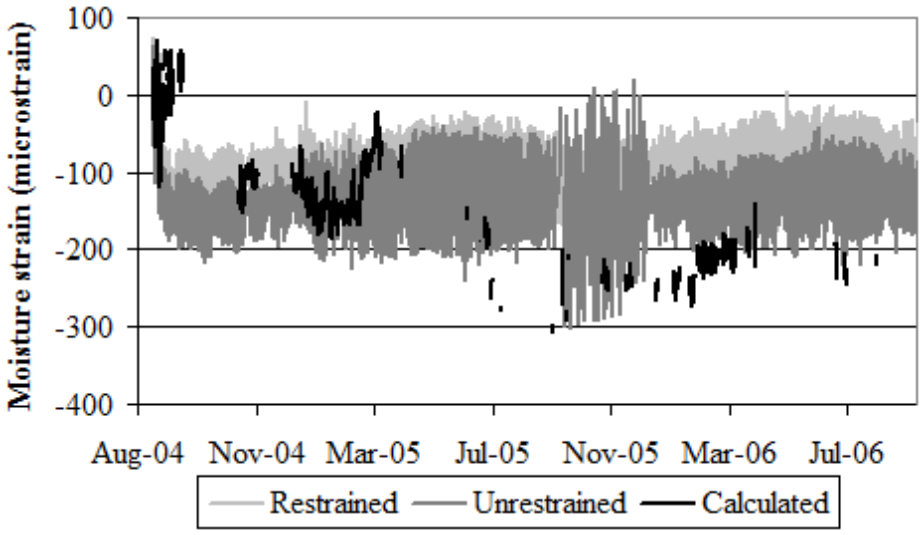

Figure 6.25. Calculated and measured moisture-related strain at the slab surface and midpanel.

The seasonal variation in the calculated moisture-related strain and the measured strain due to moisture and other factors are compared in Figure 6.26. The calculated and measured strain follows the same seasonal trends. The calculated and measured moisture-related strain is negative throughout the two-year period. The average seasonal measured moisture-related strain is similar for the two years, while the calculated strain exhibits a significant increase in the second year after construction. During the first year after paving, the calculated strain is slightly smaller in magnitude than the measured strain, and during the second year after paving, the calculated strain is slightly larger in magnitude than the measured strain. During the second year after paving, the measured strain due to moisture-related and slab restraining conditions constitutes 39 percent of the total strain calculated for the case of the restrained slabs and 59 percent for the case of the unrestrained slabs.

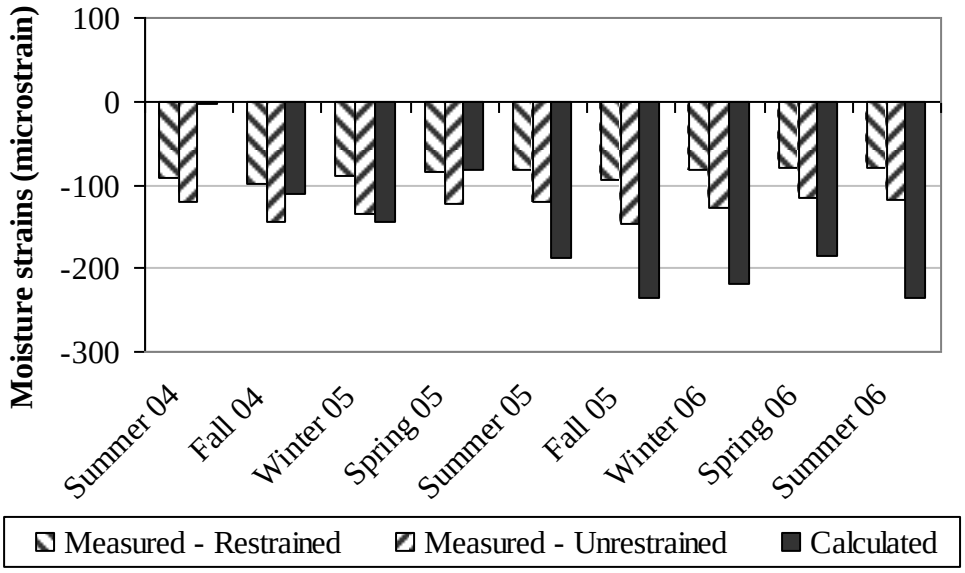

Figure 6.26. Seasonal variation in moisture-related strain at the slab surface.

As temperatures increase and the concrete expands, the width of the joint decreases to accommodate the increase in length of the slab. The joint width will continue to decrease with increasing temperature until the joint locks-up. Strain measurements are used to determine the temperature at which the joint will lock. The variation in average total strain with respect to temperature change is plotted for the midpanel sensors measuring concrete movement in the longitudinal direction at the top of the restrained and unrestrained slabs. The strain versus temperature variation is presented in Figure 6.27 and Figure 6.28. At the top of the unrestrained and restrained slabs, the temperature ranges between 0˚F and 111˚F, and the transverse joints lock-up starting at a temperature of 96˚F.

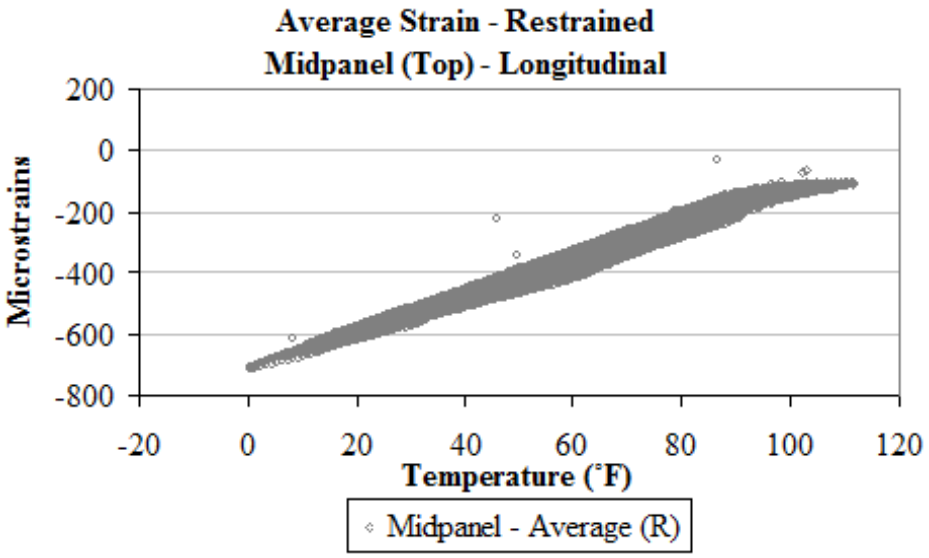

Figure 6.27. Variation in strain with temperature, in the longitudinal direction at midpanel for top of restrained slabs.

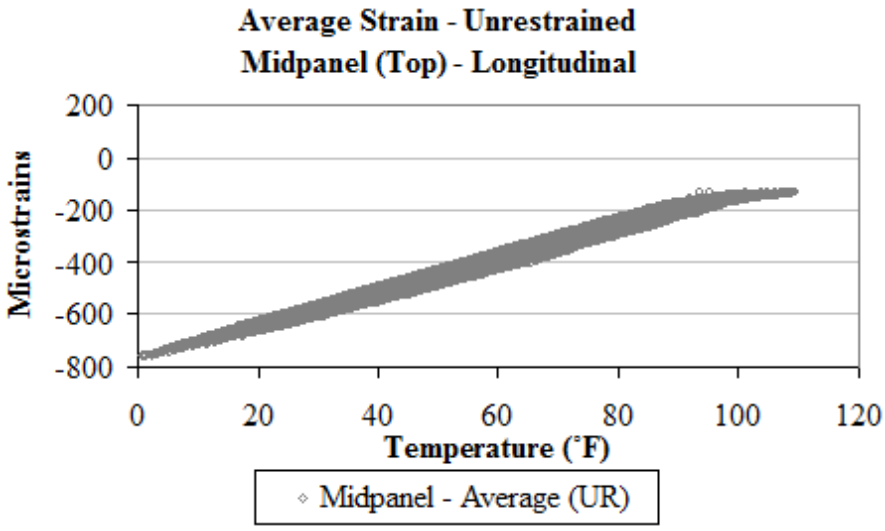

Figure 6.28. Variation in strain with temperature, in the longitudinal direction at midpanel for top of unrestrained slabs.

During seasons when temperatures are high, strain increases until the joints lock-up. During seasons when temperatures are low, strain is not large enough to cause lock-up of the joints. The seasonal range of concrete temperatures recorded by the static strain gages is presented in Table 6.4 for both the restrained and unrestrained slabs. The table summarizes data collected from the sensors measuring strain in the longitudinal direction at the top of the midpanel locations. It indicates that lock-up of the transverse joint does not occur during the fall and winter, but takes place during the spring and summer seasons. The minimum strain recorded by the midpanel sensors at the time the transverse joints were locked reached -105 microstrain for the restrained slabs and -130 microstrain for the unrestrained slabs. At lock-up, the magnitude of the strain in the unrestrained slab is 24 percent larger than for the restrained slabs. This confirms that the restraining conditions of the slab cause a decrease in the total allowable joint opening in the slab, when compared to similar slabs with less restraint.

Table 6.4. Temperatures at transverse joints lock-up for the restrained and unrestrained slabs.

	Range of Temperatures (˚F)		**Temperature at joint lock-up (˚F)**
	Restrained slabs	**Unrestrained slabs**	
Summer	50 to 111	51 to 109	96
Fall	11 to 89	12 to 87	--
Winter	0 to 77	0 to 75	--
Spring	31 to 108	32 to 106	96

The variation in total strain with temperature was also plotted for strain measured in the transverse direction to determine whether the longitudinal joints also lock-up at high temperatures. Figure 6.29 presents the variation in average total strain with respect to temperature change for the sensors measuring movement in the transverse direction along the transverse joint at the top of the unrestrained slab. The figure shows that expansion in the transverse direction is not restricted to a maximum limit, even though concrete temperatures recorded by the sensors exceed the 96˚F limit at which transverse joints lock-up. This indicates that the presence of the curb and gutter does not restrain the slab sufficiently to prevent

expansion of the slab in the transverse direction. This was observed in the strain measured in the transverse direction by all the sensors located at the transverse joints of the unrestrained and restrained slabs.

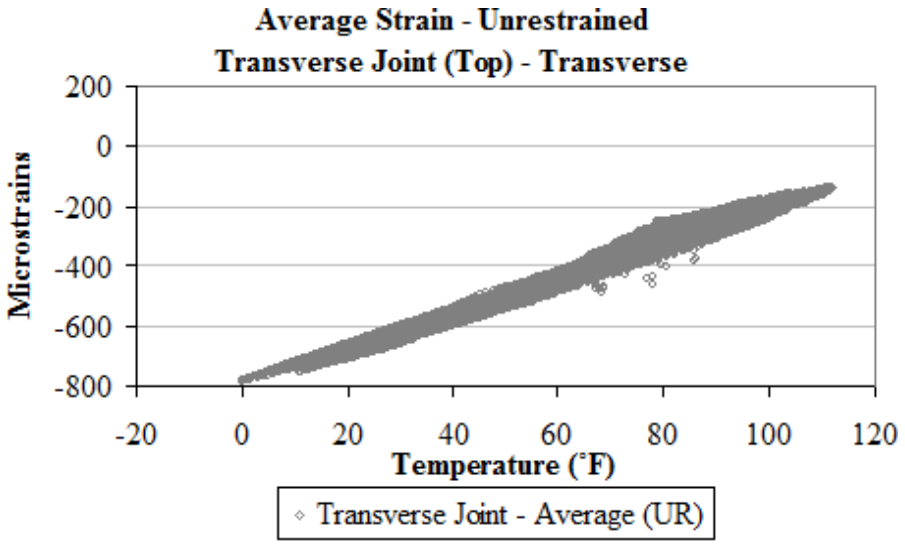

Figure 6.29. Variation in strain with temperature, in the transverse direction along the transverse joints for top of unrestrained slabs.

6.2.2.2 Effect of slab restraining conditions

In this section, the effects of the different slab restraining conditions on the development of strain in the slab are examined. The investigated factors include depth within the slab, presence of dowel bars or tie bars, and slab length in the direction of movement.

The boundary conditions at the top and bottom of the slab are different. The bottom of the slab is fully bonded to the asphalt treated permeable base (Wells et al. 2005), while the slab surface is free from restraint. The total strain measured at the midpanel locations at the top and bottom portions of the restrained and unrestrained slabs are compared to each other in Figure 6.30. The strains at the bottom of the slab are typically the same because the primary restraint is from friction between the base and slab which is the same for restrained and unrestrained slabs. The total strain measured at the bottom portion of the restrained slab is 12 percent lower than at

the top portion of the slab, and the total strain at the top of the unrestrained slab is 22 percent lower than at the top portion of the slab. Since the sensors are equidistant from the surface and the base layer, the comparison between the strain measured at the top and bottom of the slab gives an indication of the effect of the base restraint on the strain measurements. The difference in moisture content between the top and bottom of the slab also contributes to the difference between the strain at the top and bottom of the slab.

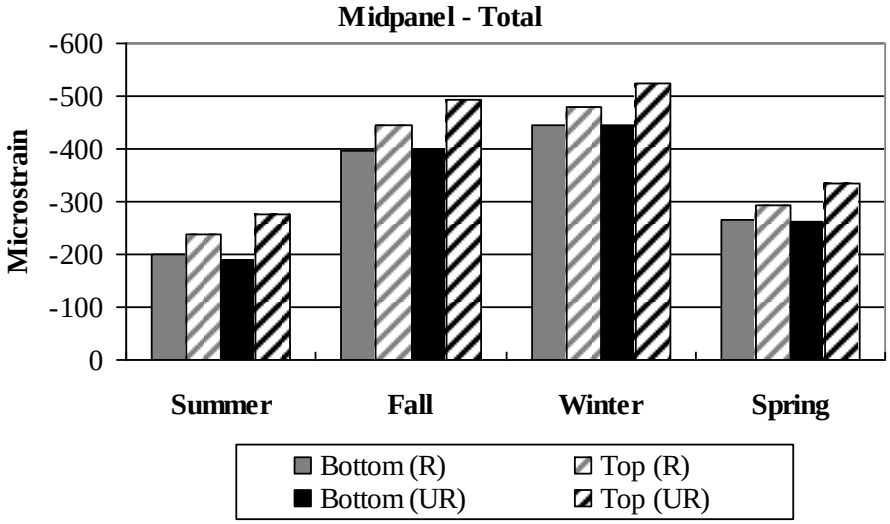

Figure 6.30. Total strain at the top and bottom of the restrained and unrestrained slabs at midpanel in the longitudinal direction.

The total strain can be separated into that due to temperature effects and that due to other remaining factors including moisture and creep. Slab restraining conditions reduce the total strain. The thermal strain analyzed in this section is that due to uniform temperature changes across the slab depth, and does not take into account the daily changes in temperature gradients. As a result, it is expected that the temperature-induced strain presented does not vary depending on the sensor location within the slab depth. This is shown in Figure 6.31, which presents a comparison between the temperature-induced strain measured in the longitudinal direction at midpanel. Based on this figure, the temperature-induced strain measured at the bottom portion of the restrained slab is 7 percent lower than at the top portion of the slab, and the temperature-

induced strain at the bottom of the unrestrained slab is 10 percent lower than at the top portion of the slab. This difference in temperature-induced strain does not account for the 12 and 22 percent differences in total strain between the top and bottom portions of the slab. Therefore, a comparison between the midpanel strain due to the remaining factors, which include moisture and restraints is also plotted and is presented in Figure 6.32. Based on this figure, the strain due to the remaining factors is on average similar at the bottom and top of the restrained slabs, and 28 percent lower at the bottom of the unrestrained slab, when compared to the strain at the top portions of the slab.

Similarly, a comparison between the strain measured at the top and bottom of the slab was carried out for the sensors at all locations within the restrained and unrestrained slabs. The comparison showed that the temperature-induced strain at the bottom of the slab is 1 to 12 percent lower than the strain measured at the top for the restrained slab, and 2 to 29 percent for the unrestrained slab. On the other hand, at the bottom portion of the slab, the strain due to the remaining factors is significantly lower in magnitude than that at the top of the slab. The strain at the bottom of the slab is 14 to 67 percent lower than that measured at the top of the restrained slab, and 29 to 69 percent lower than that measured at the top of the unrestrained slab.

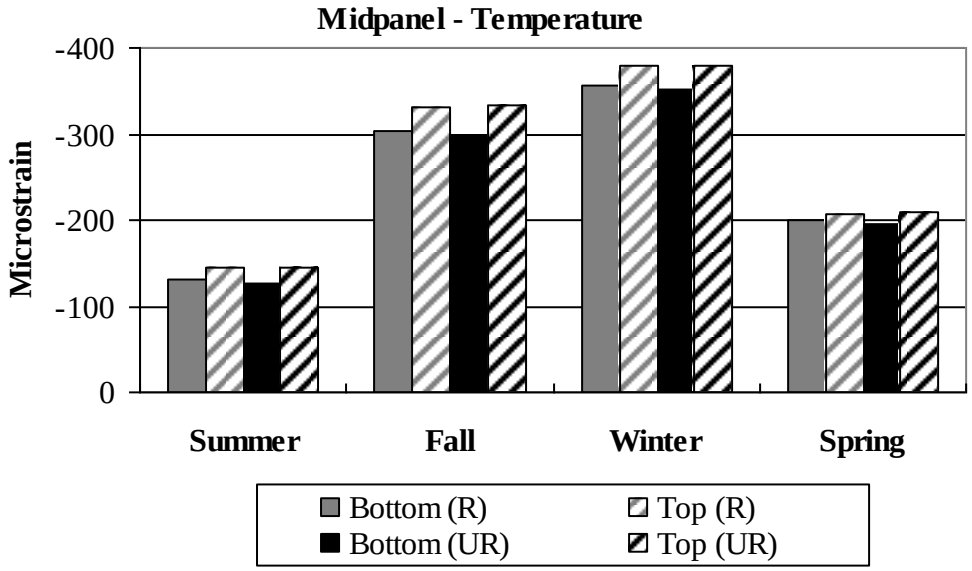

Figure 6.31. Temperature-induced strain at the top and bottom of the restrained and unrestrained slabs at midpanel in the longitudinal direction.

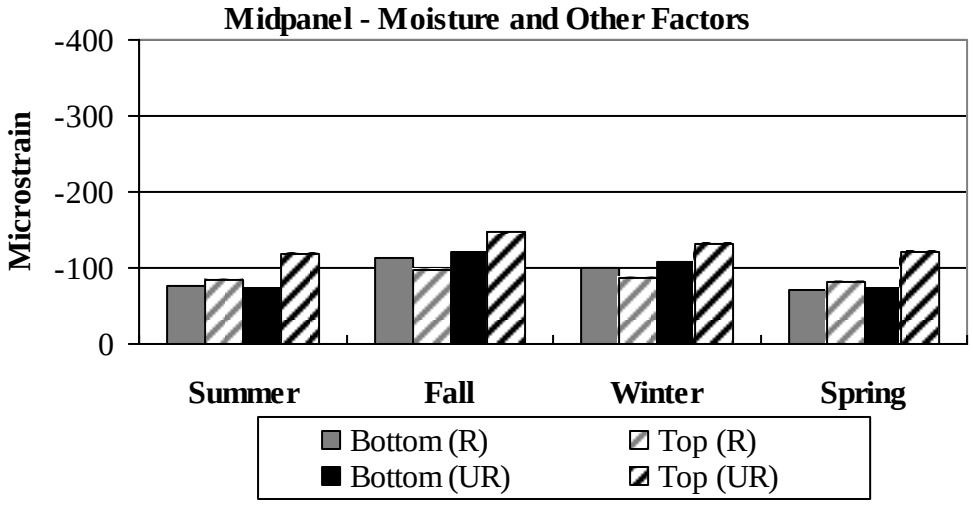

Figure 6.32. Strain due to moisture and other factors at the top and bottom of the restrained and unrestrained slabs at midpanel in the longitudinal direction.

Another factor restraining slab movement is the presence of dowel bars along the transverse joints. As previously mentioned, dowel bars are placed along the transverse joints for the purpose of minimizing joint faulting. Dowels restrict the slab from free contraction, reduce slab deflections along the transverse joint and affect the curling-induced stresses, especially in the regions surrounding the dowels. Dowels also restrict the slab curvature causing a redistribution of stresses in the slabs (Wells 2005; Vandenbossche 2003). In this section, the effect of the presence of dowel bars along the transverse joints on the development of concrete strain is examined. For this purpose, strain data collected from the restrained and unrestrained slabs are compared to each other.

Figure 6.33 presents a comparison between the total strain measured in the transverse direction along the transverse joint of the restrained and unrestrained slab. At the top of the slab, the total strain measured in the unrestrained slab is 20 percent higher than that in the restrained slab. At the bottom of the slab, the measured strain is similar and within 1 percent. Separating the total strain into the different components, it was found that the temperature-induced strain is not affected by the presence of dowel bars. However, the strain due to the restraining conditions showed a 42 percent increase in measured strain in the absence of dowel bars, compared to the case when dowel bars are present.

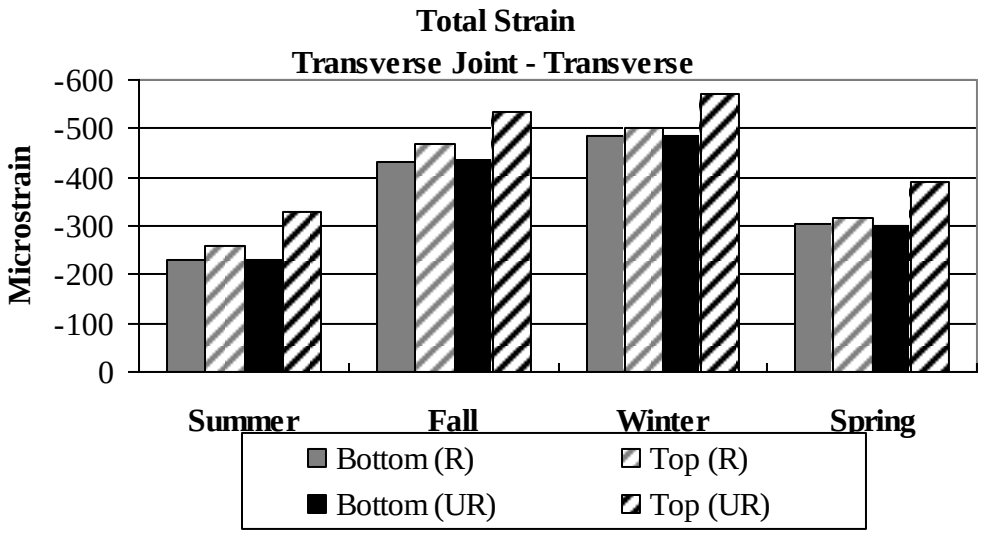

Figure 6.33. Total strain at the top of the restrained and unrestrained slabs along the transverse joint in the transverse direction.

Tie bars were placed along the transverse joints to keep the joints tight and prevent the infiltration of water into the pavement structure. Keeping the joint tight allows the load to be transferred from one slab to the other through aggregate interlock. In this section, the effect of the presence of tie bars along the longitudinal joints on the development of concrete strain is examined. For this purpose, strain data collected from the restrained and unrestrained slabs is compared.

Figure 6.34 presents a comparison between the total strain measured in the longitudinal direction along the centerline longitudinal joints of the restrained and unrestrained slabs. At the top and bottom portions of the slab, the total strain measured in the restrained and unrestrained slabs is within 3 percent. Separating the total strain into the different components, it was found that the temperature-induced strain and the strain due to the remaining factors are also not affected by the presence of tie bars along the joints.

Similarly, a comparison between the strain measured in the longitudinal direction at the restrained and unrestrained slab corners along the centerline joint was also carried out. The total strain is within 4 percent, also indicating that the tie bars do not affect the development of strains in the slabs. The same observations were made for the sensors located at the top, mid-depth and bottom of the slabs.

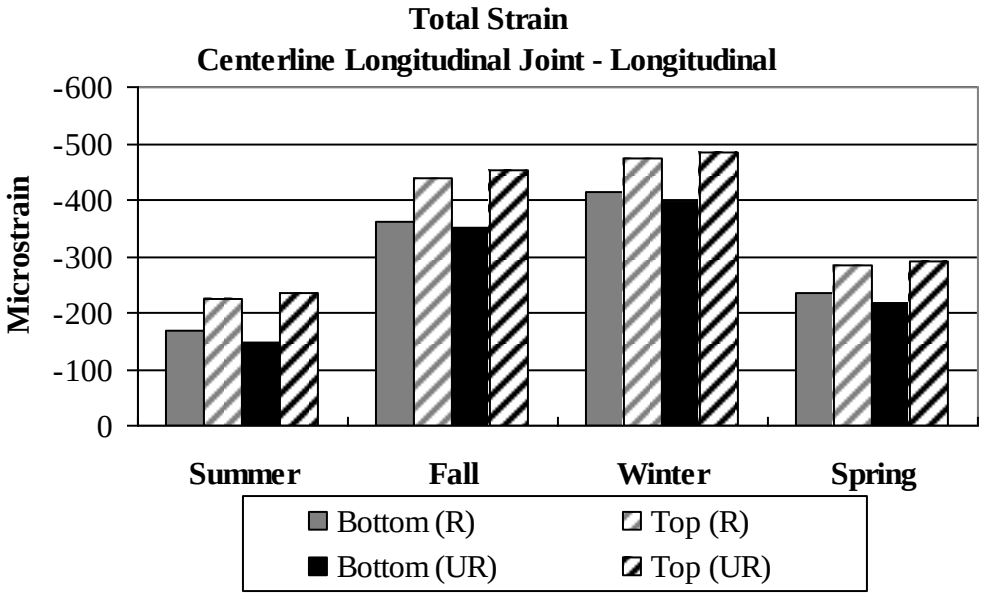

Figure 6.34. Total strain at the top of the restrained and unrestrained slabs along the centerline longitudinal joint in the longitudinal direction.

The effect of the slab length and type of adjacent boundary conditions on the development of strain in the concrete is examined herein. In the transverse direction, the slab is approximately 12 feet wide and is restrained by the curb and gutter on one side and by the eastbound lane on the other side. In the longitudinal direction, the slab is approximately 15 feet long and is restrained by the adjacent slabs on both sides, with dowels in the case of the restrained slab. Strain data collected from the sensors located along the longitudinal joint measuring strain in the longitudinal direction is compared to data collected from sensors located along the transverse joint measuring strain in the transverse direction of the unrestrained slab.

Figure 6.35 presents a comparison between the total strain measured in the longitudinal and transverse directions along the longitudinal and transverse joints of the unrestrained slab. At the top portion of the slab, the total strain measured in the transverse direction is 5 to 29 percent larger than that measured in the longitudinal direction. At the bottom portions of the slab, the difference is 18 to 37 percent. This indicates that when the slab length is longer and is restrained by adjacent slabs, the restraint is increased and the measured strain is lower.

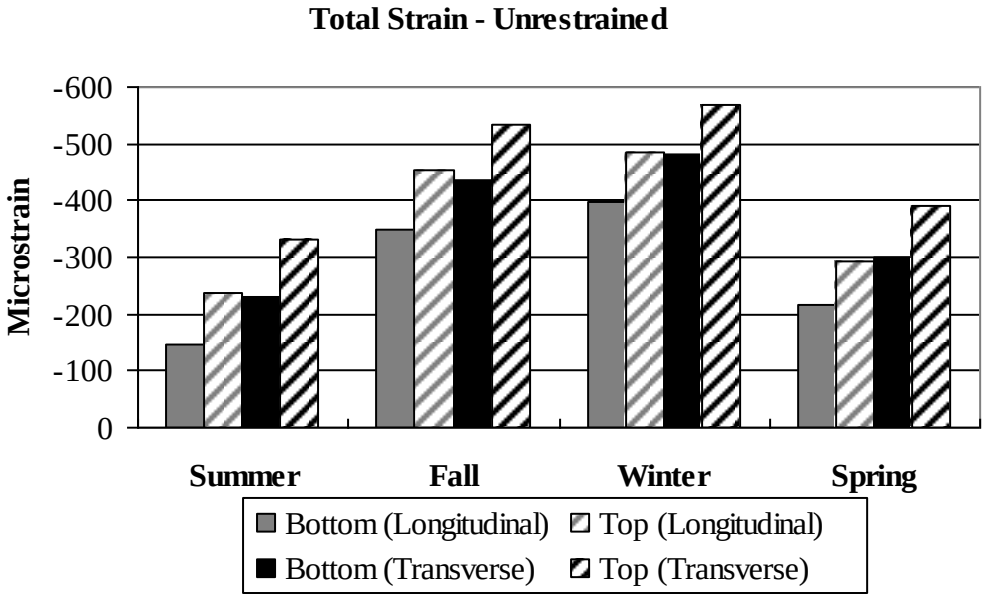

Figure 6.35. Total strain along the centerline longitudinal joints (longitudinal direction) and the transverse joints (transverse direction) at the top of the unrestrained slabs.

In summary, it was found that the bond provided at the slab/base interface reduces the slab surface strain by 12 to 22 percent, the presence of dowel bars reduces the strain by 20 percent, and the longer slab length with adjacent slabs reduce the strain by 5 to 29 percent. On the other hand, it was found that the presence of tie bars does not affect the strain at the slab surface.

6.2.3 Slab curvature

Equation 6-10 was used to calculate the curvature based on the strain measured by the static strain sensors located at the top and bottom of the slab corners, in a rosette configuration. Figure 6.36 and Figure 6.37 show the average curvature based on the strain measured in the diagonal direction for the restrained and unrestrained slabs during the first two years after construction. These figures indicate that the average curvature trends were similar for the restrained and unrestrained slabs during the first two years after construction: the range of curvatures is relatively small during the winters and larger during the summers. This is expected because the

slabs are subjected to small temperature gradients during the winter season (resulting in smaller amounts of curvature)and larger temperature gradients during the summer seasons (resulting in smaller amounts of curvature). The computed curvatures are predominantly (>99 percent of values) positive or curled upward, which is a similar trend to that observed with the curvature calculated based on temperature and moisture measurements. This supports the theory that the slabs will be more susceptible to top-down than bottom-up cracking.

Figure 6.38 presents a plot of curvature versus equivalent linear temperature gradient data using the strain data from the restrained and unrestrained slabs for the month of April 2006 only (to limit the number of points being plotted). The month of April was selected because this month typically exhibits the widest range of temperature gradients and would, therefore, encompass the majority of the gradients experienced throughout the year. These strains represent both built-in and transient gradients. Note that the slopes of the trend lines for the restrained and unrestrained slab data are similar.

Figure 6.38 suggests that the gradients present when the slabs are flat are 1.03˚F/in for the restrained slab and 1.88˚F/in for the unrestrained slab. This is equivalent to a zero-curvature temperature difference (i.e., an effective built-in temperature difference) of 12.4˚F for a 12-in thick restrained slab and a 22.6˚F temperature difference for a 12-in unrestrained slab. The default value for effective built-in temperature difference currently suggested in the MEPDG is 10˚F, regardless of whether the slab is doweled or undoweled. The MEPDG default value is close to that measured in this study for the restrained slab but does not appear to be appropriate for unrestrained (i.e., undoweled) slabs.

The built-in construction gradient was 0.31˚F/in. The differences between this value and the effective built-in temperature gradients computed above are 0.72˚F/in for the restrained slabs and 1.57˚F/in for the unrestrained slabs. This restraint of free deformation results in substantially higher levels of stress. The curvatures due only to long-term drying shrinkage and the built-in gradient (i.e., the x-axis intercepts in Figure 6.38) are 0.0010 1/ft for the restrained slabs and 0.0017 1/ft for the unrestrained slabs. The curvature of the restrained slabs is more than 50 percent lower than that of the unrestrained slabs.

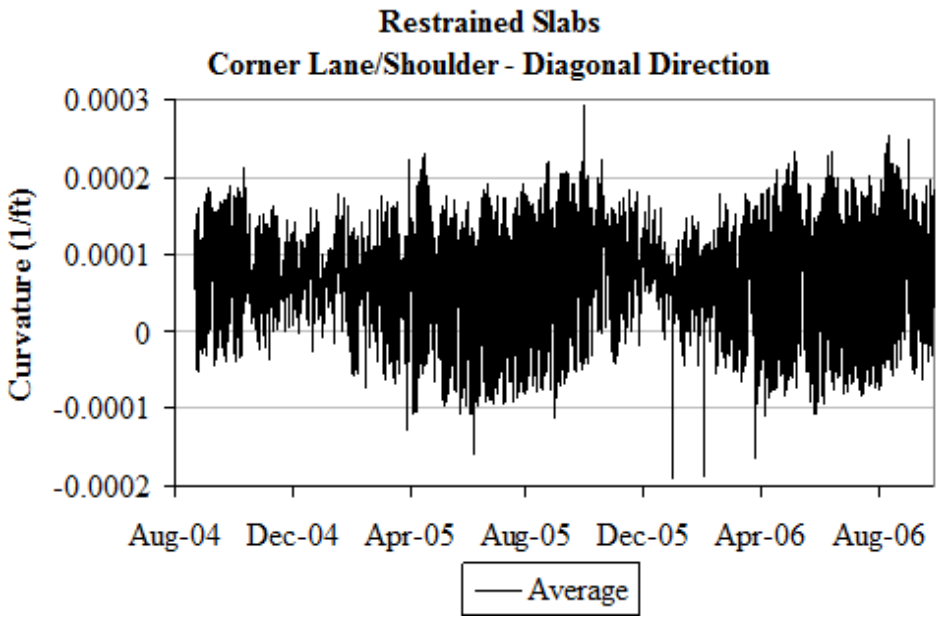

Figure 6.36. Average curvature for the restrained slabs, based on the corner strain in the diagonal direction along the shoulder.

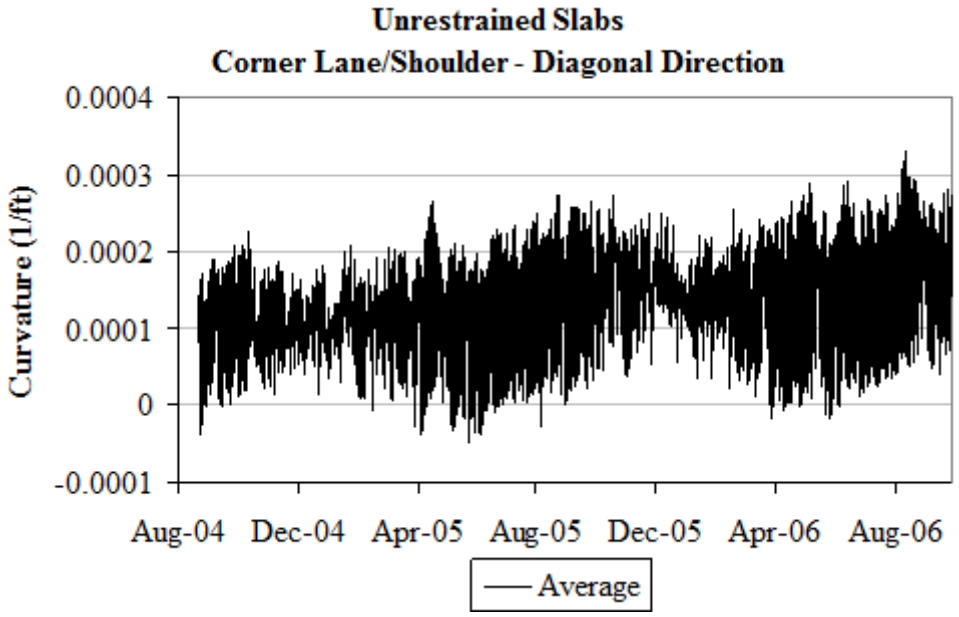

Figure 6.37. Average curvature for the unrestrained slabs, based on the corner strain in the diagonal direction along the shoulder.

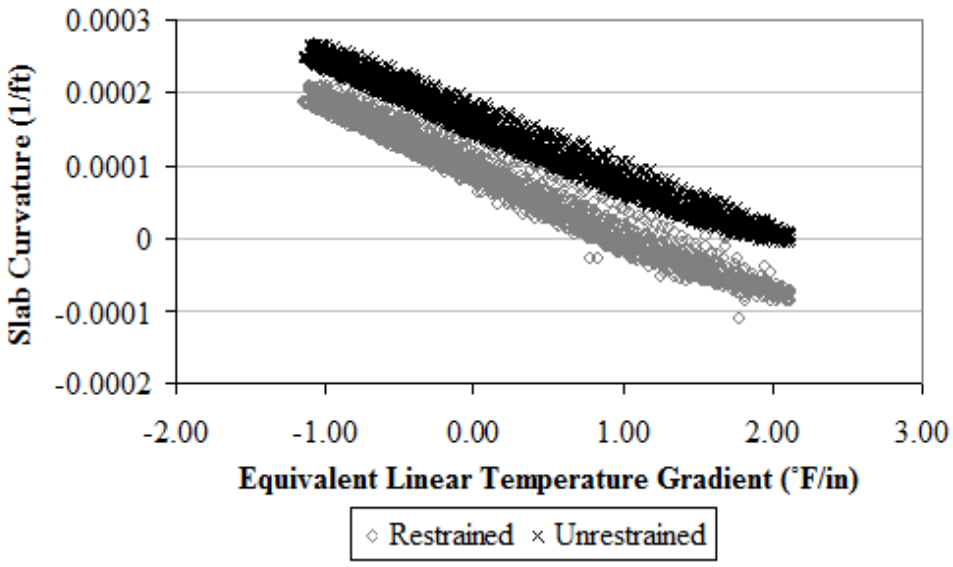

Figure 6.38. Variation of average curvature with equivalent linear temperature gradient for the restrained and unrestrained slabs (April 2006).

It is somewhat surprising that the slopes of the trend lines for the restrained and unrestrained slabs are so similar. These similar slopes indicate that the rates of change in curvature with changes in the temperature gradient are similar for the restrained and unrestrained slabs. An estimate of the maximum curvature caused strictly by the temperature gradient observed throughout the month can be obtained by subtracting out the curvature due to the built-in gradient and the drying shrinkage. In doing this, it was found that the maximum and minimum curvatures corresponding to the minimum and maximum gradients experienced throughout the month were 0.0010 1/ft and -0.0020 1/ft, for both the restrained and unrestrained slabs. Therefore, the additional restraint provided by the dowel and tie bars does not significantly reduce slab deformation resulting from daily temperature fluctuations. These trends were also observed for the curvature estimated from strain in the longitudinal and transverse directions. Similar observations can be made from the data reported by Vandenbossche (2003).

Plots similar to Figure 6.38 were made for strain data collected at various times throughout the first two years after paving. Linear regression analyses were performed so that the y-intercept could be established for each data set. The y-intercept represents the curvature in the slab when a transient temperature gradient is not present. For the purpose of this discussion,

this condition will be referred to as the "zero-gradient curvature." The zero-gradient curvature histories were determined for the restrained and unrestrained slabs for the first two years after paving, as shown in Figure 6.39. These curvatures represent the effects of the built-in gradients as well as drying shrinkage. Some of this drying shrinkage is reversible, as can be seen by the seasonal fluctuations. Rewetting during wet seasons (e.g., springtime) reverses a portion of the drying shrinkage and reduces the observed curvature. The shrinkage (and, therefore, the curvature) is regained during the drier seasons. This yearly fluctuation in curvature is about 0.0003 1/ft for both the restrained and unrestrained slabs.

The dowel and tie bars do not appear to have a significant effect on changes in slab curvature attributed to the seasonal fluctuations in drying shrinkage. They do, however, have a substantial effect on the long-term effects of shrinkage on observed slab curvature. Figure 6.39 shows that the overall trend of the zero-gradient curvature for the restrained slab is relatively flat while there is an obvious increase in the zero-gradient curvature with time for the unrestrained slab. The longer-term reduction in slab curvature for restrained slab helps to insure the presence of more uniform support beneath the slab and, therefore, reduces vehicle load-related stress. These reductions in vehicle load-related stress are at least partially offset by the increase in the critical slab stress (particularly those at the top of the slab near mid-panel) due to the restraint of curvature.

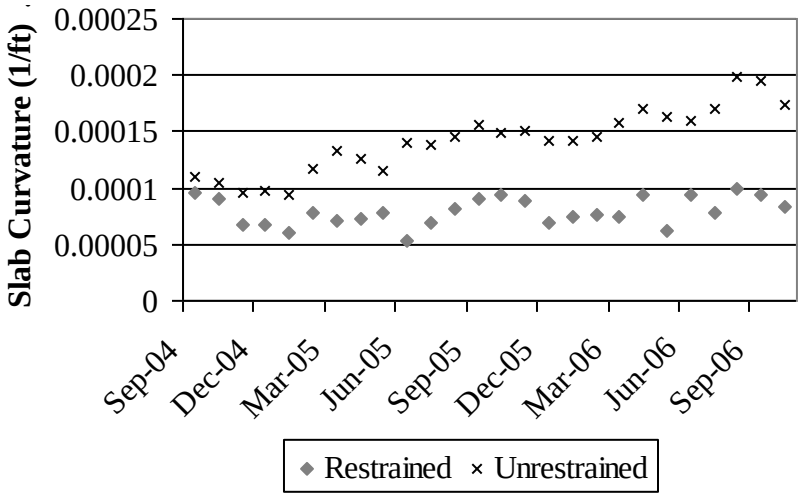

Figure 6.39. Curvature when the temperature gradient is zero.

Figure 6.40 presents a comparison between the average curvature estimated from the calculated thermal gradient and moisture gradient-induced strain and the total strain measured at slab corner at the lane/shoulder joint (in the diagonal direction). The figure shows that, with the exception of the first summer, the average curvature is positive indicating that the slab is, on average, curled upward throughout the two-year period. The magnitude of the moisture-induced curvature is larger than the magnitude of the thermal curvature. The curvature due to the effects of temperature and moisture gradients represents an estimate of the curvature of an ideally free slab (unrestrained and unbonded to the base, with free shrinkage). Both curvatures are counteracted by the slab restraining conditions and the actual slab curvature is smaller than the calculated curvature for both restrained and unrestrained slabs. The difference between the calculated and measured curvatures can provide an estimate of the residual stress in the slabs due to the effects of the slab restraints. The slab restraining conditions include friction along the base and slab weight in the case of the unrestrained slabs, and in the case of the restrained slabs, there is the added effect of the dowel bars along the transverse joints.

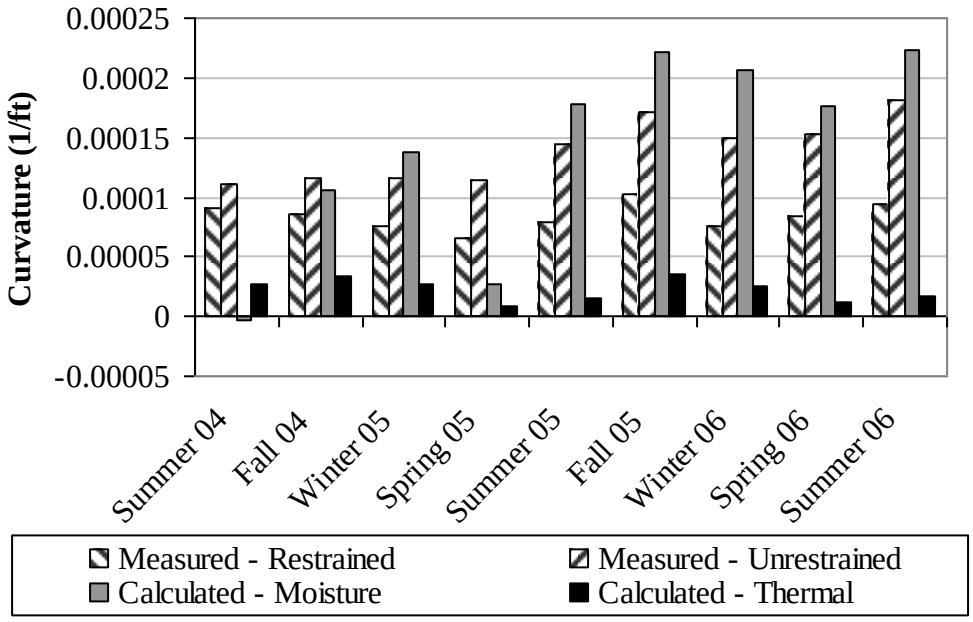

Figure 6.40. Seasonal average slab curvature based on the measured and calculated strains.

The slab curvature calculated in this section is compared to the slab curvature calculated based on the surface profile testing. The difference between the two curvatures is used to estimate the effect of moisture on the drying shrinkage of the concrete and is presented in section 6.4.

6.2.4 Summary

Based on the static strain measurements in the concrete slab, it was found that the slab movement is affected by seasonal variation in temperature and moisture conditions. It was also found that the slabs are restrained by the friction at the slab/base interface and restraint along the transverse and longitudinal joints. The strain is negative throughout the first two years after construction, indicating that the slabs are in a state of contraction. The variation in strain follows seasonal trends. The low temperature observed during the winter season causes the slab to contract and thereby results in the lowest strain measurements. The higher temperature observed during the summer causes the least amount of contraction in the slabs and therefore the strain measurements are largest. This was observed in both the restrained and unrestrained slabs.

Moisture and creep induced strain does not fluctuate much throughout the different seasons, while the temperature induced strain exhibits a larger amount of fluctuation. This is due to the fact that the moisture and creep conditions do not vary much throughout the year when compared to the temperature conditions, which are continuously changing. During the fall and summer, temperature has the greatest effect on strain; while during the winter and spring, moisture and creep induced strain is larger than temperature induced strain. This is also observed in both the restrained and unrestrained slabs.

The joint width continues to decrease with increasing temperature until the joints lock-up. Lock-up of the transverse joint occurs at temperatures higher than 96˚F, while the curb and gutter do not provide enough restraint to cause lock-up of the longitudinal joint.

Strain data from the restrained and unrestrained slabs was compared to investigate the different restraint conditions. It was found that the bond at the slab/base interface, the presence of dowel bars and the slab length with adjacent slabs all provide comparable restraint on the slab. However, the presence of tie bars does not provide sufficient restraint to affect the strain in the slab.

The curvatures estimated from strain in the longitudinal, diagonal and transverse directions show that curvature for the restrained slab is smaller by 20 to 50 percent when compared to the unrestrained slab. The dowel and tie bars restrict upward and downward movement at the outer portion of the slab, and cause the majority of the curvature to develop in the central portion of the slab.

6.3 SLAB SURFACE PROFILE MEASUREMENTS

In this section, the curling and warping of the slab due to seasonal temperature and moisture conditions are discussed. For this, seasonal surface profile measurements were made to capture changes in the shape of the slab under various temperature and moisture gradients.

Surface profile measurements were made using a Dipstick™, manufactured by Face Construction Technologies, Inc. (FACE 2004). The Dipstick™, shown in Figure 6.41, is a highly sensitive device that measures the relative difference in elevation between successive points along the slab surface. Surface profile measurements were made on the restrained and unrestrained slabs in the longitudinal, diagonal, and transverse directions, along the lines shown in Figure 6.42.

The Dipstick™ runs were initiated from the top of invar rods located near the transverse joints along the shoulder, placed in the ground at a depth of approximately 12 feet. The invar rods have a low coefficient of thermal expansion, which allows the top of the rods to remain relatively unaffected by the changing temperature conditions throughout the year. In addition, the upper portion of the invar rods was encased in grease-filled polyvinylchloride (PVC) tubing to protect the rods from the expansive stresses that may be induced by frost exposure. The top of the rods is expected to maintain a constant elevation throughout the year and is used as a benchmark for all slab surface profile measurements (Wells et al. 2005).

Figure 6.41. Surface profile measurements using the Dipstick™.

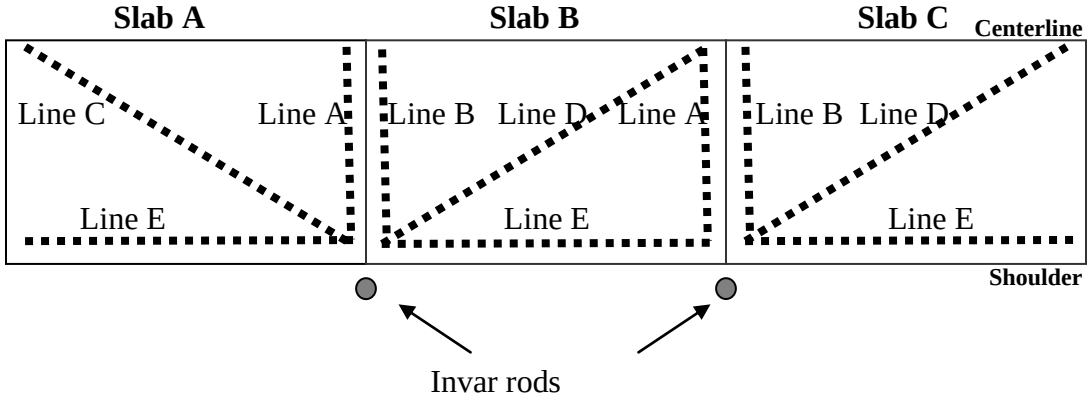

Figure 6.42. Surface profile measurement paths along the concrete slabs (Wells et al. 2005).

The data collected from the Dipstick™ was first corrected for the slope of the slabs in the transverse, longitudinal and diagonal directions. As previously mentioned in Chapter 3, this section of the roadway has, on average, a 2 percent transverse slope and a 2.4 percent longitudinal slope. As a result, the slopes of the slabs affect the surface profile measurements. Each measured profile consisted of walking the Dipstick™ back and forth along the lines drawn on the slab, starting and ending with the top of the invar rod. The difference between the data measured in both directions is calculated for every point along the line, and the average of the differences is considered to be the bias of the operator. Then, the readings were corrected for the bias and the average between the readings taken in the approach direction and those taken in the leave direction was used to calculate the slope of the profile. Finally, the average profile data was corrected for the calculated slope of the profile. This procedure helps ensure that surface irregularities are removed from the profiles.

The next and final step in the data manipulation process was to make sure that the measured profile is zeroed. This was carried out by subtracting out the profile present at a temperature gradient corresponding to the built-in gradient, for every profile and every seasonal outing. As previously mentioned in Chapter 4, the restrained and unrestrained slabs set with a built-in construction gradient of 0.31°F/in. This implies that the slabs will be curled upward whenever the gradient is less than 0.31°F/in.

During the two-year period after construction of the pavement, surface profile measurements were carried out seasonally, four times a year. The seasonal data collection includes continuously walking the Dipstick™ across the paths shown in Figure 6.42 for a one-day period extending between midnight and 6:00 P.M. The dates of the data collection outings representing each season are provided in Table 6.5. Surface profile measurements were taken for a one-week period shortly after paving. Unfortunately, Dipstick™ testing was not carried out for the fall 2005 season.

The slab temperature and moisture conditions during the Dipstick test dates are presented first, followed by the results of the seasonal surface profile measurements. In addition, the curvature of the slabs was estimated based on the surface profiles and the corresponding corner displacement was calculated, as presented in sections 6.3.3 and 6.3.4. Finally, a summary of the findings of this section is presented.

Table 6.5. Surface profile measurements test dates representing each season.

Season	Test Date
Summer 2004	August 16 to 19 and August 22, 2004
Fall 2004	November 16, 2004
Winter 2005	March 3, 2005
Spring 2005	April 6, 2005
Summer 2005	September 22, 2005
Fall 2005	---
Winter 2006	February 1, 2006
Spring 2006	April 18, 2006
Summer 2006	July 20, 2006

6.3.1 Temperature and moisture conditions during seasonal Dipstick™ testing

Dipstick™ testing was performed under different temperature and moisture conditions representing the different seasons. The concrete temperature is characterized in terms of the weighted average temperature and the equivalent linear temperature gradient, while the concrete moisture conditions are characterized in terms of the relative humidity and the corresponding equivalent temperature difference across the slab. The variation in the measured temperature and relative humidity in the slab over the two-year period were presented in Chapter 5. The concrete temperature and moisture conditions during the Dipstick™ test dates are presented in this section.

The temperature of the slab during Dipstick™ testing is summarized in Table 6.6. Since each test date represents a season, the table lists the weighted average temperature and the equivalent linear gradient by season. The average slab temperature ranged between 31˚F (winter 2005) and 90˚F (summer 2006). The daily variation in the concrete weighted average temperature during the Dipstick™ test dates is presented in Figure 6.43 and Figure 6.44.

Table 6.6. Seasonal slab temperature and equivalent linear gradient during profile testing.

	Weighted Average Slab Temperature (˚F)			Equivalent Linear Temperature Gradient (˚F/in)		
Season	**Maximum**	**Minimum**	**Average**	**Maximum**	**Minimum**	**Average**
Summer 04	81	71	75	0.98	-0.97	-0.16
Fall 04	49	42	45	0.72	-0.60	-0.06
Winter 05	36	27	31	0.92	-0.85	-0.25
Spring 05	69	52	60	2.42	-0.51	0.65
Summer 05	82	68	75	1.67	-0.88	0.08
Fall 05	--	--	--	--	--	--
Winter 06	42	39	40	0.44	-0.32	-0.12
Spring 06	74	57	65	2.11	-0.94	0.31
Summer 06	97	83	90	1.85	-0.73	0.29

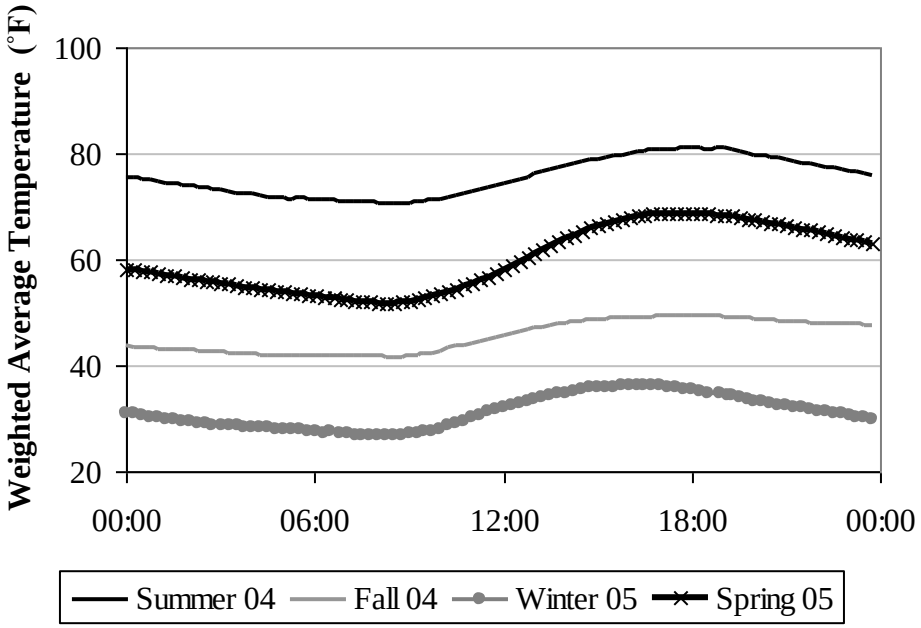

Figure 6.43. Midpanel weighted average concrete temperature during Dipstick™ testing performed the first year after paving.

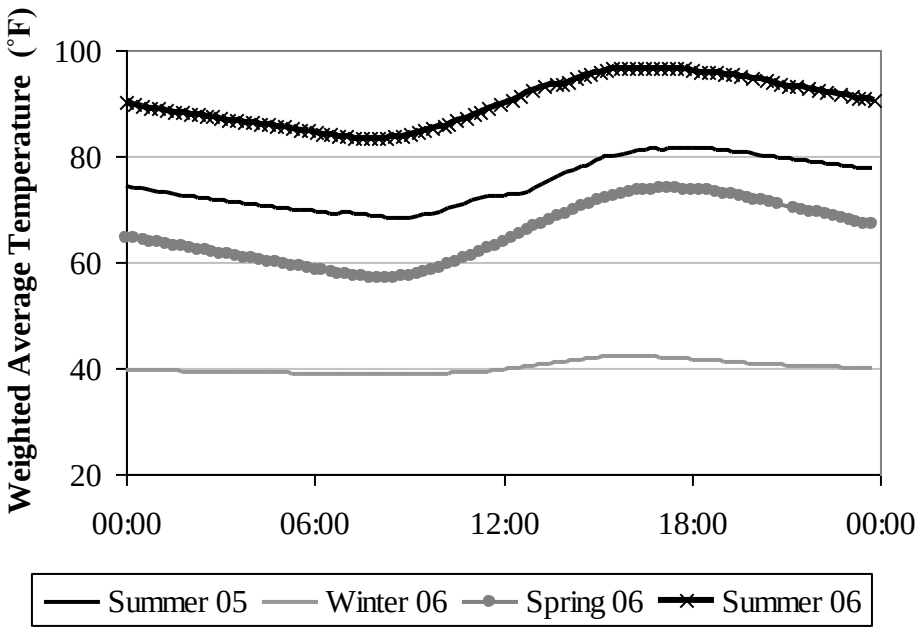

Figure 6.44. Midpanel weighted average concrete temperature during Dipstick™ testing performed the second year after paving.

During the Dipstick™ test dates, the equivalent linear temperature gradient covered positive and negative values. The widest range of values throughout the test days was recorded during the spring season, followed by the summer season. The narrowest range of values throughout the test days was recorded during the winter season. The largest positive gradient during the test days was 2.42˚F/in and occurred during the spring of 2005. The largest negative gradient was -0.97˚F/in and it occurred during the summer of 2004 test date. The daily variation in the concrete equivalent linear temperature gradient during testing is presented in Figure 6.45 and Figure 6.46.

The concrete moisture condition during the Dipstick™ testing is presented in Figure 6.47 and Figure 6.48. These figures were generated based on the moisture sensors located at midpanel and along the slab edge. The figures show the average concrete relative humidity for each season. As previously stated in Chapter 5, the concrete relative humidity during the second year after paving is lower than the concrete relative humidity during the first year after paving. The moisture is highest during the spring of 2005 and lowest during the winter of 2006.

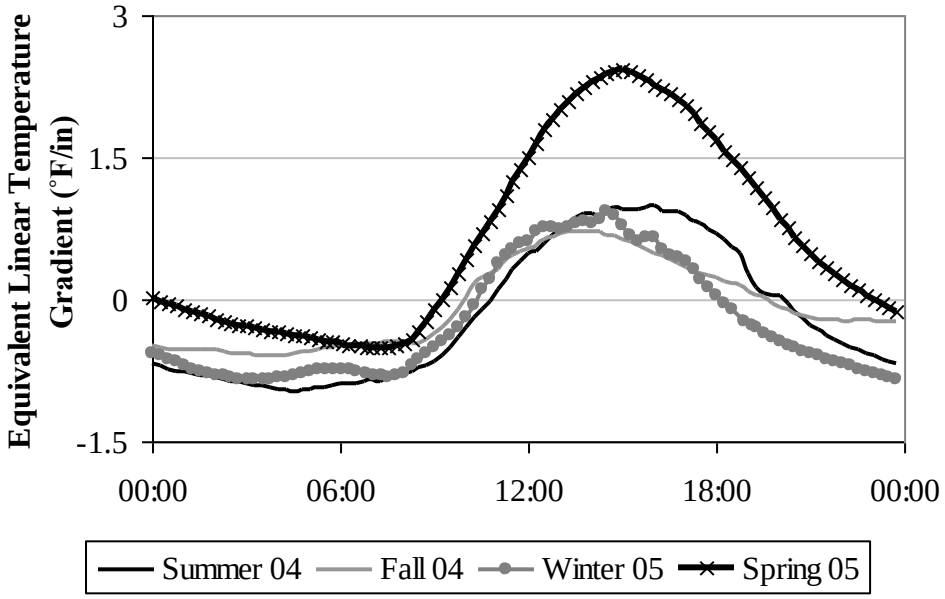

Figure 6.45. Midpanel equivalent linear temperature gradient during Dipstick™ testing performed the first year after paving.

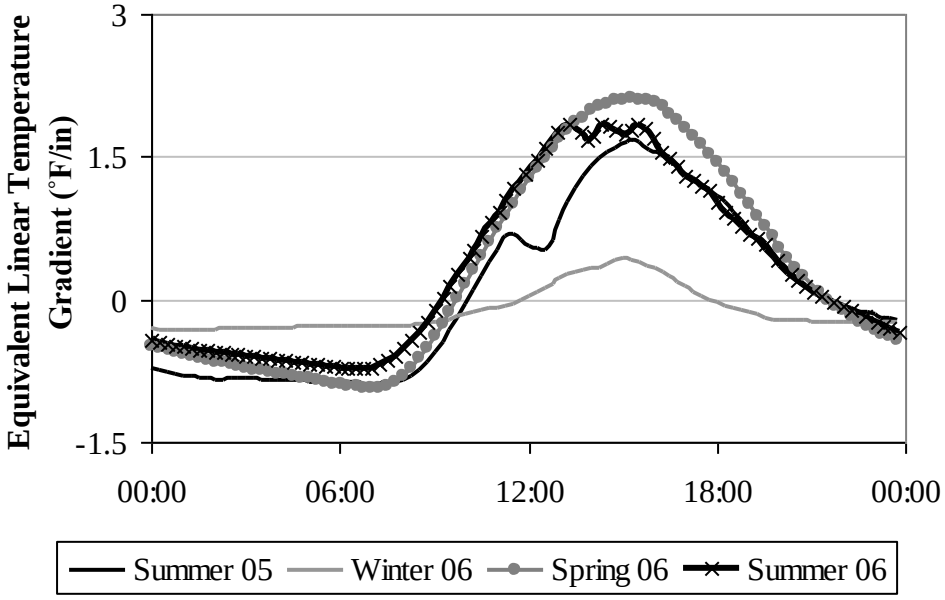

Figure 6.46. Midpanel equivalent linear temperature gradient during Dipstick™ testing performed the second year after paving.

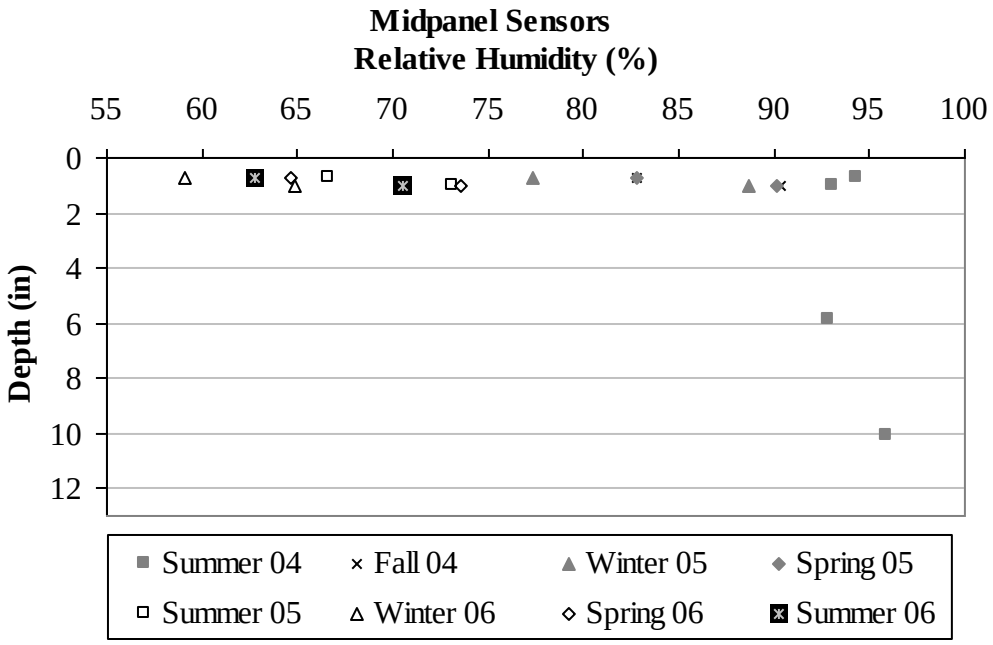

Figure 6.47. Concrete moisture content at midpanel during Dipstick™ testing.

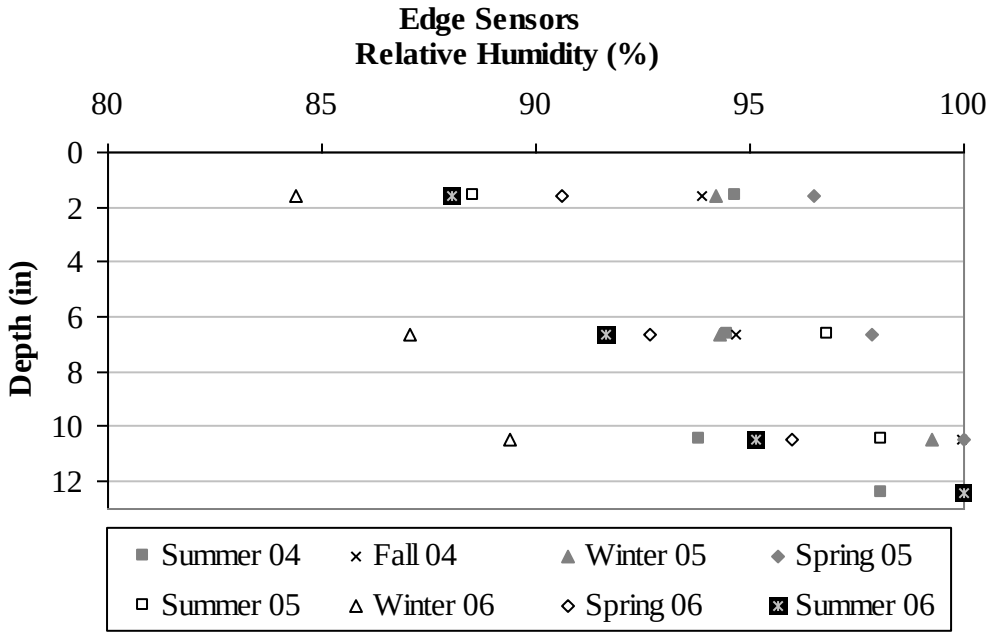

Figure 6.48. Concrete moisture content at the slab edge during Dipstick™ testing.

Based on the concrete moisture measurements at the time of testing, the corresponding equivalent temperature difference and equivalent temperature gradient across the slab are determined by following the procedure described in section 6.1.4. The variation of the equivalent temperature difference during each test date is calculated based on the moisture measurements at the slab edge and are presented in Figure 6.49 and Figure 6.50 for the first two years after construction. During most seasons, the equivalent temperature difference does not vary significantly during the same day. The equivalent temperature difference varies between 12˚F and -50˚F throughout the two-year period.

The equivalent temperature gradients across the slab corresponding to the equivalent temperature differences are presented in Figure 6.51 and Figure 6.52 for the first two years after construction. The equivalent gradient varies between 1˚F/in and -4˚F/in throughout the two-year period.

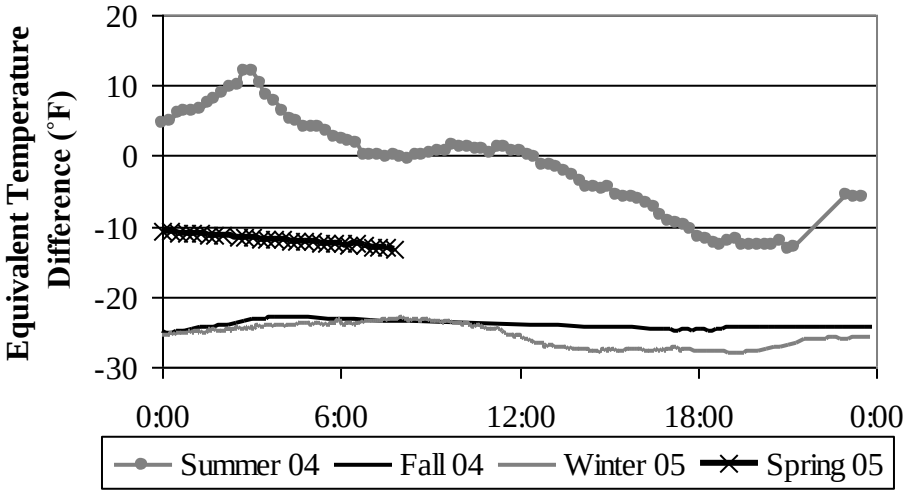

Figure 6.49. Equivalent temperature difference due to moisture during Dipstick™ testing the first year after construction.

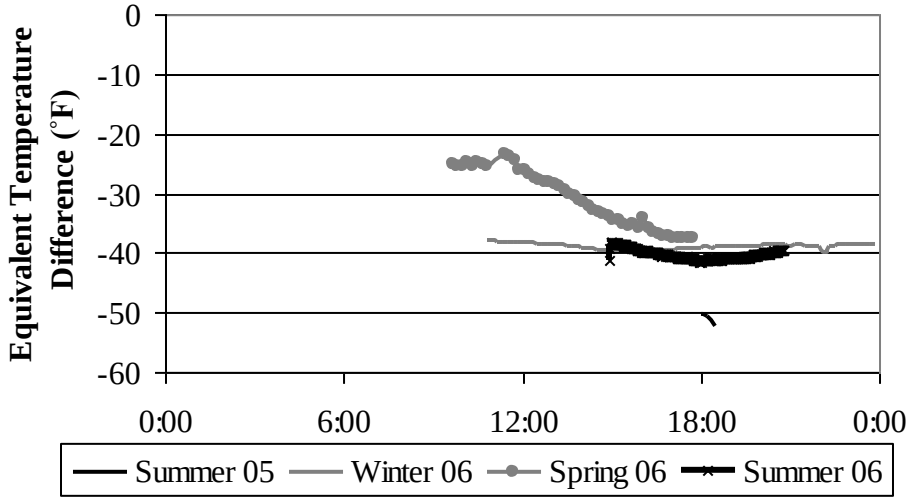

Figure 6.50. Equivalent temperature difference due to moisture during Dipstick™ testing the second year after construction.

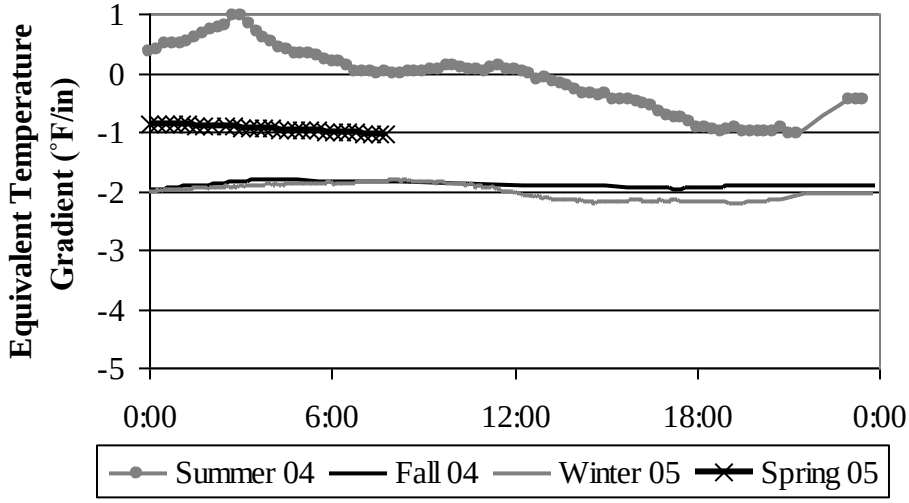

Figure 6.51. Equivalent temperature gradient due to moisture during Dipstick™ testing the first year after construction.

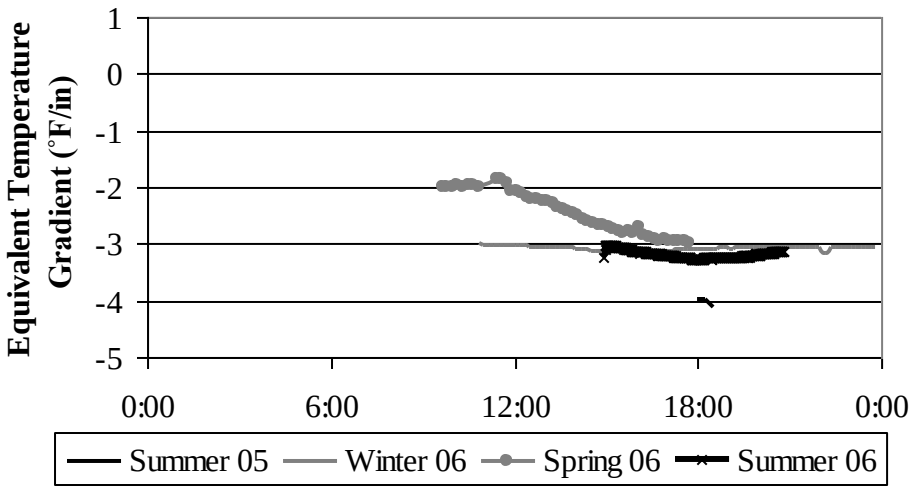

Figure 6.52. Equivalent temperature gradient due to moisture during Dipstick™ testing the second year after construction.

Based on the previous figures, the equivalent temperature conditions due to moisture were averaged for each test day. They are summarized in Table 6.7 for the two-year period.

Table 6.7. Equivalent temperature difference and gradient due to moisture warping for profile test dates.

Season	Test Date	Equivalent Temperature Difference (˚F)	Equivalent Temperature Gradient (˚F/in)
Summer 04	22-Aug-04	-1.4	-0.11
Fall 04	11-Nov-04	-24.3	-1.92
Winter 05	3-Mar-05	-25.3	-2.00
Spring 05	6-Apr-05	-11.9	-0.94
Summer 05	22-Sep-05	-45.2	-3.58
Fall 05	--	--	--
Winter 06	1-Feb-06	-38.9	-3.08
Spring 06	18-Apr-06	-31.0	-2.45
Summer 06	20-Jul-06	-40.2	-3.18

6.3.2 Surface profile measurements

The Dipstick™ was able to provide a dynamic representation of the surface profile of the slab as daily temperature gradients caused it to curl. For each test date, the measured profile is zeroed to the slab surface profile during the same test date corresponding to the built-in construction gradient of 0.31˚F/in. By doing this, the effect of the built-in temperature gradient is taken into account in the surface profiles. However, since the surface profiles are zeroed to a profile during the same test date, and not to the actual surface profile that represents the built-in gradient, the effect of moisture on the slab curvature is not taken into account.

Seasonal profiles were measured in the longitudinal, transverse and diagonal directions of the restrained and unrestrained Slabs A, B and C. A complete set of the profile measurements carried out during the first three years after paving are available in the one-year and the three-year reports (Wells et al. 2005; Asbahan et al. 2006; McCracken et al. 2008). A complete set of all profile measurements for the restrained and unrestrained slabs in the diagonal, longitudinal and transverse directions for the first two years after construction (eight data collection outings) is provided in Appendix C. Only some of the figures are presented in this section. The general seasonal trends observed in the variation in the slab surface profile are presented in this section, for the restrained and unrestrained slabs.

Profiles measured for restrained Slab C in the diagonal direction during four of the test dates representing each of the fall, winter, spring and summer seasons are shown in Figure 6.53 to Figure 6.56. The test date during which profile testing covered the widest range of slab curvatures is presented for every season. The figures indicate that the restrained slab surface is subjected to positive and negative curvature during each test date. During the early morning hours, when the temperature gradient is negative, the slab tends to curl upward, and during the afternoon hours, when the temperature gradient is positive, the slab tends to curl downward.

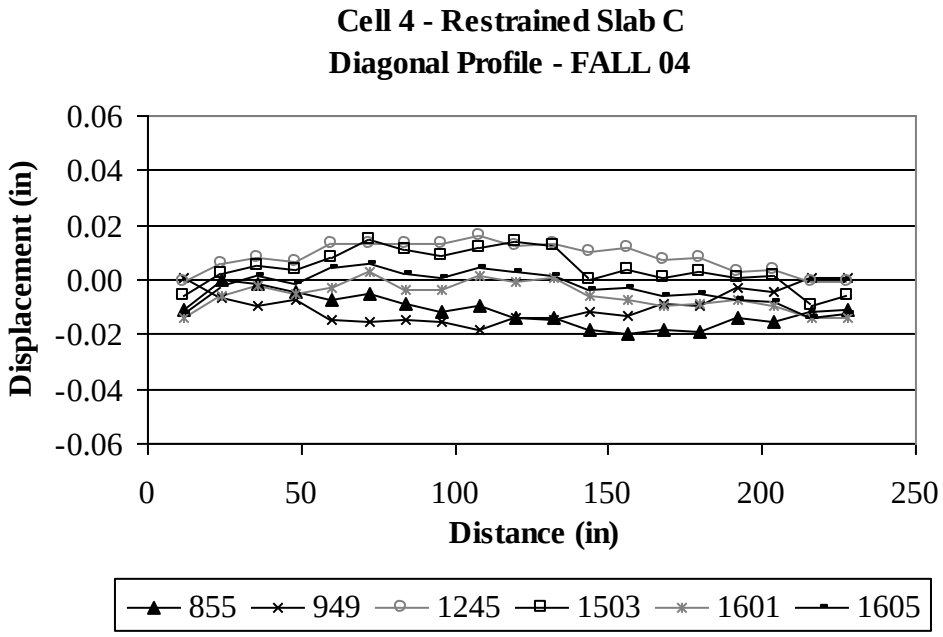

Figure 6.53. Diagonal surface profiles for restrained Slab C in the fall of 2004.

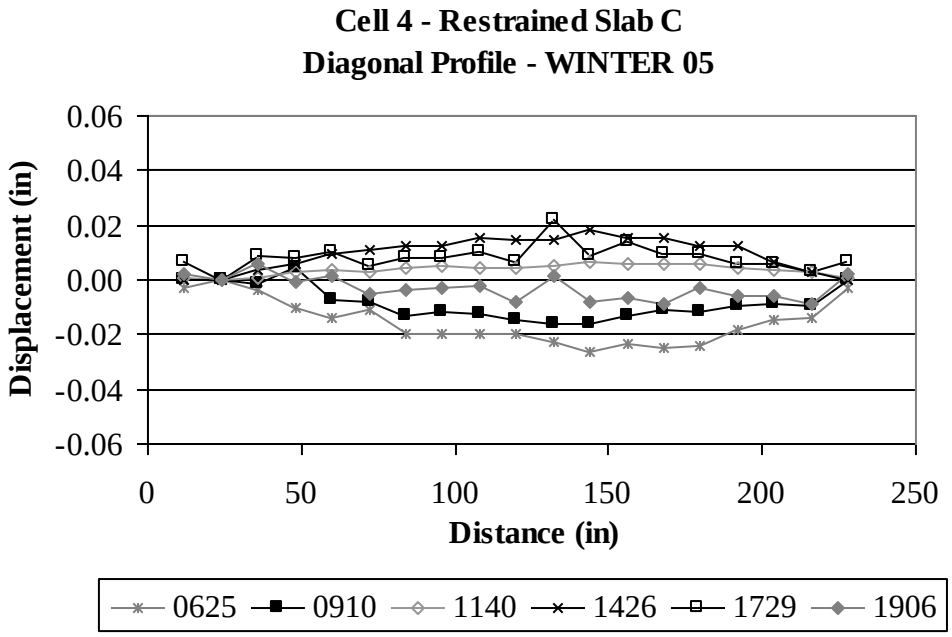

Figure 6.54. Diagonal surface profiles for restrained Slab C in the winter of 2005.

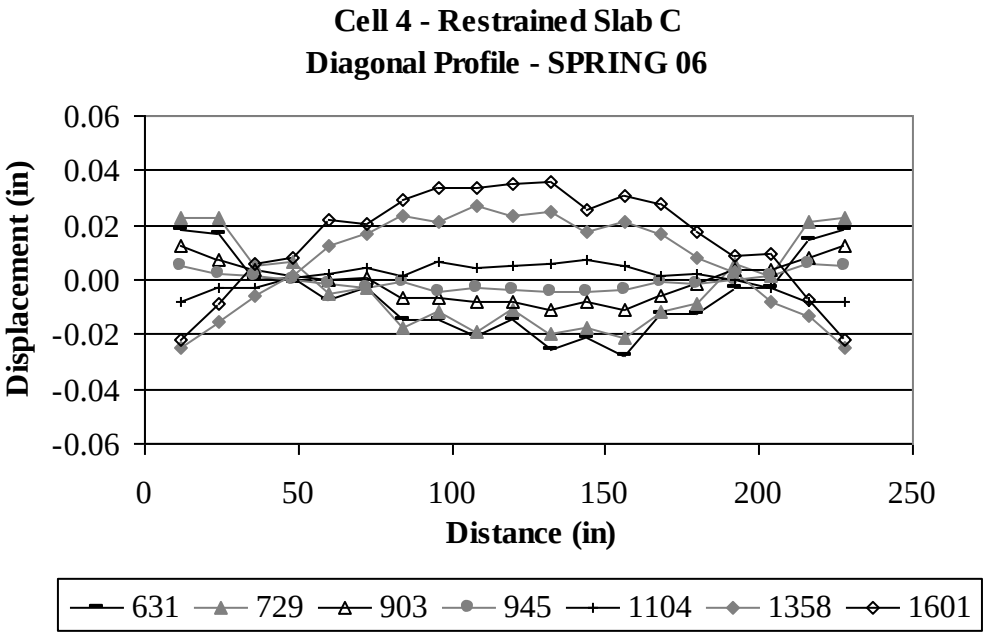

Figure 6.55. Diagonal surface profiles for restrained Slab C in the spring of 2006.

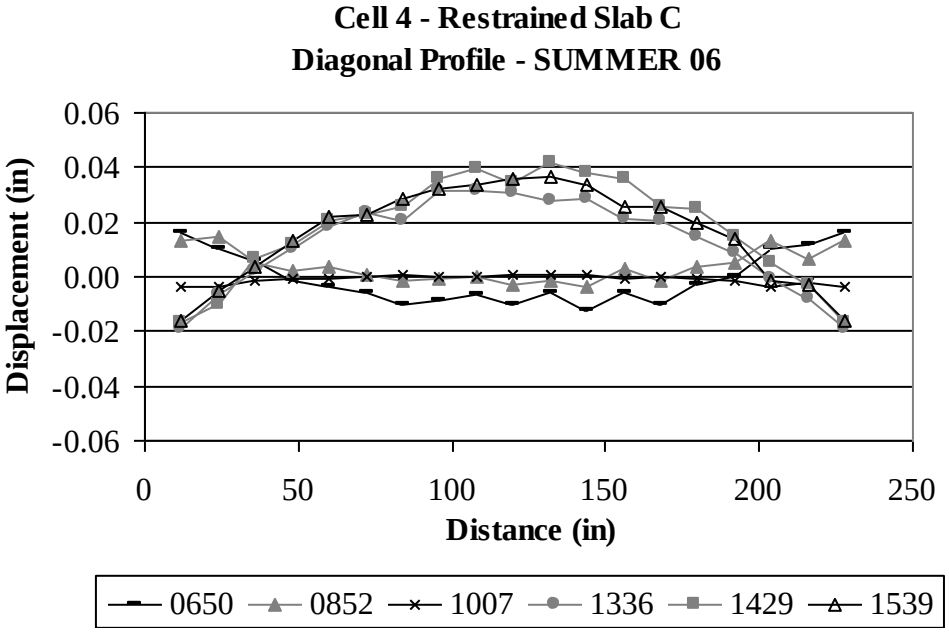

Figure 6.56. Diagonal surface profiles for restrained Slab C in the summer of 2006.

During the fall and winter, the maximum slab displacement at midpanel is within 0.02 inch, while during the summer and spring, the slab displacement at midpanel reaches 0.04 inch (in the case of positive curvature). This is expected since the slab is subjected to a wider range of temperature gradients during the summer and spring, compared to the fall and winter, as previously presented in section 5.1.1. In addition, the displacement at the slab edges varies within 0.02 inch, during the summer and spring, and is much less than that during the fall and winter. To verify this statement, the curvature of the slab and the corresponding corner displacement will be calculated based on the measured profiles, and will be presented in sections 6.3.3 and 6.3.4. Similar trends were observed for the longitudinal and transverse profiles of restrained Slab C and the diagonal, longitudinal and transverse profiles of restrained Slabs A and B.

Profiles measured for unrestrained Slab A in the diagonal direction during four of the test dates representing fall, winter, spring and summer seasons are shown in Figure 6.57 to Figure 6.60. The figures indicate that the unrestrained slab is also subjected to positive and negative curvature during each test date. The profiles show downward curvature during the fall 2004 season because the equivalent linear gradient was less than the construction gradient during most of the data collection period. During the early morning hours, when the temperature gradient is negative, the slab tends to curl upward, and during the afternoon hours, when the temperature gradient is positive, the slab tends to curl downward. The maximum slab displacement at midpanel varies between -0.04 and 0 inch during the fall, between 0.01 and -0.01 inch during the winter, and between -0.02 and 0.04 inch during the spring and summer. This is similar to what was observed for the case of the restrained slabs. The larger curvature (both negative and positive) is expected during the summer and spring due to the wider range of temperature gradients during these two seasons. In addition, the displacement at the unrestrained slab edge varies within 0.03 inch, during the summer and spring, and is much less than that during the fall and winter. To verify this statement, the curvature of the slab and the corresponding corner displacement will be calculated and compared to the temperature gradients in the slab at the time of the profile measurements. This will be presented in sections 6.3.3 and 6.3.4. Similar trends were observed for the longitudinal and transverse profiles of unrestrained Slab A and the diagonal, longitudinal and transverse profiles of unrestrained Slabs B and C.

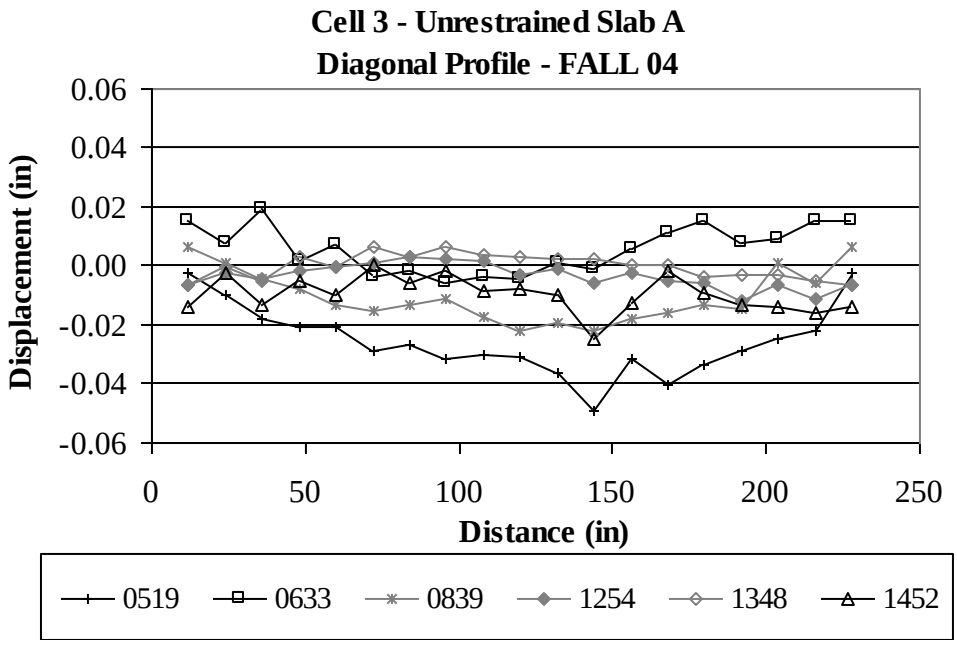

Figure 6.57. Diagonal surface profiles for unrestrained Slab A in the fall of 2004.

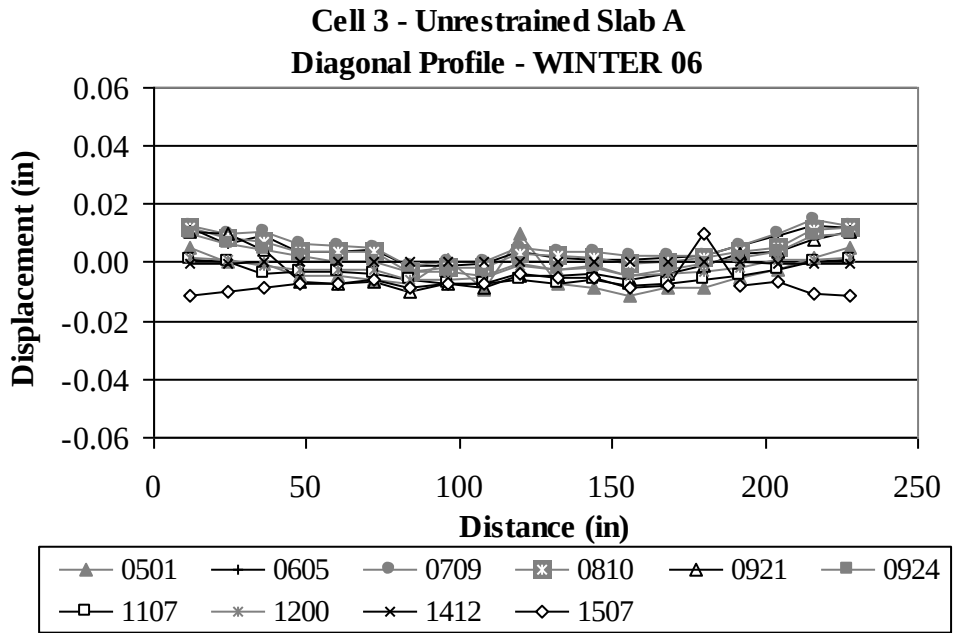

Figure 6.58. Diagonal surface profiles for unrestrained Slab A in the winter of 2006.

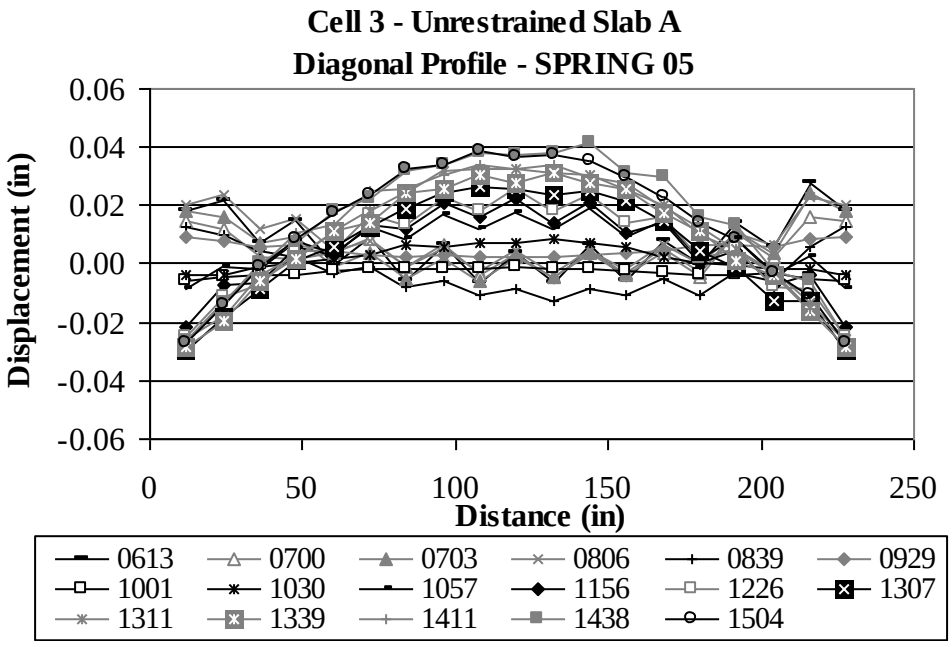

Figure 6.59. Diagonal surface profiles for unrestrained Slab A in the spring of 2005.

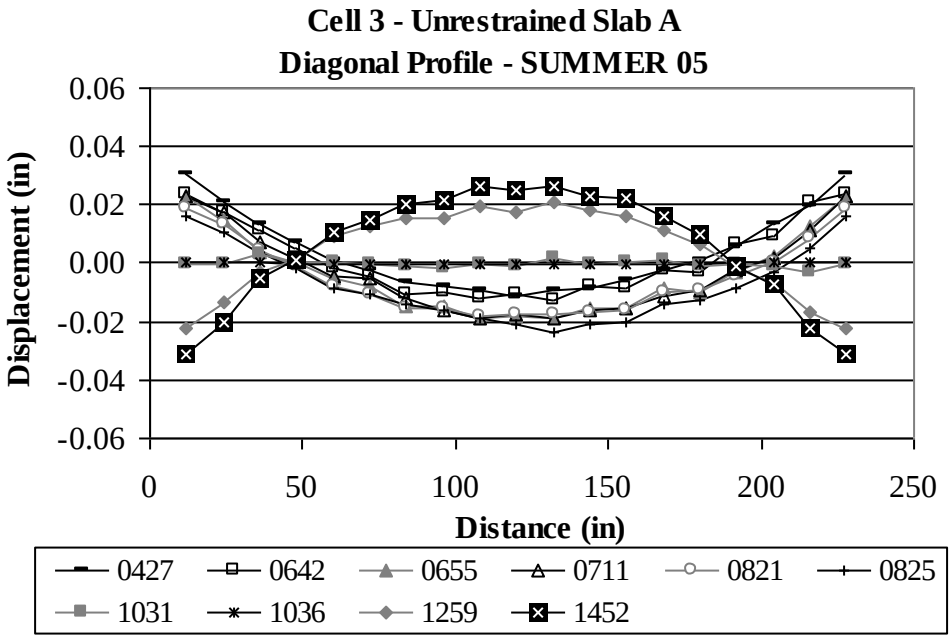

Figure 6.60. Diagonal surface profiles for unrestrained Slab A in the summer of 2005.

Based on the surface profiles provided in this section and in Appendix C, the unrestrained slabs exhibit larger movements at the edge of the slab and the restrained slabs exhibit larger movements at midpanel. The restraint provided by the dowels at the transverse joint reduces the displacement at the edge of the slab from ±0.03 inch to ±0.02 inch. Due to this restraint imposed on the restrained slab edges, the stresses increase at the edge. The redistribution of stresses within the slab causes a reduction in the stress at midpanel, which in turn allows the midpanel to deflect more than the edge (Wells et al. 2005). This behavior was observed for the profiles measured in all slabs and in the three directions.

6.3.3 Slab curvature

In this section, the slab curvature is estimated based on the measured surface profile and a relationship between slab curvature and temperature gradient is developed. First, a second order polynomial was fitted to the first few feet of the measured profiles. Then, the second derivative of the deflection profile was taken to estimate the radius of curvature of the slab. By combining the profile data with the equivalent linear temperature gradient derived from the midpanel thermocouples, the relationship between slab curvature and equivalent linear temperature gradient was defined. Plots of curvature versus equivalent linear temperature gradient for the diagonal, longitudinal and transverse profiles of both unrestrained and restrained slabs were generated for data collected during the first three years after paving (Asbahan et al. 2006; McCracken et al. 2008). Surface profile data collected during the first two years after construction was used to generate the plots presented in Figure 6.61 and Figure 6.62, which are based on the diagonal profiles of restrained Slab C and unrestrained Slab A.

A linear relationship between slab curvature and equivalent linear temperature gradient can be distinguished. The slope of the line indicates the rate of change in curvature with changes in equivalent linear gradient. As the temperature gradient in the slab increases, the curvature of the slab decreases; a negative curvature indicates downward slab curvature and a positive curvature indicate upward curvature. In general, the graphs are consistent in showing that the slopes of the lines are relatively close to each other throughout the seasons. An exception is the slopes estimated for the September 2005 (Summer 2005) testing, which are somewhat steeper than for the remaining seasons.

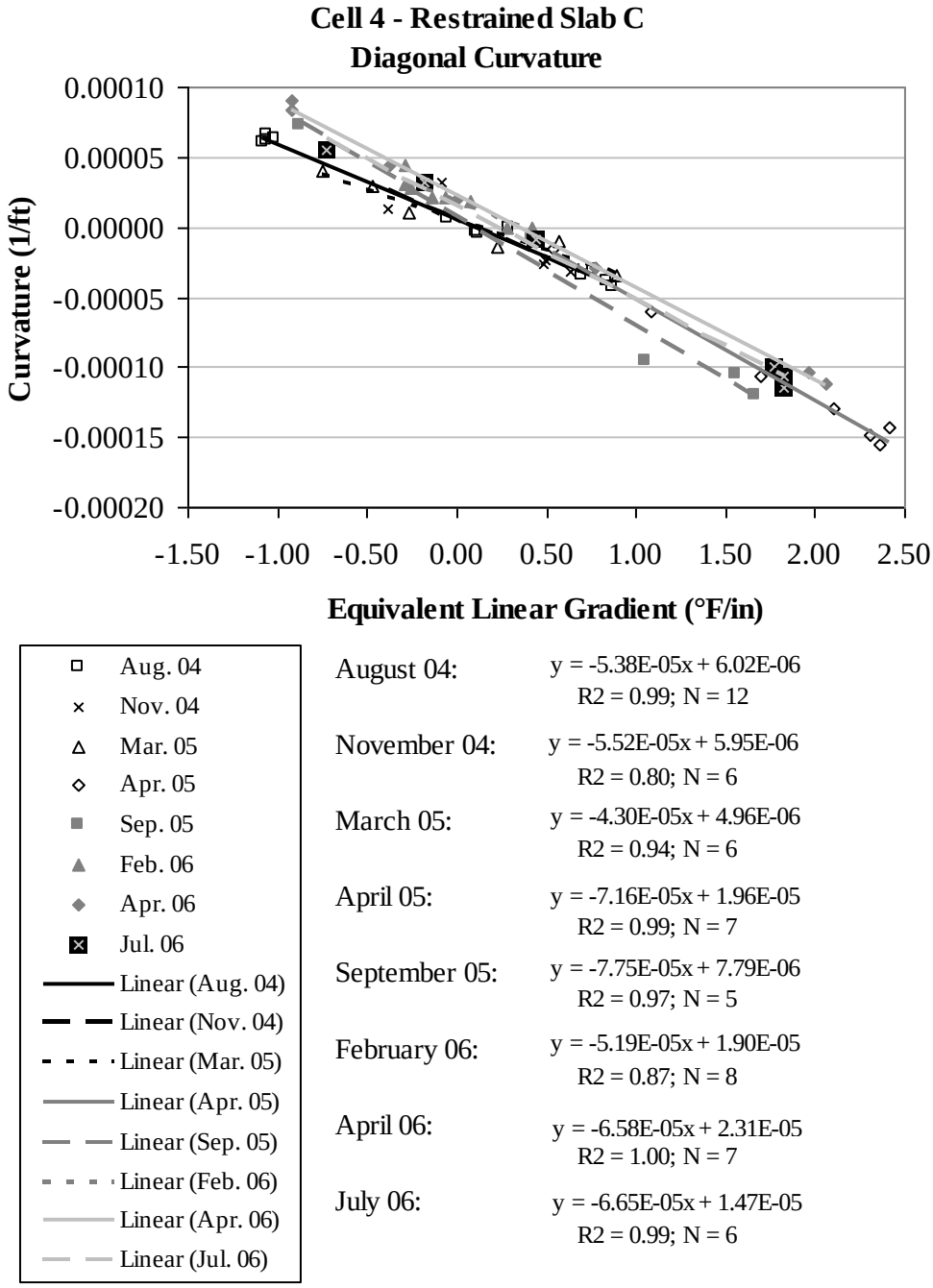

Figure 6.61. Curvature versus equivalent linear gradient for the diagonal profile of restrained Slab C.

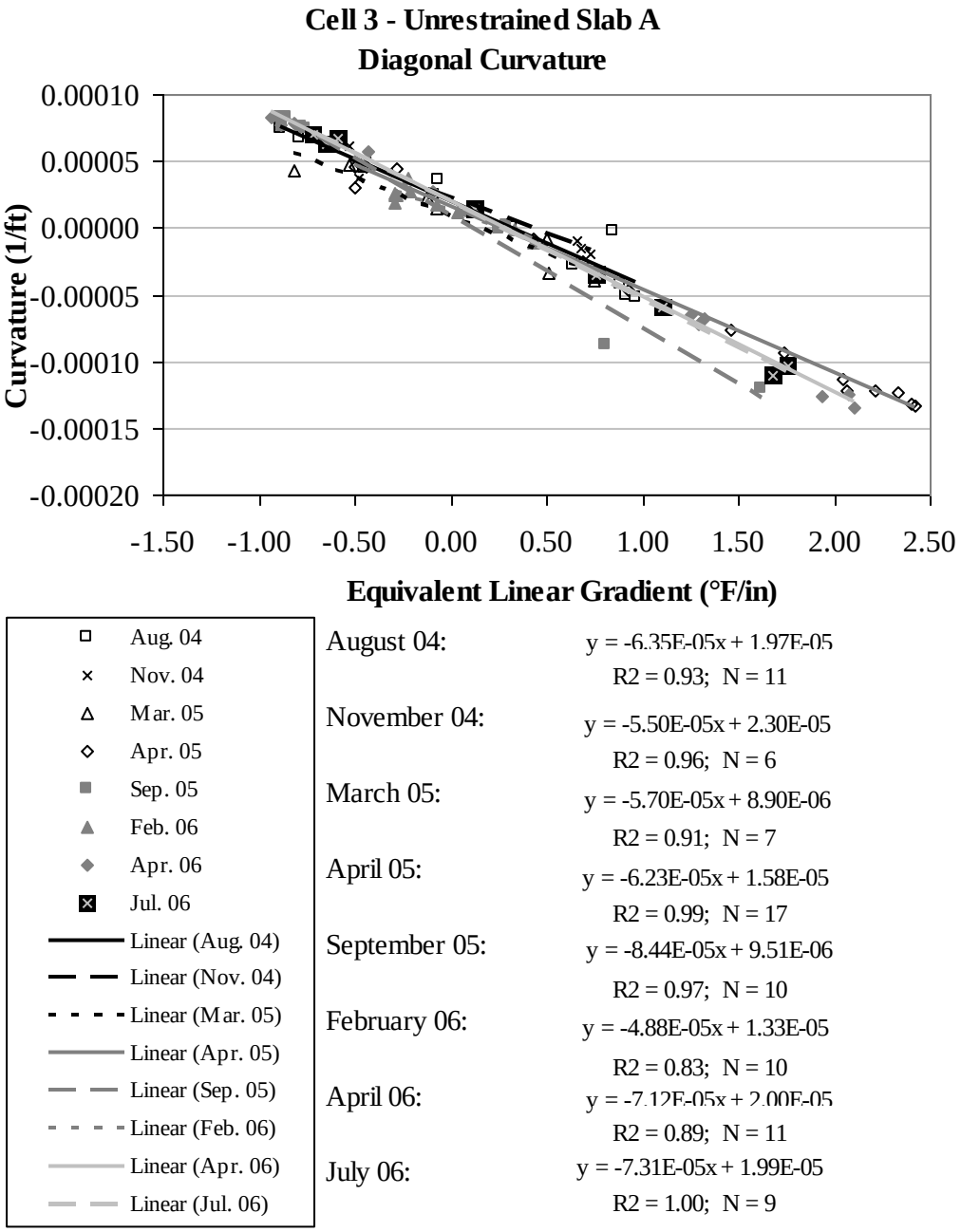

Figure 6.62. Curvature versus equivalent linear gradient for the diagonal profile of unrestrained Slab A.

The slopes of the lines are similar for the restrained and unrestrained slabs and fall within 9 percent of each other. This is consistent with the observation made in section 6.2.3 for the curvatures based on the strain measurements. The magnitude of the curvature is also similar between the restrained and unrestrained slabs and ranges between -0.0017 1/ft and 0.0015 1/ft. These values are similar to the temperature-related curvature calculated based on the temperature measurements, as shown in Figure 6.21.

A comparison between the variation in the curvature with change in equivalent linear temperature gradient of the restrained and unrestrained slabs is presented in Figure 6.63 based on the diagonal profiles. Unlike in Figure 6.38, comparing the curvatures based on the strain data, the data points in Figure 6.63 are relatively collinear because the effect of drying shrinkage is removed.

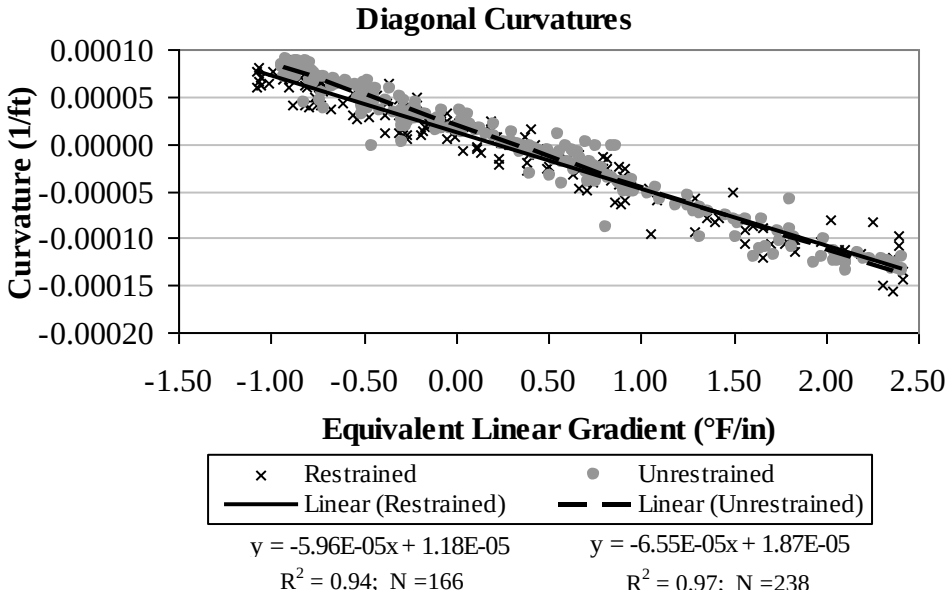

Figure 6.63. Curvature versus equivalent linear gradient for the diagonal profiles of restrained and unrestrained slabs.

6.3.4 Slab corner displacement

In this section, the corner displacement is calculated based on the slab curvature and a relationship between corner displacement and equivalent linear temperature gradient is presented.

The profile measurement starts from the top of the invar rods, the subsequent Dipstick™ reading is taken on the curb and gutter and the third reading is taken at a marked point on the slab located at a distance of four inches away from each edge, as shown in Figure 6.64. Based on the estimated curvature, and knowing the exact point where the profiles are initiated, the displacement of the slab corner can be calculated. The corner displacement is estimated for each profile by using the first surface profile measurement located on the slab and backcalculating the displacement at the corresponding distance away based on the profile curvature. The diagonal profiles are used to estimate the corner displacements, the transverse profiles are used to estimate the displacements four inches away from the corner in the longitudinal direction. The longitudinal profiles are used to estimate the displacements four inches away from the corner in the transverse direction (Asbahan et al. 2006).

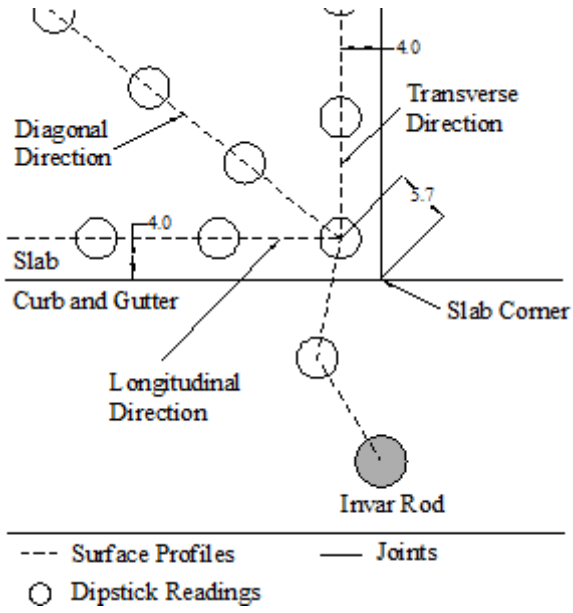

Figure 6.64. Plan showing the start point of the surface profiles in all directions (Asbahan et al. 2006).

Figure 6.65 and Figure 6.66 show the variation of the corner displacement estimated using the diagonal profiles for restrained Slab C and unrestrained Slab A with respect to the equivalent linear temperature gradient. The slope of the line indicates the rate of change in corner displacement with changes in equivalent linear gradient. The corner displacement decreases with increasing gradient. However, Figure 6.65 indicates that the rates of change for the November 04 and March 05 test dates are smaller than the rates for the other data collection outings. The range of equivalent linear gradients covered during both these test dates is smaller compared to the other outings, as well. This indicates that there was not sufficient data to give an overall grasp of the change in slab corner displacement that accompanies changes in temperature gradient. In addition, for the November 04 testing, the coefficient of correlation is approximately 16 percent, which indicates that the relationship between the temperature gradient and the corner displacement is poor for that data set.

The corner deflections for the diagonal profiles of the unrestrained and restrained slabs are compared to each other for the same equivalent linear temperature gradient. The equivalent linear temperature gradients varied between -1.0˚F/in to 2.5˚F/in during the time periods when surface profile measurements were being taken. The range of corner displacements for the restrained and unrestrained slabs is provided in Table 6.8. This represents the range of corner displacements for all slabs (Slabs A, B and C). For the same gradient, the estimated corner displacement is similar for the restrained and unrestrained slabs. The maximum positive corner displacement is 40 mils for both the restrained and unrestrained slabs, and the maximum negative corner displacement is -35 mils for the restrained slabs and -40 mils for the unrestrained slabs. This indicates that the slabs encounter comparable measurable maximum displacement, irrespective of the restraint provided by the dowel bars and tie bars along the transverse and longitudinal joints, respectively.

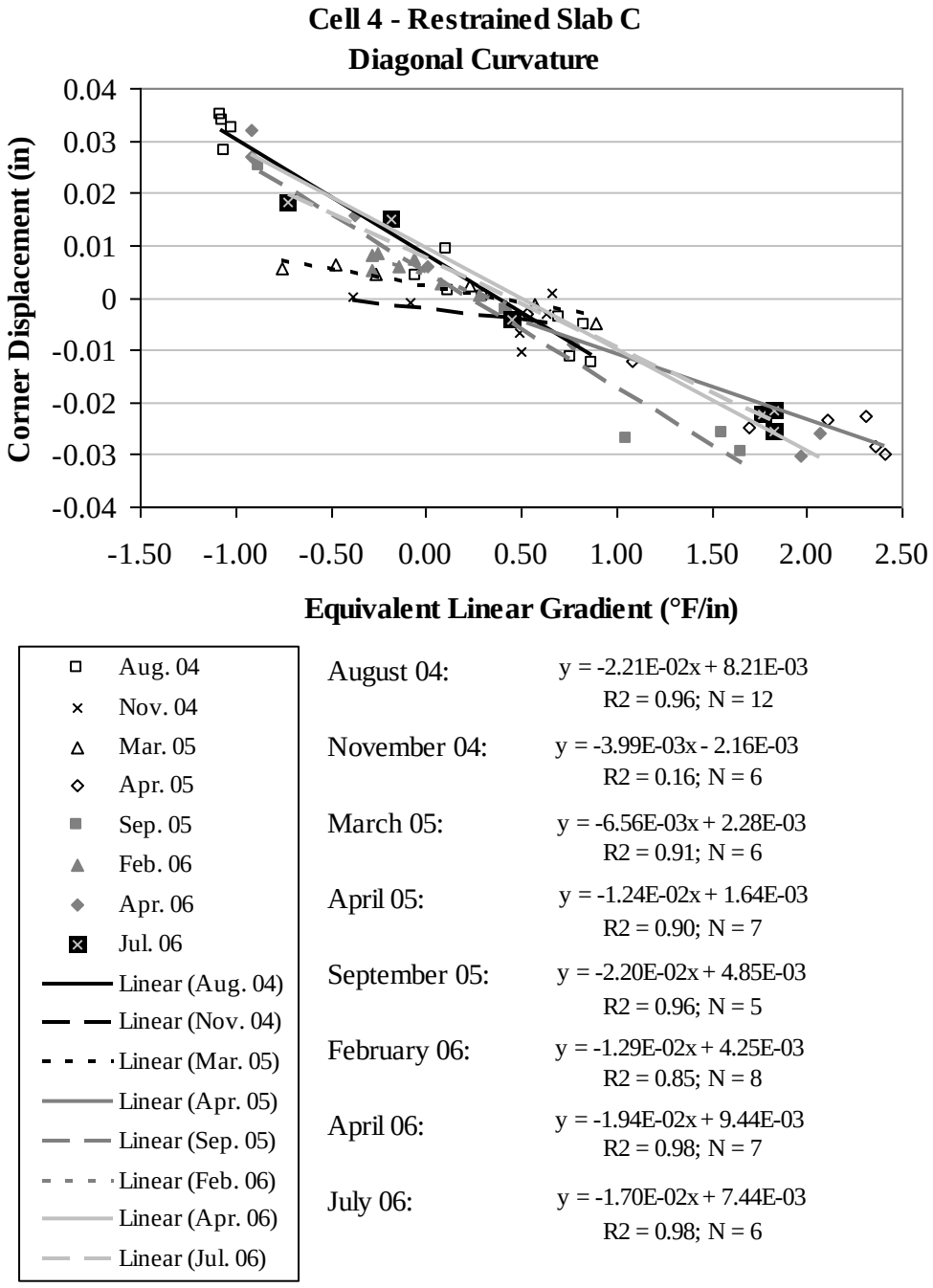

Figure 6.65. Corner displacement versus equivalent linear gradient for the diagonal profiles of restrained Slab C.

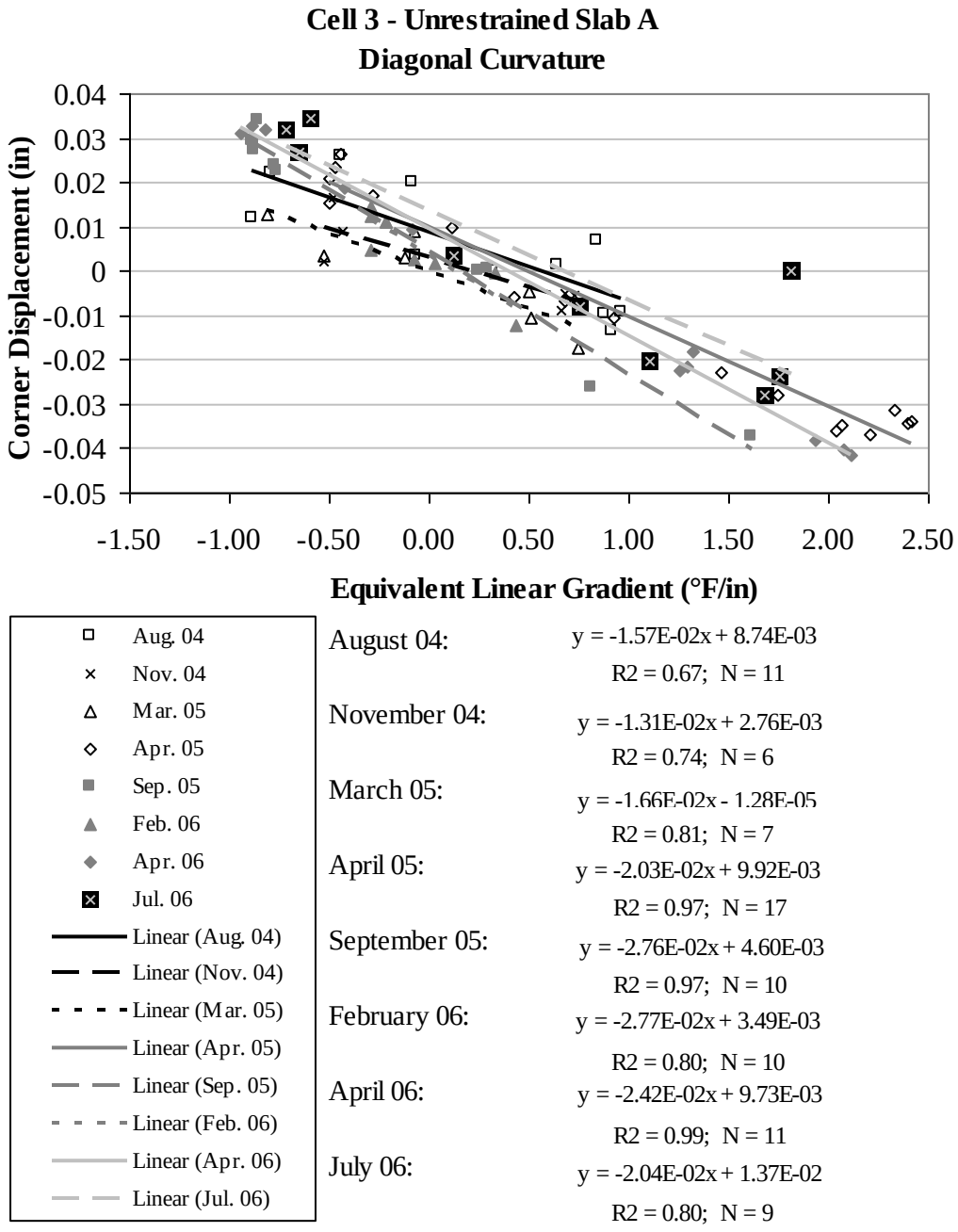

Figure 6.66. Corner displacement versus equivalent linear gradient for the diagonal profiles of unrestrained Slab A.

Table 6.8. Ranges of corner displacement for different equivalent linear temperature gradients for unrestrained and restrained Slabs A, B and C.

	Corner Deflections from Diagonal Profiles (Slabs A, B and C) (mils)					
Equivalent Linear Temperature Gradient (˚F/in)	**Restrained Slabs**			**Unrestrained Slabs**		
-1.0	5	to	40	10	to	40
0.0	-10	to	15	-5	to	20
0.31	-15	to	15	-10	to	15
1.0	-30	to	0	-25	to	0
2.0	-35	to	-15	-40	to	-20

6.3.5 Summary

The restraint provided by the dowels at the transverse joint reduces the displacement at the edge of the slab from ±0.03 inch to ±0.02 inch. Due to this restraint imposed on the restrained slab edges, the stress increases at the edge. This behavior was observed in the longitudinal, diagonal and transverse directions.

The seasonal profiles show positive curvature during the fall season and both positive and negative curvature during the remaining seasons. The slab deformation is relatively small during the winter season to the point were the slabs are almost flat, although it must be remembered that the effect of the moisture gradients (drying shrinkage) has been removed. Large deformations occur during the spring and summer. The largest upward curvature was measured in the spring and the largest downward curvature in the fall and summer. The slab curvature based on the Dipstick™ data is similar in value to the curvature calculated based on the temperature measurements.

Slab curvature decreases with increasing equivalent linear gradients at a constant rate irrespective of the season of the year. This was confirmed by all data collected throughout the two-year period, with some exceptions. The rate of the change in curvature with a change in gradient is similar for the restrained and unrestrained slabs. Unlike the curvature based on the strain measurements, the curvatures are relatively collinear for both types of slabs because the effect of drying shrinkage is not accounted for.

6.4 EFFECT OF MOISTURE ON CONCRETE DRYING SHRINKAGE

In the previous sections, the slab curvature was estimated based on the calculated surface thermal and moisture strains (section 6.1.5), based on the strain measurements (section 6.2.3) and based on the surface profile measurements (section 6.3.3). In this section, the slab curvature estimated from the three types of data is compared for the days when Dipstick™ testing was performed during the two-year period after construction. The results are used in evaluating the effect of moisture on the drying shrinkage for the restrained and unrestrained slabs.

6.4.1 Restrained slabs

First, the curvatures calculated based on the VW sensors and the Dipstick™ data are compared. Figure 6.67 to Figure 6.71 compare the curvature that was estimated based on the strain data to the curvature based on the surface profile data for restrained Slab A, for the Dipstick™ test dates during the first year after paving. The curvatures provided in the figures are estimated based on strain data collected from the VW sensors in the corner of the slab adjacent to the lane/shoulder joint and in the longitudinal, diagonal and transverse directions. The curvature estimated using the Dipstick™ data is based on surface profiles that begin in the slab corner adjacent to the lane/shoulder joint and extend in the same three directions. The figures show that the curvatures estimated from the surface profiles and the strain data follow the same general daily trends, with smaller curvature values resulting from estimates that are based on the measured strain data, in most cases.

Appendix D includes a full set of the remaining figures comparing curvatures estimated from the surface profiles to those from the strain gages, for restrained Slabs A, B and C, for the second year after construction. The trend line for the curvature estimated from the surface profile is shifted downward and has a flatter slope with respect to the trend line for the curvature obtained from the strain gage data. The downward shift means that the computed curvature under/overestimate actual total curvature because the process of zeroing out the profile measurement removes the effects of everything except the transient temperature gradient.

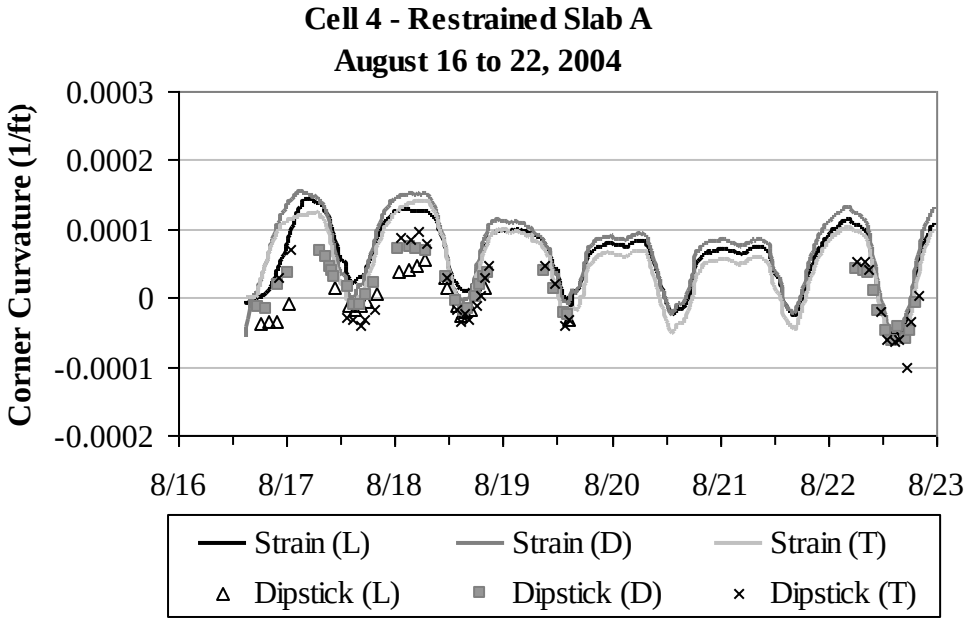

Figure 6.67. Curvature estimated from surface profiles and vibrating wire gages for restrained Slab A during the summer of 2004.

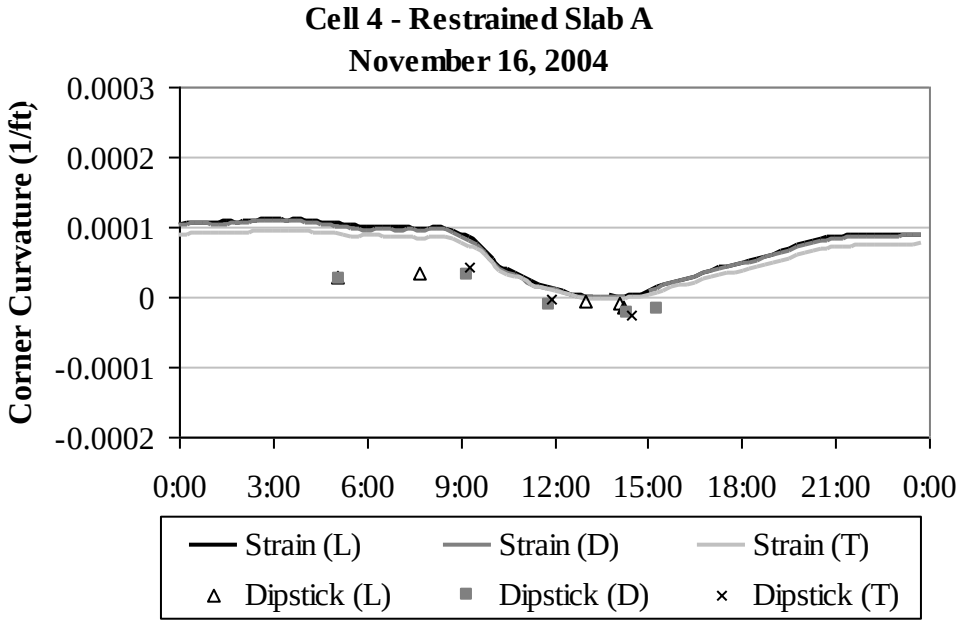

Figure 6.68. Curvature estimated from surface profiles and vibrating wire gages for restrained Slab A during the fall of 2004.

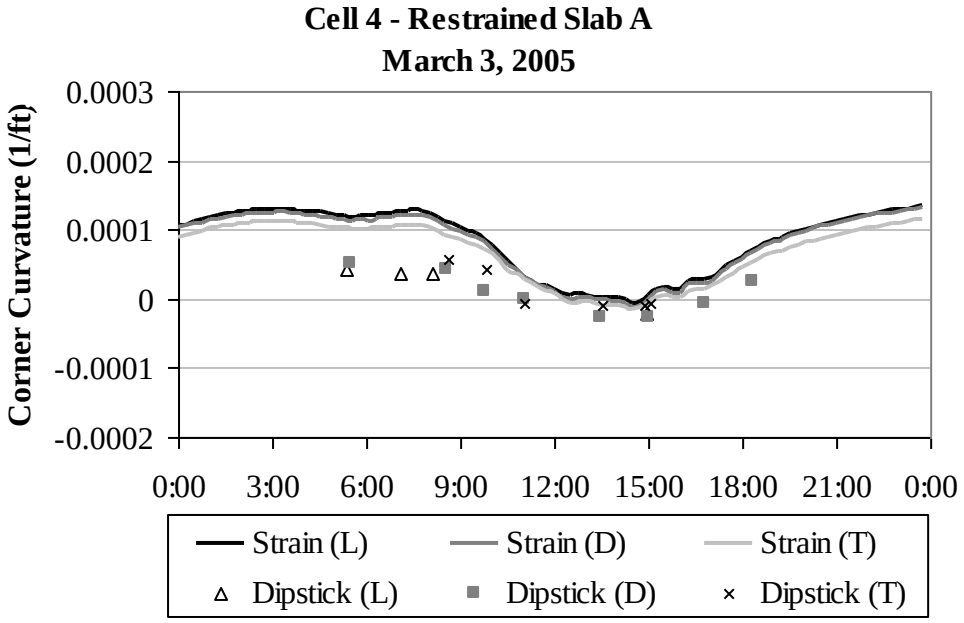

Figure 6.69. Curvature estimated from surface profiles and vibrating wire gages for restrained Slab A during the winter of 2005.

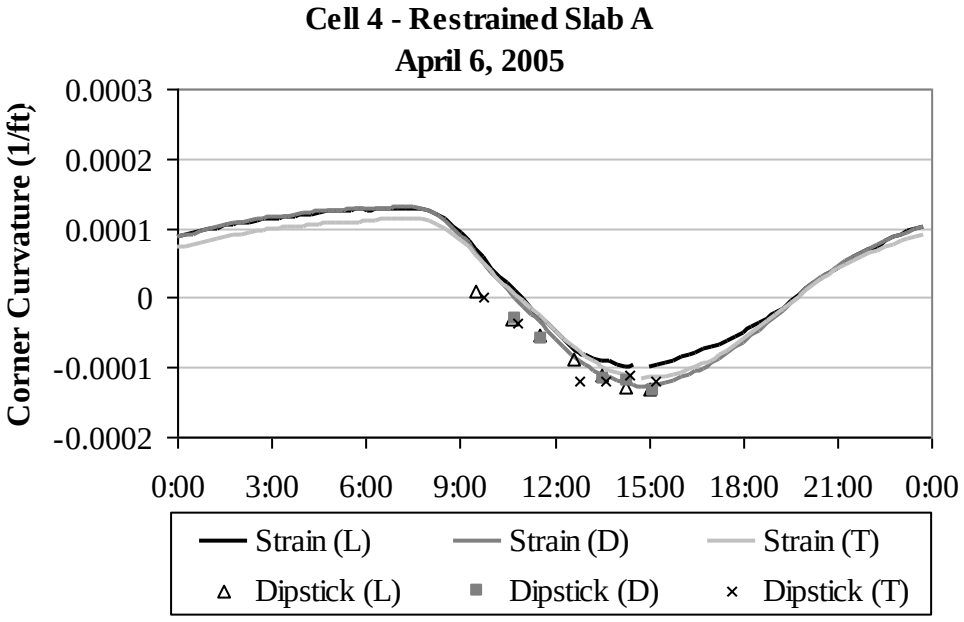

Figure 6.70. Curvature estimated from surface profiles and vibrating wire gages for restrained Slab A during the spring of 2005.

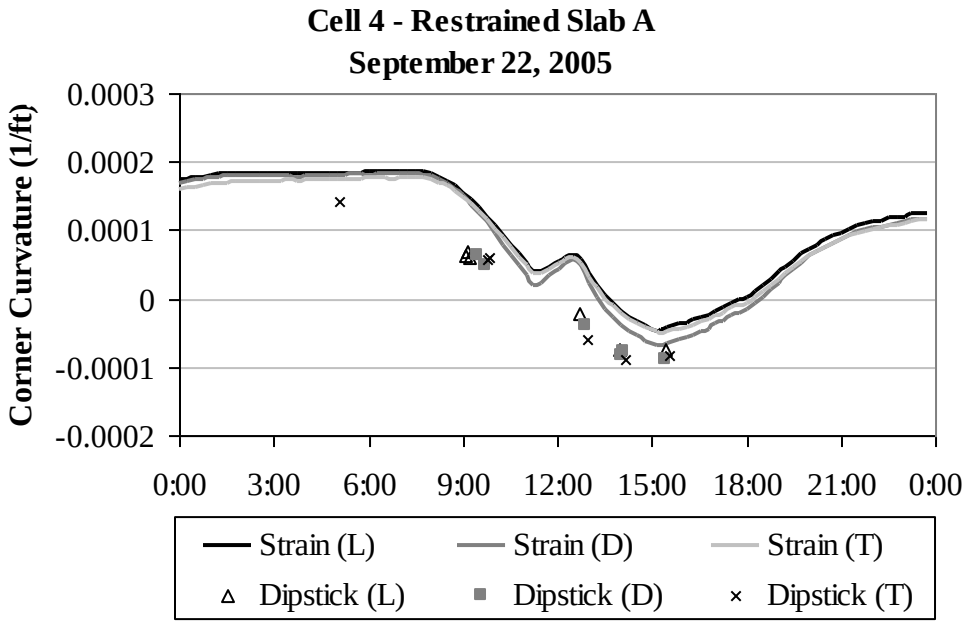

Figure 6.71. Curvature estimated from surface profiles and vibrating wire gages for restrained Slab A during the summer of 2005.

The curvature estimated using the two methods are different because of the different components that are accounted for when using each method. As previously presented in section 2.3, slab curling and warping is due to several factors, including the following: daily and seasonal variations in temperature, seasonal variations in moisture and the presence of a built-in construction gradient. The response of the slab to these different factors is highly affected by concrete material properties such as coefficient of thermal expansion, drying shrinkage, creep and elastic modulus. In addition, the response of the slab is also highly affected by factors that reduce the slab movement, which include: slab self-weight, friction at the slab/base interface and restraints along the transverse and longitudinal joints.

Estimating the slab curvature based on strain data takes into account the variation in temperature and moisture conditions, the built-in construction gradient, as well as other factors affecting the slab movement such as concrete material properties and slab restraining conditions. However, the slab curvature estimated based on the surface profile measurement does not take into account all these factors. As previously mentioned in section 6.3, for each Dipstick™ test date, the surface profiles are zeroed to a profile representing the built-in construction gradient.

This establishes that the slab is flat when the temperature gradient is equal to the built-in gradient. This is not entirely true because it does not take into account the effect of moisture changes on concrete drying shrinkage over time or creep.

The majority of the drying shrinkage that will occur throughout the life of the slab will occur within the first couple of years after casting. Upon rewetting, concrete expands to reverse a portion of the drying shrinkage but some of the shrinkage that occurs on first drying is irreversible. The main factors that affect the reversible portion of drying shrinkage are the seasonal climatic conditions (ARA 2004). As a result, the difference in slab curvature as estimated from the two methods can be attributed to the effect of drying shrinkage of concrete.

Figure 6.72 and Figure 6.73 present comparisons of slab curvature calculated based on temperature and moisture measurements with curvature estimated based on strain measurements (diagonal direction only) and curvature based on surface profile measurements (diagonal direction only). All data presented were collected during a single day in the fall of 2004 and the winter of 2005. The figures show that the curvatures derived from surface profile data closely fit the trend line for curvatures based on temperature measurements. Curvature due to moisture-induced strains is relatively constant throughout the test day. This confirms the previous statement that the primary difference between the curvatures computed using strain data and surface profile data is due to the effects of moisture and creep.

The same pattern was observed when comparing the calculated curvature due to the calculated thermal and moisture-induced strain (based on the temperature and moisture measurements) to the curvature from the strain measurements and the Dipstick™ data for the remaining seasons and slabs. Unfortunately, in some cases, the curvature due to the moisture-induced strain was not available due to the gaps in the collected moisture data. The figures comparing the curvature due to the thermal and moisture-induced strain to the curvature based on the strain measurements and the Dipstick™ data for the remaining seasons are also included in Appendix D, for restrained Slab A.

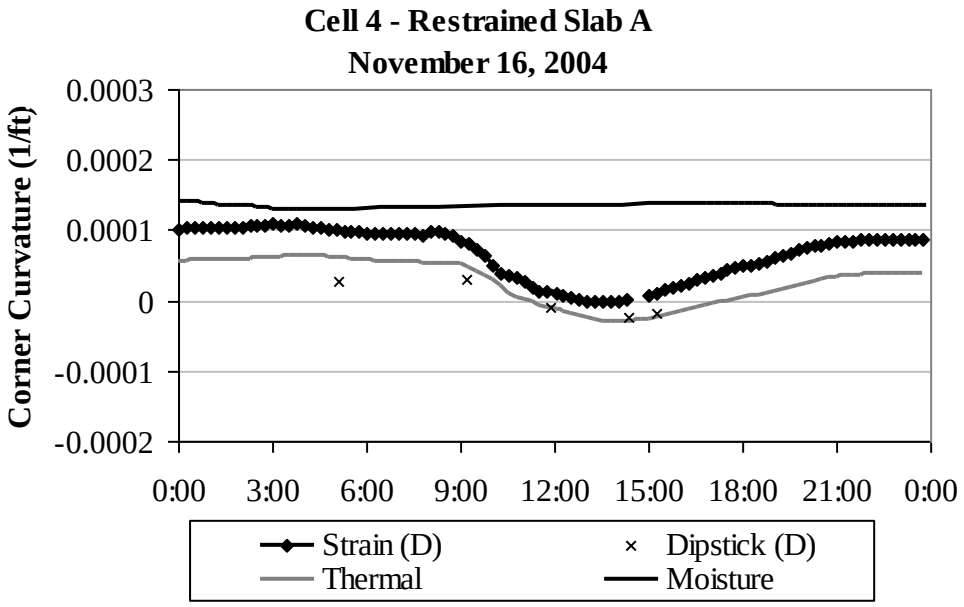

Figure 6.72. Comparison between curvatures estimated from the three types of data for restrained Slab A during the fall of 2004.

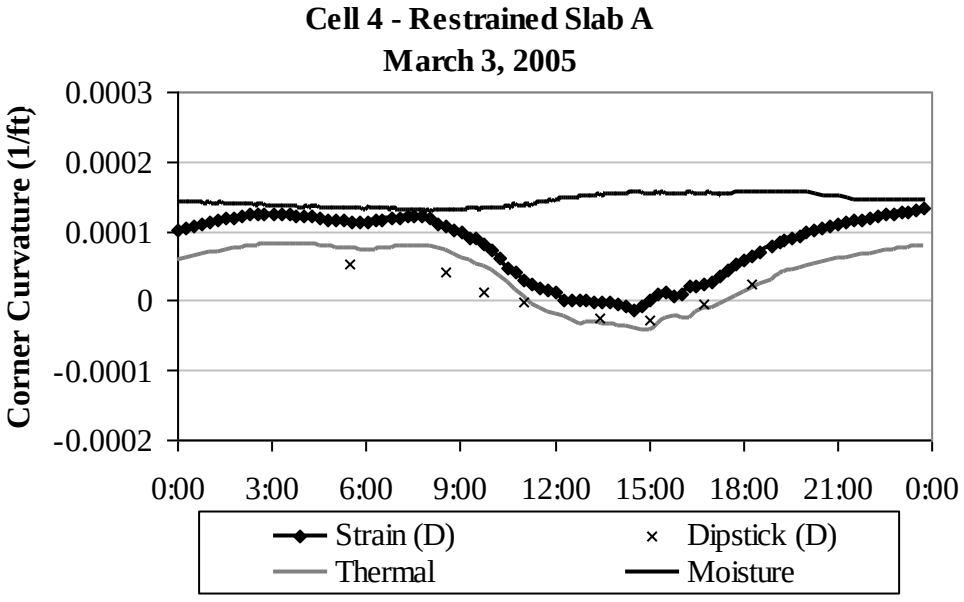

Figure 6.73. Comparison between curvatures estimated from the three types of data for restrained Slab A during the winter of 2005.

The difference between the curvatures estimated from the strain data and those estimated from the surface profile measurements were calculated for every profile measured during every outing. The differences for the restrained slabs are presented in Figure 6.74 for the two-year period following construction based on surface profiles measured in the diagonal direction. The figure shows that the calculated differences are mostly positive indicating that the curvature based on the strain data is, in general, larger than the curvature based on the surface profile measurements. This implies that the surface profile measurements underestimate the slab curvature because they do not take into account the effect of moisture, which contributes to an upward slab curvature (positive). The figure also shows that the difference in curvature is not constant throughout the two-year period, although a distinct trend in variation cannot be detected. This implies that the drying shrinkage at the slab surface is increasing with time due to the decreasing concrete moisture over the two-year period (as previously shown in section 5.2) and that there are seasonal fluctuations as well. Similar trends were observed for the restrained slab curvatures in the longitudinal and transverse directions.

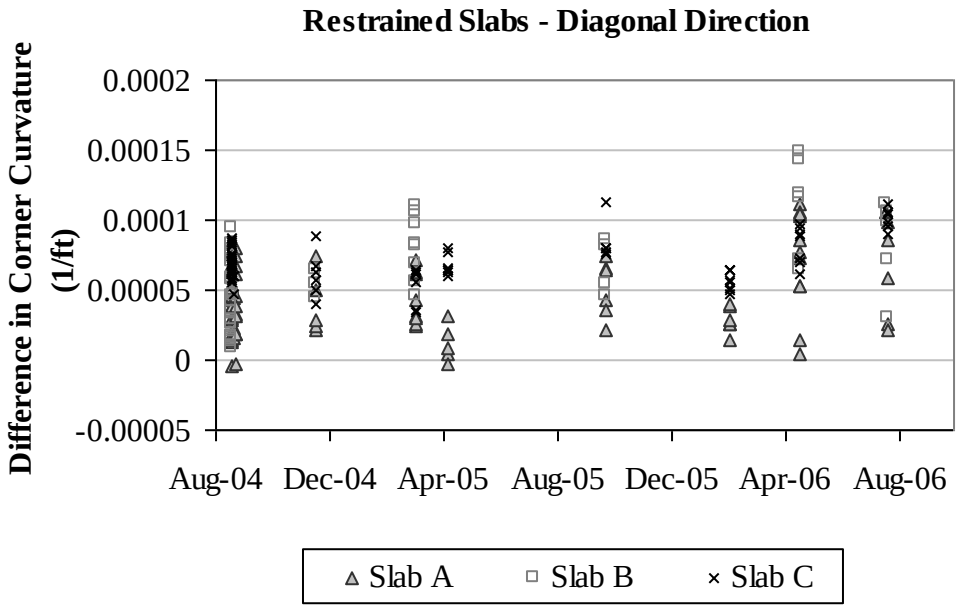

Figure 6.74. Difference in slab curvature for the restrained slabs in the diagonal direction.

Moreover, the differences indicate a scatter in the data for every test day. This is most likely due to difference in the restraining conditions along the slabs. For example, it is highly possible that the dowel bars or tie bars get slightly shifted from their original position during construction, indicating that the same exact restraining conditions are not replicated for the three slabs. Also, the joint cracking pattern will potentially have an effect on the crack widths at the transverse joints. Joints that cracked first were wider than the joints that cracked later.

6.4.2 Unrestrained slabs

Similar to the procedure followed for the restrained slabs, the curvature estimated based on the strain data and the surface profile data for unrestrained Slab A is presented in Figure 6.75 and Figure 6.76. This data is for the summer 2004 and spring 2005 data collection outings. The curvature provided in the figures is estimated based on strain data collected from sensors in the corner of the slab adjacent to the lane/shoulder joint and in the longitudinal, diagonal and transverse directions. The curvature estimated based on the Dipstick^{TM} data is based on the surface profiles measured at the slab corner adjacent to the lane/shoulder joint in the same three directions. The same trends that were observed for the restrained slabs are also observed for the unrestrained slabs. The curvature estimated based on the strain data is greater than that for the surface profiles. As expected, the curvature shows a decrease during the early hours of the day and an increase during the early hours of the night. This is consistent with the peak positive curvature (upward) which occurs in the early morning hours and the peak negative curvature (downward) which occurs in the late afternoon/early evening.

Appendix D also includes a full set of figures comparing curvatures estimated from the surface profiles to those from the strain gages, for unrestrained slabs A, B and C, for the remaining seasonal Dipstick^{TM} outings. The observed trends are similar to those for the restrained slabs. All the figures show that the curvature estimated from the surface profiles is shifted downward compared to the curvature obtained from the strain gages. Based on the discussion presented in section 6.4.1, the difference in slab curvatures as estimated from the two methods can be attributed to the effect of moisture on the drying shrinkage of concrete.

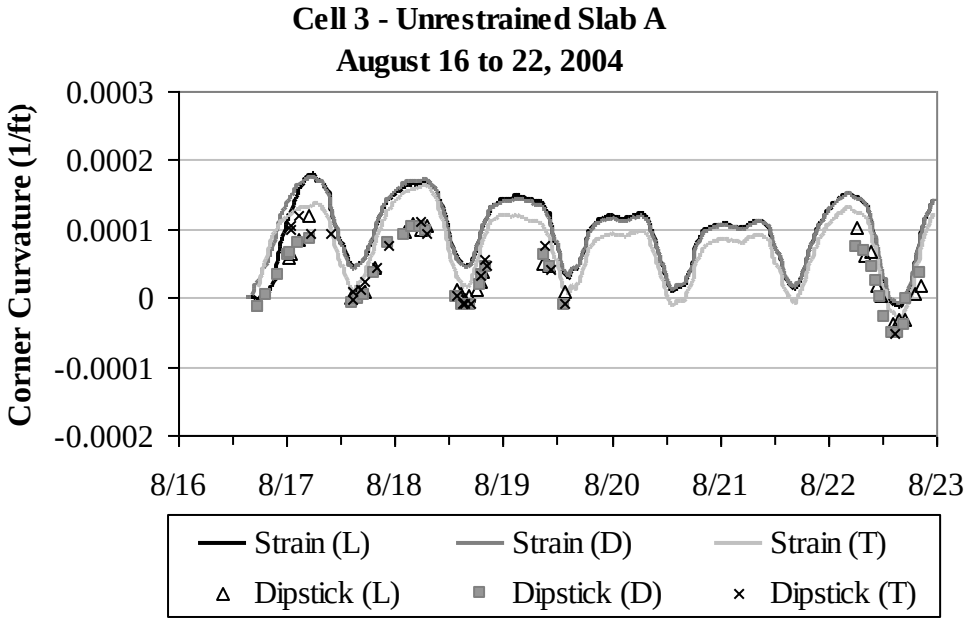

Figure 6.75. Curvature estimated from surface profiles and vibrating wire gages for unrestrained Slab A during the summer of 2004.

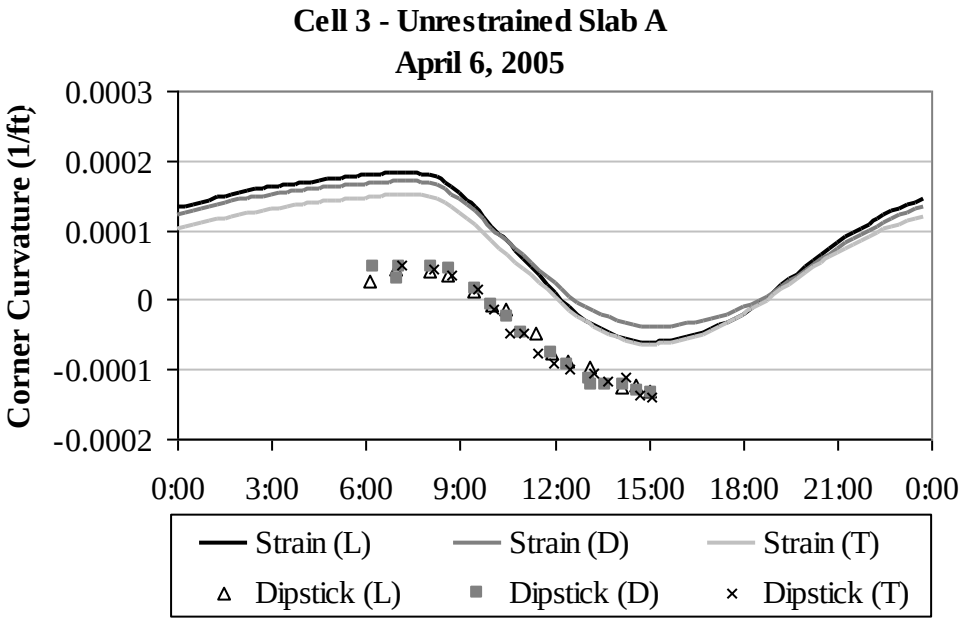

Figure 6.76. Curvature estimated from surface profiles and vibrating wire gages for unrestrained Slab A during the spring of 2005.

Similarly to what was carried out for the restrained slabs, the slab curvature estimated based on the calculated thermal and moisture strain in section 6.1.5 is compared to the curvature estimated based on the strain measurements and the seasonal surface profiles for restrained Slab A, for the Dipstick™ test dates during the winter of 2005, as presented in Figure 6.77. To avoid congestion, the figure only provides the curvature estimated based on strain data and Dipstick™ data in the diagonal direction. Similarly to the restrained slabs, the curvature estimated based on the Dipstick™ data matches up with the curvature due to the thermal strain and the curvature due to the moisture-induced strain is relatively constant throughout the test day. This also confirms the previous statement that the difference between the curvature from the strain data and the curvature from the Dipstick™ data is due to the effect of moisture.

The same pattern was observed when comparing the curvature due to the calculated thermal and moisture-induced strains to the curvature from the strain measurements and the Dipstick™ data for the remaining seasons and slabs. Unfortunately, in some cases, the curvature due to the moisture-induced strain was not available due to the gaps in the collected concrete moisture data. The figures comparing the curvature due to the thermal and moisture-induced strains to the curvatures based on the strain measurements and the Dipstick™ data for the remaining seasons are also included in Appendix D, for unrestrained Slab A.

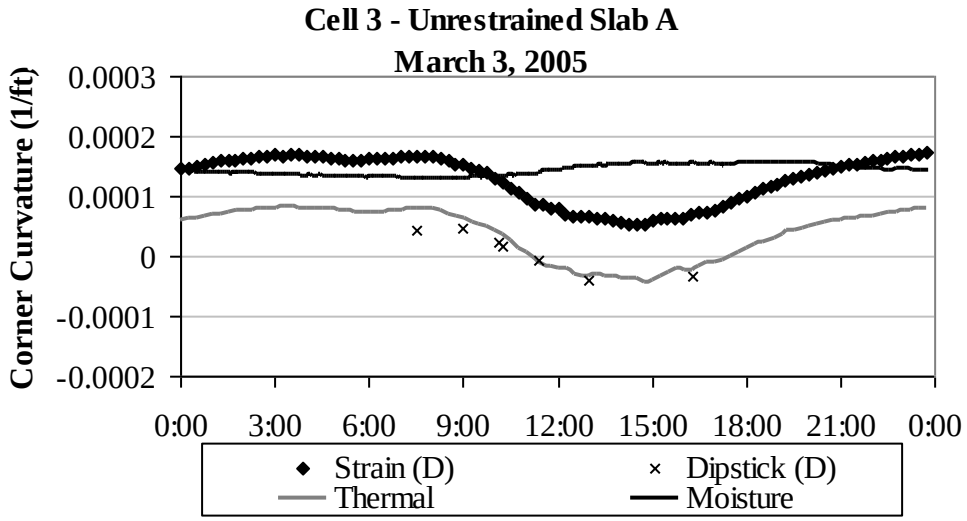

Figure 6.77. Comparison between curvatures estimated from the three types of data for unrestrained Slab A during the winter of 2005.

The difference between the curvature estimated from the strain data and the curvature estimated from the surface profile measurements was calculated for every profile measured during every seasonal outing. The differences for the unrestrained slabs are presented in Figure 6.78 for the two-year period following construction based on the surface profiles measured in the diagonal direction. With the exception of the differences calculated for the summer 2004 season, the figure shows that the calculated differences are positive indicating that the curvature based on the strain data is larger than the curvature based on the surface profile measurements. This implies that the surface profile measurements underestimate the slab curvature because they do not take into account the effect of moisture, which contributes to an upward slab curvature (positive). The figure also shows that the difference in curvature increases throughout the two-year period, implying that the drying shrinkage at the slab surface is increasing with time. Similar trends were observed for the curvatures of the unrestrained slabs in the longitudinal and transverse directions.

In addition, Figure 6.78 does not show a wide range of scatter in the differences calculated for every test day for the unrestrained slabs, when compared to Figure 6.74 showing the same data for the restrained slabs. This indicates that the unrestrained slabs exhibit a more repeatable pattern of behavior. Part of this might be attributed to the fact that the measured curvatures are higher for the unrestrained slab which spreads the data over a wider range, compared to the restrained slabs.

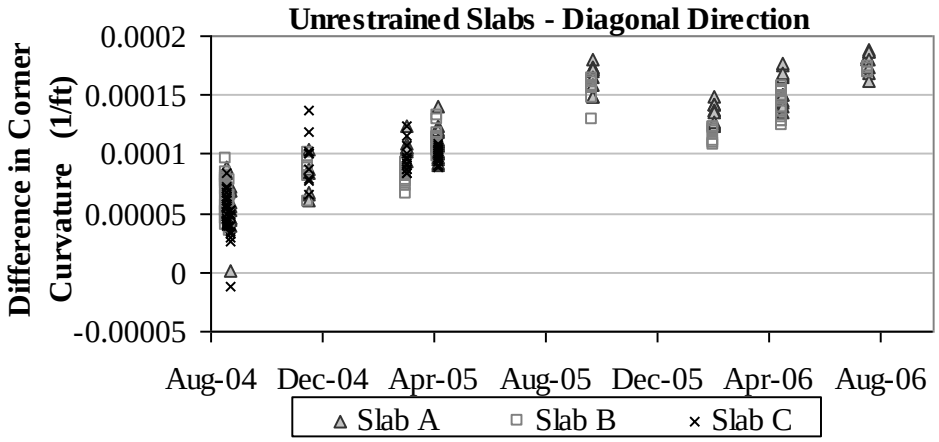

Figure 6.78. Difference in slab curvatures for the unrestrained slabs in the diagonal direction.

6.4.3 Comparison between restrained and unrestrained slabs

The slab curvature calculated based on the temperature and moisture measurements is compared to the curvature estimated based on the strain measurements and the seasonal surface profiles in Figure 6.79 for the restrained and unrestrained slabs during the month of March in 2005. To avoid congestion, the figure only provides the curvature estimated based on strain data and Dipstick™ data in the diagonal direction. According to the figure, the curvature estimated based on the Dipstick™ data matches up with the curvature due to the thermal strain and the curvature due to the moisture-induced strain is relatively constant throughout the test day. This confirms the previous statement that the difference between the curvature from the strain data and the curvature from the Dipstick™ data is due to the effect of moisture and creep.

It can also be concluded from Figure 6.79 that the addition of curvature due to temperature and moisture measurements results in a computed total curvature that is larger than the curvature estimated using strain measurements. This indicates that creep and slab restraint (in both restrained and unrestrained slabs) cause a reduction in slab curvature when compared with the total curvature computed using calculated thermal and moisture gradients. For example, for the test day in March of 2005 that was used in Figure 6.79, unrestrained slab curvatures computed using the VW data are an average of 30 percent lower than curvatures computed using strains estimated from temperature and moisture measurements. This reduction can be attributed to the effects of slab self-weight and creep. For the restrained slabs, the average reduction is 56 percent and can be attributed to the effects of dowel bars, tie bars, slab self-weight and creep.

A comparison of the curvatures of the restrained and unrestrained slabs leads to the conclusion that the presence of dowel and tie bars along the joints reduces the slab curvature by an average of 38 percent on this project. Reduced curvature affects the development of slab stresses: joint restraint increases temperature- and moisture-related stresses (until creep and stress relaxation reduce this effect), but can reduce load-induced stresses by providing more uniform slab support. This reduction in curvature for restrained slabs was observed for all three curvature estimation techniques.

The same pattern was observed when comparing the curvature calculated based on the temperature and moisture measurements available to the curvature from the strain measurements and the Dipstick™ data for the remaining seasons and slabs.

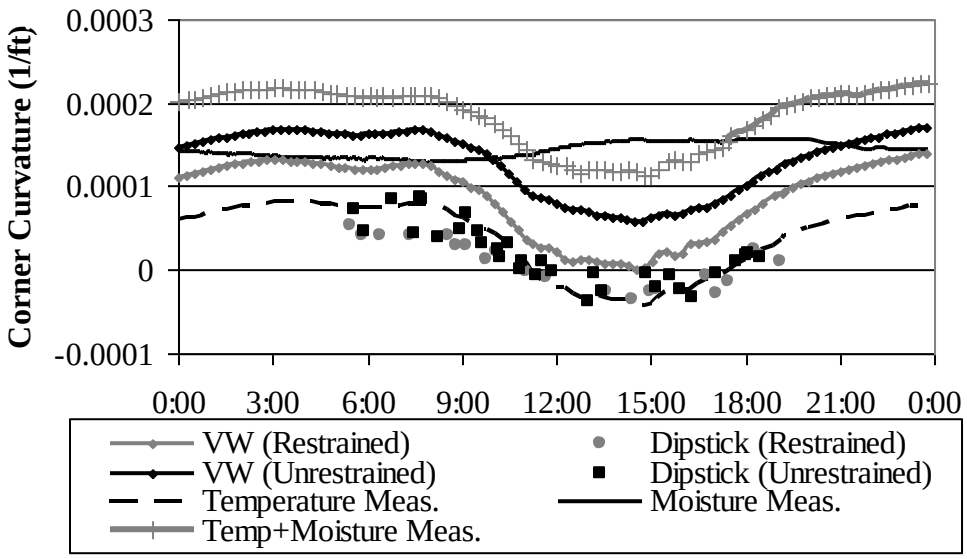

Figure 6.79. Comparison between calculated curvatures based on VW, Dipstick™ and temperature and moisture measurements during the test day of March in 2005 for restrained and unrestrained slabs.

The differences between curvatures estimated using strain data and those estimated using surface profile measurements were calculated for every profile measured during every field data collection outing. Figure 6.80 presents a summary of the differences in curvatures for the restrained and unrestrained slabs for the two-year period following paving (using surface profiles measurements obtained along the slab diagonal). The figure shows that the calculated differences (VW-based curvature minus profile-based curvature) are positive at all times more than a few months after construction. This is consistent with the fact that curvatures based on surface profile measurements in this study represent departures from zero-gradient deformations measured on the day of testing and do not, therefore, take into account the effects of moisture-related deformation, which would otherwise increase upward (positive) slab curvature. Figure 6.80 also shows that the difference in the curvatures varies over the two-year period, suggesting that the drying shrinkage at the slab surface is generally increasing with time as the slabs dry, but that there are seasonal fluctuations as well. Similar trends were observed for the slab curvatures in the longitudinal and transverse directions. Figure 6.80 shows that the curvature differences are smaller for the restrained slabs, confirming the previously stated finding that slab edge restraint reduces the curvature produced by moisture gradients.

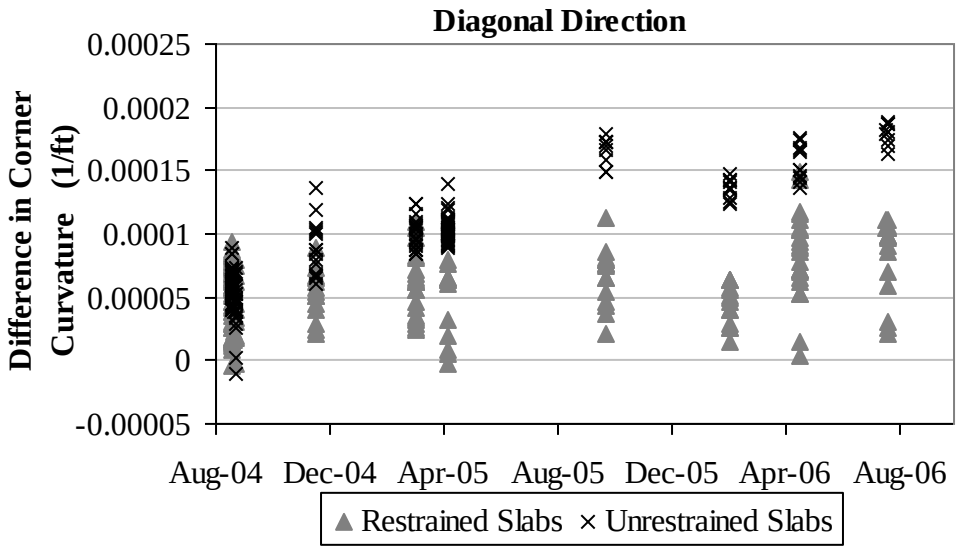

Figure 6.80. Comparison between the difference in corner curvatures for the restrained and unrestrained slabs in the diagonal direction.

Figure 6.80 also shows that the rate of increase in the curvature differences over time is five times larger (on average) for the unrestrained slabs than for the restrained slabs. This further illustrates the effects of slab restraint due to dowel bars on slab curvature due to drying shrinkage and supports the previously stated findings based on Figure 6.39.

There is significant scatter in the restrained slab curvature difference data for every test date. This scatter is most likely due to differences in the restraining conditions along the slabs. For example, it is possible that there is variability in dowel "looseness" (due to construction factors) and other restraining factors between the instrumented slabs. In addition, joint cracking patterns can affect the effective width of transverse joints (e.g., joints that crack sooner after paving are often wider than joints that crack later), which can affect the stiffness of doweled joints (i.e., reduced stiffness at wider doweled joints). This scatter in slab curvature differences was not observed for the unrestrained slabs; the unrestrained slabs exhibited a more repeatable pattern of behavior.

To isolate the effect of moisture, creep and slab restraint on the slabs, the curvature calculated based on the measured temperatures was subtracted from the curvature calculated based on the total strain measurements. The data is presented in Figure 6.81 for both restrained

and unrestrained slabs. Figure 6.81 shows that the curvature influenced by moisture, creep and slab restraint generally increases throughout the two-year period, particularly for the unrestrained slabs. Since the slab restraining conditions do not change for each type of slab, the figure indicates that the moisture causes an increase in the slab curvature which is counteracted by the effect of creep on the slabs. However, the overall combined effect of both factors causes an increase in the slab curvature.

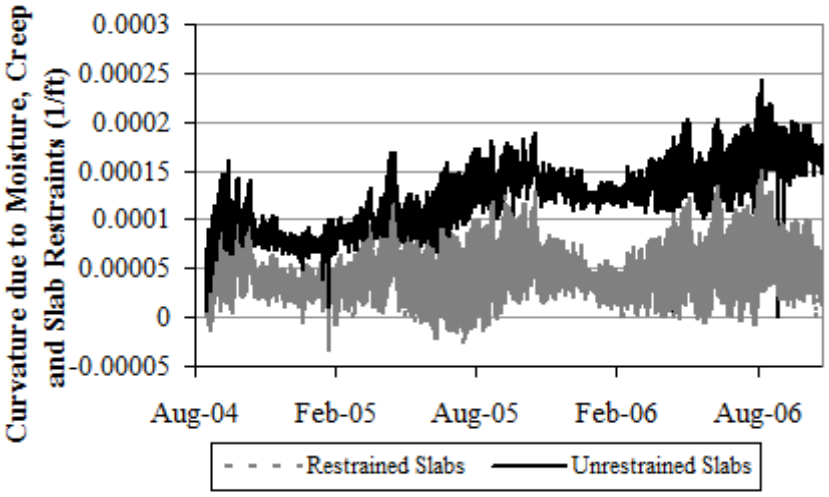

Figure 6.81. Curvature due to moisture, creep and slab restraint, based on VW measurements in the diagonal direction for restrained and unrestrained slabs.

6.4.4 Summary

Based on the slab curvatures calculated, it was found that slabs are predominantly curled upward within a few months after paving and they remain that way, resulting in increased potential for top-down fatigue cracking (rather than the bottom-up fatigue cracking that has traditionally been assumed in concrete pavement design). This finding was confirmed using curvatures computed from slab strain measurements, which showed that the slabs on this project were curled upward about 99 percent of the time.

6.5 SUMMARY AND CONCLUSIONS

In this chapter, the seasonal variation in the deformation of the restrained and unrestrained slabs when subjected to different temperature and moisture conditions were characterized. The slab deformations were quantified in terms of static strains measured inside the slabs combined with surface profile measurements taken using a Dipstick^{TM}. The data was analyzed over a period of two years after construction of the pavement.

The strain is negative throughout the first two years after construction, indicating that the restrained and unrestrained slabs are in a state of contraction. The variation in strains follows seasonal trends. The lowest temperatures observed during the winter season caused the largest contractions of the concrete slabs, and the strain measurements were lowest. While, the largest temperatures observed during the summer caused the least amount of contraction in the slabs and the strain measurements were highest.

Strain data from the restrained and unrestrained slabs was compared to investigate the different restraint conditions. It was found that the bond provided at the slab/base interface reduces the slab surface strain by 12 to 22 percent and the presence of dowel bars reduces the strain by 20 percent. However, it was found that the presence of tie bars does not affect the strain at the slab surface. The dowel and tie bars restrict upward and downward movement at the outer portion of the slab, and cause more curvature to develop in the central portion of the slab. This results in smaller slab curvature for the restrained slab. Surface profile measurements confirmed the findings based on the static strain measurements.

Curvature in the restrained slab was more than 60 percent lower than curvature of the unrestrained slabs. This restraint of temperature- and moisture-related deformation can result in substantially higher levels of environmental slab stress, which decrease over time with creep and stress relaxation and may also be partially offset by reduced load-related stresses (due to more uniform support of restrained slabs).

The difference in the slab curvature estimated using static strain measurements and those estimated using surface profile data can be attributed primarily to the effects of concrete drying shrinkage, which is not considered in the profile-based curvature values developed in this study. Drying shrinkage at the slab surface was observed to increase with time during the two-year period of this study, and the rate of increase in slab curvature due to drying shrinkage is larger

for the unrestrained slabs than for the restrained slabs. Some of this drying shrinkage is reversible, as can be seen by the seasonal fluctuations in slab curvature, with shrinkage and slab curvature decreasing during wet seasons and increasing again during drier seasons.

The additional restraint provided by the dowel and tie bars does not appear to significantly reduce slab curvature resulting from daily temperature fluctuations or from reversible drying shrinkage. It does have a substantial effect on reducing slab curvature due to long-term drying shrinkage.

The effect of moisture and creep on the slabs was isolated. The rate of increase in slab curvature over time is larger for the unrestrained slabs, compared to the restrained slabs, indicating that the effect of creep on the curvature of the unrestrained slabs is more pronounced than on the restrained slabs, as would be expected.

7.0 SLAB STRESS BASED ON FINITE ELEMENT METHODS

As mentioned in Chapter 1, the second objective of this research is to examine the effects of seasonal variations in temperature and moisture throughout the slab depth on stresses in the slab and examine the effects of different slab restraining conditions on the slab deformation and stress. In this chapter, this objective is achieved by modeling the pavement structure using a two-dimensional finite element program to study the effects of the presence of different temperature and moisture gradients on stresses inside the slab. The models are calibrated using strains measured in the field to provide a better understanding of the response of restrained and unrestrained concrete slabs to environmental loads.

The structural performance of the pavement was monitored by carrying out seasonal Falling Weight Deflectometer (FWD) testing. The results from the FWD tests are used to characterize the seasonal support conditions (subgrade k-values), stiffness of the concrete and base layers and the load transfer efficiency across transverse and longitudinal joints. These are needed to adequately model the restrained and unrestrained slabs. The program ISLAB2000 (Khazanovich et al. 2000) is used to model the pavement.

This program contains the following advanced features that distinguish it from other rigid pavement analysis programs that are based on plate theory (ARA 2004):

- a wide selection of subgrade models, including Winkler, elastic solid, Pasternak, Kerr-Vlasov, and Zhemochkin-Sinitsyn-Shtaerman.
- an ability to analyze the effect of the independent actions of two pavement layers.
- an ability to analyze the effect of linear and nonlinear temperature distribution throughout the pavement thickness.
- an ability to analyze partial-depth cracks.

Although other general-purpose finite element packages are more powerful and capable, and can conduct three-dimensional nonlinear dynamic analysis, they usually demand considerable computational resources, as well as time for developing a structural model for each problem. In addition, a study was conducted to compare the results from one of the general-purpose finite element programs (ABAQUS, which is widely used in pavement design research) and ISLAB2000 and an excellent correlation was found between the predicted stresses and deflections from both programs (Hammons 1997). The main advantage of using ISLAB2000 over other general-purpose finite element programs is the computational time required for the program.

The first section of this chapter presents the results of the seasonal FWD tests that will be used to model the pavement structure. The second section describes the inputs used in developing the finite element models for the restrained and unrestrained slabs. The third section discusses the validation of the finite element models and the fourth section presents the stresses generated in the slabs and the effect of various parameters on slab stresses. Finally, the last section summarizes the results and conclusions made regarding the development of stress in the slabs.

7.1 STRUCTURAL PERFORMANCE OF THE PAVEMENT BASED ON FWD TESTING

FWD testing was carried out seasonally to describe the structural performance of the pavement by characterizing the foundation conditions representing the material underneath the concrete slabs, identifying the presence of voids under the slabs and evaluating the efficiency of the transverse joints to transfer loads across adjacent slabs. FWD testing consists of dropping three loads on a plate placed on the surface of the slab and recording the corresponding deflections at various locations along the slab surface. The plate used to load the pavement and the sensors measuring slab deflections are shown in Figure 7.1. FWD testing is performed at midpanels, adjacent to the transverse joints and along the slab corners. The results of the tests carried out at midpanel are used to backcalculate the k-values representing the stiffness of the underlayers. The results of the tests carried out along the transverse joints are used to evaluate the load

transfer efficiency across the joints. The results of the tests carried out at the corner locations are used to identify the presence of voids under the slabs. The results of the FWD testing will be used as inputs in the finite element model to represent the stiffness of the foundation layers, the concrete and base layers, as well as the stiffness of the joints. More details of the FWD testing and test results are included in other publications (Wells et al. 2005; Asbahan et al. 2006; McCracken et al. 2008).

During the two-year period after construction of the pavement, FWD testing was carried out seasonally, four times a year. The dates of the data collection outings representing each season are provided in Table 7.1. Unfortunately, it was not possible to carry out FWD testing during the summer 2004 and fall 2005 seasons. With the exception of the fall 2004 season, the FWD testing and the Dipstick™ testing were carried out within a week from each other. The slab temperature and moisture conditions during the FWD test dates are similar to those during the Dipstick™ test dates, previously presented in Chapter 6. The slab temperature and moisture conditions affect the response of the pavement structure when subjected to FWD loadings. As a result, the stiffness of the foundation, the load transfer efficiency across transverse joints, and the possible presence of voids under the slabs are also affected.

Figure 7.1. Falling weight deflectometer (FWD) load plate and sensor configuration.

Table 7.1. FWD test dates representing each season.

Season	Test Date
Summer 2004	---
Fall 2004	October 11, 2004
Winter 2005	March 10, 2005
Spring 2005	April 1, 2005
Summer 2005	October 6, 2005
Fall 2005	---
Winter 2006	February 2, 2006
Spring 2006	April 19, 2006
Summer 2006	July 19, 2006

In this section, the slab temperature and moisture conditions at the time FWD testing was performed are presented first, followed by a general background describing the procedure that was followed to evaluate the slab structural performance. Then, the seasonal support conditions, the stiffness of the concrete slabs and base layer, and the load transfer efficiency of the transverse joints and longitudinal joints are presented. The final section summarizes the results obtained that will be used in the finite element modeling of the pavement structure.

7.1.1 Temperature and moisture conditions during FWD testing

FWD testing was performed under different temperature and moisture conditions representing the different seasons. Similarly to what was carried out in section 6.3, the concrete temperature conditions are characterized in terms of the weighted average temperature and the equivalent linear temperature gradient, while the concrete moisture conditions are characterized in terms of the relative humidity. The variations in the measured concrete temperatures and relative humidity during the two-year period were presented in Chapter 5; the concrete temperature and moisture conditions during the FWD test dates are presented in this section.

The concrete temperature conditions present on the FWD test dates are summarized in Table 7.2. Since each test date represents a season, the table lists the weighted average temperatures and the equivalent linear gradients by seasons. The measured temperatures were lowest during the winter seasons, followed by the fall, then the spring and the highest

temperatures were measured during the summer seasons. The average slab temperatures ranged between 34˚F (winter 2005) and 90˚F (summer 2006). The daily variations of the concrete weighted average temperatures during the FWD test dates are presented in Figure 7.2 and Figure 7.3. The temperatures show a decrease during the early morning hours and an increase during the afternoon hours.

Table 7.2. Seasonal slab temperatures and equivalent linear gradients during FWD testing.

	Weighted Average Slab Temperature (˚F)			Equivalent Linear Temperature Gradient (˚F/in)		
Season	**Maximum**	**Minimum**	**Average**	**Maximum**	**Minimum**	**Average**
Summer 04	--	--	--	--	--	--
Fall 04	63	53	58	1.03	-0.97	-0.23
Winter 05	39	29	34	1.03	-0.77	-0.09
Spring 05	61	52	57	1.19	-0.69	0.15
Summer 05	80	68	74	1.59	-0.66	0.20
Fall 05	--	--	--	--	--	--
Winter 06	45	38	42	0.77	-0.45	0.11
Spring 06	76	59	67	2.11	-0.85	0.36
Summer 06	97	83	90	2.07	-0.73	0.35

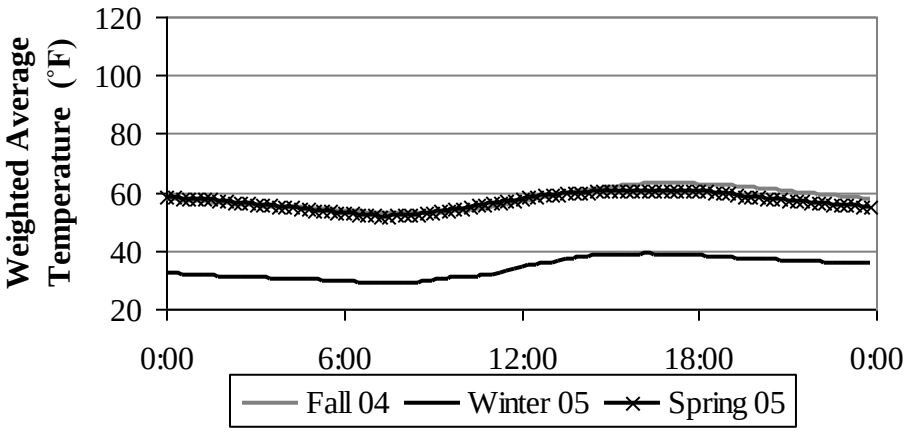

Figure 7.2. Midpanel weighted average concrete temperatures during FWD testing for the first year after paving.

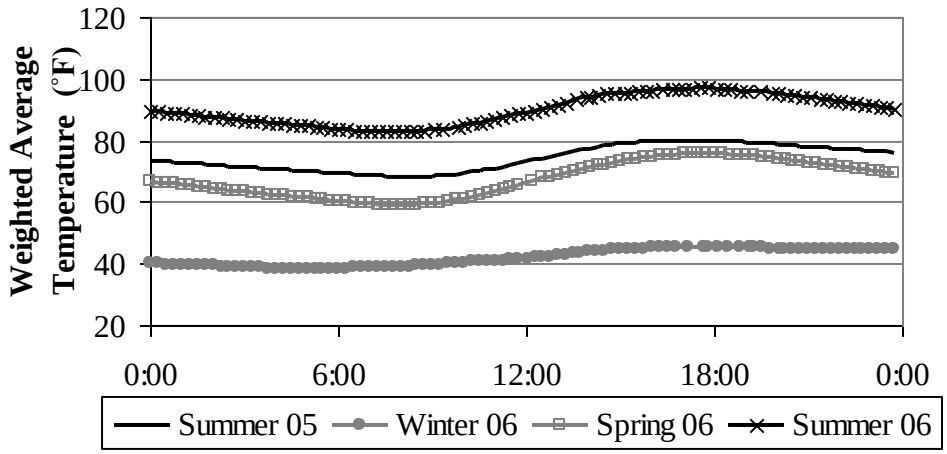

Figure 7.3. Midpanel weighted average concrete temperatures during FWD testing for the second year after paving.

During the FWD test dates, the equivalent linear temperature gradients covered positive and negative values. The widest range of values was recorded during the spring and summer seasons. The narrowest range of values was recorded during the winter 2006 season. The largest positive gradient was 2.11˚F/in and was recorded during the spring 2006 test date and the largest negative gradient was -0.97˚F/in and was recorded during the fall 2004 test date. The daily variations of the concrete equivalent linear temperature gradients during the FWD test dates are presented in Figure 7.4 and Figure 7.5. The peak positive gradients are recorded during the afternoon hours and the peak negative gradients are recorded during the early morning hours.

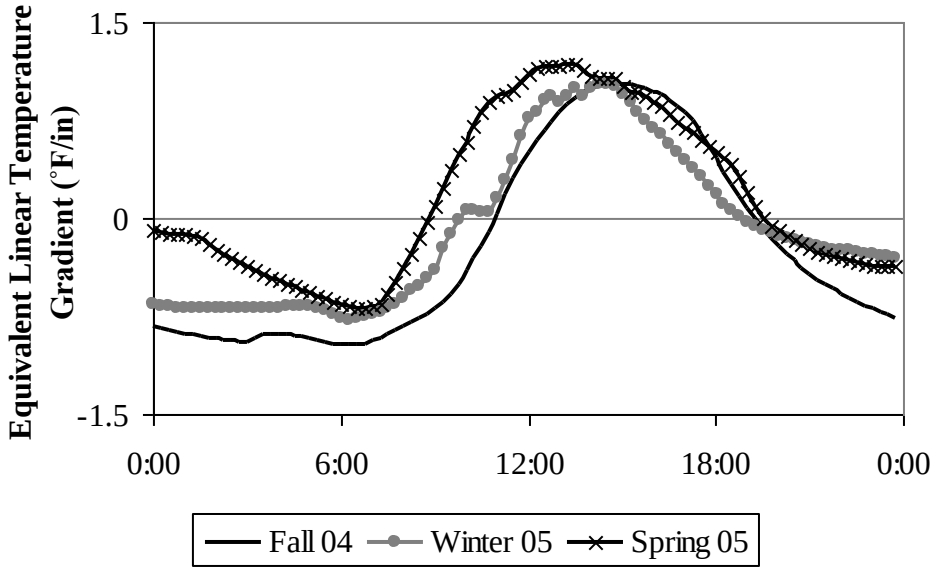

Figure 7.4. Midpanel equivalent linear temperature gradients during FWD testing for the first year after paving.

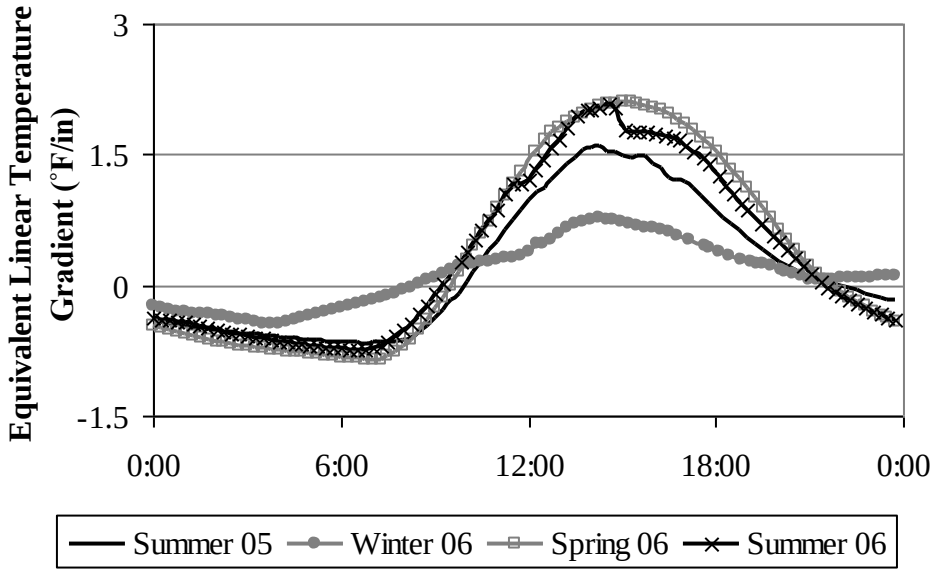

Figure 7.5. Midpanel equivalent linear temperature gradients during FWD testing for the second year after paving.

The concrete moisture conditions during the FWD test dates are presented in Figure 7.6 and Figure 7.7 based on the moisture sensors at midpanel and at the slab edge. The figures show the average concrete relative humidity for the FWD test date representing each season. As previously stated in Chapter 5, the concrete relative humidity levels are lower during the second year after paving compared to the first year after paving. The concrete moisture levels were highest during the spring 2005 and lowest during the winter 2006 season.

Based on the concrete moisture measurements at the time of testing, the corresponding equivalent temperature difference and equivalent temperature gradient across the slab are determined by following the procedure described in section 6.1.4. The variation of the equivalent temperature difference during each test date is calculated based on the moisture measurements at the slab edge and are presented in Figure 7.8 and Figure 7.9 for the first two years after construction. The equivalent temperature difference for the moisture gradients does not vary significantly during the test dates. The equivalent temperature difference varies between -46˚F and -4˚F throughout the two-year period. This range is similar to the range of equivalent temperatures for the moisture gradients measured during the Dipstick™ test dates (-50˚F to -4˚F based on section 6.3.1, excluding the first few days after construction).

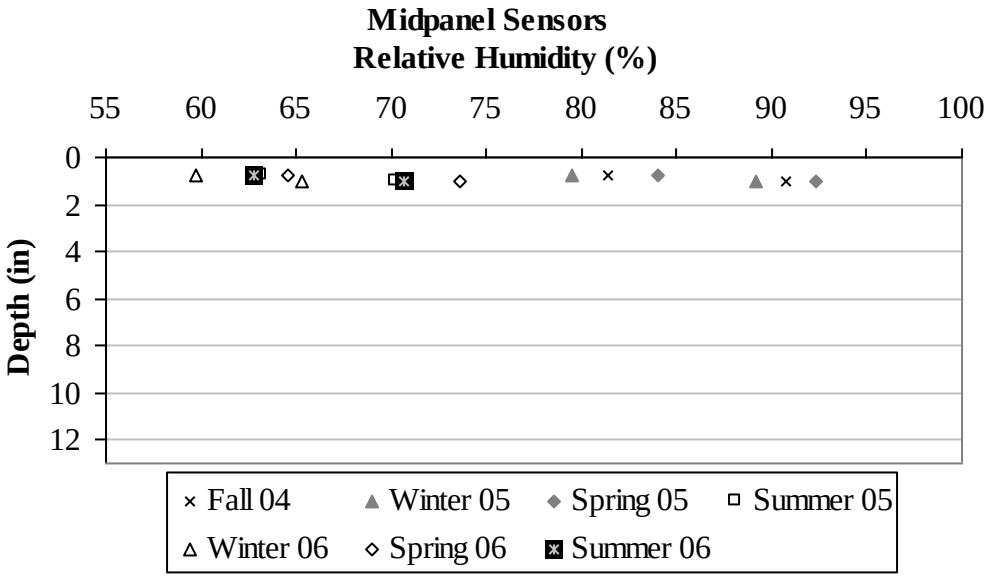

Figure 7.6. Moisture content of the concrete at midpanel during FWD testing.

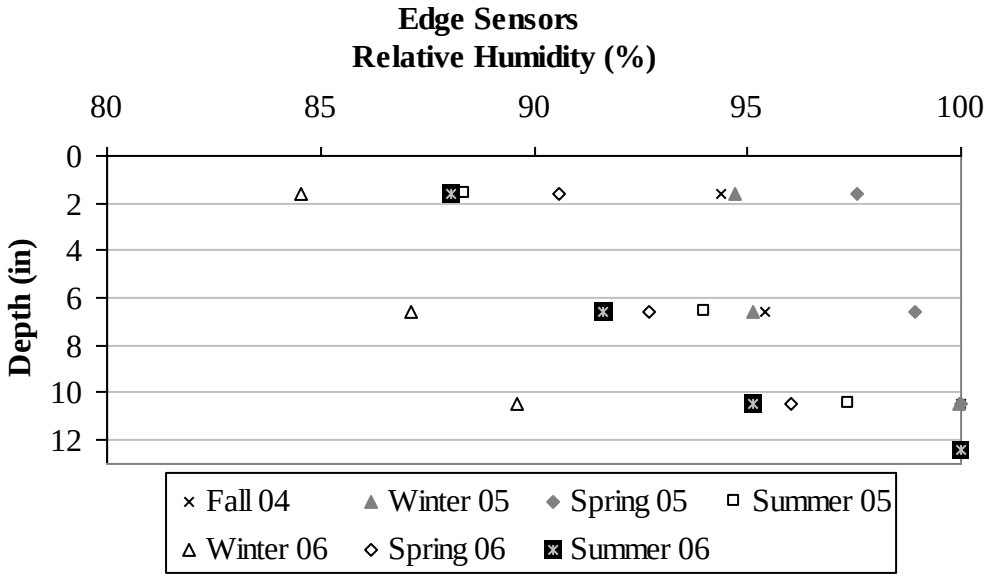

Figure 7.7. Moisture content of the concrete at the edge of the slab during FWD testing.

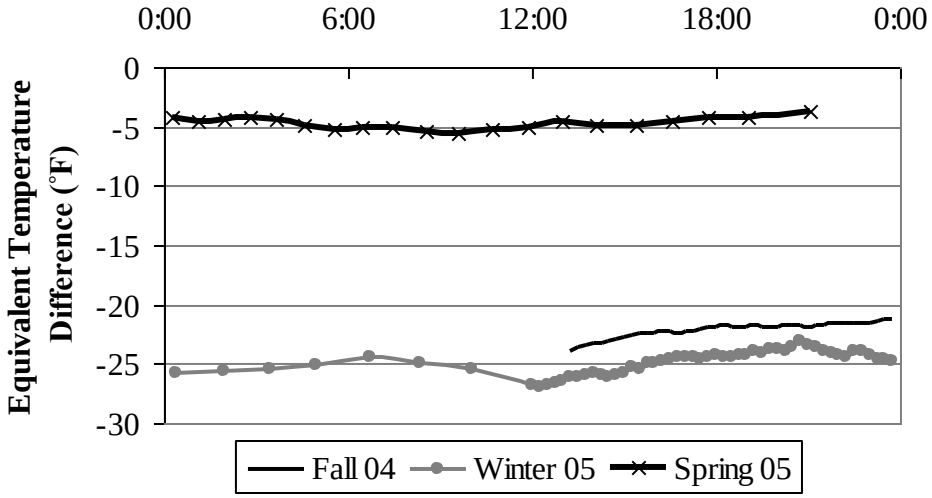

Figure 7.8. Equivalent temperature difference due to moisture during FWD testing for the first year after construction.

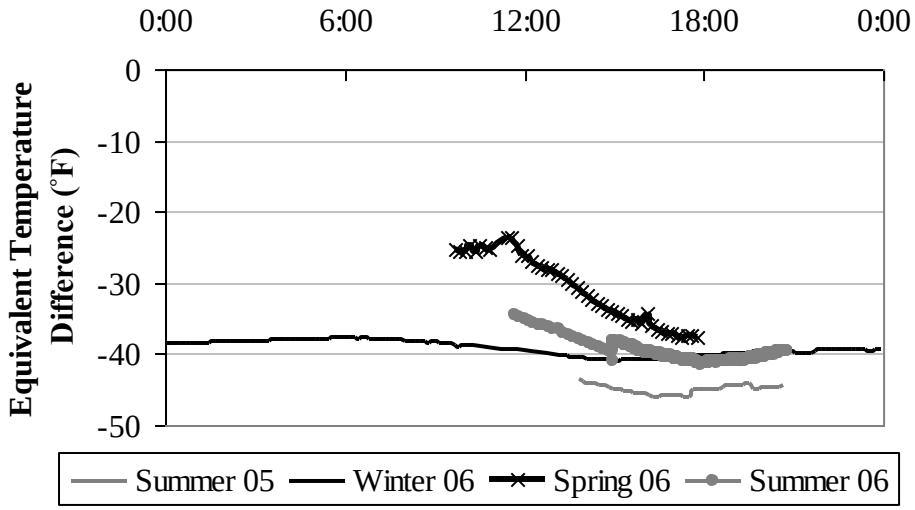

Figure 7.9. Equivalent temperature difference due to moisture during FWD testing for the second year after construction.

The equivalent temperature gradients across the slab corresponding to the equivalent temperature differences for the moisture gradients are presented in Figure 7.10 and Figure 7.11 for the FWD test dates during the first two years after construction. The equivalent gradient varies between -3.6˚F/in and -0.3˚F/in throughout the two-year period, which is also similar to the equivalent gradient measured for the Dipstick™ test dates (-4˚F/in to -0.3˚F/in based on section 6.3.1, excluding the first few days after construction).

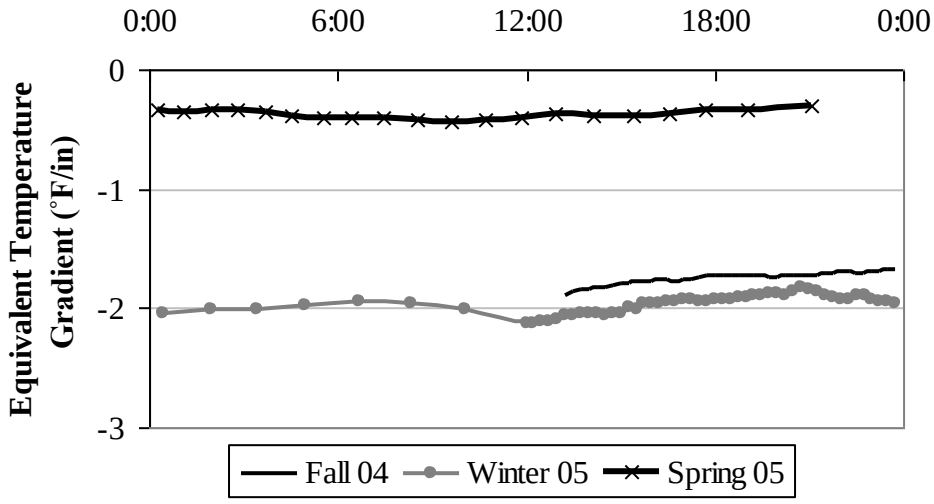

Figure 7.10. Equivalent temperature gradient due to moisture during FWD testing for the first year after construction.

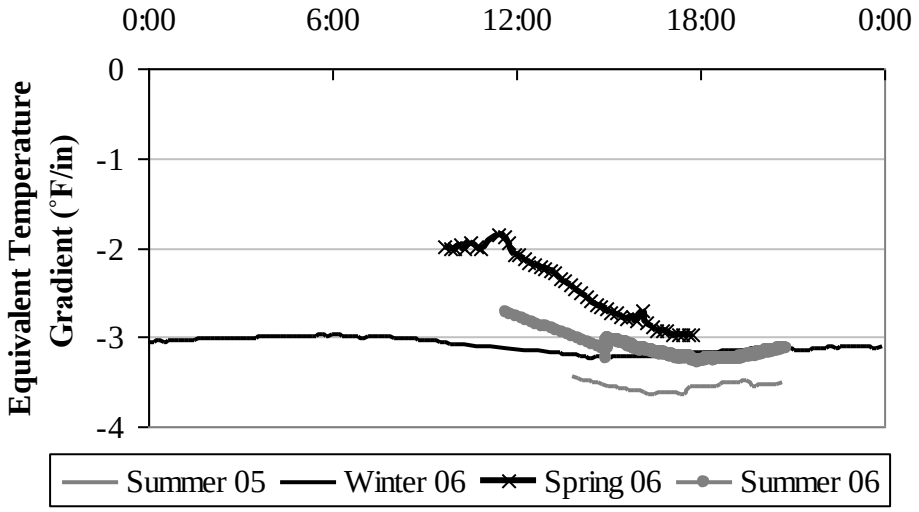

Figure 7.11. Equivalent temperature gradient due to moisture during FWD testing for the second year after construction.

Based on the previous figures, average equivalent temperature conditions due to moisture were selected to represent each FWD test day and are summarized in Table 7.3 for the two-year period. The average equivalent temperature and corresponding temperature gradient are similar to those for the Dipstick™ test dates, which were presented in Table 6.6.

Table 7.3. Equivalent temperature difference and gradient due to moisture during profile test dates.

Season	Test Date	Equivalent Temperature Difference (˚F)	Equivalent Temperature Gradient (˚F/in)
Summer 04	---	---	---
Fall 04	11-Oct-04	-22.1	-1.75
Winter 05	10-Mar-05	-24.9	-1.97
Spring 05	1-Apr-05	-4.7	-0.37
Summer 05	6-Oct-05	-45.0	-3.55
Fall 05	---	--	--
Winter 06	2-Feb-06	-39.1	-3.09
Spring 06	19-Apr-06	-31.0	-2.45
Summer 06	19-Jul-06	-40.1	-3.17

7.1.2 Background

The deflection data collected during FWD testing at midpanels can be used to backcalculate the material response parameters for each layer in a rigid pavement structure. Back calculation is based on plate theory, whereby all measured deflections are attributed to compression of the subgrade and bending of the plates and the main assumption being that compression does not take place in the upper layers (Khazanovich et al. 2001; Hall et al. 1997). The seasonal k-values representing the composite stiffness of all layers beneath the slab are backcalculated by using the AREA method (Hall et. al 1997). The backcalculation procedure is briefly presented in this section.

The seasonal FWD testing was carried out using a 7-sensor configuration, as shown in Figure 7.12. The first step involves calculating the AREA parameter based on the deflection basin measured for approximately a 9-kip load, by using Equation 7-1.

$$AREA_{60} = 4 + 6\frac{d_8}{d_0} + 5\frac{d_{12}}{d_0} + 6\frac{d_{18}}{d_0} + 9\frac{d_{24}}{d_0} + 18\frac{d_{48}}{d_0} + 12\frac{d_{60}}{d_0} \qquad \text{(Equation 7-1)}$$

Where: $AREA_{60}$ = AREA parameter, and

d_r = Deflection measured by the sensor located at a distance r from the load plate

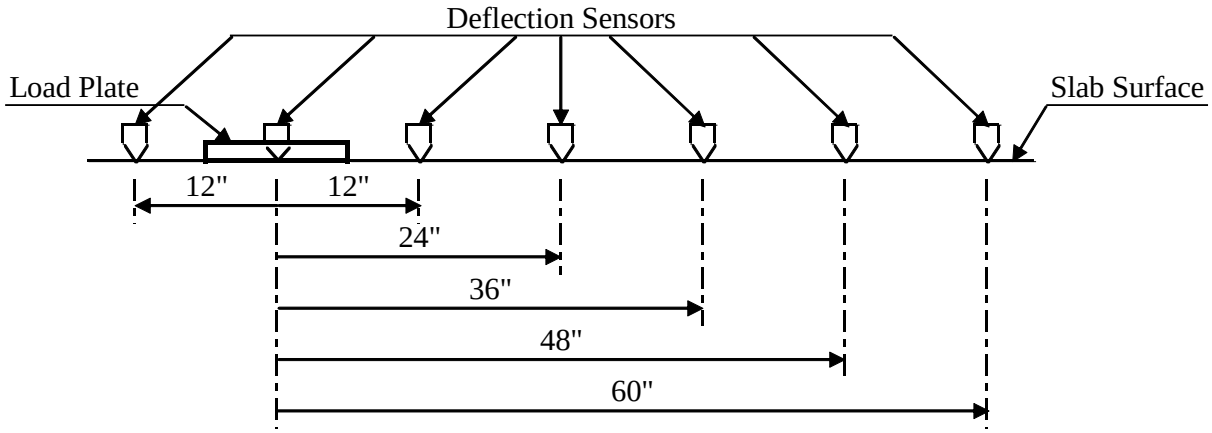

Figure 7.12. Sensor configuration used in the FWD tests.

The AREA parameter is then used to estimate the radius of relative stiffness, based on Equation 7-2. The radius of relative stiffness represents the stiffness of the slab with respect to the stiffness of the underlying layers.

$$l = \left(\frac{\ln\left(\frac{k_1 - AREA_{60}}{k_2} \right)}{-k3} \right)^{\frac{1}{k_4}} \qquad \text{(Equation 7-2)}$$

where: l = radius of relative stiffness, inches

k_1, k_2, k_3 and k_4 are regression coefficients. For the sensor configuration shown in Figure 7.12, the coefficients are as follows: $k_1 = 60$, $k_2 = 289.708$, $k_3 = 0.698$ and $1/k_4 = 2.566$.

The radius of relative stiffness is then used to calculate the modulus of subgrade reaction, based on Equation 7-3. According to the available literature, the k-value established using a static load is 1 to 3 times lower than the k-value for the same structure established using a dynamic load (AASHTO 1993). The static k-value will be used in the finite element modeling and will be obtained by multiplying the backcalculated dynamic k-value by a factor of 0.5, as recommended by the current pavement design guide (AASHTO 1993).

$$k = \frac{Pd_r^*}{d_r l^2} \qquad \text{(Equation 7-3)}$$

Where: P = applied load, lbs,

d_r = measured load at a distance r from the applied load, inches,

d_r^* = nondimensional deflection coefficient corresponding to the sensor located at a distance r from the applied load, calculated based on Equation 7-4.

$$d_r^* = ae^{-be^{-cl}} \qquad \text{(Equation 7-4)}$$

Where: r represents the distance between the sensor and the applied load,

a, b and c are regression coefficients depending on the sensor location

The modulus of elasticity of the concrete slab is calculated for each k-value based on Equation 7-5.

$$E = \frac{12\, l^4 k(1-\mu^2)}{h_{PCC}^3} \qquad \text{(Equation 7-5)}$$

where: E = elastic modulus of the slab

μ = Poisson's ratio of the concrete

l = radius of relative stiffness

k = modulus of subgrade reaction of the underlying layers

h_{PCC} = slab thickness

Concrete pavements are generally analyzed as slab-on-grade structures with no structural contributions attributed to the underlying base or subbase layers. However, the underlying layers can affect the structural performance of the pavement, particularly if bonding between the slab and base occurs. In the case of slabs bonded to the underlying base layer, the effective pavement

structure becomes larger and the behavior of the overall pavement changes (Khazanovich et al. 2001). As previously mentioned in Chapter 3, the push-off test and cores taken from the concrete on the field have shown that the jointed plain concrete slabs are bonded to the underlying asphalt-treated base layer. As such, the effect of the bond between the two layers needs to be taken into account when backcalculating the stiffness of the layers. For the case of a slab bonded to the underlying layer, the flexural stiffness of the fictitious homogeneous plate may be derived using Equations 7-6 and 7-7 (Khazanovich et al. 2001).

$$x = \frac{\frac{h_1^2}{2} + \beta h_2\left(h_1 + \frac{h_2}{2}\right)}{h_1 + \beta h_2} \qquad \text{(Equation 7-6)}$$

$$E_1 = \frac{h_1^3}{h_1^3 + \beta h_2^3 + 12h_1\left(x - \frac{h_1}{2}\right)^2 + 12\beta h_2\left(h_1 - x + \frac{h_2}{2}\right)^2} E_e \qquad \text{(Equation 7-7)}$$

where: h_1 = thickness of upper plate (concrete)

h_2 = thickness of lower plate (base)

E_1 = modulus of upper plate (concrete)

E_2 = modulus of lower plate (base)

E_e = modulus of fictitious effective composite homogeneous plate which is equivalent to the actual two-plate system

β = ratio of the modulus of the lower plate to the modulus of the upper plate = E_2/E_1 = E_{base} / E_{PCC} = 1/15, for an open graded hot-mixed, hot-laid asphalt concrete base layer (Khazanovich et al. 2001).

For each season, and at each midpanel test location, the modulus of subgrade reaction, the modulus of elasticity of the concrete slab and the modulus of elasticity of the base layer were determined by adopting the previously-mentioned procedure. The results will be presented in sections 7.1.3 and 7.1.4.

In addition, deflection data collected during FWD testing along both sides of the transverse joints, in the wheelpath, can be used to estimate the load transfer efficiency (LTE) of the joints. When one side of the joint is loaded, a portion of the applied load is transferred across to the adjacent slab, causing both sides of the joint to deflect. A comparison between the

deflections measured across both sides of the joint gives an indication of the efficiency of the aggregate interlock and/or dowel bars to transfer the load across the joint. LTE is dependent on many factors including temperature, base/subgrade support, and the aggregate interlock (Khazanovich 2003). LTE is evaluated using the ratio of the maximum deflection of the loaded slab to the deflection of the unloaded slab, as presented in Equation 7-8. The results of the evaluation of the LTE across transverse joints will be summarized in section 7.1.5.

$$LTE = \frac{\delta_{ul}}{\delta_l} \times 100\% \qquad \text{(Equation 7-8)}$$

where: LTE = Load transfer efficiency, percent

δ_{ul} = Deflection measured on the unloaded side of the joint

δ_l = Deflection measured on the loaded side of the joint

7.1.3 Seasonal support conditions

The seasonal average values of the dynamic modulus of subgrade reaction are presented in Figure 7.13 and Figure 7.14 for the restrained and unrestrained slabs. These averages will be used to represent the stiffness of the underlayers in the finite element modeling of the pavement structure.

During the winter season, the base and underlayers are subjected to low temperatures, which cause the layers to freeze. This induces an increase in the stiffness of the underlayers and would indicate a high k-value. Therefore, it is expected that the FWD testing carried out during the winter would indicate the highest k-values. However, based on the figures, this is not the case. During both tests carried out in the winter, the backcalculated k-values were amongst the lowest compared to the remaining seasons. When examining the temperature and moisture conditions during the winter FWD test dates, the winter 2005 and fall 2004 tests were carried out under similar moisture and temperature gradient conditions, however, the temperatures during the winter 2005 test date were much lower than those during the fall 2004 test date. When examining the temperatures of the underlayers during the winter 2005 testing, previously presented in section 5.1, the temperatures were starting to increase and the underlayers can be considered to be in a thawing condition. This explains the low k-values that are similar to those

of the fall 2004 testing. Moreover, when examining the temperature and moisture conditions during the winter 2006 testing, the temperatures were higher than those recorded during the previous winter, and they were higher than the freezing temperature. This indicates that the underlayers were not frozen and therefore, there is no reason to expect their stiffness to be high (Asbahan et al. 2006).

Moreover, FWD testing during the summer is expected to represent the normal pavement conditions, and FWD testing during the fall and spring seasons is expected to be lower due to the increased moisture conditions in the slabs. Based on Figure 7.13 and Figure 7.14, the spring k-values are consistent with the expectations for the unrestrained slabs, but are not consistent for the restrained slabs. When examining the temperature and moisture conditions during the spring 2006 season the temperature conditions are similar to those of the summer, however, the moisture in the concrete slabs is higher than that during the summer. The lower concrete moisture during the summer causes the presence of a higher negative moisture gradient in the slabs, which in turn causes an increase in the upward curvature of the slabs. The slab curvature affects the results of the backcalculation and an increased downward curvature could be construed as causing a void under the midpanel location, which would result in a lower stiffness of the underlayers (Asbahan et al. 2006).

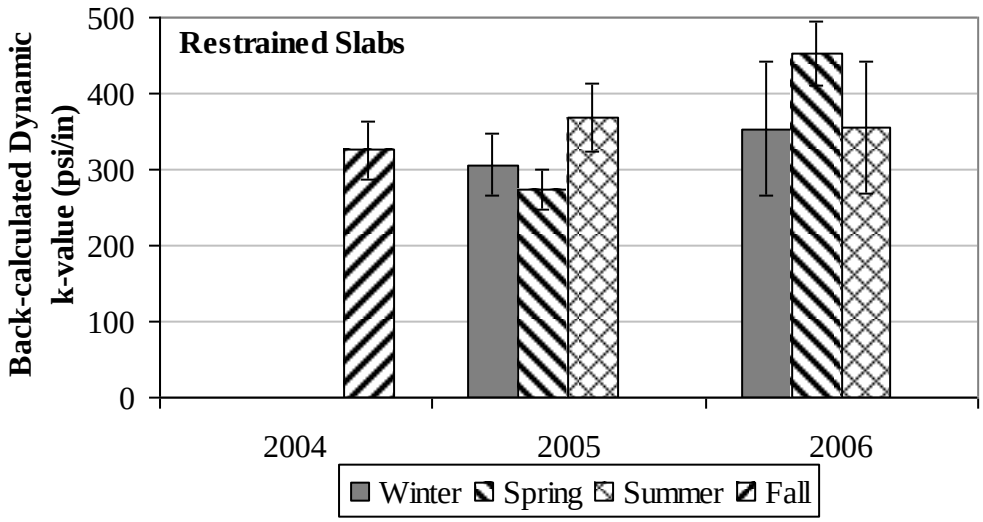

Figure 7.13. Backcalculated seasonal modulus of subgrade reaction for restrained slabs.

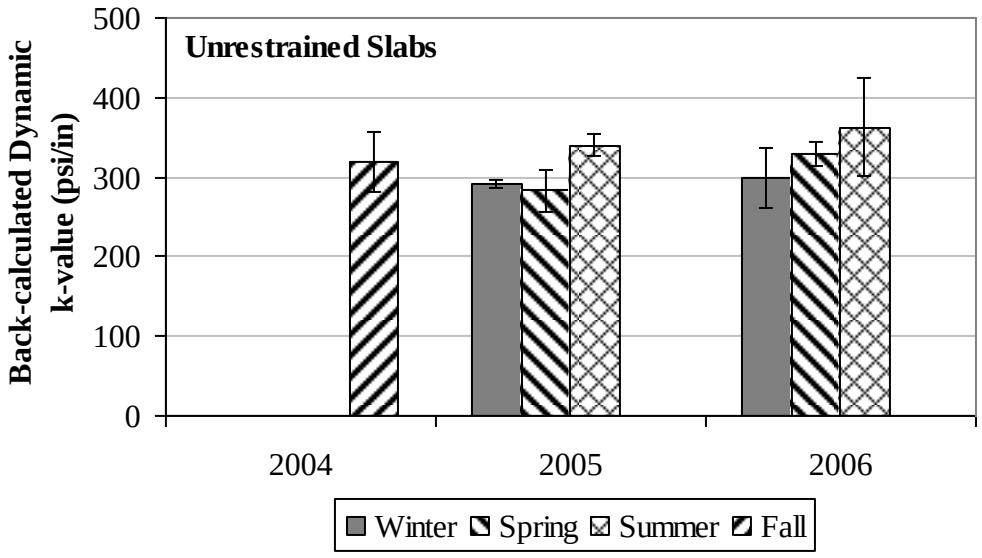

Figure 7.14. Backcalculated seasonal modulus of subgrade reaction for unrestrained slabs.

A more thorough interpretation of the causes of the unexpected backcalculation results does not constitute a part of the scope of this study. A more detailed analysis was undertaken and the findings were documented in McCracken et al. (2008) and McCracken (2008).

Moreover, the backcalculation results indicate that the k-values of the restrained slabs are slightly higher than those of the unrestrained slabs, as shown in Figure 7.15. On average, the k-values are higher by 12 percent for the winter season, 19 percent for the spring, 3 percent for the summer and 2 percent for the fall. The differences between the k-values for the restrained and unrestrained slabs are not significant and may be attributed to variability in the support conditions under the slab. As a result, an average of the k-values for the restrained and unrestrained slabs will be used when modeling the support conditions under the slab. These will be presented at the end of this section.

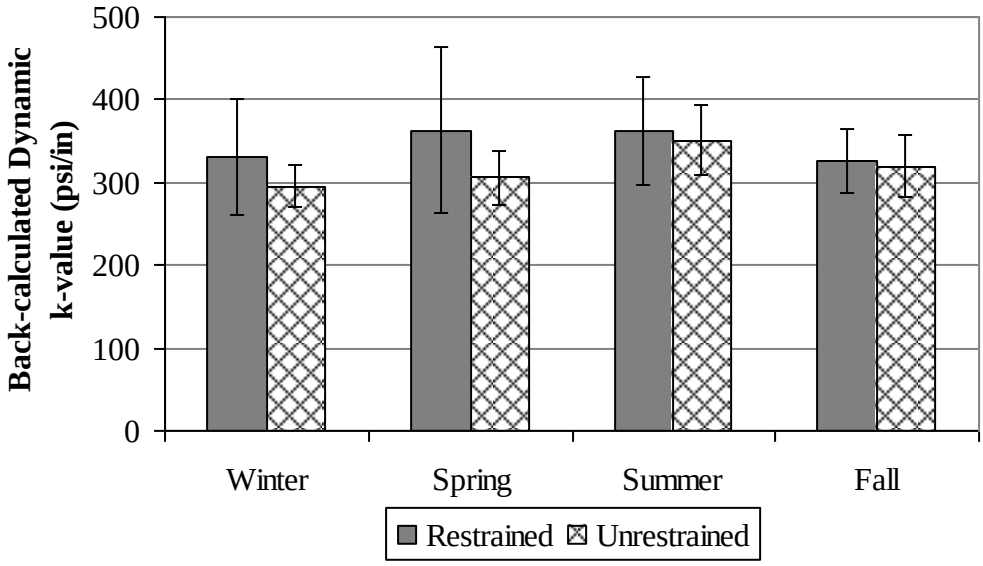

Figure 7.15. Comparison between seasonal average backcalculated k-values for restrained and unrestrained slabs.

FWD testing was conducted at the slab corners to evaluate the presence of voids under the slabs. The detailed results are presented in other references and therefore will not be repeated here (Asbahan et al. 2006; McCracken et al. 2008). In summary, it was found that no voids were present under the corners of the restrained or unrestrained slabs, indicating that the slabs are in full contact with the base layer during the first two years after paving.

7.1.4 Stiffness of the concrete slabs and base layer

The modulus of elasticity of the concrete and the modulus of elasticity of the ATPB were calculated using Equations 7-5 and 7-7, previously presented in section 7.1.2 and the results are presented in this section. The moduli of elasticity will be used to represent the stiffness of the slab and base layer in the finite element model of the pavement structure.

The modulus of elasticity of the concrete was calculated for FWD load drops corresponding to 9,000 kips at midpanel, and the values were averaged to obtain one modulus value representative of all the slabs. The seasonal average values of the modulus of elasticity of the concrete slabs are presented in Figure 7.16. Since the FWD load is a dynamic load, the

modulus of elasticity estimated based on the backcalculated k-values is considered a dynamic modulus. According to the available literature, the static concrete modulus is approximately 80 percent of the dynamic concrete modulus (AASHTO 1993). As previously mentioned in Chapter 3, concrete cylinders were cast from the mix at the time of paving and were subjected to static elastic modulus testing in the lab. The results from this testing are shown in Figure 7.16. According to the figure, the dynamic modulus of elasticity is 20 to 30 percent larger than the static modulus, which is consistent with the available literature (AASHTO 1993). The static concrete modulus values will be used to model the pavement structure and are presented at the end of this section.

The modulus of elasticity of the ATPB layer was calculated by multiplying the dynamic concrete modulus by the β factor, as previously presented in section 7.1.2. The seasonal average values of the ATPB modulus of elasticity are presented in Figure 7.17. The modulus of elasticity of the ATPB layer varies between 320,000 and 535,000 psi, with an average of 393,000 psi over the two-year period. Since the ATPB modulus is calculated based on the dynamic concrete modulus and since the dynamic modulus is 20 to 30 percent larger than the static modulus, the ATPB modulus can be reduced by an average of 25 percent to obtain the ATPB modulus for design purposes.

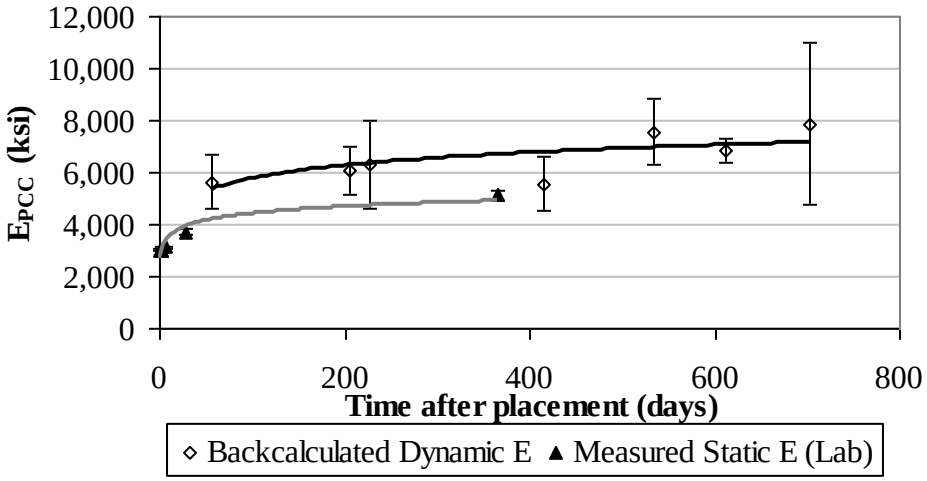

Figure 7.16. Concrete modulus of elasticity based on FWD test results and measurements made in the lab in accordance with ASTM C469.

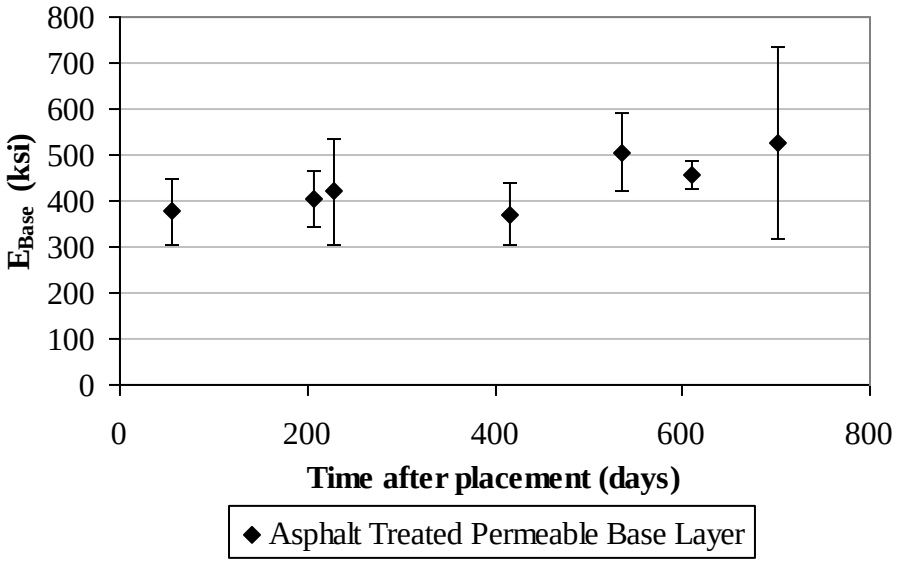

Figure 7.17. Modulus of elasticity of ATPB layer based on FWD test results.

The stiffness of the base layer varies depending on its temperature, as shown in Figure 7.18 (Asbahan et al. 2006; McCracken et al. 2008). Therefore, the stiffness corresponding to the average ATPB temperature during the Dipstick™ test days will be reduced by 25 percent and used to model the pavement structure. The ATPB temperature at the time the Dipstick™ measurements were made are presented in Figure 7.19 and Figure 7.20 with the average temperatures and corresponding moduli of elasticity are summarized in Table 7.4.

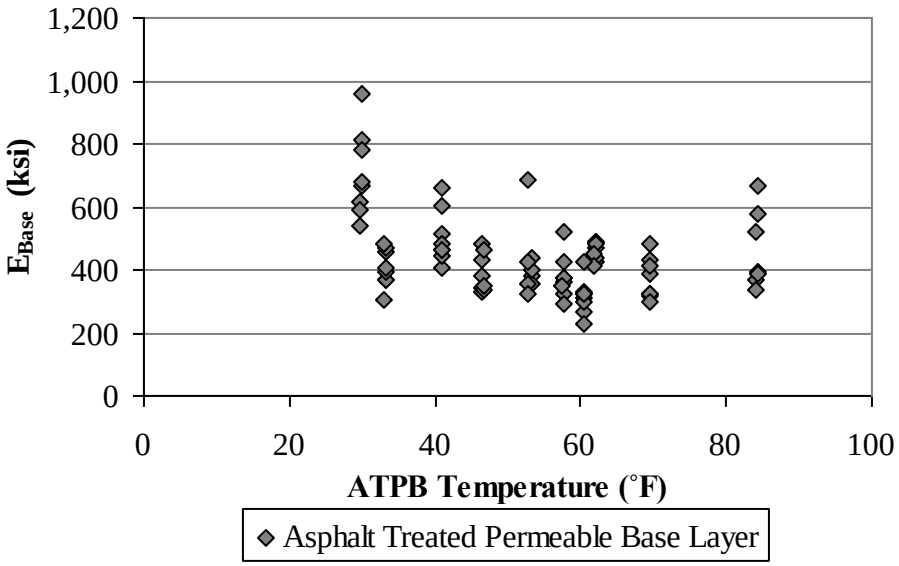

Figure 7.18. Variation of backcalculated ATPB modulus of elasticity with temperature.

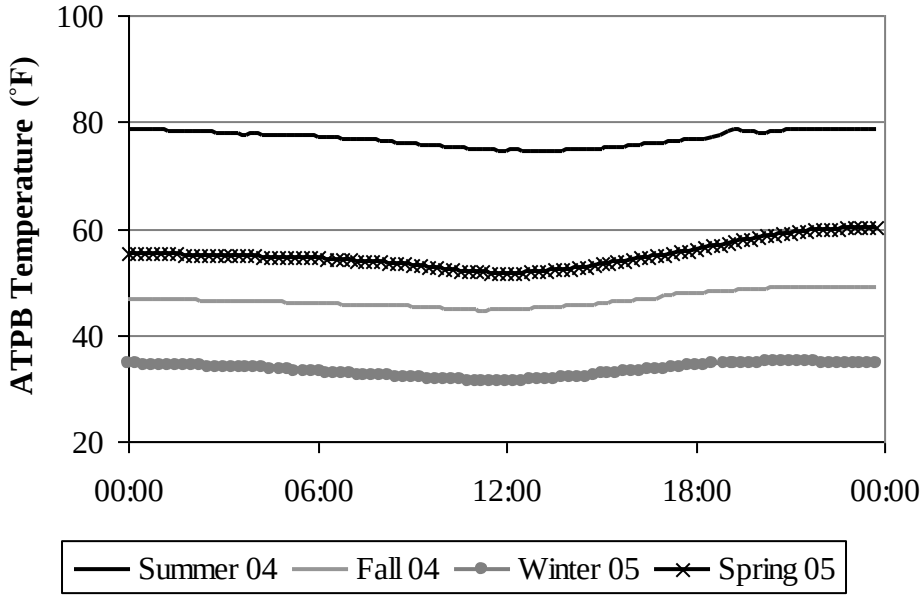

Figure 7.19. ATPB temperature during Dipstick™ test dates for the first year after construction.

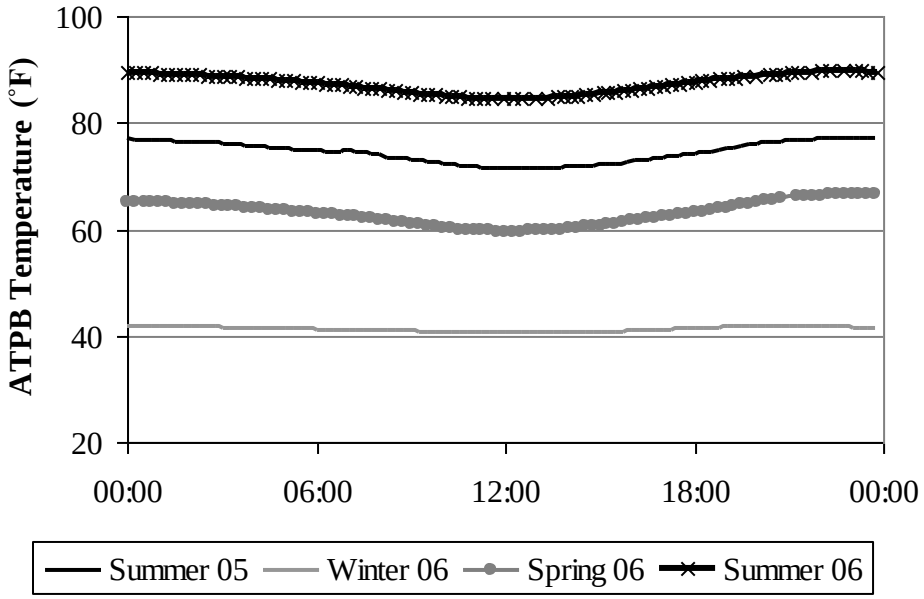

Figure 7.20. ATPB temperature during Dipstick™ test dates for the second year after construction.

Table 7.4. ATPB temperature and corresponding elasticity modulus for use in the finite element model.

Season	T_{ATPB} (˚F)	E_{Base} (psi)	
		Backcalculated	Reduced
Summer 2004	86	525,000	420,000
Fall 2004	47	390,000	312,000
Winter 2005	33	405,000	325,000
Spring 2005	55	400,000	320,000
Summer 2005	74	450,000	360,000
Fall 2005	--	--	--
Winter 2006	41	505,000	404,000
Spring 2006	63	465,000	372,000
Summer 2006	87	525,000	420,000

7.1.5 Load transfer efficiency across transverse joints

The measured load transfer efficiency will be used to model the stiffness of the transverse joint. A thorough analysis of the variations in the LTE over the two-year period was undertaken in the one-year and three-year reports (Asbahan et al. 2006; McCracken et al. 2008). The relevant results are summarized in this section.

During the first two years after construction of the pavement, the LTE varied between 41 and 94 percent for the restrained slabs and 31 and 88 percent for the unrestrained slabs. The average seasonal LTEs are presented in Figure 7.21 and Figure 7.22 for both the restrained and unrestrained slabs. As expected, the LTE of the restrained slabs are on average 40 percent higher than those of the unrestrained slabs. Moreover, the LTE of the restrained slabs does not vary significantly throughout the two-year period, compared to the LTE of the unrestrained slabs.

During the winter, the LTE for the undoweled joints is expected to be lowest due to the extremely low temperatures that cause the slabs to contract and the joints to open wider, thus decreasing the load transfer efficiency of the joints. This behavior was not observed during the first year after paving, but was present in the second and third year. The discrepancy in the behavior of the LTEs during the first year after paving was attributed to the fact that the slabs had not yet "broken apart" due to repeated loading during that first year (Asbahan et al. 2006). A more thorough analysis of the behavior of the joints does not constitute a part of this research study and is discussed in detail in other publications (McCracken et al. 2008; McCracken 2008).

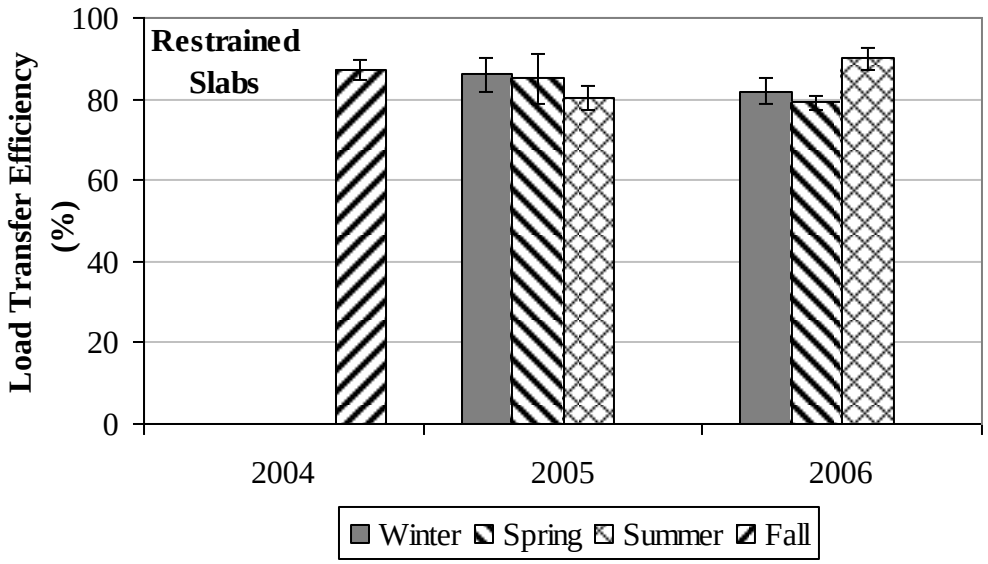

Figure 7.21. Seasonal variation of LTE across transverse joints for restrained slabs.

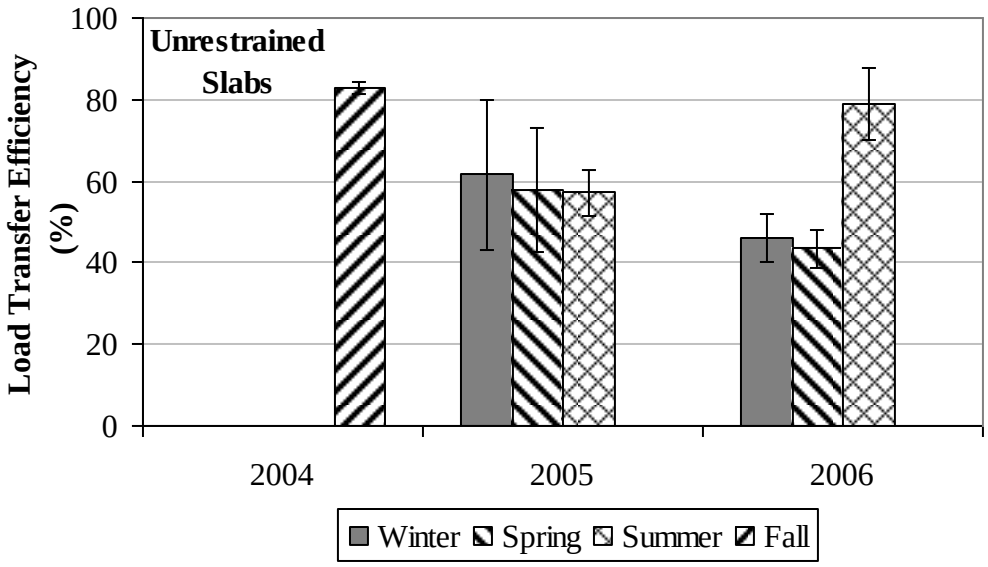

Figure 7.22. Seasonal variation of LTE across transverse joints for unrestrained slabs.

7.1.6 Load transfer efficiency across longitudinal joints

The longitudinal LTE along the centerline joint was estimated based on the slab shape factor. This method was used by other researchers and found to give reasonable results (McCracken et al. 2008). The slabs are 15-foot long by 12-feet wide and the longitudinal LTE is estimated by multiplying the transverse LTE by a factor of 15 over 12 or 1.25. The transverse LTE was determined for each of the joints during each season and the results were presented in section 7.1.5. Table 7.5 provides the longitudinal LTE for the restrained and unrestrained slabs incorporated into the finite element models.

Table 7.5. Load transfer efficiency across longitudinal joints.

Season	Longitudinal Load Transfer Efficiency (%)	
	Restrained Slabs	Restrained Slabs
Summer 2004	--	--
Fall 2004	100	100
Winter 2005	100	77
Spring 2005	100	72
Summer 2005	100	71
Fall 2005	--	--
Winter 2006	100	57
Spring 2006	100	53
Summer 2006	100	98

7.1.7 Summary

In summary, the structural performance of the pavement structure was evaluated based on the results of FWD testing carried out seasonally on site. The seasonal support conditions were evaluated by estimating the stiffness or k-value of the underlayers, the stiffness or modulus of elasticity of the concrete slabs and the ATPB layer, as summarized in Table 7.6. The seasonal static k-values were estimated by multiplying the backcalculated dynamic values by a factor of

0.50, the modulus of elasticity of the concrete is based on the results of the lab measurements (static values) and the modulus of elasticity of the ATPB is determined based on the ATPB temperature at the time the Dipstick™ testing was performed. The concrete modulus of elasticity during the second year after construction is assumed to be equal to that measured at a concrete age of one year. In addition, the interface between adjacent slabs will be modeled based on the average LTEs determined for both restrained and unrestrained slabs, which are summarized in Table 7.5 (longitudinal joints) and Table 7.6 (transverse joints). Due to the absence of FWD test data representing the summer of 2004, it is assumed that the seasonal support conditions representing the summer of 2004 are similar to those representing the fall of 2004 (as shown in Table 7.6).

Table 7.6. Summary of seasonal support conditions based on FWD testing.

Season	k-value (psi/in)	E_{PCC} (psi)	E_{Base} (psi)	Transverse Load Transfer Efficiency (%)	
				Restrained Slabs	Unrestrained Slabs
Summer 2004	--	3,100,000	420,000	--	--
Fall 2004	162	4,200,000	311,200	87	83
Winter 2005	150	4,700,000	324,000	86	62
Spring 2005	139	4,750,000	320,000	85	58
Summer 2005	179	5,000,000	358,400	80	57
Fall 2005	--	--	--	--	--
Winter 2006	167	5,000,000	404,000	82	46
Spring 2006	203	5,000,000	372,000	79	43
Summer 2006	179	5,000,000	420,000	90	79

The analysis also indicated that voids were not present under the slab corners at the time the FWD tests were being carried out. This indicates that the slabs are in full contact with the base layer during the first two years after paving and that there is no need to model voids under the slabs.

7.2 DEVELOPMENT OF THE FINITE ELEMENT MODELS

As previously mentioned, the pavement structure is modeled using the two-dimensional finite element program ISLAB2000 to study the effects of the presence of different temperature and moisture gradients on stresses inside the slab. The slab is modeled as a medium-thick plate and the pavement structure is modeled as an equivalent two-layer system. The model will be calibrated using strains measured in the field to provide a better understanding of the response of restrained and unrestrained slabs to environmental loads. In this section, the details of the development of the finite element models are presented. This includes: mesh, geometry and slab thickness, concrete and base material properties, subgrade stiffness, joint parameters, and environmental loads.

7.2.1 Mesh and geometry

The pavement was modeled as a six-slab system with three slabs in the longitudinal direction and two in the transverse direction. For comparison purposes, a free slab was also modeled. The slabs are 15 feet long and 12 feet wide. A uniform mesh with a 6-inch spacing was used, which resulted in 30 elements in the longitudinal direction and 24 elements in the transverse direction, of each slab.

The model consists of a plate (representing the concrete and base layers) resting on a Winkler (dense liquid) foundation, as shown in Figure 7.23. The stiffness of the concrete and base are represented by the modulus of elasticity, detailed in section 7.2.3. The stiffness of the foundation is represented with the static k-values determined in section 7.1.

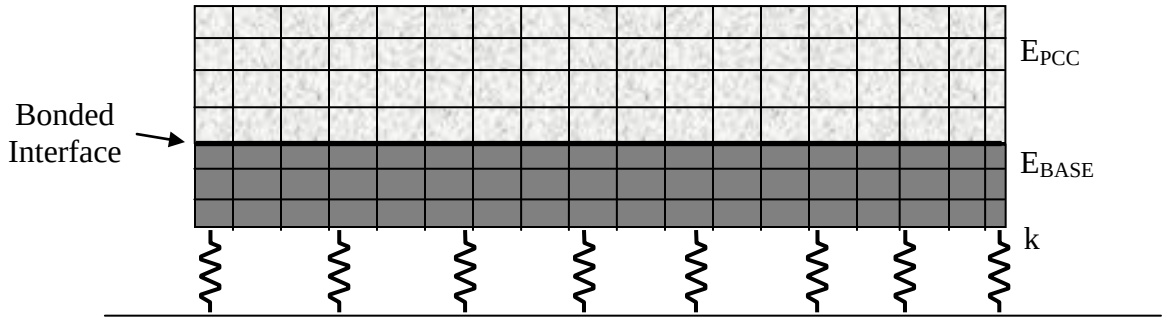

Figure 7.23. Plate resting on a Winkler foundation.

7.2.2 Slab thickness

At the construction stage, the field survey showed that there was some variability in the slab thicknesses. The thickness of the slab is slightly larger along the lane/shoulder joint when compared to the centerline joint, as shown in Figure 7.24. The unrestrained slab thickness varies between 12.8 and 14.0 inches along the lane/shoulder joint, and between 12.4 and 12.7 inches along the centerline joint. The restrained slab thickness varies between 12.2 and 14.0 inches along the lane/shoulder joint, and between 12.0 and 12.8 inches along the centerline joint (Wells et al. 2005). The average slab thickness along the diagonal direction is calculated to estimate the average slab thickness for the finite element modeling and presented in Table 7.7. The unrestrained slabs will be modeled using a thickness of 13.0 inches and the restrained slabs will be modeled using a thickness of 12.5 inches.

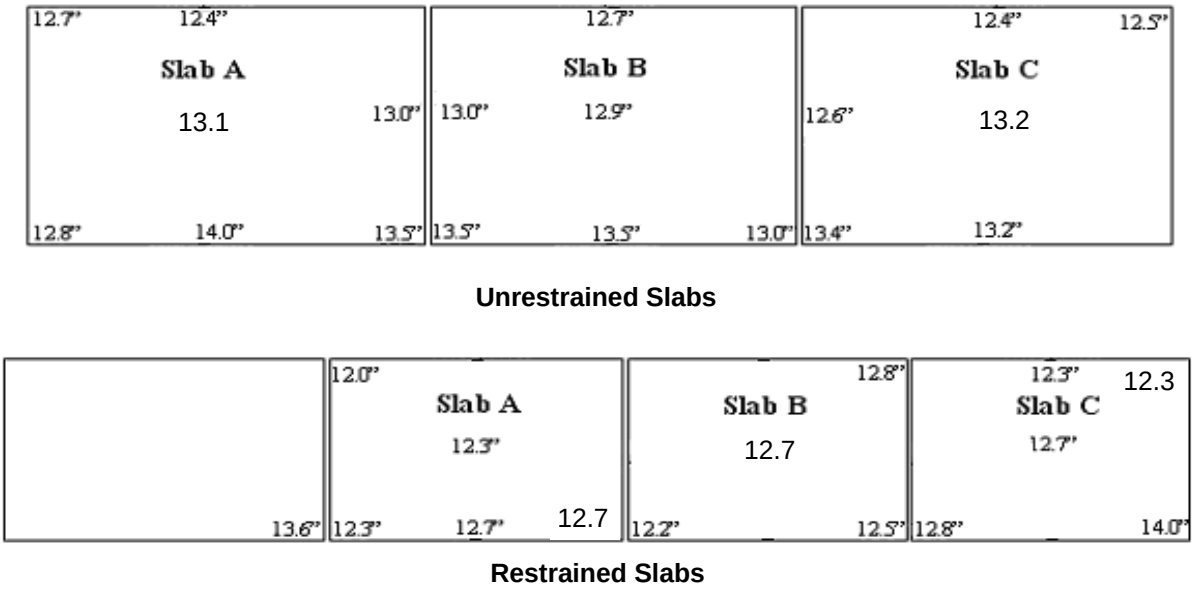

Figure 7.24. Surveyed thicknesses for restrained and unrestrained slabs (Wells et al. 2005).

Table 7.7. Average restrained and unrestrained slab thicknesses.

		Surveyed Slab Thickness (in)			
Type of Slab	**Slab**	**Corner Lane/Shoulder Joint**	**Midpanel**	**Corner Centerline Joint**	**Average**
Unrestrained	A	13.5	13.1	12.7	13.1
	B	13.5	12.9	N/A	13.2
	C	13.4	13.2	12.5	13.0
Restrained	A	12.7	12.3	12.0	12.3
	B	12.2	12.7	12.8	12.6
	C	12.8	12.7	12.3	12.6

7.2.3 Base, subbase and subgrade

The finite element model consists of a concrete pavement over an asphalt treated base resting on a dense liquid foundation. The seasonal support conditions were defined based on the results of FWD testing by estimating the stiffness or k-value of the underlayers and the moduli of elasticity of the concrete slab and the ATPB layer, as discussed in section 7.1 and summarized in Table 7.6. The bond characteristics between the slab and the base were defined as fully bonded based on the results of the push-off test (Wells et al. 2005). Other layer properties are summarized in Table 7.8.

Table 7.8. PCC and ATPB property inputs based on measured values.

	PCC	**ATPB**
Thickness (in.)		
Unrestrained Slabs	13.0	4.0
Restrained Slabs	12.5	
Elastic Modulus	Varies - See Table 7.6	
Poisson's Ratio	0.17	0.35
Coefficient of Thermal Expansion (/°F)	5.70×10^{-6}	1.10×10^{-6}
Unit Weight (lbs/ft^3)	145	148
Interface With PCC Layer	---	Bonded

7.2.4 Joints

ISLAB2000 allows the user to estimate joint parameters by assigning the load transfer efficiency at the joints or by specifying the joint parameters (such as dowel bar properties and/or aggregate interlock properties).

The longitudinal joints for both restrained and unrestrained slabs were modeled by specifying the average joint LTEs that were previously summarized in Table 7.5. The transverse joints for the unrestrained slabs were also modeled by specifying the average joint LTEs that

were previously summarized in Table 7.6. However, for the restrained slabs, the transverse joints were modeled by specifying the dowel and aggregate parameters. The ISLAB model includes 1.5-inch diameter dowel bars placed every 12 inches, with the properties described in Table 7.9.

Table 7.9. Dowel properties used for modeling the transverse joints of the restrained slabs.

Item	Value
Outside diameter (in.)	1.5
Inside diameter (in.)	0.0
Joint width (in.)	0.1
Elastic Modulus (psi)	29,000,000
Poisson's ratio	0.20
Dowel Support Modulus	1,500,000
Length (in.)	12.0
Spacing (in.)	12.0

Aggregate interlock across the transverse joints of the restrained slabs can be described by a spring stiffness referred to as the AGG factor and defined by Equation 7-9.

$$AGG = \left(\frac{\frac{1}{LTE_{joint}} - 0.01}{0.012} \right)^{-\frac{1}{0.849}} \times k \times \ell \qquad \text{(Equation 7-9)}$$

Where: AGG = AGG factor

LTE_{joint} = Total joint LTE, percent

ℓ = Radius of relative stiffness, inches calculated using a permutation of Equation 7-2, shown by Equation 7-10

k = modulus of subgrade reaction, presented in section 7.1.7.

$$\ell = \sqrt[4]{\frac{E_{PCC} h_{PCC}^3}{12\, k(1-\mu^2)}} \qquad \text{(Equation 7-10)}$$

The AGG factors were calculated for the different seasons and are presented in Table 7.10.

Table 7.10. AGG factors used for modeling the transverse joints of the restrained slabs.

Season	AGG Factor
Summer 2004	--
Fall 2004	158,300
Winter 2005	137,100
Spring 2005	116,100
Summer 2005	94,300
Fall 2005	--
Winter 2006	112,900
Spring 2006	105,300
Summer 2006	256,700

7.2.5 Environmental loads

The environmental loads on the pavement are modeled based on the measured temperature and moisture conditions during the Dipstick™ test dates. Peak negative and positive temperature gradients measured during each of the Dipstick™ test dates are selected for the finite element modeling. These conditions are selected for calibration because they represent the times when the slab curvatures are at their peak maximum and minimum values. The curvatures corresponding to these temperature conditions are predicted by ISLAB2000 and compared to the curvatures based on the measured strain data, to validate the finite element models.

The concrete temperature and moisture conditions during the days when Dipstick™ testing was carried out were previously presented and summarized in section 6.3.1. The peak positive and negative temperature gradients for each Dipstick™ test date were determined from the data collected by the thermocouples and are presented in Figure 7.25 and Table 7.11.

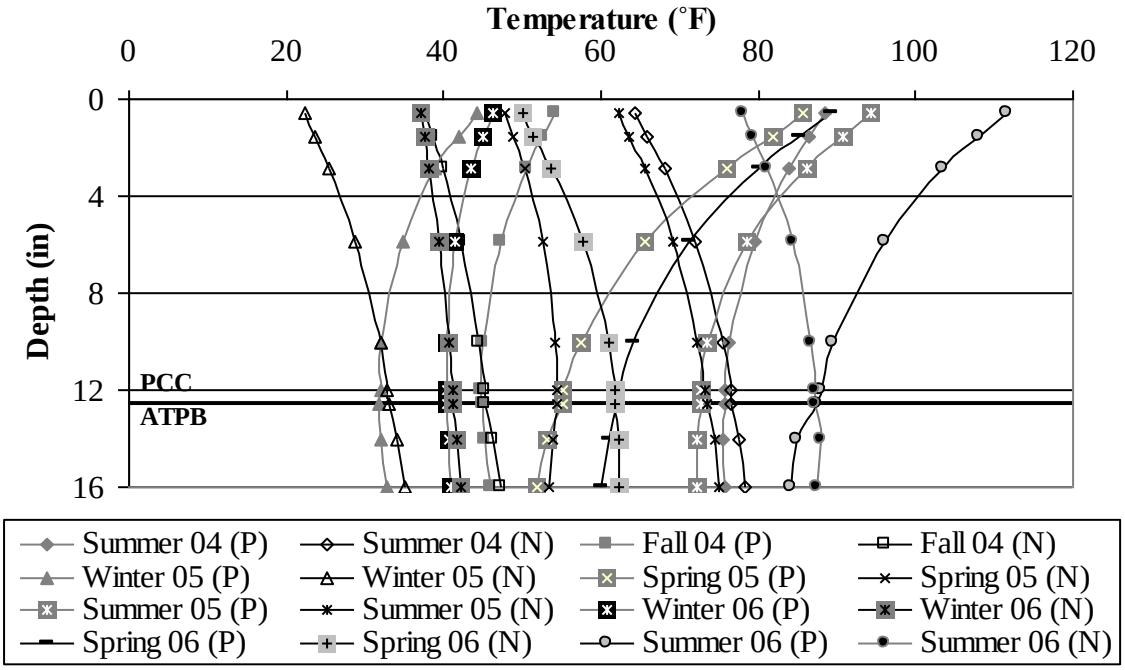

Figure 7.25. Peak temperature profiles selected for use in the finite element model.

Table 7.11. Peak temperature conditions for the Dipstick™ test dates.

	Peak Positive Temperature		Peak Negative Temperature	
Season	**Equivalent Temperature Gradient (˚F/in)**	**Slab Weighted Average Temperature (˚F)**	**Equivalent Temperature Gradient (˚F/in)**	**Slab Weighted Average Temperature (˚F)**
Summer 04	0.98	80.1	-0.97	71.9
Fall 04	0.72	47.8	-0.60	42.2
Winter 05	0.92	35.6	-0.85	28.7
Spring 05	2.42	66.5	-0.51	52.2
Summer 05	1.67	79.8	-0.88	69.0
Fall 05	---	---	---	---
Winter 06	0.44	42.0	-0.32	39.4
Spring 06	2.11	72.0	-0.94	57.4
Summer 06	1.85	96.5	-0.73	84.0

The environmental loads used in the finite element model need to be corrected for the effect of moisture on the slab and the effect of the built-in temperature gradient, determined to be 0.31˚F/in in Chapter 4. The concrete moisture gradient present during each test date was previously presented in section 6.3.1, along with the corresponding equivalent linear temperature gradients. The equivalent linear gradients based on the temperature and moisture measurements are presented in Table 7.12, along with the gradients after correction for the built-in temperature condition, referred to as the "effective" gradients. The "effective" gradient is calculated by summing the temperature and moisture gradients and subtracting the built-in temperature gradient from the sum. The effective gradient will be used to model the environmental conditions in the restrained and unrestrained slabs.

The temperature profiles representing the effective gradients modeled are graphically shown in Figure 7.26 and the actual temperatures are summarized in Table 7.13. With the exception of the effective profiles modeled for the summer of 2004 and the spring of 2005, the effective gradients are negative, indicating that the slab curvature is expected to be upward.

Table 7.12. Modeled environmental loads for peak positive and negative temperature conditions.

	Equivalent Temperature Gradient (˚F/in)			
Season	**Peak Positive Temperature**	**Peak Negative Temperature**	**Moisture**	**Effective**
Summer 04	0.98		-0.48	0.19
		-0.97	0.40	-0.88
Fall 04	0.72		-1.91	-1.50
		-0.60	-1.81	-2.72
Winter 05	0.92		-2.20	-1.59
		-0.85	-1.93	-3.09
Spring 05	2.42		-1.04	1.07
		-0.51	-1.04	-1.85
Summer 05	1.67		-3.49	-2.13
		-0.88	-3.49	-4.68
Fall 05	0.44		-3.13	-3.00
		-0.32	-3.00	-3.63
Winter 06	2.11		-1.99	-0.19
		-0.94	-1.99	-3.24
Spring 06	1.85		-3.07	-1.53
		-0.73	-3.25	-4.29

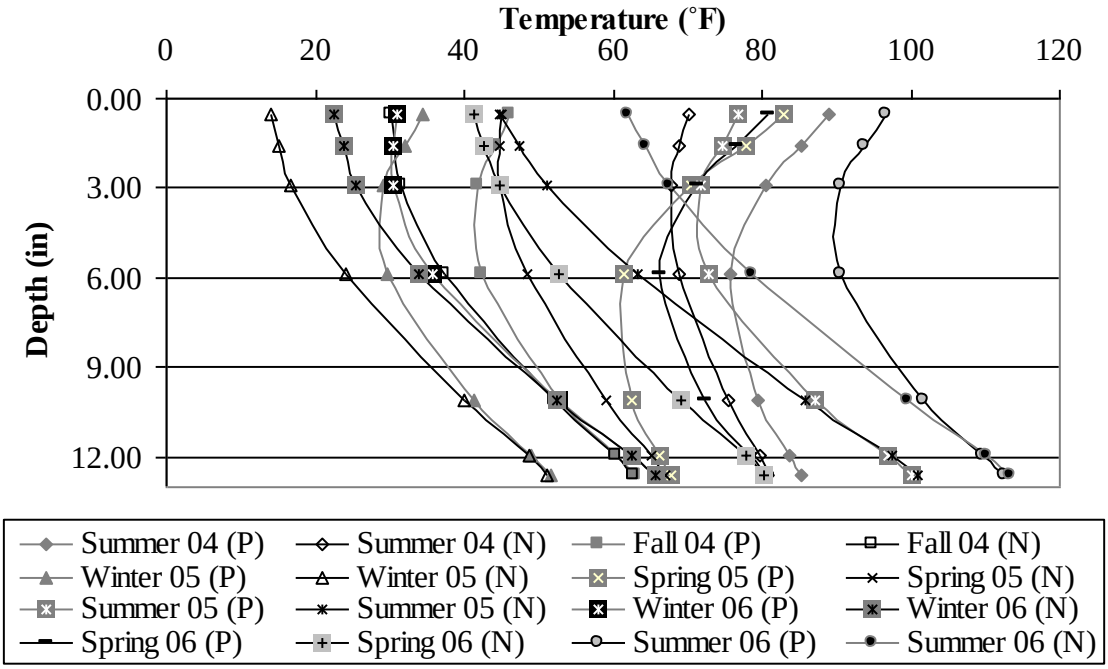

Figure 7.26. Effective temperature profiles used in the finite element model.

Table 7.13. Modeled nonlinear temperature profiles considered in each model.

	PCC							ATPB	
Depth (in)	**0.53**	**1.58**	**2.88**	**5.88**	**10.06**	**11.96**	**12.58**	**14**	**16**
Temperature (˚F)	88.9	85.2	80.6	75.8	79.4	83.7	85.2	75.5	75.7
	70.1	69.0	67.9	68.9	75.5	79.6	80.8	77.6	78.3
	46.1	44.3	42.0	42.4	53.1	60.5	63.1	45.2	46.0
	30.2	30.7	31.6	37.4	52.1	60.3	62.8	46.3	47.3
	34.5	32.2	29.2	29.8	41.2	49.1	51.7	32.1	32.9
	14.1	15.1	16.7	24.1	40.1	48.6	51.2	34.1	35.2
	83.0	77.8	70.5	61.4	62.4	66.2	67.9	53.2	51.8
	45.0	44.7	44.8	48.4	59.1	65.2	67.1	54.0	53.3
	76.7	74.6	71.9	72.9	87.2	96.9	100.3	72.3	72.2
	44.8	47.3	51.1	63.2	85.9	97.5	101.0	74.4	75.1
	31.0	30.6	30.5	35.9	52.7	62.6	65.8	40.6	40.9
	22.6	23.7	25.5	33.9	52.5	62.6	65.8	41.6	42.1
	80.7	76.5	71.3	66.3	72.3	78.4	80.7	60.9	60.0
	41.5	42.7	44.8	52.8	69.2	77.9	80.3	62.3	62.3
	96.6	93.8	90.6	90.5	101.7	109.8	112.6	85.0	84.2
	61.9	64.3	67.7	78.8	99.6	110.2	113.3	88.0	87.3

There are three methods available to model temperature profiles throughout the depth of the slab and base using ISLAB2000: linear, quadratic, and nonlinear. As previously mentioned in section 2.4, research has shown that replacing an actual distribution by a linear approximation determined based on the temperatures at the top and bottom of the slab leads to an overestimation of maximum stresses for daytime conditions and the underestimation of maximum stresses in the slab for nighttime conditions (Armaghani et al. 1987; Choubane and Tia 1992; Mirambell 1990). Therefore, selecting a nonlinear effective temperature analysis is expected to result in more accurate predictions of the slab deformation and stress. A nonlinear temperature analysis was selected for validation and analysis of the finite element models, with temperature nodes placed at the locations corresponding to the thermocouples and the temperatures presented in Table 7.13.

Moreover, since the interface between the concrete and the ATPB was defined as a bonded interface, the reference temperature is a required input for both layers. The reference temperature is the temperature at which the slab is free from thermal stresses and is that corresponding to the time of set of the slabs. The reference temperatures were determined based on the analysis presented in Chapter 4 and are summarized in Table 7.14.

Table 7.14. Reference temperatures for the pavement layers.

Layer	**Reference Temperature (˚F)**
Concrete	104.1
ATPB	90.6

7.3 VALIDATION OF THE FINITE ELEMENT MODELS

This section presents the validation of the finite element models developed for the restrained and unrestrained slabs described in the previous section based on field data collected from the static vibrating wire gages. The slab curvatures predicted by the finite element model are compared to the curvatures based on the measured VW data and corresponding to the same temperature and moisture conditions described in the previous section.

The slab curvatures estimated based on the strain data, along the diagonal direction, as previously presented in section 6.2.3, are used to compare to the curvature predicted by the finite element method. The predicted slab curvature was calculated by fitting a second order polynomial to the first few feet of the predicted surface profile. The accuracy of the finite element method in predicting the slab curvature is evaluated using statistical analysis. First, the predicted curvature is plotted versus the measured curvature, as shown in Figure 7.27. The correlation coefficient (R^2) between predicted and measured was equal to 0.82 for the restrained slabs and 0.85 for the unrestrained slabs (p less than 0.001 for both cases), indicating that the finite element method explains 82 and 85 percent of the total variability in curvature predictions for the 16 data points (for each type of slab).

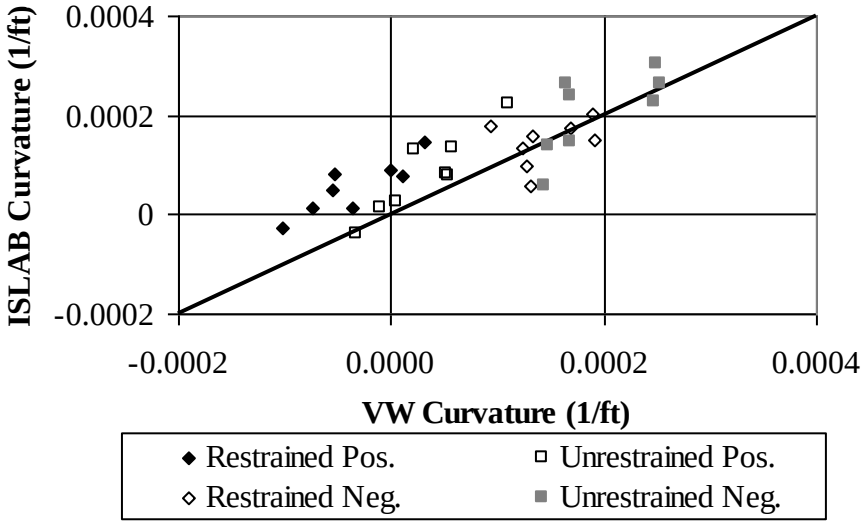

Figure 7.27. Predicted versus measured curvatures for restrained and unrestrained slabs.

In addition, the scatter around the one-to-one line in Figure 7.27 is an indication of the residual error involved in the curvature estimated using the finite element method. The residuals representing the difference between the predicted and measured weighted curvatures were plotted against the measured curvature, and are presented in Figure 7.28. The figure shows a horizontal band with no abnormalities or trends, implying that the data used in the analysis is independent.

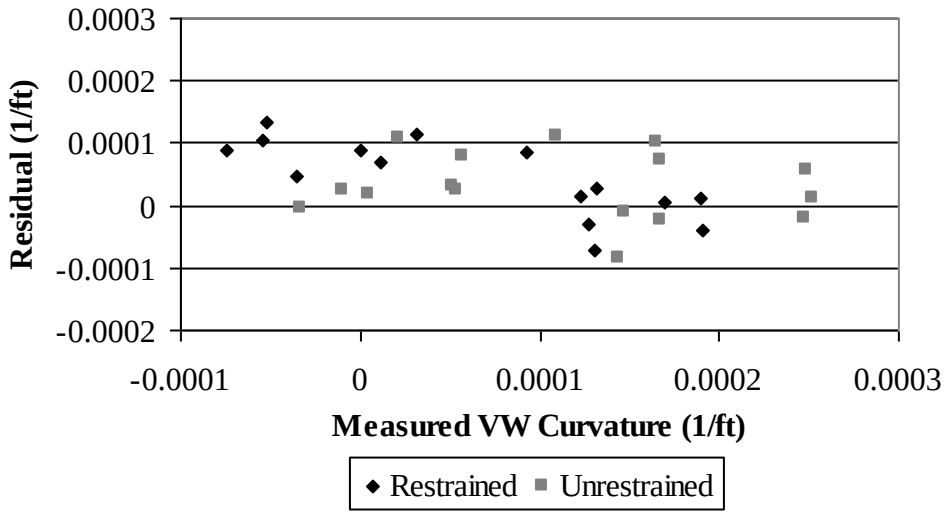

Figure 7.28. Residual versus measured curvature for restrained and unrestrained slabs.

Having established that the predicted slab curvature is similar to the measured, the relationship between the predicted slab curvature and the effective equivalent linear temperature gradient is examined. Similar to the results obtained in sections 6.2.3 and 6.3.3 for the strain and surface profile data, Figure 7.29 shows that the predicted slab curvature decreases with an increase in the gradient. However, the slopes on the best-fit lines are not similar for the restrained and unrestrained slabs. This was expected since the predicted curvatures correspond to environmental conditions that already take into account the presence of the moisture gradient.

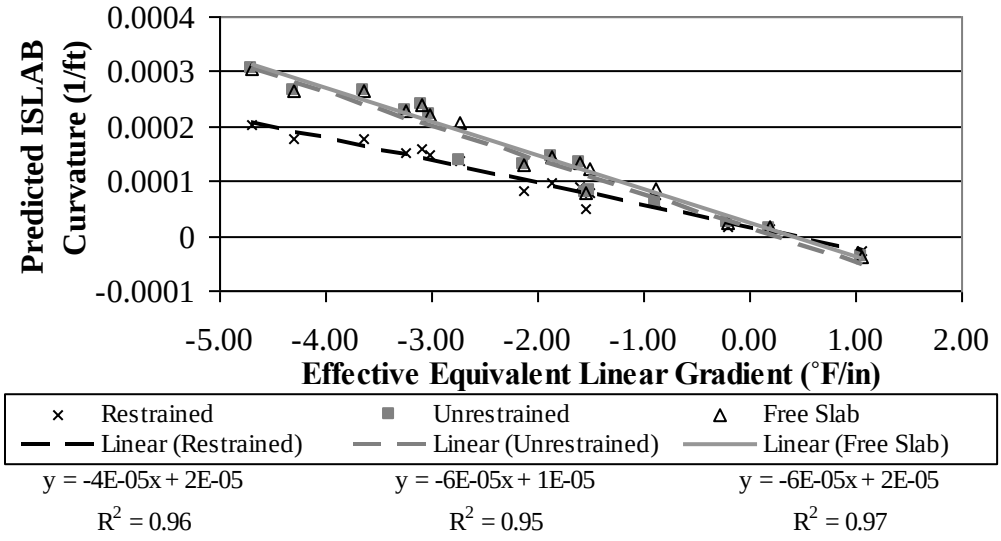

Figure 7.29. Predicted curvature versus effective equivalent linear temperature gradient.

The curvature of the restrained slab is 1 to 39 percent lower compared to the unrestrained slab. The results of the finite element method are consistent with the observations made based on the strain measurements whereby the restrained slab curvature was 20 to 50 percent lower than that of the unrestrained slab (section 6.2.3). This indicates that the restraint provided by the dowel bars and tie bars along the joints causes the restrained slabs to undergo a smaller amount of curvature than the unrestrained slabs.

7.4 CURLING AND WARPING STRESSES

Having validated the finite element models developed for this research, the effects of different parameters on slab stress is examined in this section. These parameters include slab restraint, the effect of the built-in construction gradient, the moisture gradient, the slab temperature at set and the bond between the slab and the base layer. The effect of approximating the nonlinear temperature profile by an equivalent linear temperature profile is also examined. The first section establishes the terminology used throughout the rest of this chapter regarding the cases analyzed to evaluate the effects of the different parameters.

7.4.1 Terminology

The finite element models are used to model several environmental loading conditions to evaluate the effects of different parameters on the development of stress in the slabs. The terminology used to differentiate between the cases is defined in the following:

- The built-in temperature (BT) gradient, previously established in Chapter 4. The equivalent linear built-in temperature (BELT) gradient of 0.31˚F/in may be used in the analysis or the nonlinear built-in temperature (BNLT) gradient may be used, based on the measured profile. The BT does not include drying shrinkage.
- The transient temperature gradient representing the measured temperature profile at the time of interest is characterized as an equivalent linear (TELT) gradient, or a nonlinear (TNLT) gradient.
- The transient moisture equivalent linear (TELM) gradient represents the temperature gradient equivalent to the measured moisture profiles at the time of interest.
- The composite nonlinear gradient (CNL), which represents the temperature and moisture gradients in the slab, corrected for the effect of the built-in temperature gradient. This is the same as the "effective" gradient, previously defined in section 7.2.5, as:

  CNL = TNLT + TELM – BNLT

  The CNL gradient is used to model the environmental conditions in the restrained and unrestrained slabs and represents the measured conditions in the slab and the validated models. All the remaining cases analyzing the effects of other parameters are compared to this base case.
- The composite equivalent linear (CEL) gradient represents the equivalent linear temperature and moisture gradients in the slab, corrected for the effect of the built-in temperature gradient, defined as:

  CEL = TELT + TELM – BELT

7.4.2 Results of the validated finite element models

For the validated models, the temperature loading caused by the CNL gradient was modeled to establish a base case and study the effects of other parameters on stress development in the slabs. This section presents the results of the validated models.

The critical midpanel stress was estimated using finite element analysis and the results are summarized in Table 7.15. When negative gradients are present in the concrete (which represents the modeled CNL gradient for most of the analyzed cases), critical stresses are expected at the top of the slab. According to Table 7.15, the bottom of the slab is always in compression, for both restrained and unrestrained slabs (with the exception of one of the March 2005 cases for the unrestrained slab) while the top of the restrained slabs is in tension for half the cases and the top of the unrestrained slabs is in compression for all the cases (with the exception of one of the November 2004 cases). In summary, the restrained slabs are exhibiting the expected behavior (tension at the top and compression at the bottom), while the unrestrained slabs are mostly in compression along the top and bottom.

When a positive gradient is present, the critical stress is expected to occur at the bottom of the slab. According to Table 7.15, the bottom and top of the slab (restrained and unrestrained) are both in compression when a positive gradient is present. The bottom of the slab is in compression for both restrained and unrestrained slabs. However, the compressive stress in the restrained slab is larger than in the unrestrained slab. The top of the slab exhibits higher tensile stress in the restrained slab than in the unrestrained slab.

Figure 7.30 and Figure 7.31 show the range of the midpanel critical stress that develops at the top and bottom of the restrained and unrestrained slabs versus the CNL gradients analyzed. For the restrained slabs, the largest tensile stress in the top of the slab is associated with the peak negative gradient. For the unrestrained slabs, the only peak tensile stress in the top of the slab is associated with one of the November 2004 cases.

Table 7.15. Critical midpanel stress corresponding to peak CNL gradients.

Date	Peak Positive Gradient (ºF/in)	Peak Negative Gradient (ºF/in)	CNL Gradient (ºF/in)	Slab Weighted Average Temp. (ºF)	Midpanel Stress (psi)[1]			
					Restrained Slabs		Unrestrained Slabs	
					Top	Bottom	Top	Bottom
22-Aug-04	0.98		0.18	80.1	-183	-46	-185	-36
		-0.97	-0.89	71.9	-21	-20	-25	-3
16-Nov-04	0.72		-1.51	47.8	-87	-134	-87	-92
		-0.60	-2.73	42.2	87	-88	91	-37
3-Mar-05	0.92		-1.60	35.6	-135	-130	-298	-84
		-0.85	-3.10	28.7	127	-46	-175	3
6-Apr-05	2.42		1.06	66.5	-406	-66	-386	-105
		-0.51	-1.86	52.2	28	-69	-149	-31
22-Sep-05	1.67		-2.14	79.8	-85	-355	-252	-286
		-0.88	-4.69	69.0	324	-238	-91	-164
1-Feb-06	0.44		-3.01	42.0	41	-162	-258	-101
		-0.32	-3.64	39.4	161	-119	-200	-61
18-Apr-06	2.11		-0.20	72.0	-312	-204	-338	-187
		-0.94	-3.25	57.4	190	-134	-114	-75
20-Jul-06	1.85		-1.54	96.5	-123	-349	-220	-296
		-0.73	-4.30	84.0	315	-269	-44	-199

Note: [1] Tension is positive.

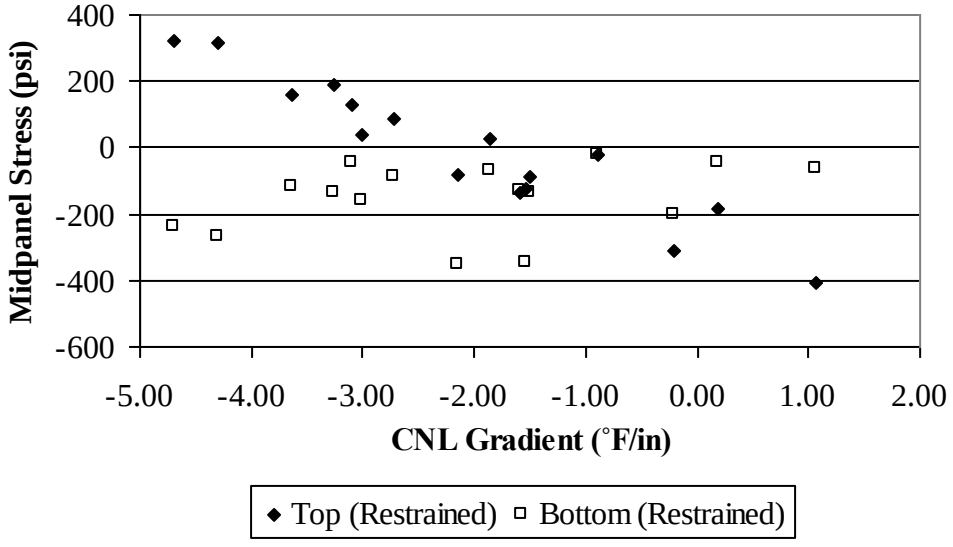

Figure 7.30. Stress at the top and bottom of the restrained slab for the peak CNL gradients.

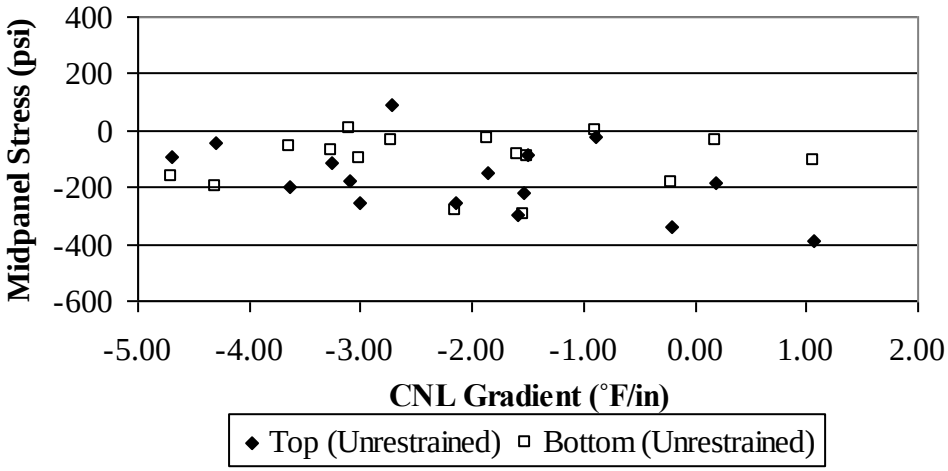

Figure 7.31. Stress at the top and bottom of the unrestrained slab for the peak CNL gradients.

7.4.3 Effect of the transient temperature gradient

To isolate the effects of the moisture gradient and the built-in construction gradient, the finite element models were re-analyzed with the original temperature loads modeled as a transient nonlinear temperature distribution or TNLT gradients. The TNLT loads were previously presented in Figure 7.25 and Table 7.11 (section 7.2.5). The results are presented in this section.

The critical midpanel stress estimated using the finite element analysis is summarized in Table 7.16 for the peak negative TNLT gradients and Table 7.17 for the peak positive TNLT gradients. In the case of negative gradients, the top and bottom of the restrained slab are both in tension, due to the high set temperature. Moreover, the top of the unrestrained slab is in compression in some of the cases, while the bottom of the slabs is in tension, which is also not typical of this type of loading.

When the average temperature of the slab is higher than the set temperature, compressive stresses are generated because the expansion of the slab is restrained by the bond between the slab and the base. Tensile stresses are therefore expected to be generated when the average slab temperature is lower than the set temperature. The set temperature for the slabs was 104˚F and the slab weighted average temperature is lower than 104˚F for all the modeled cases. This would result in the development of tensile stress in the both restrained and unrestrained slabs.

Table 7.16. Critical midpanel stress corresponding to peak negative TNLT gradients.

Date	Peak Negative TNLT Gradient (ºF/in)	Slab Weighted Average Temp. (ºF)	Midpanel Stress (psi)[1]			
			Restrained Slabs		Unrestrained Slabs	
			Top	Bottom	Top	Bottom
22-Aug-04	-0.97	71.9	94	80	90	88
16-Nov-04	-0.60	42.2	46	149	46	154
3-Mar-05	-0.85	28.7	76	210	-45	213
6-Apr-05	-0.51	52.2	60	166	-13	159
22-Sep-05	-0.88	69.0	112	98	22	106
1-Feb-06	-0.32	39.4	-4	218	-89	214
18-Apr-06	-0.94	57.4	127	148	19	158
20-Jul-06	-0.73	84.0	120	87	53	88

Note: [1] Tension is positive.

Table 7.17. Critical midpanel stress corresponding to peak positive TNLT gradients.

Date	Peak Positive TNLT Gradient (ºF/in)	Slab Weighted Average Temp. (ºF)	Midpanel Stress (psi)[1]			
			Restrained Slabs		Unrestrained Slabs	
			Top	Bottom	Top	Bottom
22-Aug-04	0.98	80.1	-142	115	-144	107
16-Nov-04	0.72	47.8	-158	154	-161	146
3-Mar-05	0.92	35.6	-234	194	-229	161
6-Apr-05	2.42	66.5	-255	255	-241	111
22-Sep-05	1.67	79.8	-242	171	-221	78
1-Feb-06	0.44	42.0	-152	212	-182	190
18-Apr-06	2.11	72.0	-268	245	-251	124
20-Jul-06	1.85	96.5	-200	189	-183	67

Note: [1] Tension is positive.

Figure 7.32 and Figure 7.33 show the range of the midpanel critical stress that develops at the top and bottom of the restrained and unrestrained slabs for the TNLT gradients in Table 7.16 and Table 7.17. Both figures show that the tensile stress at the top of slab decreases with an increase in temperature gradient, while the tensile stress at the bottom of slab only slightly varies with the TNLT gradient.

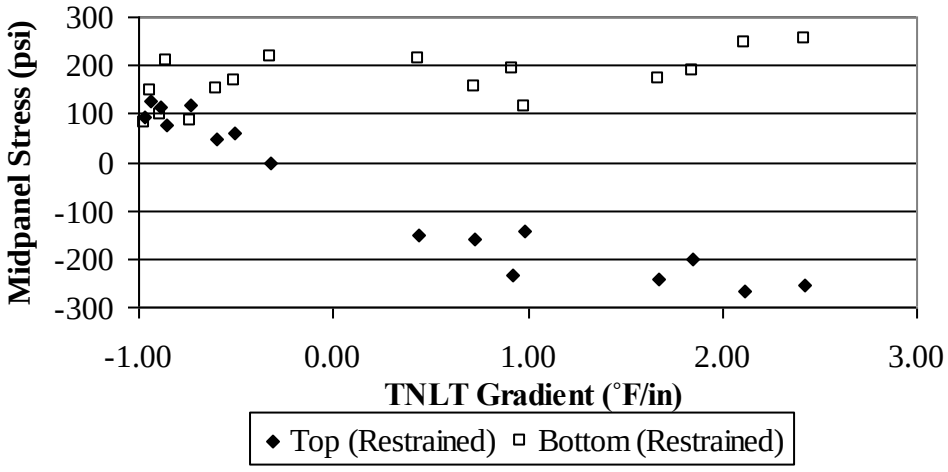

Figure 7.32. Stress at the top and bottom of the restrained slab for the peak TNLT gradients.

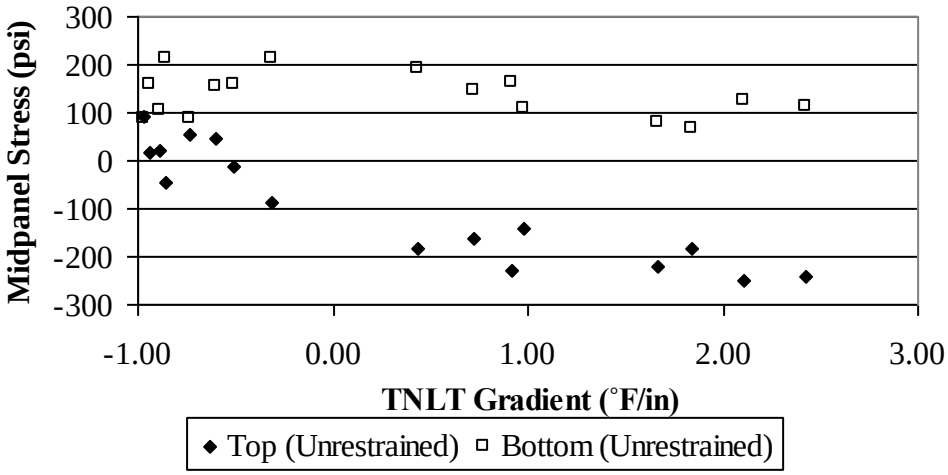

Figure 7.33. Stress at the top and bottom of the unrestrained slab for the peak TNLT gradients.

Figure 7.34 shows the variation in the critical midpanel stress with the weighted average slab temperature for each negative gradient. The figure shows the critical stress in the top of the slab increases with an increase in slab temperature, while the critical stress in the bottom of the slab decreases with an increase in slab temperature. As the slab temperature approaches the temperature at set time, the critical tensile stresses shift in location from the top of the slab at midpanel to the bottom of the slab. This was observed for both restrained and unrestrained slabs.

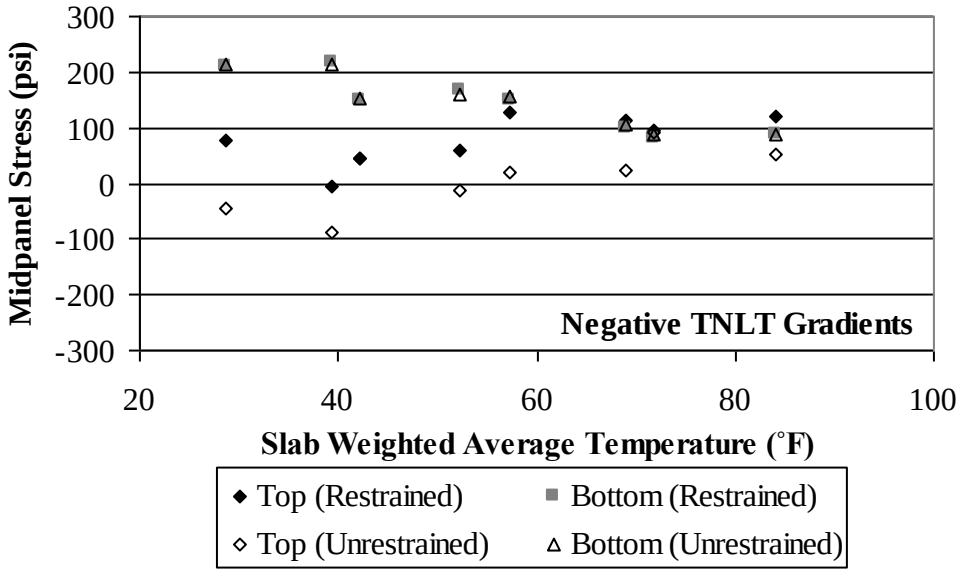

Figure 7.34. Variation of critical midpanel stress with weighted average slab temperature for each peak negative TNLT gradient.

Figure 7.35 shows the variation of the critical midpanel stress with changes in the weighted average slab temperature for the positive gradients. The figure indicates that the magnitude of the critical stress is not significantly affected by the weighted average slab temperature of the slab for positive gradients.

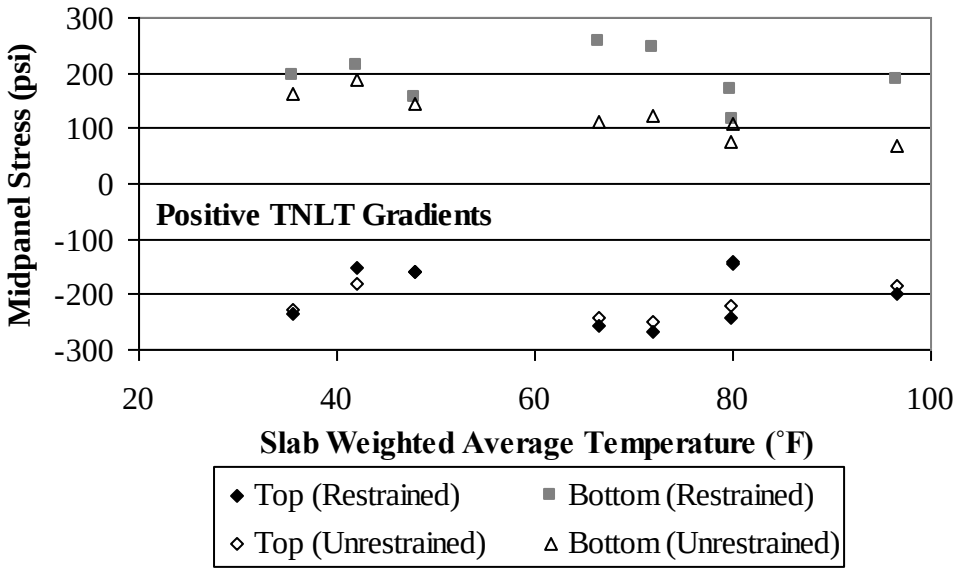

Figure 7.35. Variation of critical midpanel stress with weighted average slab temperature for each peak positive TNLT gradient.

The stress predicted for the peak TNLT gradient is compared to the stress predicted for the base case, where the temperature loading represents the CNL gradients (section 7.4.2), to quantify the effect of neglecting the moisture gradient and the built-in temperature gradient. Figure 7.36 shows a comparison between the predicted stresses for the restrained slab, and Figure 7.37 show a comparison between the predicted stresses for the unrestrained slab.

For positive gradients, the figures indicate that neglecting the moisture and built-in temperature gradients results in an underestimation of the compressive stress in the top of the slab (by an average of 40 percent for the restrained and 20 percent for the unrestrained slabs), and a shift from compressive stress to tensile stress at the bottom of the slab. This shift is expected since moisture gradients are equivalent to negative temperature gradients, which counteract the effects of the positive gradients. For the negative gradients, the figures indicate that neglecting the moisture and built-in temperature gradients results in an underestimation of tensile stress at the top of the restrained slabs (by an average of 50 percent), an underestimation of compressive stress at the top of the unrestrained slabs (by an average of 67 percent), and a shift from compressive stress to tensile stress at the bottom of the slabs.

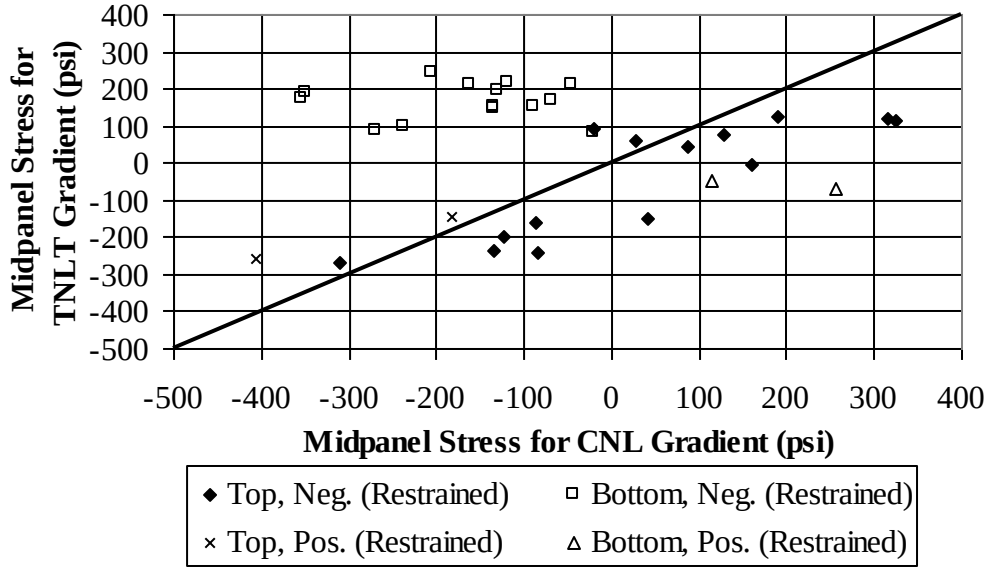

Figure 7.36. Comparison of stress generated by the TNLT gradient and the CNL gradient in the restrained slab.

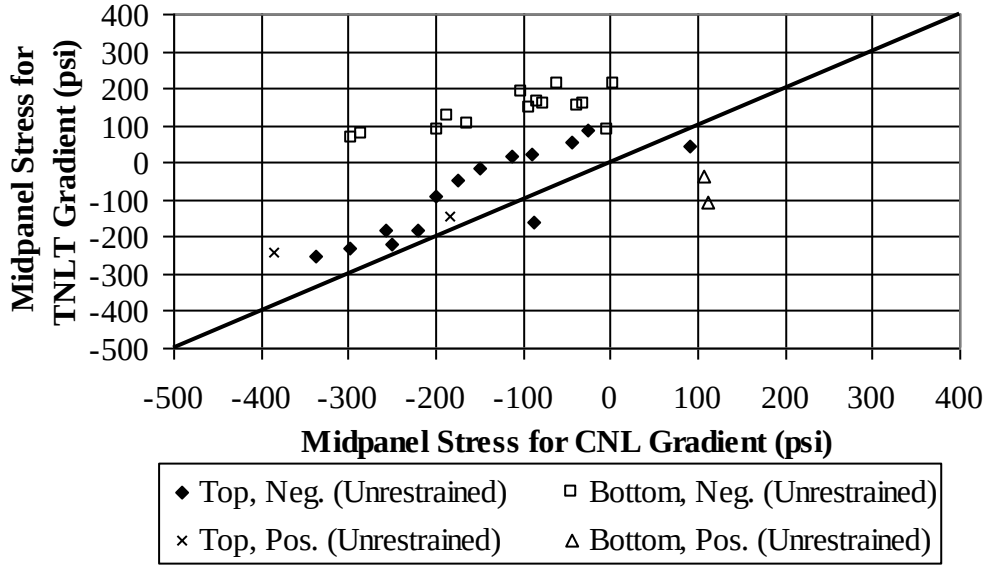

Figure 7.37. Comparison of stress generated by the TNLT gradient and the CNL gradient in the unrestrained slab.

7.4.4 Effect of the moisture gradient

To isolate the effect of the moisture gradient, the finite element models were re-analyzed with the transient temperature loads (TNLT gradient) corrected only for the built-in nonlinear temperature (BNLT) gradient of 0.31˚F/in, or TNLT – BNLT, instead of the composite nonlinear (CNL) gradient. The corrected temperature profiles are presented in Figure 7.38 and the corresponding temperature gradients are presented in Table 7.18. The results of the stress predictions are presented in this section.

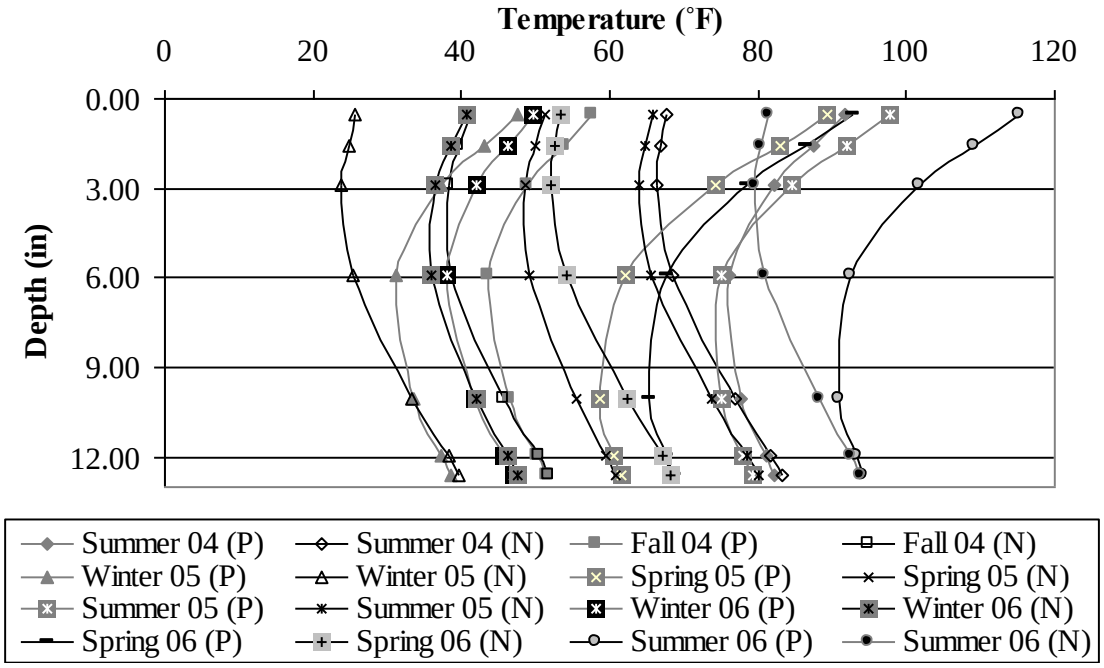

Figure 7.38. Transient temperature profiles corrected for the built-in temperature gradient, or TNLT – BNLT.

Table 7.18. Equivalent linear temperature gradient accounting for the transient nonlinear temperature (TNLT) gradient and the built-in temperature (BNLT) gradient.

	Equivalent Temperature Gradient (˚F/in)		
Season	**Peak Positive Temperature**	**Peak Negative Temperature**	**Corrected**
Summer 04	0.98		0.67
		-0.97	-1.28
Fall 04	0.72		0.41
		-0.60	-0.91
Winter 05	0.92		0.61
		-0.85	-1.16
Spring 05	2.42		2.11
		-0.51	-0.82
Summer 05	1.67		1.36
		-0.88	-1.19
Fall 05	0.44		0.13
		-0.32	-0.63
Winter 06	2.11		1.80
		-0.94	-1.25
Spring 06	1.85		1.54
		-0.73	-1.04

The critical midpanel stresses estimated from the finite element analysis for the corrected negative and positive temperature gradients are graphically shown in Figure 7.39 and Figure 7.40 for the restrained and unrestrained slabs.

For the negative gradients, the top of the restrained and unrestrained slabs is in compression, while the bottom of the slabs is in compression for most of the cases. As previously mentioned in section 7.4.2, tensile stresses are expected to be generated when the average slab temperature is lower than the set temperature, which is the case for this analysis. For the positive gradients, both the top and bottom of the restrained and unrestrained slab is in compression, for most of the cases.

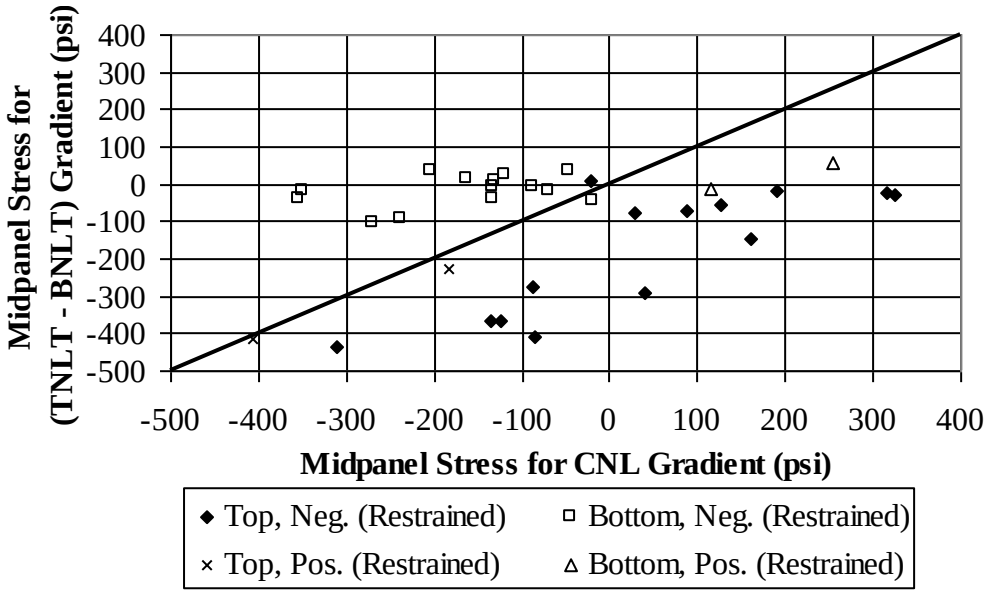

Figure 7.39. Comparison of stress generated by the (TNLT-BNLT) gradient and the CNL gradient in the restrained slab.

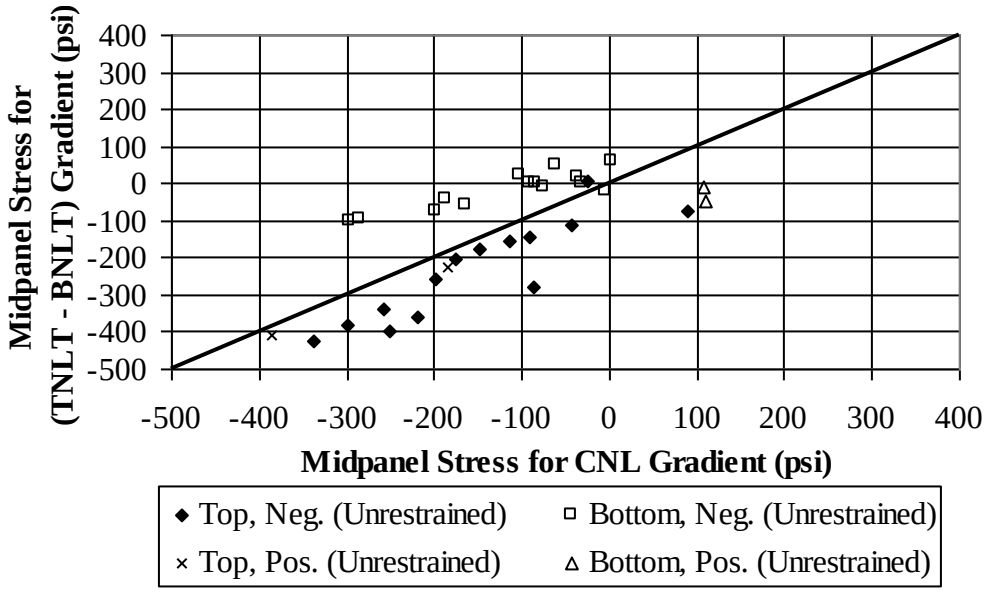

Figure 7.40. Comparison of stress generated by the (TNLT-BNLT) gradient and the CNL gradient in the unrestrained slab.

In the case of negative TNLT gradients, the corrected gradients (TNLT-BNLT) are larger in magnitude compared to the TNLT gradients. This is expected to result in larger tensile stress at the top of the slab and larger compressive stress at the bottom of the slab. In the case of positive TNLT gradients, the corrected gradients are lower. This is expected to result in smaller compressive stress at the top of the slab and larger tensile stress at the bottom of the slab. The stress predicted for the corrected (TNLT-BNLT) gradients is compared to the stress predicted for the CNL gradients to quantify the effect of neglecting the moisture gradient. Figure 7.41 and Figure 7.42 show a comparison between the predicted stress for the case of a positive TNLT gradient, and Figure 7.43 and Figure 7.44 show a comparison between the predicted stress for the case of a negative TNLT gradient.

For the positive gradients, Figure 7.41 and Figure 7.42 indicate that neglecting the moisture gradient while accounting for the built-in construction gradient results in an overestimation of the compressive stress in the top of the slab (by an average of 29 percent for the restrained and 57 percent for the unrestrained slabs), a shift from compressive stress to tensile stress at the bottom of the restrained slab, and an underestimation of the compressive stresses in the bottom of the unrestrained slabs (by an average of 17 percent). This shift is expected since moisture gradients are equivalent to negative temperature gradients, which counteract the effects of the positive TNLT gradients selected. Moreover, as expected, the compressive stress caused by the composite CNL gradient is smaller at the top of the slab and the tensile stress is larger at the bottom of the slab, compared to the stress due to the corrected transient nonlinear temperature (TNLT – BNLT) profiles.

For the negative gradients, Figure 7.43 and Figure 7.44 indicate that neglecting the moisture gradient results in a shift from tensile to compressive stress at the top of the restrained slab and an overestimation of compressive stress at the top of the unrestrained slabs (by an average of 69 percent). It also results in an underestimation of compressive stress at the bottom of the restrained slab (by an average of 32 percent) and the bottom of the unrestrained slab (by an average of 72 percent). Moreover, as expected, the tensile stress caused by the composite CNL gradient is larger at the top of the slab and the compressive stress is larger at the bottom of the slab, compared to the stress due to the transient profiles corrected for the built-in gradient (TNLT – BNLT).

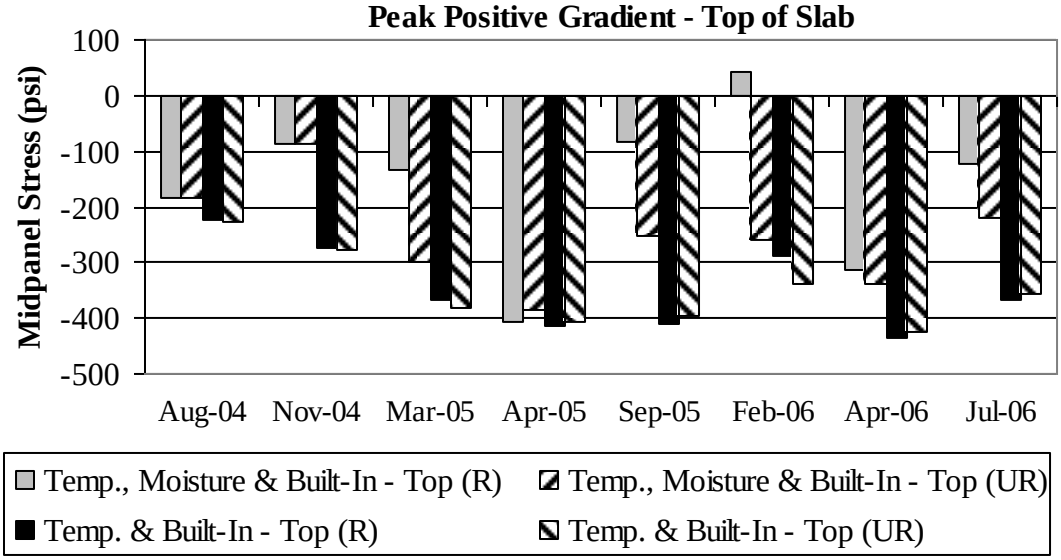

Figure 7.41. Stress at the top of the slab when considering the CNL gradient with and without the moisture or TELM gradient, for peak positive TNLT gradients.

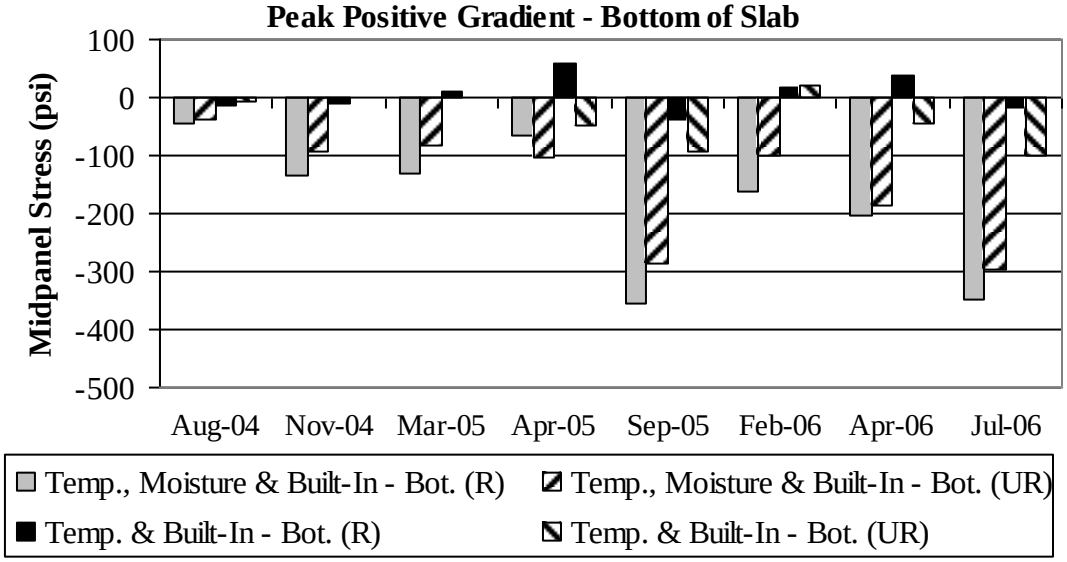

Figure 7.42. Stress at the bottom of the slab when considering the CNL gradient with and without the moisture or TELM gradient, for peak positive TNLT gradient.

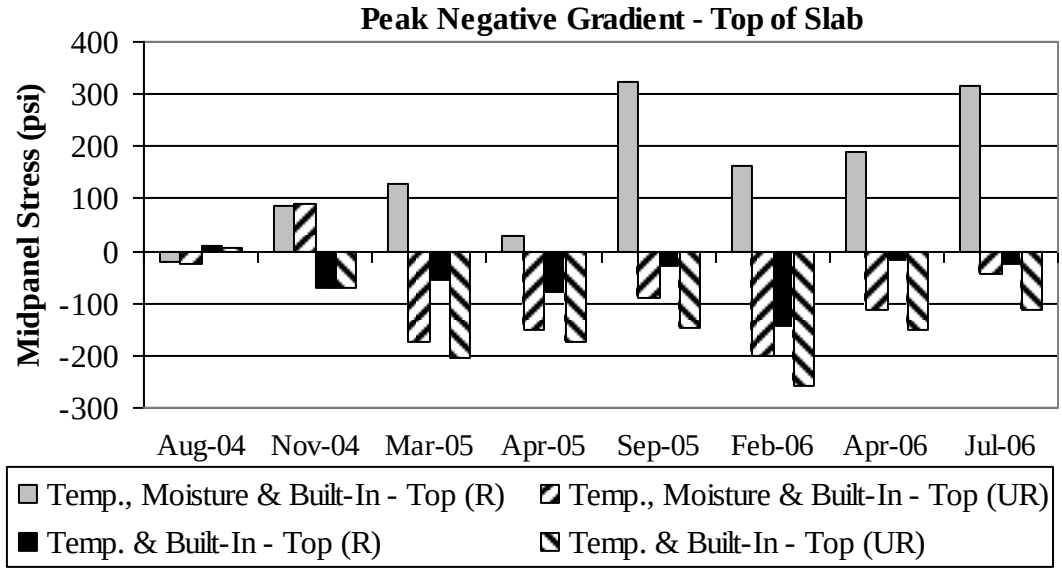

Figure 7.43. Stress at the top of the slab when considering the CNL gradient with and without the moisture or TELM gradient, for peak negative TNLT gradient.

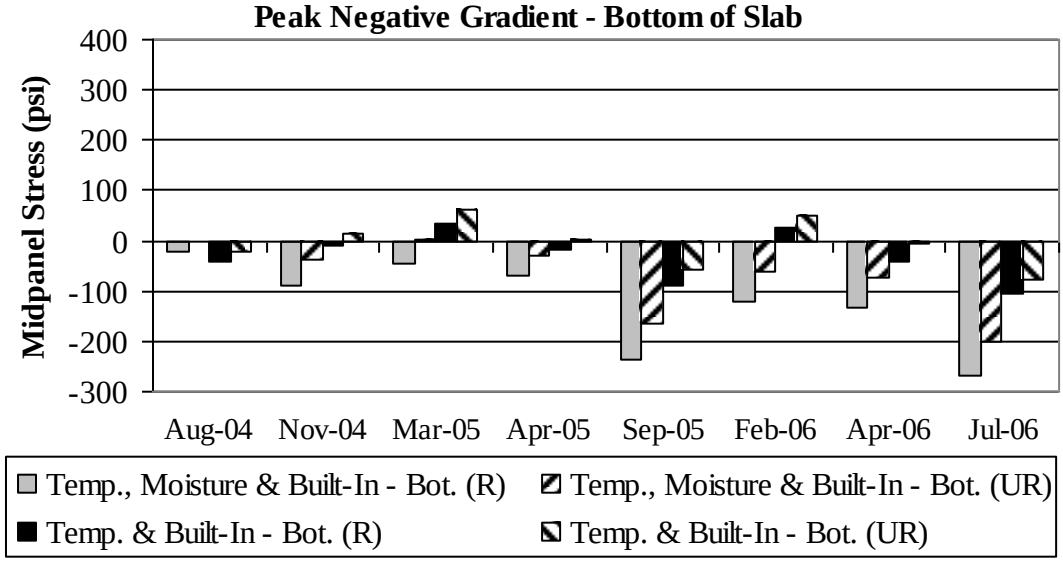

Figure 7.44. Stress at the bottom of the slab when considering the CNL gradient with and without the moisture or TELM gradient, for peak negative TNLT gradient.

7.4.5 Effect of the temperature at set time

To isolate the effect of the slab and base temperatures at set time, the finite element models were re-analyzed with the reference temperatures set equal to the weighted average slab temperature present in the field at the time the gradient was measured. The weighted average slab temperature and the asphalt base layer temperature were presented in Table 7.11 and Table 7.13. The results of the stress predictions are presented in this section.

The critical midpanel stress estimated from the finite element analysis neglecting the effect of the slab and base temperature at set time is presented in Table 7.19 for the restrained and unrestrained slabs. For the negative gradients, the top of the restrained and unrestrained slabs are in tension for half of the cases, while the bottom of the slab is in compression. This is consistent with the expected behavior (tension at the top and compression at the bottom) for this type of loading. This confirms the statements in the previous sections that the temperature at set time is influencing the expected slab behavior in the presence of negative gradients. For the positive gradients, the top and bottom of the restrained and unrestrained slabs is in compression, with the compression at the top of the slab larger than at the bottom of the slab. This can be considered consistent with the expected behavior (compression at the top and tension at the bottom) in that the top of the slab is in higher compression than the bottom of the slab.

Figure 7.45 and Figure 7.46 show the range of the critical midpanel stress that develops at the top and bottom of the restrained and unrestrained slabs for each composite CNL gradient analyzed, when neglecting the temperature at set time. This is similar to the results obtained when the slabs were subjected to the CNL gradient loading with the measured set time temperature of 104˚F. For the restrained slabs, the largest tensile stress at the top of the slab is associated with the peak negative gradients. The critical midpanel tensile stress decreases with an increase in the composite CNL gradient and the compressive stress increases with increasing gradient. For the unrestrained slabs, the critical midpanel stress does not vary much with the gradient and is smaller in magnitude than for the restrained slabs, when neglecting the set temperature.

Table 7.19. Critical midpanel stresses corresponding to modeled gradients neglecting the effect of the slab and base temperatures at set time.

Date	Peak Positive Gradient (ºF/in)	Peak Negative Gradient (ºF/in)	Effective Gradient (ºF/in)	Slab Weighted Average Temp. (ºF)	Midpanel Stress (psi)[1]			
					Restrained Slabs		Unrestrained Slabs	
					Top	Bottom	Top	Bottom
22-Aug-04	0.98		0.18	80.1	-174	-113	-173	-103
		-0.97	-0.89	71.9	-3	-121	-4	-104
16-Nov-04	0.72		-1.51	47.8	-50	-285	-49	-240
		-0.60	-2.73	42.2	134	-273	137	-216
3-Mar-05	0.92		-1.60	35.6	-85	-327	-177	-279
		-0.85	-3.10	28.7	190	-287	-26	-224
6-Apr-05	2.42		1.06	66.5	-336	-134	-324	-193
		-0.51	-1.86	52.2	69	-229	-82	-135
22-Sep-05	1.67		-2.14	79.8	-64	-435	-202	-364
		-0.88	-4.69	69.0	360	-372	-8	-289
1-Feb-06	0.44		-3.01	42.0	103	-400	-111	-326
		-0.32	-3.64	39.4	228	-374	-43	-298
18-Apr-06	2.11		-0.20	72.0	-295	-292	-295	-280
		-0.94	-3.25	57.4	236	-310	3	-254
20-Jul-06	1.85		-1.54	96.5	-116	-375	-203	-324
		-0.73	-4.30	84.0	340	-362	14	-286

Note: [1] Tension is positive.

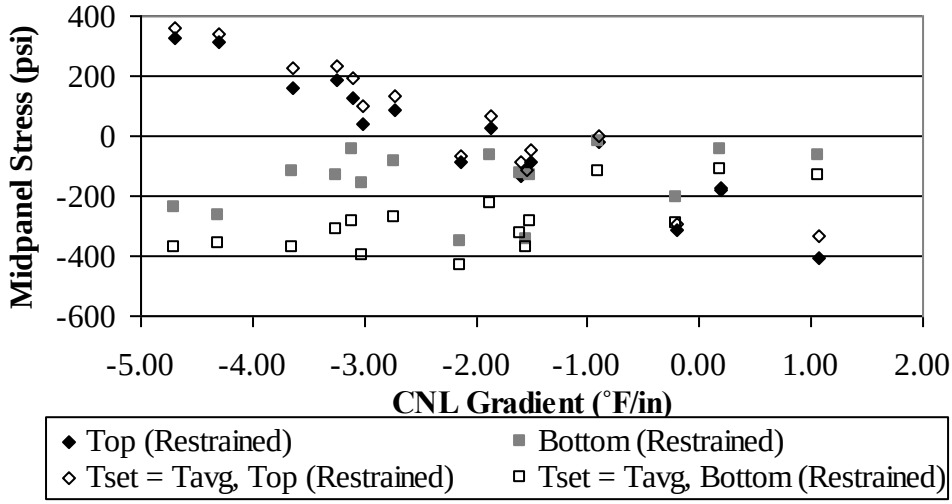

Figure 7.45. The effect of neglecting set temperature on stress development for restrained slabs.

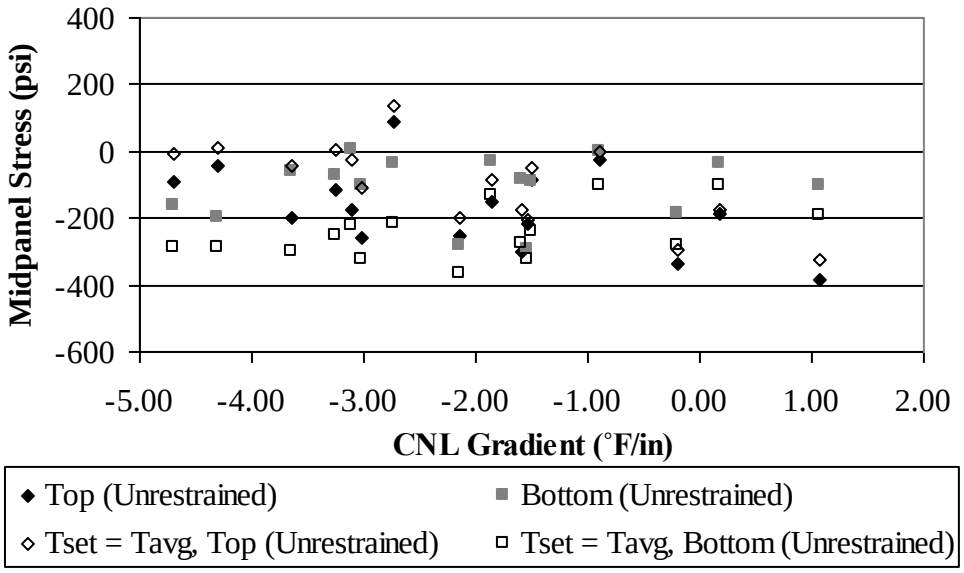

Figure 7.46. The effect of neglecting set temperature on stress development for unrestrained slabs.

The stress predicted in this section is compared to the stress predicted for the CNL case presented in section 7.4.2 to quantify the effect of neglecting the effect of the slab and base temperature at set time. Figure 7.47 and Figure 7.48 show a comparison between the predicted stress for restrained and unrestrained slabs.

For the positive gradients, the figures indicate that neglecting the effect of the temperature at set time results in an underestimation of the compressive stress at the top of the slab (by an average of 20 percent) and an overestimation of the compressive stress in the bottom of the slab (by more than 200 percent). For the negative gradients, neglecting the effect of the temperature at set time results in an overestimation of tensile stress at the top of the slab (by an average of 31 percent), and an overestimation of compressive stress at the bottom of the slab (by more than 200 percent).

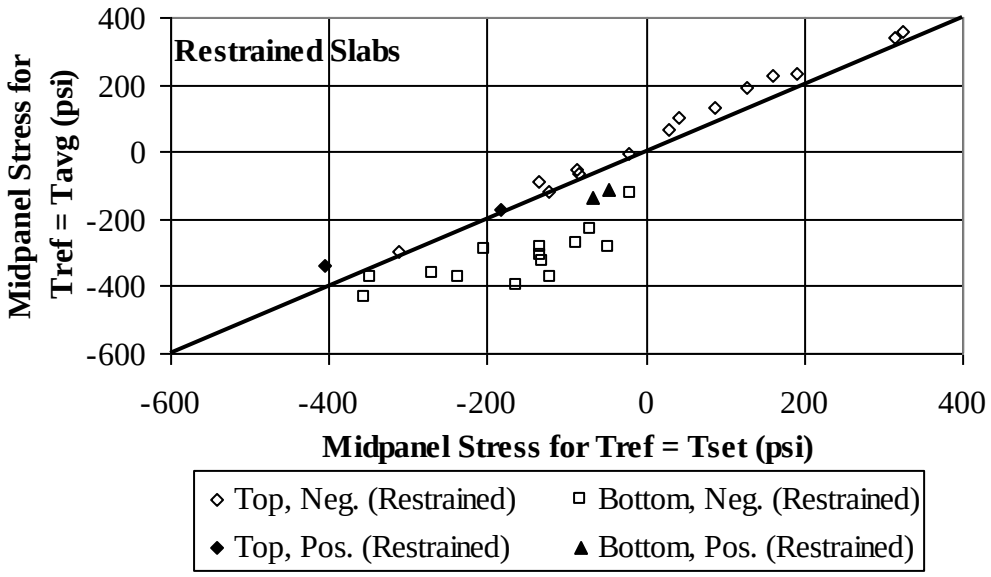

Figure 7.47. Comparison of stress generated by neglecting the effect of the set temperature in restrained slabs.

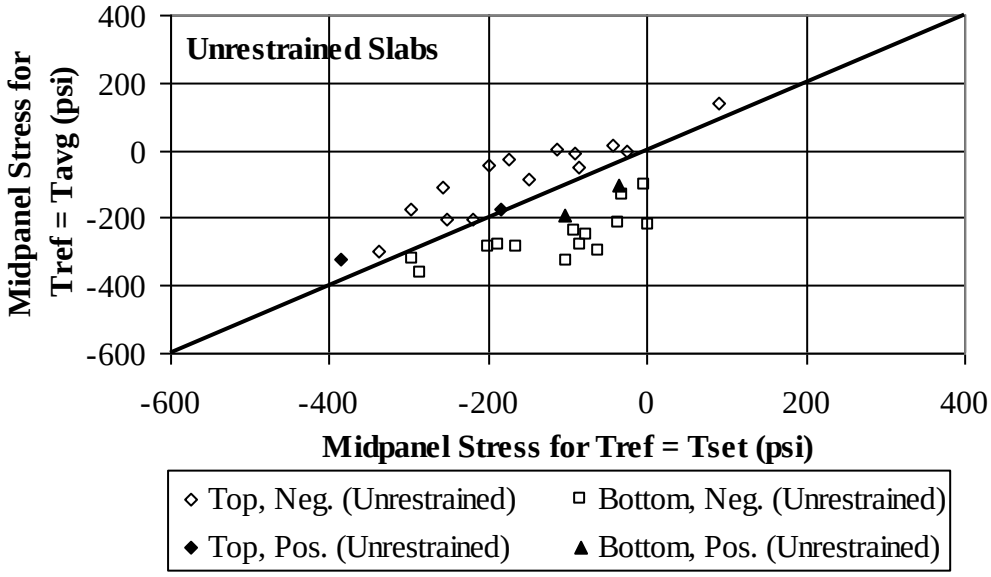

Figure 7.48. Comparison of stress generated by neglecting the effect of the set temperature in unrestrained slabs.

The peak stress that developed in the slab for the base case, where the temperature loading represents the CNL gradients, is compared to the peak stress generated for each of the previously described cases to examine the influence of each of the different parameters. The average difference between each case and the base case is summarized in Table 7.20 for the stress at the top of the slab and Table 7.21 for the stress at the bottom of the slab. The influence of the various parameters is larger for the stress at the bottom of the slab, compared to the top of slab. For the top of slab, the stress is mostly affected by the moisture gradient at the day of interest. For the bottom of the slab, the stress is mostly affected by the temperature gradient at the time of interest. Neglecting the reference temperature has the most significant effect on stress at the bottom of the slab (up to 300 percent increased stress for unrestrained slabs). In addition, the stress in the unrestrained slab is more affected by the moisture gradient and the reference temperature, compared to the restrained slab.

Table 7.20. Average percent difference between the peak stress at the top of slab, compared to the base case.

	Ave. Difference in Stress at Top of Slab, %[(1)]			
	Restrained Slab		**Unrestrained Slab**	
	Positive Gradient	**Negative Gradient**	**Positive Gradient**	**Negative Gradient**
Composite nonlinear (CNL = TNLT + TELM – BNLT)	100	100	100	100
Temperature (TNLT)	17	98	10	148
Temperature and Moisture (TNLT + TELM)	47	-72	67	151
Temperature and Built-in (TNLT - BNLT)	-29	169	-57	-2
Reference Temperature = Temperature at gradient measurement	-2	-31	25	71

Note: (1) $Average\ \%\ Difference = \frac{\sigma_{CNL} - \sigma_i}{\sigma_{CNL}} \times 100\ \%$

Table 7.21. Average percent difference between the peak stress at the bottom of slab, compared to the base case.

	Ave. Difference in Stress at Bottom of Slab, %[(1)]			
	Restrained Slab		Unrestrained Slab	
	Positive Gradient	Negative Gradient	Positive Gradient	Negative Gradient
Composite nonlinear (CNL = TNLT + TELM – BNLT)	100	100	100	100
Temperature (TNLT)	257	303	232	-196
Temperature and Moisture (TNLT + TELM)	147	235	149	10
Temperature and Built-in (TNLT - BNLT)	109	68	83	-206
Reference Temperature = Temperature at gradient measurement	-92	-237	-121	307

Note: (1) $Average\ \%\ Difference = \frac{\sigma_{CNL} - \sigma_i}{\sigma_{CNL}} \times 100\ \%$

7.4.6 Effect of the bond between the slab and base

To study the effect of the bond between the slab and the base, the finite element models were re-analyzed with the assumption that the slab and base are unbonded. The results of the stress predictions are presented in this section.

Neglecting the effect of the bond between the slab and base is expected to result in larger tensile stress in the top of the slab and larger compressive stress in the bottom of the slab for the case of negative gradients (which describes most of the cases analyzed). For the two cases where positive gradients were modeled, neglecting the effect of the bond between the slab and base is expected to result in larger compressive stresses at the top of the slab and larger tensile stresses at the bottom of the slab.

For the restrained slabs, modeling an unbonded condition between the slab and base did not yield any results. The analysis did not converge and therefore, no results are available. For the unrestrained slabs, the critical midpanel stresses estimated from the finite element analysis

neglecting the effect of the slab/base bond are presented in Table 7.22. Neglecting the effect of the bond along the interface is expected to allow the whole slab to curl up or down depending on the gradient; which would result in stresses that are similar along the top and bottom portions of the slab. For the negative and positive gradients, the top and bottom of the slab are in compression for all cases. For the case of the positive gradient, the stress at the top of the slab is larger than at the bottom, while for the case of the negative gradient the stress at the bottom of the slab is larger than the top. This is consistent with the expected behavior.

Table 7.22. Critical midpanel stress corresponding to modeled gradients neglecting the effect of the slab/base bond for unrestrained slabs.

Date	Peak Positive Gradient (ºF/in)	Peak Negative Gradient (ºF/in)	Effective Gradient (ºF/in)	Slab Weighted Average Temp. (ºF)	Midpanel Stress (psi)[(1)]	
					Unrestrained Slabs	
					Top	Bottom
22-Aug-04	0.98		0.18	80.1	-173	-102
		-0.97	-0.89	71.9	-8	-82
16-Nov-04	0.72		-1.51	47.8	-57	-209
		-0.60	-2.73	42.2	119	-151
3-Mar-05	0.92		-1.60	35.6	-196	-239
		-0.85	-3.10	28.7	-74	-135
6-Apr-05	2.42		1.06	66.5	-309	-214
		-0.51	-1.86	52.2	-78	-133
22-Sep-05	1.67		-2.14	79.8	-233	-303
		-0.88	-4.69	69.0	-93	-139
1-Feb-06	0.44		-3.01	42.0	-166	-224
		-0.32	-3.64	39.4	-113	-172
18-Apr-06	2.11		-0.20	72.0	-297	-277
		-0.94	-3.25	57.4	-63	-135
20-Jul-06	1.85		-1.54	96.5	-226	-276
		-0.73	-4.30	84.0	-74	-128

Note: [(1)] Tension is positive.

The stress predicted in this section is compared to the stress predicted for the CNL case presented in section 7.4.2 to quantify the effect of the slab/base bond. Figure 7.49 shows a comparison between the predicted stress for the unrestrained slab. For the positive gradients, neglecting the effect of the slab/base bond results in an increase in the stress at the top and bottom of the unrestrained slab. For the negative gradient, neglecting the effect of the slab/base bond results in similar tensile stress at the top of the slab and an overestimation of compressive stress in the bottom of the slab (by more than 200 percent).

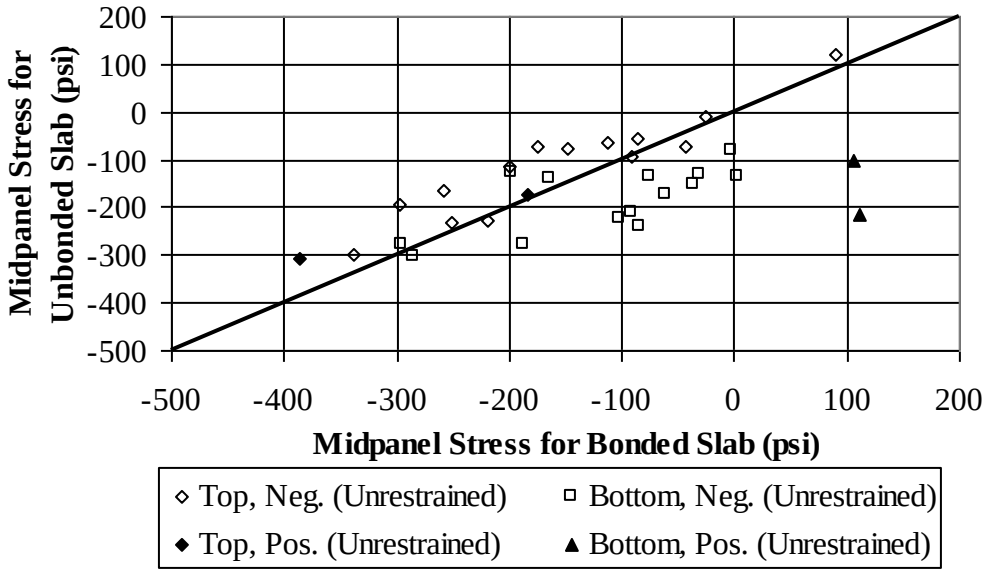

Figure 7.49. Comparison of stress generated by neglecting the effect of the slab/base bond in unrestrained slabs.

7.4.7 Effect of using effective linear environmental loads

In this section, the effect of modeling linear temperature loads (CEL gradient) instead of the nonlinear temperature profiles described in section 7.2.5 (CNL gradient) is assessed. The finite element models were re-analyzed with the temperature profiles described by three points along the slab depth: at the surface, at mid-depth and along the bottom surface of the slab. Similarly to

the effective temperature profiles described in section 7.2.5, the composite equivalent linear temperature profiles are corrected for the moisture gradient and the built-in temperature gradient (CEL = TELT + TELM – BELT), and are presented in Figure 7.50. The results of the stress predictions are presented in this section.

As previously mentioned in sections 2.4 and 7.2.5, research has shown that replacing an actual distribution by an equivalent linear approximation leads to the overestimation of maximum stresses for daytime conditions and the underestimation of maximum stresses in the slab for nighttime conditions (Armaghani et al. 1987; Choubane and Tia 1992; Mirambell 1990).

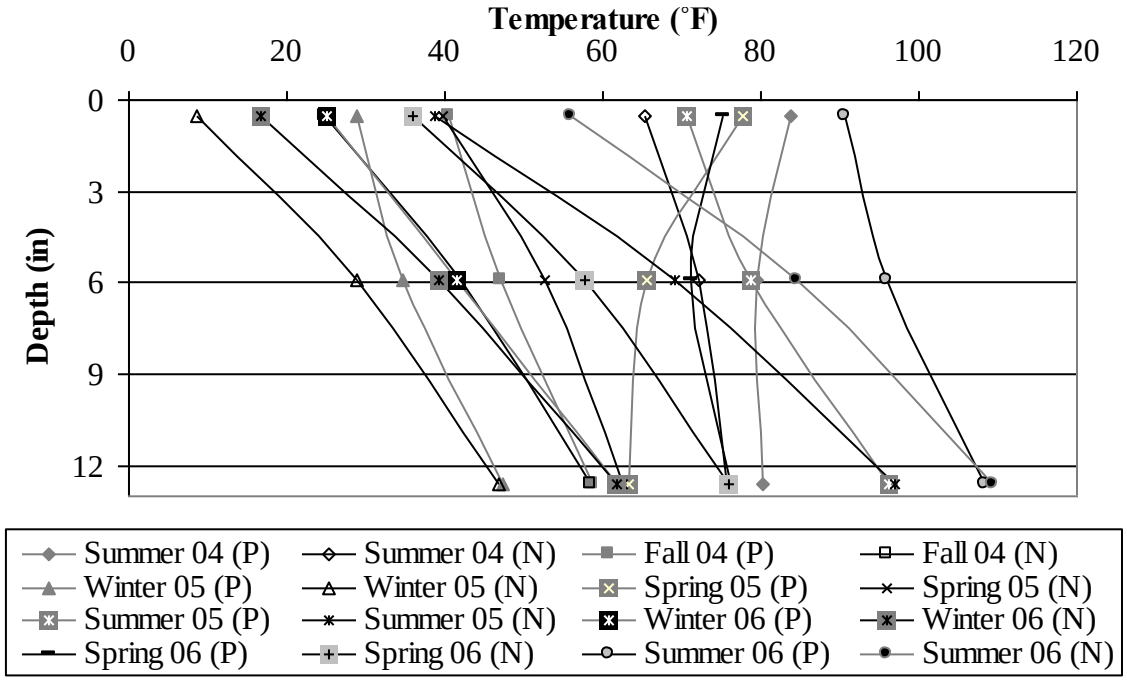

Figure 7.50. Composite equivalent linear (CEL) temperature profiles.

The critical midpanel stress estimated from the finite element analysis based on the linear temperature data is presented in Table 7.23 for the restrained and unrestrained slabs.

Table 7.23. Critical midpanel stresses corresponding to effective linear temperature profiles.

Date	Peak Positive Gradient (°F/in)	Peak Negative Gradient (°F/in)	Effective Gradient (°F/in)	Slab Weighted Average Temp. (°F)	Midpanel Stress (psi)[1]			
					Restrained Slabs		Unrestrained Slabs	
					Top	Bottom	Top	Bottom
22-Aug-04	0.98		0.18	80.1	-183	-46	-76	65
		-0.97	-0.89	71.9	-21	-20	79	87
16-Nov-04	0.72		-1.51	47.8	81	23	77	26
		-0.60	-2.73	42.2	264	53	257	57
3-Mar-05	0.92		-1.60	35.6	60	40	-100	37
		-0.85	-3.10	28.7	331	110	33	103
6-Apr-05	2.42		1.06	66.5	-406	-66	-221	66
		-0.51	-1.86	52.2	-289	0	47	93
22-Sep-05	1.67		-2.14	79.8	139	-161	-32	-155
		-0.88	-4.69	69.0	571	-74	156	-82
1-Feb-06	0.44		-3.01	42.0	41	-162	-26	11
		-0.32	-3.64	39.4	161	-119	37	45
18-Apr-06	2.11		-0.20	72.0	-311	-204	-142	-25
		-0.94	-3.25	57.4	190	-134	112	31
20-Jul-06	1.85		-1.54	96.5	102	-157	4	-153
		-0.73	-4.30	84.0	562	-101	202	-104

Note: [1] Tension is positive.

The stress predicted in this section is compared to the stress predicted for the CNL case presented in section 7.4.2 to study the effect of using equivalent linear temperature loading instead of nonlinear temperature loading. Figure 7.51 and Figure 7.52 show a comparison between the predicted stress for the restrained and unrestrained slabs. For positive gradients, using CEL temperature profiles results in similar stress at the top of the restrained slab, an underestimation of the compressive stress at the top of the unrestrained slab (by an average of 87 percent), an overestimation of the tensile stress at the bottom of the restrained slab (by an average of 45 percent) and the bottom of the unrestrained slab (by an average of 60 percent). The overestimation of the tensile stress at the bottom of the slab is consistent with the expected behavior based on research by others (Armaghani et al. 1987; Choubane and Tia 1992; Mirambell 1990). For negative gradients, using CEL temperature profiles results in an overestimation of tensile stress at the top of the restrained and unrestrained slabs (by an average

of 79 percent for the restrained and more than 200 percent for the unrestrained slabs), and an underestimation of compressive stress at the bottom of the restrained slab (by an average of 91 percent) and the bottom of the unrestrained slab (by an average of 82 percent). The overestimation of tensile stress at the top of the slabs is not consistent with the expected behavior based on research by others (Armaghani et al. 1987; Choubane and Tia 1992; Mirambell 1990).

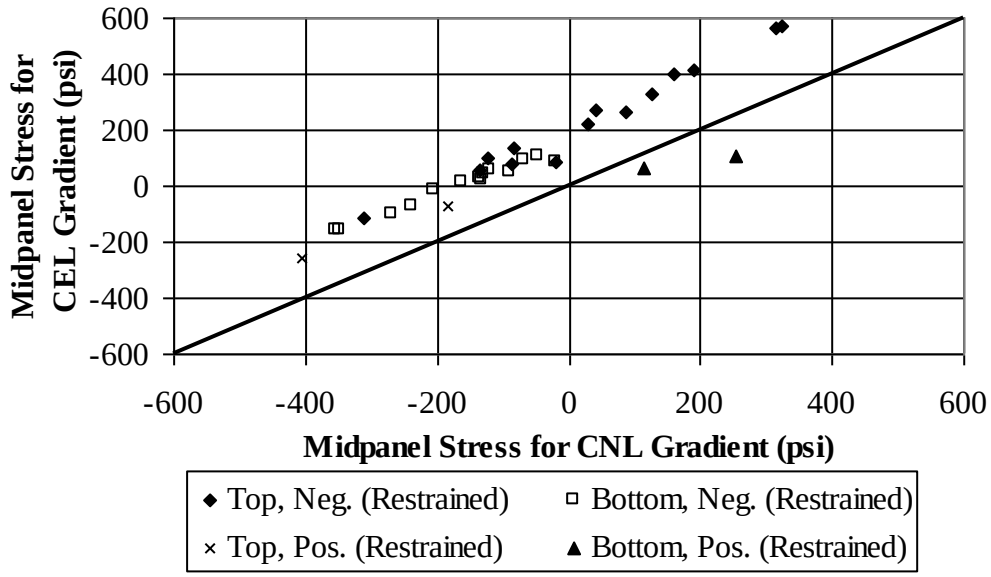

Figure 7.51. Comparison between stress predicted using an equivalent linear and a nonlinear temperature model for restrained slab.

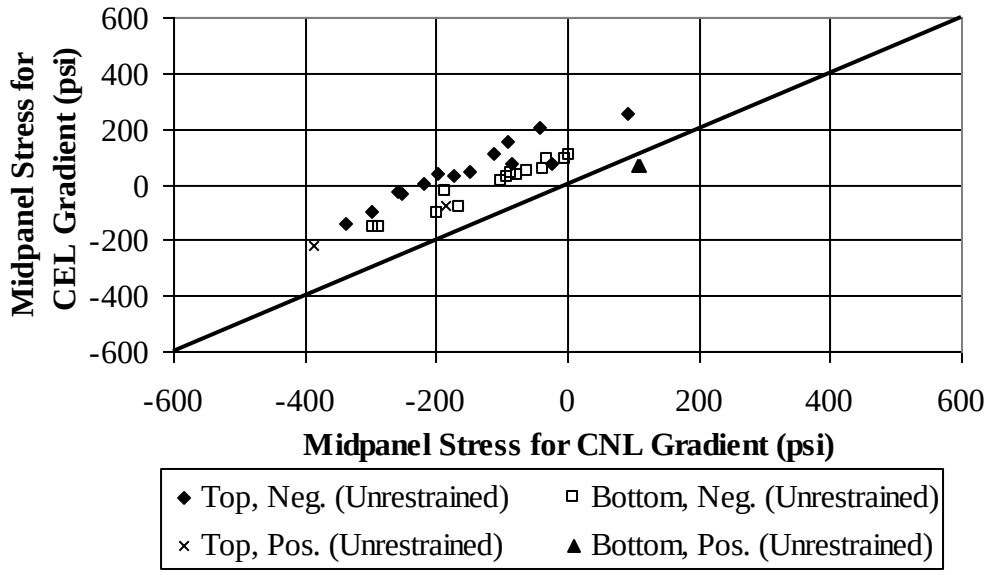

Figure 7.52. Comparison between stress predicted using an equivalent linear and a nonlinear temperature model for unrestrained slab.

7.5 SUMMARY AND CONCLUSIONS

In this chapter, the effect of seasonal variations in temperature and moisture on the development of stress in the restrained and unrestrained slabs was examined. For this purpose, the pavement structure was modeled using a two-dimensional finite element program, ISLAB2000. Inputs for the models were based on field and laboratory testing and the models were calibrated using static strains measured in the field.

The curvature of the restrained slab was lower than the unrestrained slab for the same modeled environmental loading. This was the case for both predicted curvatures and measured curvatures based on strain data. Lower curvature is expected to be accompanied with larger stress. This was true for all the cases analyzed. Critical stress in the restrained slab was on average 20 to 22 percent larger than the critical stress in the unrestrained slab while the curvature was on average 40 percent greater for the unrestrained slab.

The effect of temperature gradients on the development of stress in JPCP slabs has become a well-known factor by pavement researchers and designers. Although the effect of moisture gradients is also well-known, the extent to which moisture affects stress in slabs has not historically been considered in pavement design. An analysis of the stress generated by temperature and moisture gradients in restrained and unrestrained slabs has shown that the moisture gradient has a significant influence on stress. Neglecting the moisture gradient in the analysis results in an increased stress at the top of the slab (30 percent for the restrained and 130 percent for the unrestrained) and an increased stress at the bottom of the slab (11 percent for the restrained and 162 percent for the unrestrained).

Theoretical models for prediction of concrete temperature based on ambient climatic conditions are widely available and have been thoroughly validated based on field data. However, models predicting moisture are less common and still require more extensive research to validate them. Therefore, designers would tend to ignore the effect of moisture and only consider the effect of temperature variations. This would tend to result in a more conservative design. The cost-effectiveness of designing conservative pavement structures should be weighed against the cost of further investigating slab moisture to conceive more adequate designs.

In addition, modeling the effective temperature as a linear profile instead of a nonlinear profile resulted in an overestimation of maximum stresses for daytime conditions. While, for the nighttime conditions, this resulted in an overestimation of tensile stresses at the top of the slab and an underestimation of compressive stress at the bottom of the slab. This is the limitation of establishing the equivalent linear gradient based on equivalent deformation and not equivalent stress.

8.0 CONCLUSIONS AND RECOMMENDATIONS

This research has provided a better understanding of the effects of seasonal variations in temperature and moisture on deformation and stress development in restrained and unrestrained slabs. This chapter summarizes the conclusions that can be made from this research and recommendations for future research.

8.1 CONCLUSIONS

The following conclusions were made based on the results of this study:

- The built-in temperature gradient can be established using VW gages. The built-in temperature gradient for the instrumented test section is 0.31˚F/in and the weighted average slab temperature is 104.3˚F (section 4.5).
- In the top two inches of the slab, concrete moisture content is low during the winter (55 percent) and high during the spring (75 percent), and is primarily influenced by the frequency, duration and intensity of each rain event. In the deeper portion of the slab, the concrete moisture content remains relatively constant at 95 percent throughout the two-year period, irrespective of the ambient conditions while the bottom 2 inches of the slab remained saturated (section 5.4).
- The temperature of the concrete, the asphalt and the granular layers predicted by the EICM embedded in the MEPDG are close to those measured. The pavement performance predicted by the MEPDG over the design life was not affected by differences between the use of measured and predicted temperature and moisture profiles throughout the pavement structure (section 5.4), hence the difference found between predicted and measured temperatures does not appear to be significant.

- After the first summer following paving, the curvature of the slab is predominantly curled upward, resulting in an increased potential for top-down fatigue cracking. This was confirmed by the strain measurements, which showed that the curvature is curled upward 99 percent of the time (section 6.5).
- The overall curvature in the restrained slab is over 50 percent lower when compared to the unrestrained slab (section 6.5). This reduction in deformation resulted in a critical stress that was 20 to 22 percent larger for the restrained slab compared to the unrestrained slab (section 7.5).
- The difference in slab curvature as estimated from the static strain measurements and the surface profiles can be attributed primarily to the effect of drying shrinkage of the concrete. Although, some of this drying shrinkage is reversible, as can be seen by the seasonal fluctuations (section 6.5).
- The additional restraint provided by the dowel and tie bars does not have a significant effect on the reduction in slab curvature resulting from daily temperature fluctuations or from reversible drying shrinkage. They do have a substantial effect on the long-term drying shrinkage (up to 50 percent). This reduction in curvature will help insure more uniform support beneath the restrained slab and therefore reduce stress when vehicle loads are applied. On the other hand, the restrained curvature will increase the tensile stress on the top of the slab (section 6.5).
- The effect of moisture and creep on the slab was isolated. The rate of increase in slab curvature is larger for the unrestrained slabs, compared to the restrained slabs, indicating that the effect of creep on the curvature of the unrestrained slabs is more pronounced than on the restrained slabs, as would be expected (section 6.5).
- The presence of a moisture gradient contributes 17 to 50 percent more to the total stress than the effects of the built-in temperature gradient or the temperature at set time (section 7.5).

8.2 RECOMMENDATIONS

Based on the results of this study, the following recommendations are made:

- The finite element models developed in this study should also be used to superimpose a variety of vehicle loads and axle configurations to evaluate the combined effect of traffic and environmental loads.
- The finite element models developed in this study should also be used to evaluate the accuracy of the predicted stresses in the MEPDG. This would constitute an additional validation for the accuracy of the new design guide.
- Further research is needed to improve moisture prediction models that can be incorporated into the design process.

APPENDIX A

EARLY-AGE VIBRATING WIRE GAGE MEASUREMENTS

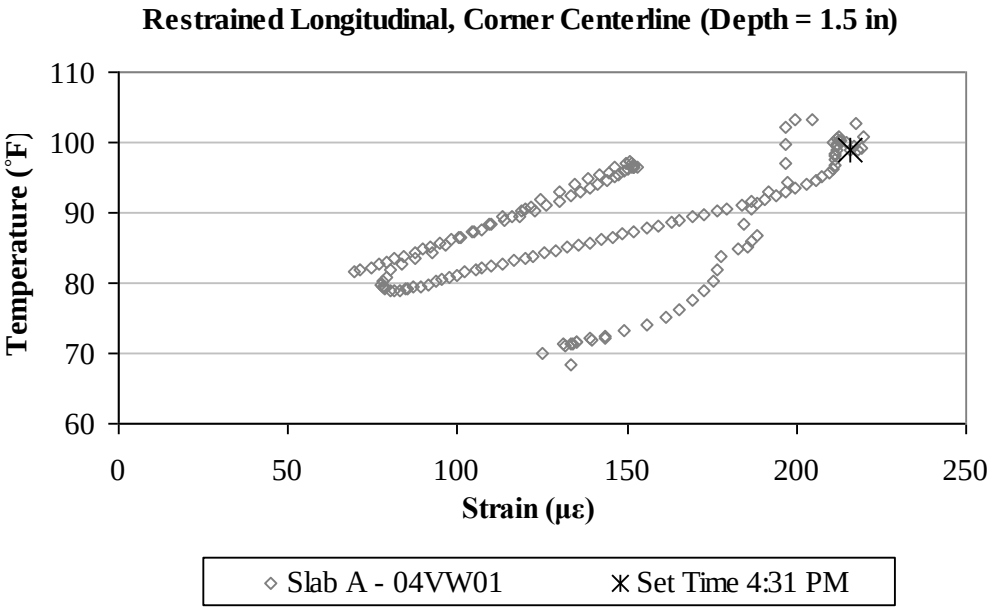

Figure A1. Early-age variation in the total strain with temperature, in the longitudinal direction, for the top sensor located at the corner along the centerline joint in restrained Slab A.

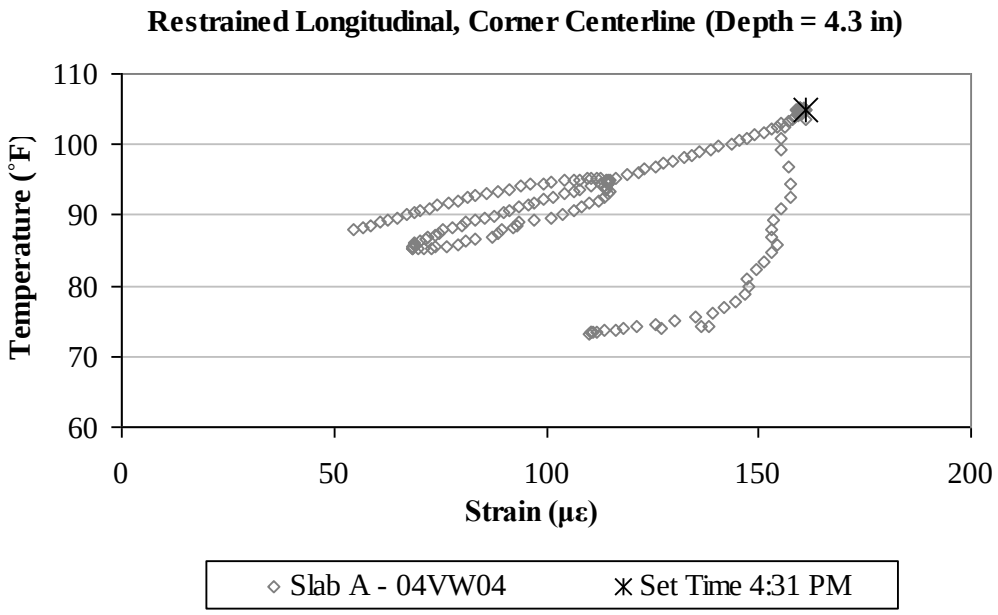

Figure A2. Early-age variation in the total strain with temperature, in the longitudinal direction, for the middepth sensor located at the corner along the centerline joint in restrained Slab A.

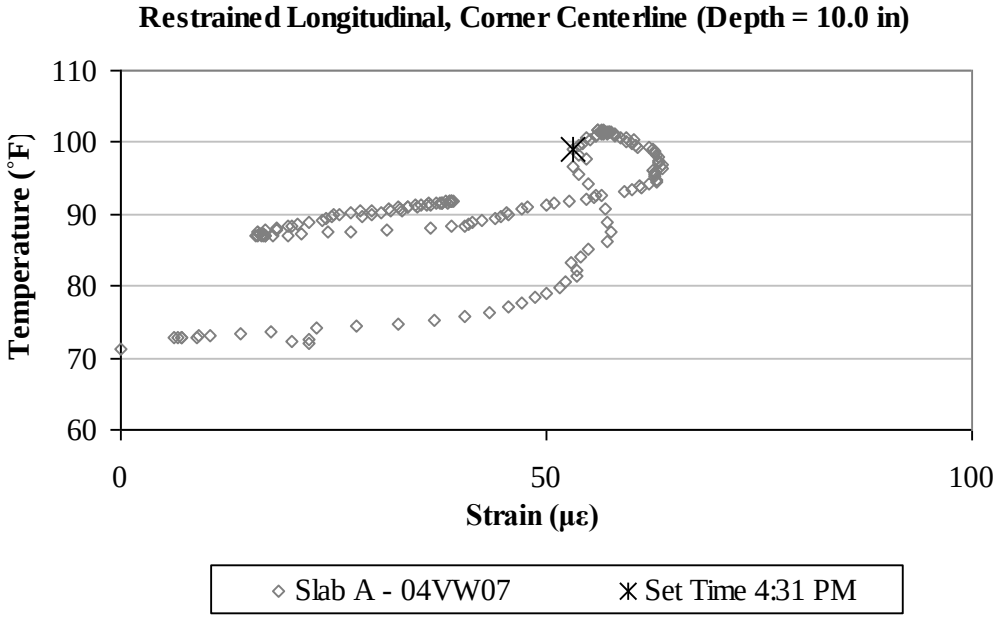

Figure A3. Early-age variation in the total strain with temperature, in the longitudinal direction, for the bottom sensor located at the corner along the centerline joint in restrained Slab A.

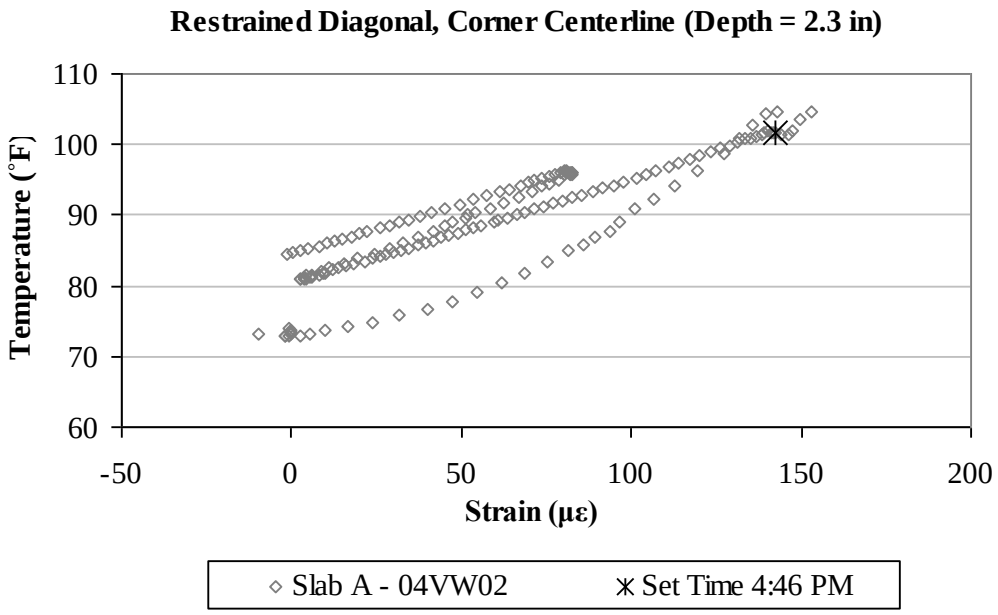

Figure A4. Early-age variation in the total strain with temperature, in the diagonal direction, for the top sensor located at the corner along the centerline joint in restrained Slab A.

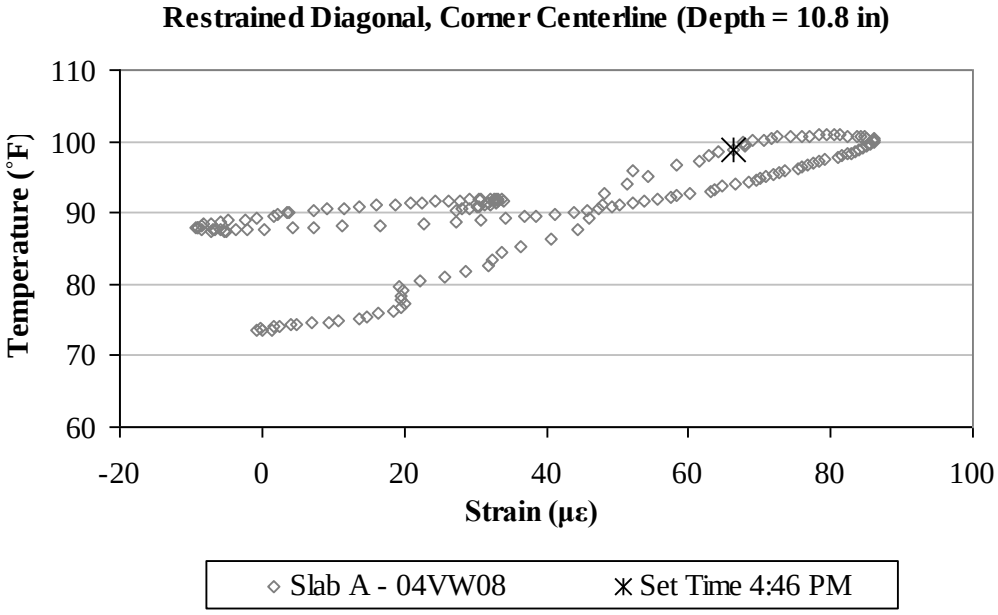

Figure A5. Early-age variation in the total strain with temperature, in the diagonal direction, for the bottom sensor located at the corner along the centerline joint in restrained Slab A.

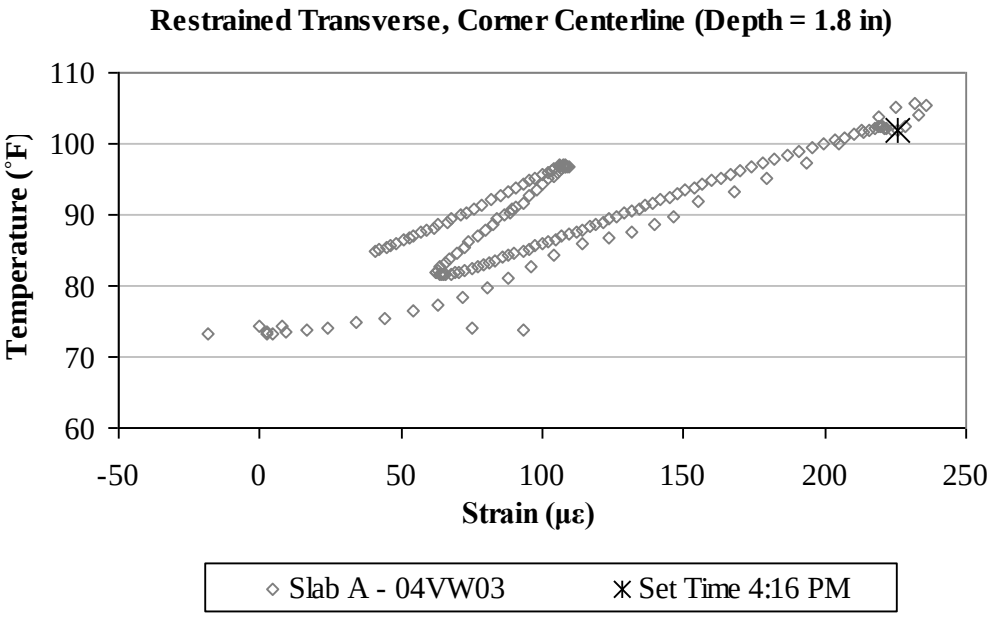

Figure A6. Early-age variation in the total strain with temperature, in the transverse direction, for the top sensor located at the corner along the centerline joint in restrained Slab A.

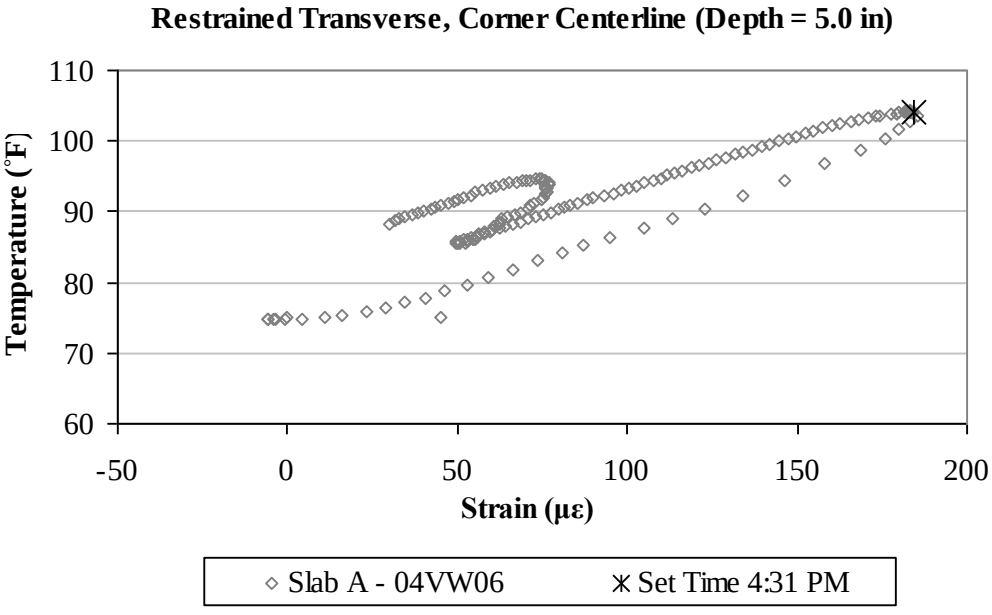

Figure A7. Early-age variation in the total strain with temperature, in the transverse direction, for the middepth sensor located at the corner along the centerline joint in restrained Slab A.

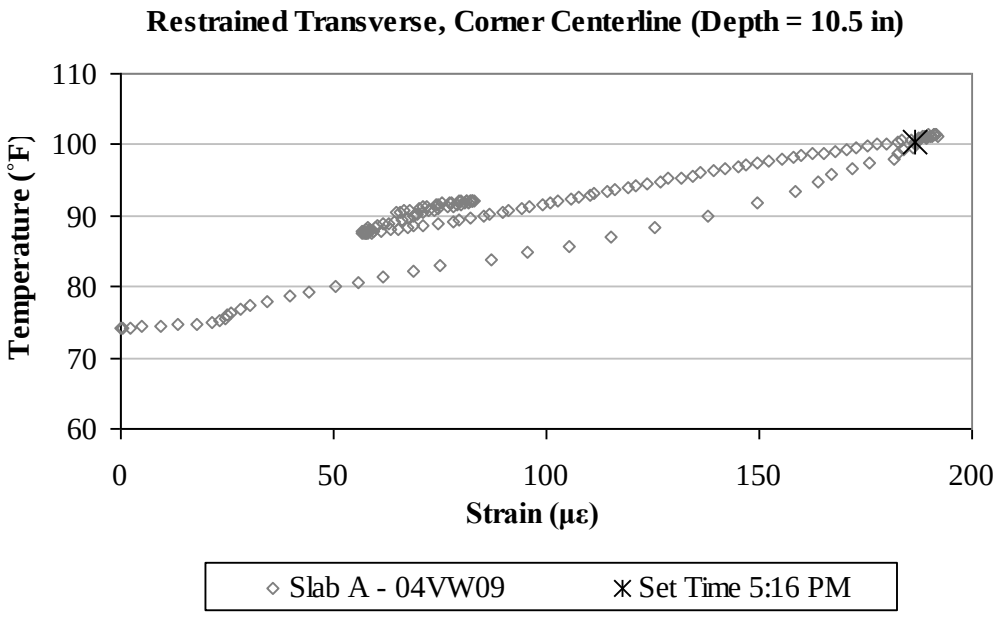

Figure A8. Early-age variation in the total strain with temperature, in the transverse direction, for the bottom sensor located at the corner along the centerline joint in restrained Slab A.

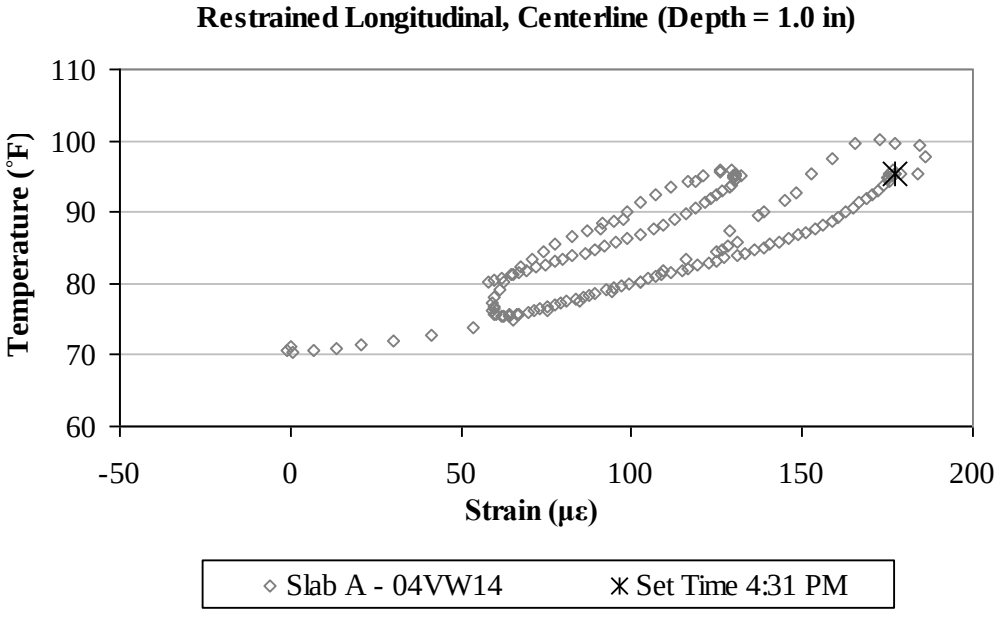

Figure A9. Early-age variation in the total strain with temperature, in the longitudinal direction, for the top sensor located along the centerline joint in restrained Slab A.

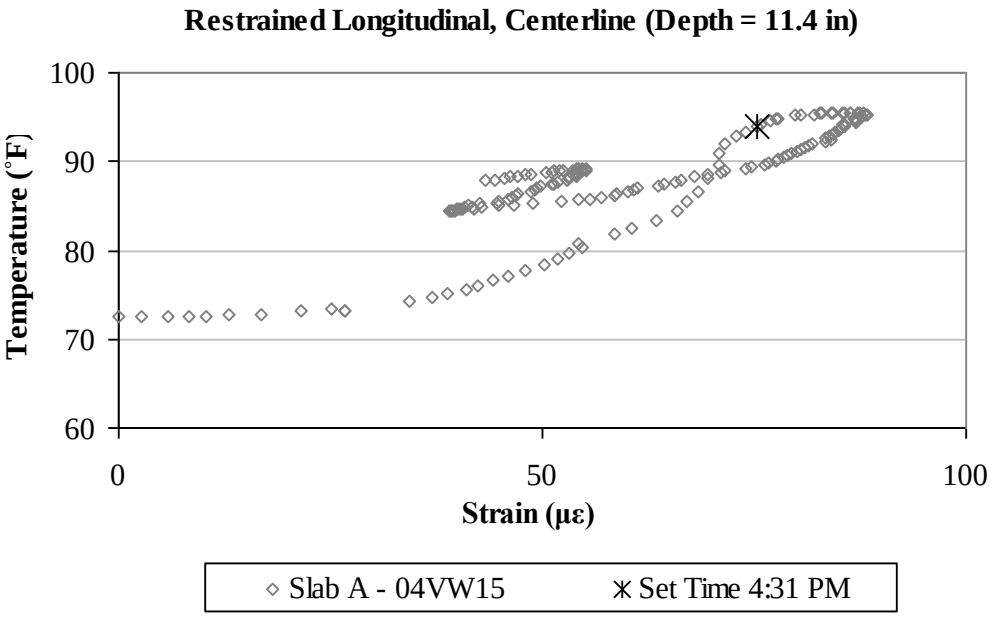

Figure A10. Early-age variation in the total strain with temperature, in the longitudinal direction, for the bottom sensor located along the centerline joint in restrained Slab A.

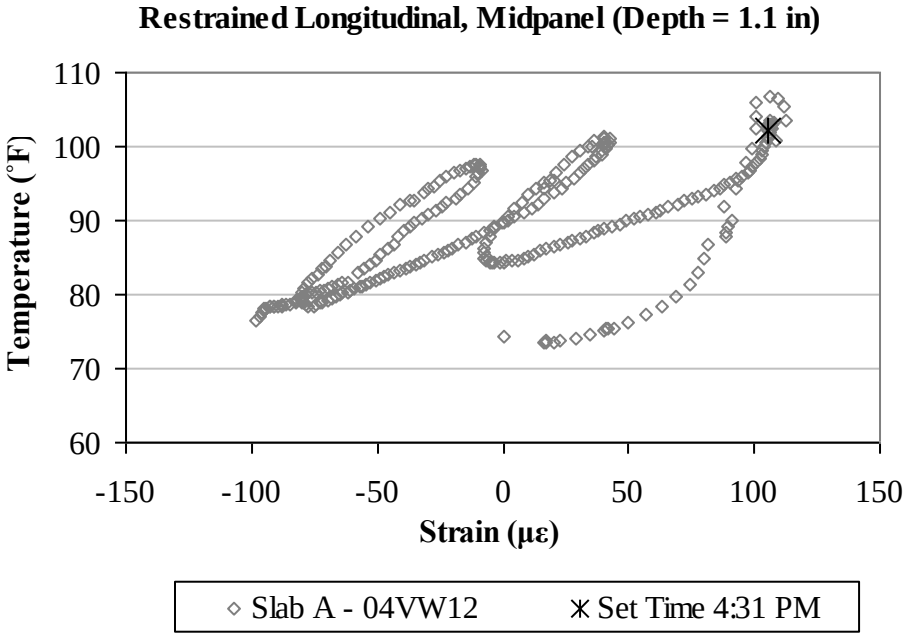

Figure A11. Early-age variation in the total strain with temperature, in the longitudinal direction, for the top sensor located at midpanel in restrained Slab A.

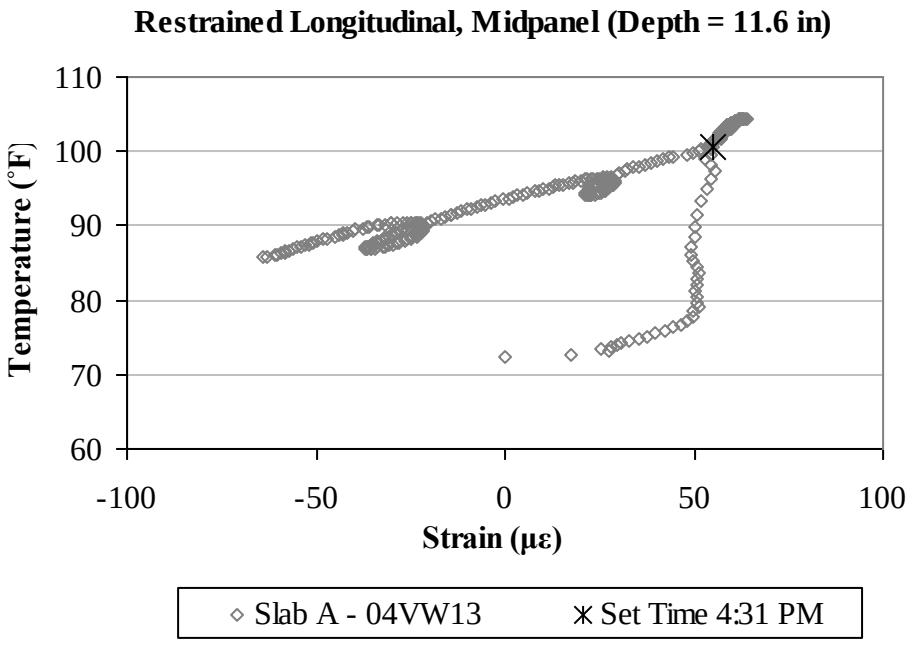

Figure A12. Early-age variation in the total strain with temperature, in the longitudinal direction, for the bottom sensor located at midpanel in restrained Slab A.

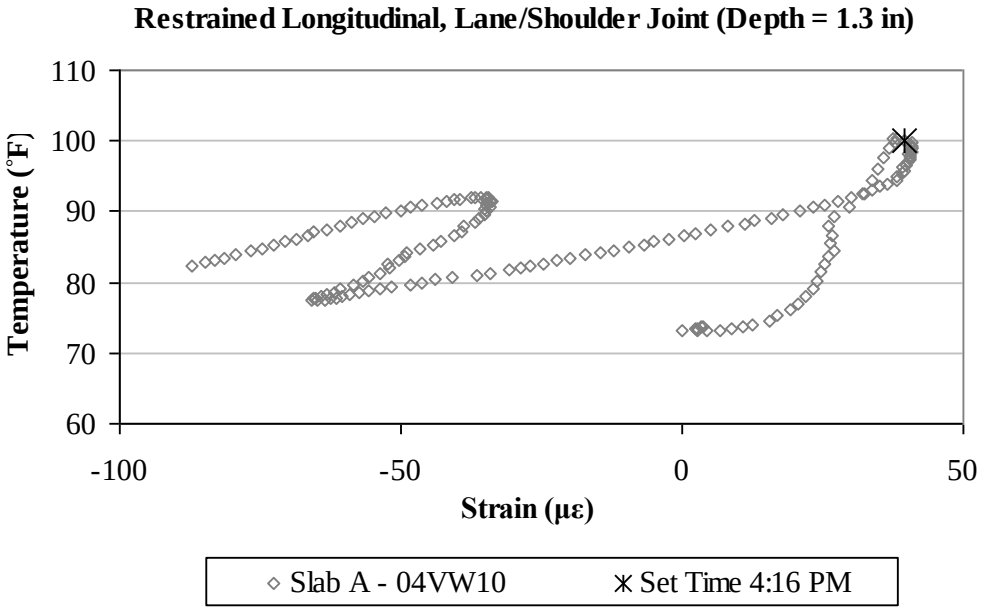

Figure A13. Early-age variation in the total strain with temperature, in the longitudinal direction, for the top sensor located along the lane/shoulder joint in restrained Slab A.

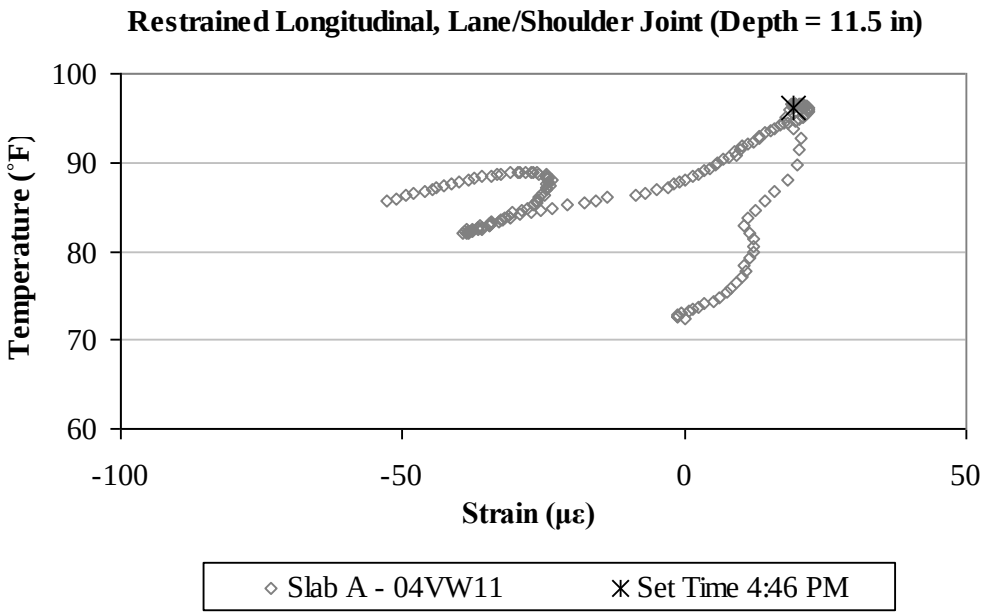

Figure A14. Early-age variation in the total strain with temperature, in the longitudinal direction, for the bottom sensor located along the lane/shoulder joint in restrained Slab A.

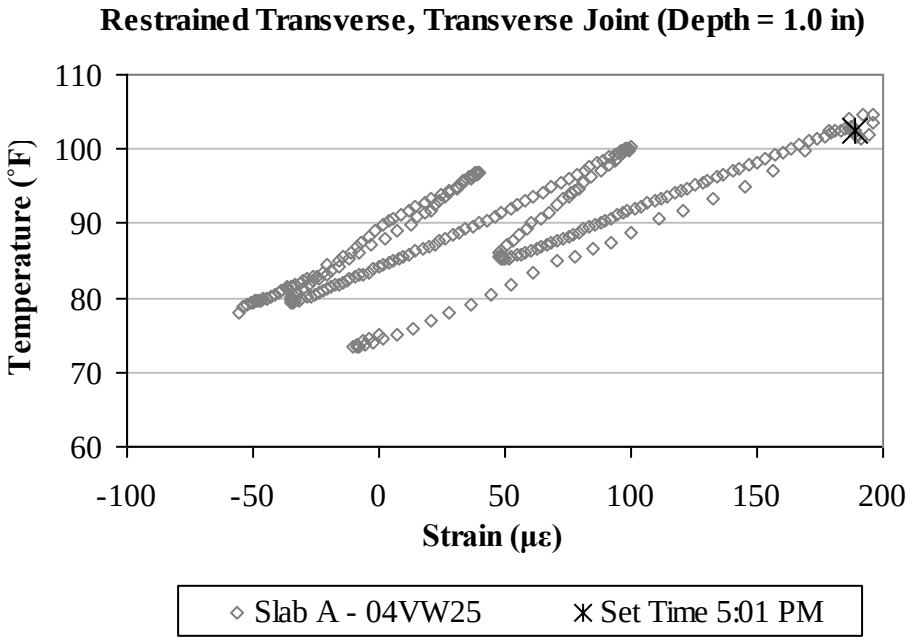

Figure A15. Early-age variation in the total strain with temperature, in the transverse direction, for the top sensor located along the transverse joint in restrained Slab A.

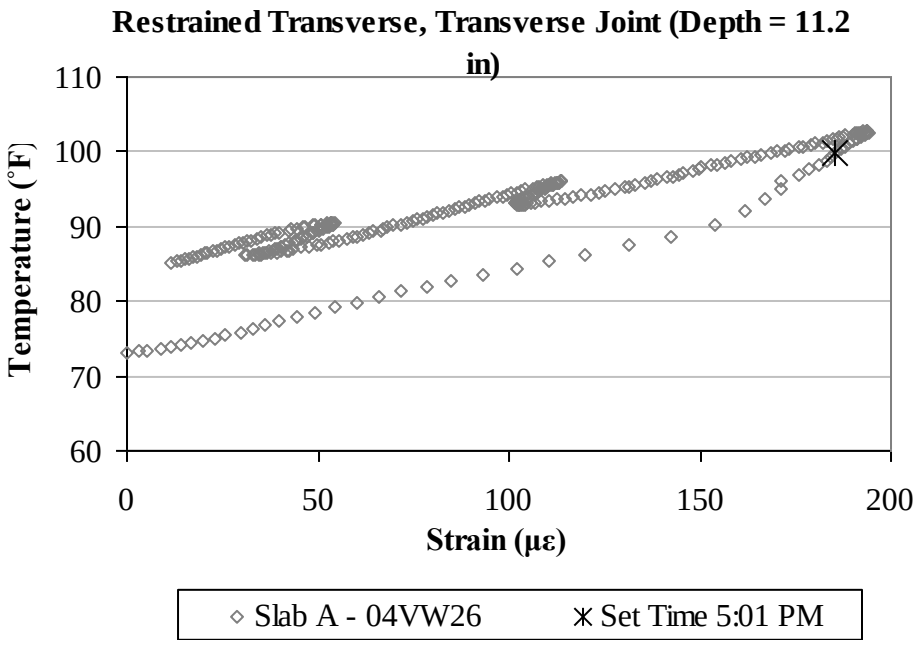

Figure A16. Early-age variation in the total strain with temperature, in the transverse direction, for the bottom sensor located along the transverse joint in restrained Slab A.

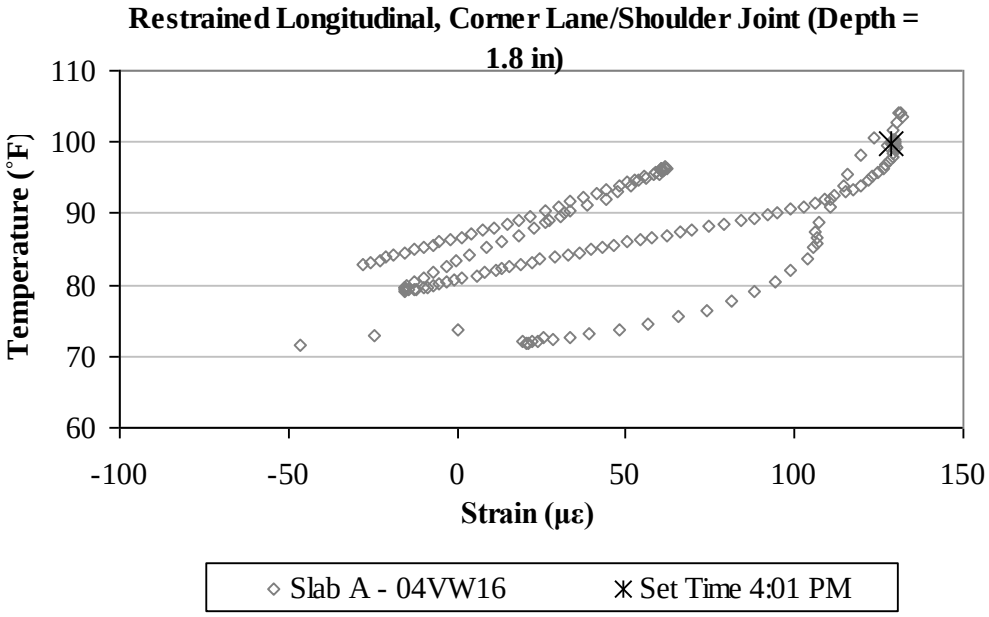

Figure A17. Early-age variation in the total strain with temperature, in the longitudinal direction, for the top sensor located at the corner along the lane/shoulder joint in restrained Slab A.

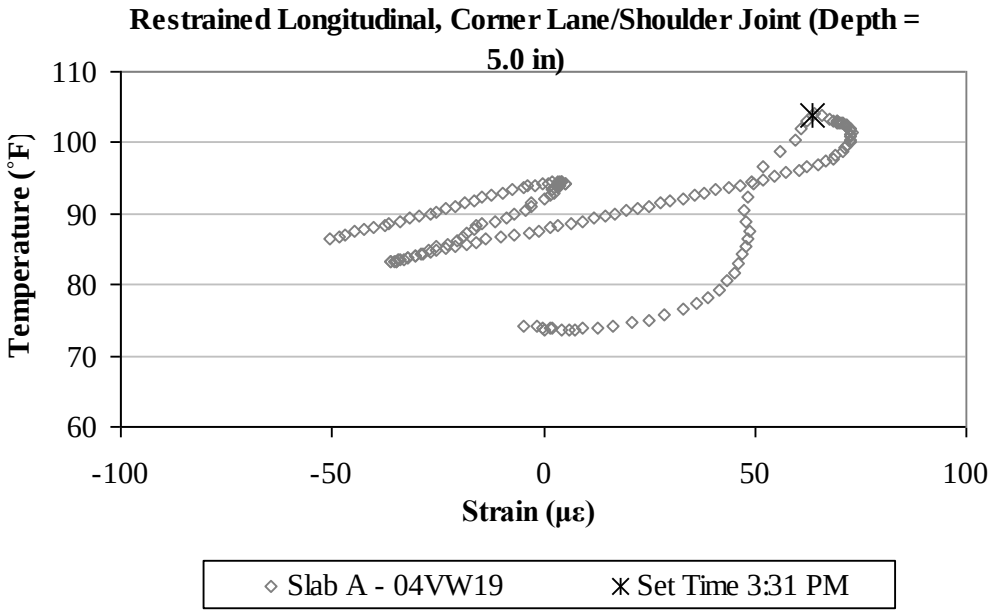

Figure A18. Early-age variation in the total strain with temperature, in the longitudinal direction, for the middepth sensor located at the corner along the lane/shoulder joint in restrained Slab A.

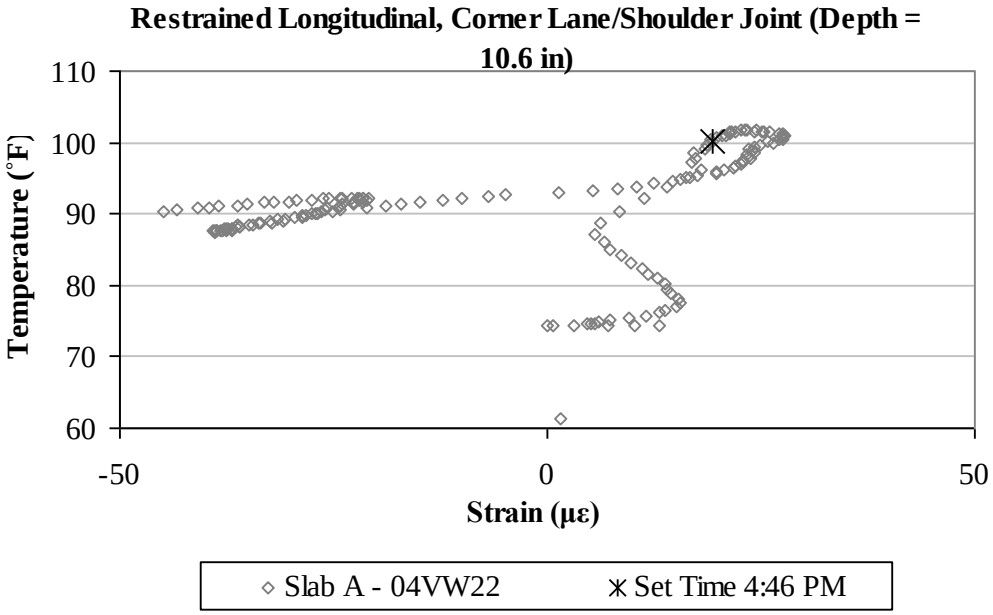

Figure A19. Early-age variation in the total strain with temperature, in the longitudinal direction, for the bottom sensor located at the corner along the lane/shoulder joint in restrained Slab A.

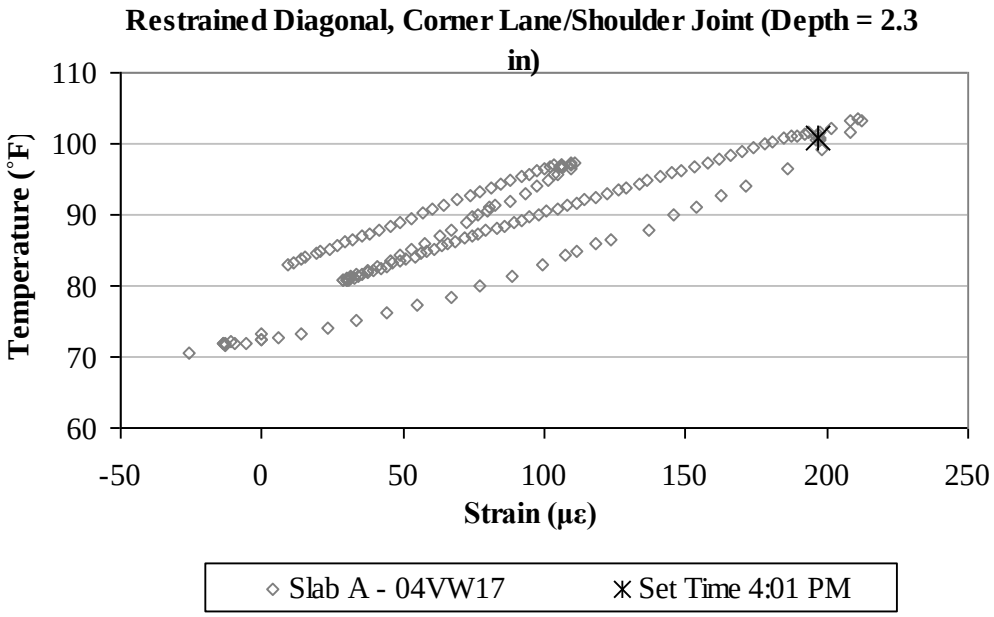

Figure A20. Early-age variation in the total strain with temperature, in the diagonal direction, for the top sensor located at the corner along the lane/shoulder joint in restrained Slab A.

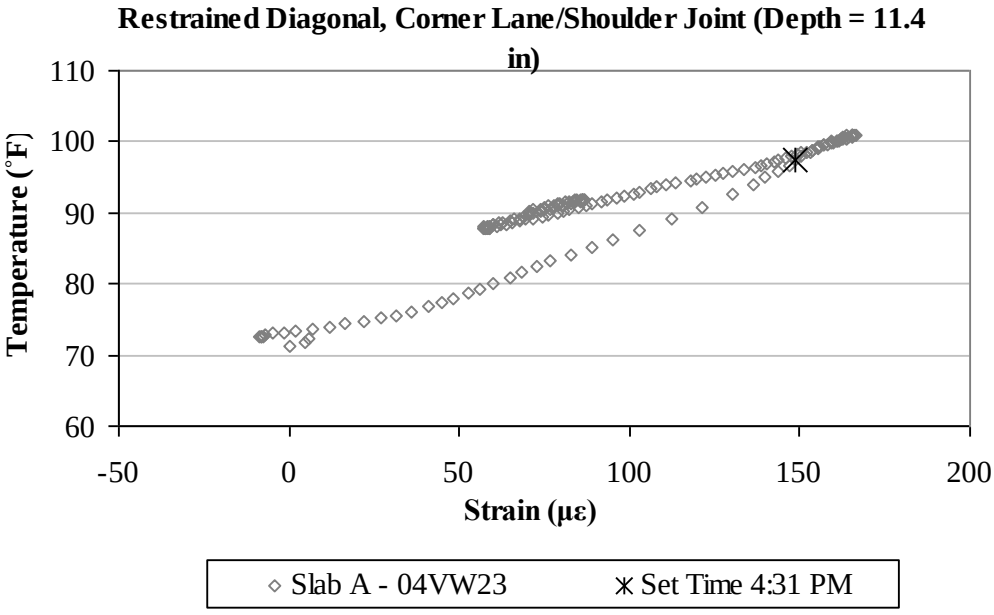

Figure A21. Early-age variation in the total strain with temperature, in the diagonal direction, for the bottom sensor located at the corner along the lane/shoulder joint in restrained Slab A.

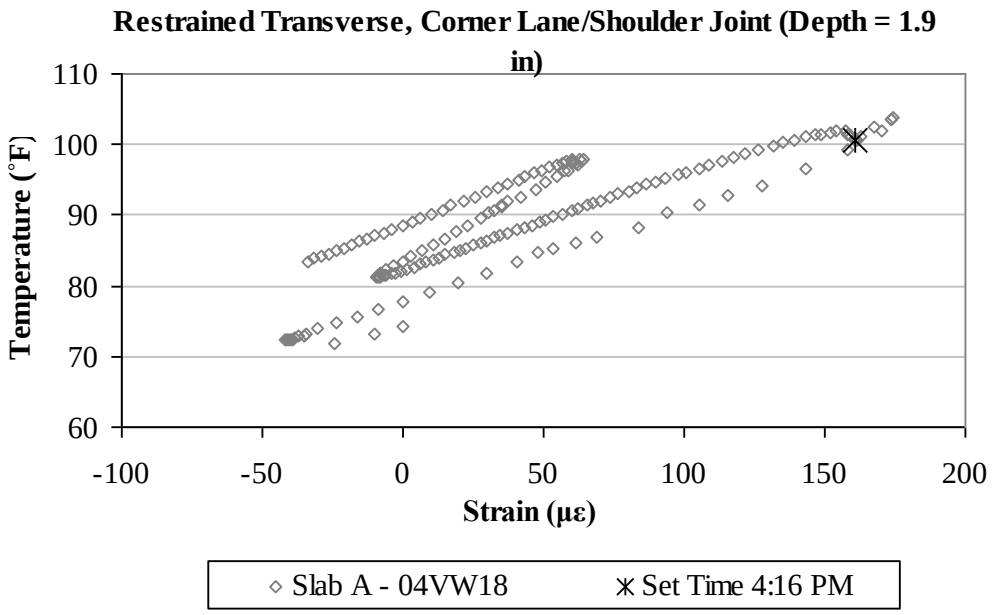

Figure A22. Early-age variation in the total strain with temperature, in the transverse direction, for the top sensor located at the corner along the lane/shoulder joint in restrained Slab A.

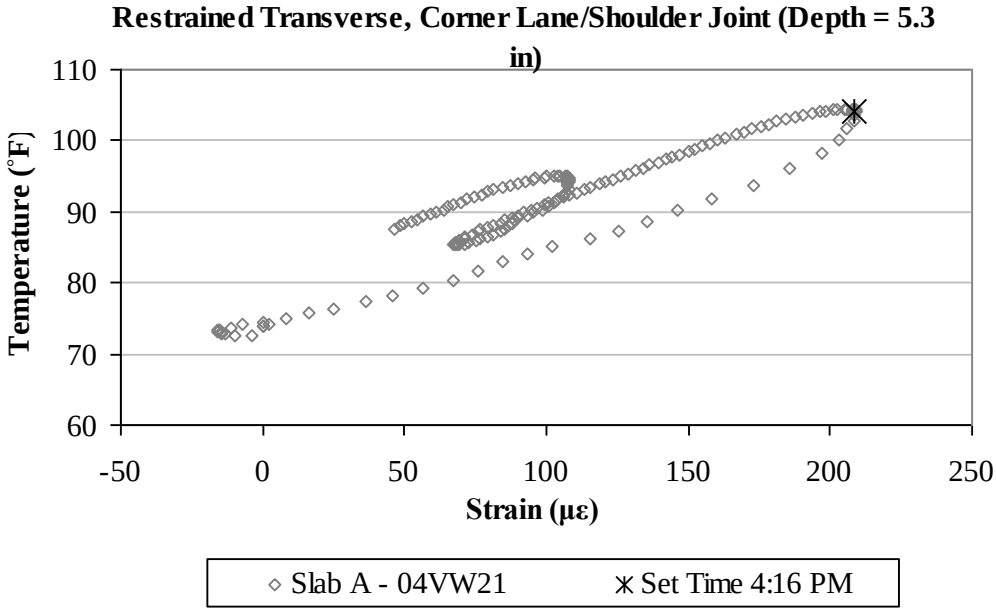

Figure A23. Early-age variation in the total strain with temperature, in the transverse direction, for the middepth sensor located at the corner along the lane/shoulder joint in restrained Slab A.

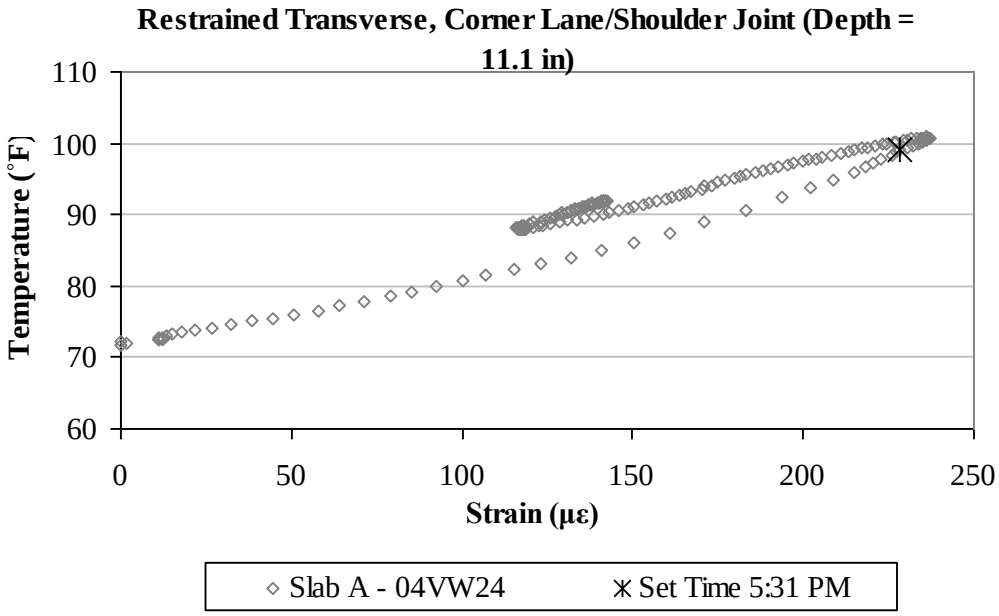

Figure A24. Early-age variation in the total strain with temperature, in the transverse direction, for the bottom sensor located at the corner along the lane/shoulder joint in restrained Slab A.

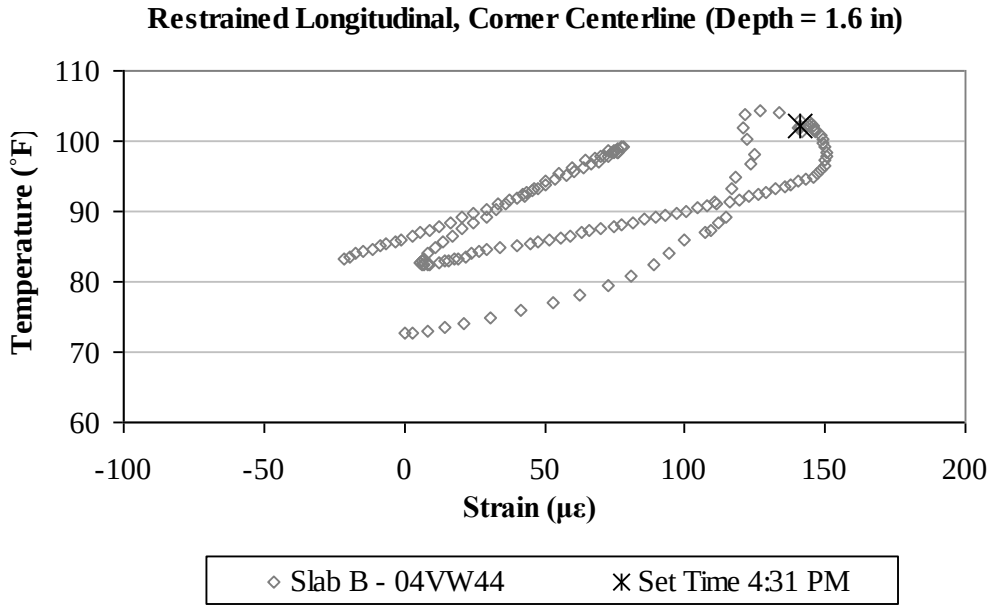

Figure A25. Early-age variation in the total strain with temperature, in the longitudinal direction, for the top sensor located at the corner along the centerline joint in restrained Slab B.

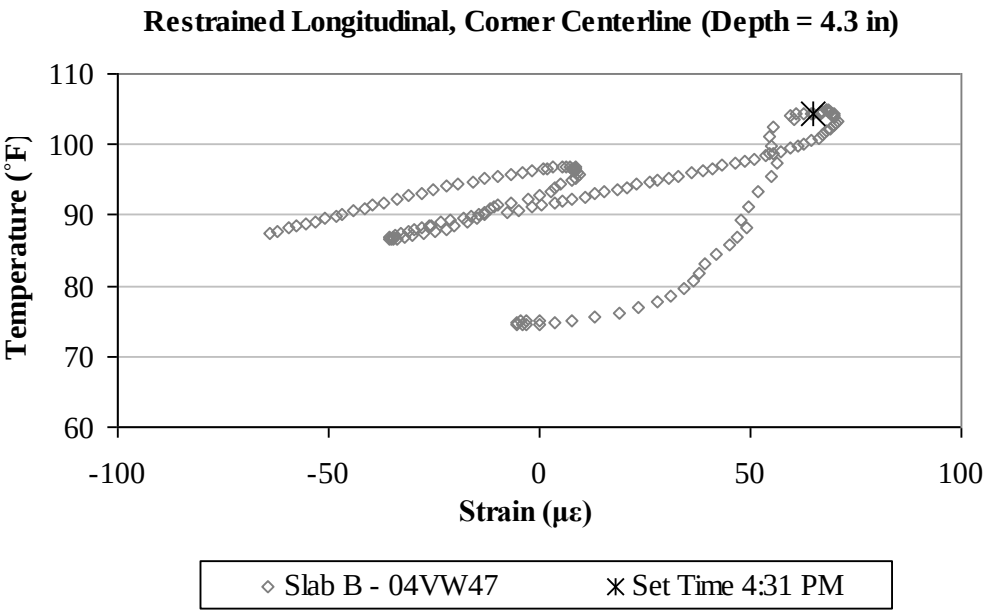

Figure A26. Early-age variation in the total strain with temperature, in the longitudinal direction, for the middepth sensor located at the corner along the centerline joint in restrained Slab B.

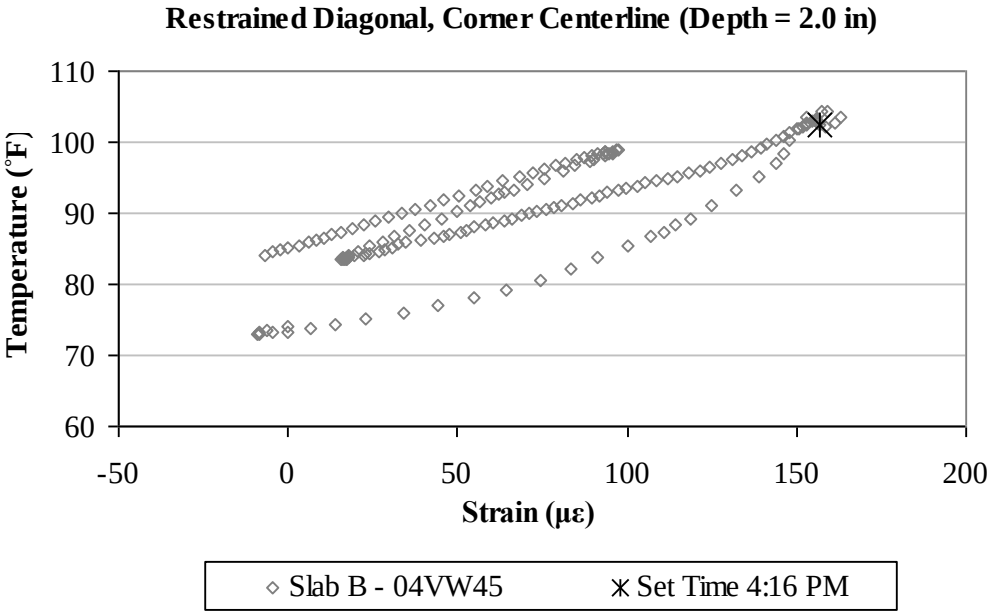

Figure A27. Early-age variation in the total strain with temperature, in the diagonal direction, for the top sensor located at the corner along the centerline joint in restrained Slab B.

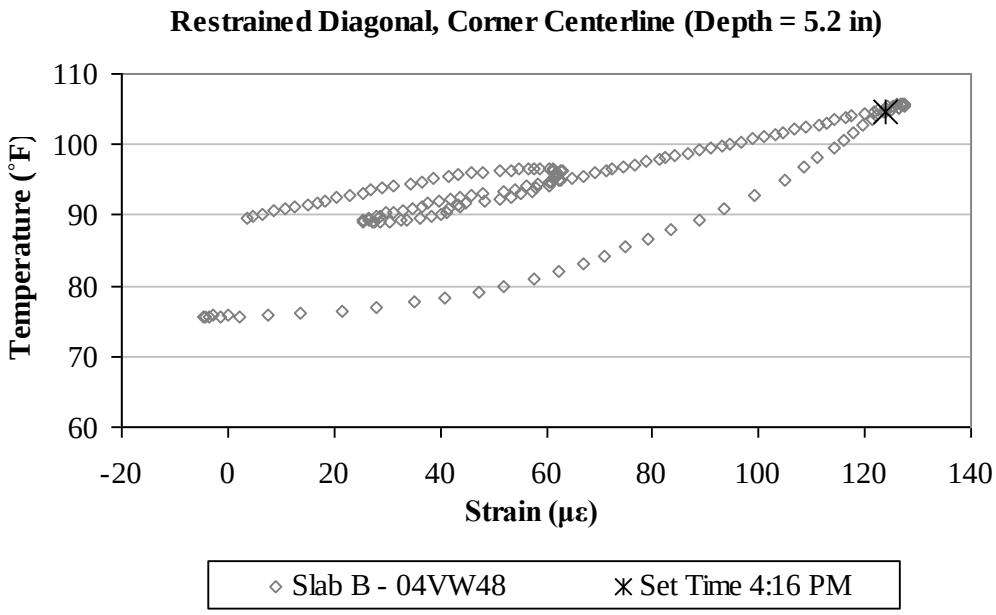

Figure A28. Early-age variation in the total strain with temperature, in the diagonal direction, for the middepth sensor located at the corner along the centerline joint in restrained Slab B.

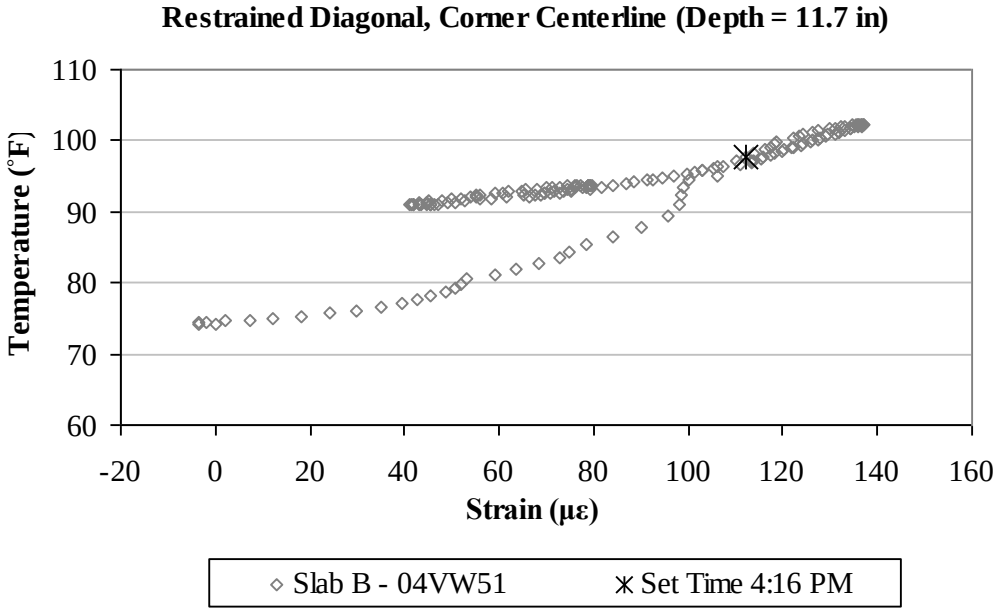

Figure A29. Early-age variation in the total strain with temperature, in the diagonal direction, for the bottom sensor located at the corner along the centerline joint in restrained Slab B.

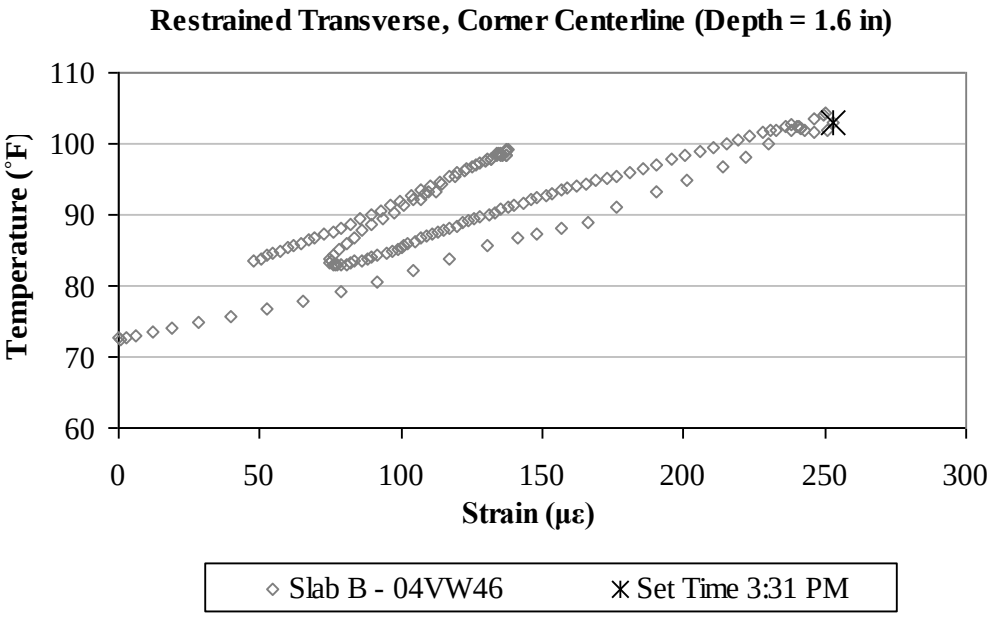

Figure A30. Early-age variation in the total strain with temperature, in the transverse direction, for the top sensor located at the corner along the centerline joint in restrained Slab B.

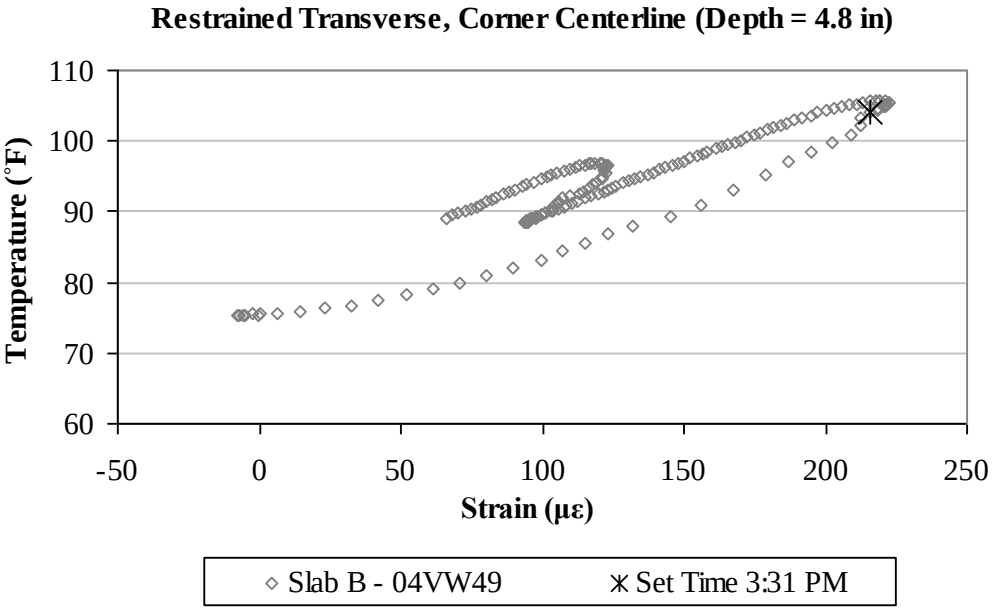

Figure A31. Early-age variation in the total strain with temperature, in the transverse direction, for the middepth sensor located at the corner along the centerline joint in restrained Slab B.

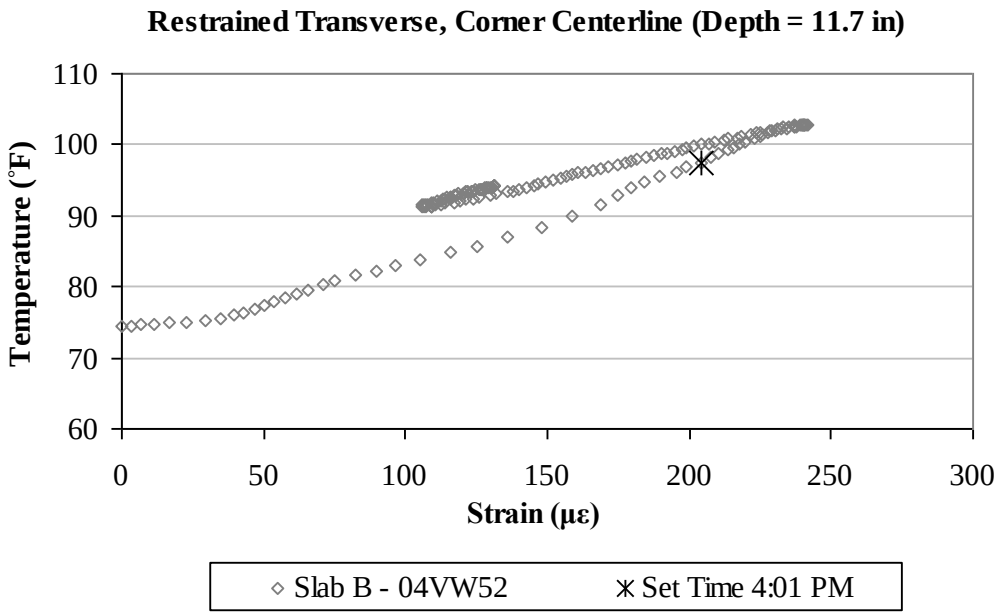

Figure A32. Early-age variation in the total strain with temperature, in the transverse direction, for the bottom sensor located at the corner along the centerline joint in restrained Slab B.

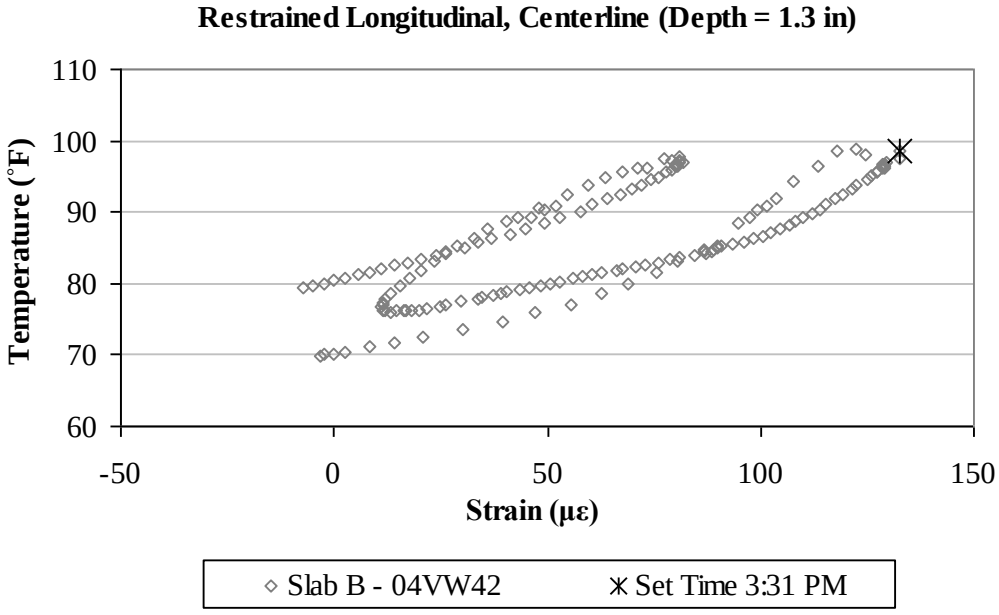

Figure A33. Early-age variation in the total strain with temperature, in the longitudinal direction, for the top sensor located along the centerline joint in restrained Slab B.

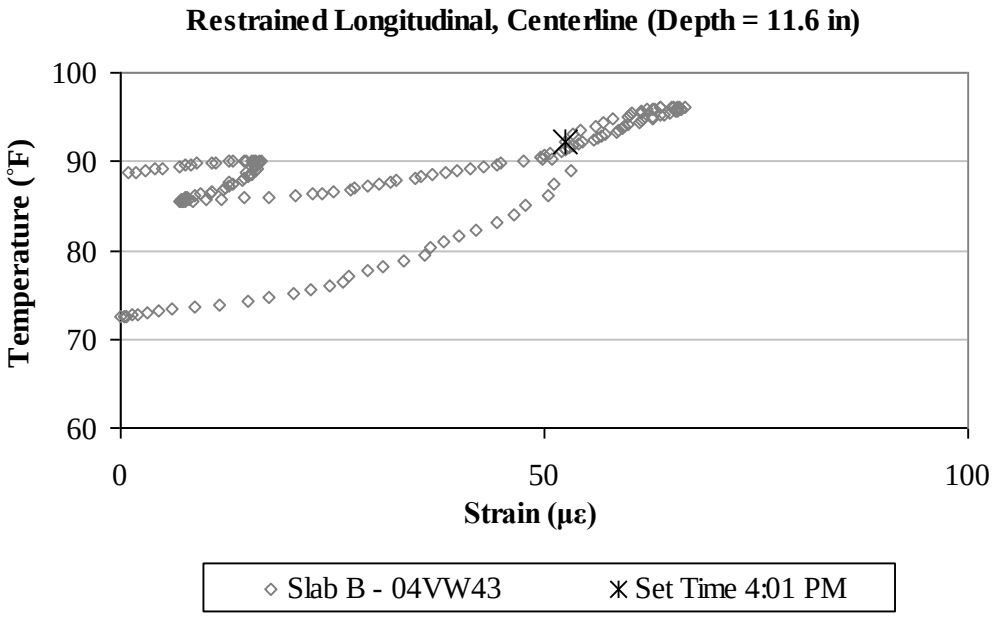

Figure A34. Early-age variation in the total strain with temperature, in the longitudinal direction, for the bottom sensor located along the centerline joint in restrained Slab B.

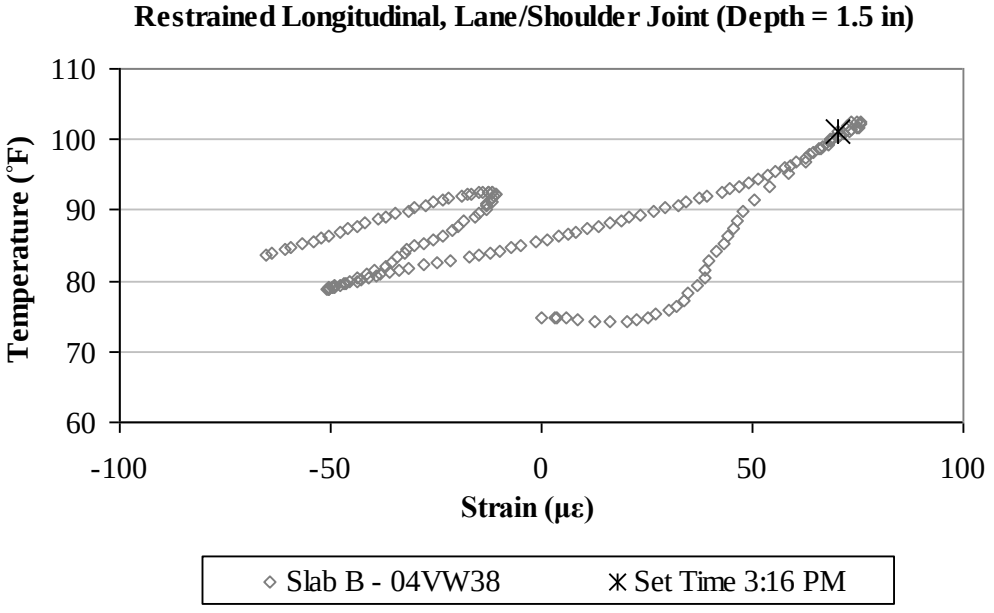

Figure A35. Early-age variation in the total strain with temperature, in the longitudinal direction, for the top sensor located along the lane/shoulder joint in restrained Slab B.

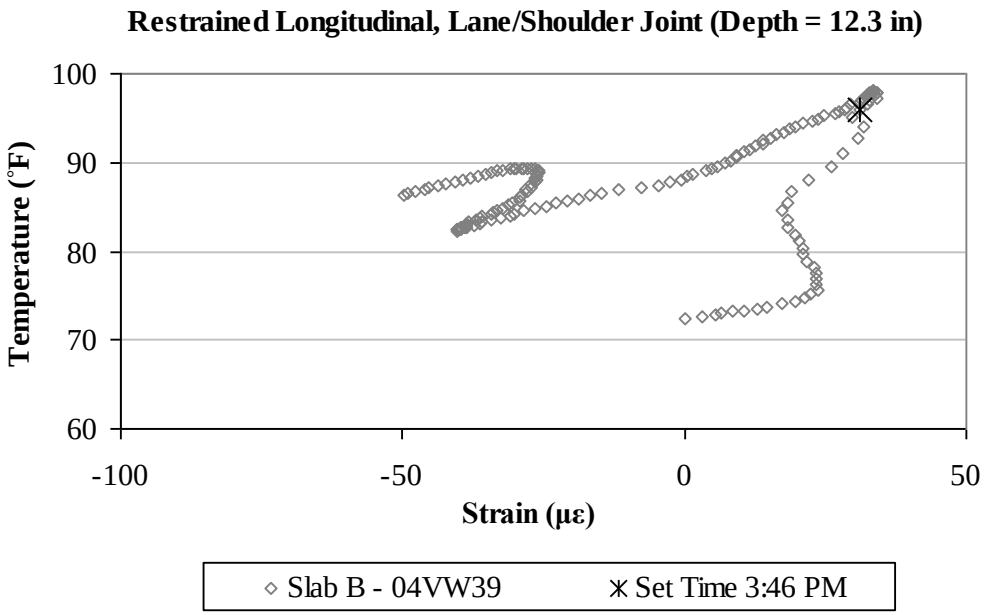

Figure A36. Early-age variation in the total strain with temperature, in the longitudinal direction, for the bottom sensor located along the lane/shoulder joint in restrained Slab B.

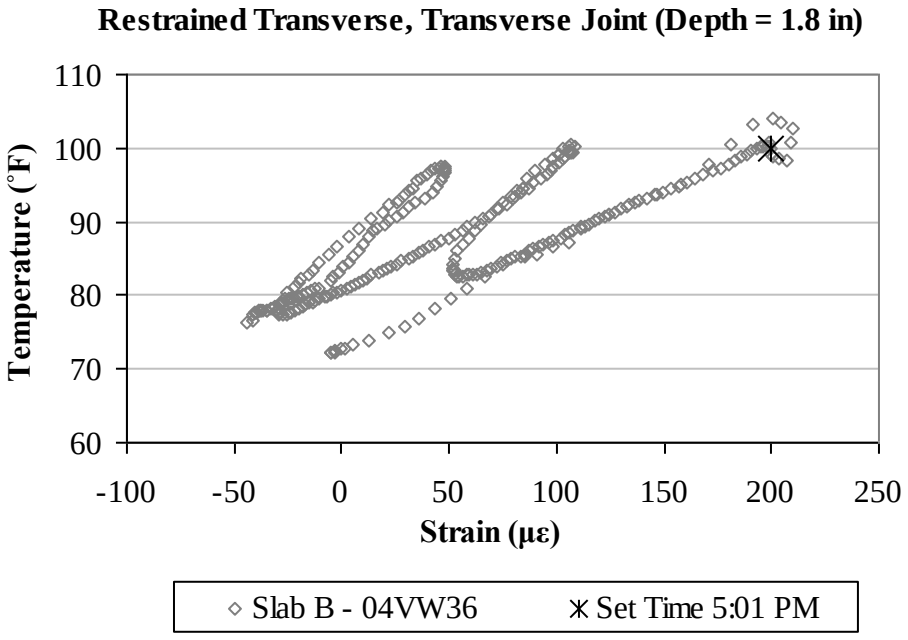

Figure A37. Early-age variation in the total strain with temperature, in the transverse direction, for the top sensor located along the transverse joint in restrained Slab B.

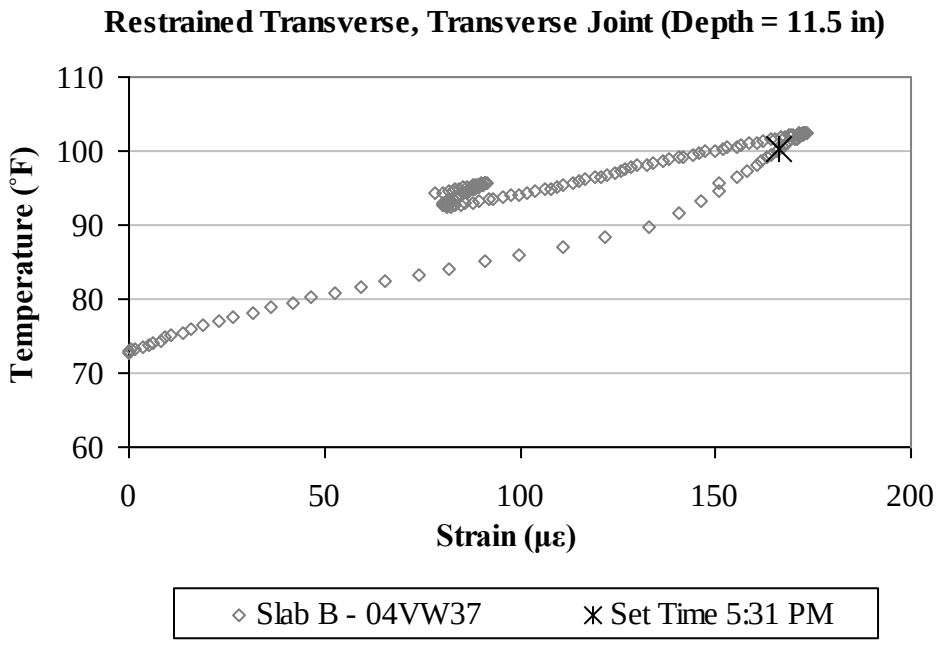

Figure A38. Early-age variation in the total strain with temperature, in the transverse direction, for the bottom sensor located along the transverse joint in restrained Slab B.

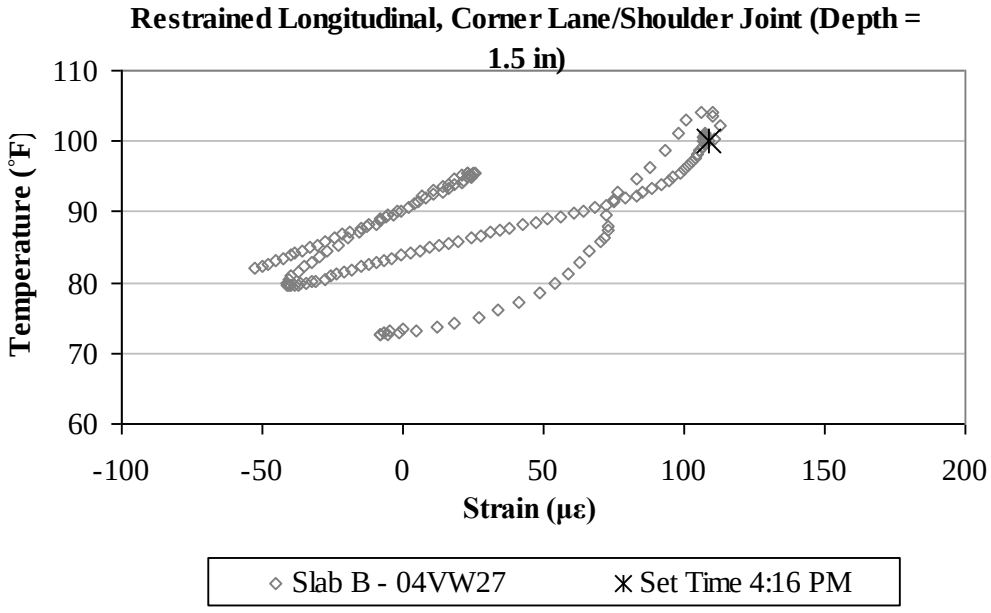

Figure A39. Early-age variation in the total strain with temperature, in the longitudinal direction, for the top sensor located at the corner along the lane/shoulder joint in restrained Slab B.

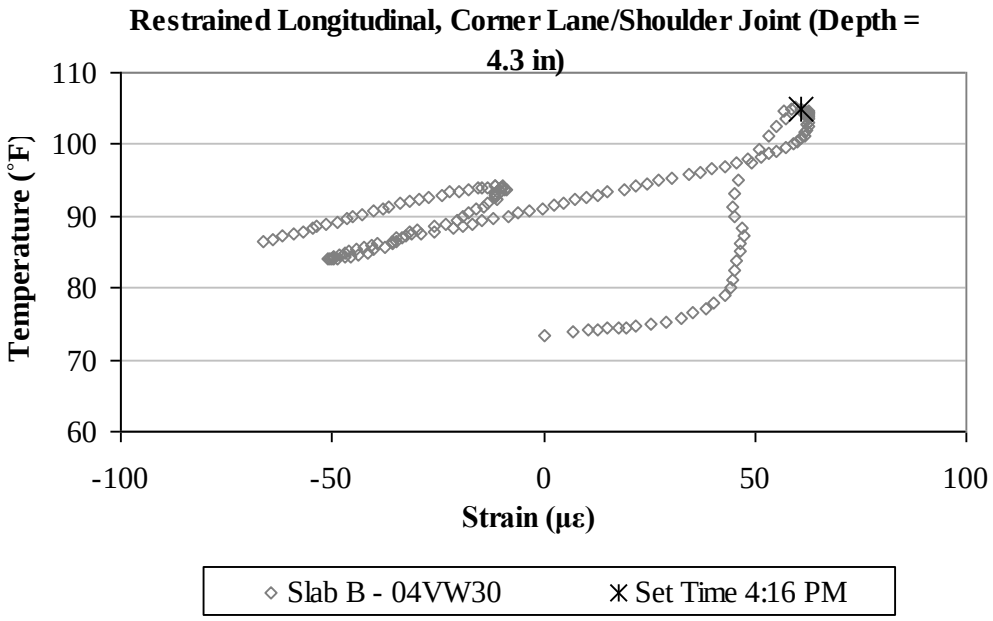

Figure A40. Early-age variation in the total strain with temperature, in the longitudinal direction, for the middepth sensor located at the corner along the lane/shoulder joint in restrained Slab B.

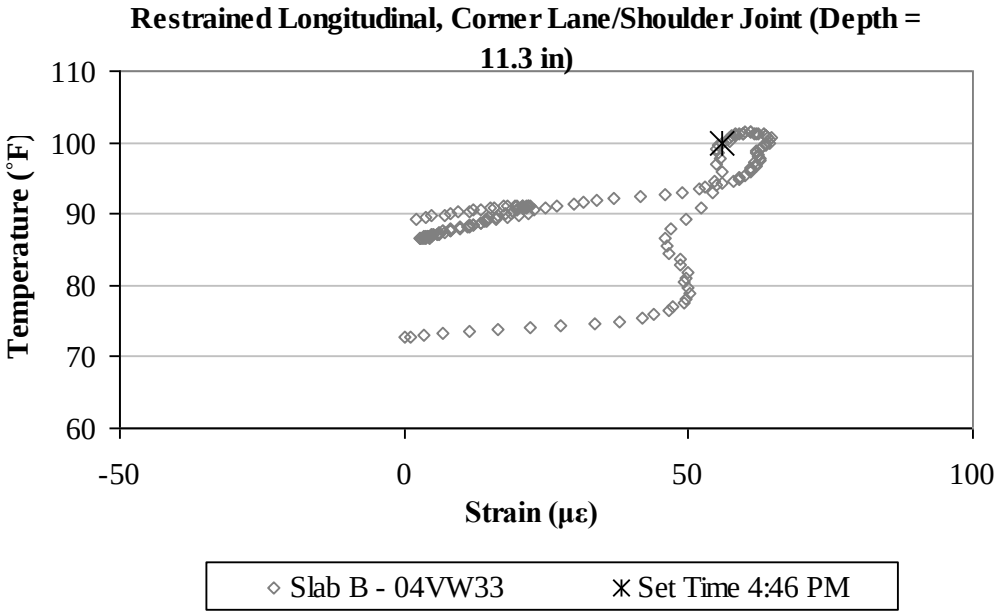

Figure A41. Early-age variation in the total strain with temperature, in the longitudinal direction, for the bottom sensor located at the corner along the lane/shoulder joint in restrained Slab B.

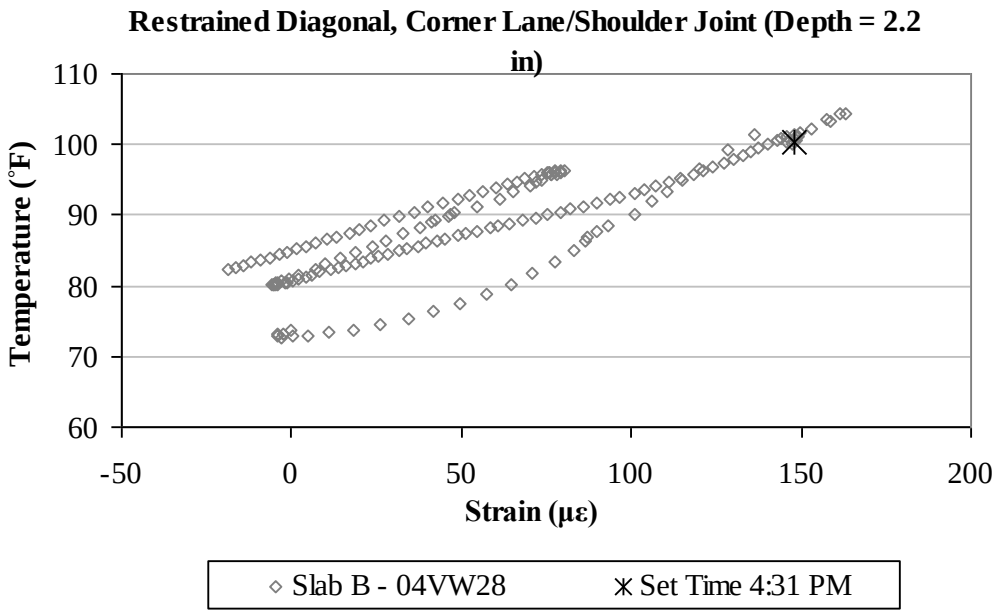

Figure A42. Early-age variation in the total strain with temperature, in the diagonal direction, for the top sensor located at the corner along the lane/shoulder joint in restrained Slab B.

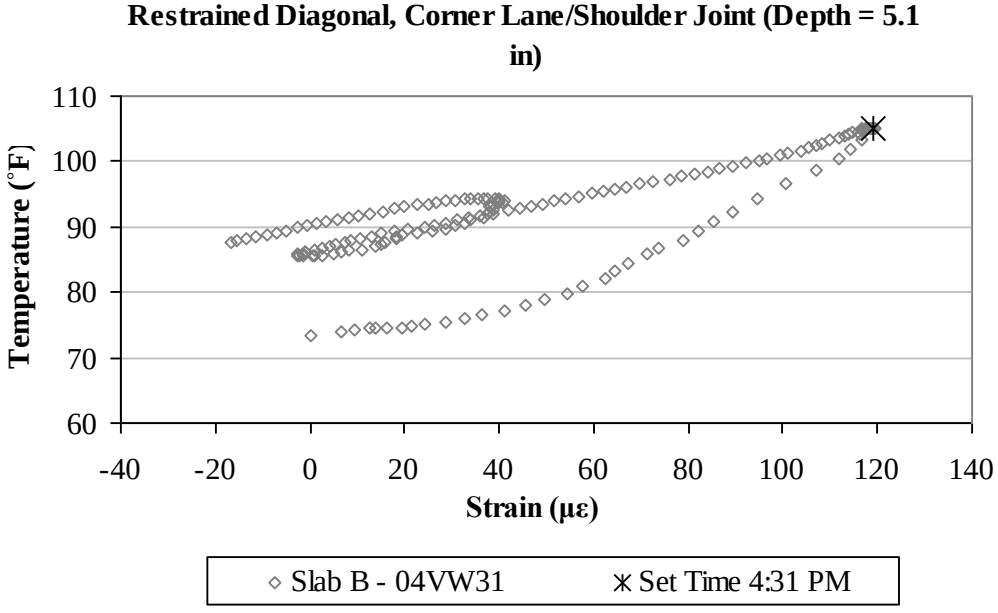

Figure A43. Early-age variation in the total strain with temperature, in the diagonal direction, for the middepth sensor located at the corner along the lane/shoulder joint in restrained Slab B.

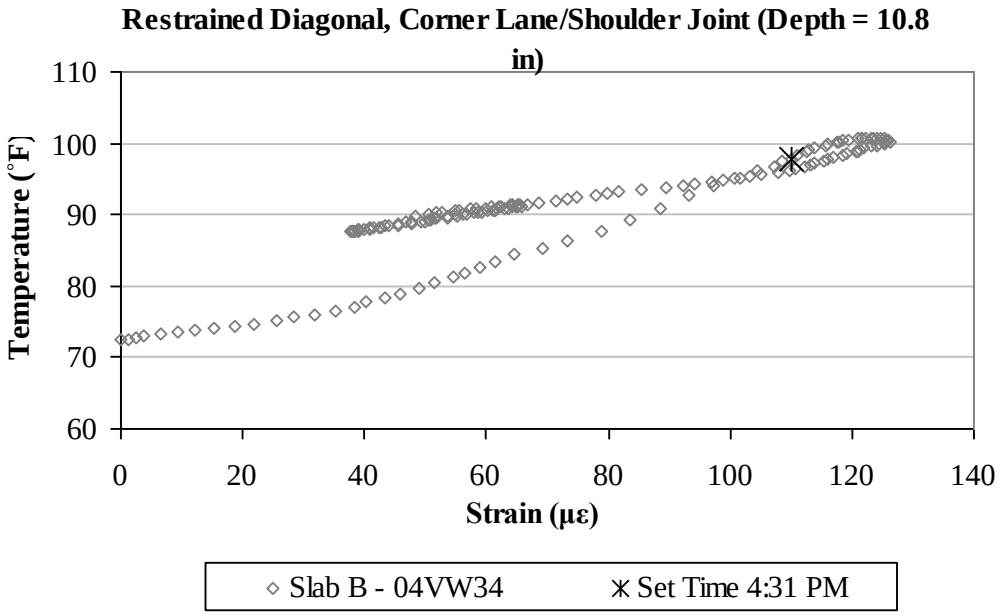

Figure A44. Early-age variation in the total strain with temperature, in the diagonal direction, for the bottom sensor located at the corner along the lane/shoulder joint in restrained Slab B.

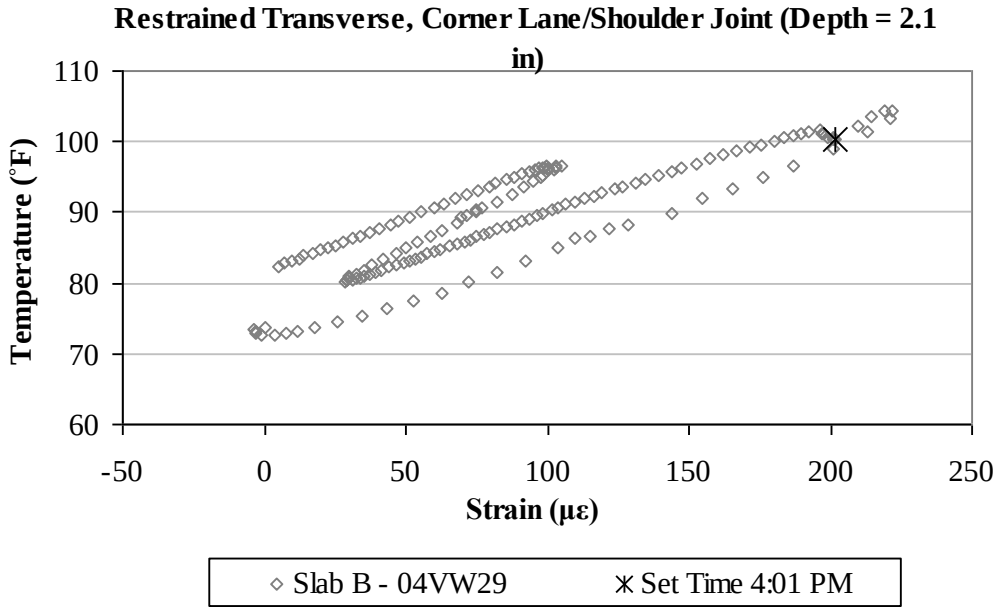

Figure A45. Early-age variation in the total strain with temperature, in the transverse direction, for the top sensor located at the corner along the lane/shoulder joint in restrained Slab B.

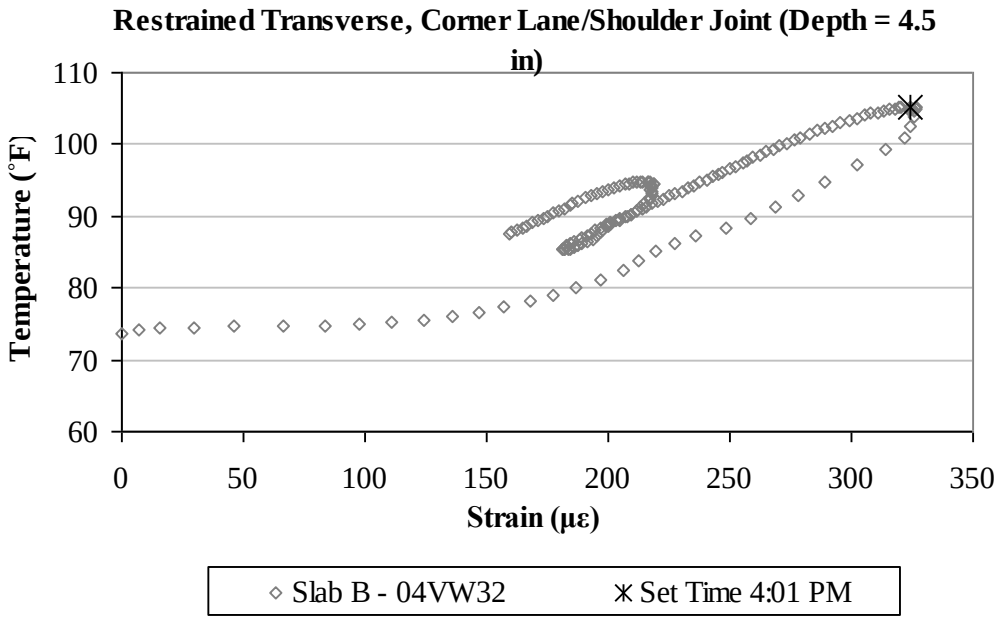

Figure A46. Early-age variation in the total strain with temperature, in the transverse direction, for the middepth sensor located at the corner along the lane/shoulder joint in restrained Slab B.

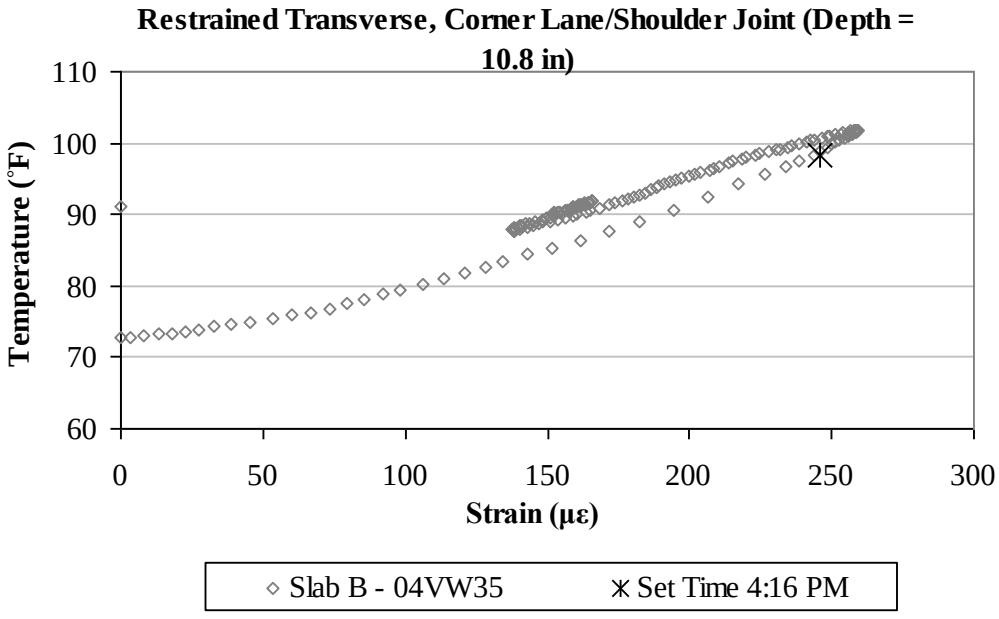

Figure A47. Early-age variation in the total strain with temperature, in the transverse direction, for the bottom sensor located at the corner along the lane/shoulder joint in restrained Slab B.

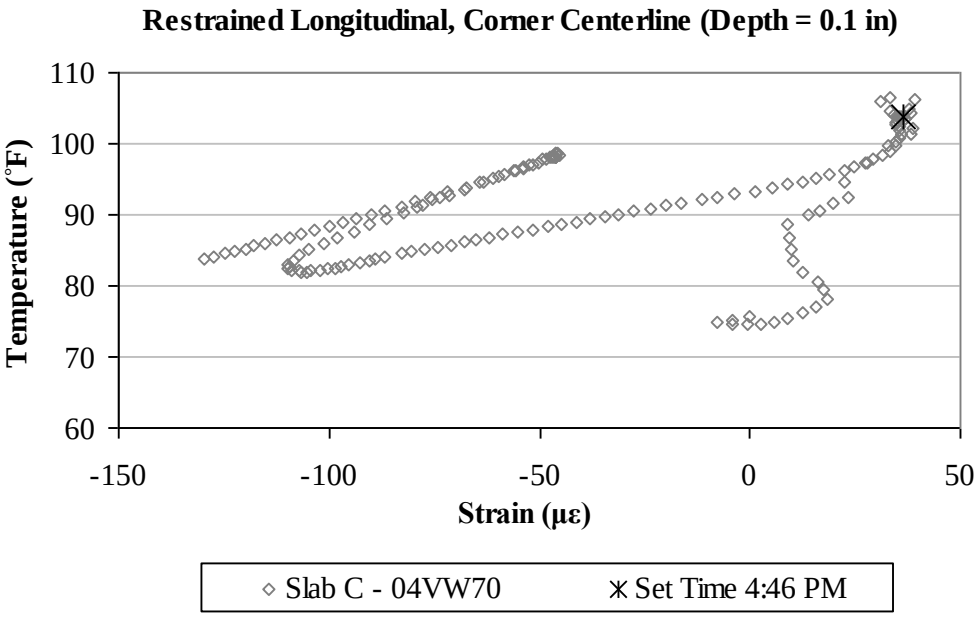

Figure A48. Early-age variation in the total strain with temperature, in the longitudinal direction, for the top sensor located at the corner along the centerline joint in restrained Slab C.

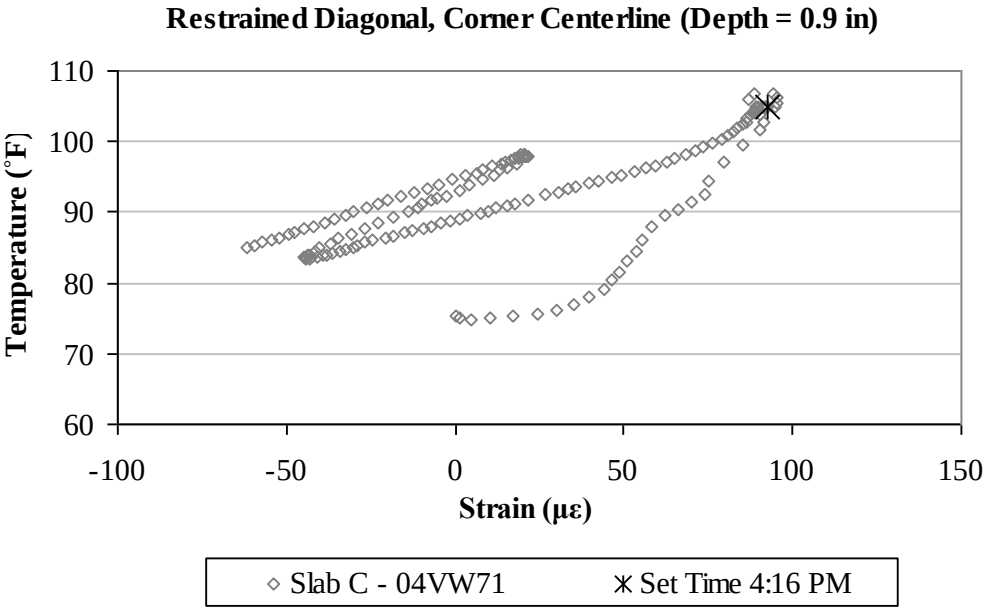

Figure A49. Early-age variation in the total strain with temperature, in the diagonal direction, for the top sensor located at the corner along the centerline joint in restrained Slab C.

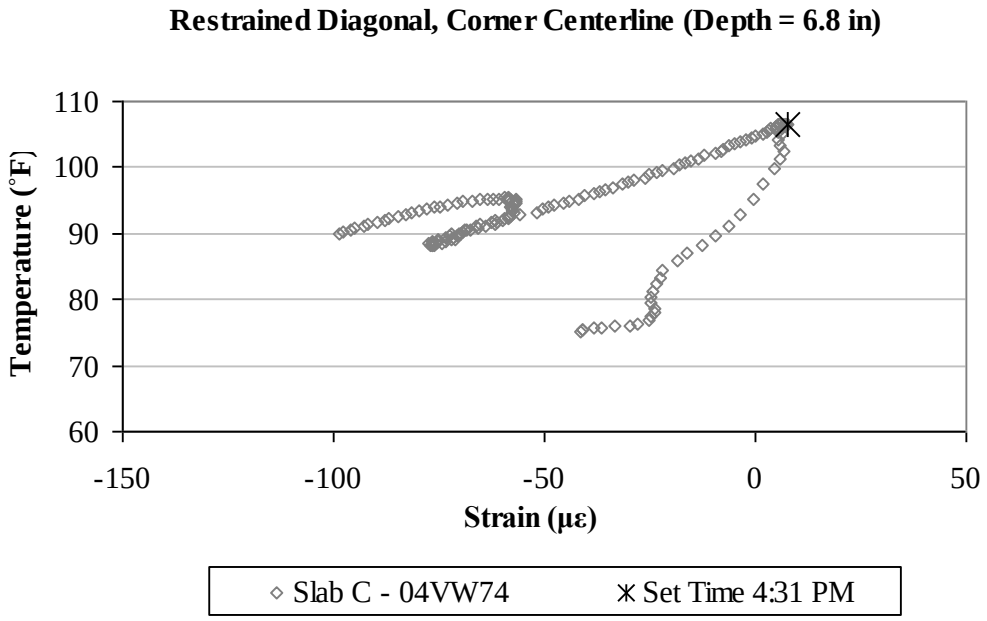

Figure A50. Early-age variation in the total strain with temperature, in the diagonal direction, for the middepth sensor located at the corner along the centerline joint in restrained Slab C.

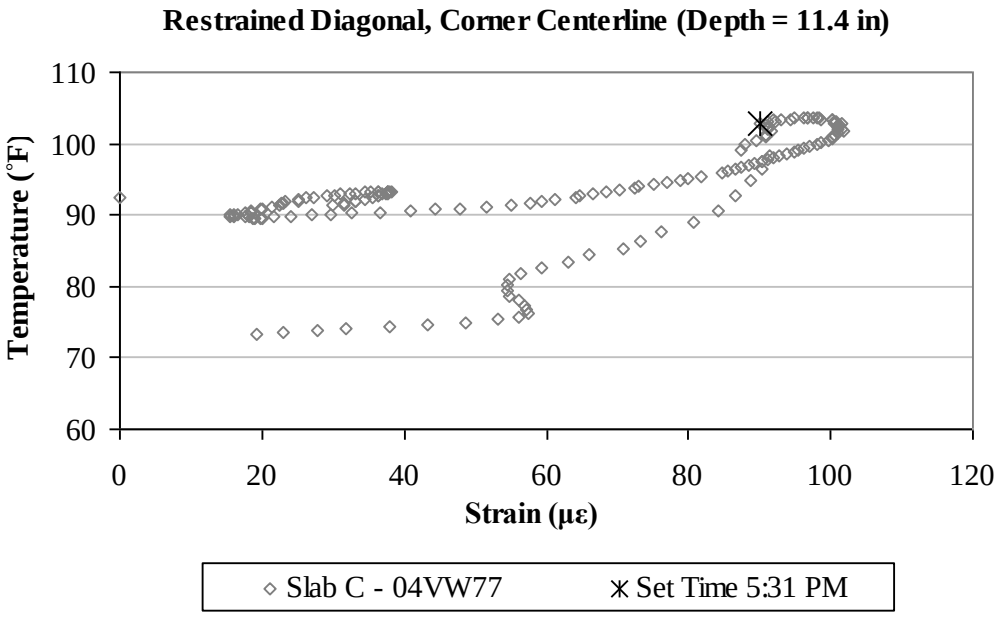

Figure A51. Early-age variation in the total strain with temperature, in the diagonal direction, for the bottom sensor located at the corner along the centerline joint in restrained Slab C.

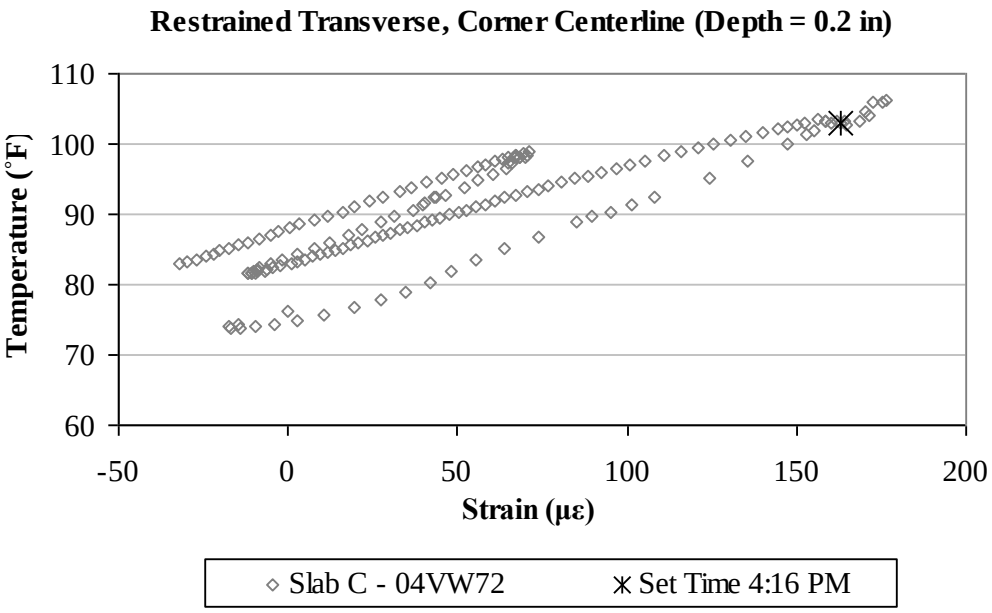

Figure A52. Early-age variation in the total strain with temperature, in the transverse direction, for the top sensor located at the corner along the centerline joint in restrained Slab C.

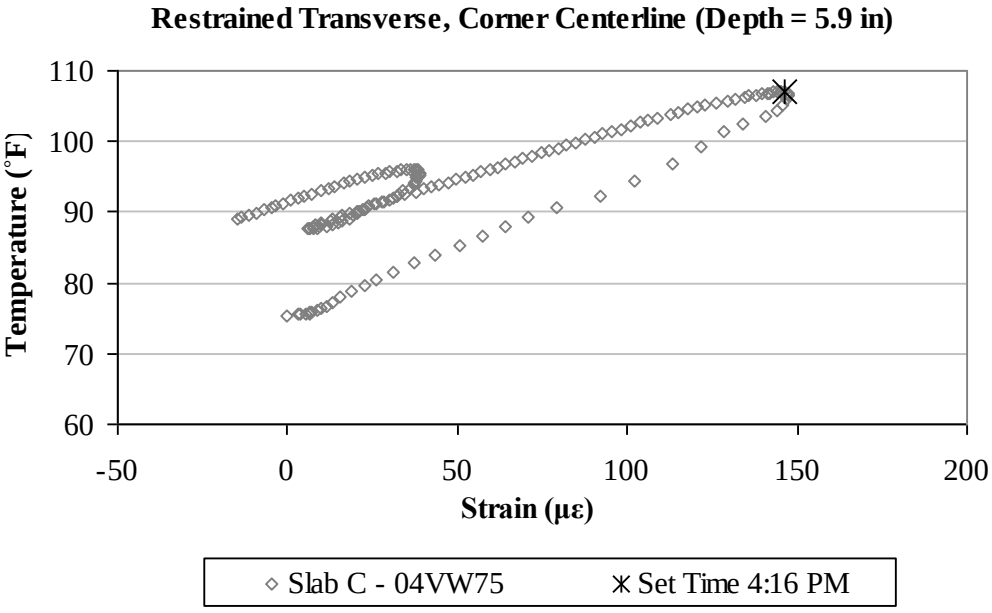

Figure A53. Early-age variation in the total strain with temperature, in the transverse direction, for the middepth sensor located at the corner along the centerline joint in restrained Slab C.

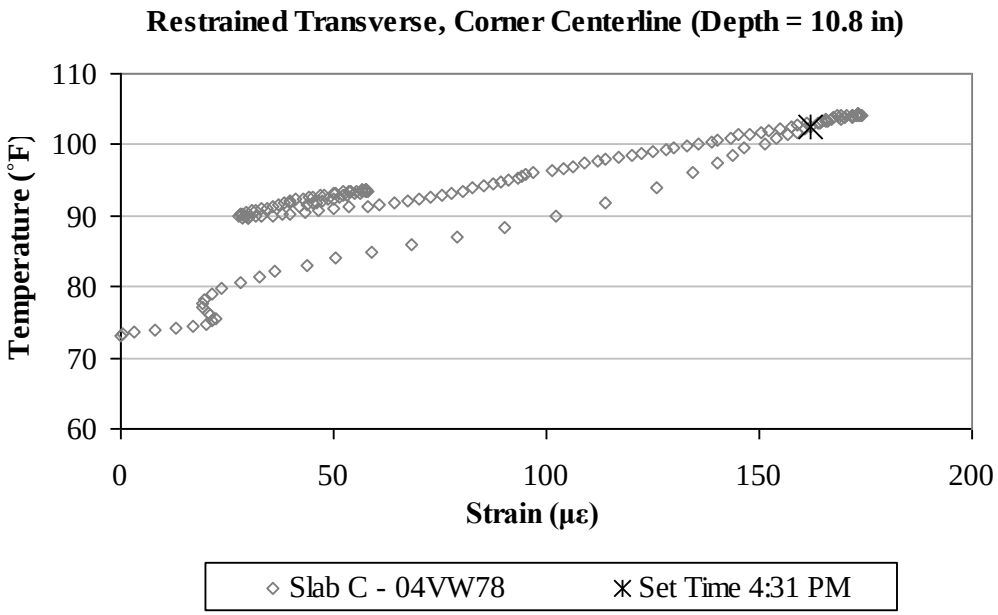

Figure A54. Early-age variation in the total strain with temperature, in the transverse direction, for the bottom sensor located at the corner along the centerline joint in restrained Slab C.

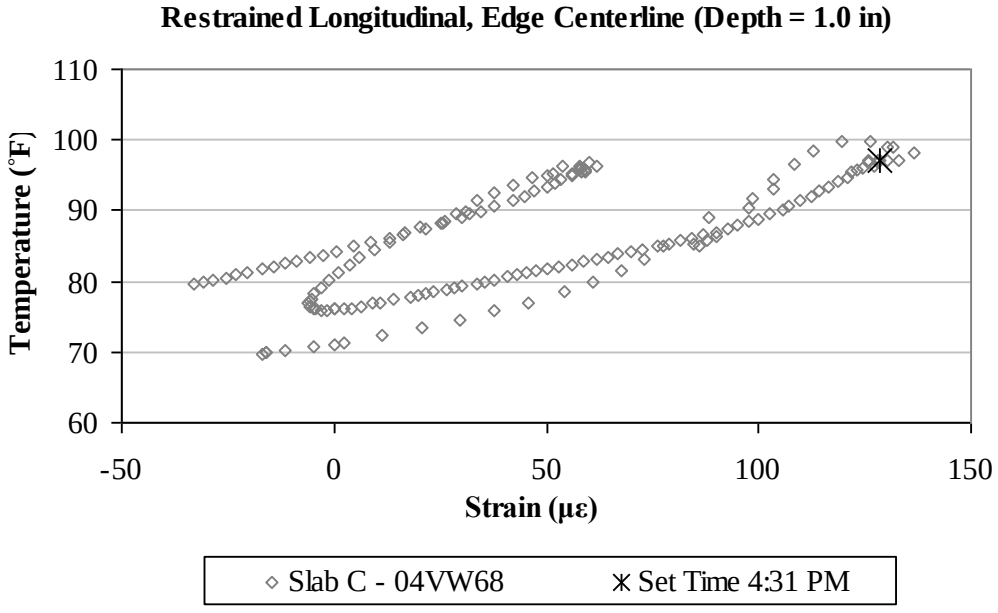

Figure A55. Early-age variation in the total strain with temperature, in the longitudinal direction, for the top sensor located along the centerline joint in restrained Slab C.

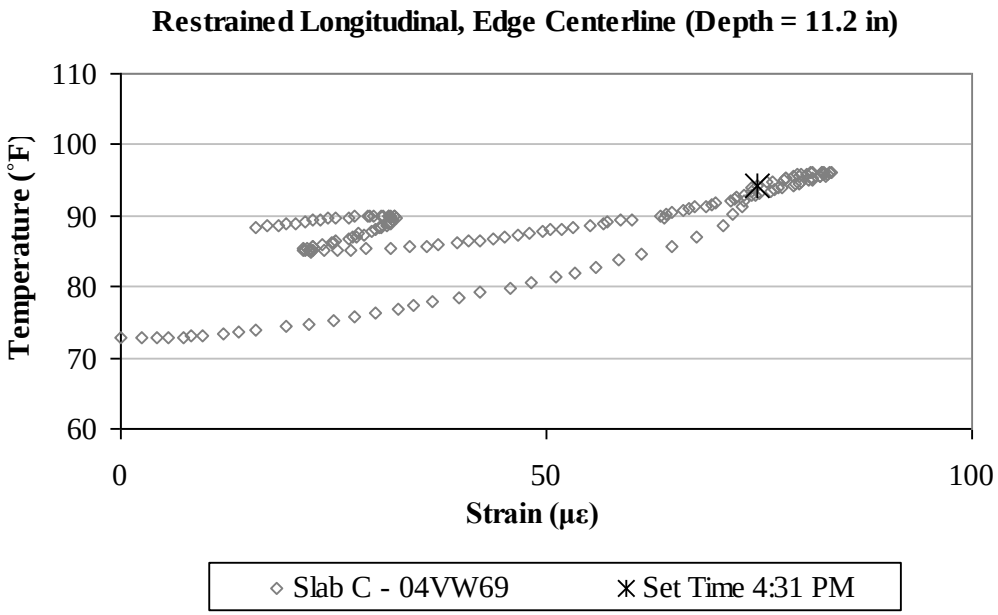

Figure A56. Early-age variation in the total strain with temperature, in the longitudinal direction, for the bottom sensor located along the centerline joint in restrained Slab C.

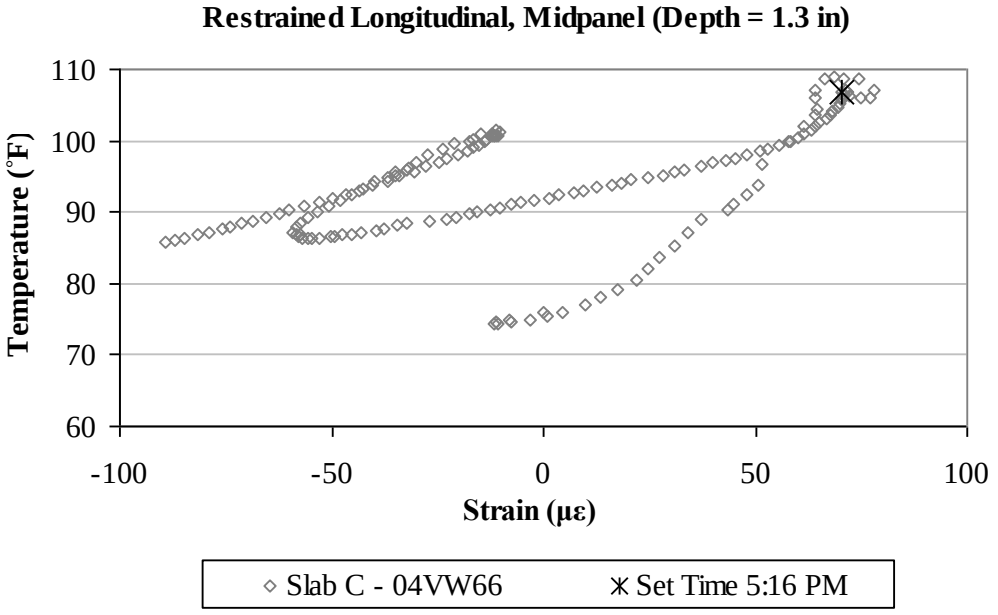

Figure A57. Early-age variation in the total strain with temperature, in the longitudinal direction, for the top sensor located at midpanel in restrained Slab C.

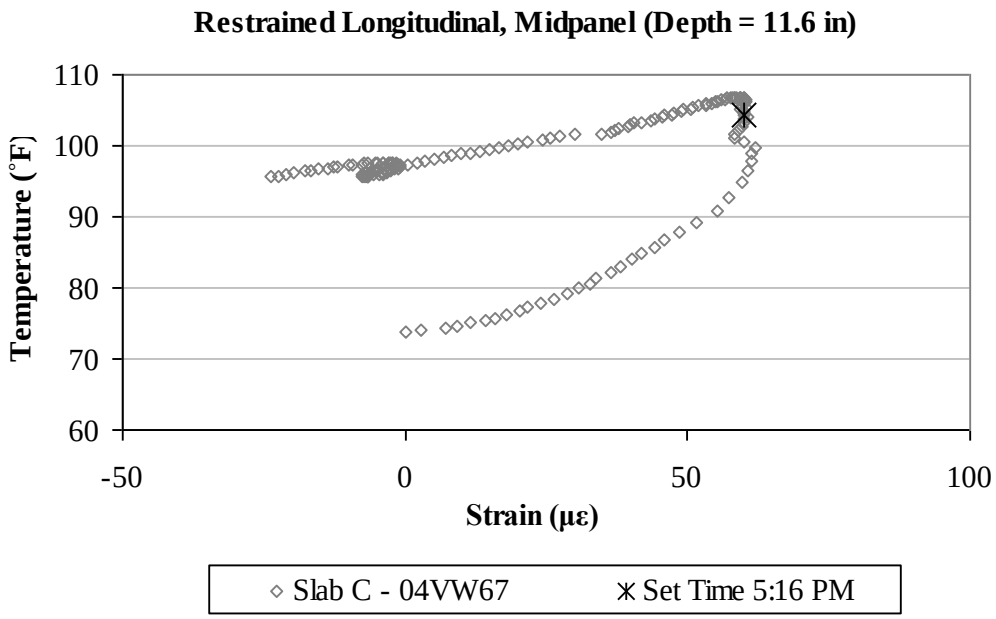

Figure A58. Early-age variation in the total strain with temperature, in the longitudinal direction, for the bottom sensor located at midpanel in restrained Slab C.

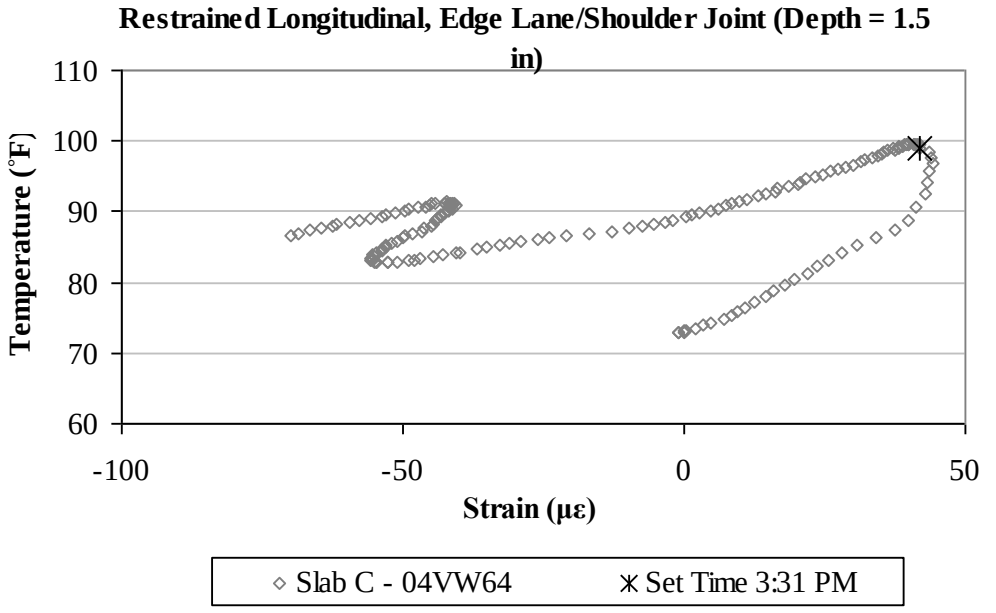

Figure A59. Early-age variation in the total strain with temperature, in the longitudinal direction, for the top sensor located along the lane/shoulder joint in restrained Slab C.

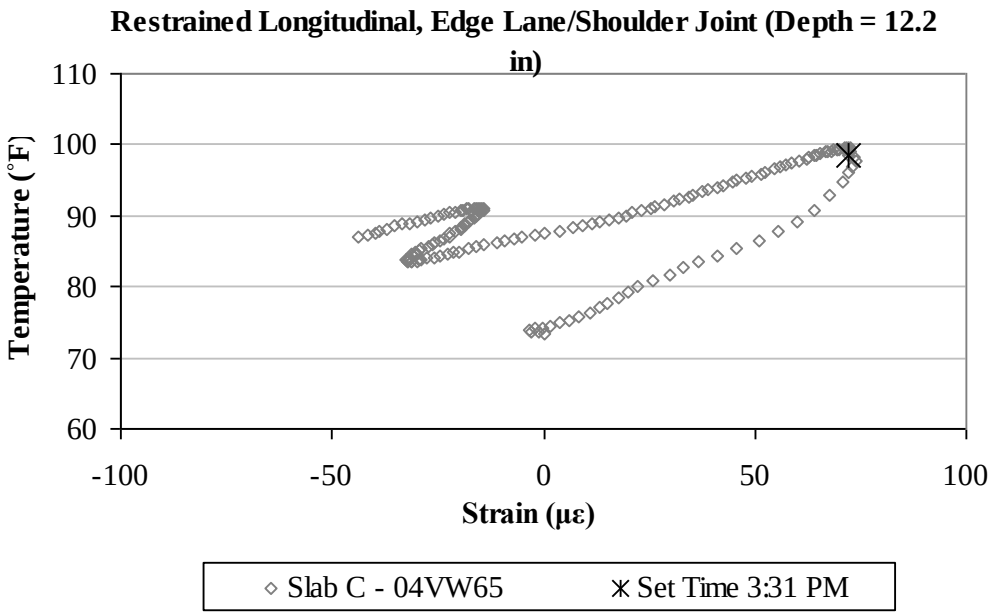

Figure A60. Early-age variation in the total strain with temperature, in the longitudinal direction, for the bottom sensor located along the lane/shoulder joint in restrained Slab C.

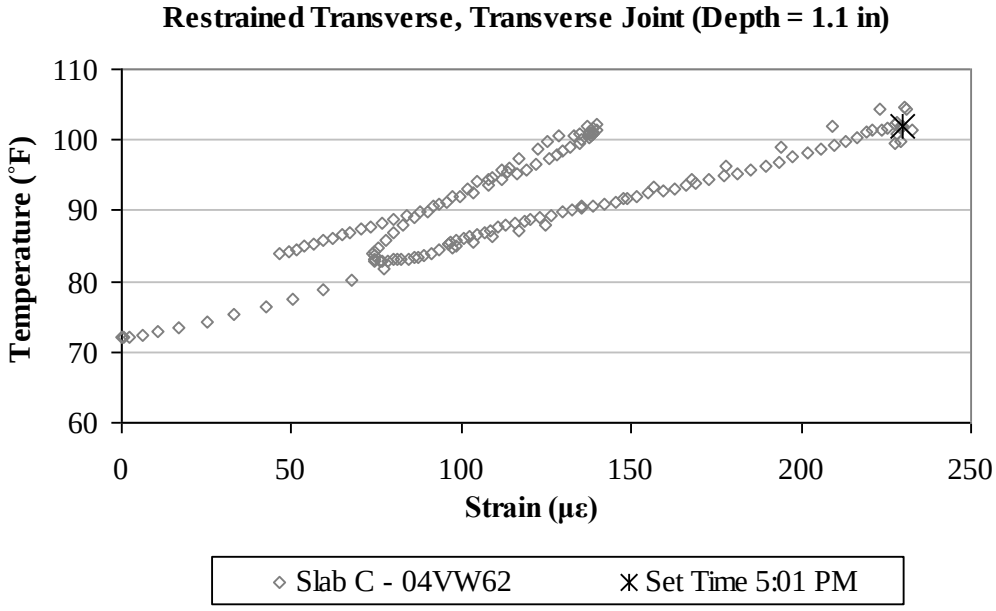

Figure A61. Early-age variation in the total strain with temperature, in the transverse direction, for the top sensor located along the transverse joint in restrained Slab C.

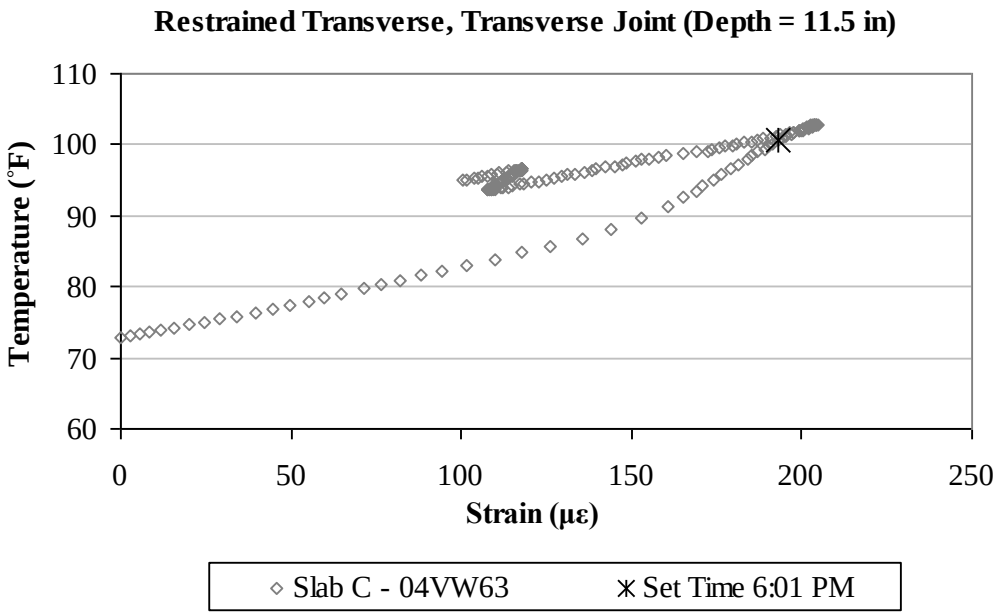

Figure A62. Early-age variation in the total strain with temperature, in the transverse direction, for the bottom sensor located along the transverse joint in restrained Slab C.

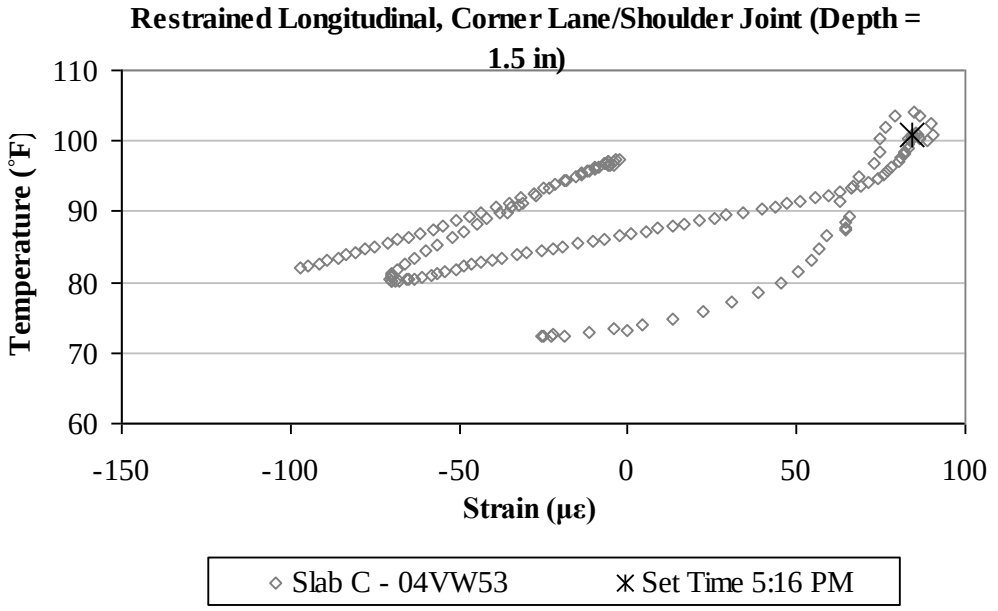

Figure A63. Early-age variation in the total strain with temperature, in the longitudinal direction, for the top sensor located at the corner along the lane/shoulder joint in restrained Slab C.

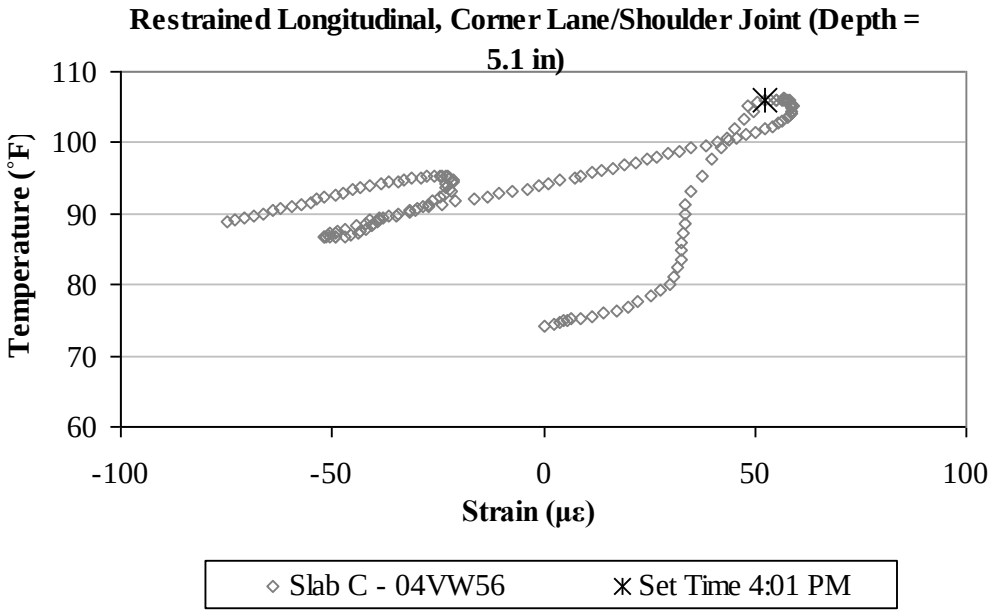

Figure A64. Early-age variation in the total strain with temperature, in the longitudinal direction, for the middepth sensor located at the corner along the lane/shoulder joint in restrained Slab C.

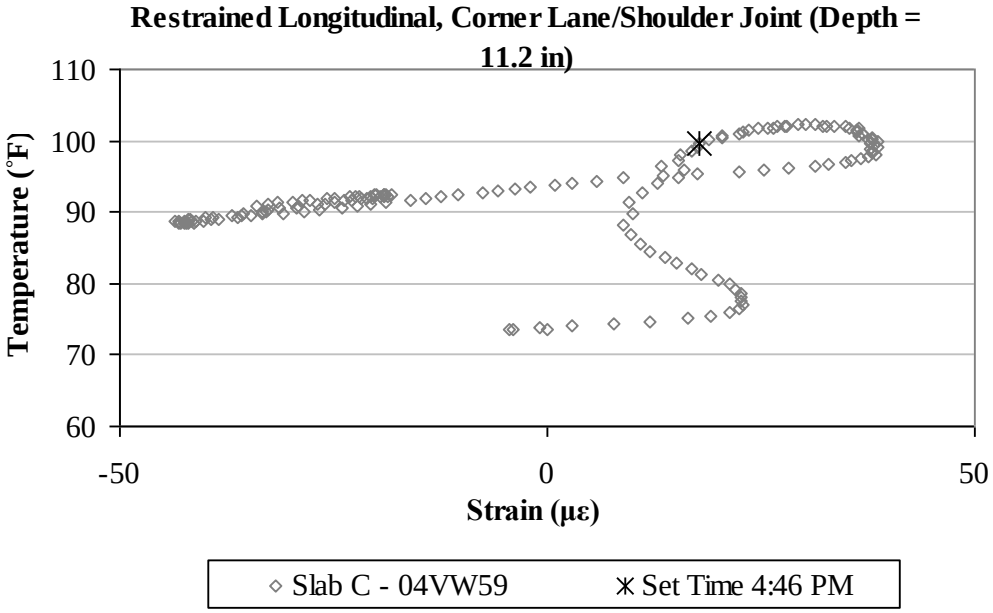

Figure A65. Early-age variation in the total strain with temperature, in the longitudinal direction, for the bottom sensor located at the corner along the lane/shoulder joint in restrained Slab C.

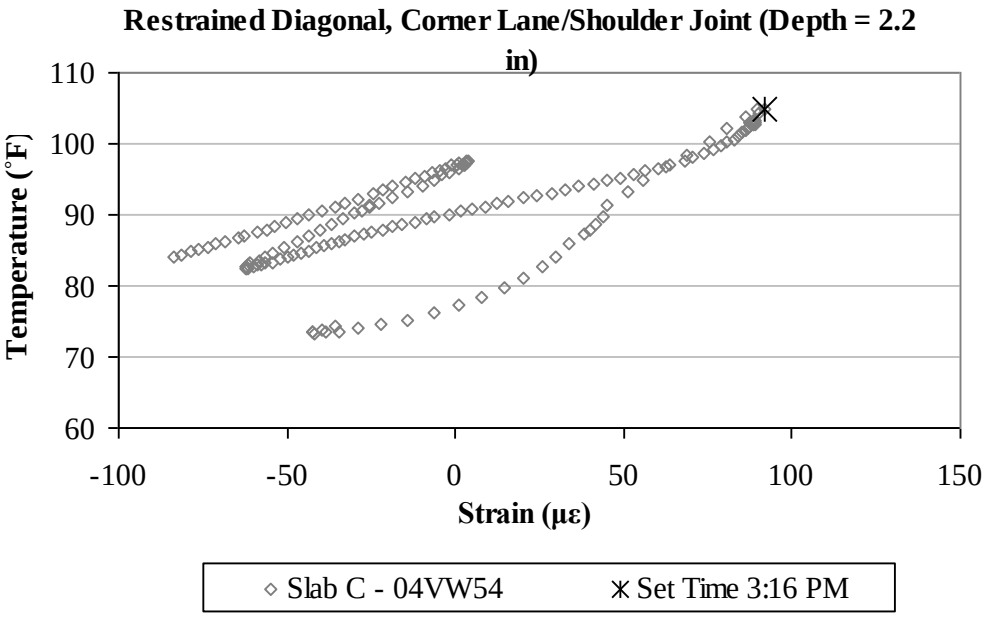

Figure A66. Early-age variation in the total strain with temperature, in the diagonal direction, for the top sensor located at the corner along the lane/shoulder joint in restrained Slab C.

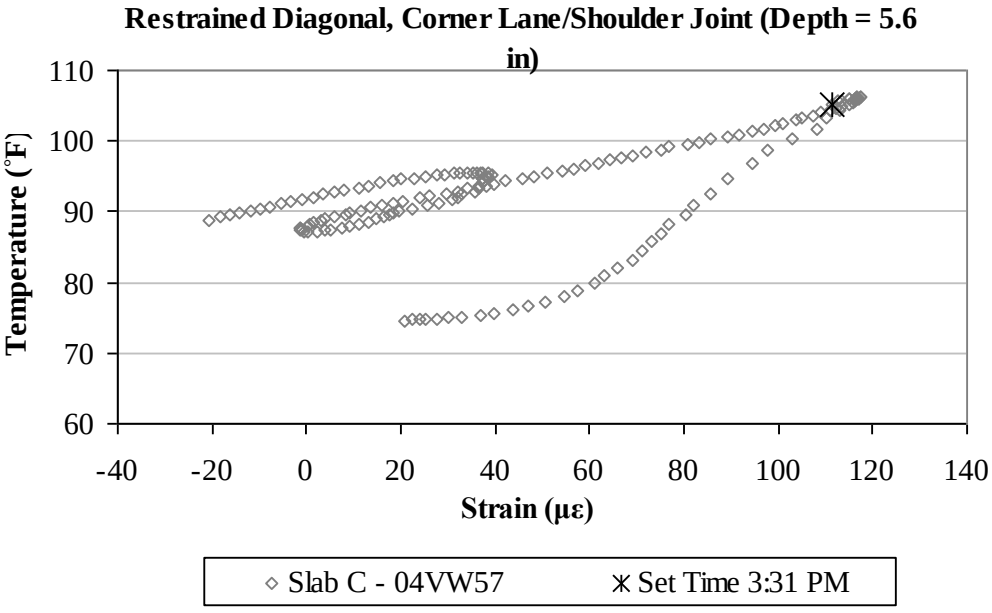

Figure A67. Early-age variation in the total strain with temperature, in the diagonal direction, for the middepth sensor located at the corner along the lane/shoulder joint in restrained Slab C.

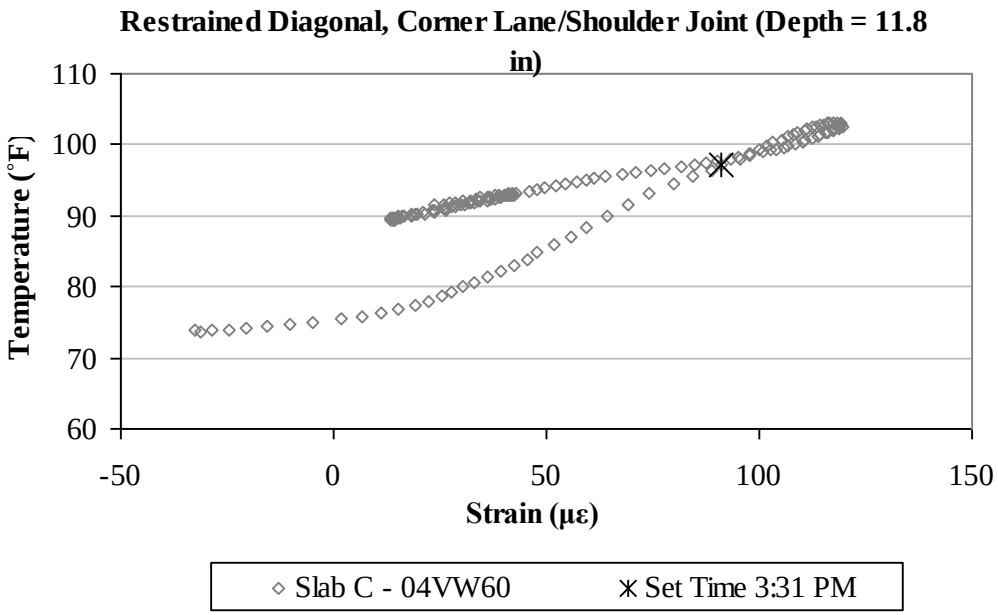

Figure A68. Early-age variation in the total strain with temperature, in the diagonal direction, for the bottom sensor located at the corner along the lane/shoulder joint in restrained Slab C.

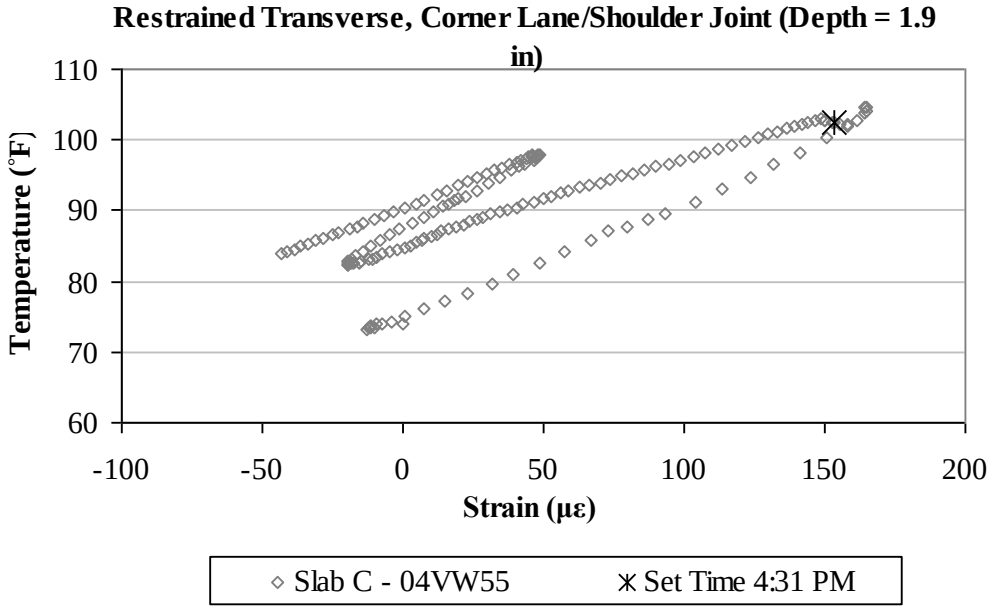

Figure A69. Early-age variation in the total strain with temperature, in the transverse direction, for the top sensor located at the corner along the lane/shoulder joint in restrained Slab C.

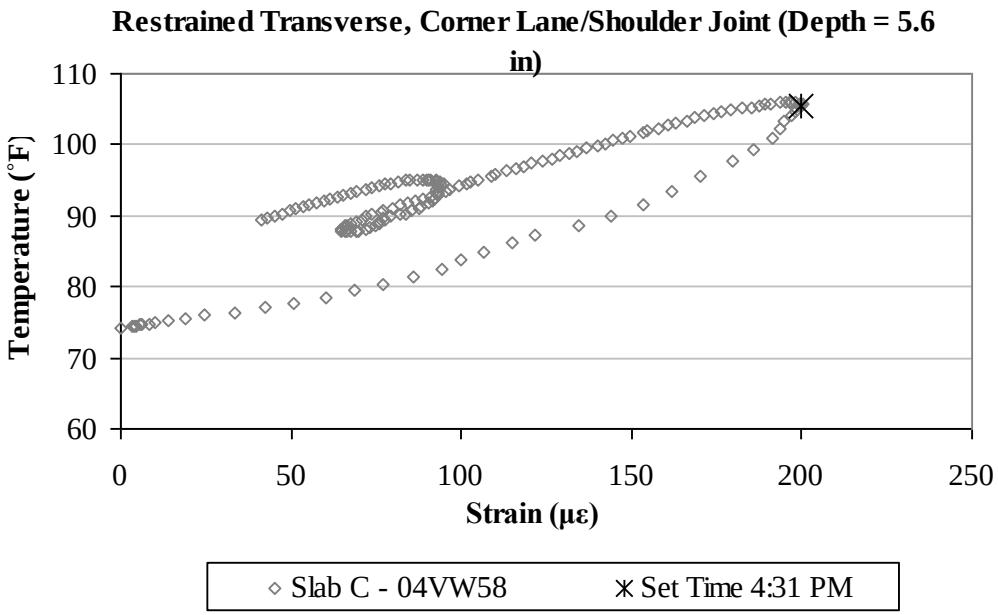

Figure A70. Early-age variation in the total strain with temperature, in the transverse direction, for the middepth sensor located at the corner along the lane/shoulder joint in restrained Slab C.

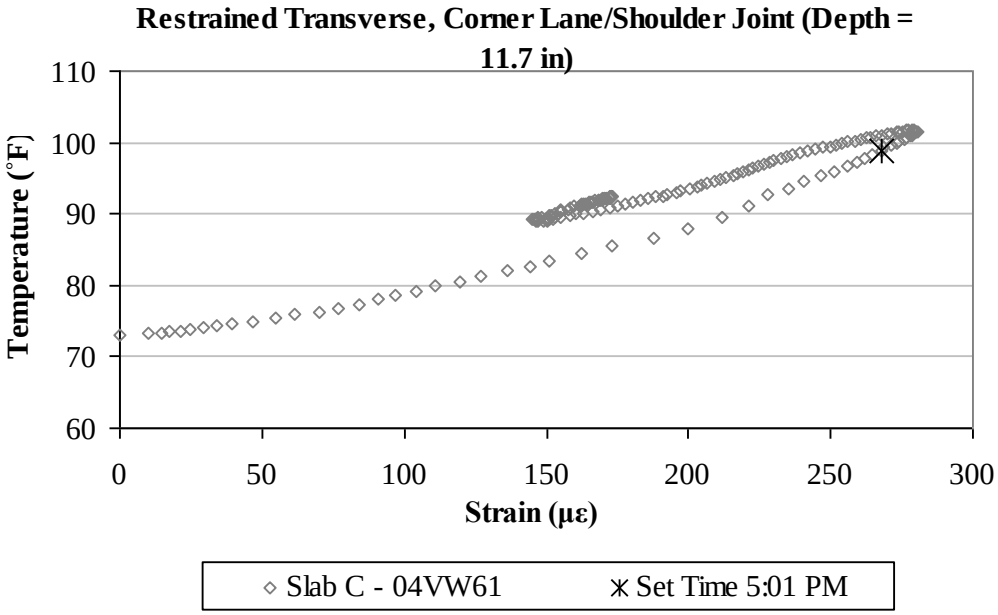

Figure A71. Early-age variation in the total strain with temperature, in the transverse direction, for the bottom sensor located at the corner along the lane/shoulder joint in restrained Slab C.

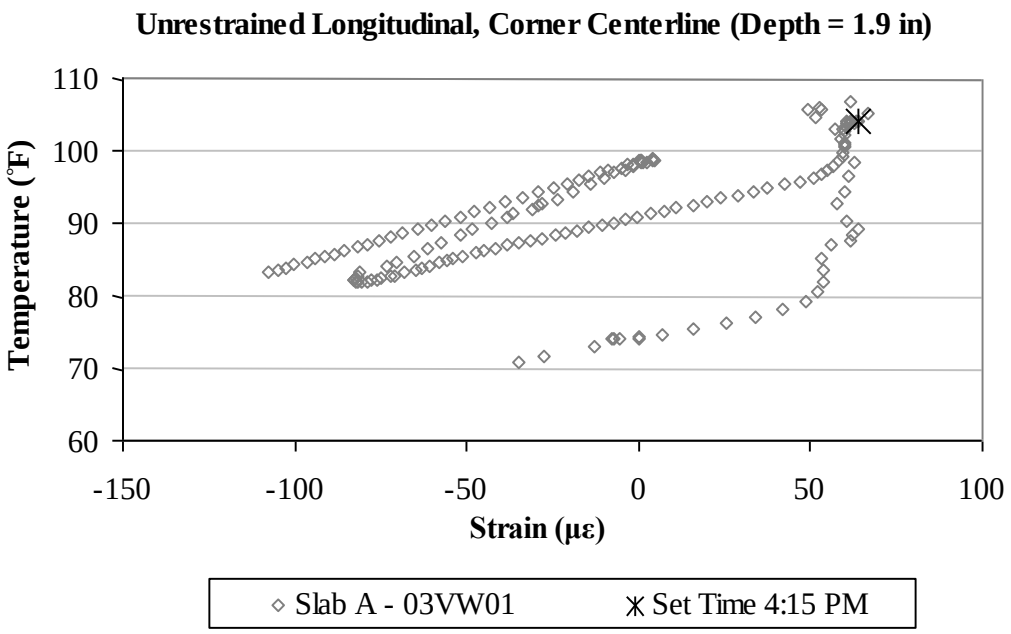

Figure A72. Early-age variation in the total strain with temperature, in the longitudinal direction, for the top sensor located at the corner along the centerline joint in unrestrained Slab A.

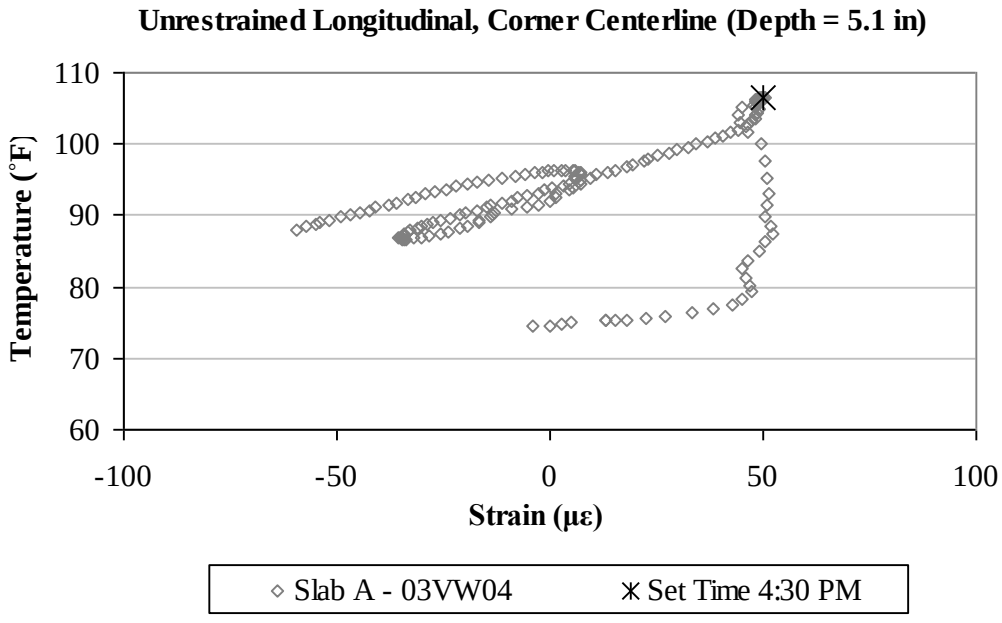

Figure A73. Early-age variation in the total strain with temperature, in the longitudinal direction, for the middepth sensor located at the corner along the centerline joint in unrestrained Slab A.

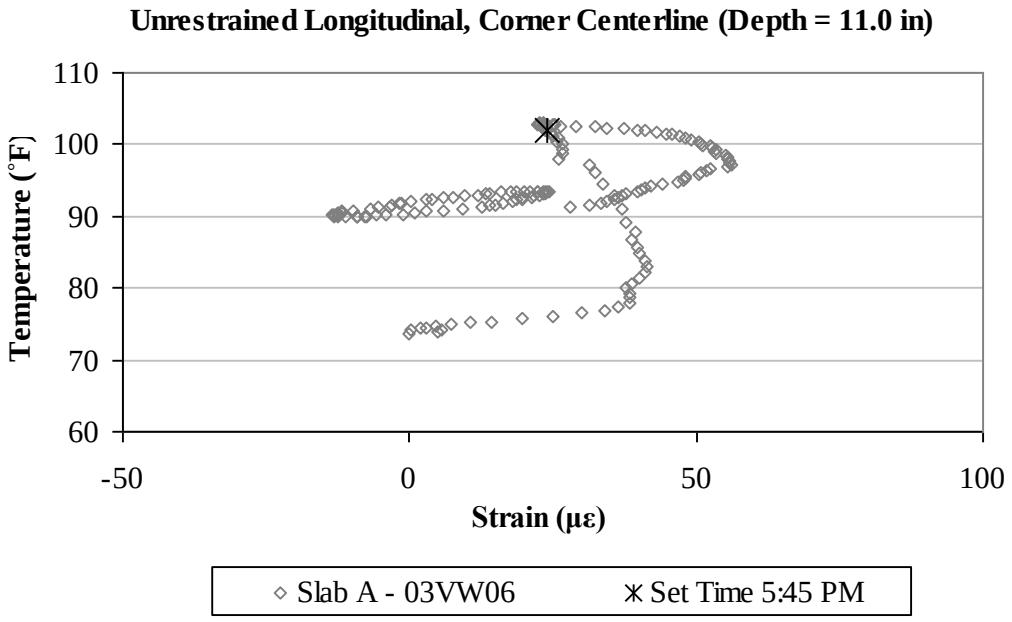

Figure A74. Early-age variation in the total strain with temperature, in the longitudinal direction, for the bottom sensor located at the corner along the centerline joint in unrestrained Slab A.

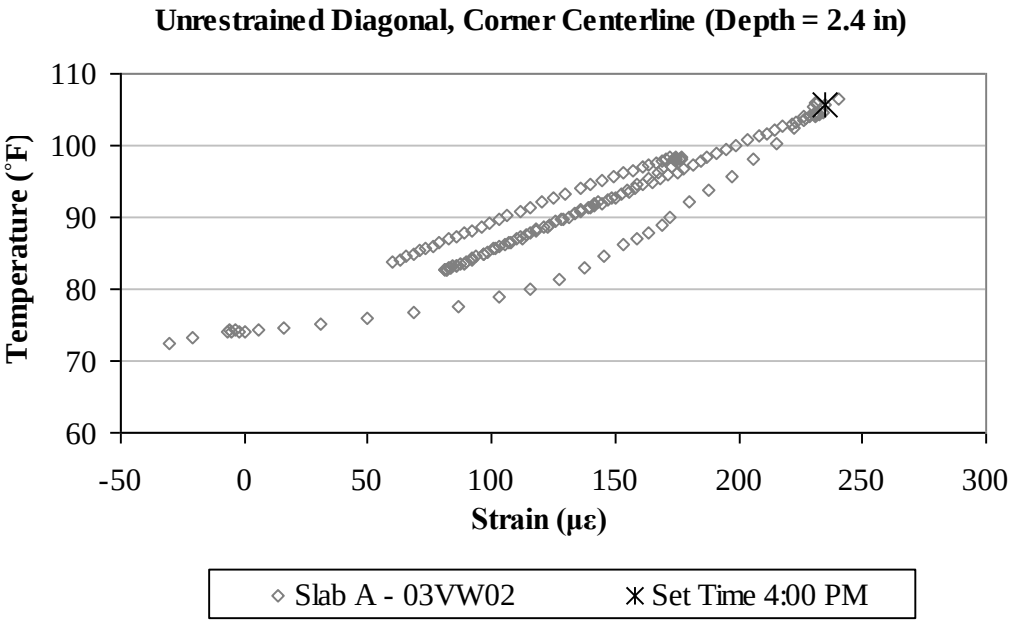

Figure A75. Early-age variation in the total strain with temperature, in the diagonal direction, for the top sensor located at the corner along the centerline joint in unrestrained Slab A.

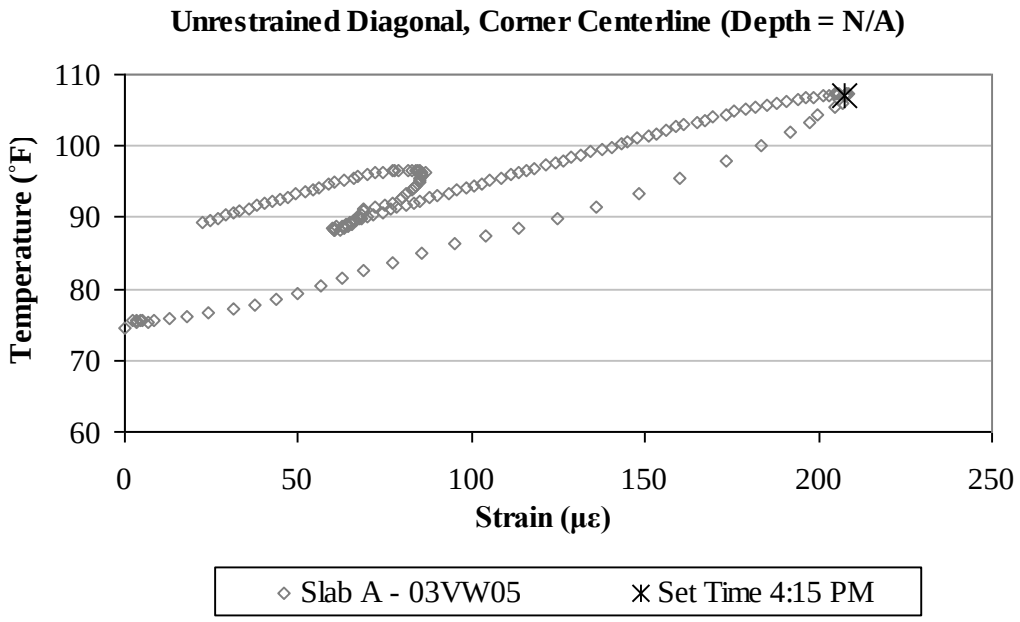

Figure A76. Early-age variation in the total strain with temperature, in the diagonal direction, for the middepth sensor located at the corner along the centerline joint in unrestrained Slab A.

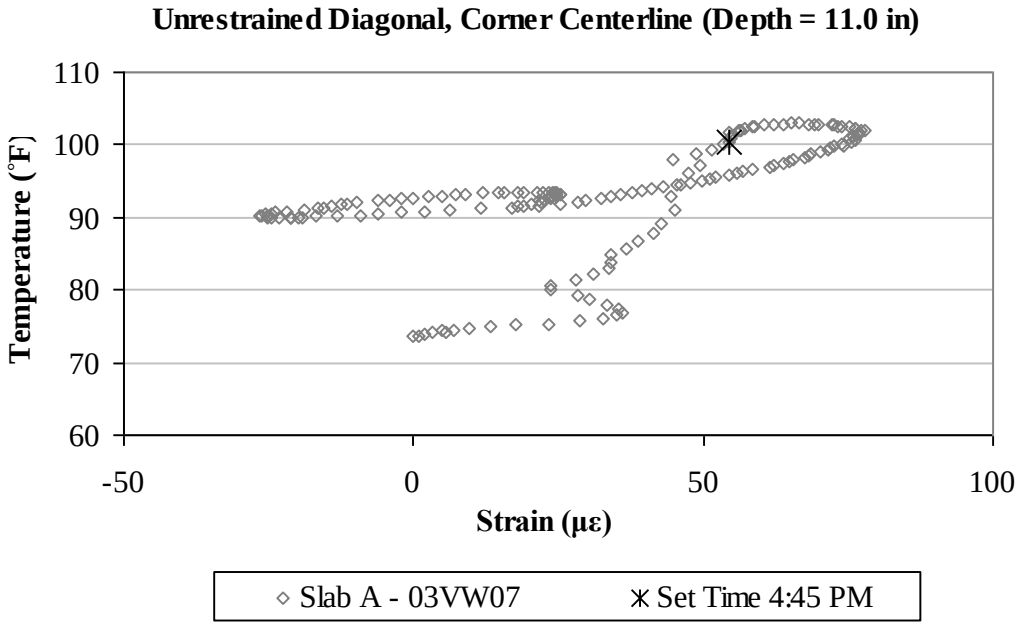

Figure A77. Early-age variation in the total strain with temperature, in the diagonal direction, for the bottom sensor located at the corner along the centerline joint in unrestrained Slab A.

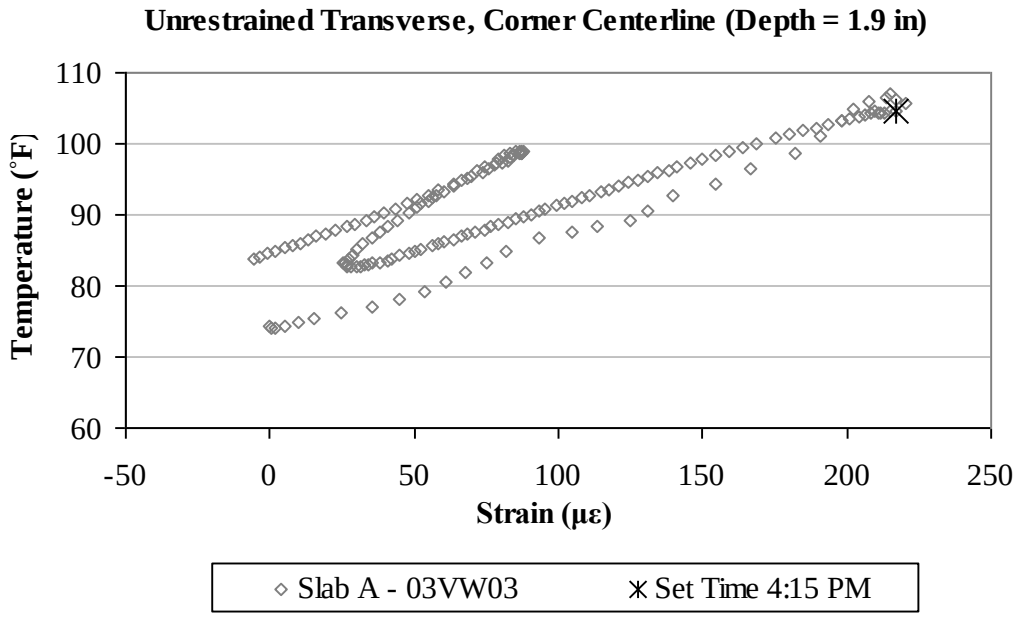

Figure A78. Early-age variation in the total strain with temperature, in the transverse direction, for the top sensor located at the corner along the centerline joint in unrestrained Slab A.

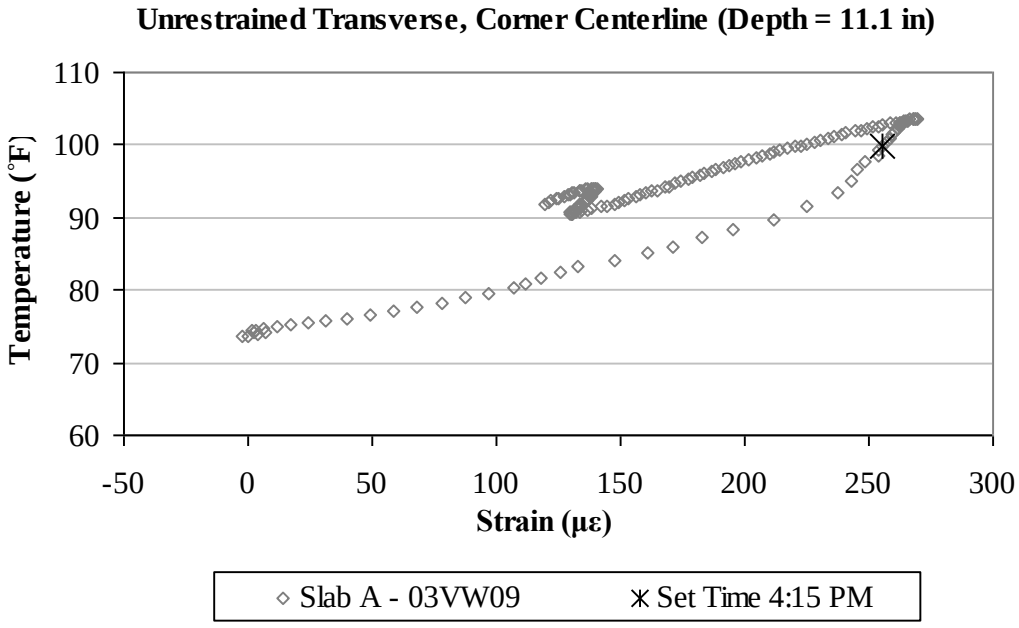

Figure A79. Early-age variation in the total strain with temperature, in the transverse direction, for the bottom sensor located at the corner along the centerline joint in unrestrained Slab A.

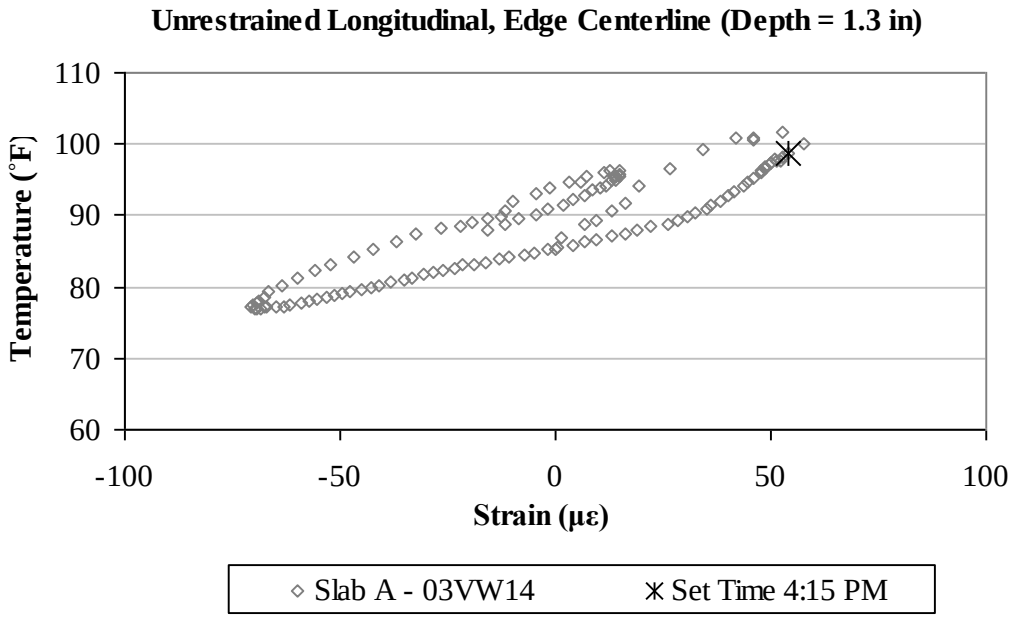

Figure A80. Early-age variation in the total strain with temperature, in the longitudinal direction, for the top sensor located along the centerline joint in unrestrained Slab A.

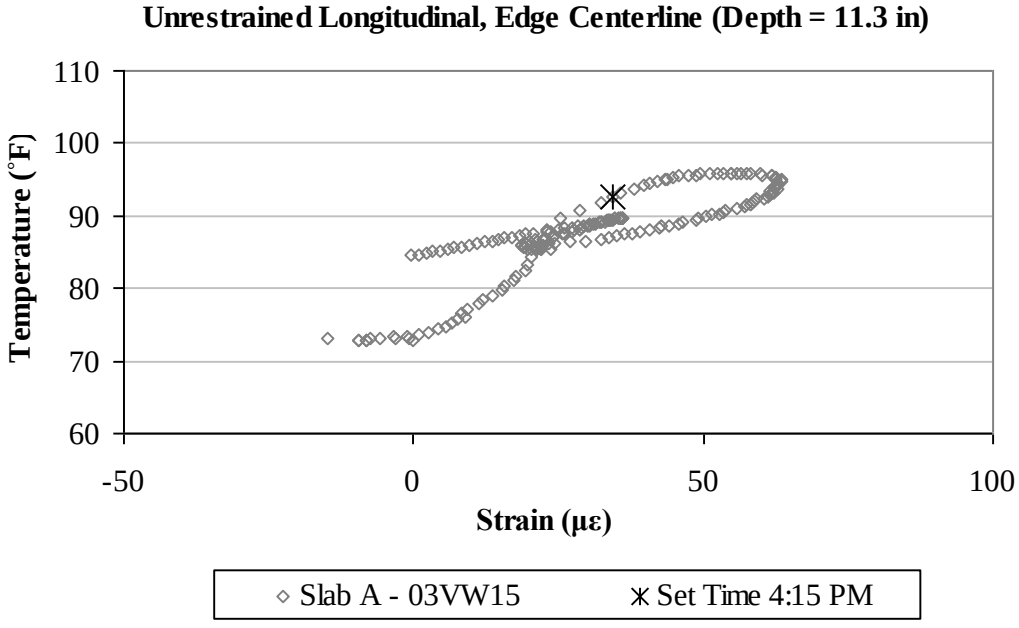

Figure A81. Early-age variation in the total strain with temperature, in the longitudinal direction, for the bottom sensor located along the centerline joint in unrestrained Slab A.

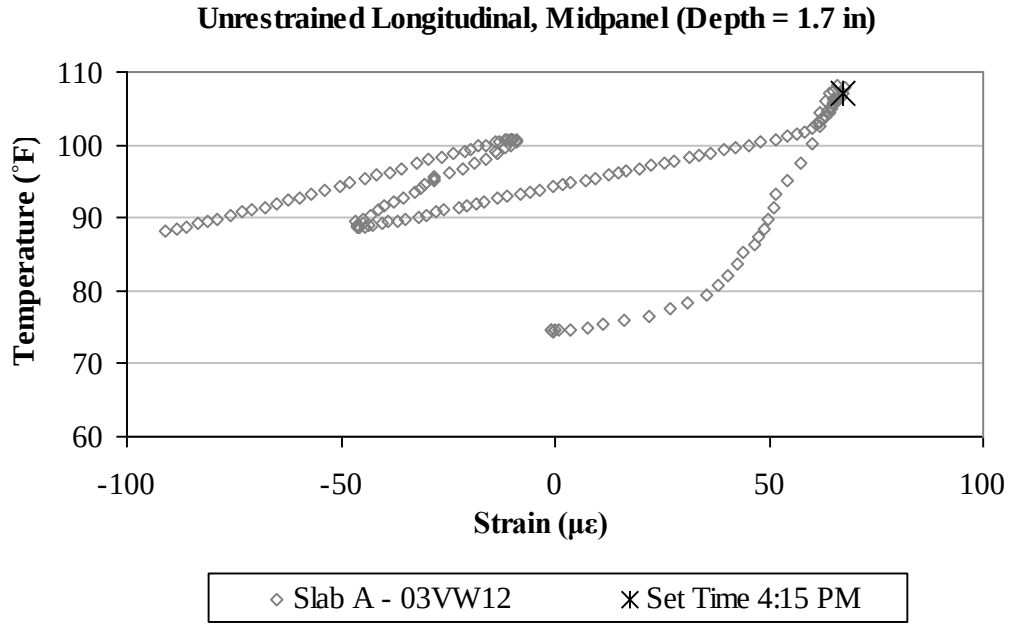

Figure A82. Early-age variation in the total strain with temperature, in the longitudinal direction, for the top sensor located at midpanel in unrestrained Slab A.

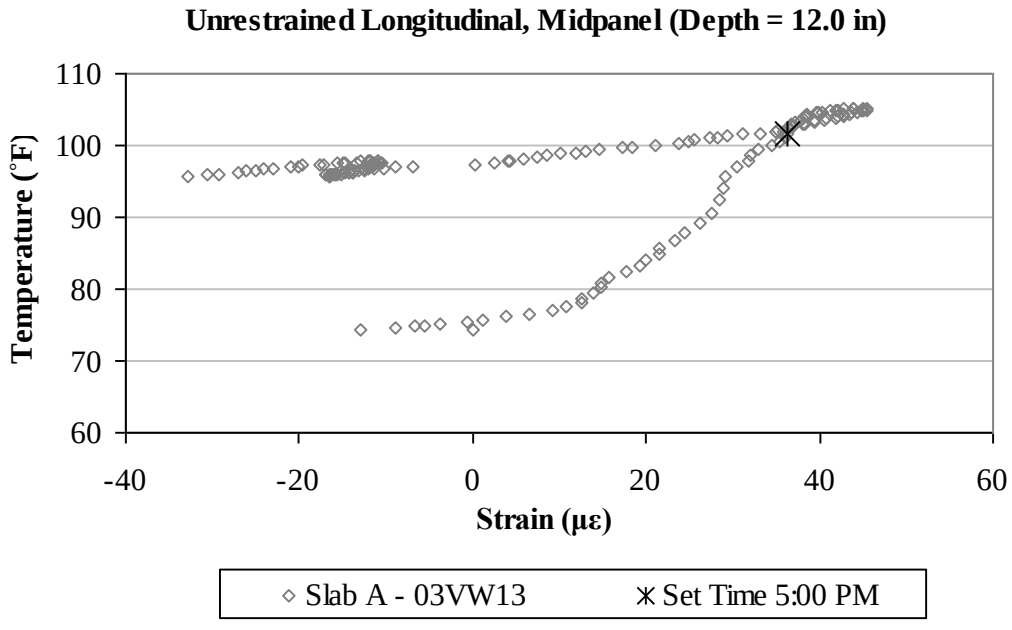

Figure A83. Early-age variation in the total strain with temperature, in the longitudinal direction, for the bottom sensor located at midpanel in unrestrained Slab A.

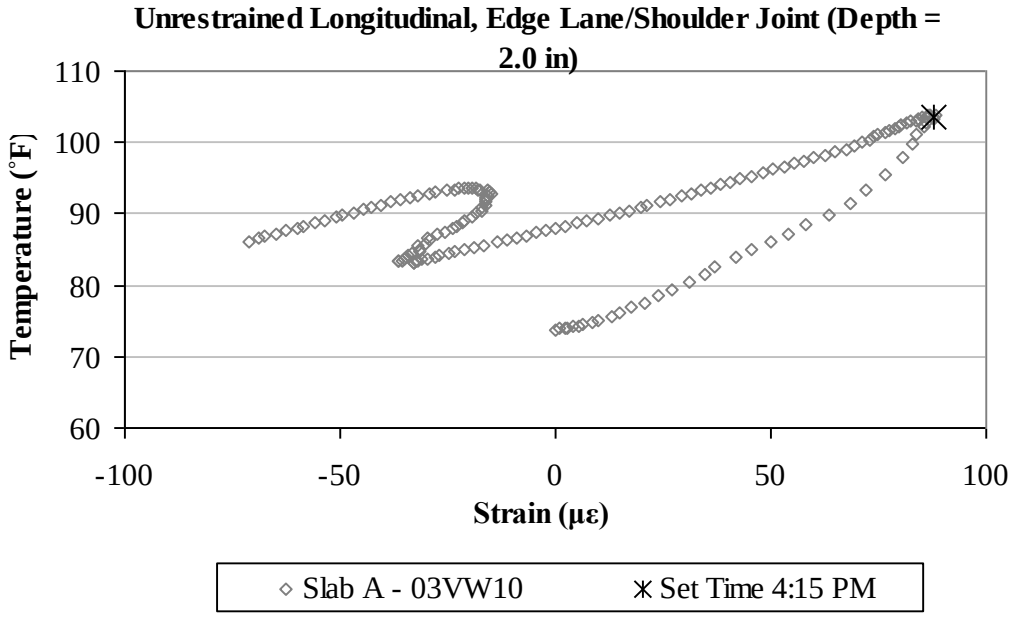

Figure A84. Early-age variation in the total strain with temperature, in the longitudinal direction, for the top sensor located along the lane/shoulder joint in unrestrained Slab A.

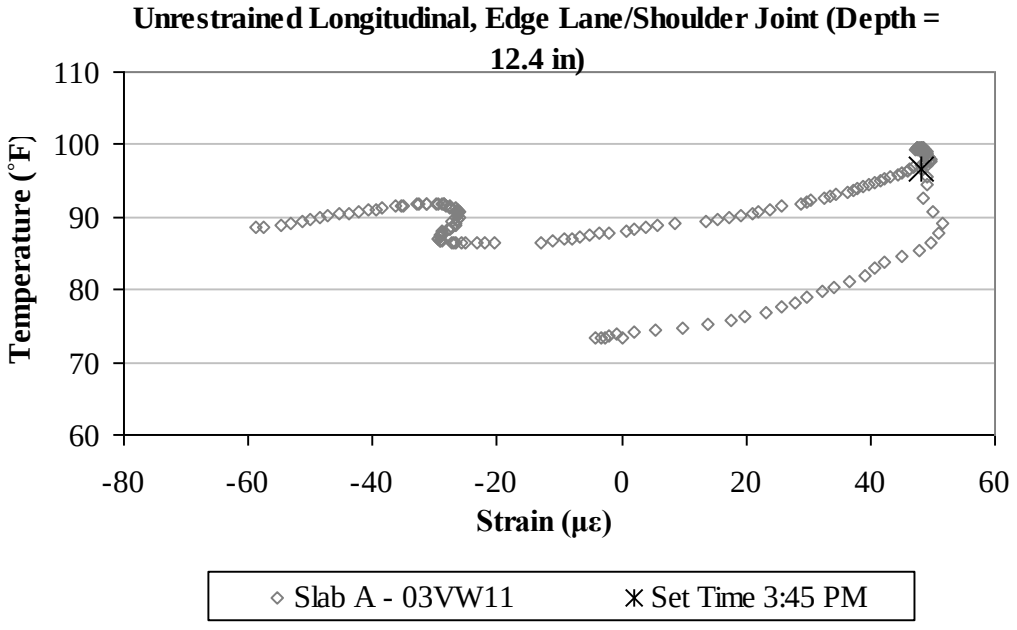

Figure A85. Early-age variation in the total strain with temperature, in the longitudinal direction, for the bottom sensor located along the lane/shoulder joint in unrestrained Slab A.

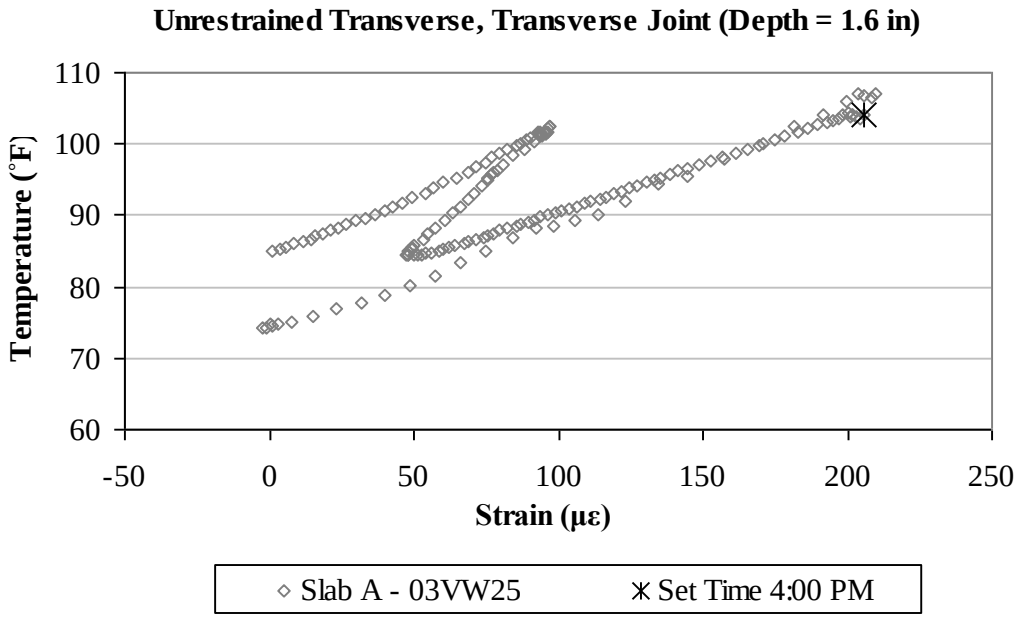

Figure A86. Early-age variation in the total strain with temperature, in the transverse direction, for the top sensor located along the transverse joint in unrestrained Slab A.

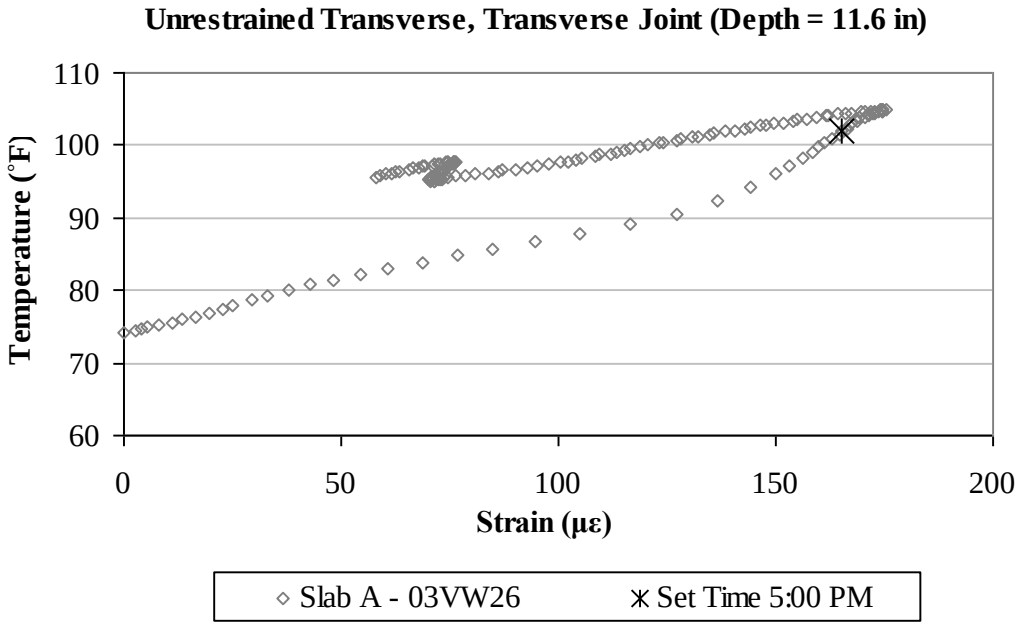

Figure A87. Early-age variation in the total strain with temperature, in the transverse direction, for the bottom sensor located along the transverse joint in unrestrained Slab A.

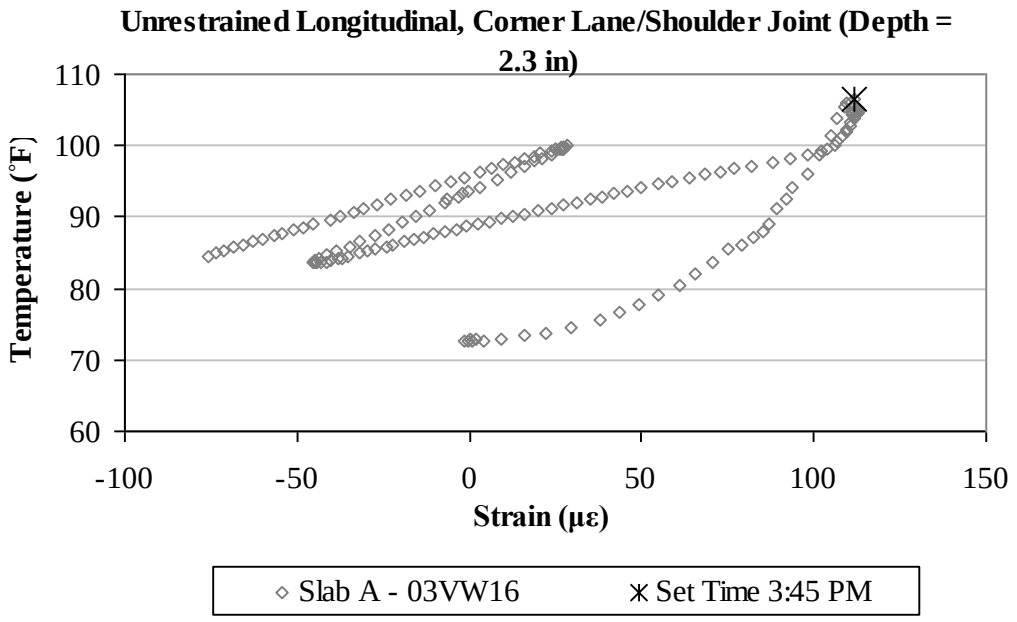

Figure A88. Early-age variation in the total strain with temperature, in the longitudinal direction, for the top sensor located at the corner along the lane/shoulder joint in unrestrained Slab A.

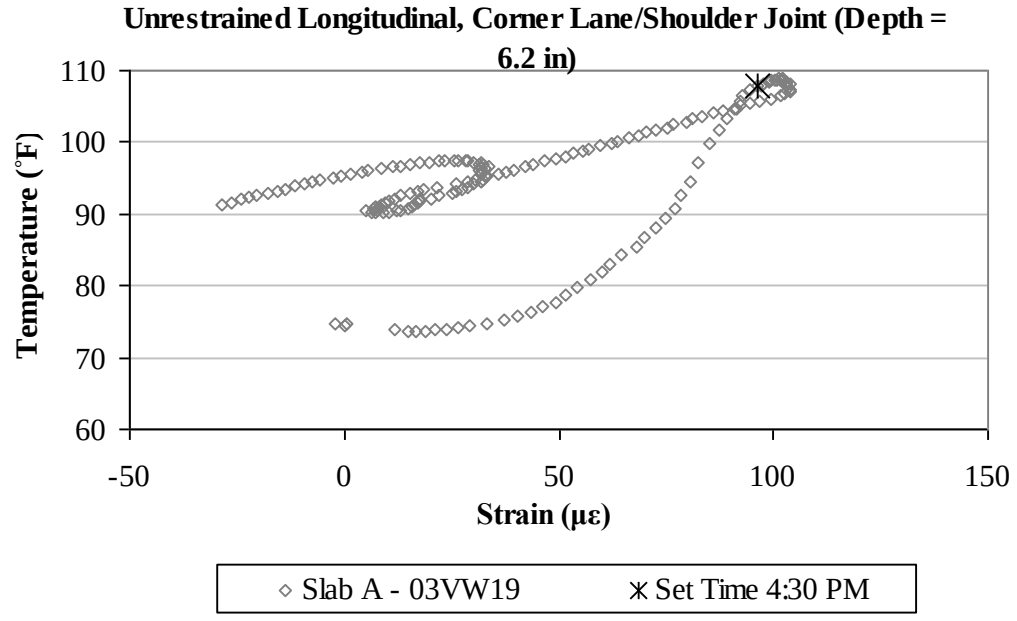

Figure A89. Early-age variation in the total strain with temperature, in the longitudinal direction, for the middepth sensor located at the corner along the lane/shoulder joint in unrestrained Slab A.

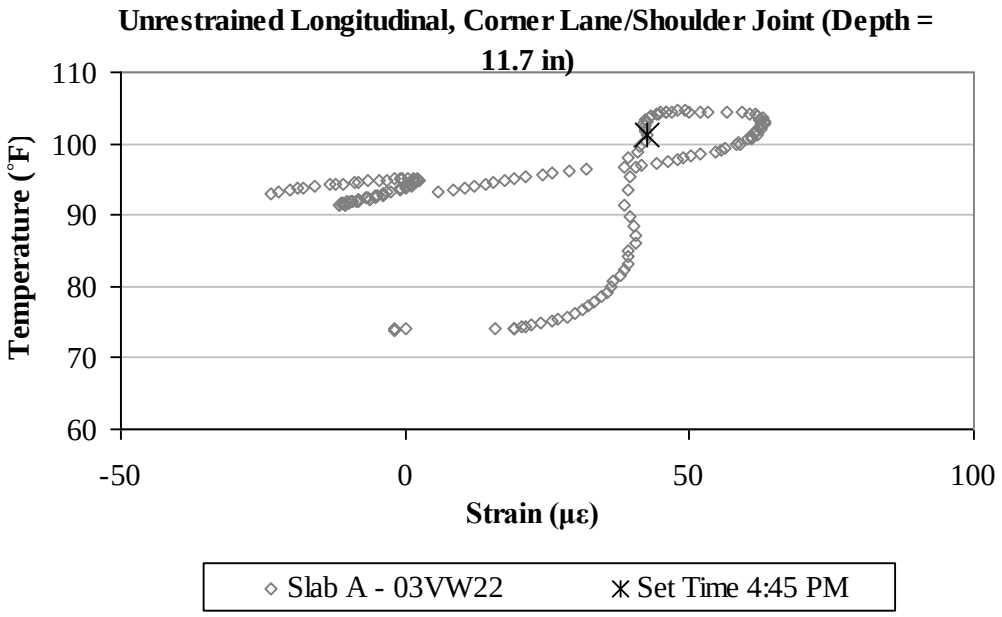

Figure A90. Early-age variation in the total strain with temperature, in the longitudinal direction, for the bottom sensor located at the corner along the lane/shoulder joint in unrestrained Slab A.

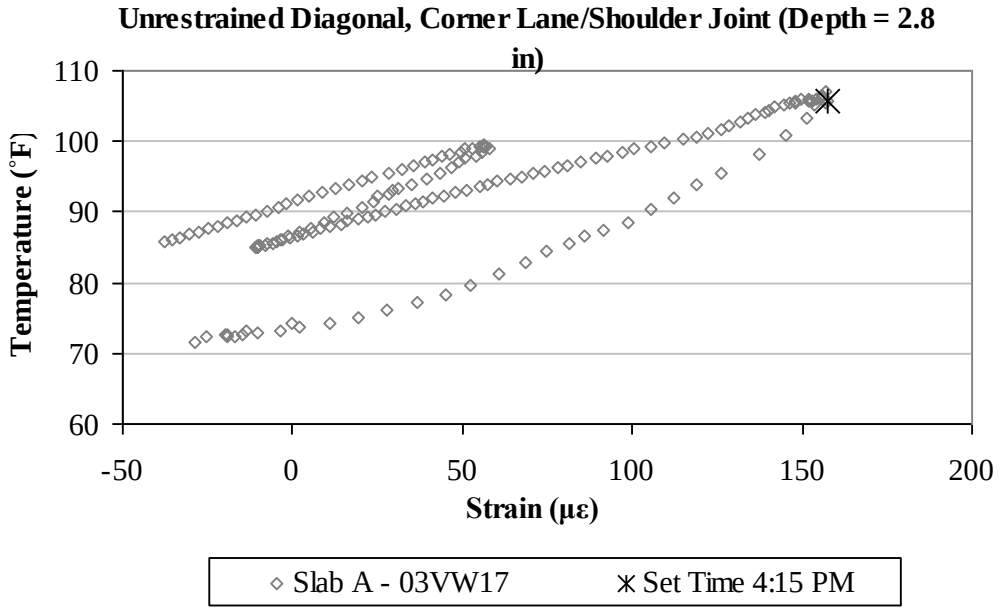

Figure A91. Early-age variation in the total strain with temperature, in the diagonal direction, for the top sensor located at the corner along the lane/shoulder joint in unrestrained Slab A.

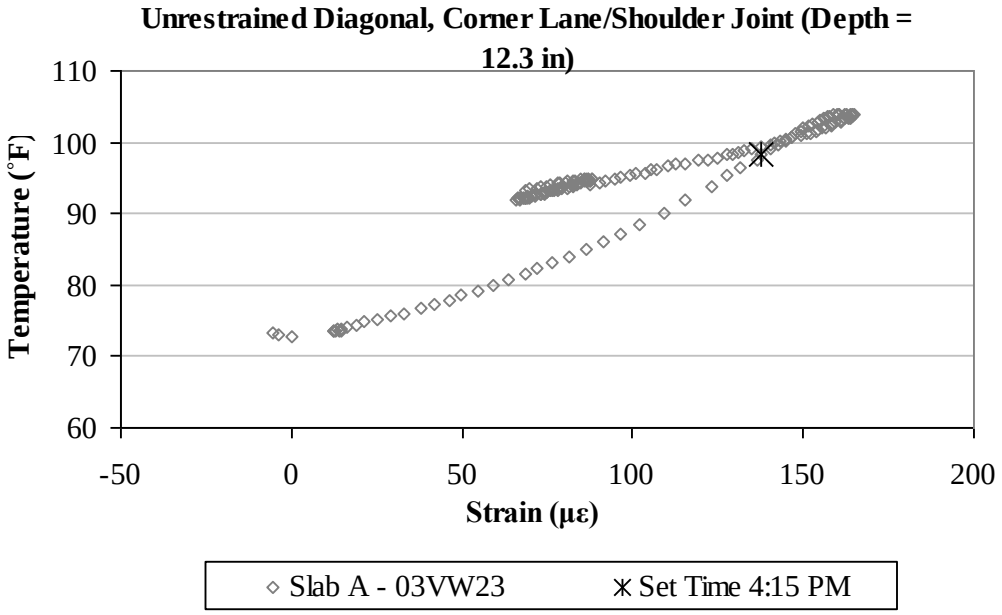

Figure A92. Early-age variation in the total strain with temperature, in the diagonal direction, for the bottom sensor located at the corner along the lane/shoulder joint in unrestrained Slab A.

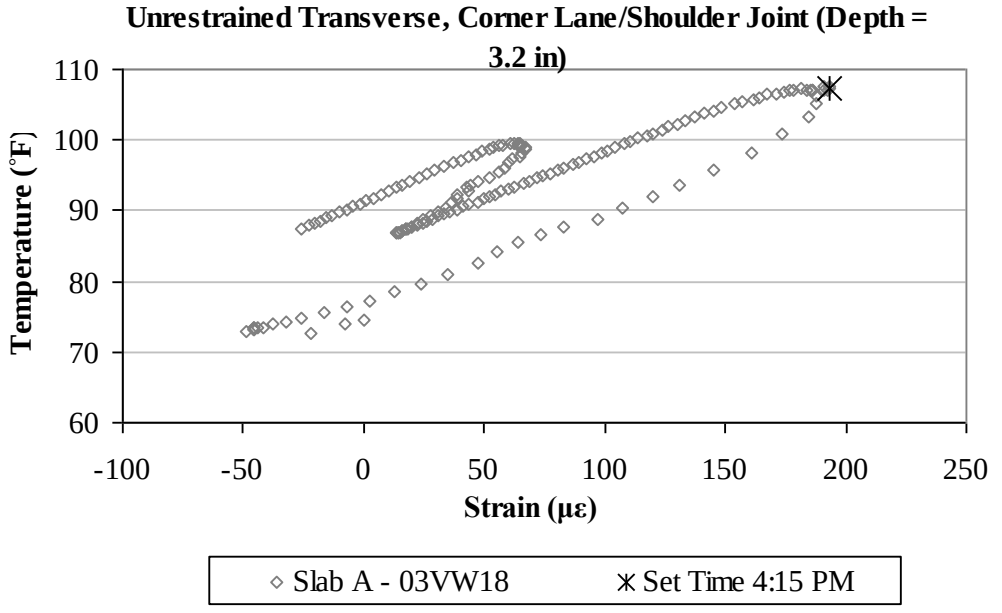

Figure A93. Early-age variation in the total strain with temperature, in the transverse direction, for the top sensor located at the corner along the lane/shoulder joint in unrestrained Slab A.

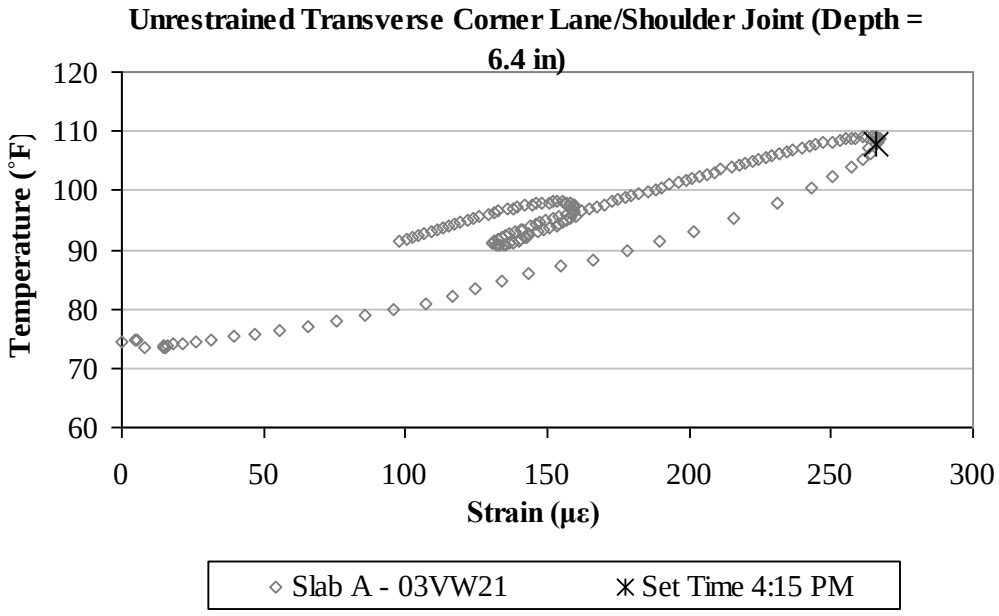

Figure A94. Early-age variation in the total strain with temperature, in the transverse direction, for the middepth sensor located at the corner along the lane/shoulder joint in unrestrained Slab A.

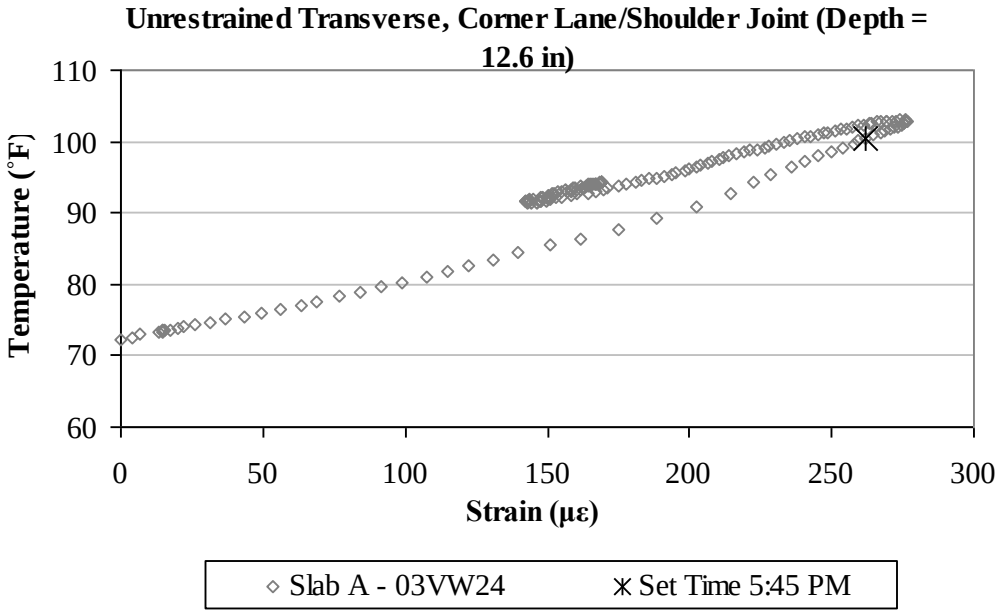

Figure A95. Early-age variation in the total strain with temperature, in the transverse direction, for the bottom sensor located at the corner along the lane/shoulder joint in unrestrained Slab A.

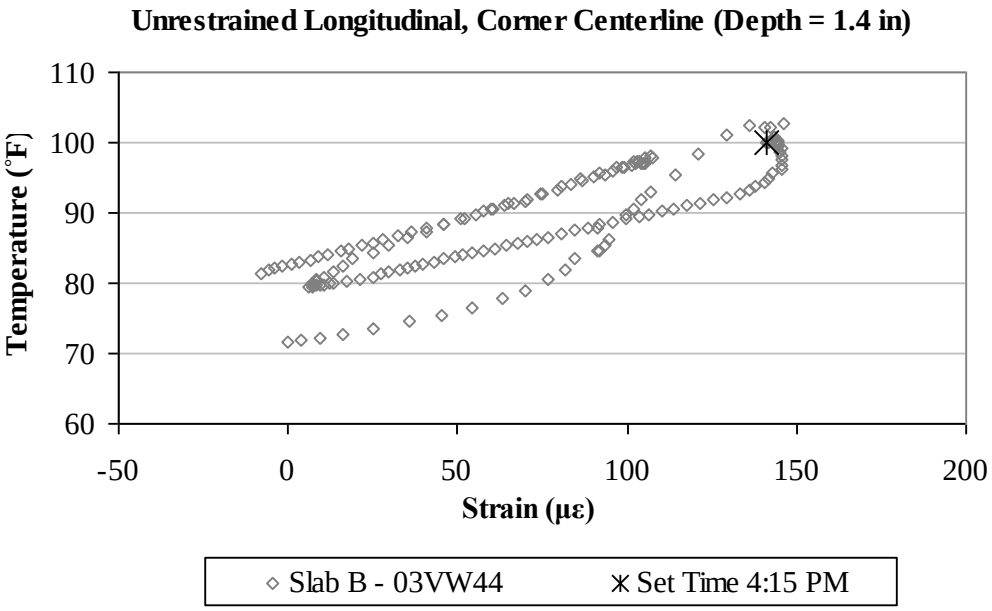

Figure A96. Early-age variation in the total strain with temperature, in the longitudinal direction, for the top sensor located at the corner along the centerline joint in unrestrained Slab B.

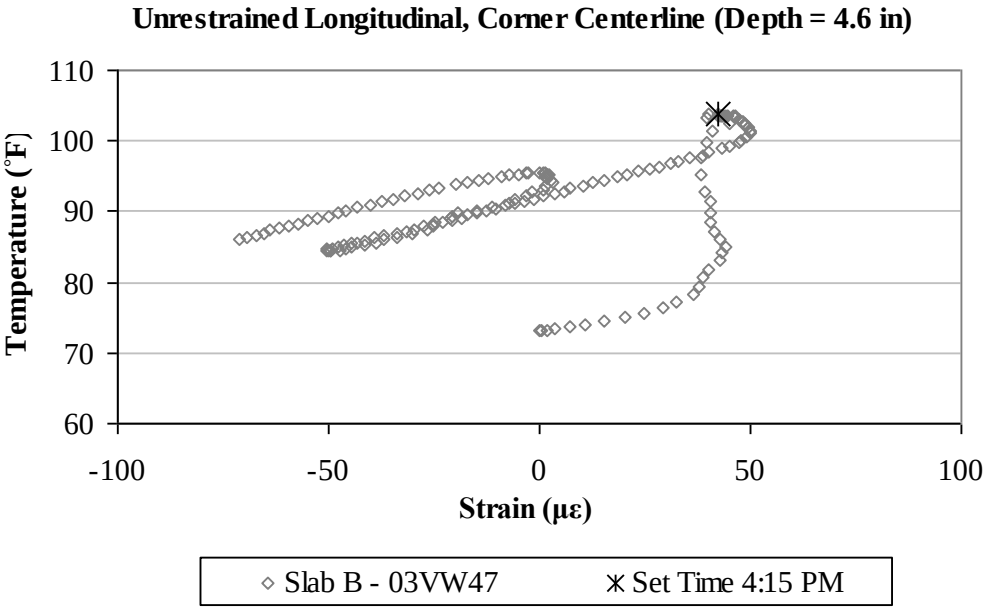

Figure A97. Early-age variation in the total strain with temperature, in the longitudinal direction, for the middepth sensor located at the corner along the centerline joint in unrestrained Slab B.

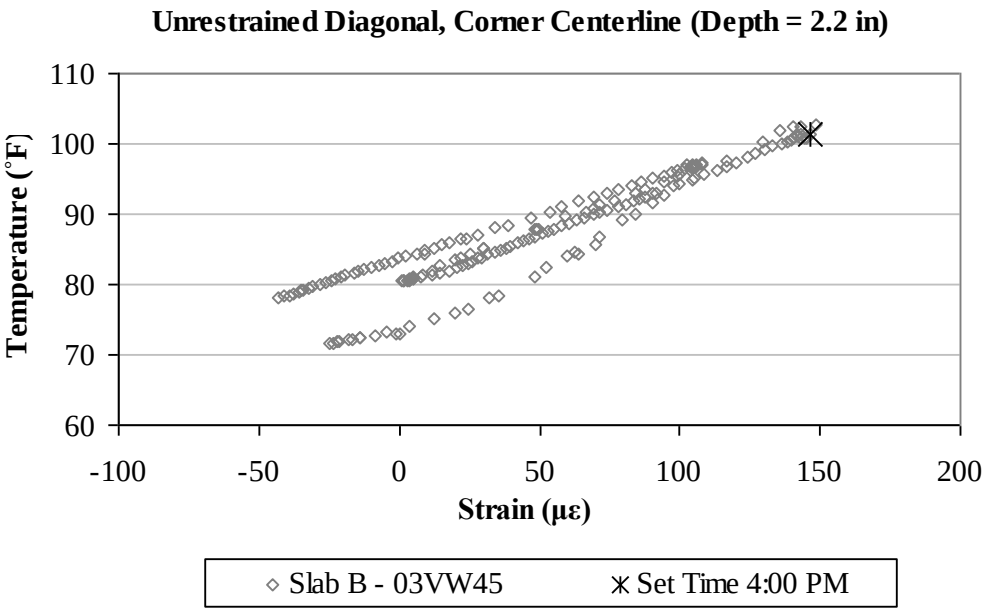

Figure A98. Early-age variation in the total strain with temperature, in the diagonal direction, for the top sensor located at the corner along the centerline joint in unrestrained Slab B.

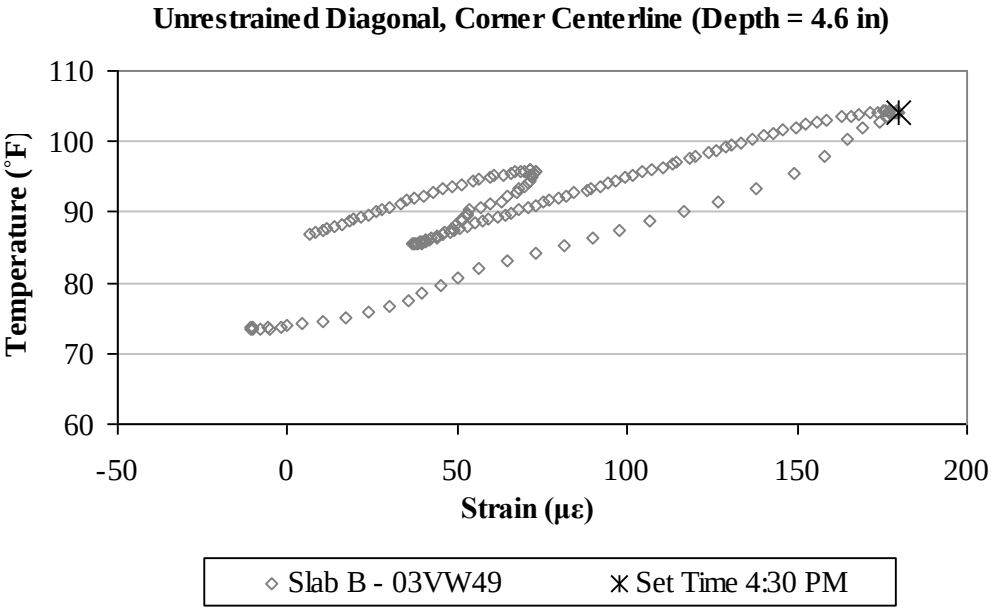

Figure A99. Early-age variation in the total strain with temperature, in the diagonal direction, for the middepth sensor located at the corner along the centerline joint in unrestrained Slab B.

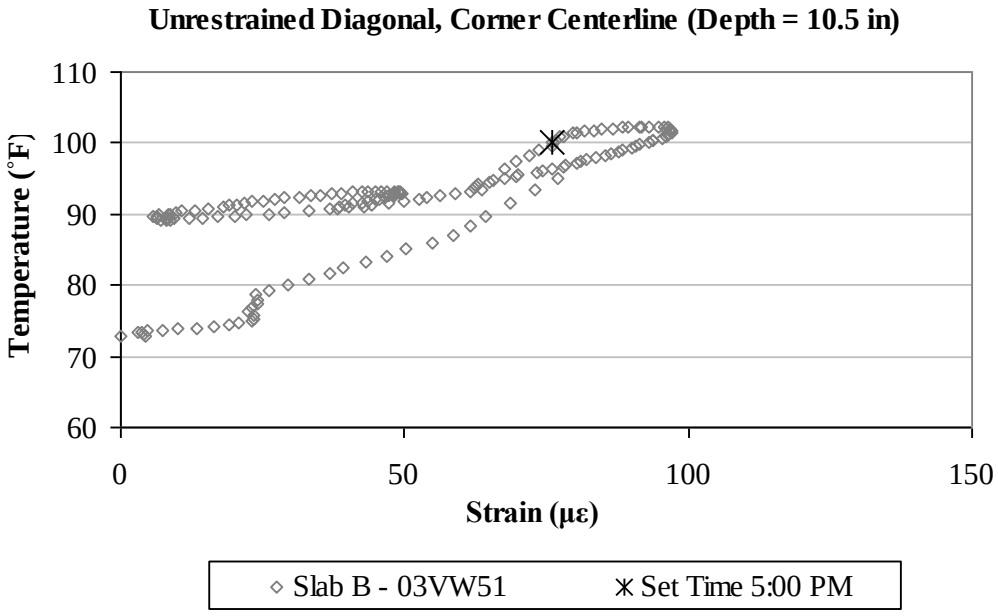

Figure A100. Early-age variation in the total strain with temperature, in the diagonal direction, for the bottom sensor located at the corner along the centerline joint in unrestrained Slab B.

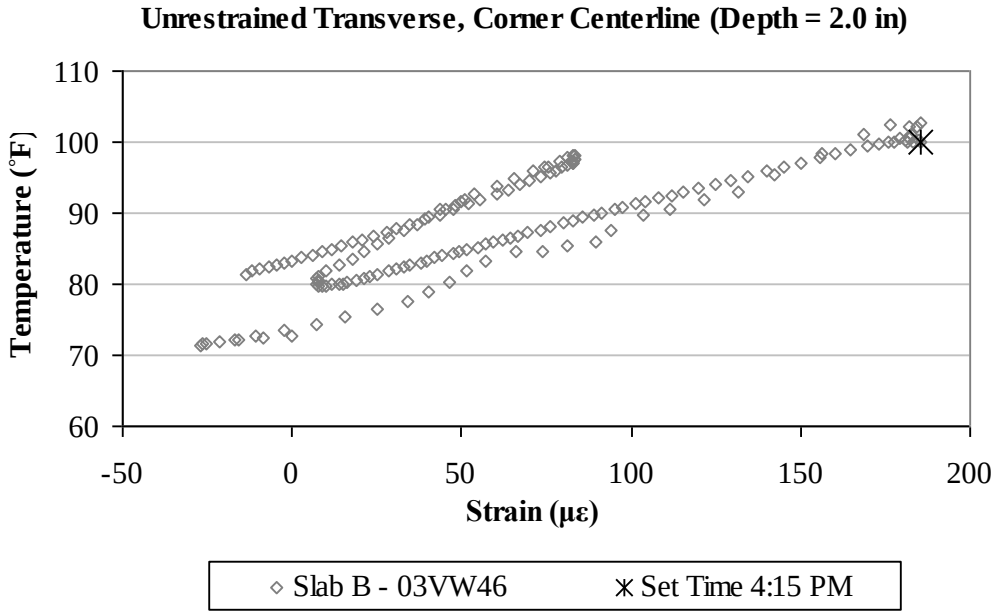

Figure A101. Early-age variation in the total strain with temperature, in the transverse direction, for the top sensor located at the corner along the centerline joint in unrestrained Slab B.

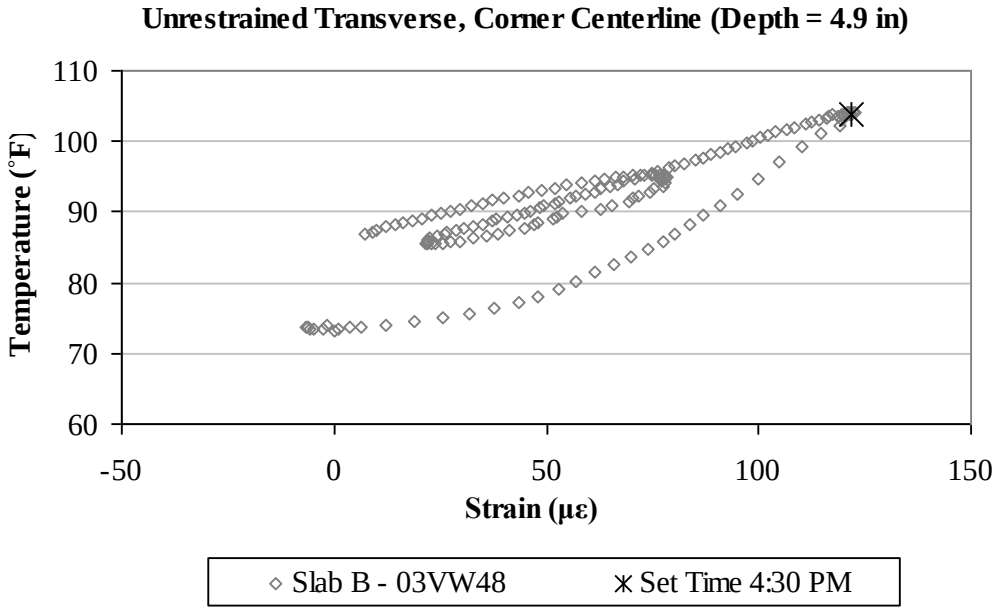

Figure A102. Early-age variation in the total strain with temperature, in the transverse direction, for the middepth sensor located at the corner along the centerline joint in unrestrained Slab B.

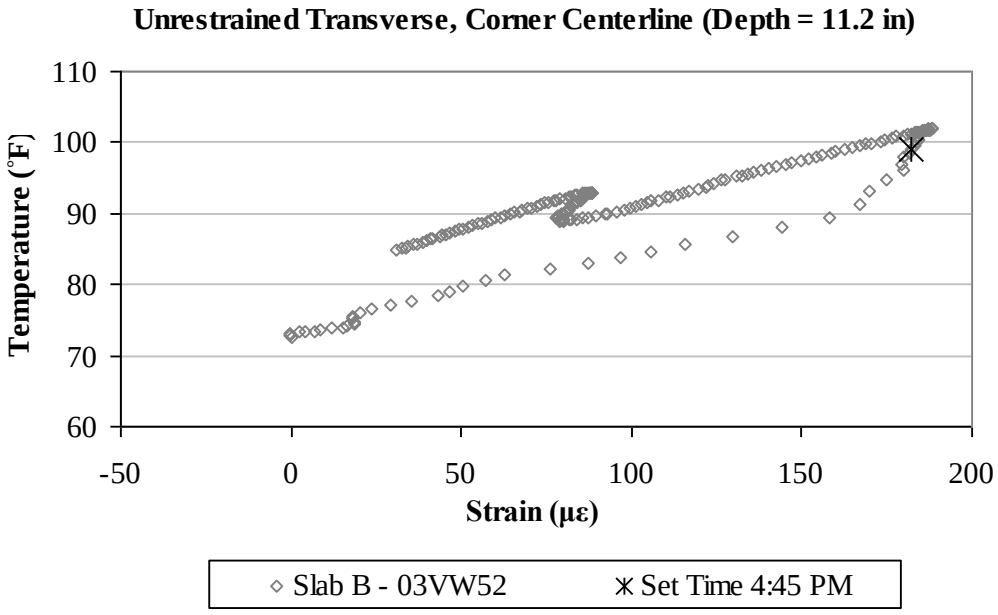

Figure A103. Early-age variation in the total strain with temperature, in the transverse direction, for the bottom sensor located at the corner along the centerline joint in unrestrained Slab B.

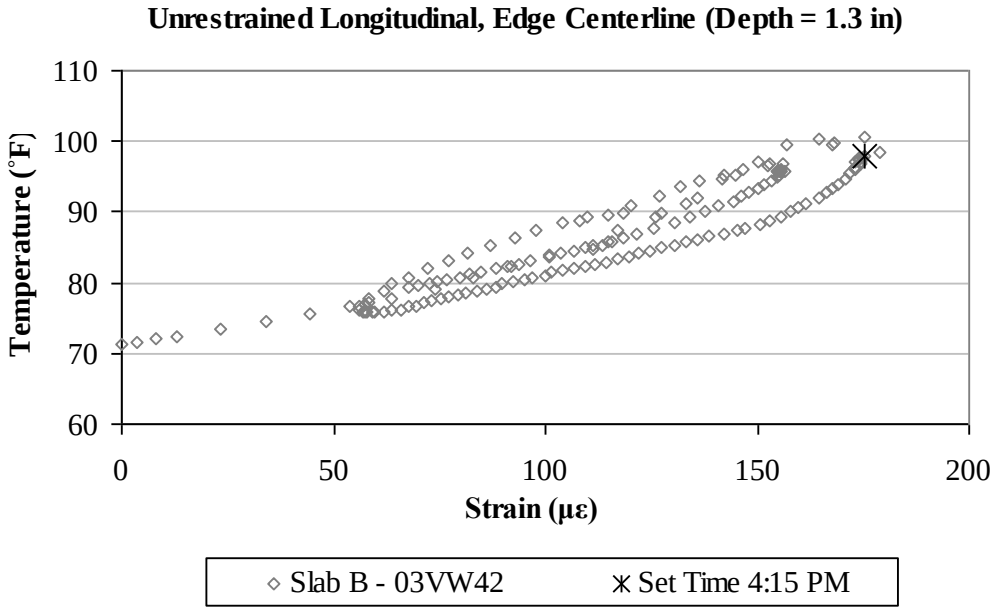

Figure A104. Early-age variation in the total strain with temperature, in the longitudinal direction, for the top sensor located along the centerline joint in unrestrained Slab B.

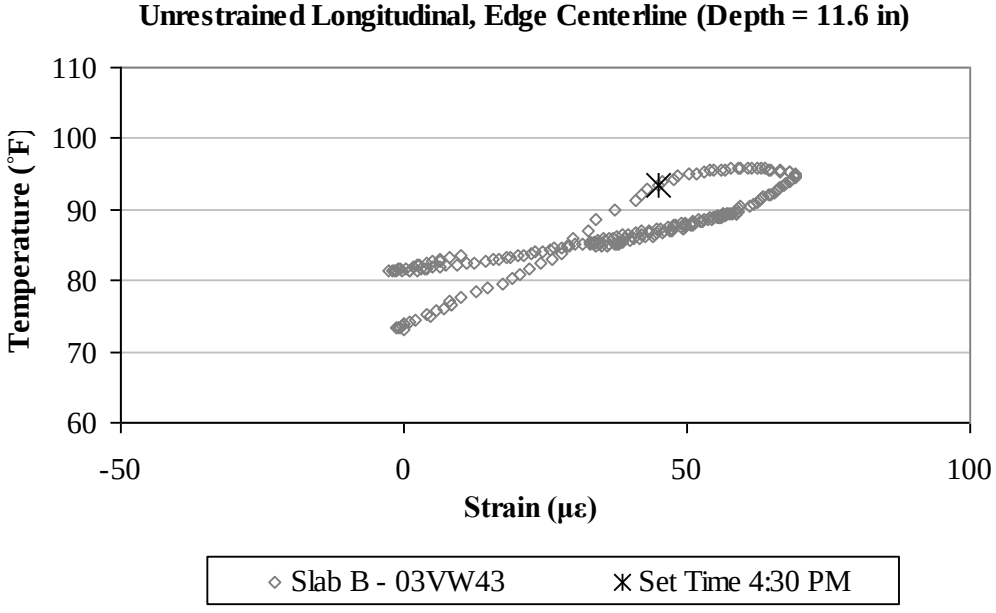

Figure A105. Early-age variation in the total strain with temperature, in the longitudinal direction, for the bottom sensor located along the centerline joint in unrestrained Slab B.

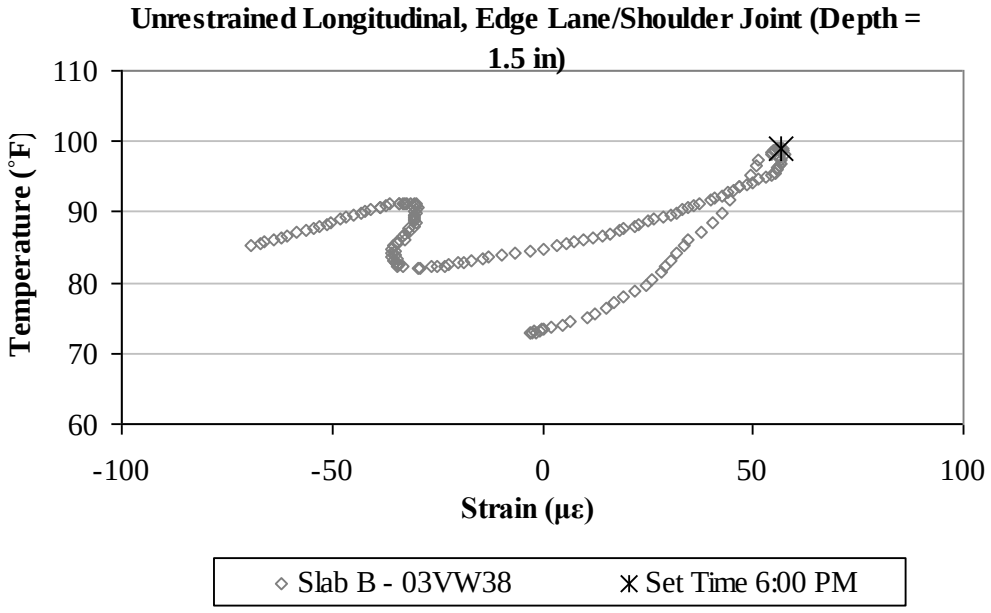

Figure A106. Early-age variation in the total strain with temperature, in the longitudinal direction, for the top sensor located along the lane/shoulder joint in unrestrained Slab B.

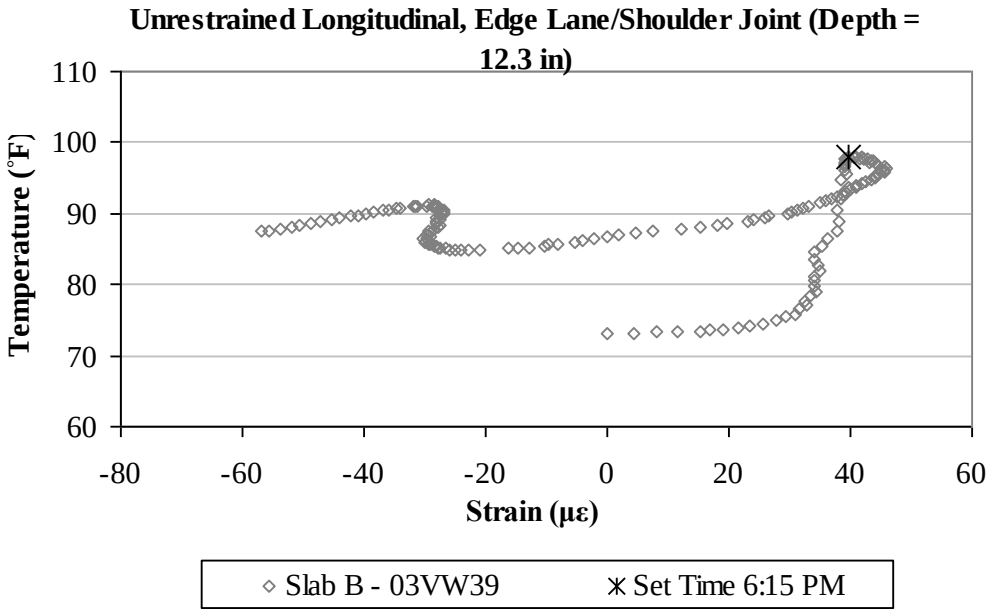

Figure A107. Early-age variation in the total strain with temperature, in the longitudinal direction, for the bottom sensor located along the lane/shoulder joint in unrestrained Slab B.

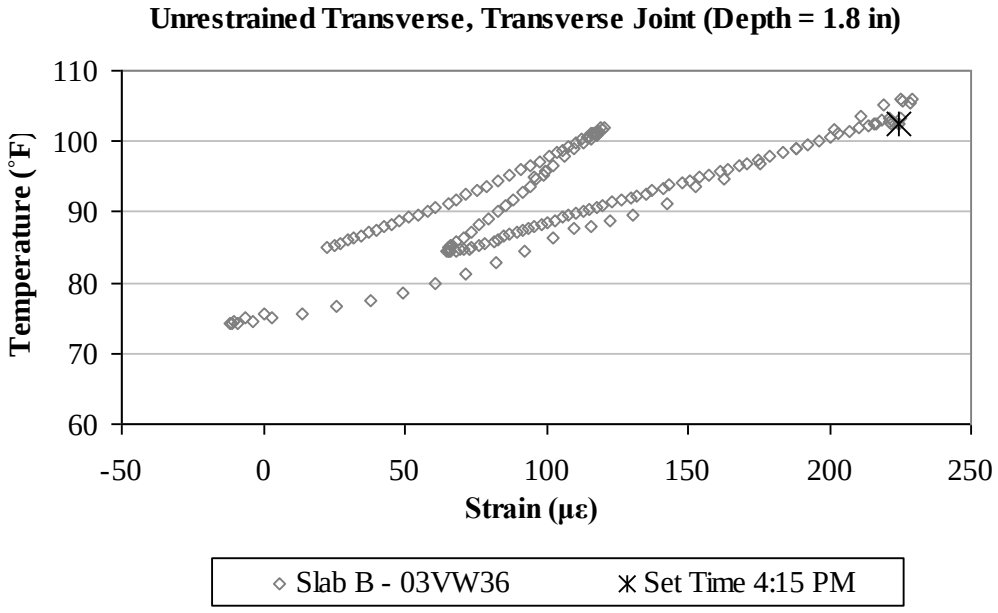

Figure A108. Early-age variation in the total strain with temperature, in the transverse direction, for the top sensor located along the transverse joint in unrestrained Slab B.

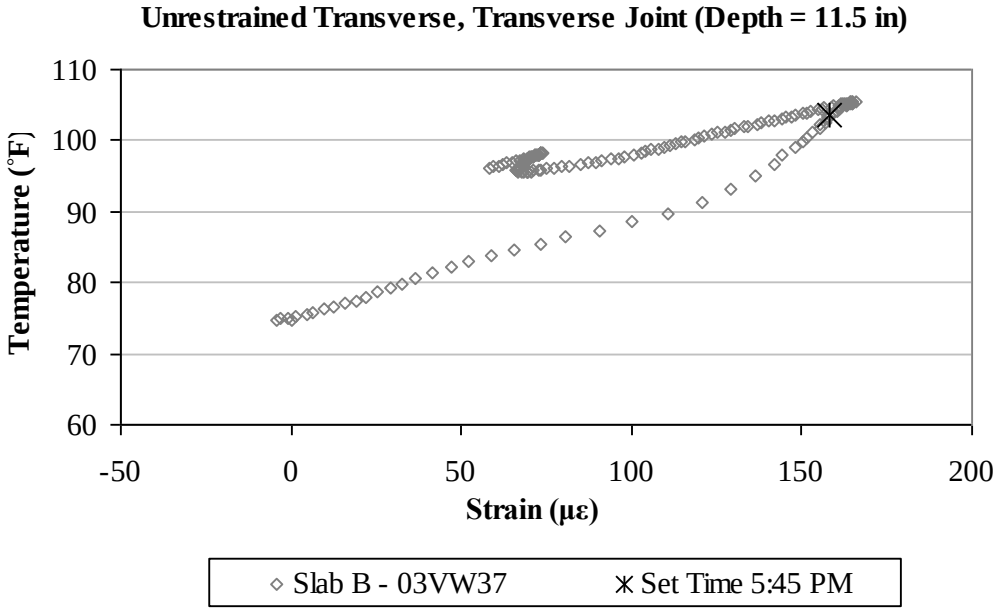

Figure A109. Early-age variation in the total strain with temperature, in the transverse direction, for the bottom sensor located along the transverse joint in unrestrained Slab B.

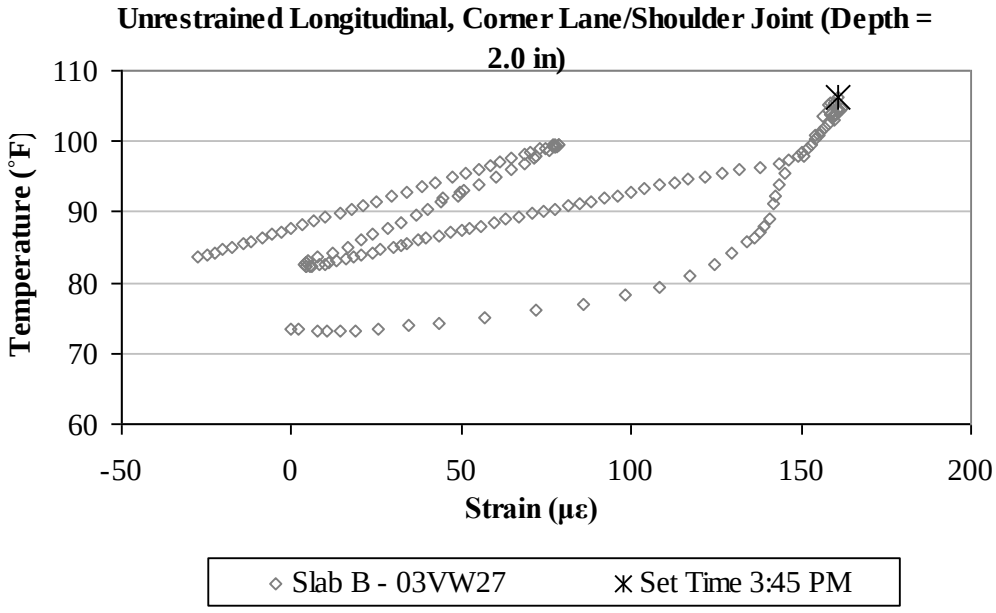

Figure A110. Early-age variation in the total strain with temperature, in the longitudinal direction, for the top sensor located at the corner along the lane/shoulder joint in unrestrained Slab B.

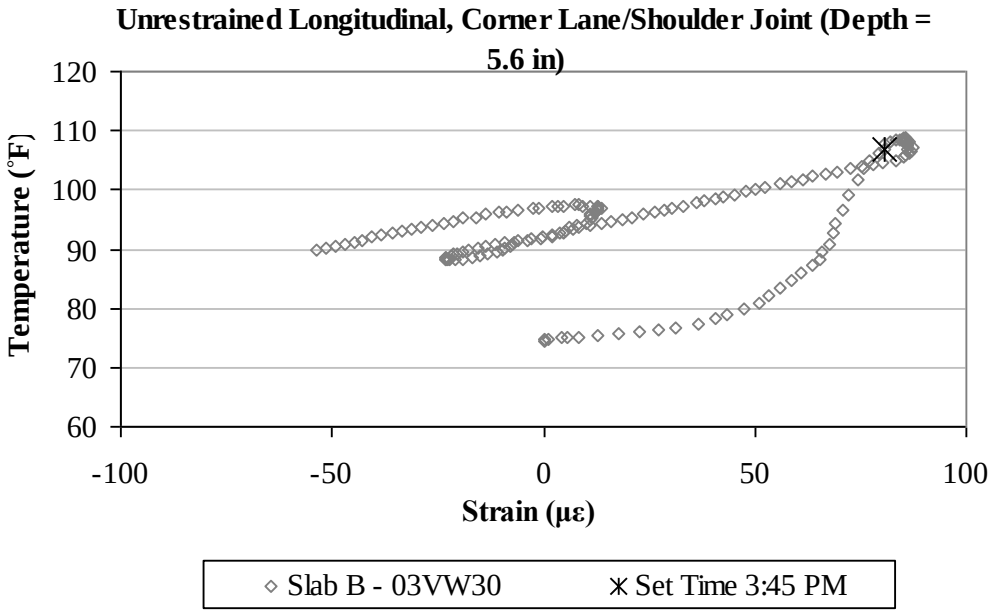

Figure A111. Early-age variation in the total strain with temperature, in the longitudinal direction, for the middepth sensor located at the corner along the lane/shoulder joint in unrestrained Slab B.

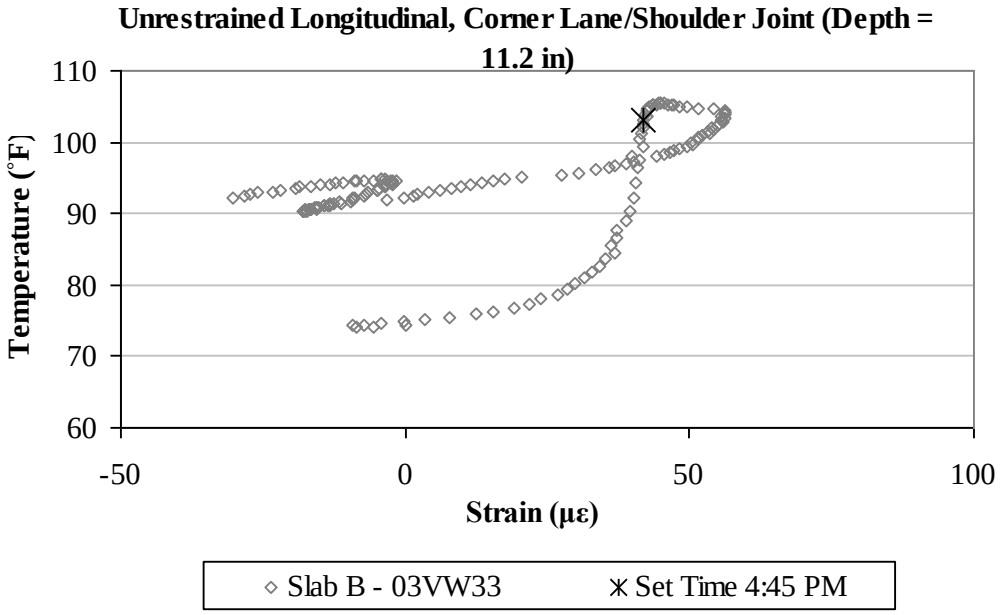

Figure A112. Early-age variation in the total strain with temperature, in the longitudinal direction, for the bottom sensor located at the corner along the lane/shoulder joint in unrestrained Slab B.

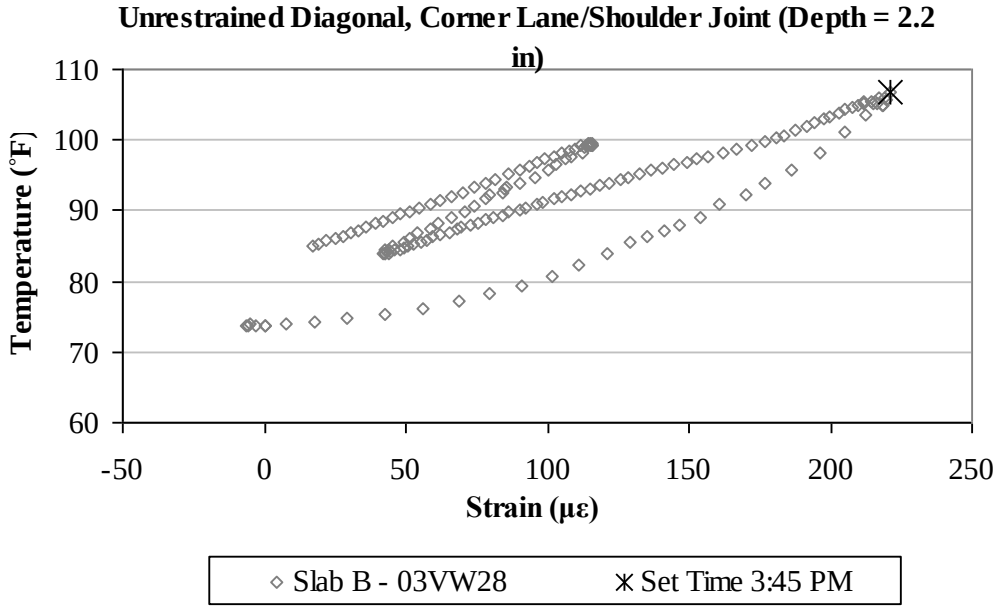

Figure A113. Early-age variation in the total strain with temperature, in the diagonal direction, for the top sensor located at the corner along the lane/shoulder joint in unrestrained Slab B.

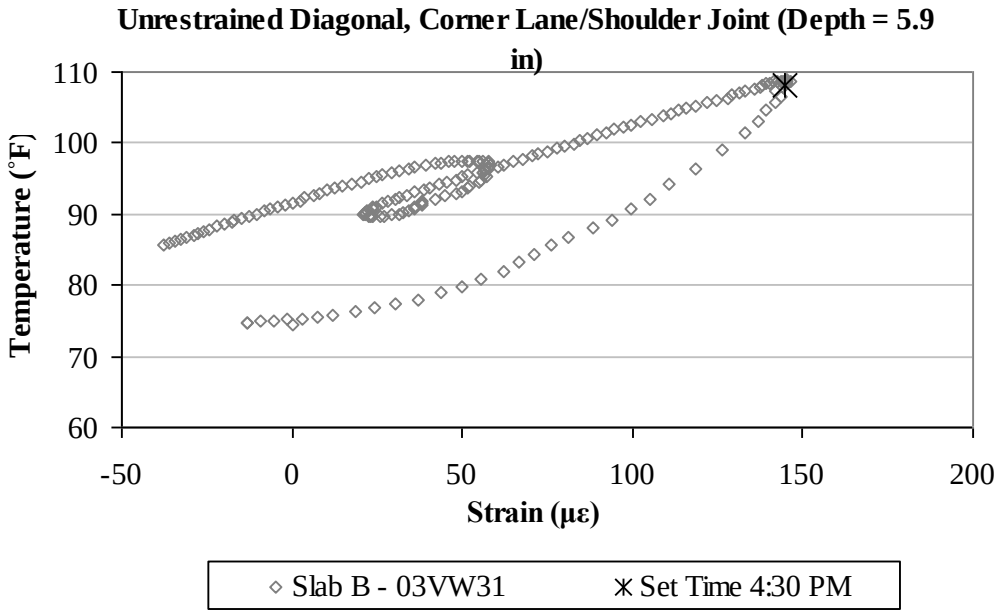

Figure A114. Early-age variation in the total strain with temperature, in the diagonal direction, for the middepth sensor located at the corner along the lane/shoulder joint in unrestrained Slab B.

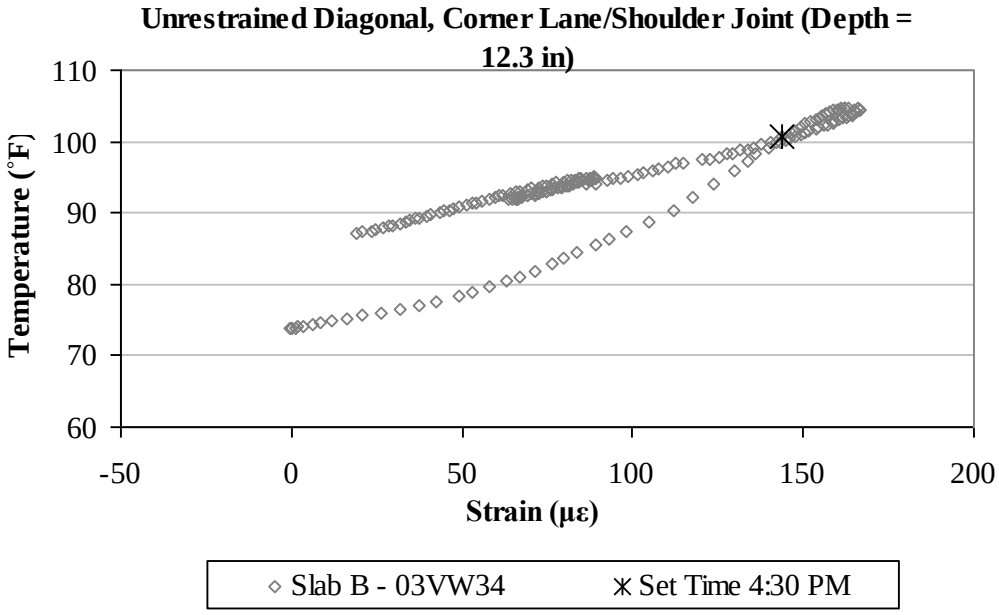

Figure A115. Early-age variation in the total strain with temperature, in the diagonal direction, for the bottom sensor located at the corner along the lane/shoulder joint in unrestrained Slab B.

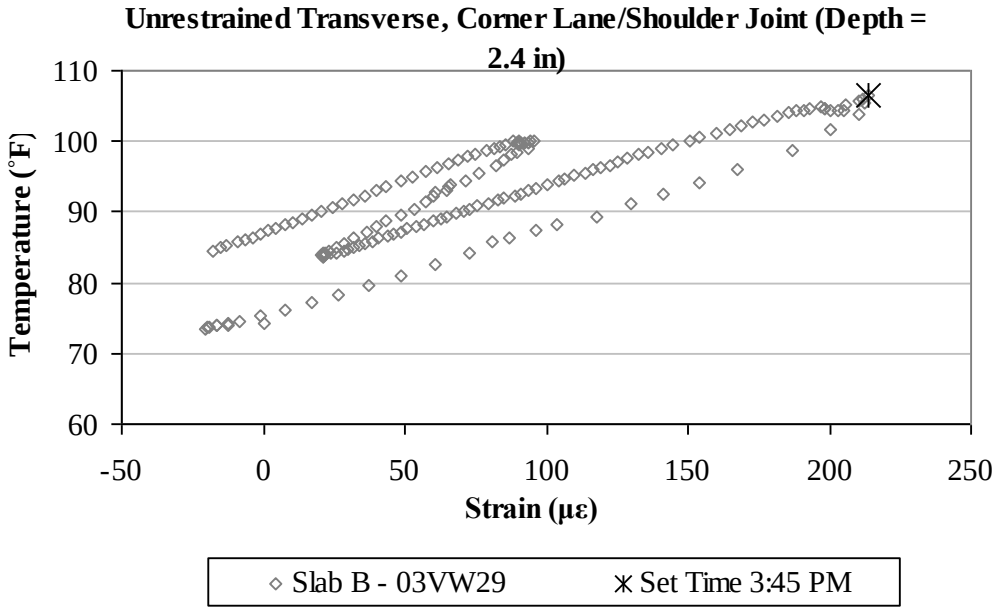

Figure A116. Early-age variation in the total strain with temperature, in the transverse direction, for the top sensor located at the corner along the lane/shoulder joint in unrestrained Slab B.

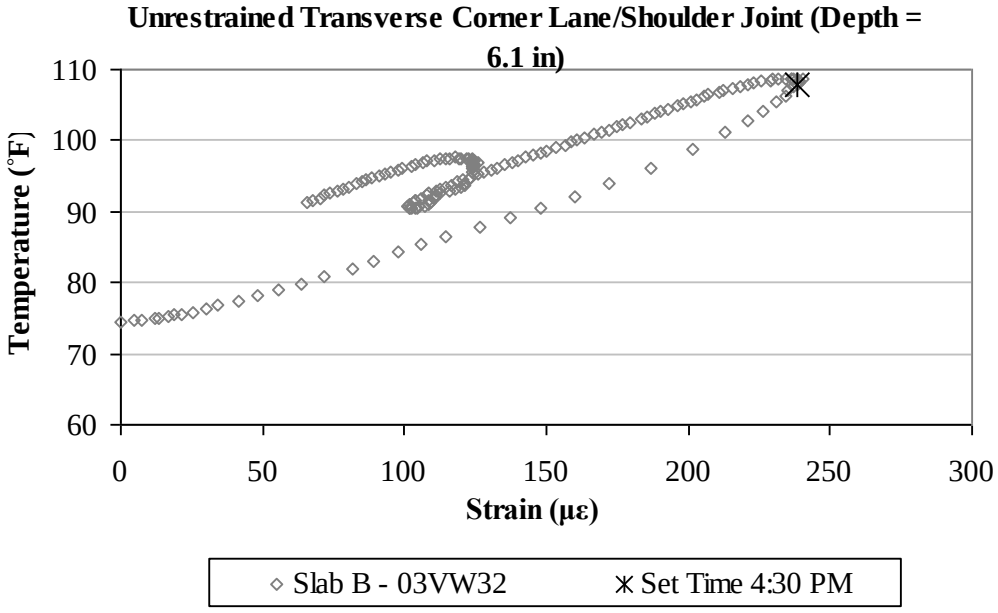

Figure A117. Early-age variation in the total strain with temperature, in the transverse direction, for the middepth sensor located at the corner along the lane/shoulder joint in unrestrained Slab B.

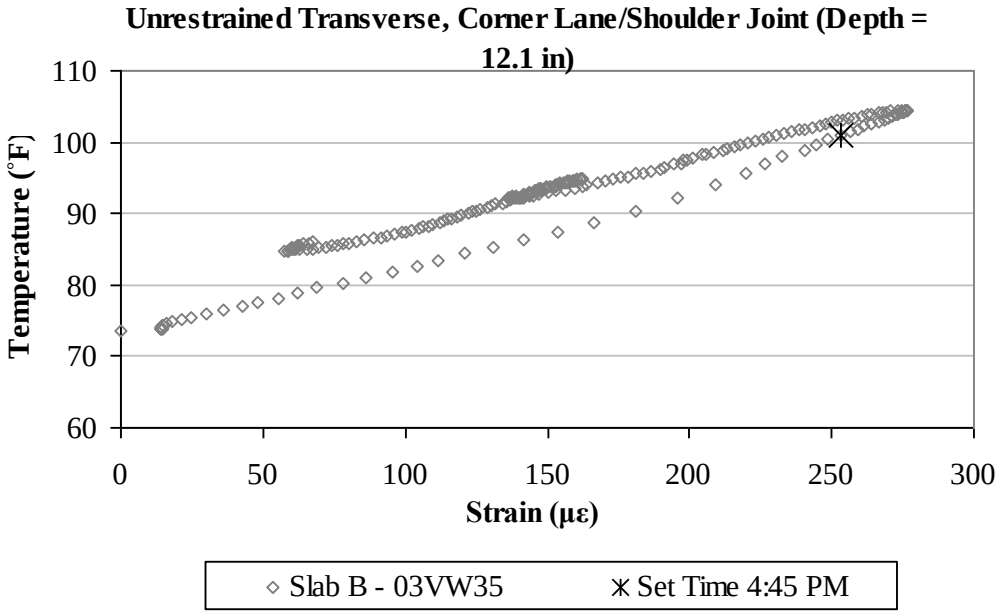

Figure A118. Early-age variation in the total strain with temperature, in the transverse direction, for the bottom sensor located at the corner along the lane/shoulder joint in unrestrained Slab B.

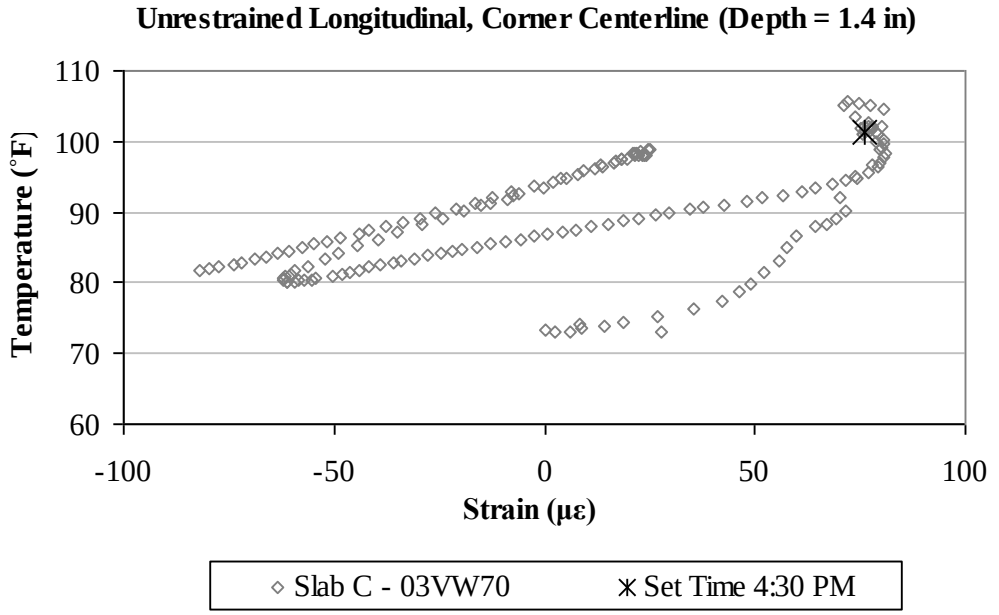

Figure A119. Early-age variation in the total strain with temperature, in the longitudinal direction, for the top sensor located at the corner along the centerline joint in unrestrained Slab C.

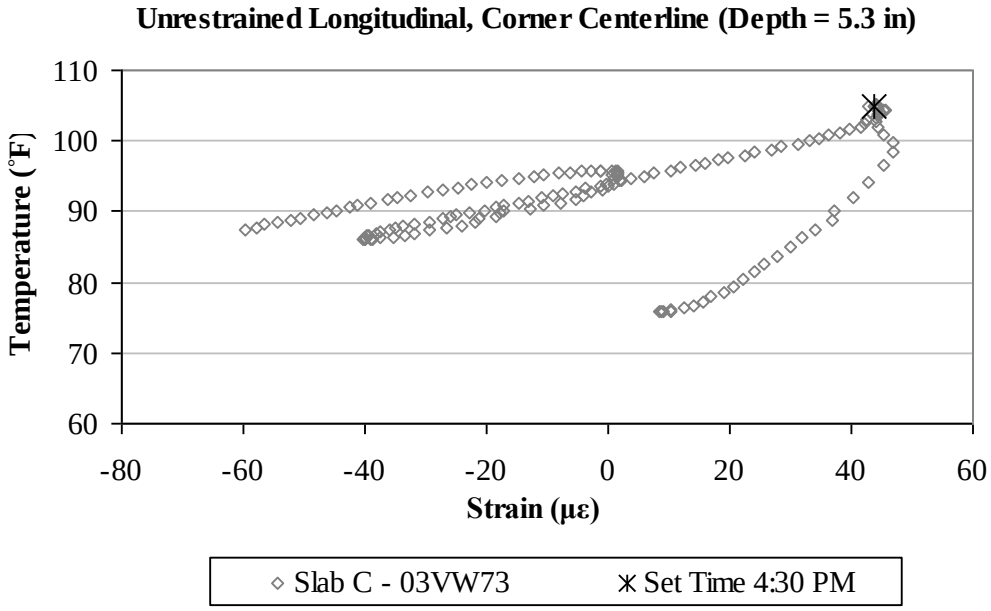

Figure A120. Early-age variation in the total strain with temperature, in the longitudinal direction, for the middepth sensor located at the corner along the centerline joint in unrestrained Slab C.

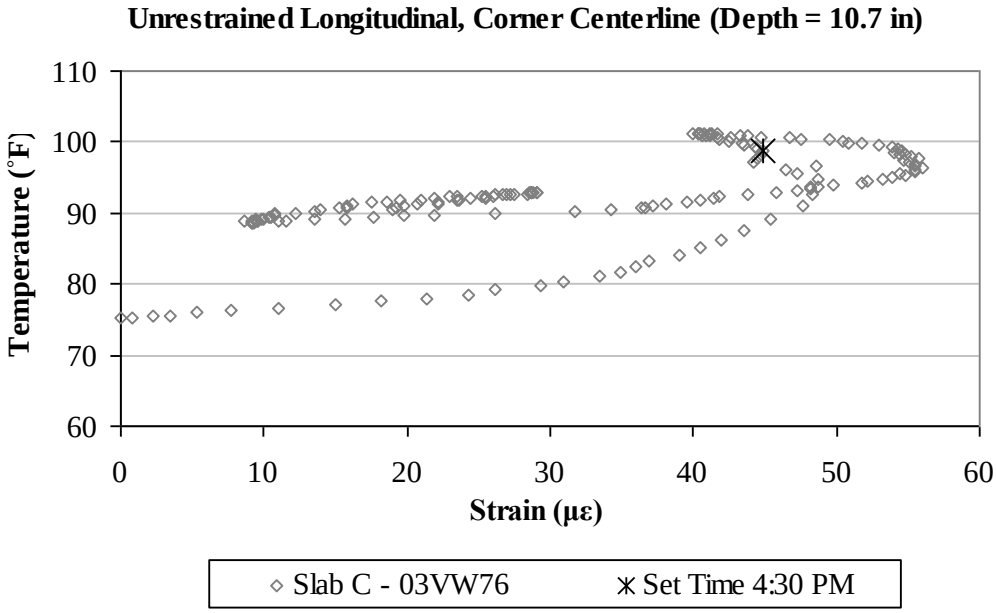

Figure A121. Early-age variation in the total strain with temperature, in the longitudinal direction, for the bottom sensor located at the corner along the centerline joint in unrestrained Slab C.

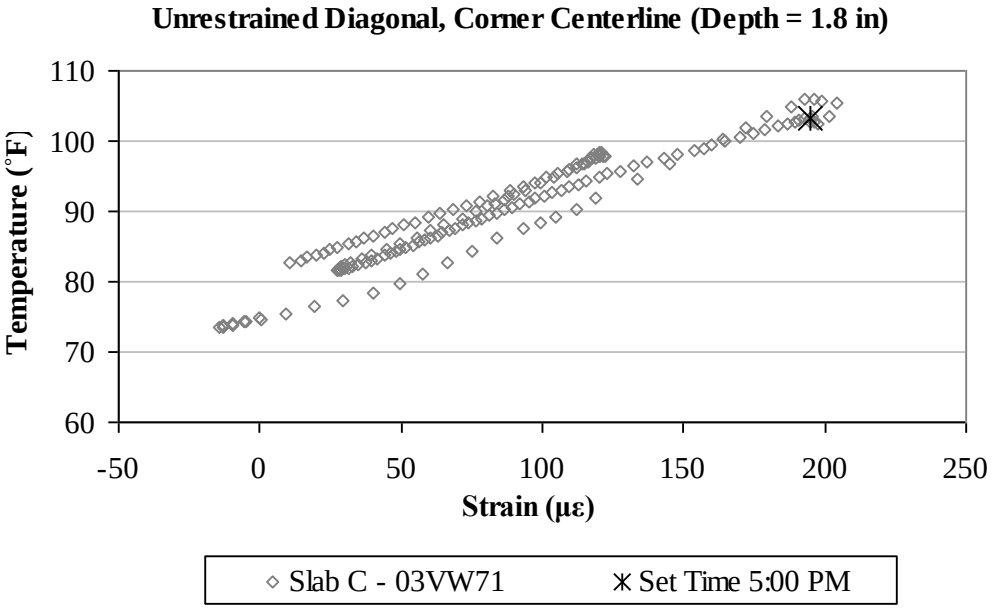

Figure A122. Early-age variation in the total strain with temperature, in the diagonal direction, for the top sensor located at the corner along the centerline joint in unrestrained Slab C.

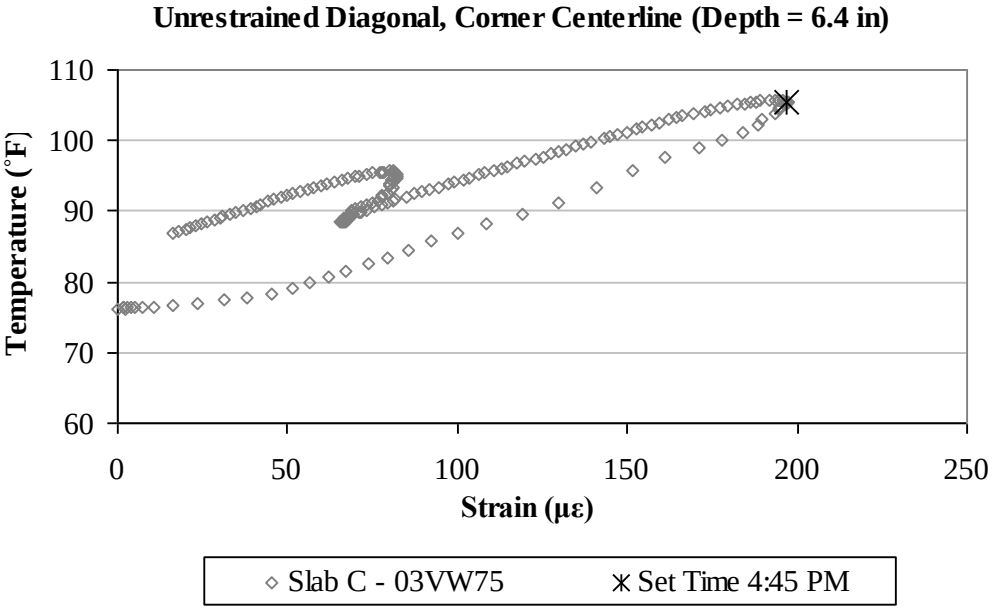

Figure A123. Early-age variation in the total strain with temperature, in the diagonal direction, for the middepth sensor located at the corner along the centerline joint in unrestrained Slab C.

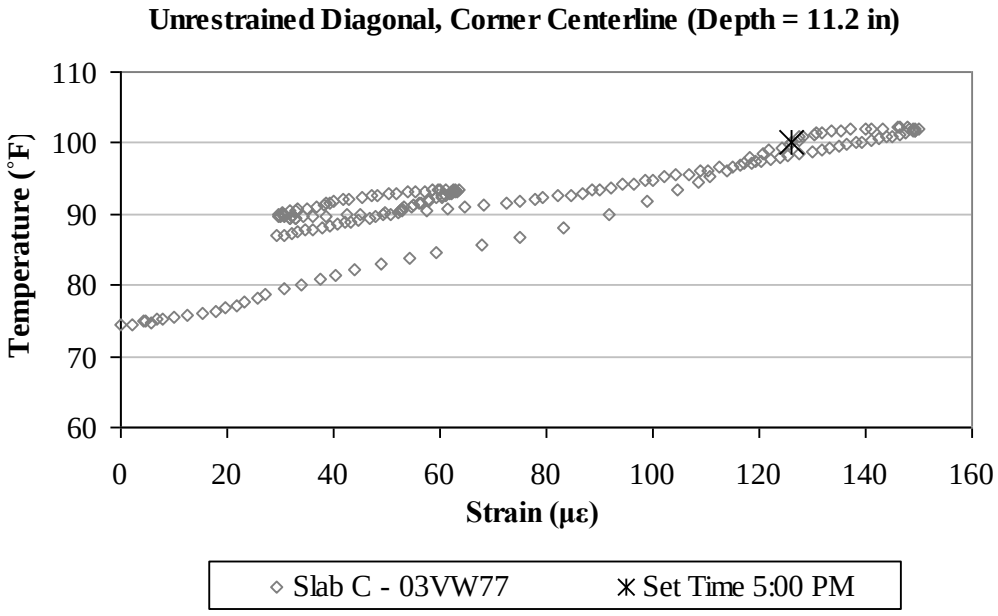

Figure A124. Early-age variation in the total strain with temperature, in the diagonal direction, for the bottom sensor located at the corner along the centerline joint in unrestrained Slab C.

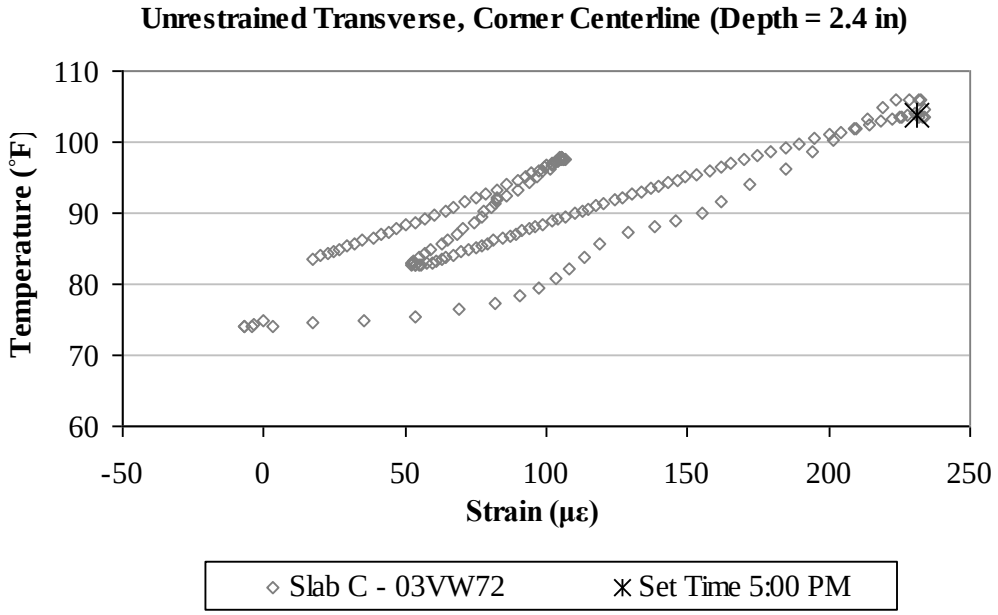

Figure A125. Early-age variation in the total strain with temperature, in the transverse direction, for the top sensor located at the corner along the centerline joint in unrestrained Slab C.

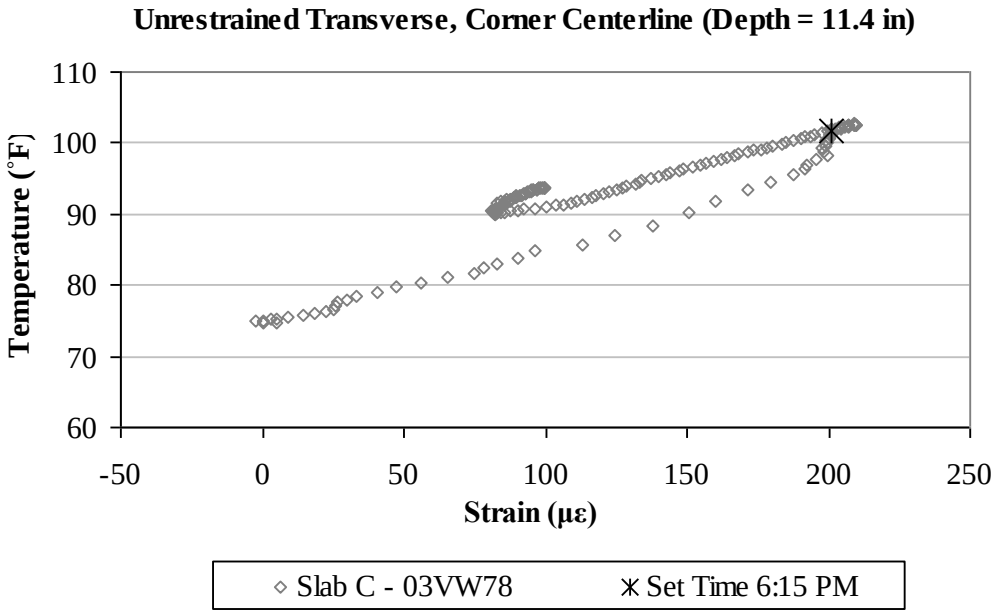

Figure A126. Early-age variation in the total strain with temperature, in the transverse direction, for the bottom sensor located at the corner along the centerline joint in unrestrained Slab C.

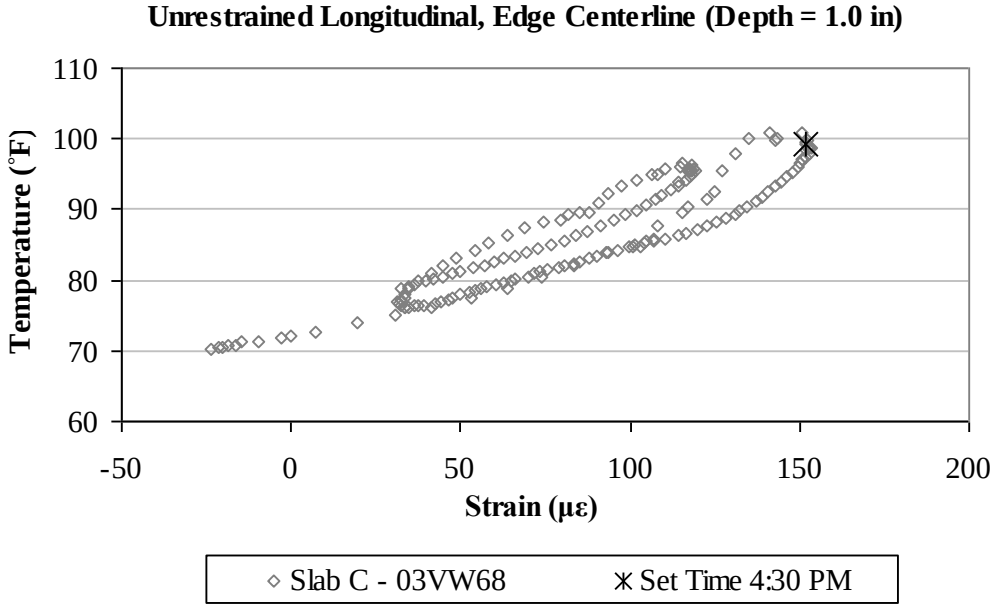

Figure A127. Early-age variation in the total strain with temperature, in the longitudinal direction, for the top sensor located along the centerline joint in unrestrained Slab C.

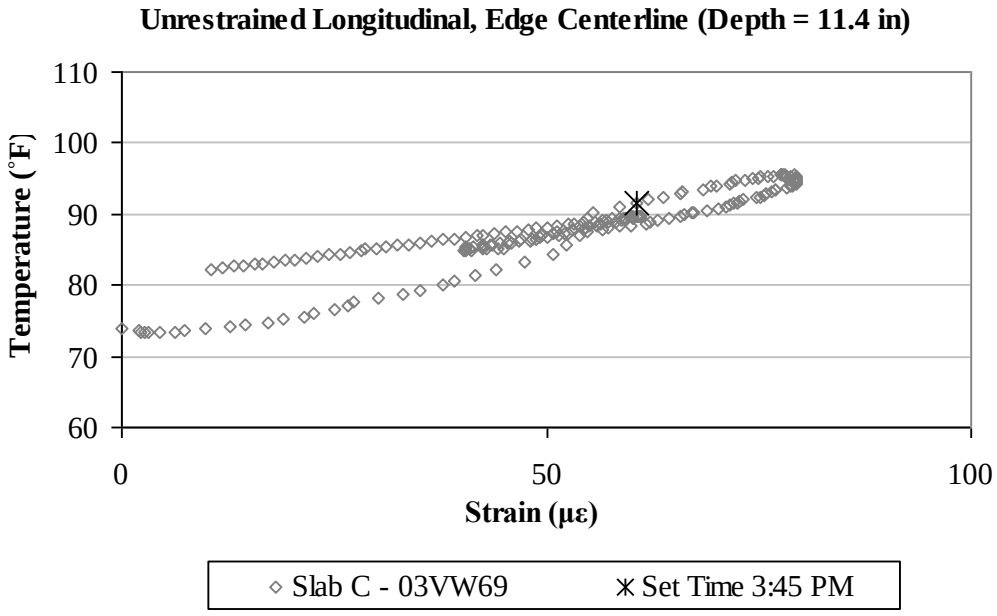

Figure A128. Early-age variation in the total strain with temperature, in the longitudinal direction, for the bottom sensor located along the centerline joint in unrestrained Slab C.

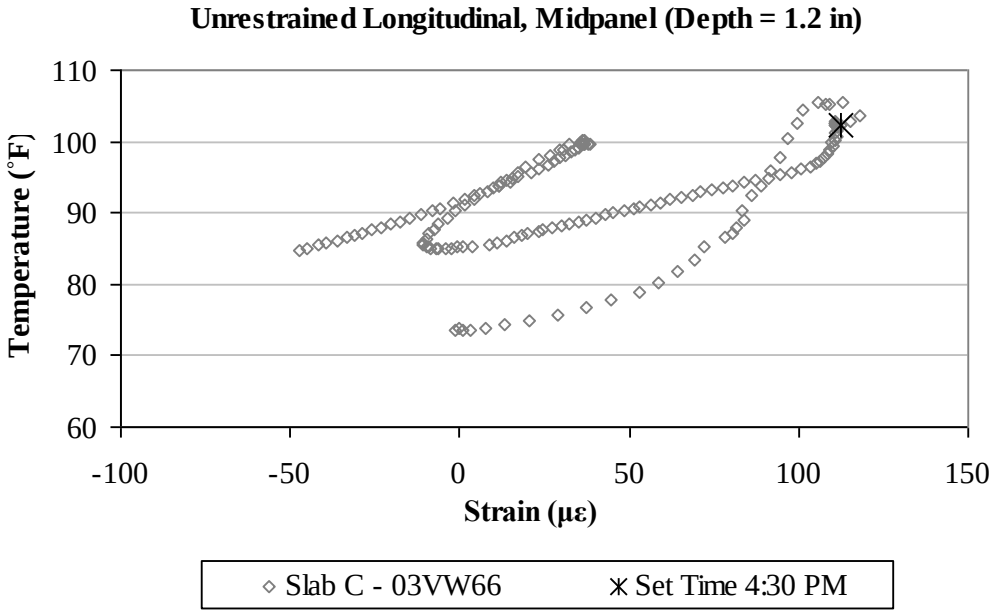

Figure A129. Early-age variation in the total strain with temperature, in the longitudinal direction, for the top sensor located at midpanel in unrestrained Slab C.

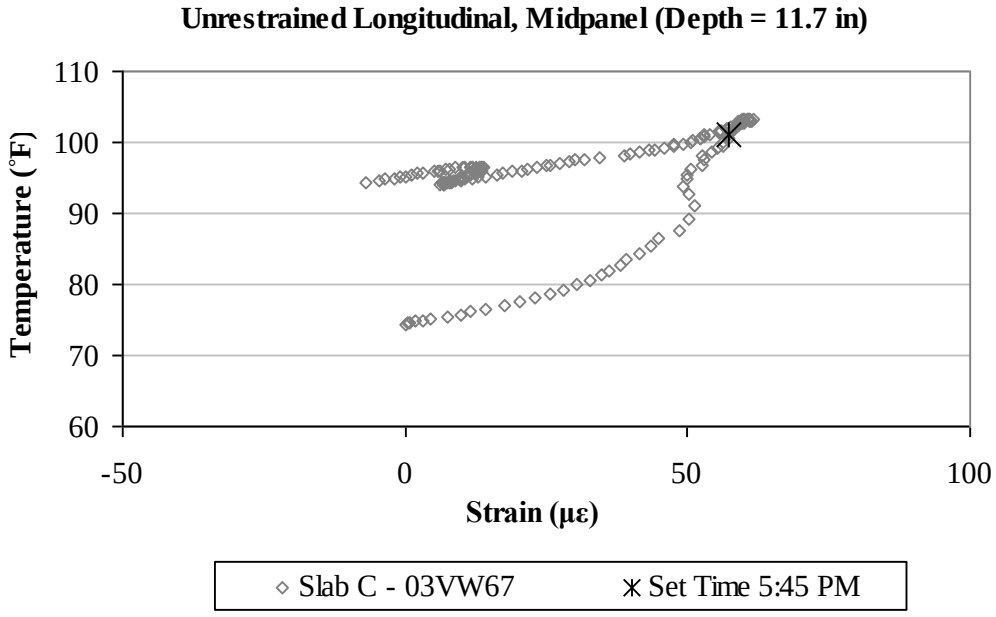

Figure A130. Early-age variation in the total strain with temperature, in the longitudinal direction, for the bottom sensor located at midpanel in unrestrained Slab C.

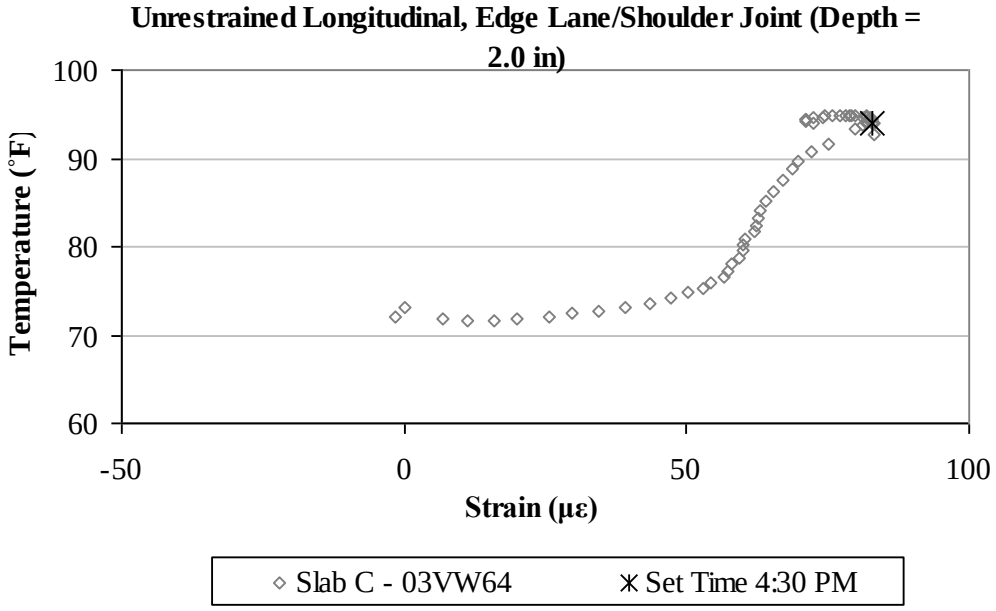

Figure A131. Early-age variation in the total strain with temperature, in the longitudinal direction, for the top sensor located along the lane/shoulder joint in unrestrained Slab C.

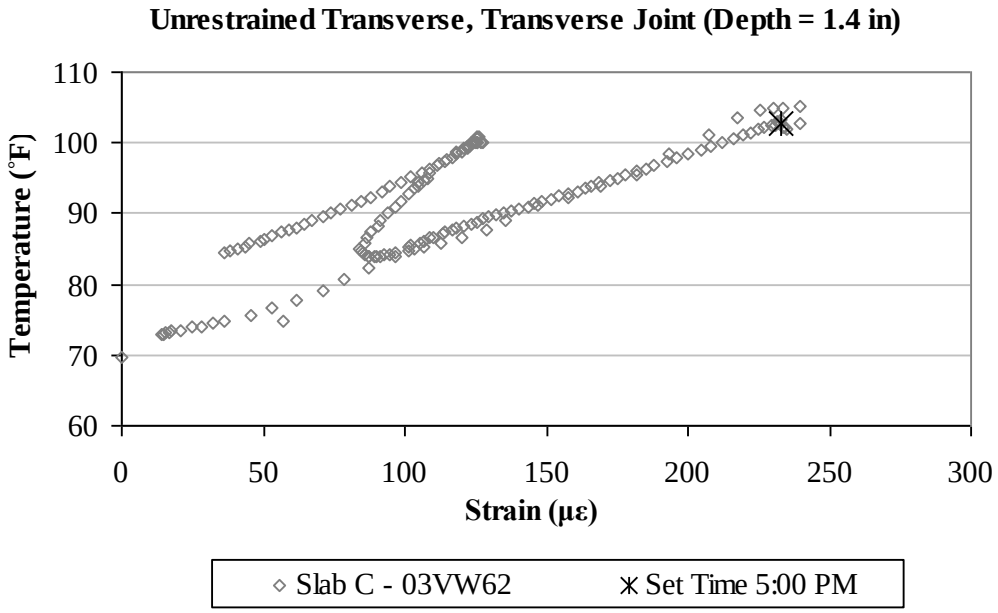

Figure A132. Early-age variation in the total strain with temperature, in the transverse direction, for the top sensor located along the transverse joint in unrestrained Slab C.

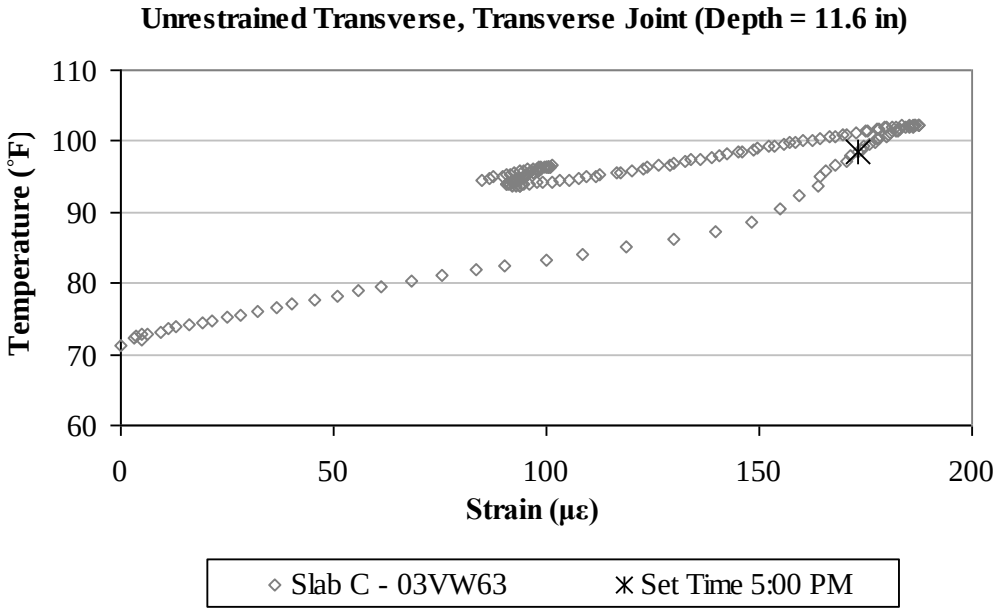

Figure A133. Early-age variation in the total strain with temperature, in the transverse direction, for the bottom sensor located along the transverse joint in unrestrained Slab C.

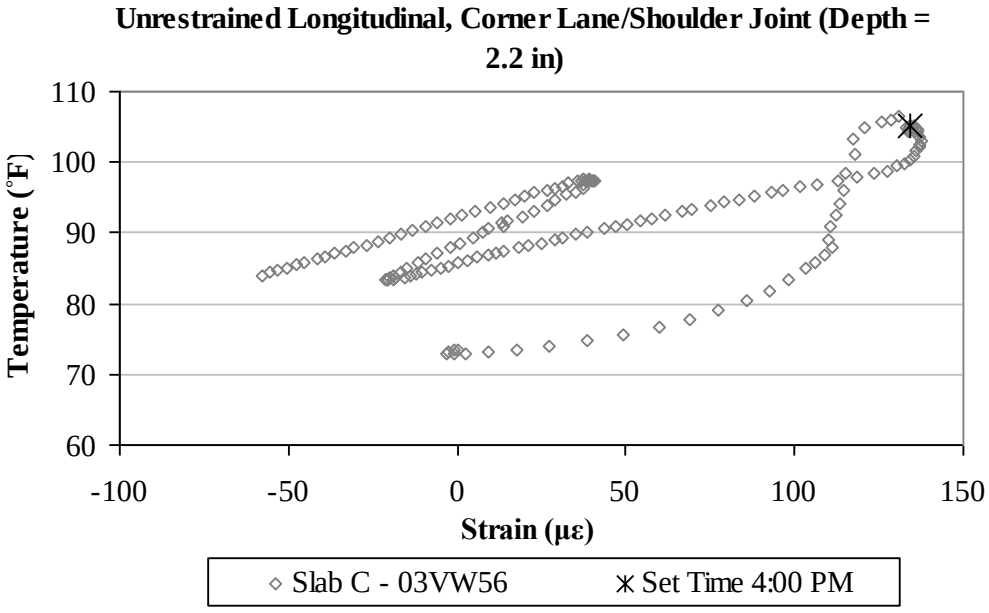

Figure A134. Early-age variation in the total strain with temperature, in the longitudinal direction, for the top sensor located at the corner along the lane/shoulder joint in unrestrained Slab C.

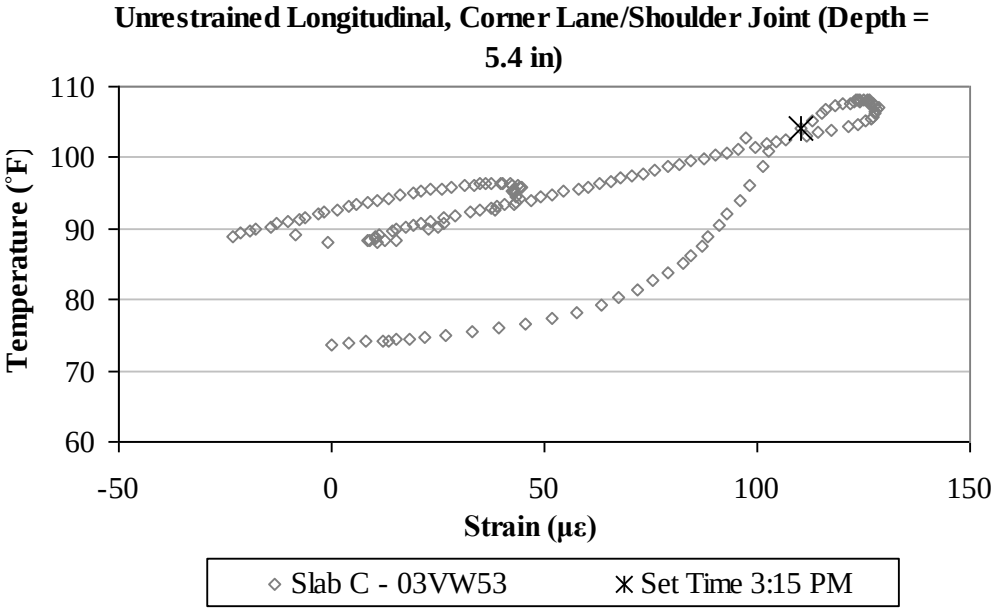

Figure A135. Early-age variation in the total strain with temperature, in the longitudinal direction, for the middepth sensor located at the corner along the lane/shoulder joint in unrestrained Slab C.

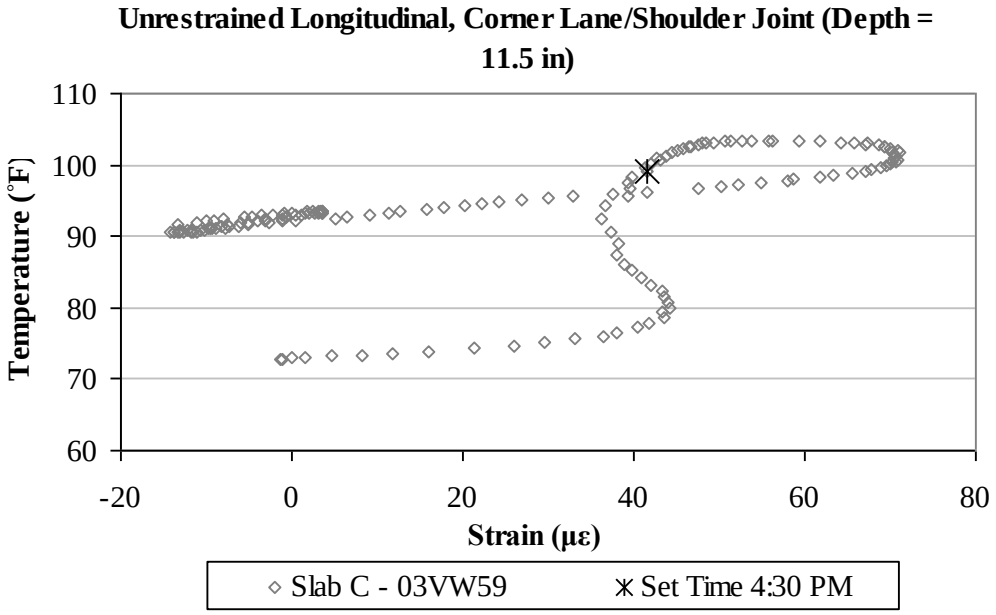

Figure A136. Early-age variation in the total strain with temperature, in the longitudinal direction, for the bottom sensor located at the corner along the lane/shoulder joint in unrestrained Slab C.

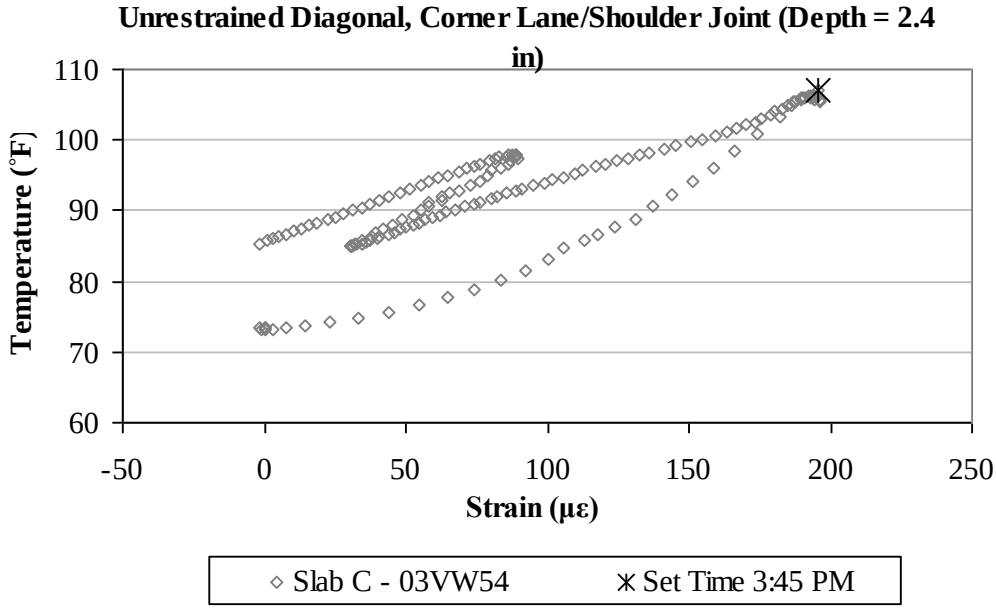

Figure A137. Early-age variation in the total strain with temperature, in the diagonal direction, for the top sensor located at the corner along the lane/shoulder joint in unrestrained Slab C.

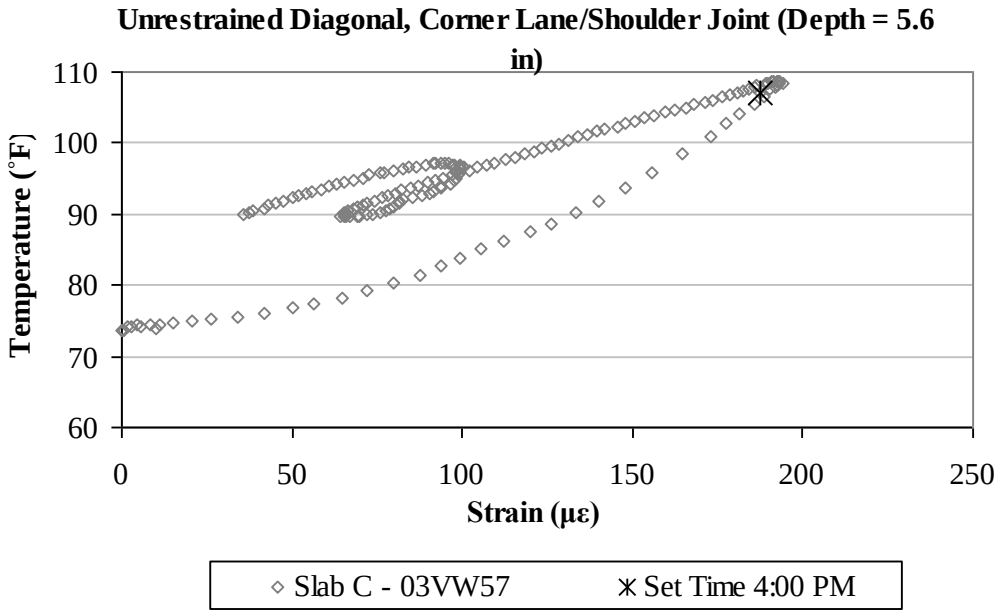

Figure A138. Early-age variation in the total strain with temperature, in the diagonal direction, for the middepth sensor located at the corner along the lane/shoulder joint in unrestrained Slab C.

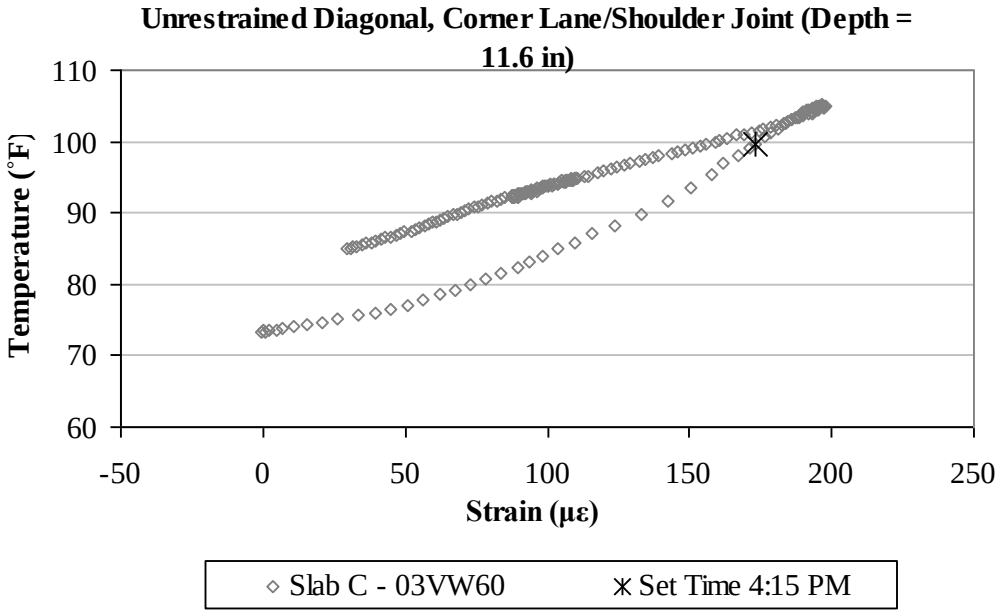

Figure A139. Early-age variation in the total strain with temperature, in the diagonal direction, for the bottom sensor located at the corner along the lane/shoulder joint in unrestrained Slab C.

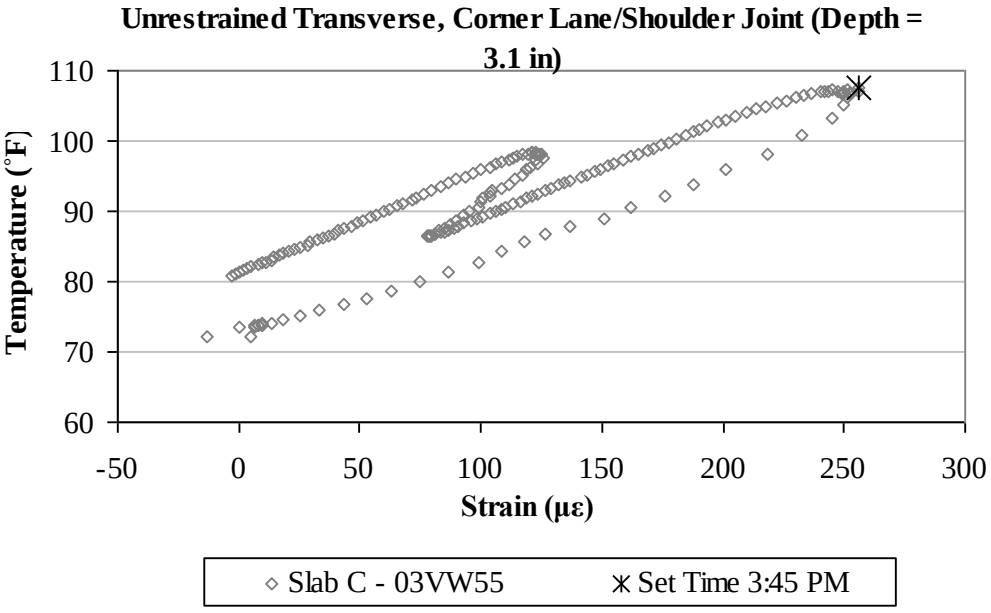

Figure A140. Early-age variation in the total strain with temperature, in the transverse direction, for the top sensor located at the corner along the lane/shoulder joint in unrestrained Slab C.

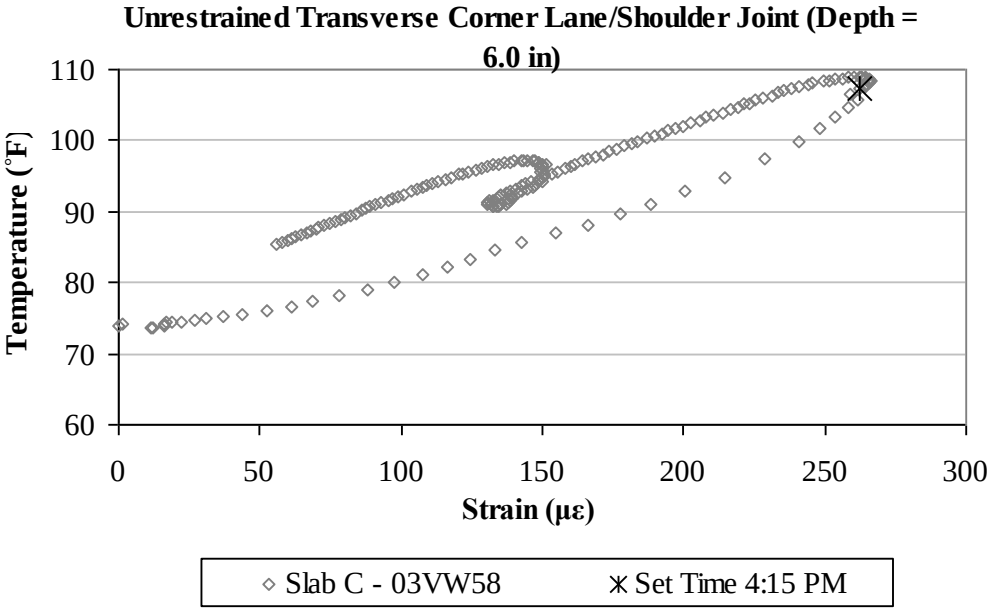

Figure A141. Early-age variation in the total strain with temperature, in the transverse direction, for the middepth sensor located at the corner along the lane/shoulder joint in unrestrained Slab C.

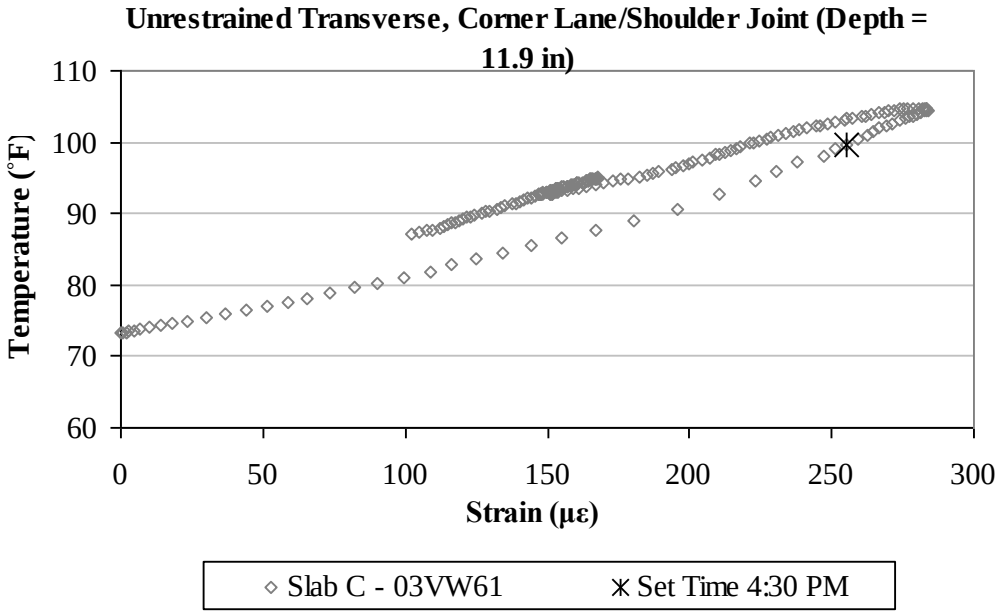

Figure A142. Early-age variation in the total strain with temperature, in the transverse direction, for the bottom sensor located at the corner along the lane/shoulder joint in unrestrained Slab C.

APPENDIX B

VIBRATING WIRE STRAIN GAGE MEASUREMENTS

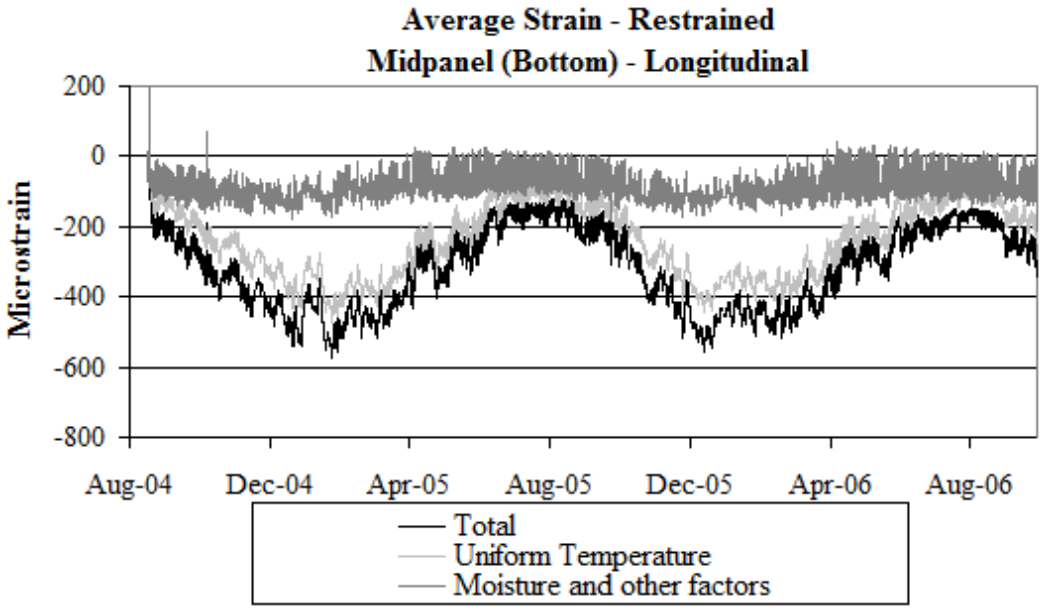

Figure B1. Strain in the longitudinal direction at midpanel at the bottom of the restrained slabs.

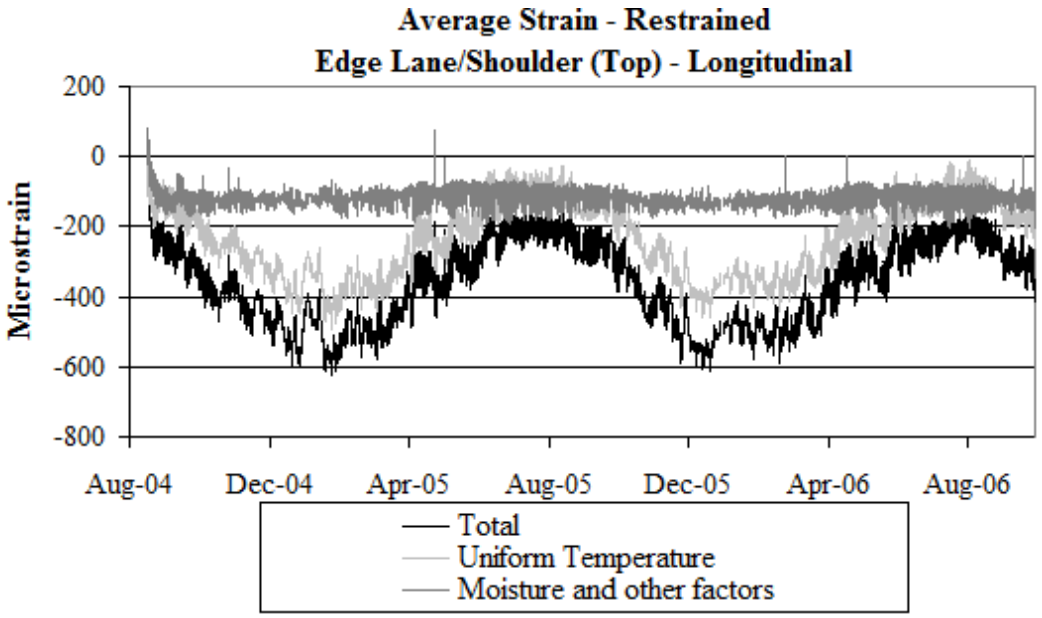

Figure B2. Strain in the longitudinal direction along the lane/shoulder joint at the top of the restrained slabs.

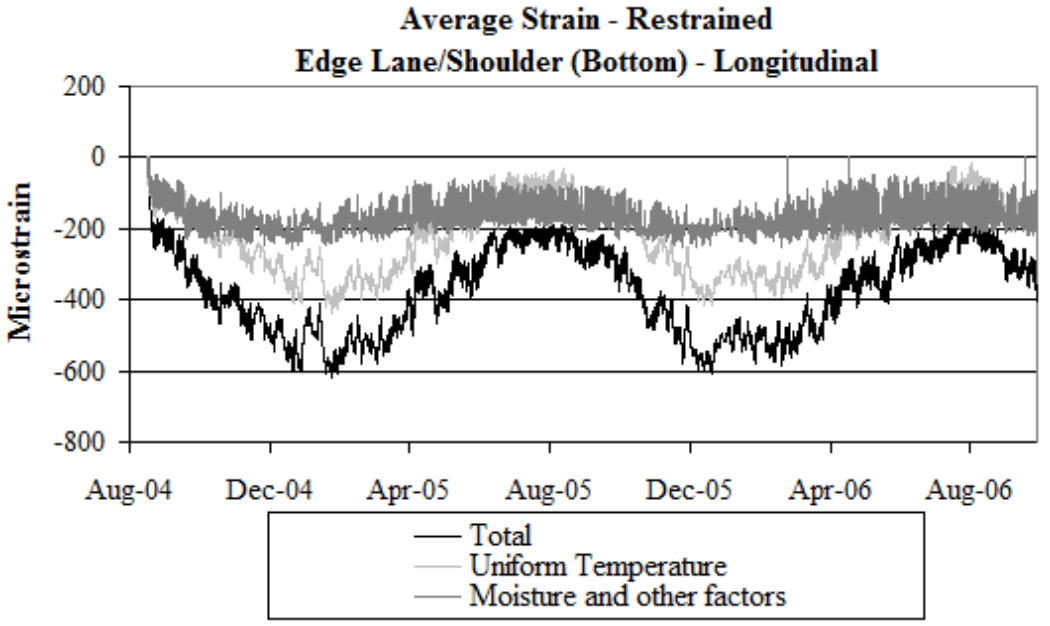

Figure B3. Strain in the longitudinal direction along the lane/shoulder joint at the bottom of the restrained slabs.

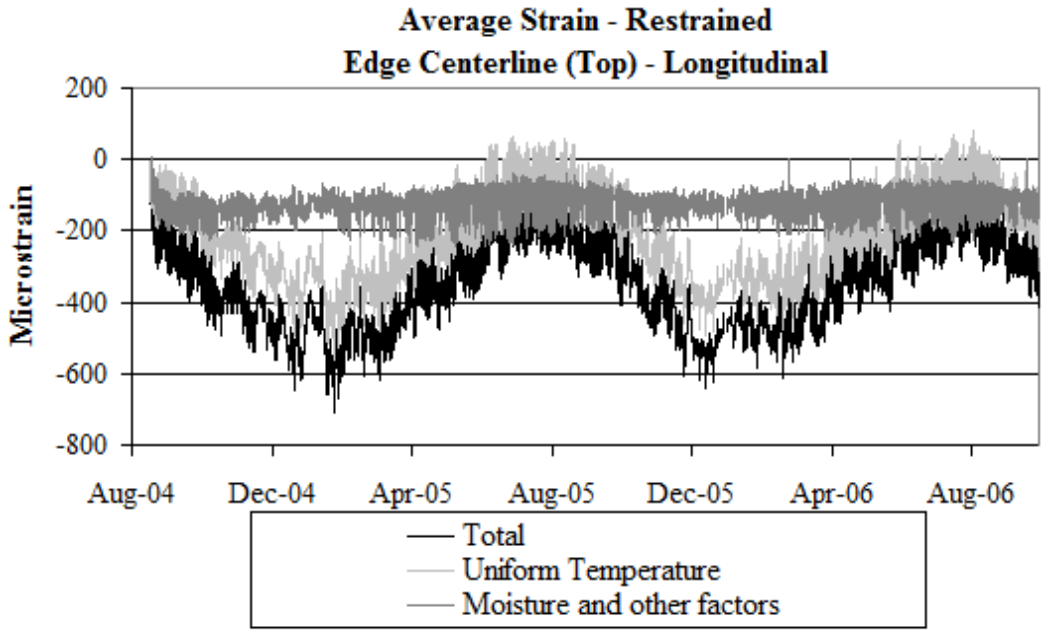

Figure B4. Strain in the longitudinal direction along the centerline joint at the top of the restrained slabs.

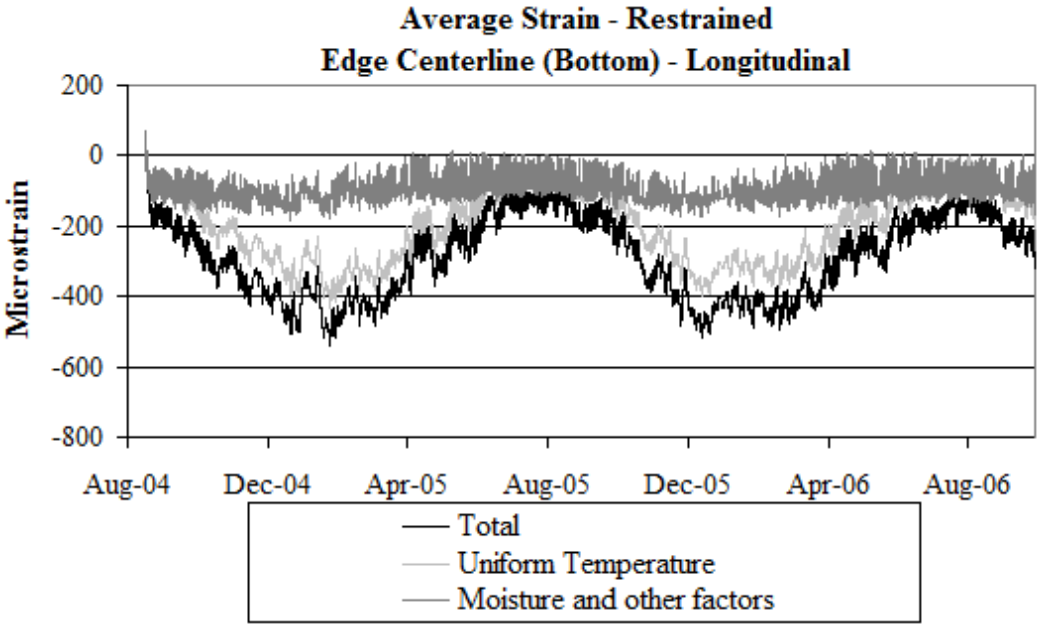

Figure B5. Strain in the longitudinal direction along the centerline joint at the bottom of the restrained slabs.

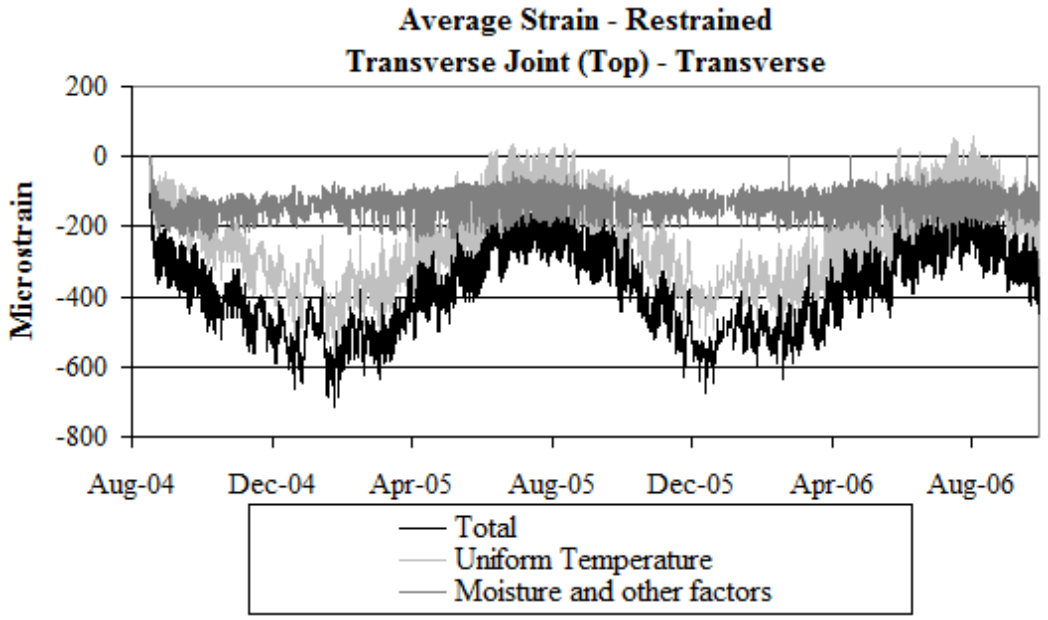

Figure B6. Strain in the transverse direction along the transverse joint at the top of the restrained slabs.

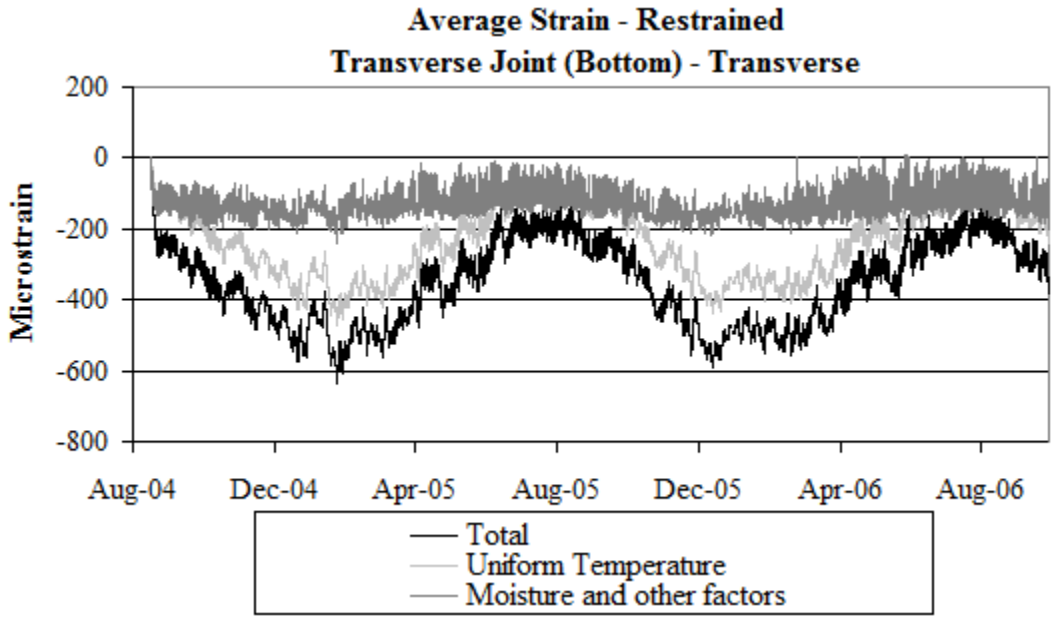

Figure B7. Strain in the transverse direction along the transverse joint at the bottom of the restrained slabs.

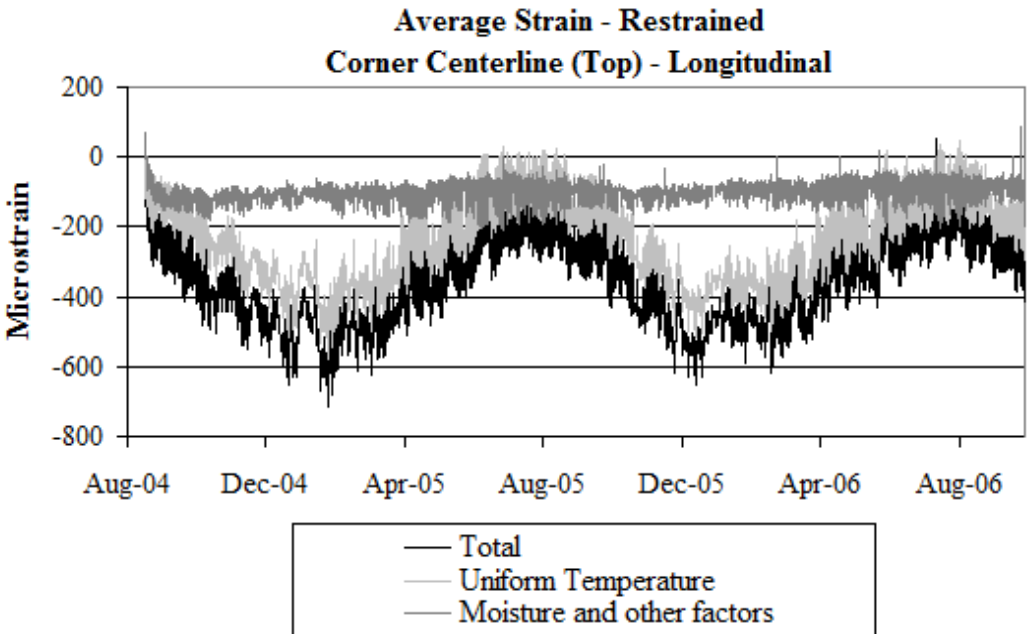

Figure B8. Strain in the longitudinal direction at the corner along the centerline joint at the top of the restrained slabs.

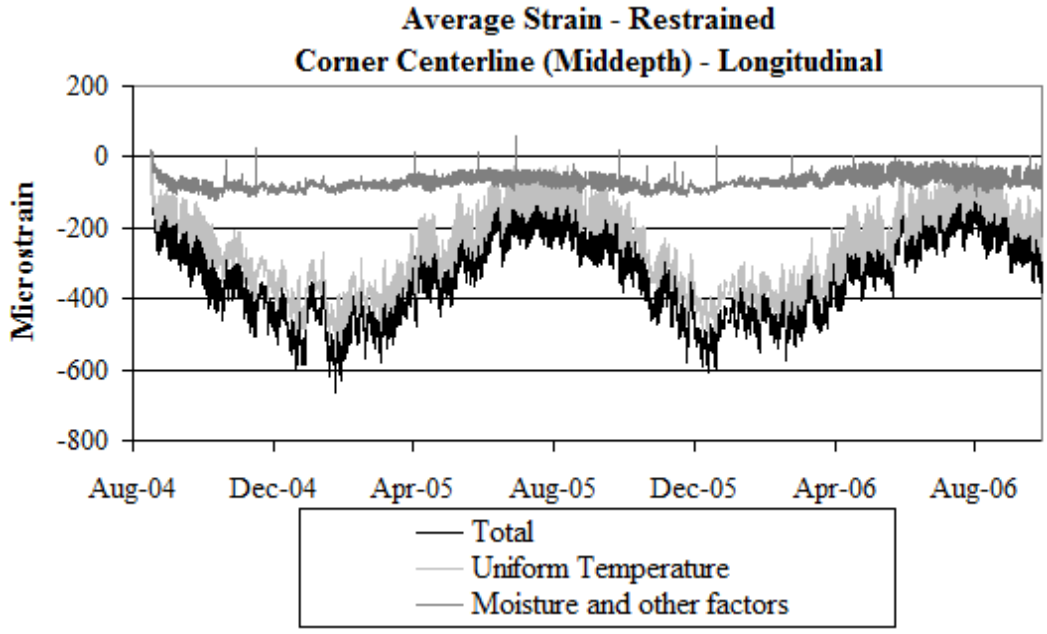

Figure B9. Strain in the longitudinal direction at the corner along the centerline joint at the middepth of the restrained slabs.

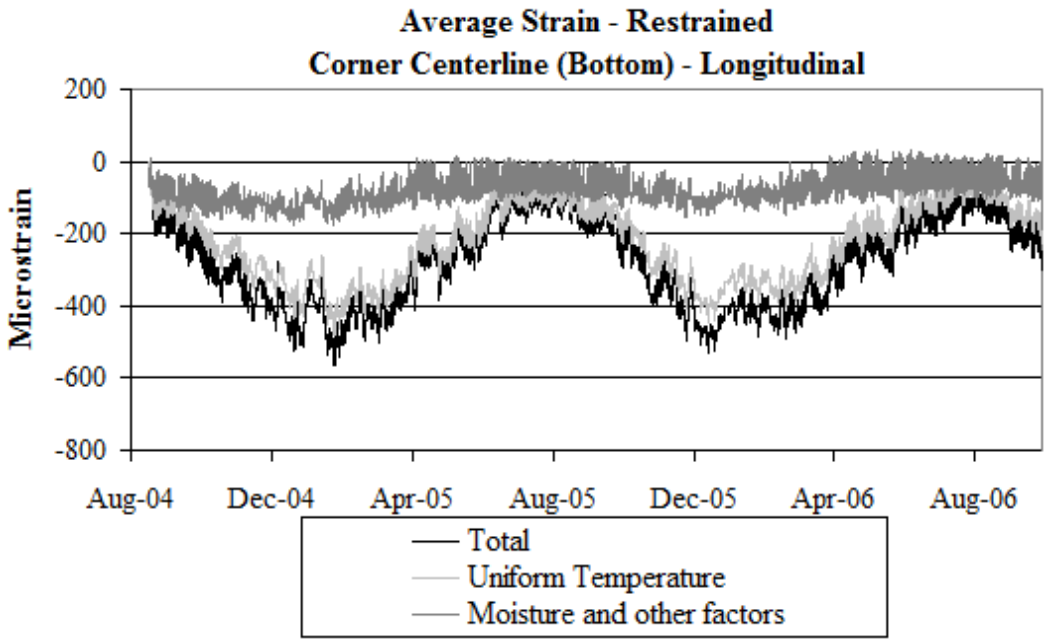

Figure B10. Strain in the longitudinal direction at the corner along the centerline joint at the bottom of the restrained slabs.

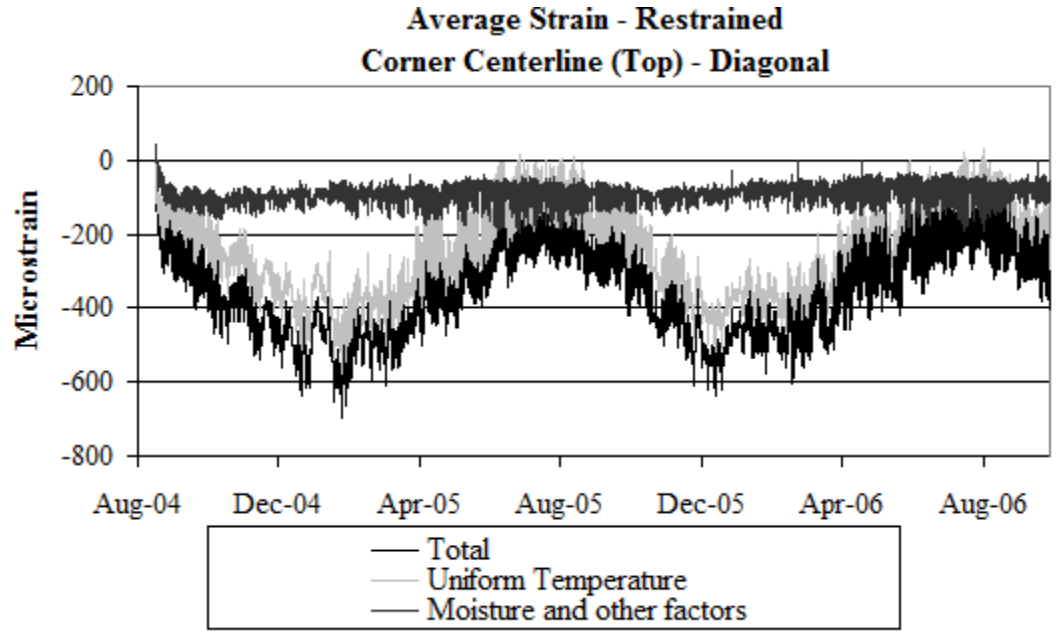

Figure B11. Strain in the diagonal direction at the corner along the centerline joint at the top of the restrained slabs.

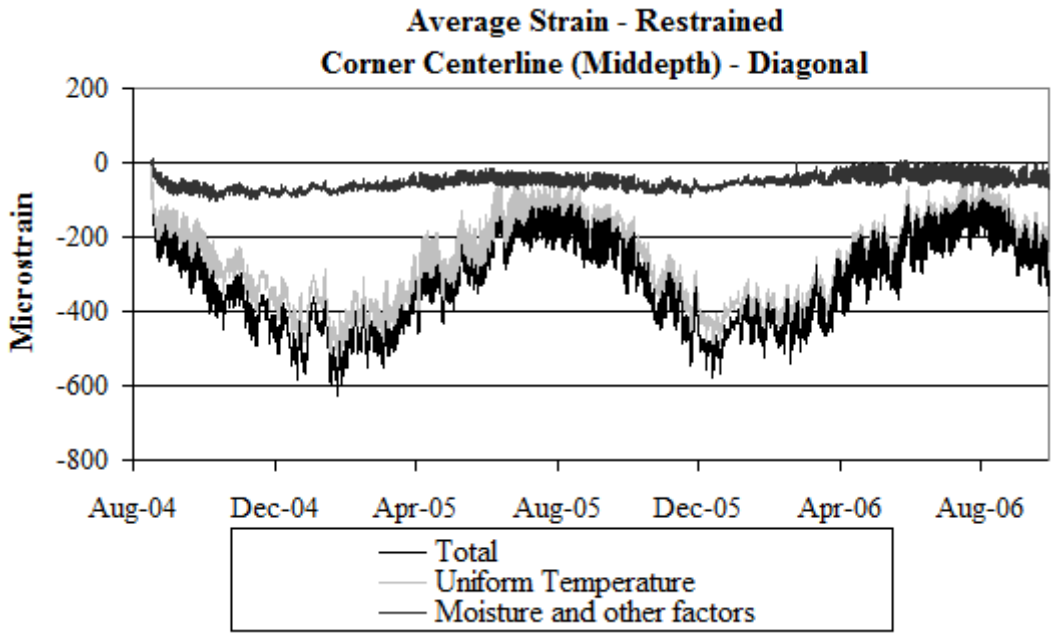

Figure B12. Strain in the diagonal direction at the corner along the centerline joint at the middepth of the restrained slabs.

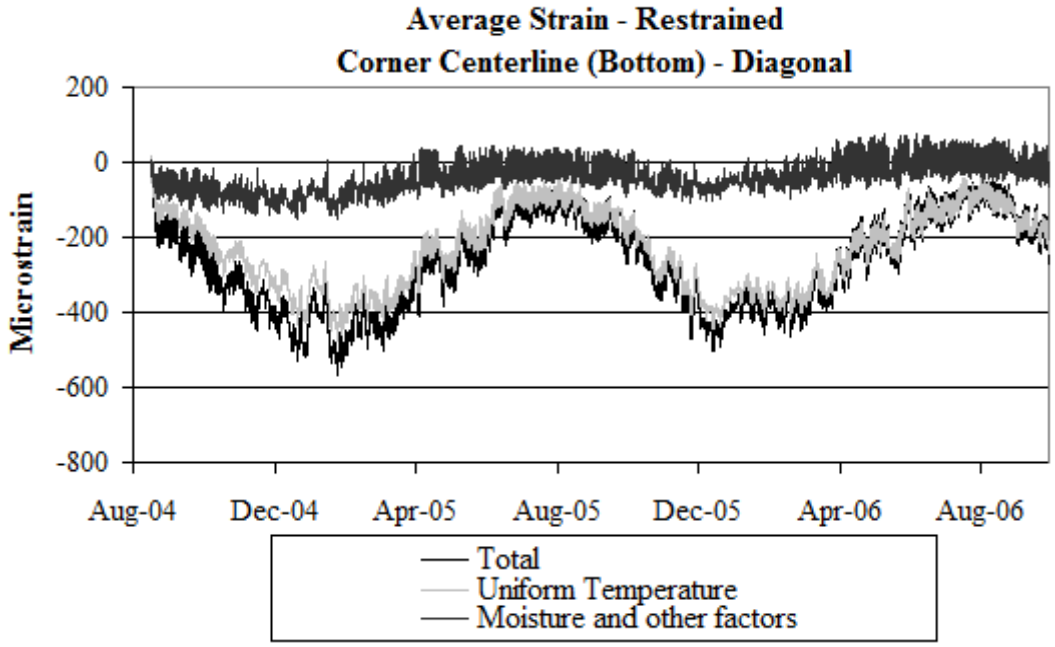

Figure B13. Strain in the diagonal direction at the corner along the centerline joint at the bottom of the restrained slabs.

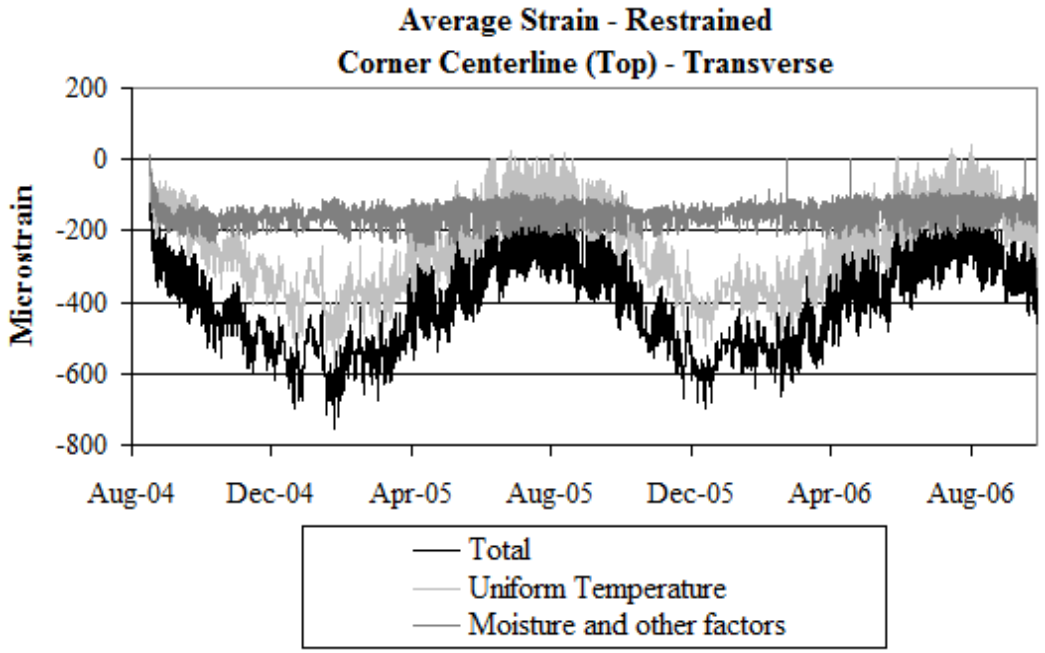

Figure B14. Strain in the transverse direction at the corner along the centerline joint at the top of the restrained slabs.

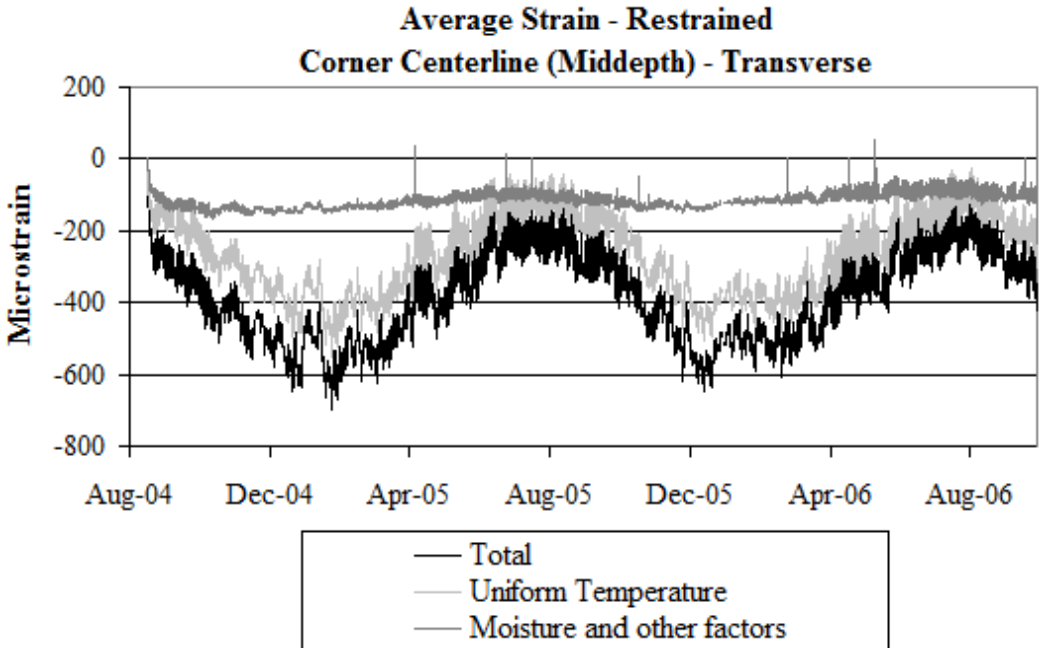

Figure B15. Strain in the transverse direction at the corner along the centerline joint at the middepth of the restrained slabs.

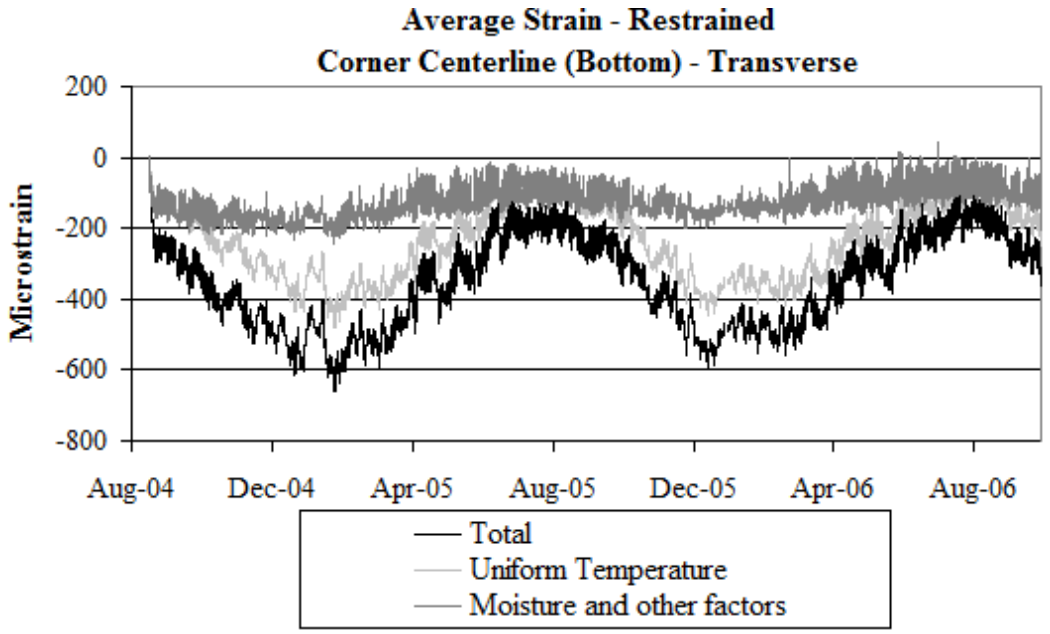

Figure B16. Strain in the transverse direction at the corner along the centerline joint at the of bottom the restrained slabs.

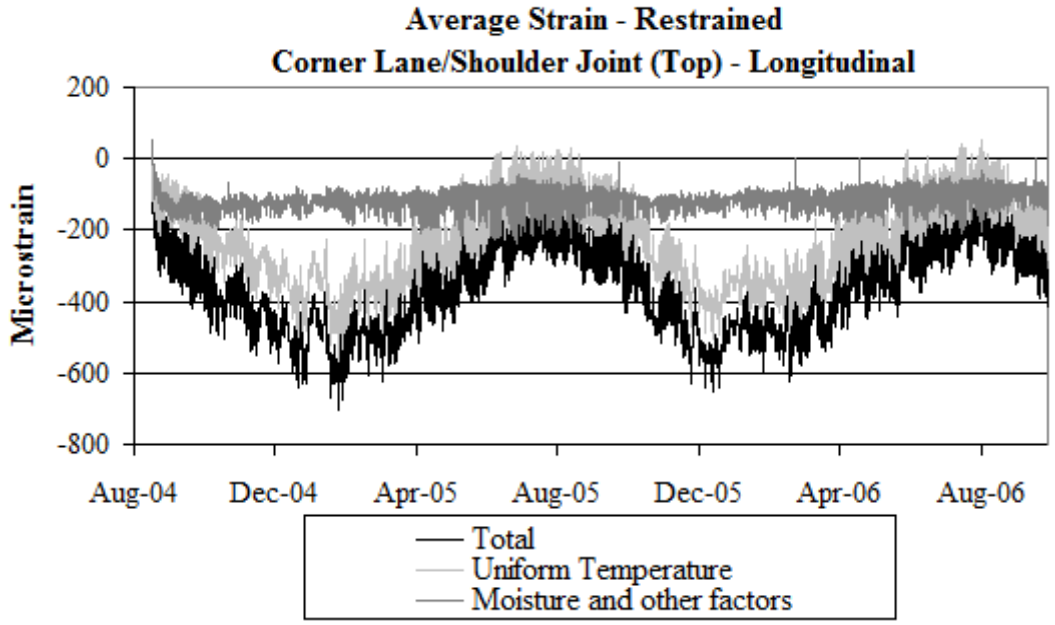

Figure B17. Strain in the longitudinal direction at the corner along the lane/shoulder joint at the top of the restrained slabs.

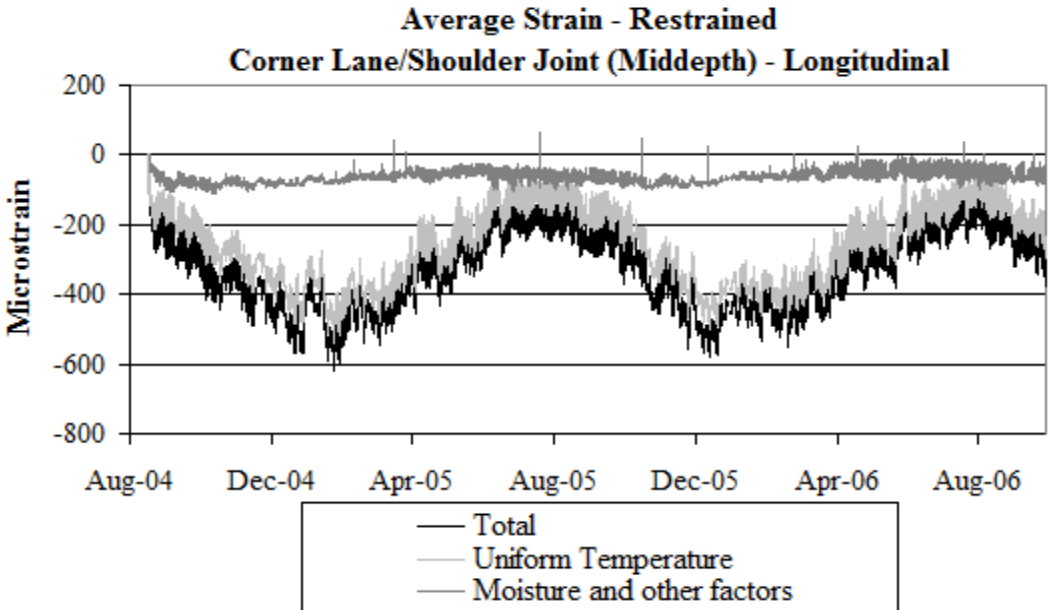

Figure B18. Strain in the longitudinal direction at the corner along the lane/shoulder joint at the middepth of the restrained slabs.

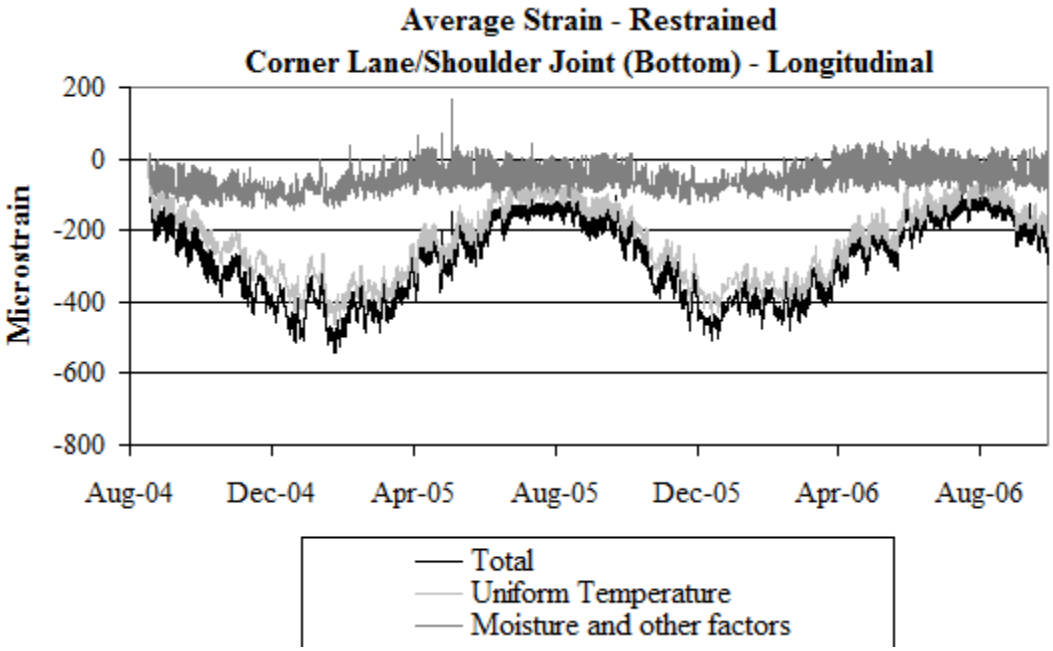

Figure B19. Strain in the longitudinal direction at the corner along the lane/shoulder joint at the bottom of the restrained slabs.

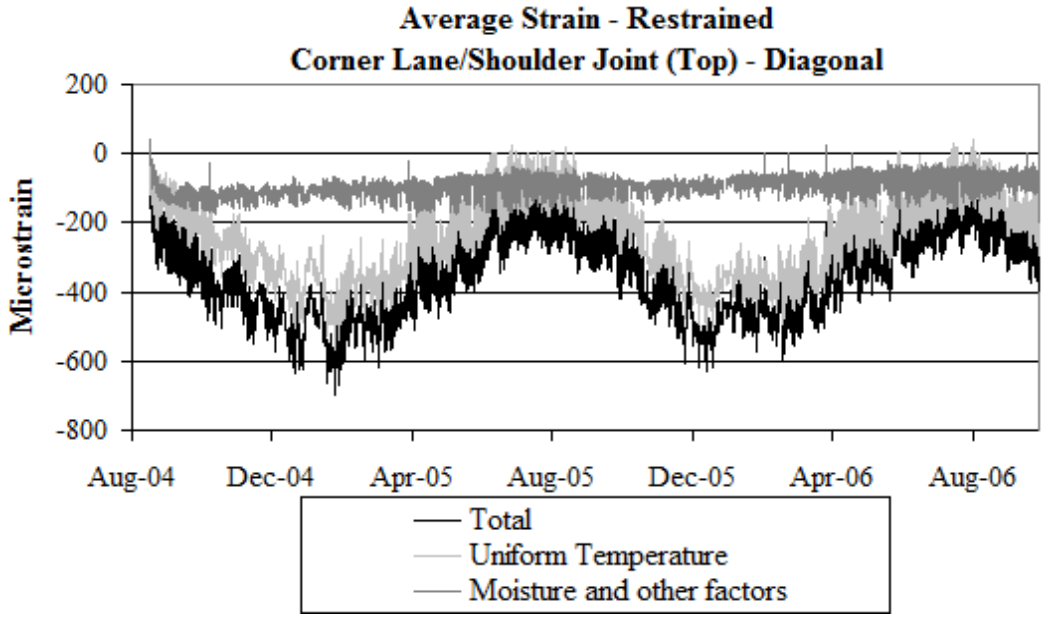

Figure B20. Strain in the diagonal direction at the corner along the lane/shoulder joint at the top of the restrained slabs.

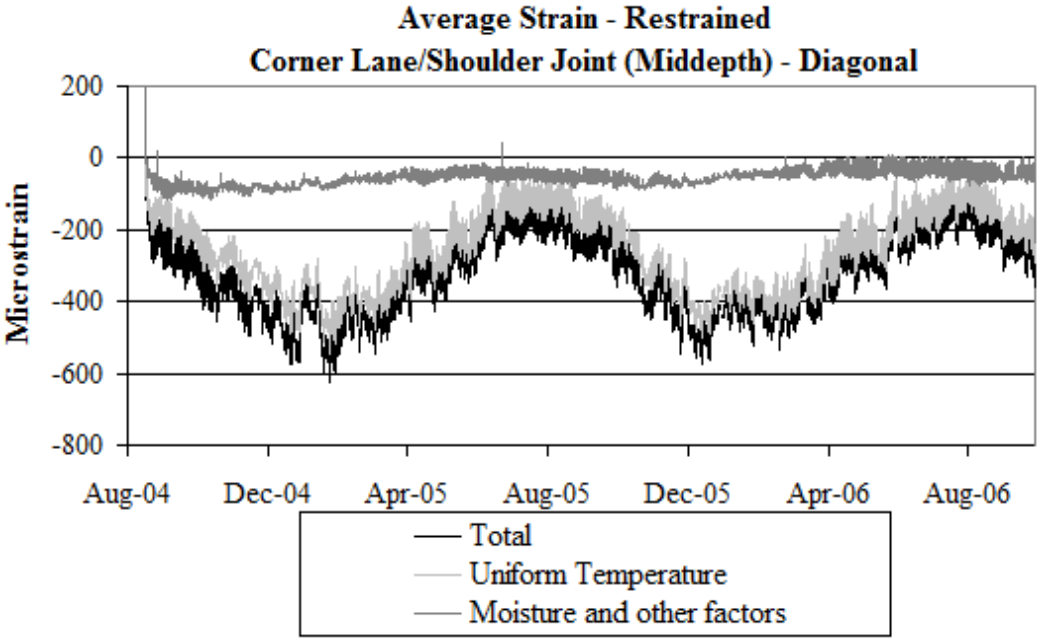

Figure B21. Strain in the diagonal direction at the corner along the lane/shoulder joint at the middepth of the restrained slabs.

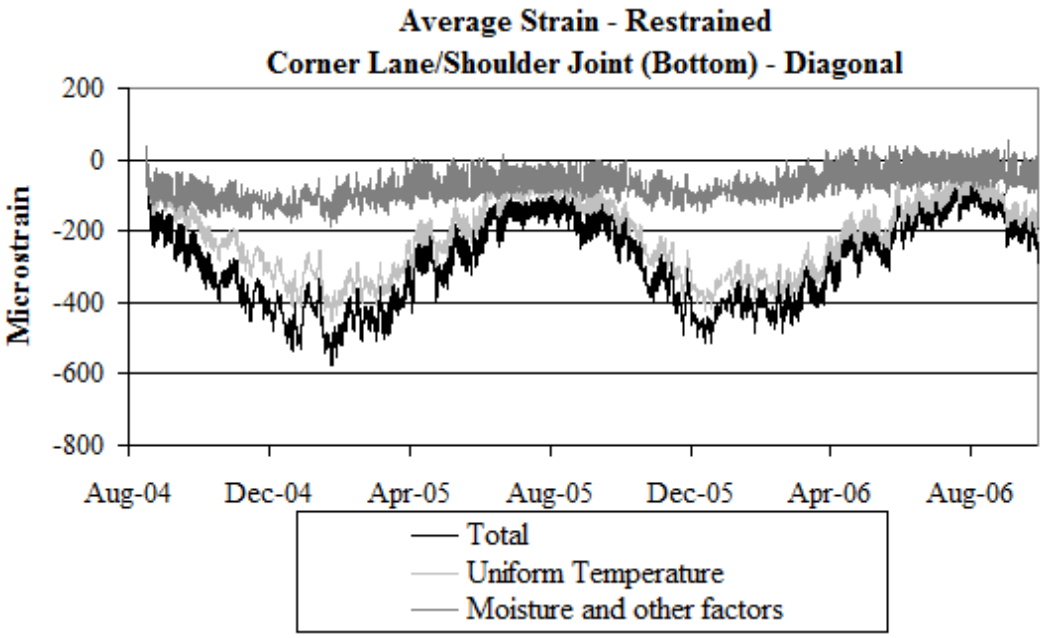

Figure B22. Strain in the diagonal direction at the corner along the lane/shoulder joint at the bottom of the restrained slabs.

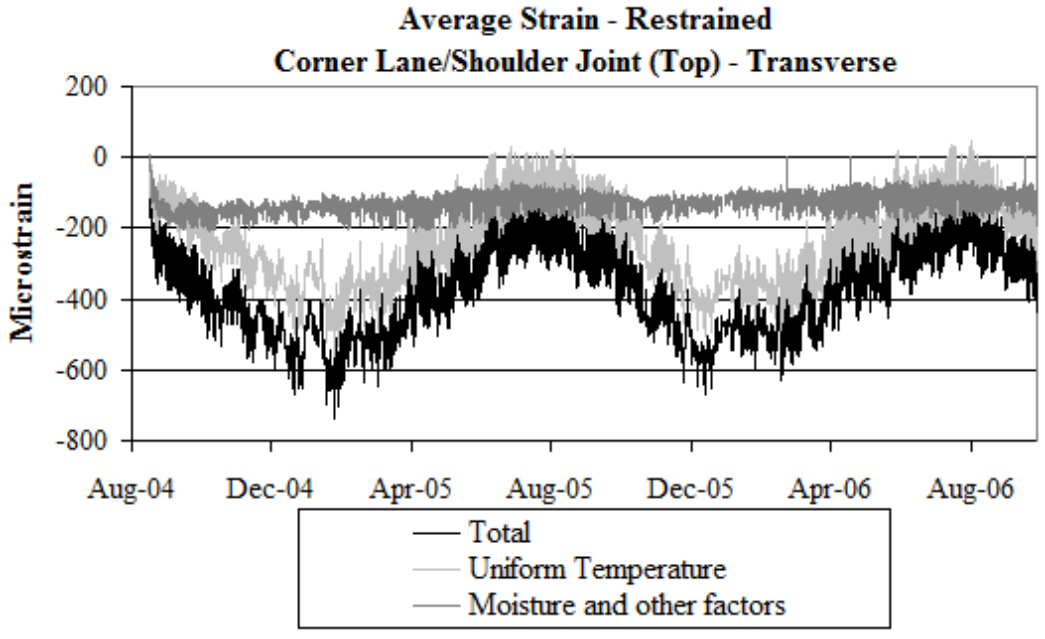

Figure B23. Strain in the transverse direction at the corner along the lane/shoulder joint at the top of the restrained slabs.

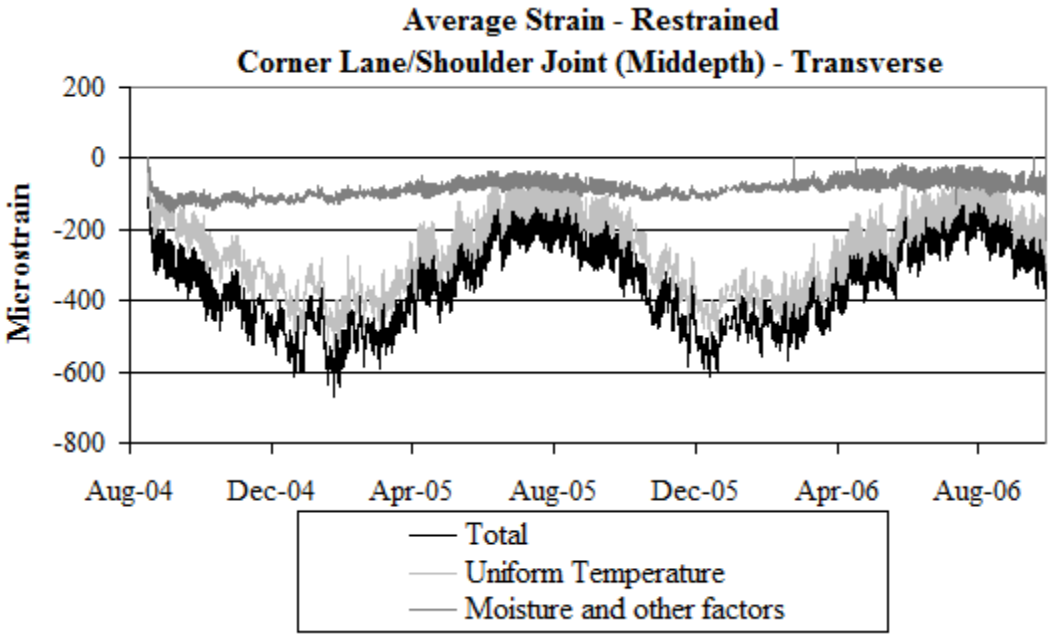

Figure B24. Strain in the transverse direction at the corner along the lane/shoulder joint at the middepth of the restrained slabs.

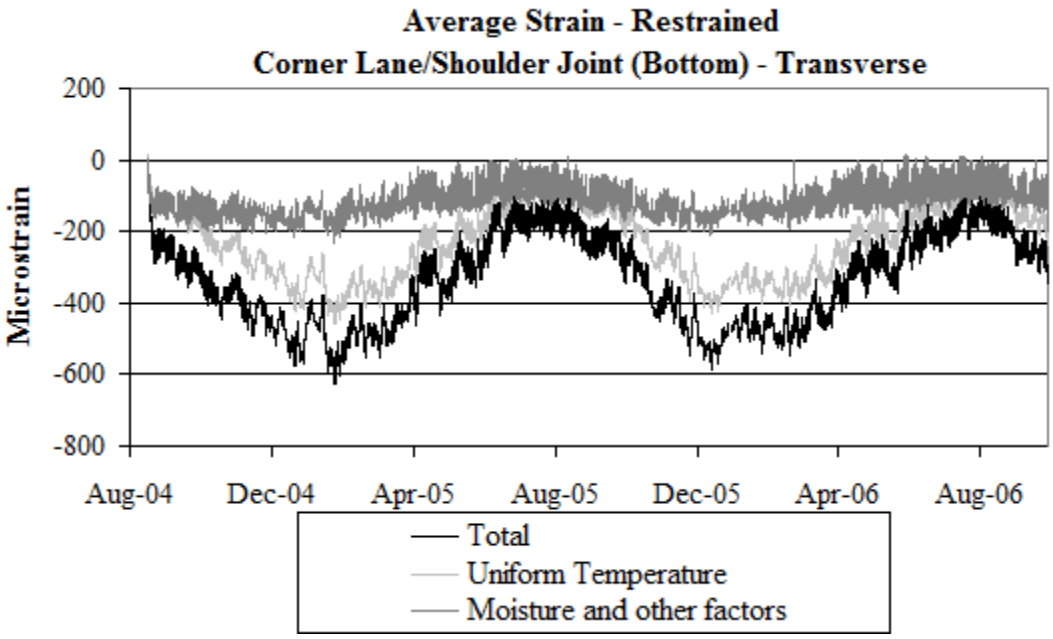

Figure B25. Strain in the transverse direction at the corner along the lane/shoulder joint at the bottom of the restrained slabs.

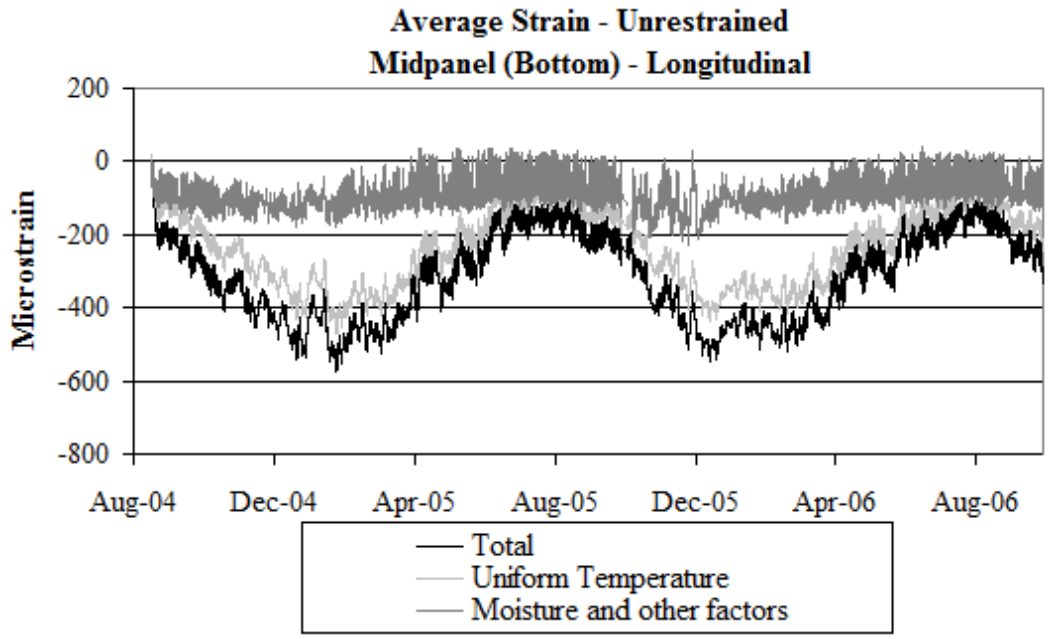

Figure B26. Strain in the longitudinal direction at midpanel at the bottom of the unrestrained slabs.

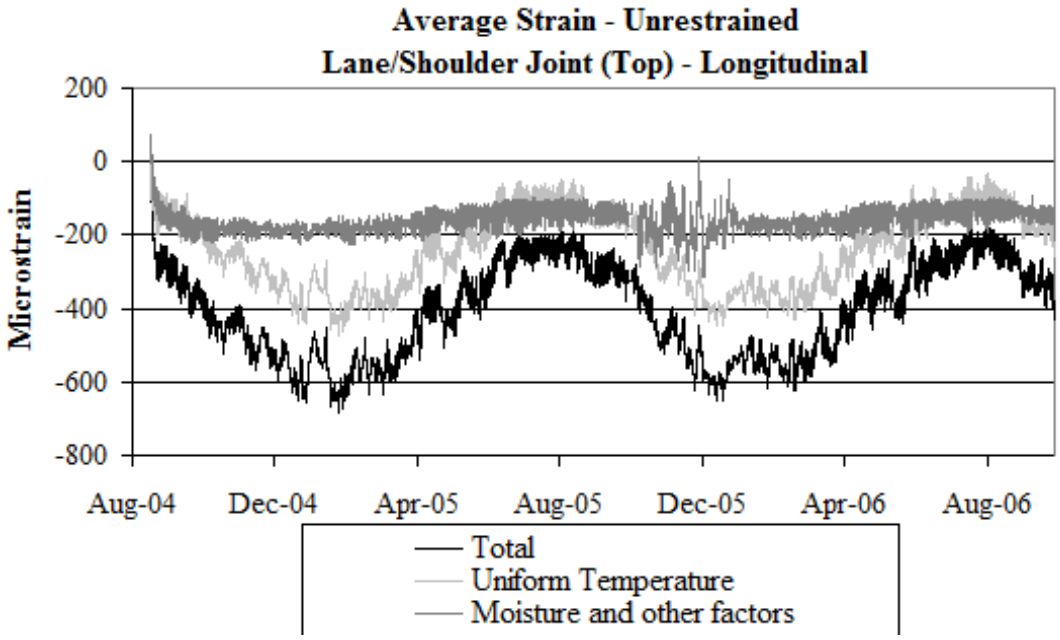

Figure B27. Strain in the longitudinal direction along the lane/shoulder joint at the top of the unrestrained slabs.

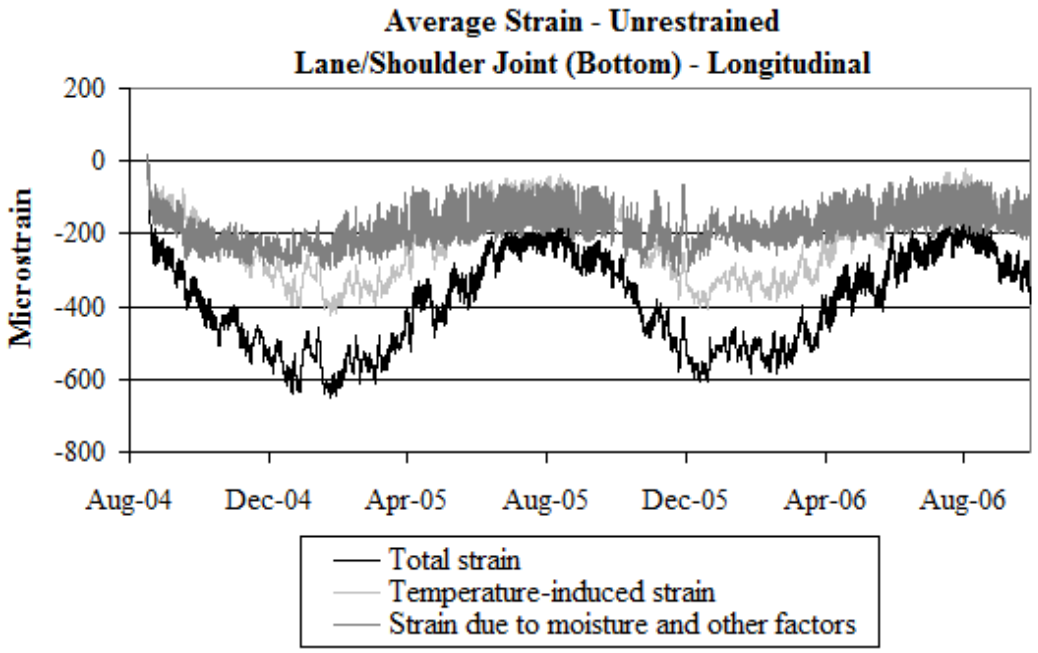

Figure B28. Strain in the longitudinal direction along the lane/shoulder joint at the bottom of the unrestrained slabs.

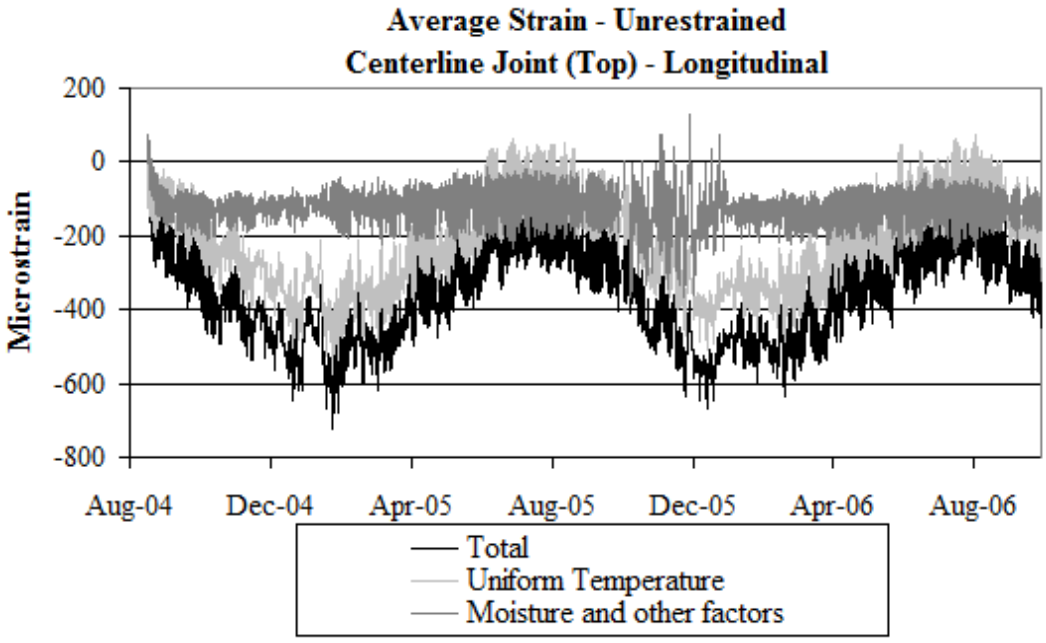

Figure B29. Strain in the longitudinal direction along the centerline joint at the top of the unrestrained slabs.

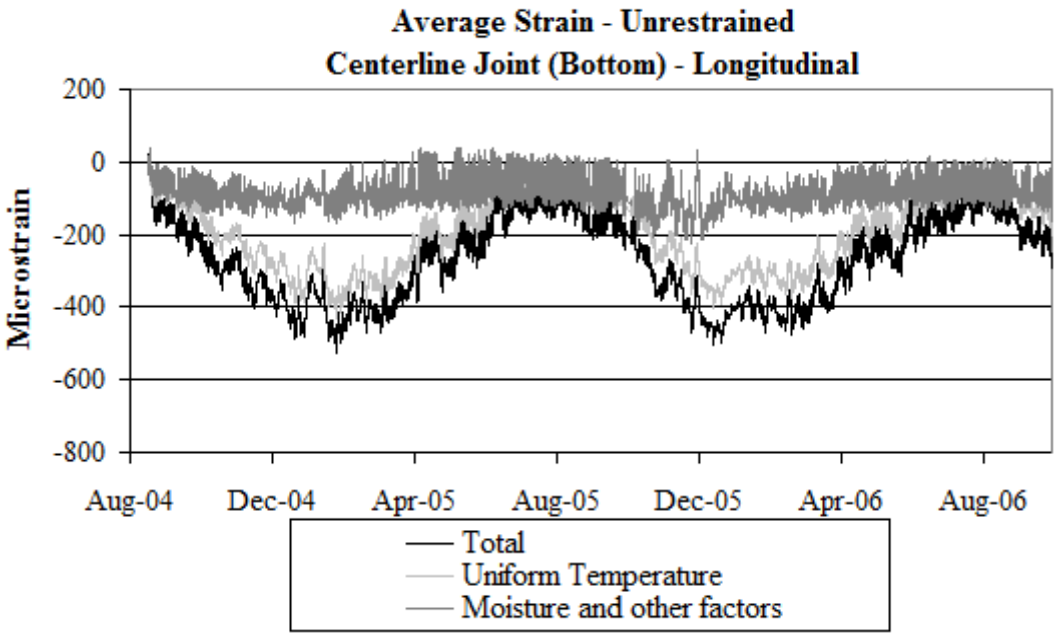

Figure B30. Strain in the longitudinal direction along the centerline joint at the bottom of the unrestrained slabs.

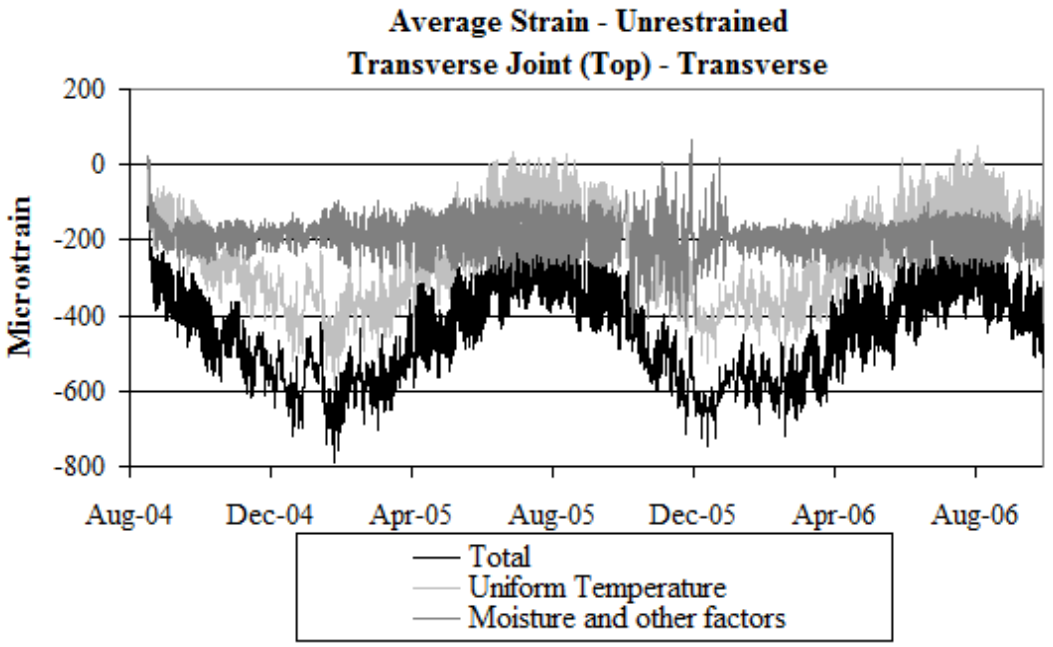

Figure B31. Strain in the transverse direction along the transverse joint at the top of the unrestrained slabs.

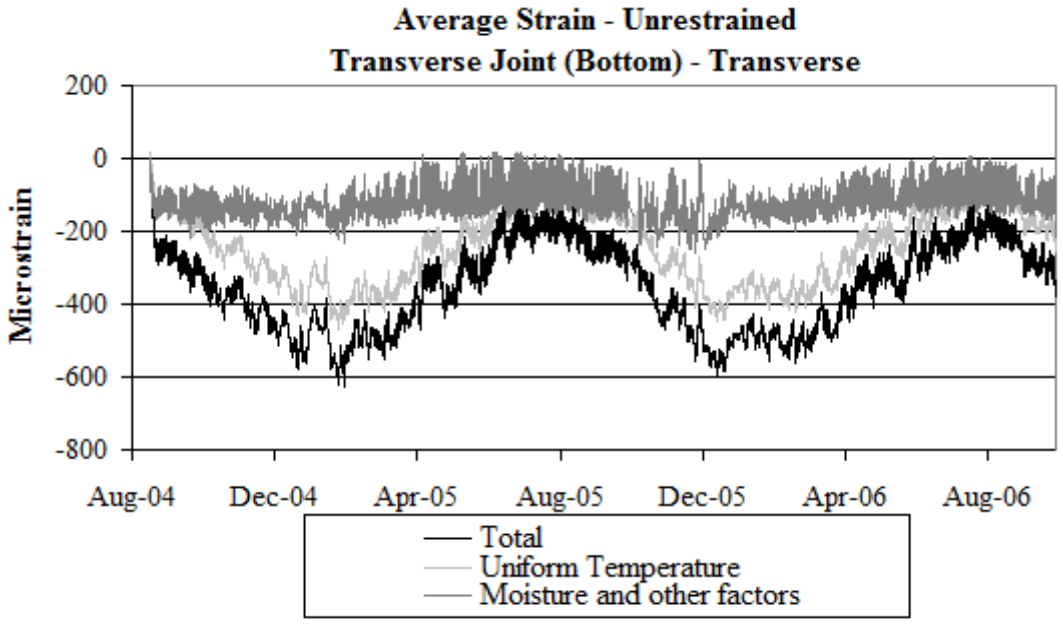

Figure B32. Strain in the transverse direction along the transverse joint at the bottom of the unrestrained slabs.

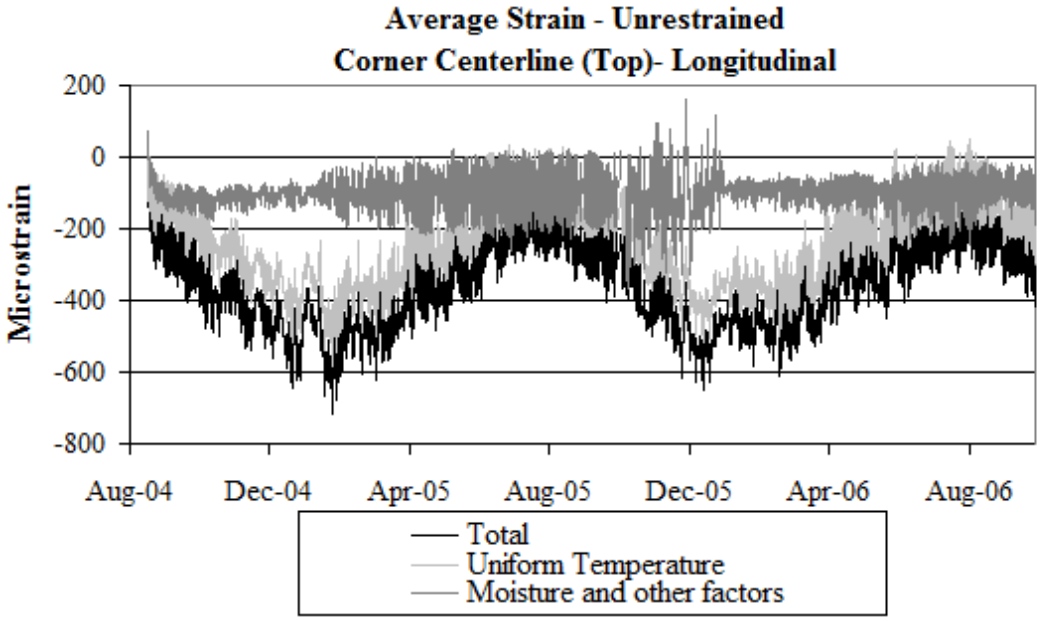

Figure B33. Strain in the longitudinal direction at the corner along the centerline joint at the top of the unrestrained slabs.

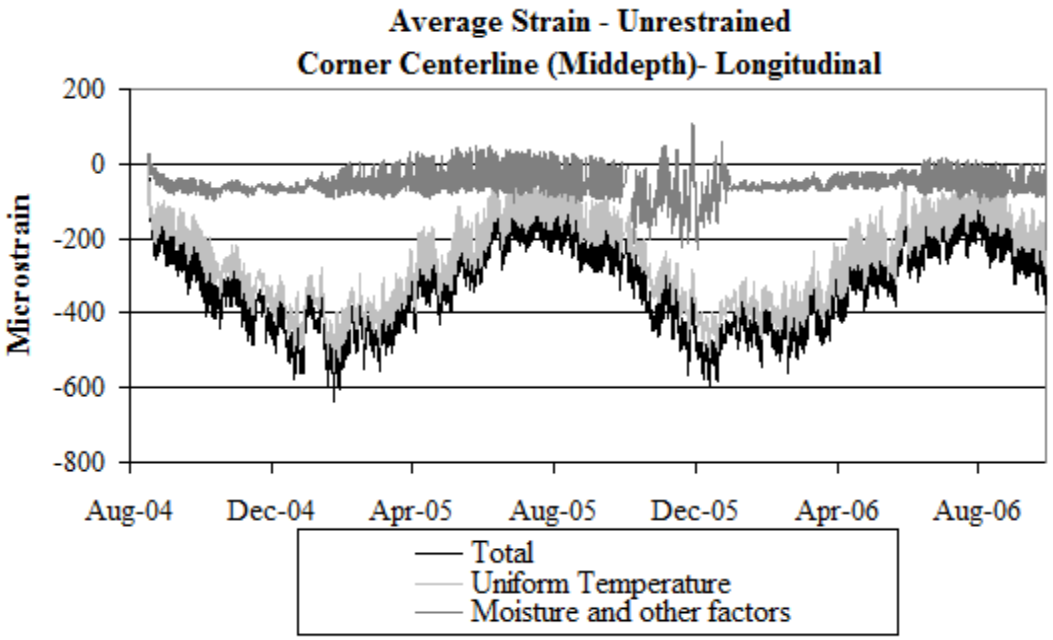

Figure B34. Strain in the longitudinal direction at the corner along the centerline joint at the middepth of the unrestrained slabs.

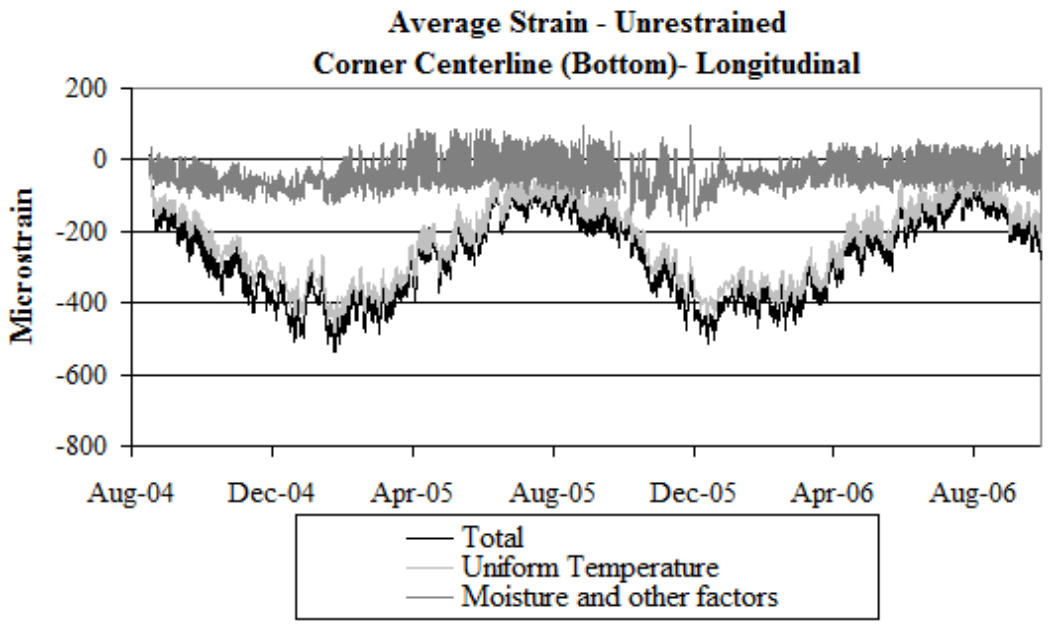

Figure B35. Strain in the longitudinal direction at the corner along the centerline joint at the bottom of the unrestrained slabs.

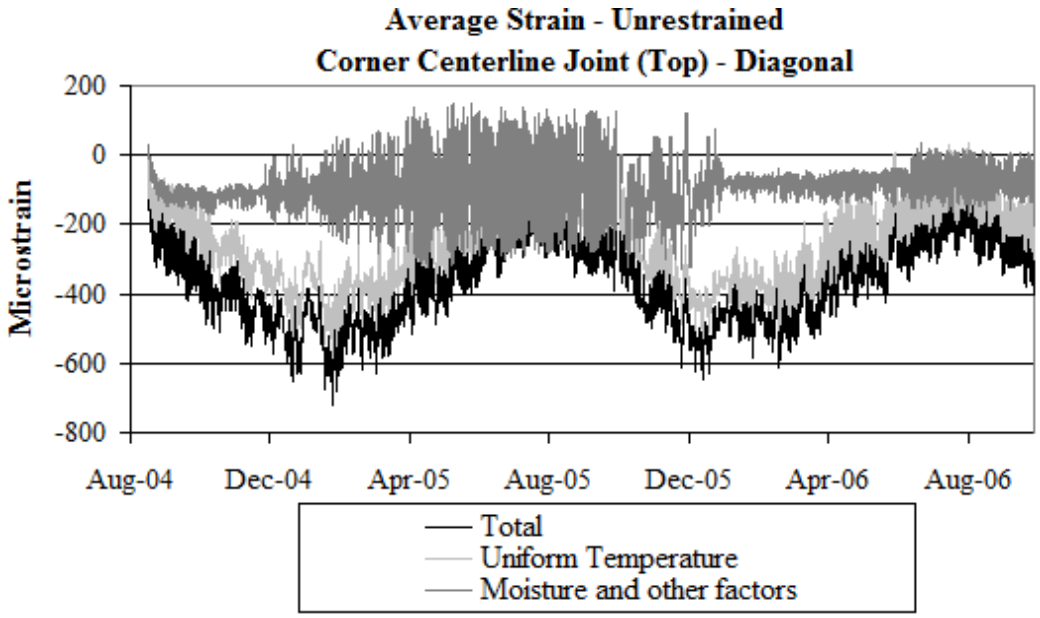

Figure B36. Strain in the diagonal direction at the corner along the centerline joint at the top of the unrestrained slabs.

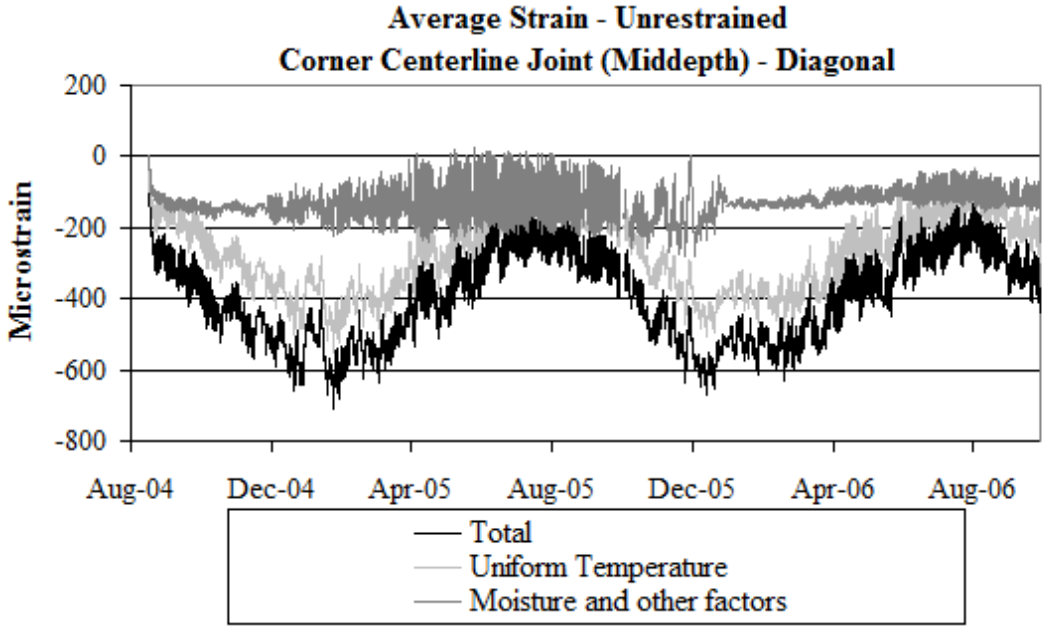

Figure B37. Strain in the diagonal direction at the corner along the centerline joint at the middepth of the unrestrained slabs.

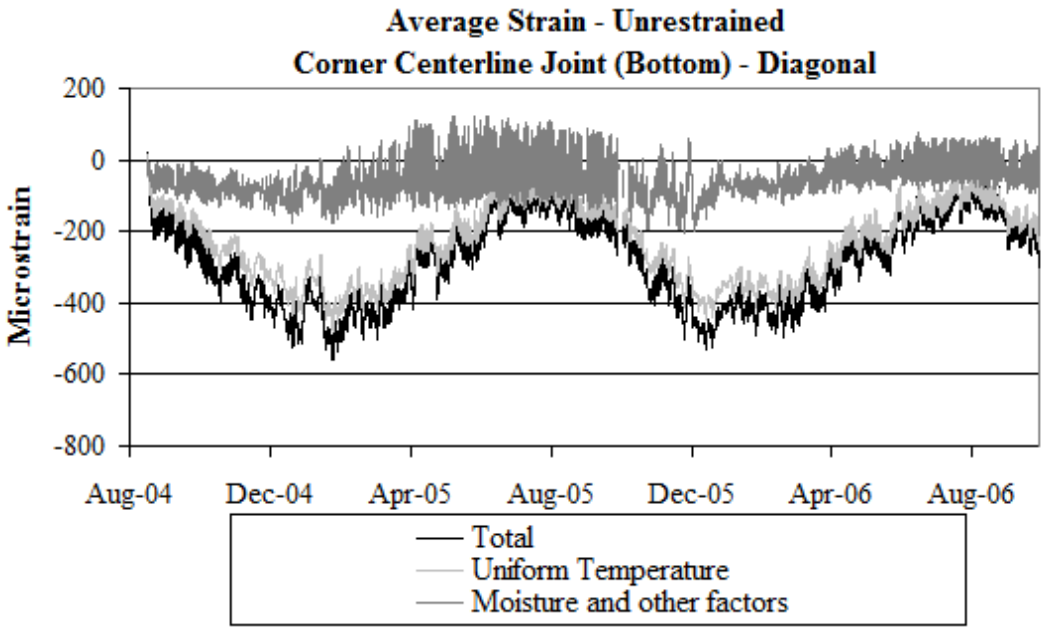

Figure B38. Strain in the diagonal direction at the corner along the centerline joint at the bottom of the unrestrained slabs.

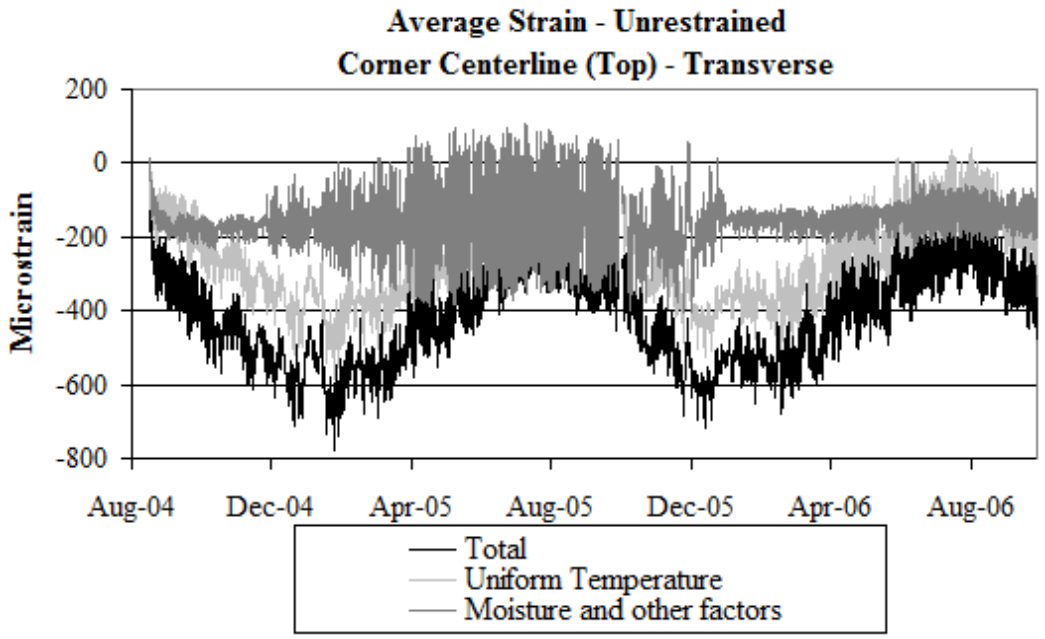

Figure B39. Strain in the transverse direction at the corner along the centerline joint at the top of the unrestrained slabs.

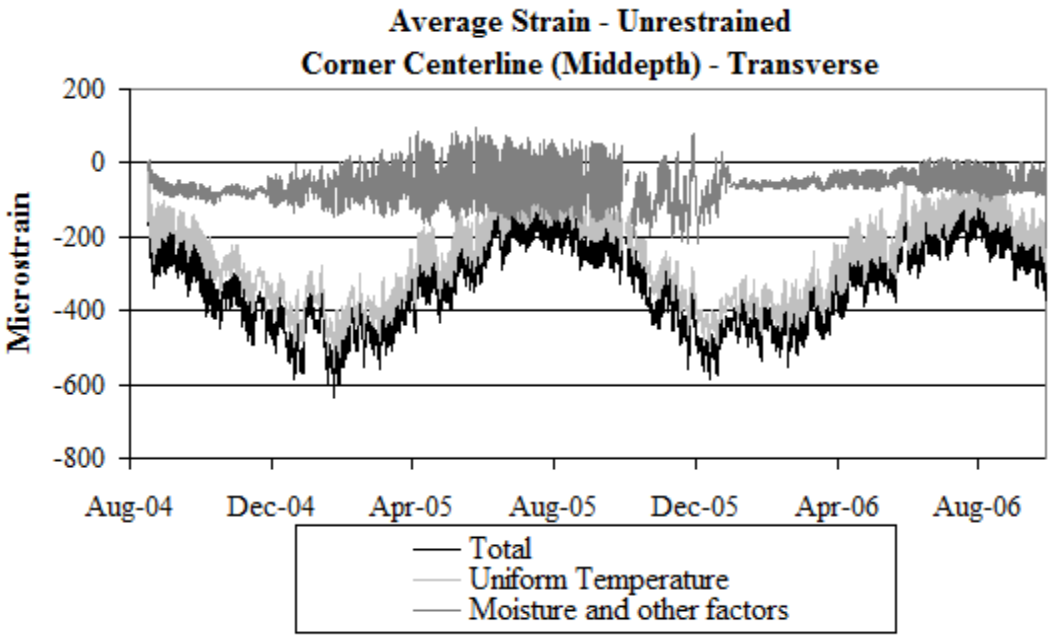

Figure B40. Strain in the transverse direction at the corner along the centerline joint at the middepth of the unrestrained slabs.

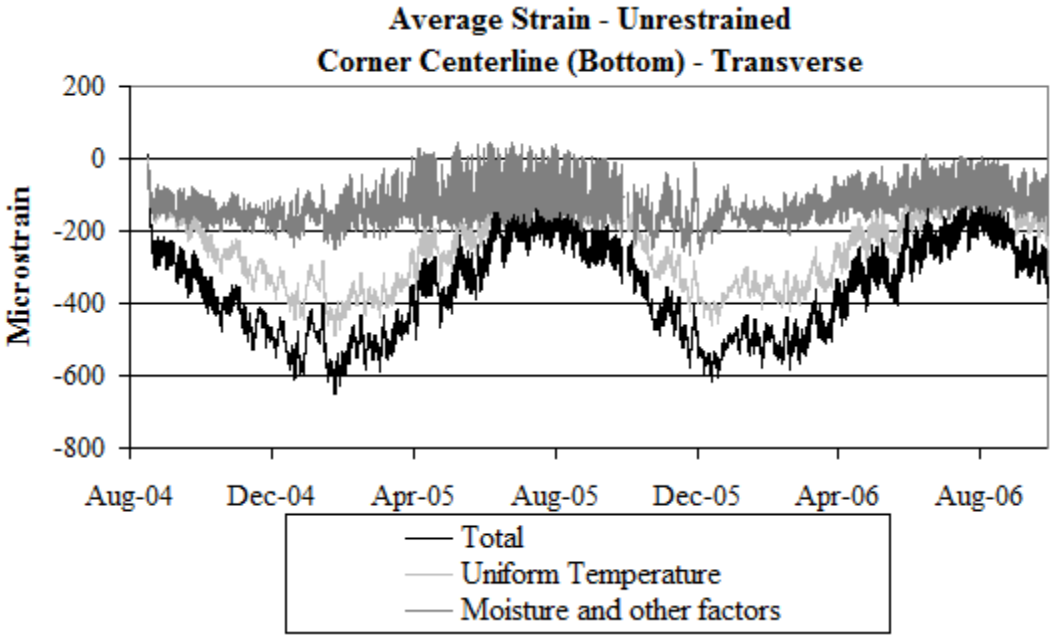

Figure B41. Strain in the transverse direction at the corner along the centerline joint at the bottom of the unrestrained slabs.

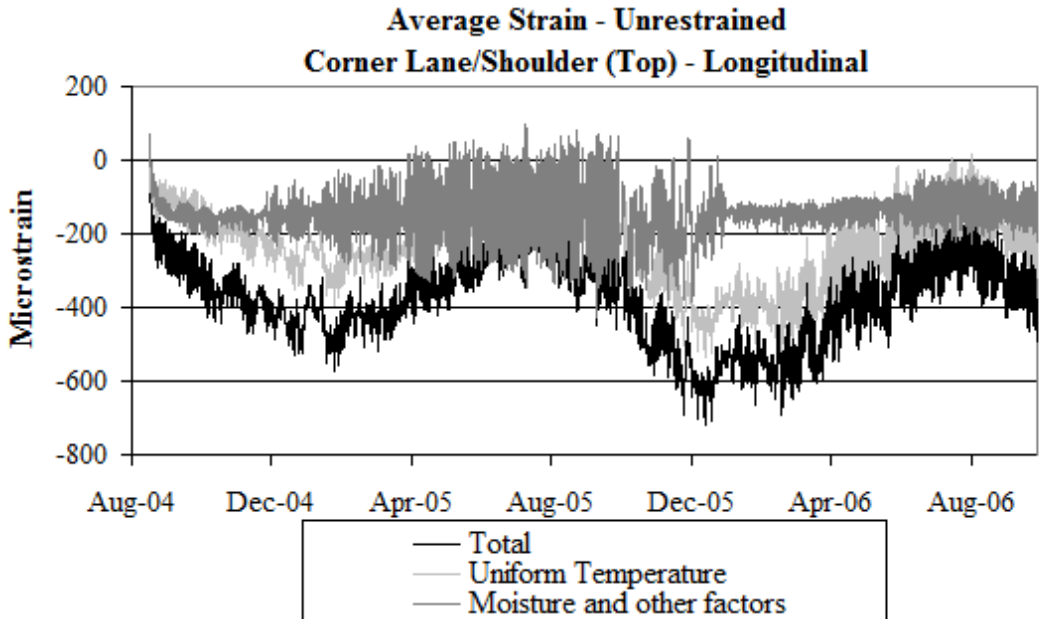

Figure B42. Strain in the longitudinal direction at the corner along the lane/shoulder joint at the top of the unrestrained slabs.

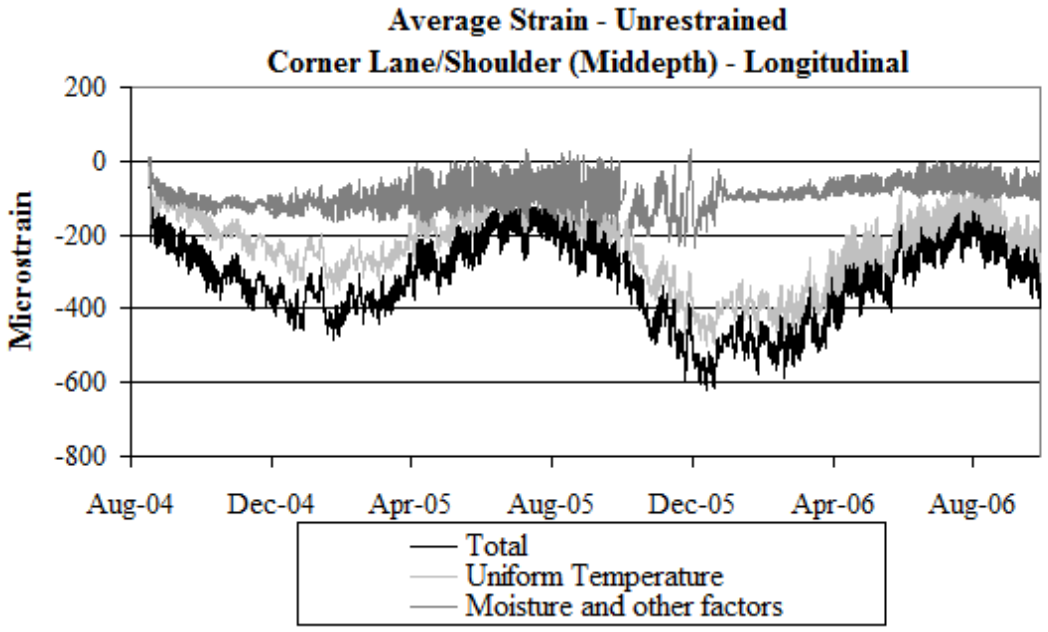

Figure B43. Strain in the longitudinal direction at the corner along the lane/shoulder joint at the middepth of the unrestrained slabs.

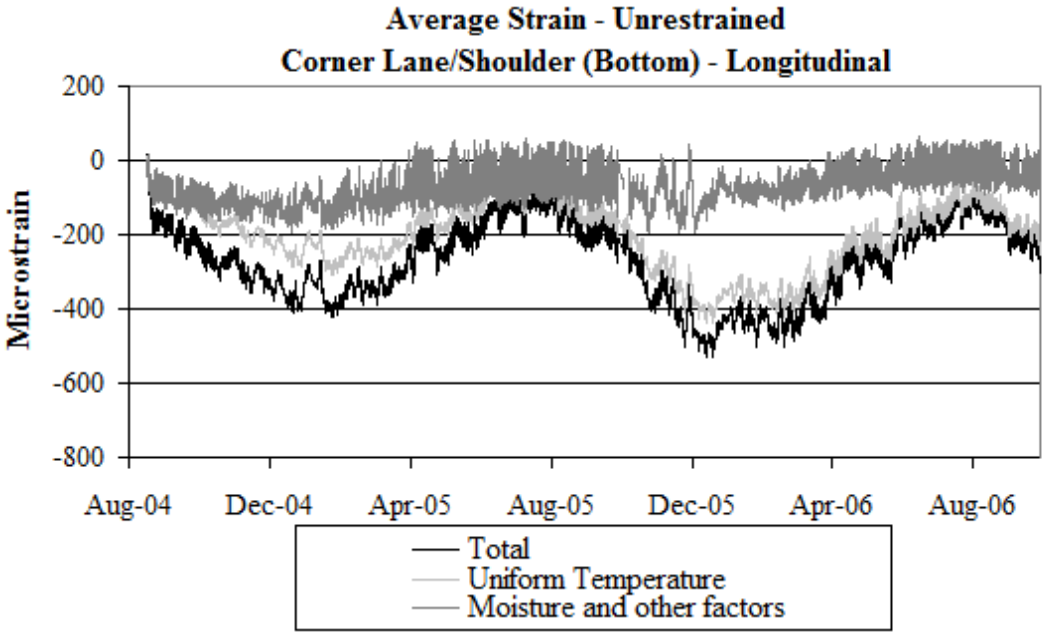

Figure B44. Strain in the longitudinal direction at the corner along the lane/shoulder joint at the bottom of the unrestrained slabs.

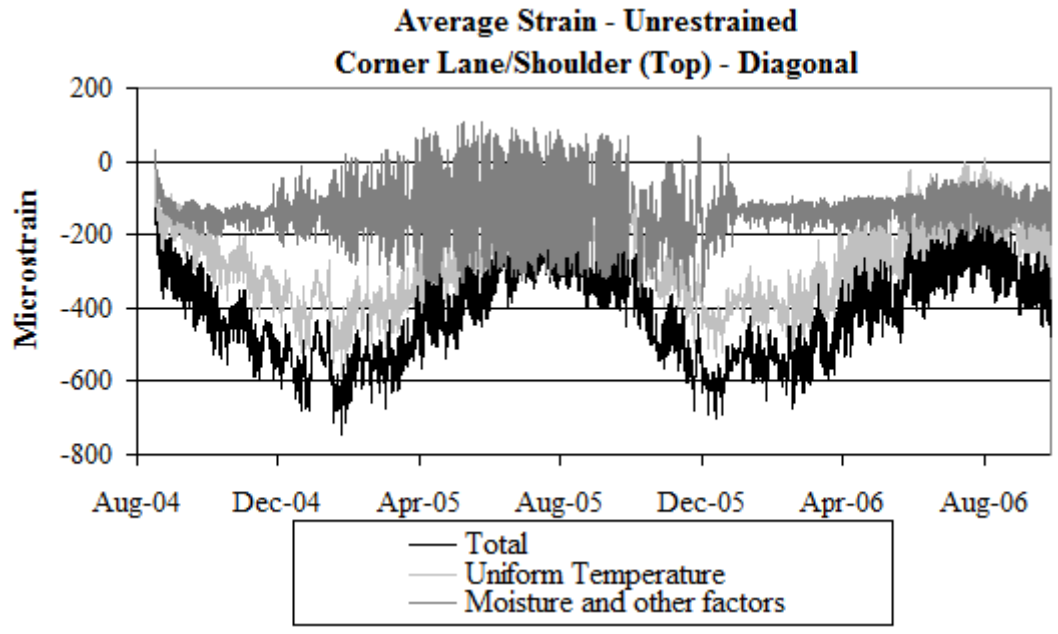

Figure B45. Strain in the diagonal direction at the corner along the lane/shoulder joint at the top of the unrestrained slabs.

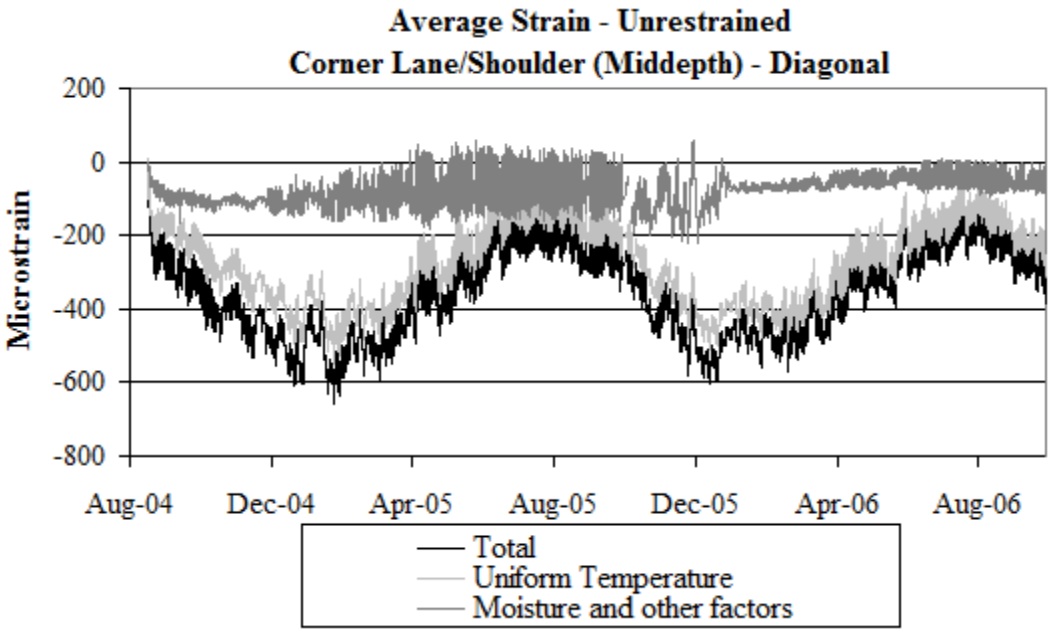

Figure B46. Strain in the diagonal direction at the corner along the lane/shoulder joint at the middepth of the unrestrained slabs.

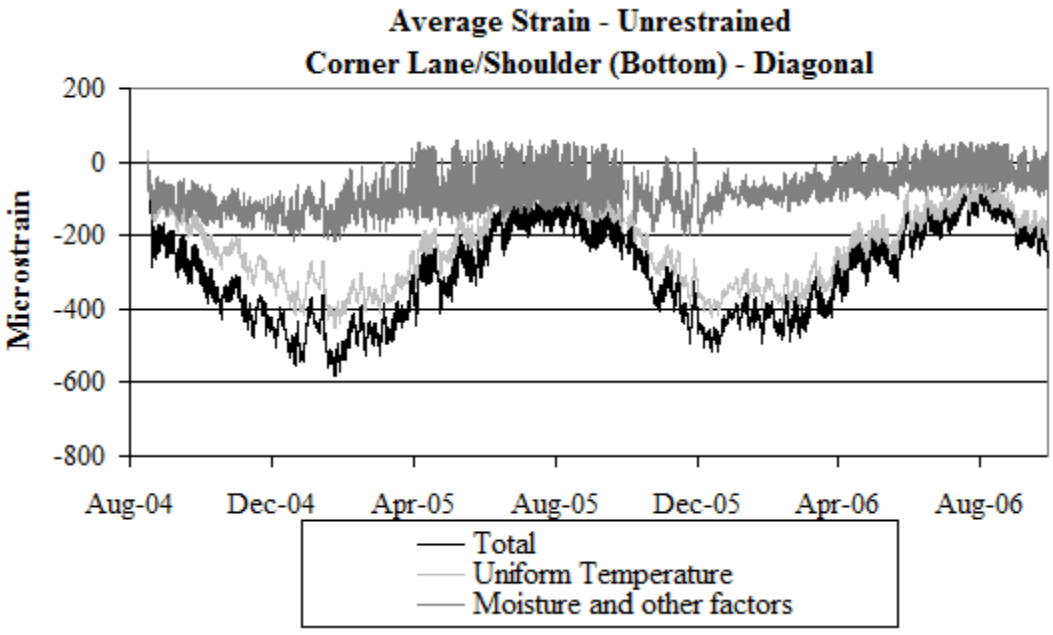

Figure B47. Strain in the diagonal direction at the corner along the lane/shoulder joint at the bottom of the unrestrained slabs.

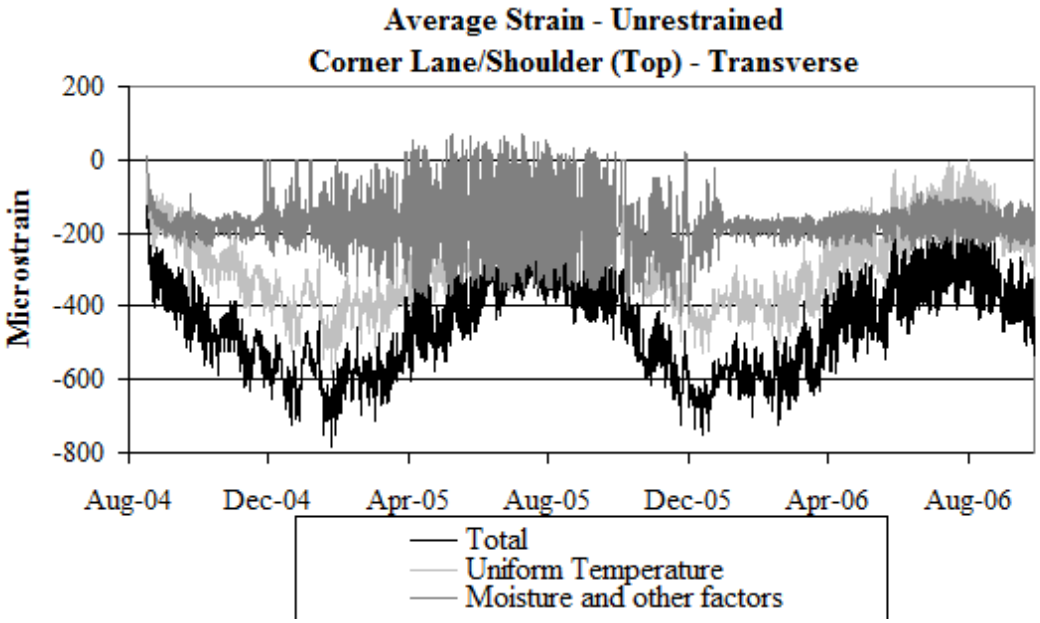

Figure B48. Strain in the transverse direction at the corner along the lane/shoulder joint at the top of the unrestrained slabs.

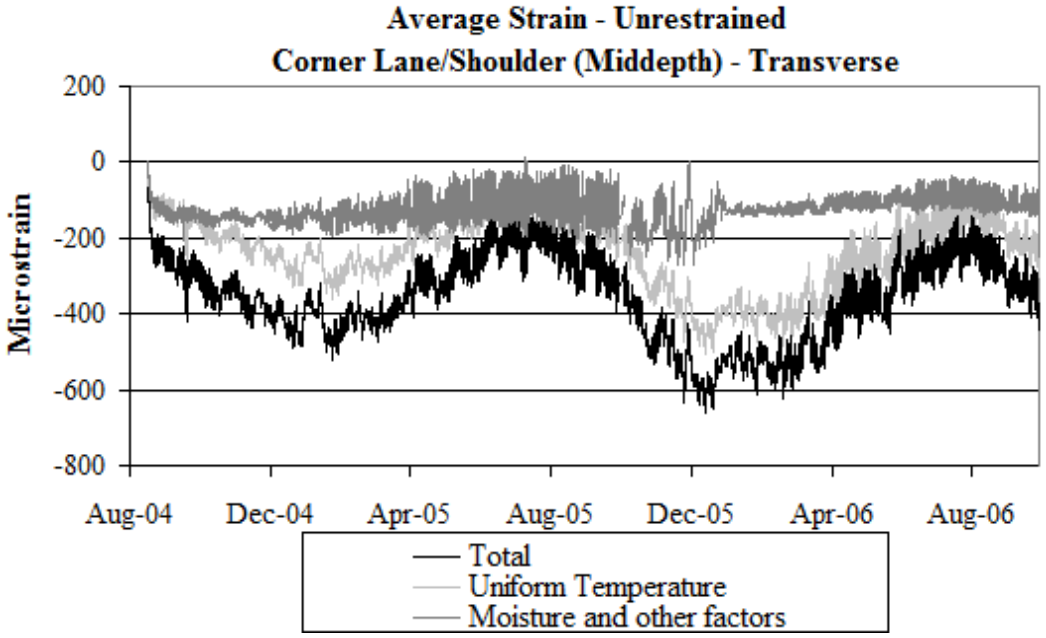

Figure B49. Strain in the transverse direction at the corner along the lane/shoulder joint at the middepth of the unrestrained slabs.

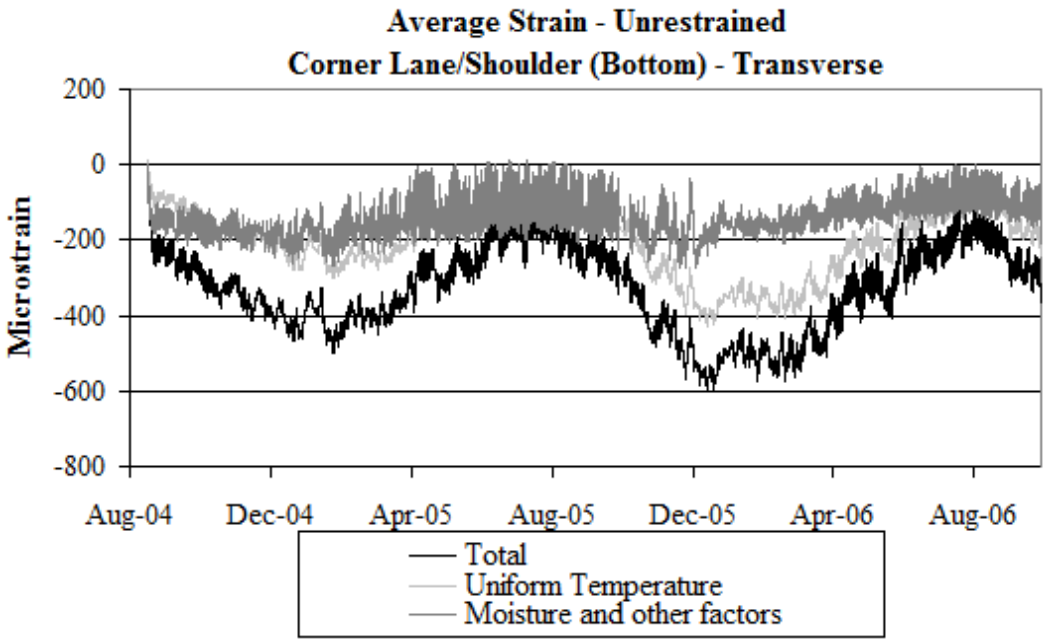

Figure B50. Strain in the transverse direction at the corner along the lane/shoulder joint at the bottom of the unrestrained slabs.

APPENDIX C

SURFACE PROFILE MEASUREMENTS

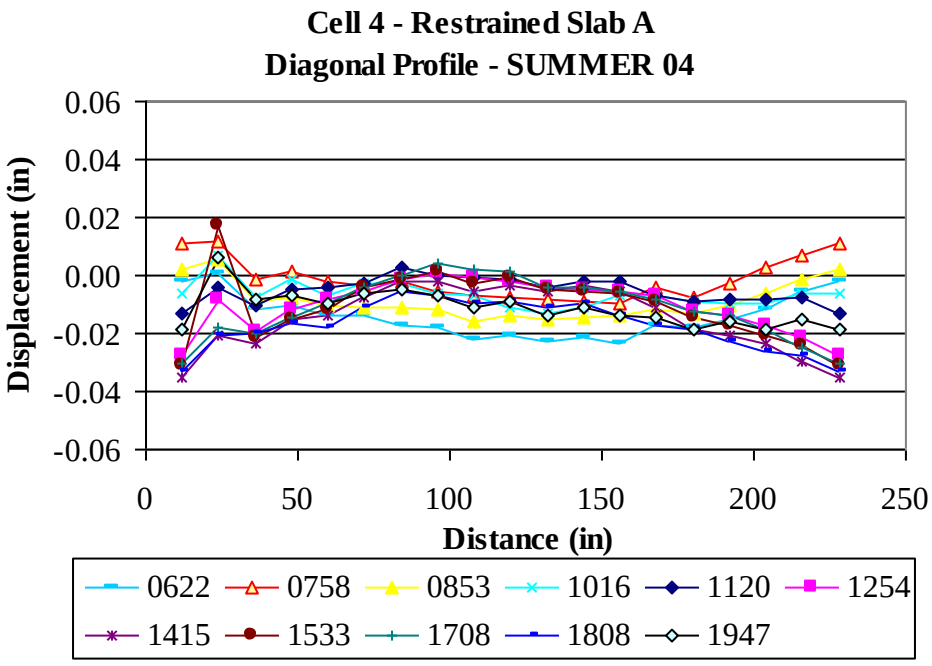

Figure C1. Restrained Slab A diagonal surface profiles for the summer of 2004.

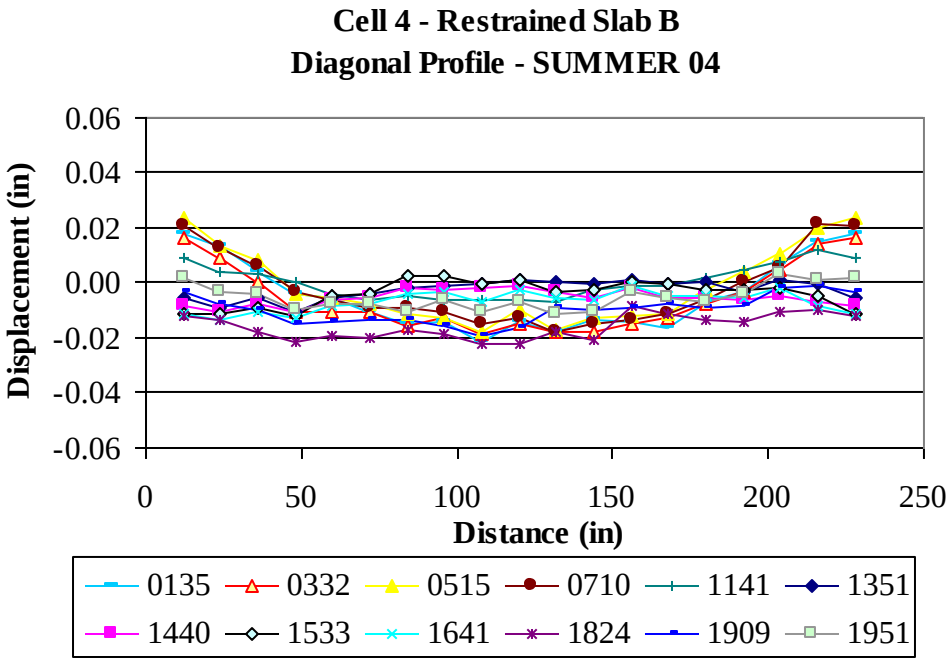

Figure C2. Restrained Slab B diagonal surface profiles for the summer of 2004.

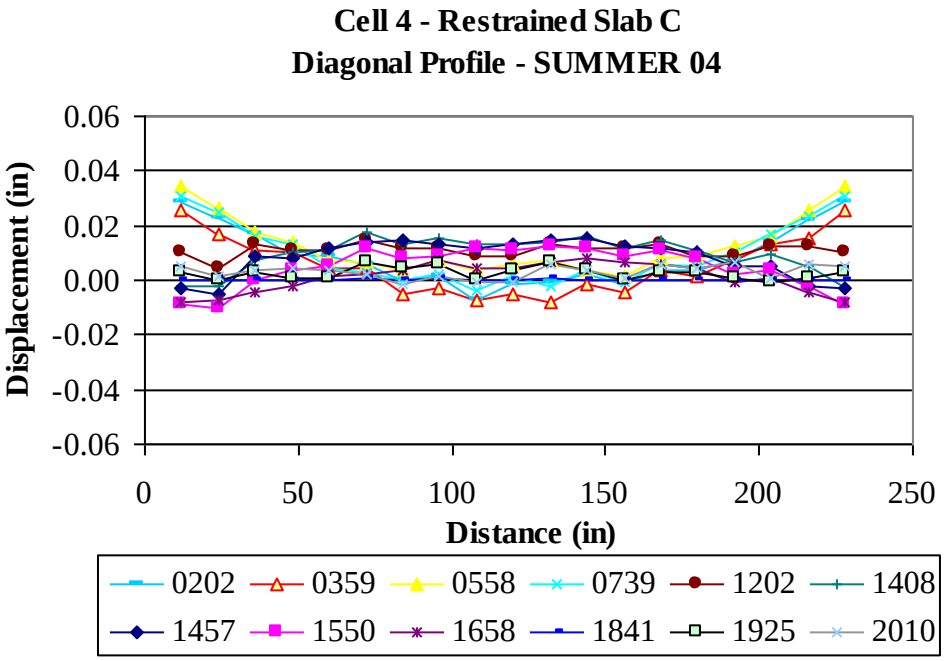

Figure C3. Restrained Slab C diagonal surface profiles for the summer of 2004.

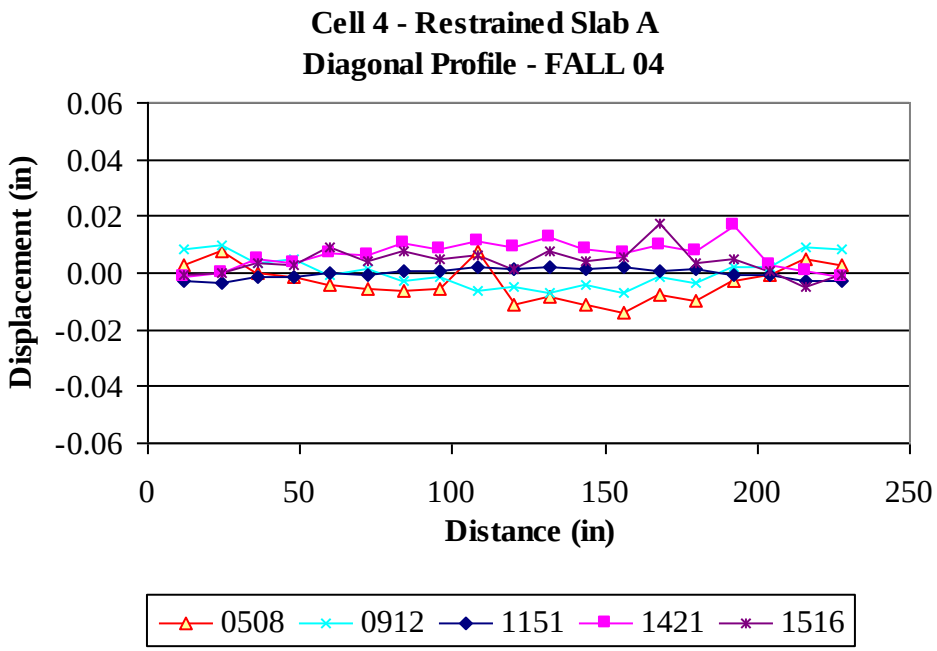

Figure C4. Restrained Slab A diagonal surface profiles for the fall of 2004.

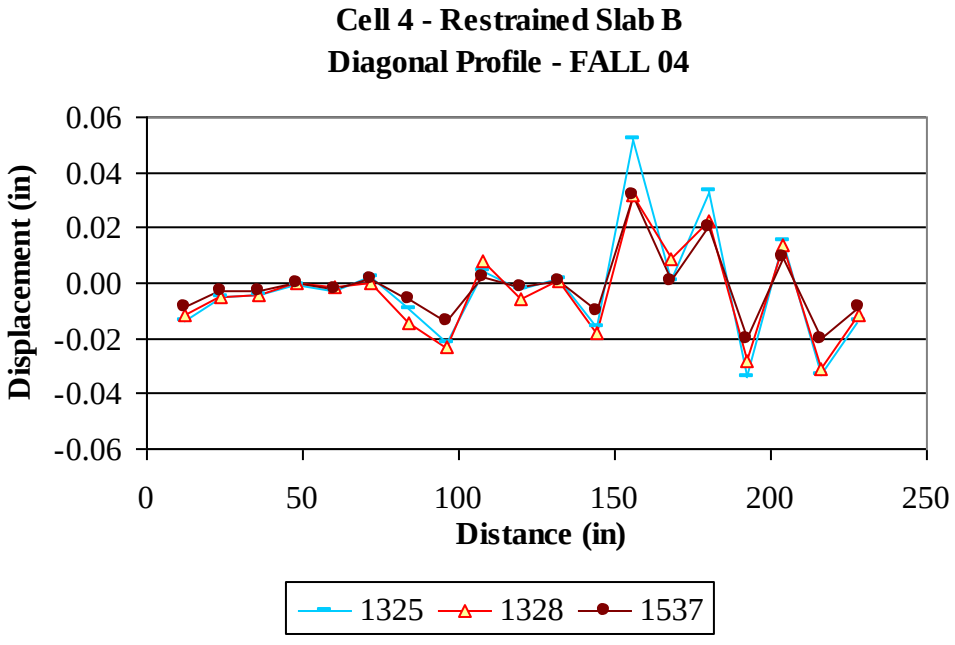

Figure C5. Restrained Slab B diagonal surface profiles for the fall of 2004 (Data was not valid).

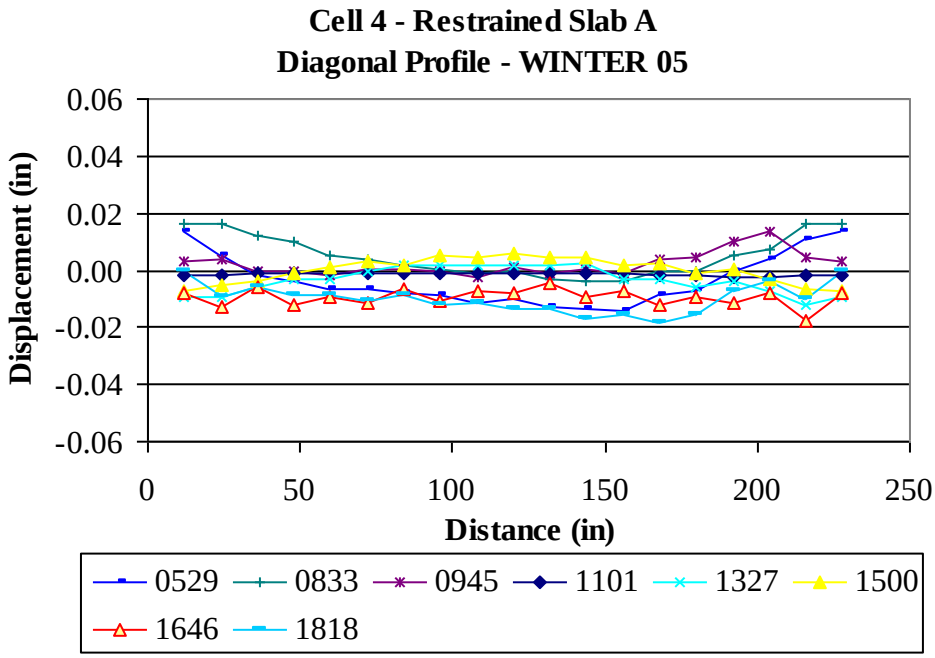

Figure C6. Restrained Slab A diagonal surface profiles for the winter of 2005.

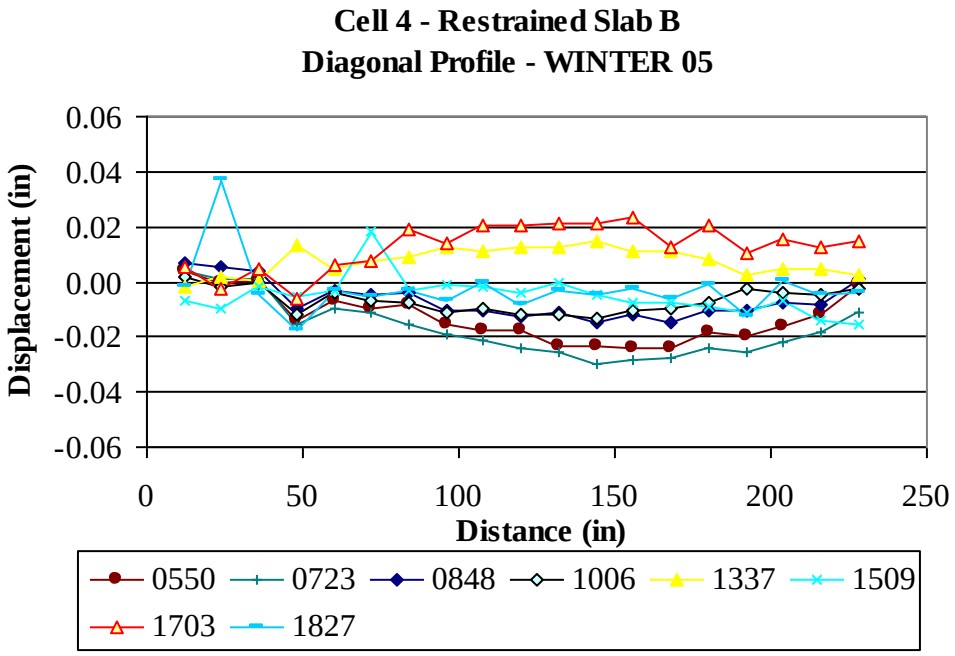

Figure C7. Restrained Slab B diagonal surface profiles for the winter of 2005.

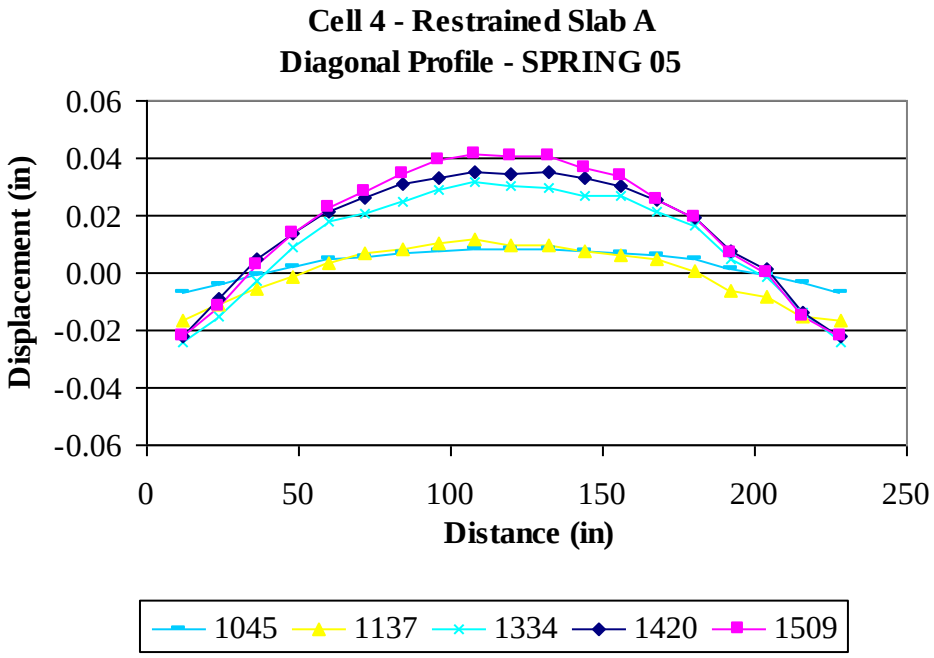

Figure C8. Restrained Slab A diagonal surface profiles for the spring of 2005.

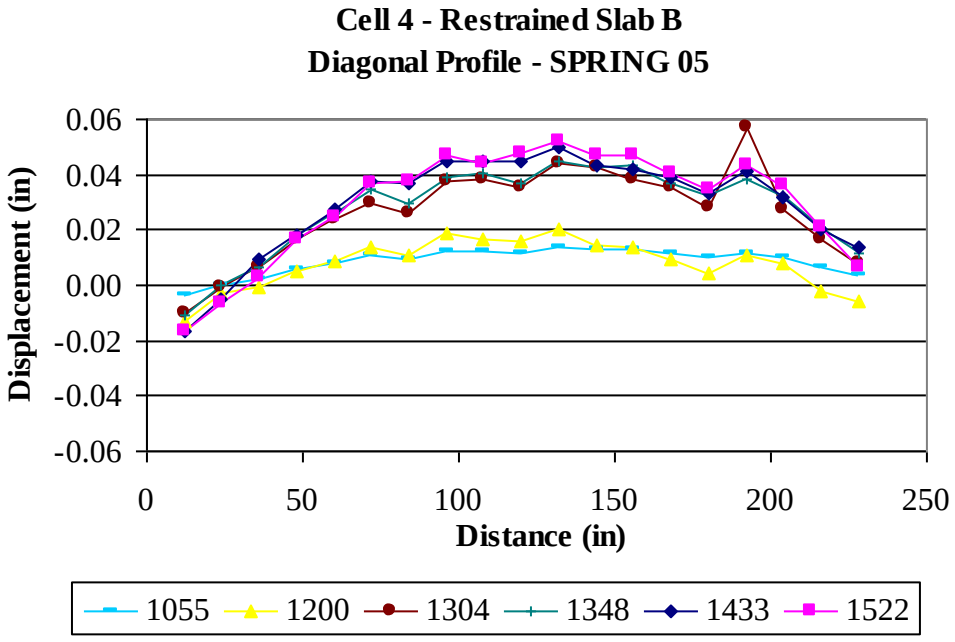

Figure C9. Restrained Slab B diagonal surface profiles for the spring of 2005.

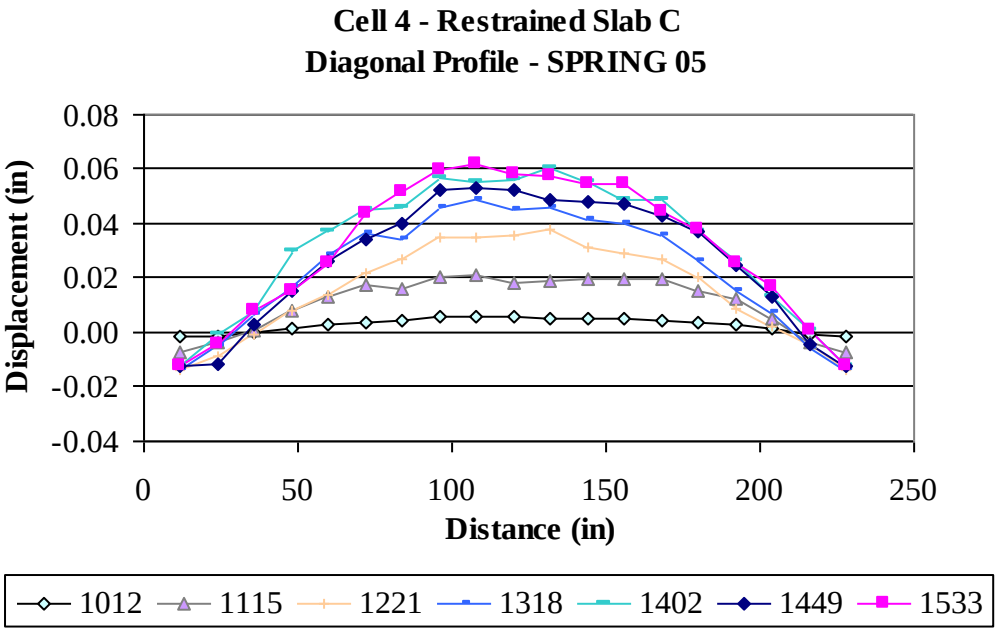

Figure C10. Restrained Slab C diagonal surface profiles for the spring of 2005.

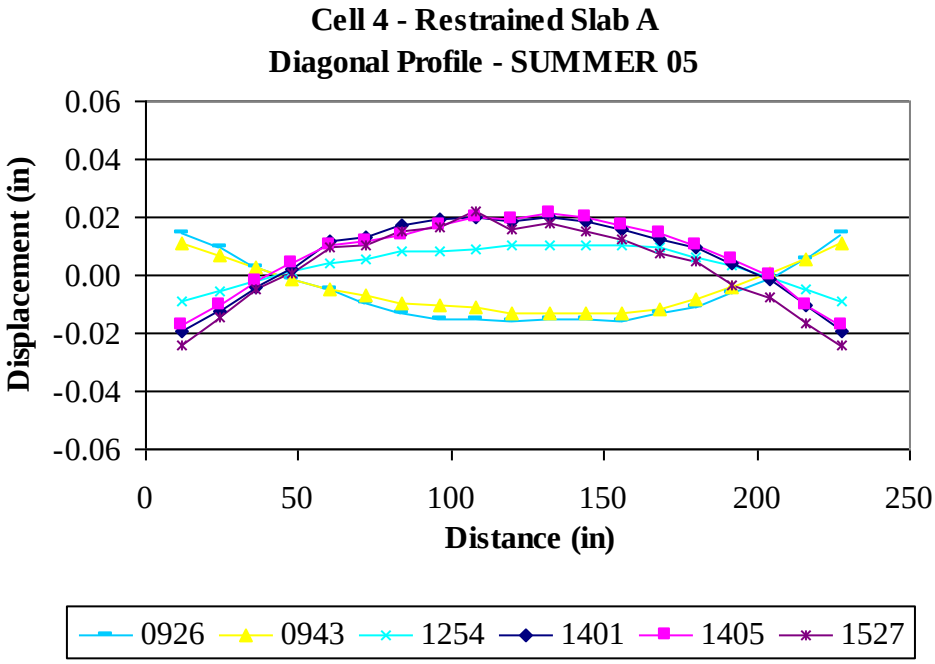

Figure C11. Restrained Slab A diagonal surface profiles for the summer of 2005.

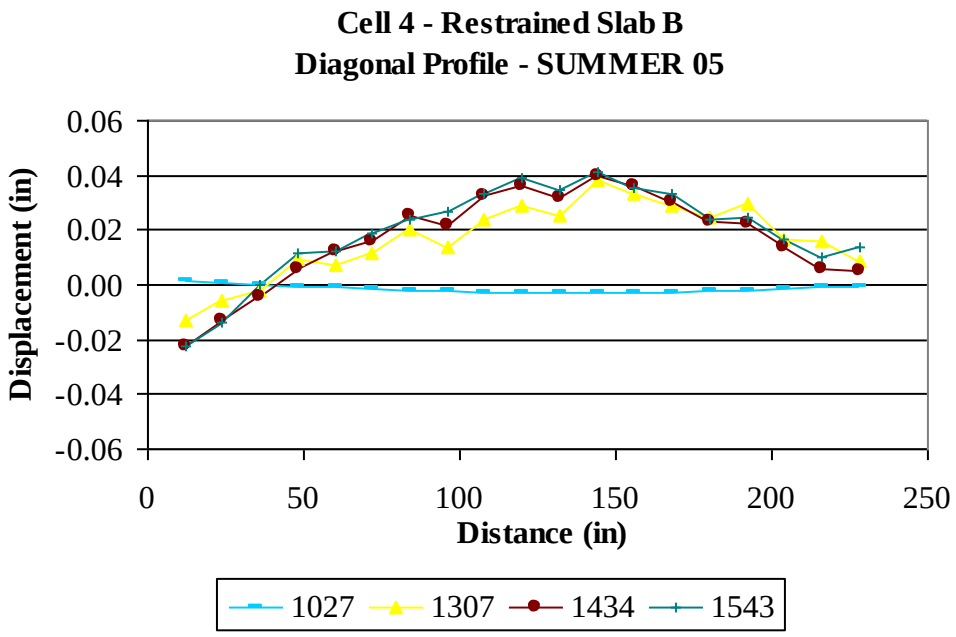

Figure C12. Restrained Slab B diagonal surface profiles for the summer of 2005.

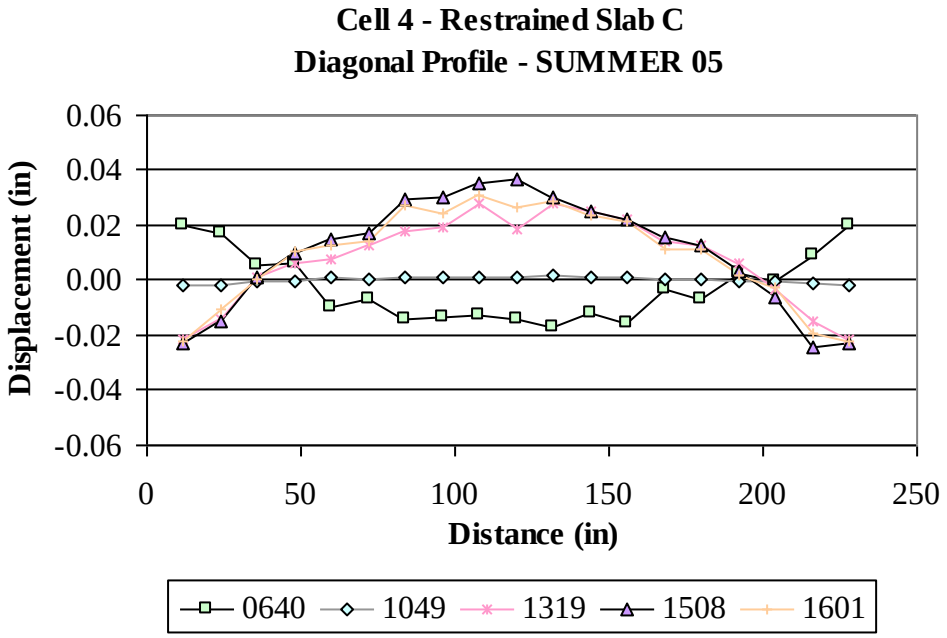

Figure C13. Restrained Slab C diagonal surface profiles for the summer of 2005.

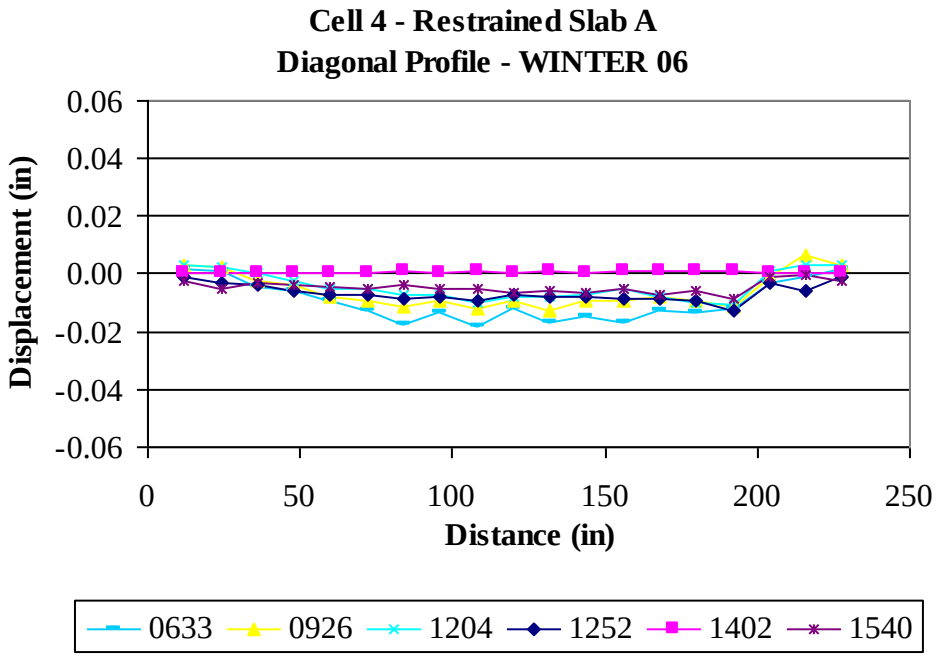

Figure C14. Restrained Slab A diagonal surface profiles for the winter of 2006.

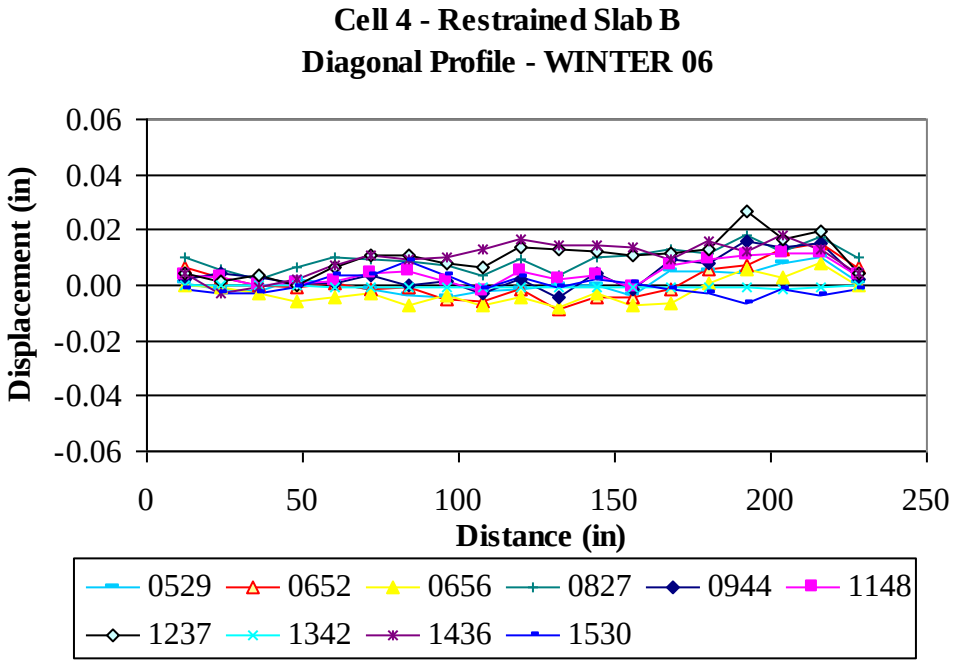

Figure C15. Restrained Slab B diagonal surface profiles for the winter of 2006.

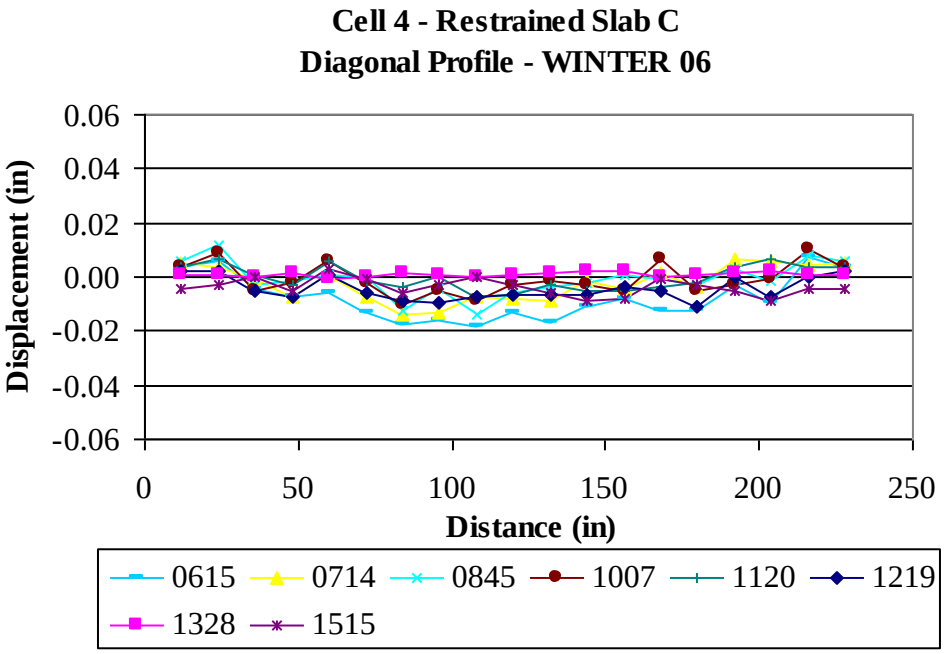

Figure C16. Restrained Slab C diagonal surface profiles for the winter of 2006.

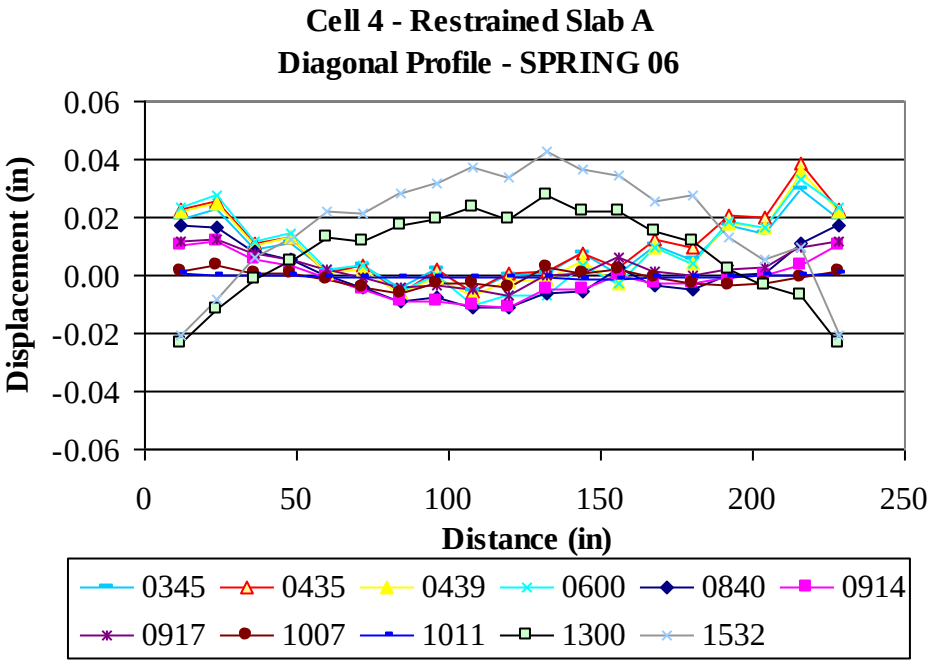

Figure C17. Restrained Slab A diagonal surface profiles for the spring of 2006.

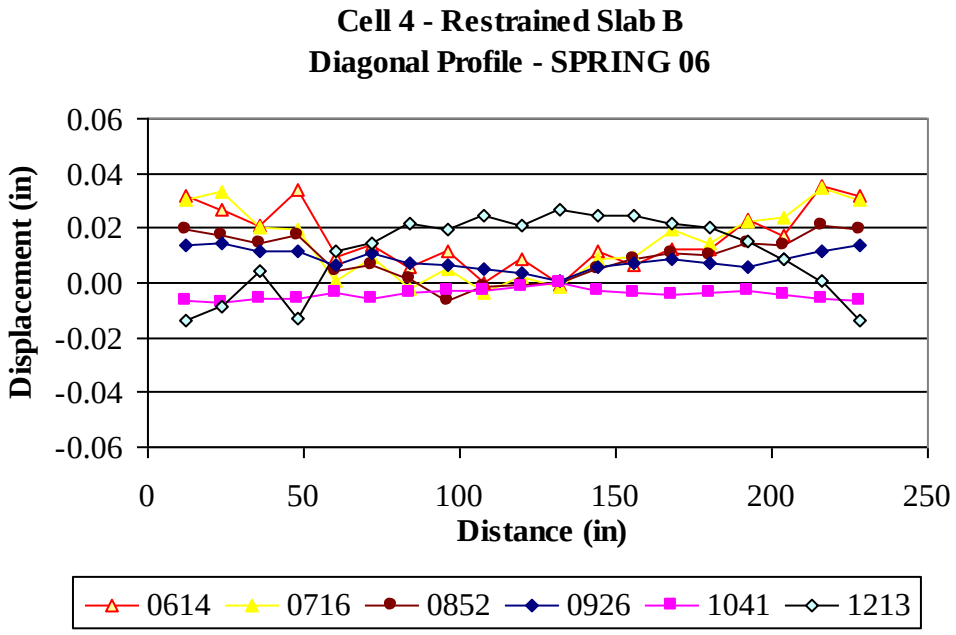

Figure C18. Restrained Slab B diagonal surface profiles for the spring of 2006.

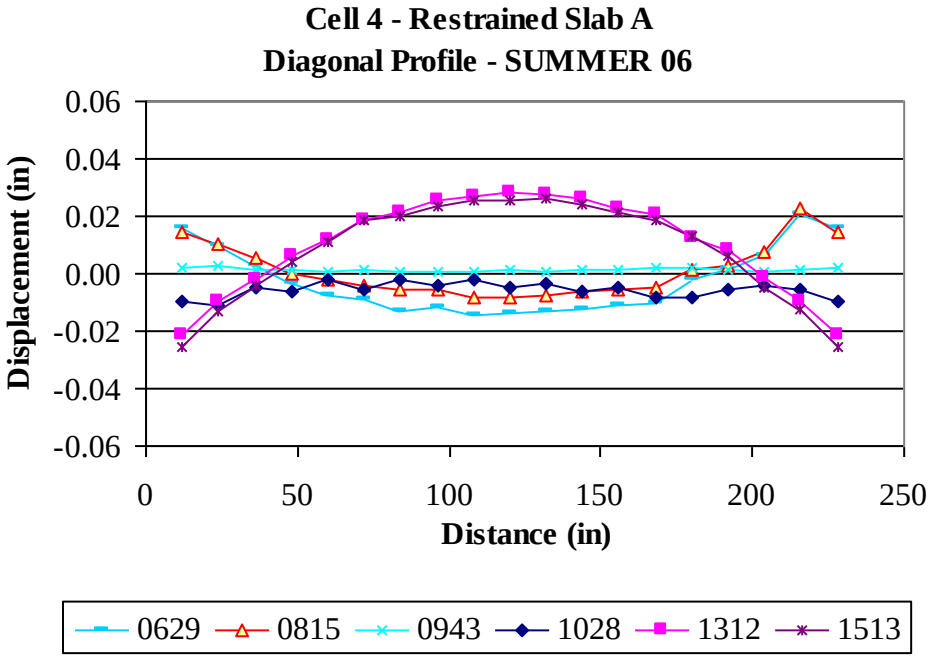

Figure C19. Restrained Slab A diagonal surface profiles for the summer of 2006.

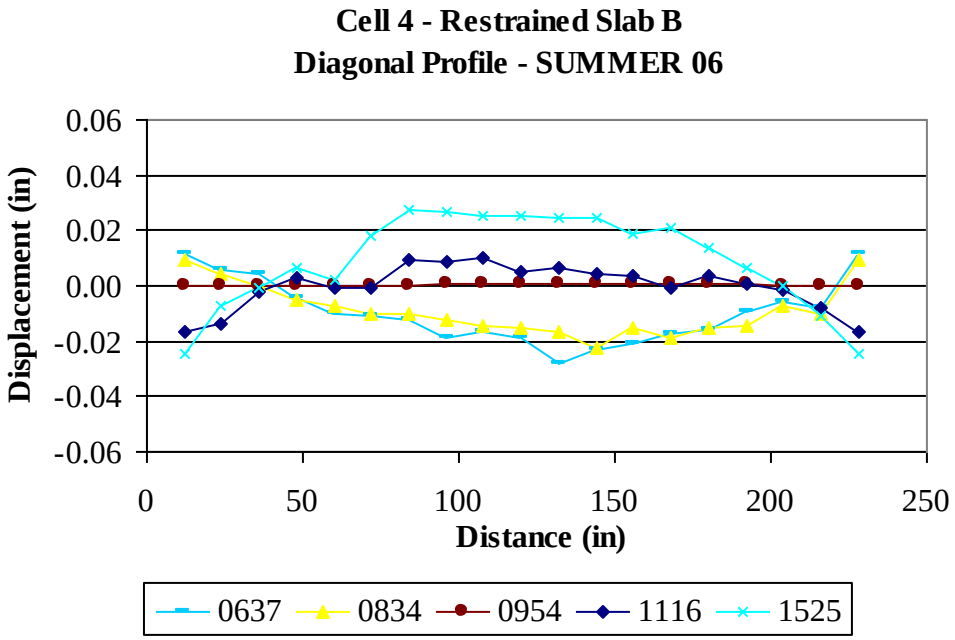

Figure C20. Restrained Slab B diagonal surface profiles for the summer of 2006.

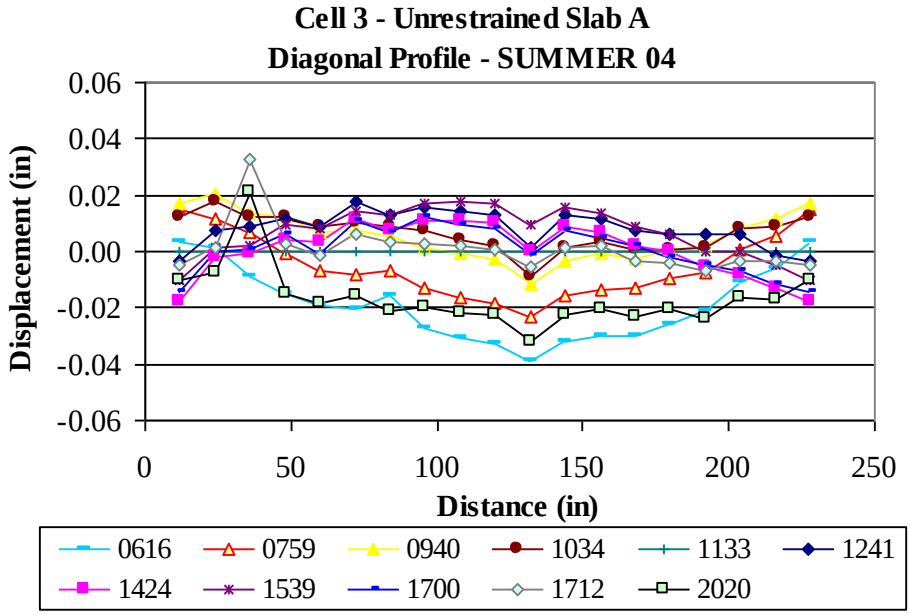

Figure C21. Unrestrained Slab A diagonal surface profiles for the summer of 2004.

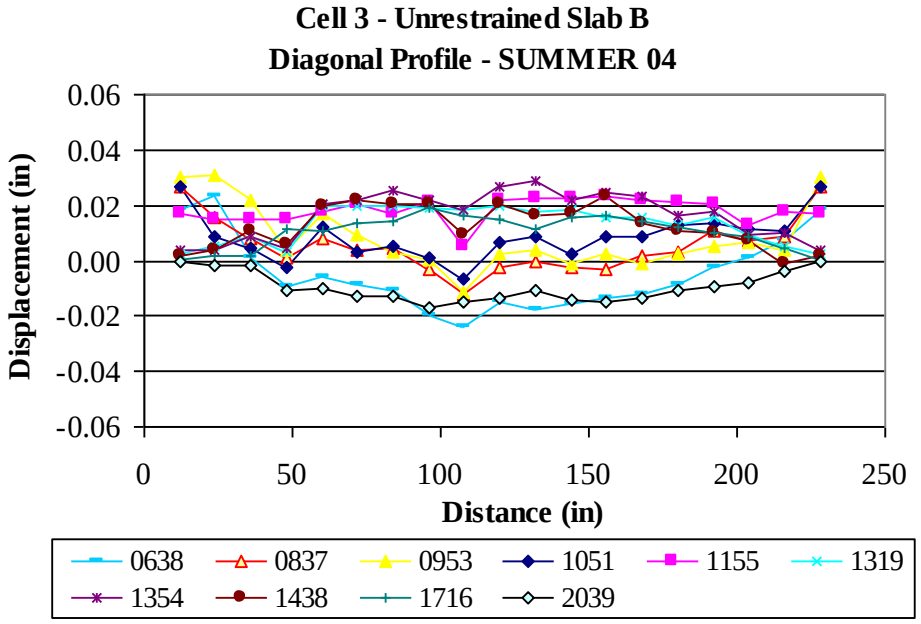

Figure C22. Unrestrained Slab B diagonal surface profiles for the summer of 2004.

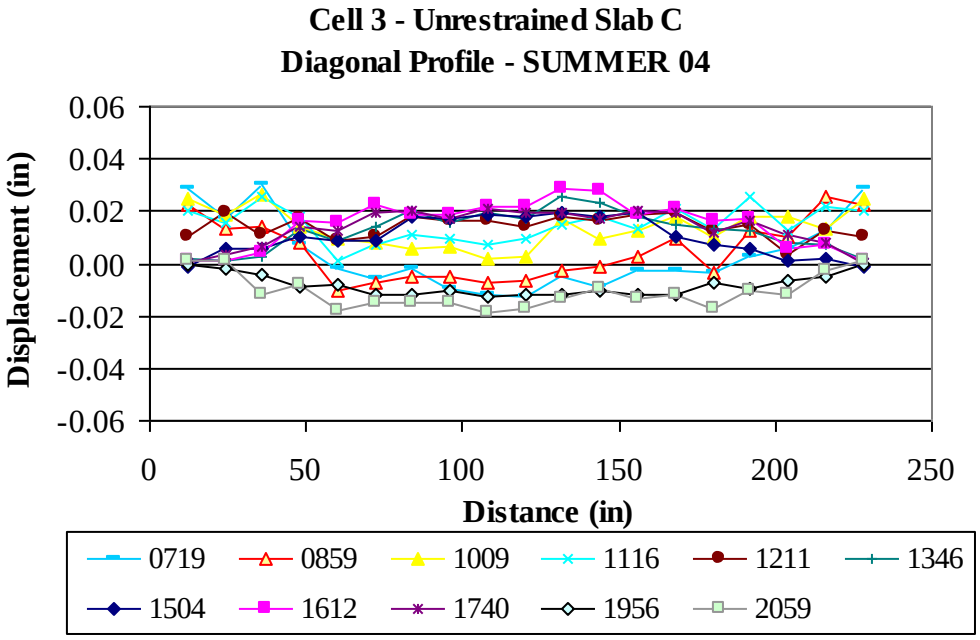

Figure C23. Unrestrained Slab C diagonal surface profiles for the summer of 2004.

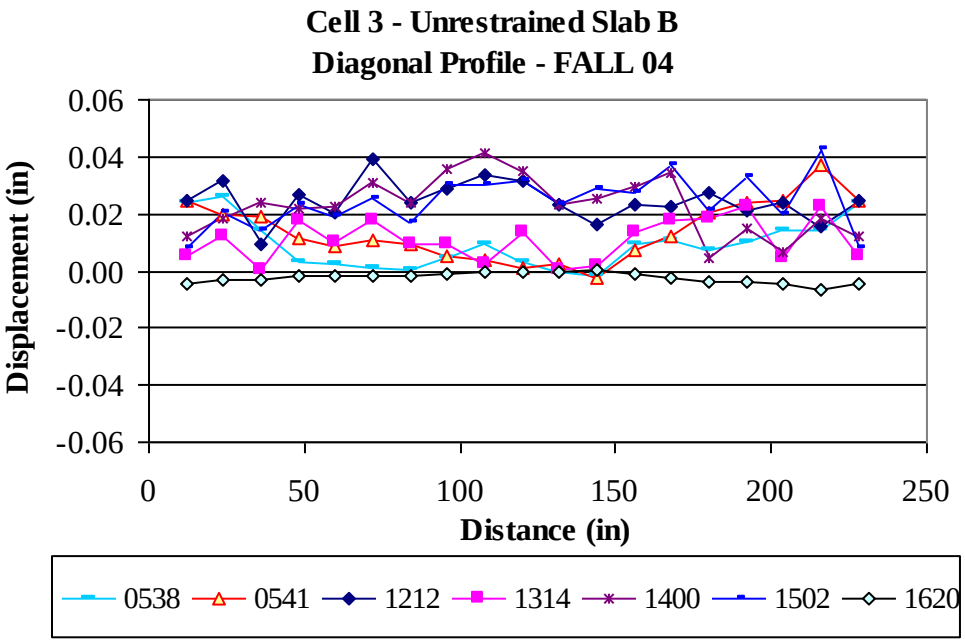

Figure C24. Unrestrained Slab B diagonal surface profiles for the fall of 2004.

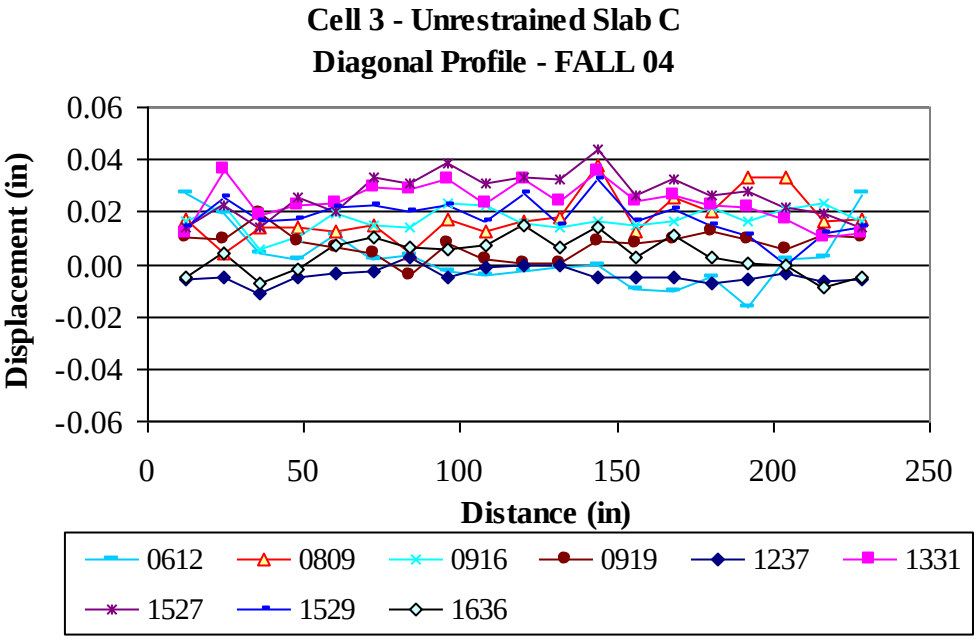

Figure C25. Unrestrained Slab C diagonal surface profiles for the fall of 2004.

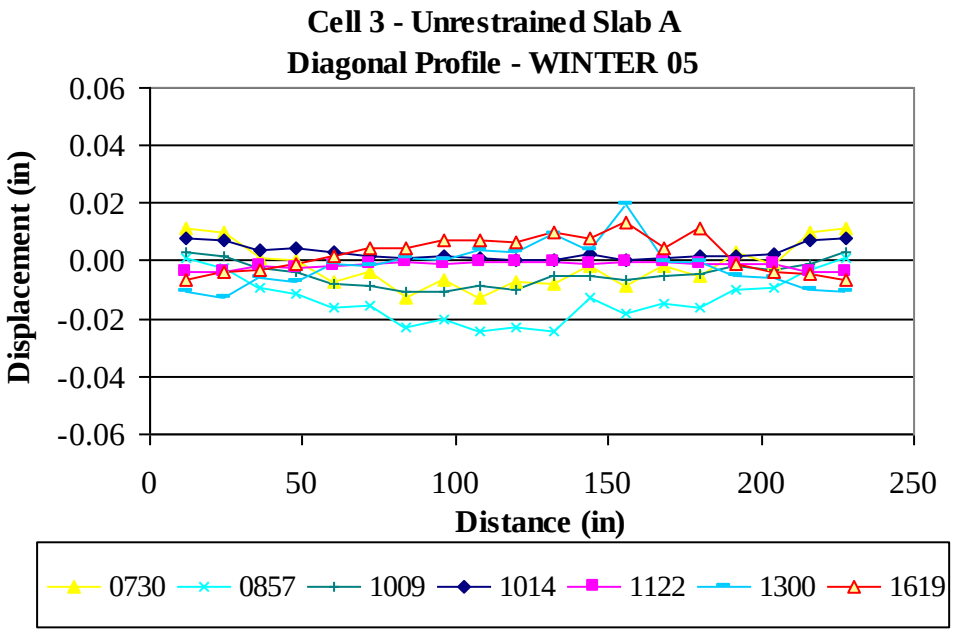

Figure C26. Unrestrained Slab A diagonal surface profiles for the winter of 2005.

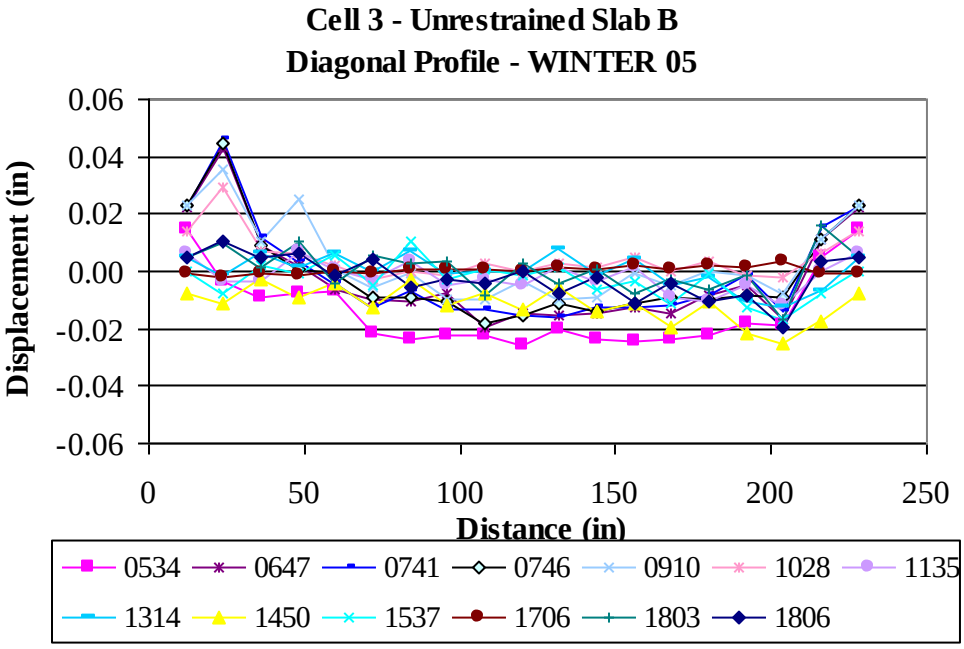

Figure C27. Unrestrained Slab B diagonal surface profiles for the winter of 2005.

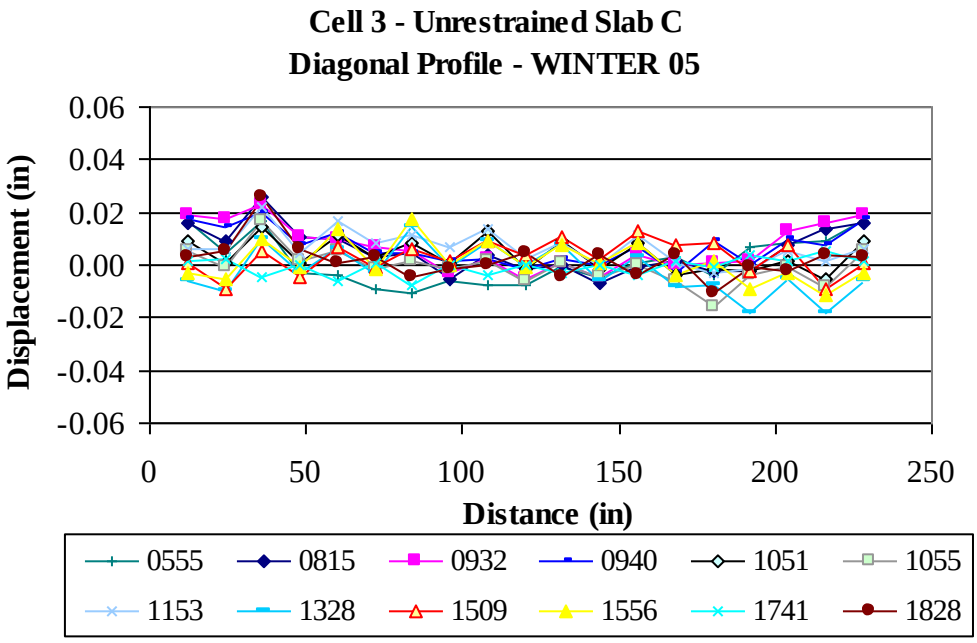

Figure C28. Unrestrained Slab C diagonal surface profiles for the winter of 2005.

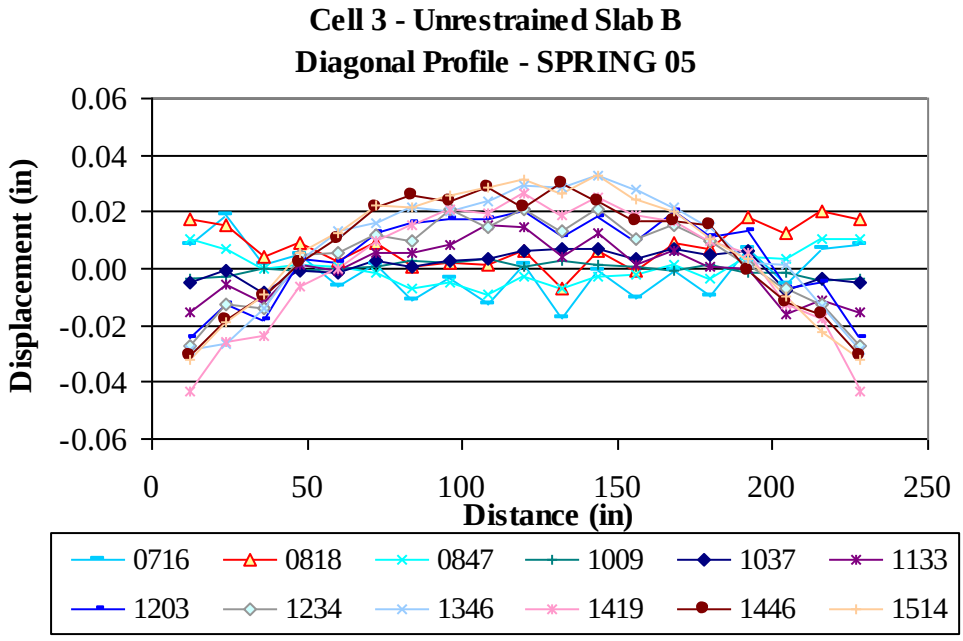

Figure C29. Unrestrained Slab B diagonal surface profiles for the spring of 2005.

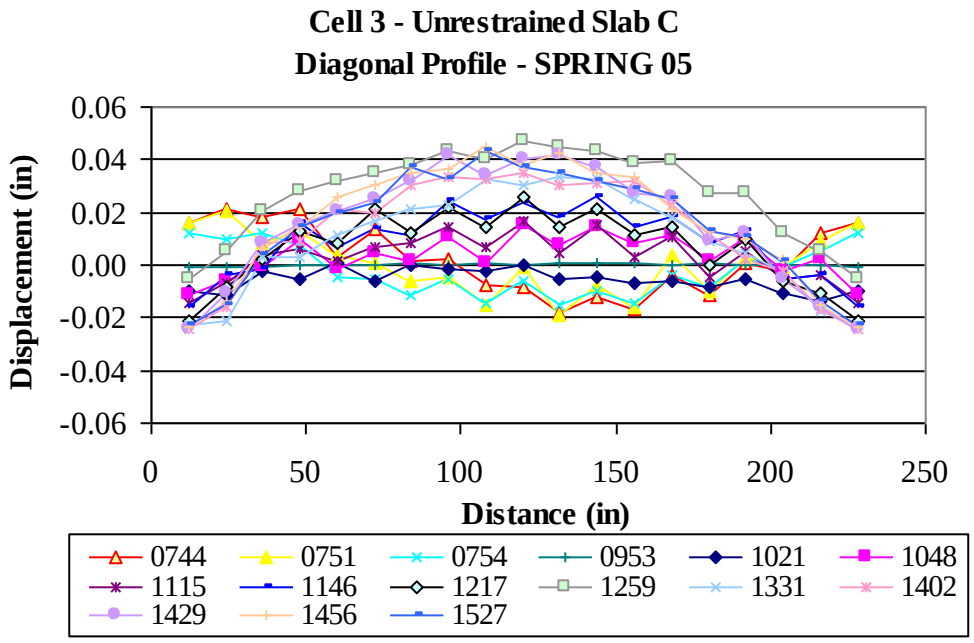

Figure C30. Unrestrained Slab C diagonal surface profiles for the spring of 2005.

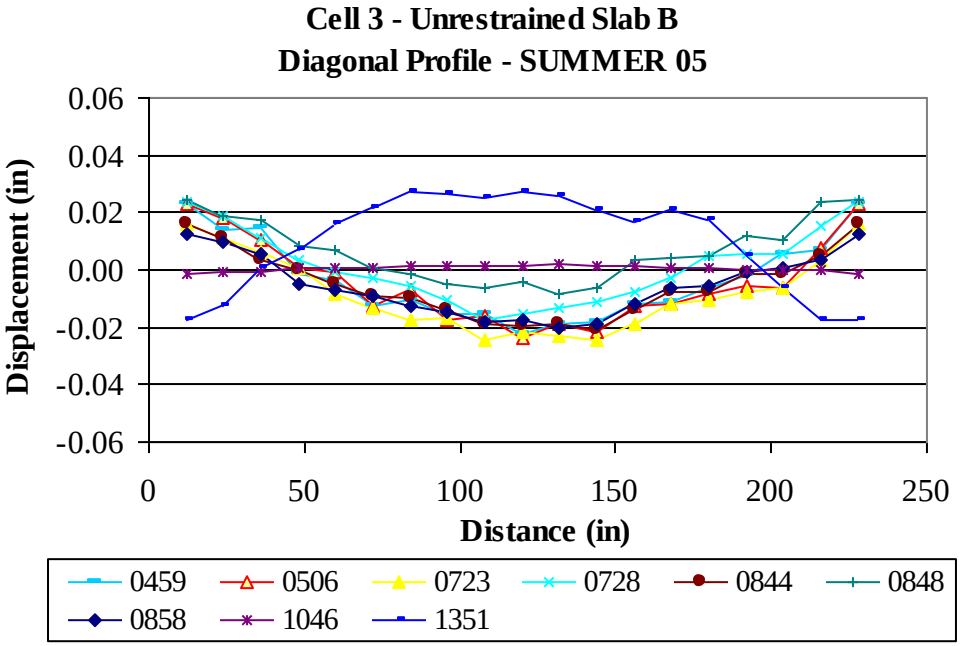

Figure C31. Unrestrained Slab B diagonal surface profiles for the summer of 2005.

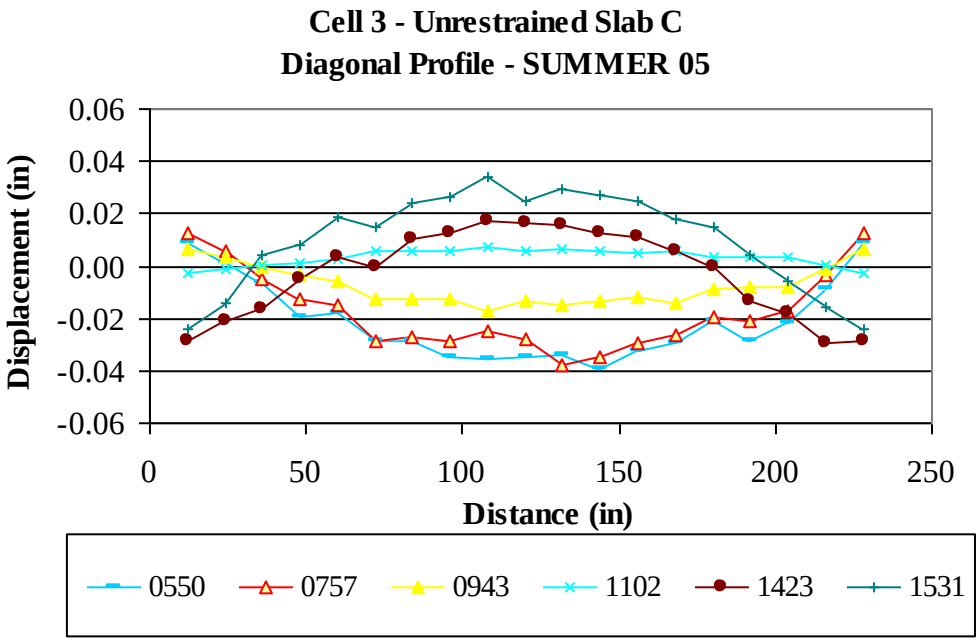

Figure C32. Unrestrained Slab C diagonal surface profiles for the summer of 2005.

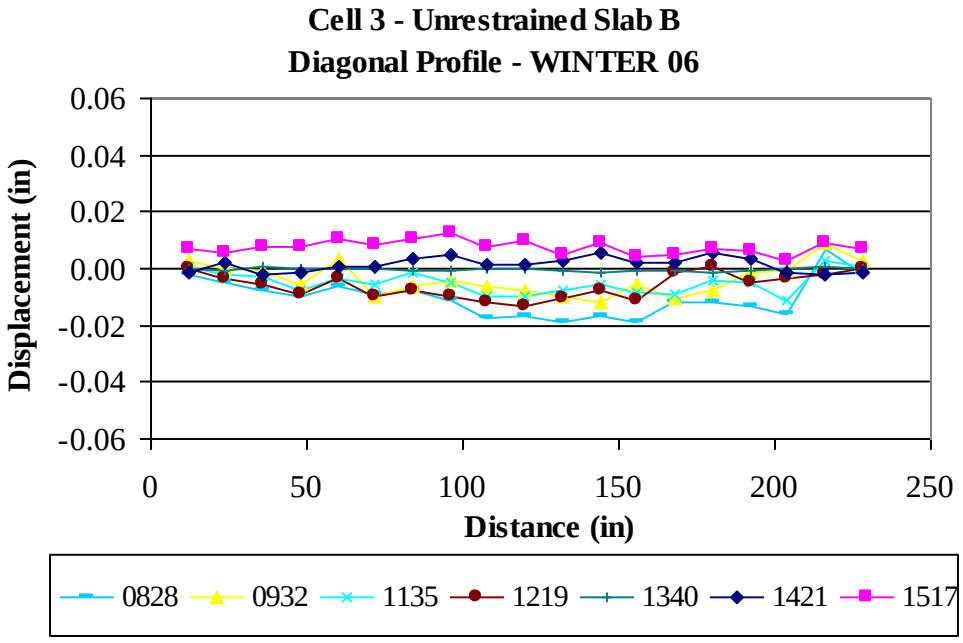

Figure C33. Unrestrained Slab B diagonal surface profiles for the winter of 2006.

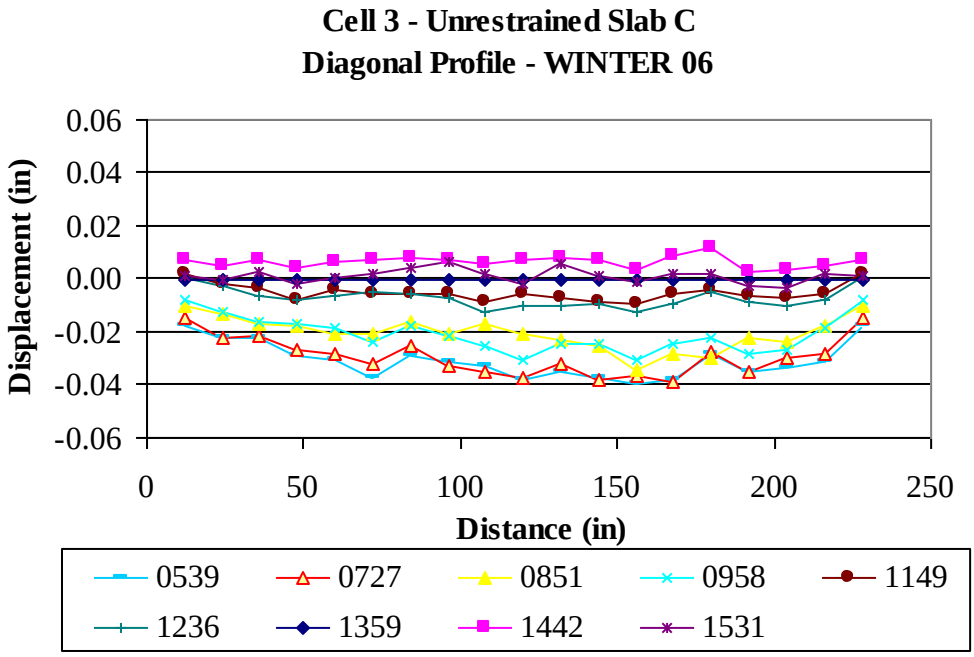

Figure C34. Unrestrained Slab C diagonal surface profiles for the winter of 2006.

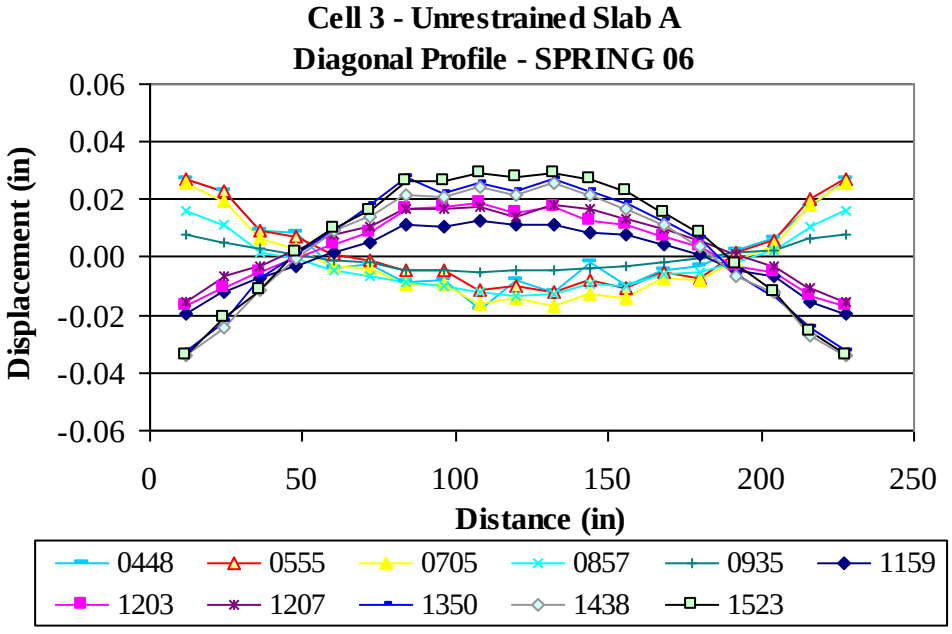

Figure C35. Unrestrained Slab A diagonal surface profiles for the spring of 2006.

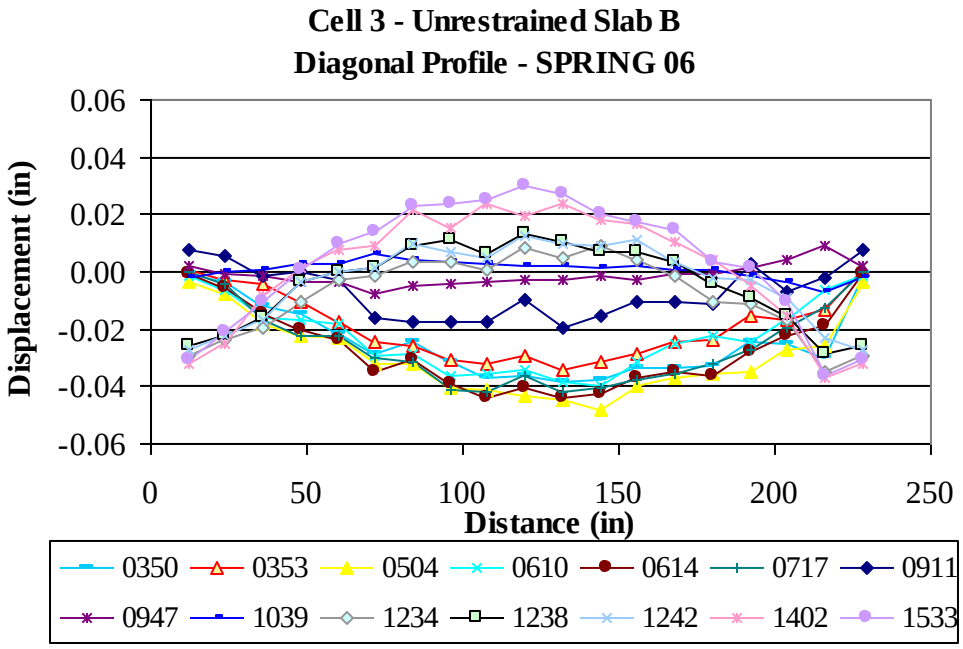

Figure C36. Unrestrained Slab B diagonal surface profiles for the spring of 2006.

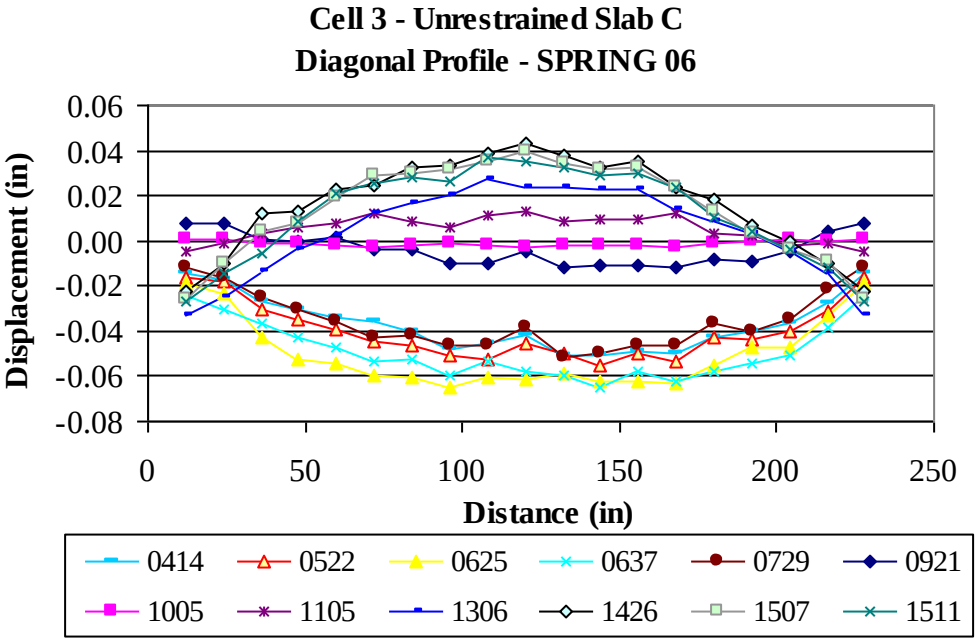

Figure C37. Unrestrained Slab C diagonal surface profiles for the spring of 2006.

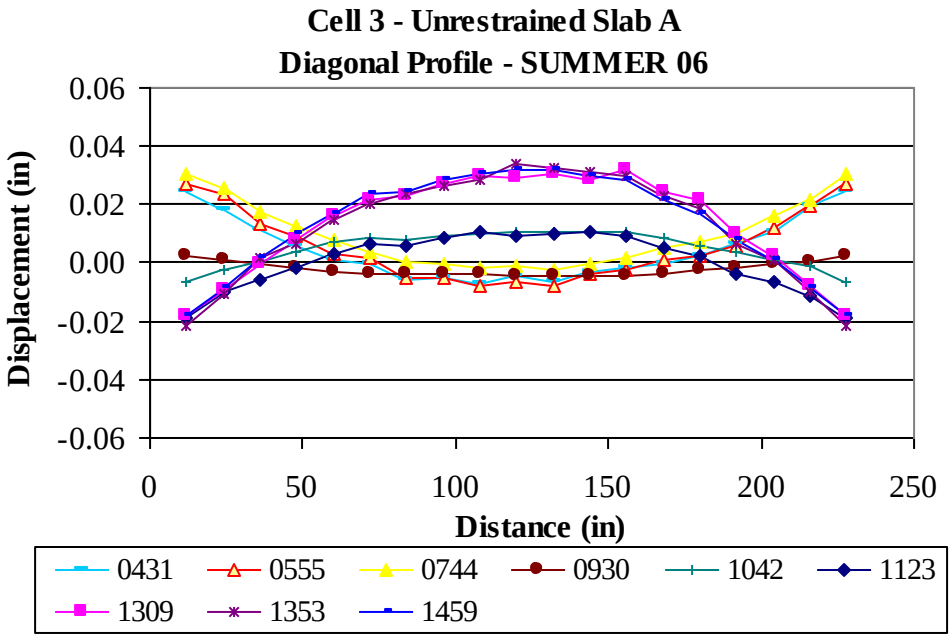

Figure C38. Unrestrained Slab A diagonal surface profiles for the summer of 2006.

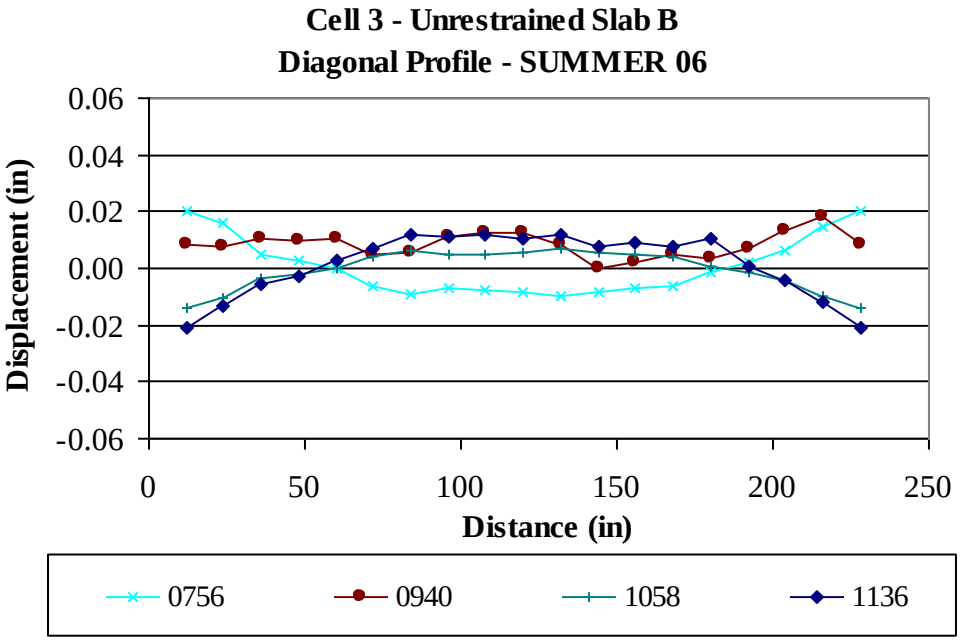

Figure C39. Unrestrained Slab B diagonal surface profiles for the summer of 2006.

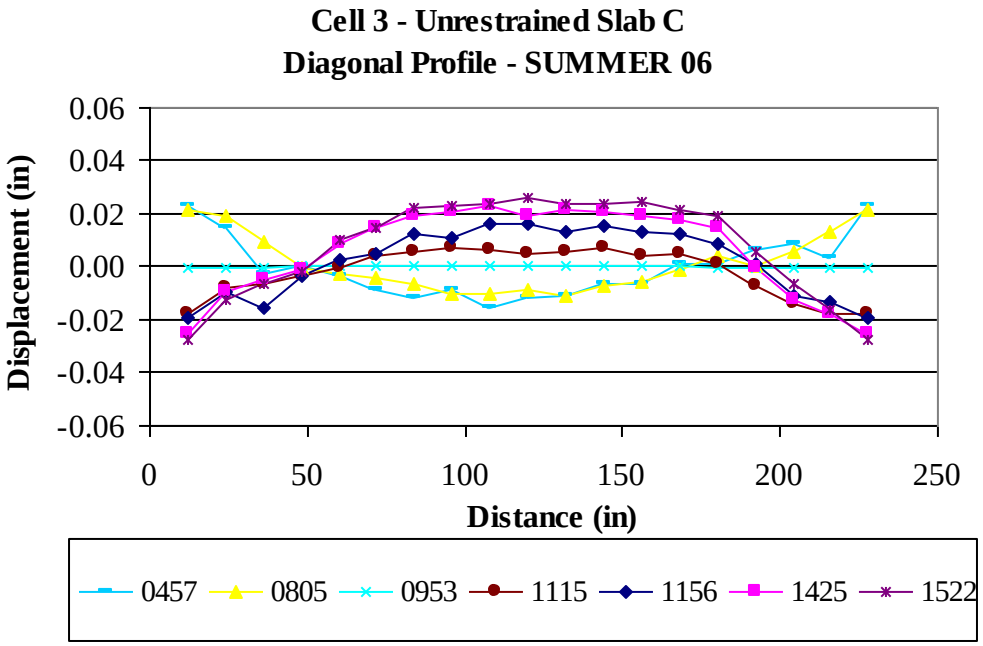

Figure C40. Unrestrained Slab C diagonal surface profiles for the summer of 2006.

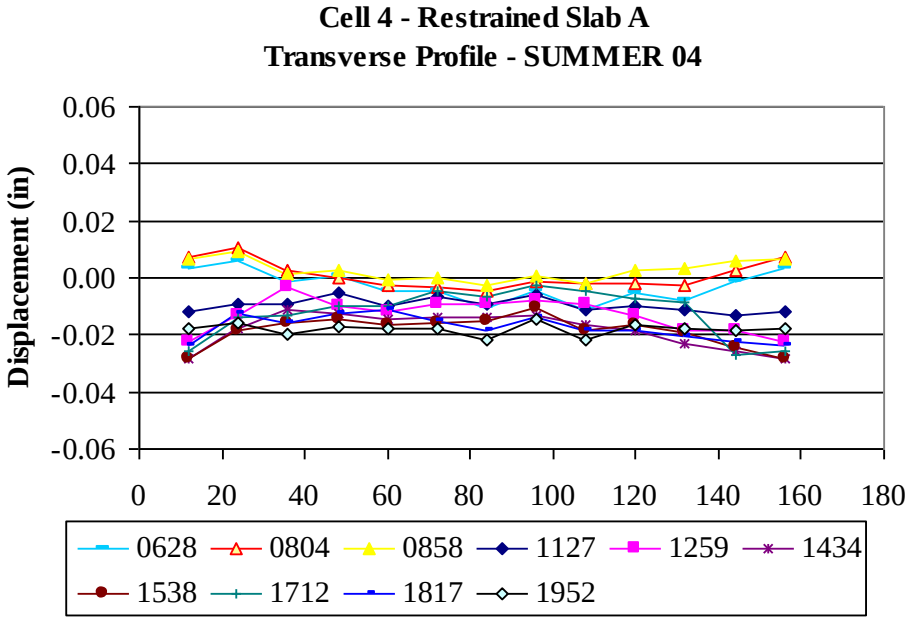

Figure C41. Restrained Slab A Line A transverse surface profiles for the summer of 2004.

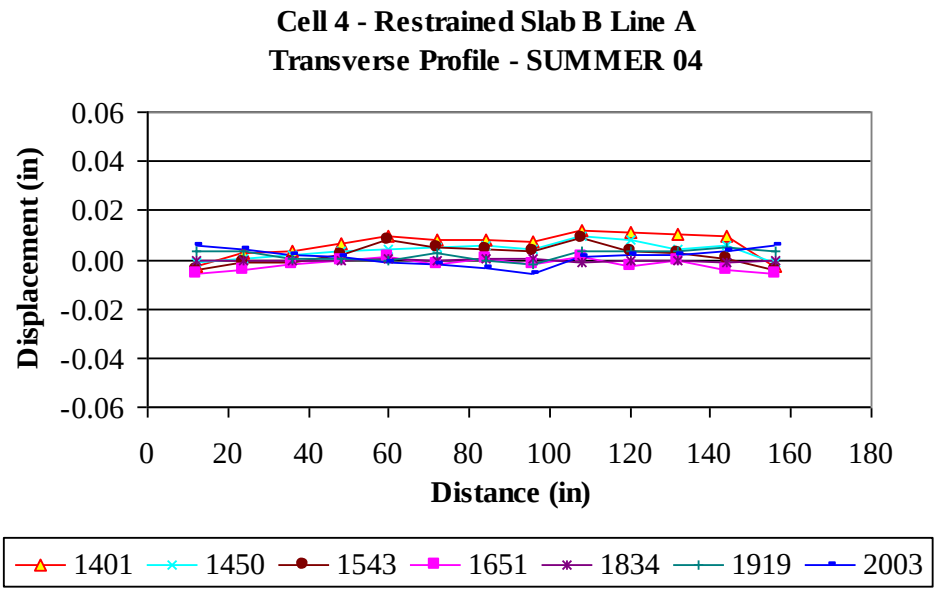

Figure C42. Restrained Slab B Line A transverse surface profiles for the summer of 2004.

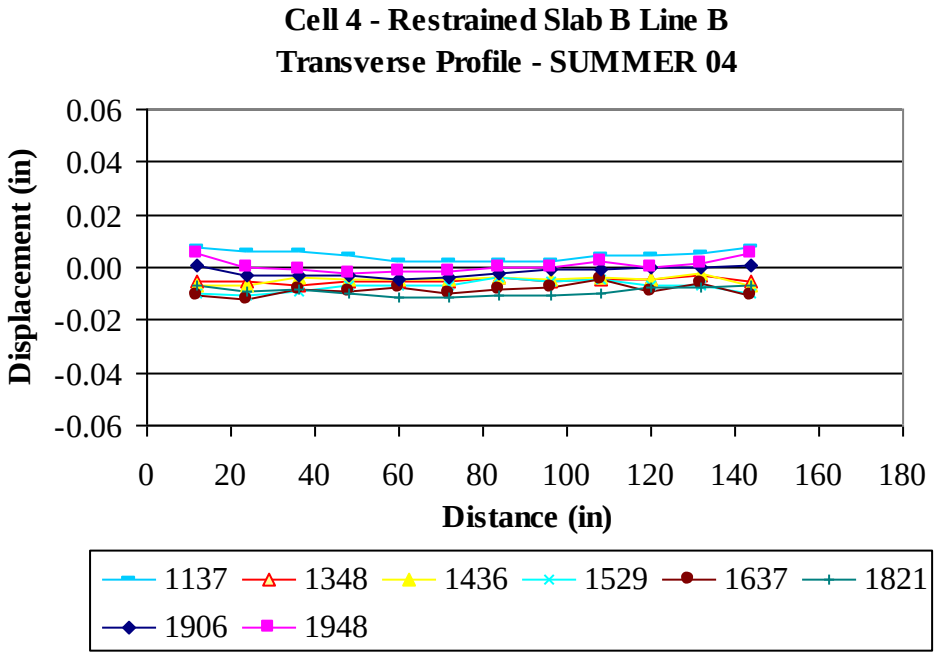

Figure C43. Restrained Slab B Line B transverse surface profiles for the summer of 2004.

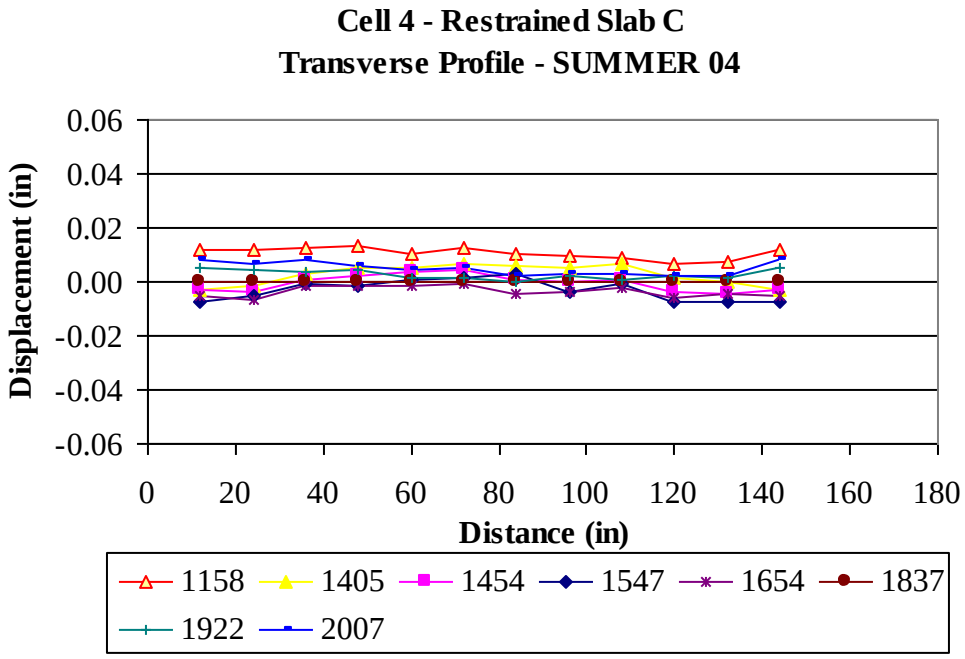

Figure C44. Restrained Slab C Line B transverse surface profiles for the summer of 2004.

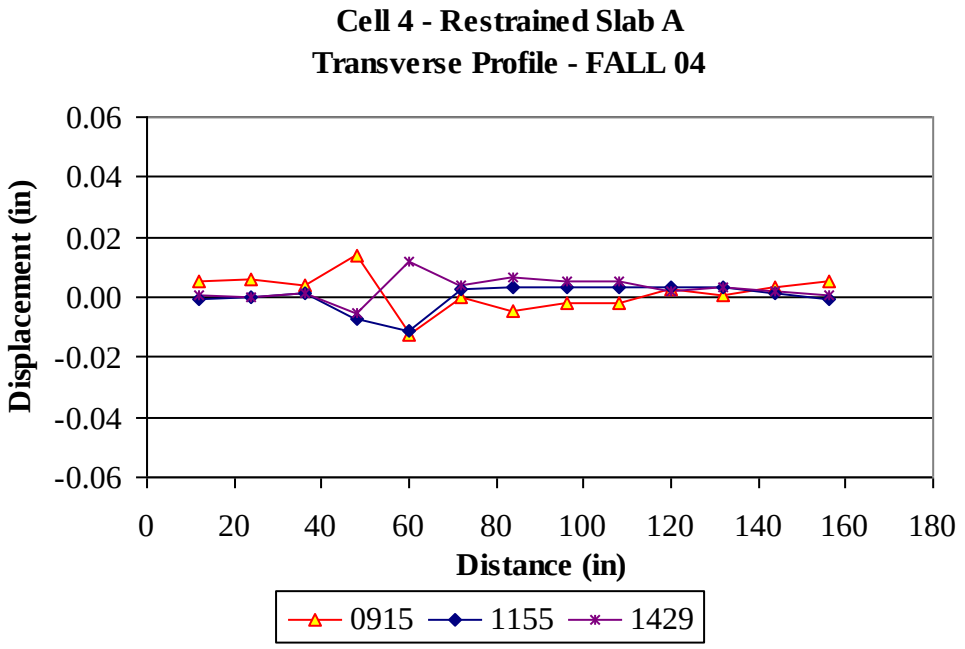

Figure C45. Restrained Slab A Line A transverse surface profiles for the fall of 2004.

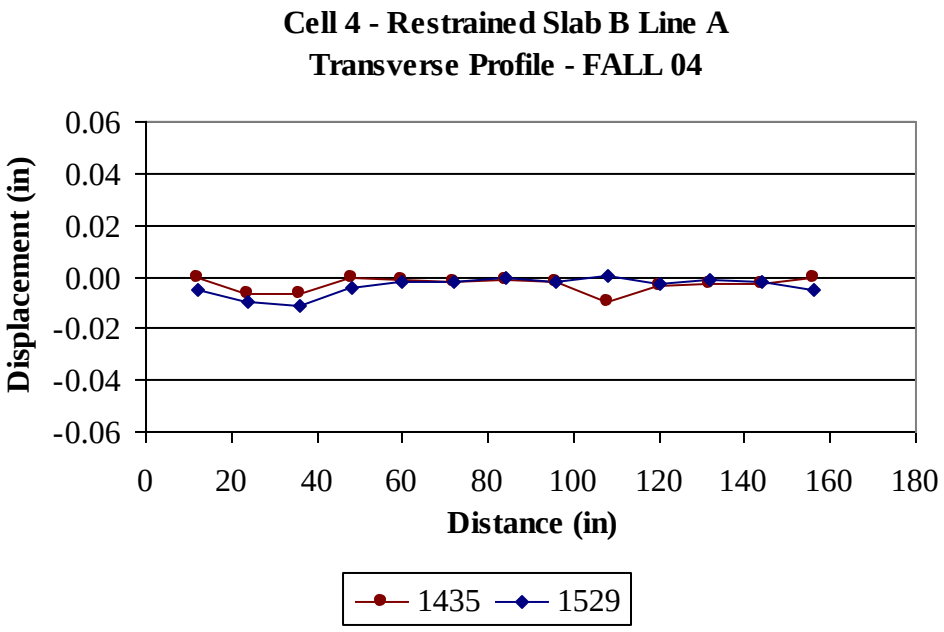

Figure C46. Restrained Slab B Line A transverse surface profiles for the fall of 2004.

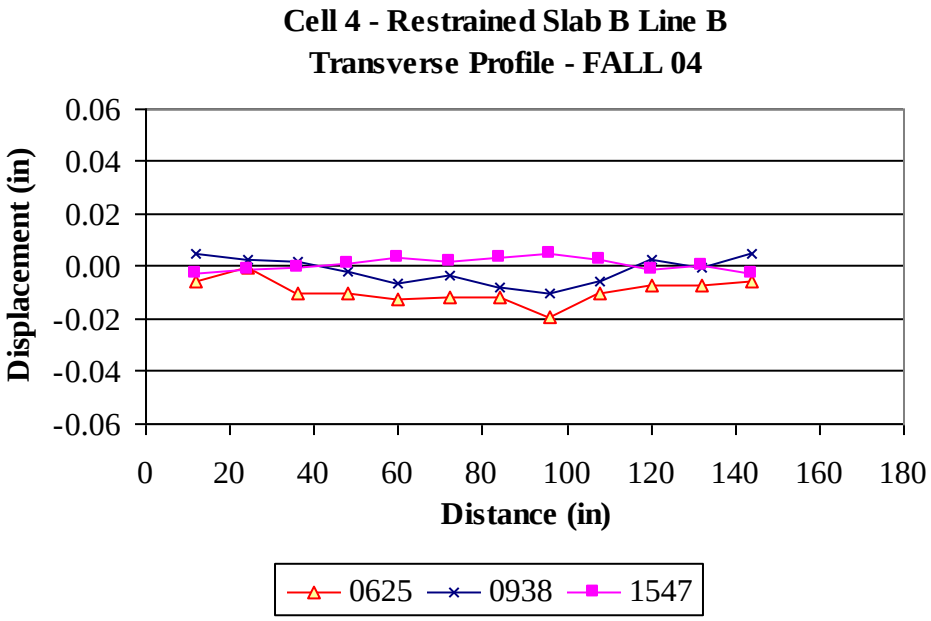

Figure C47. Restrained Slab B Line B transverse surface profiles for the fall of 2004.

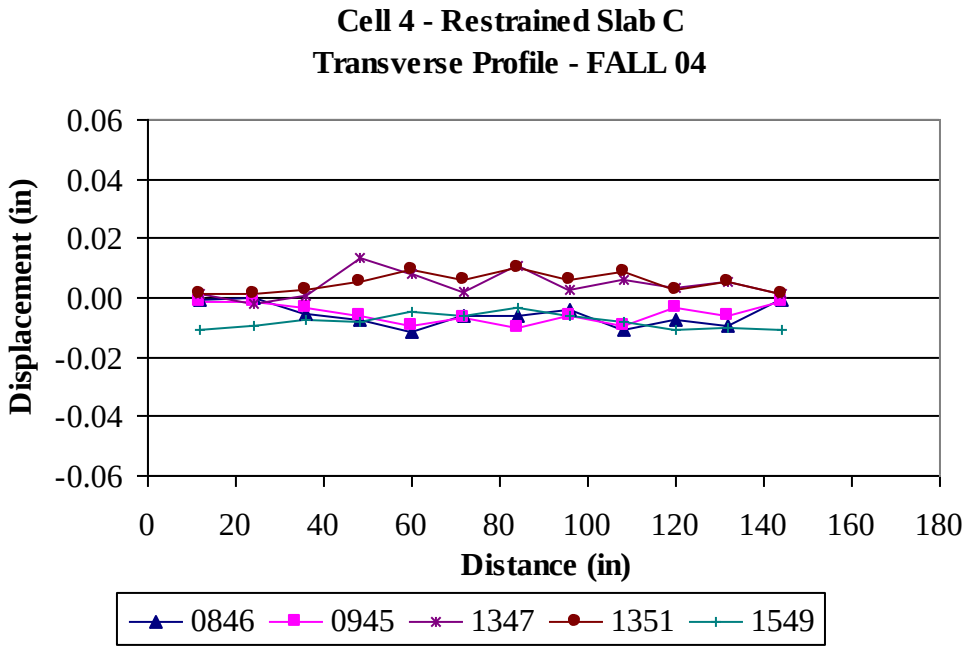

Figure C48. Restrained Slab C Line B transverse surface profiles for the fall of 2004.

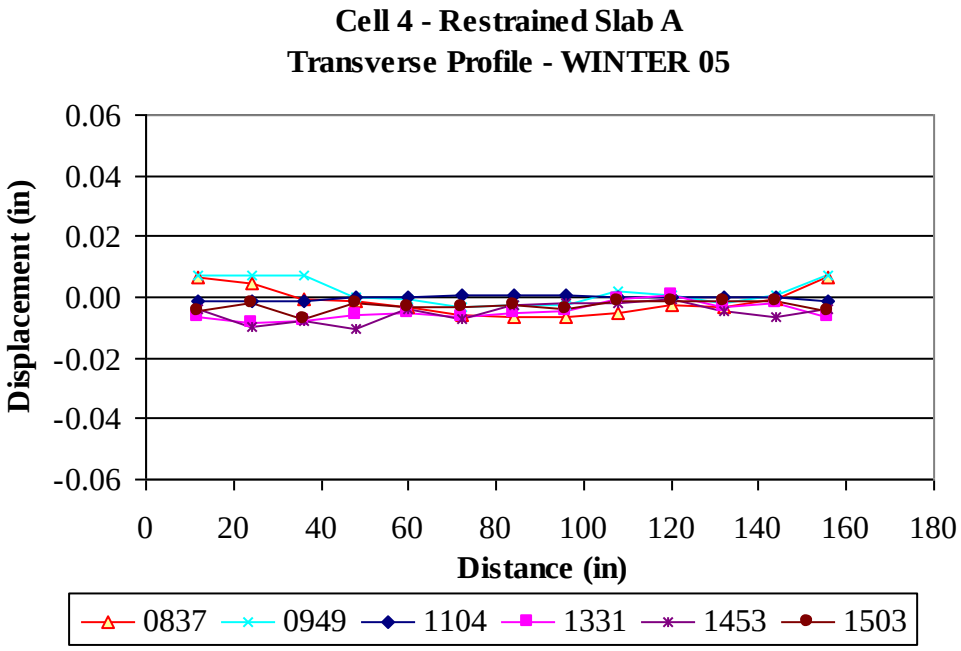

Figure C49. Restrained Slab A Line A transverse surface profiles for the winter of 2005.

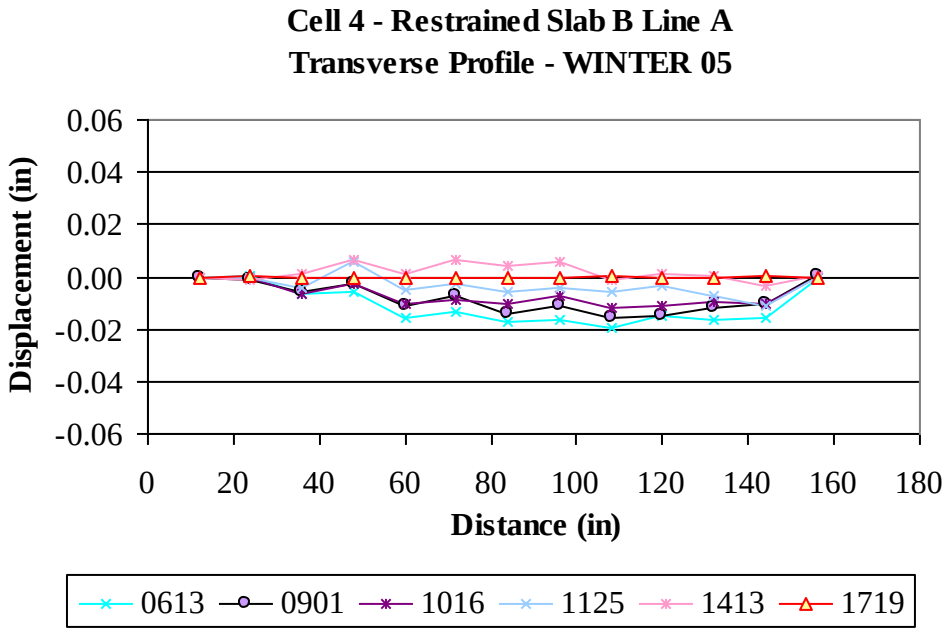

Figure C50. Restrained Slab B Line A transverse surface profiles for the winter of 2005.

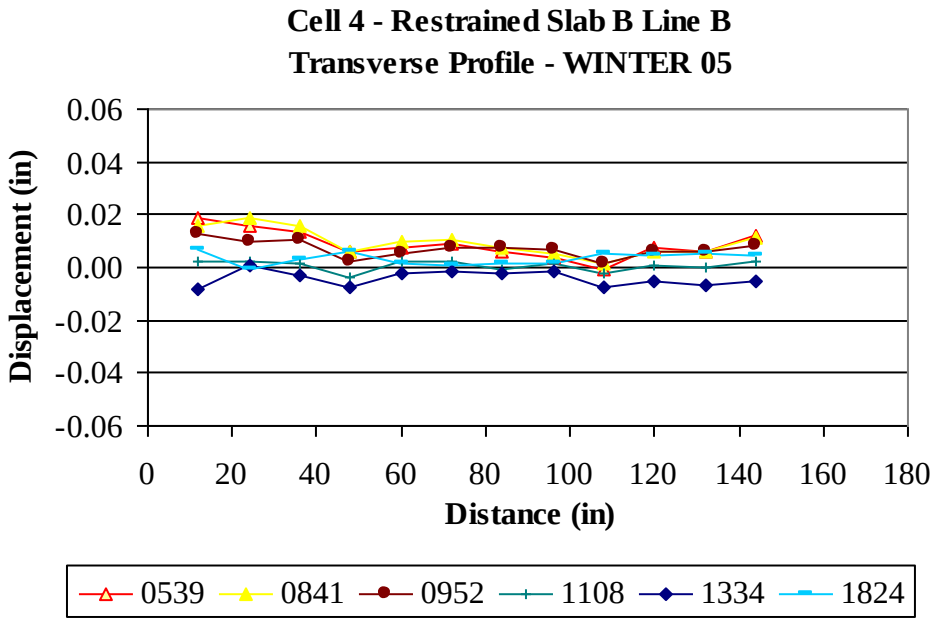

Figure C51. Restrained Slab B Line B transverse surface profiles for the winter of 2005.

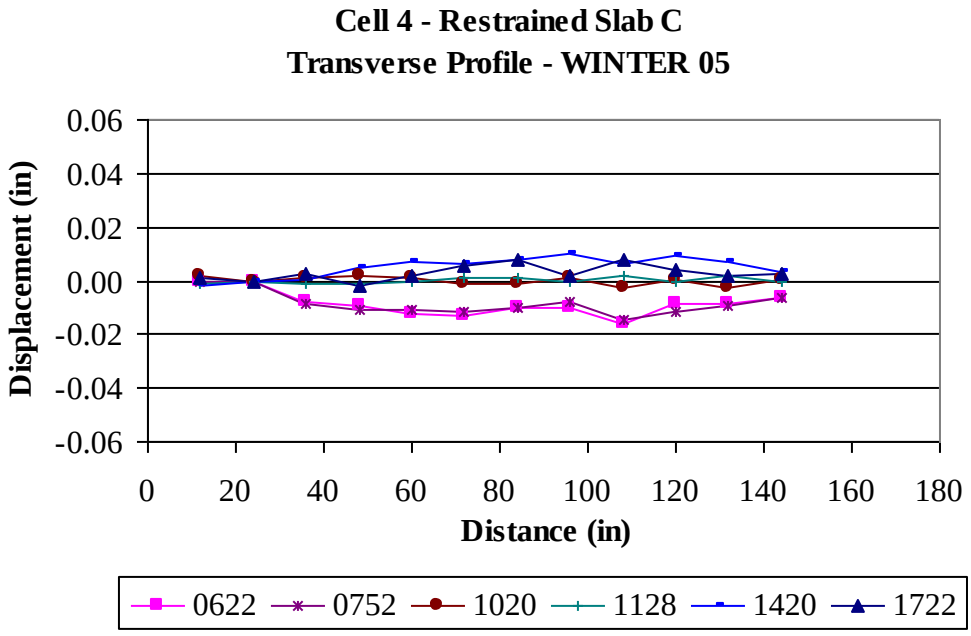

Figure C52. Restrained Slab C Line B transverse surface profiles for the winter of 2005.

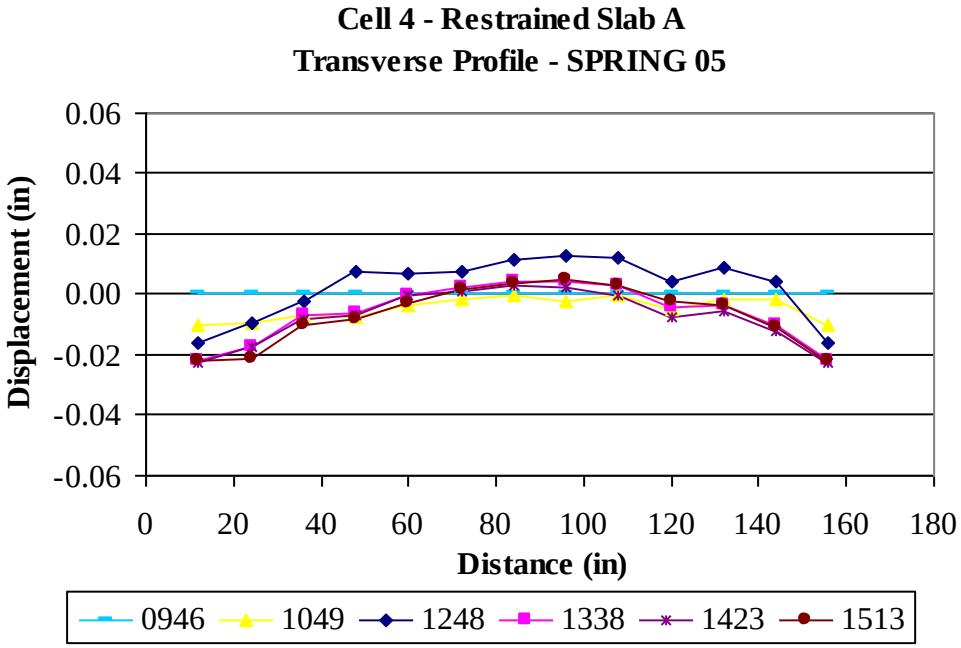

Figure C53. Restrained Slab A Line A transverse surface profiles for the spring of 2005.

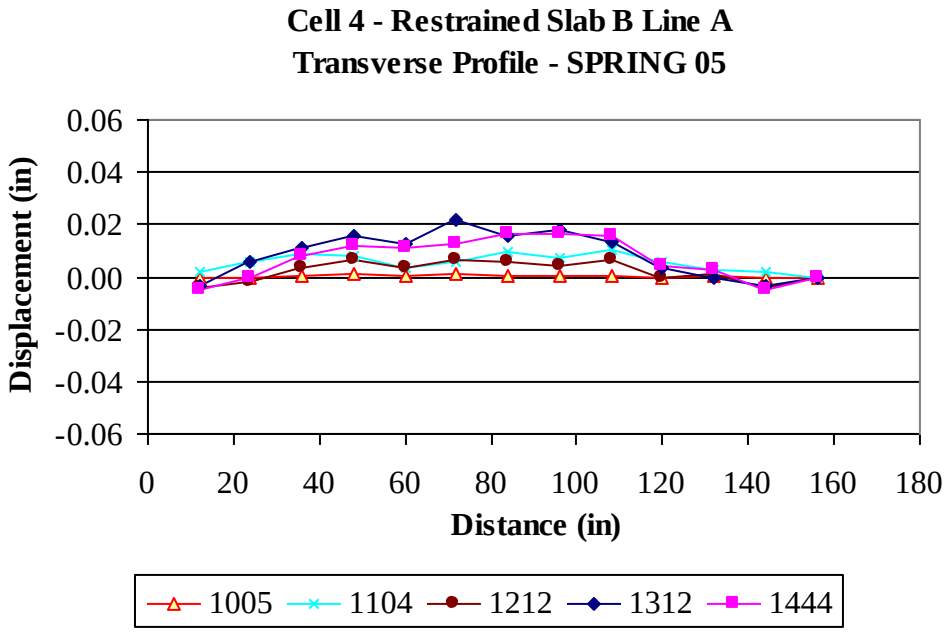

Figure C54. Restrained Slab B Line A transverse surface profiles for the spring of 2005.

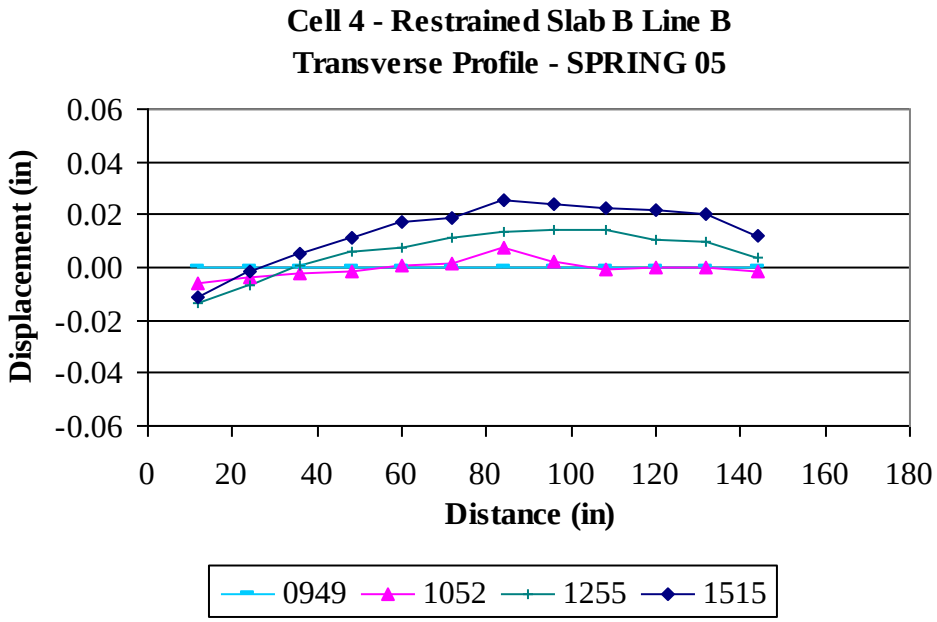

Figure C55. Restrained Slab B Line B transverse surface profiles for the spring of 2005.

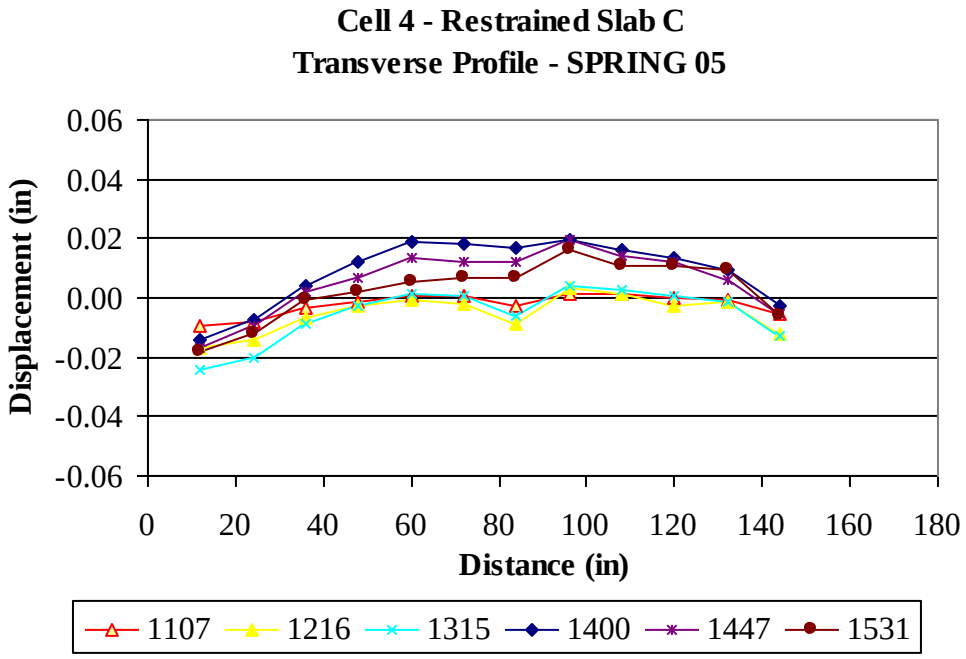

Figure C56. Restrained Slab C Line B transverse surface profiles for the spring of 2005.

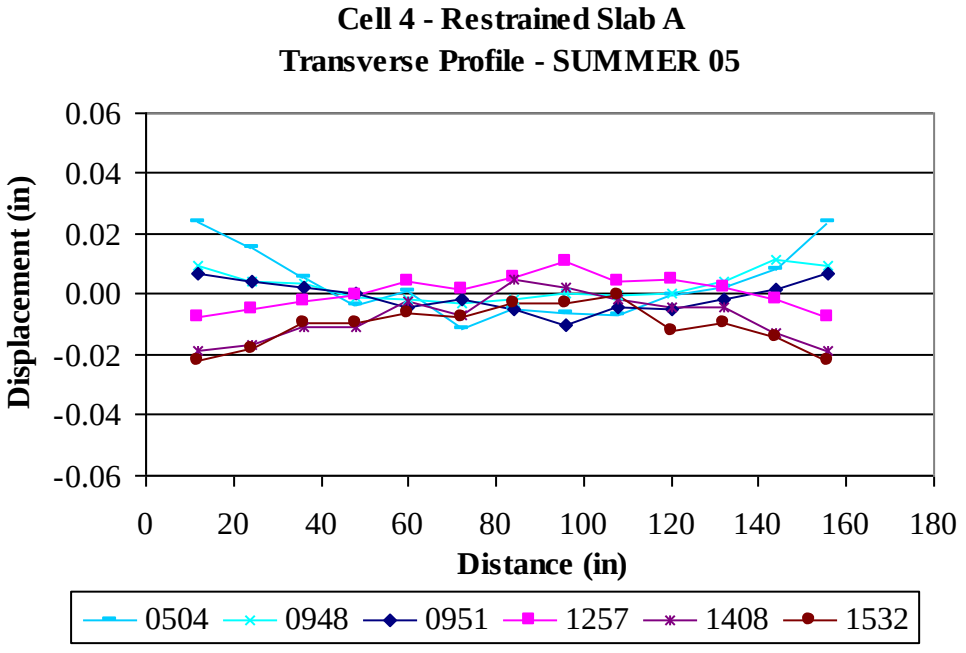

Figure C57. Restrained Slab A Line A transverse surface profiles for the summer of 2005.

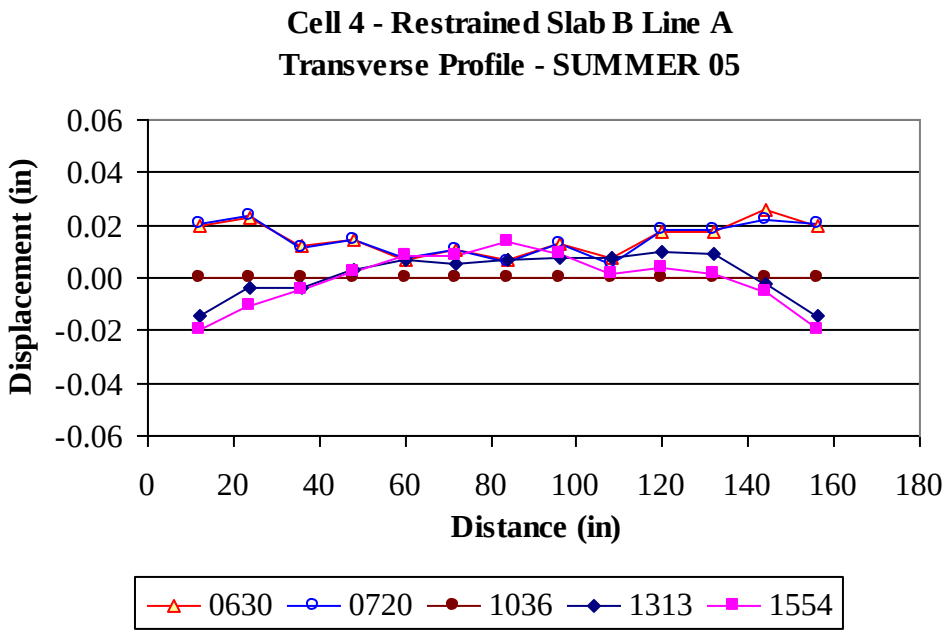

Figure C58. Restrained Slab B Line A transverse surface profiles for the summer of 2005.

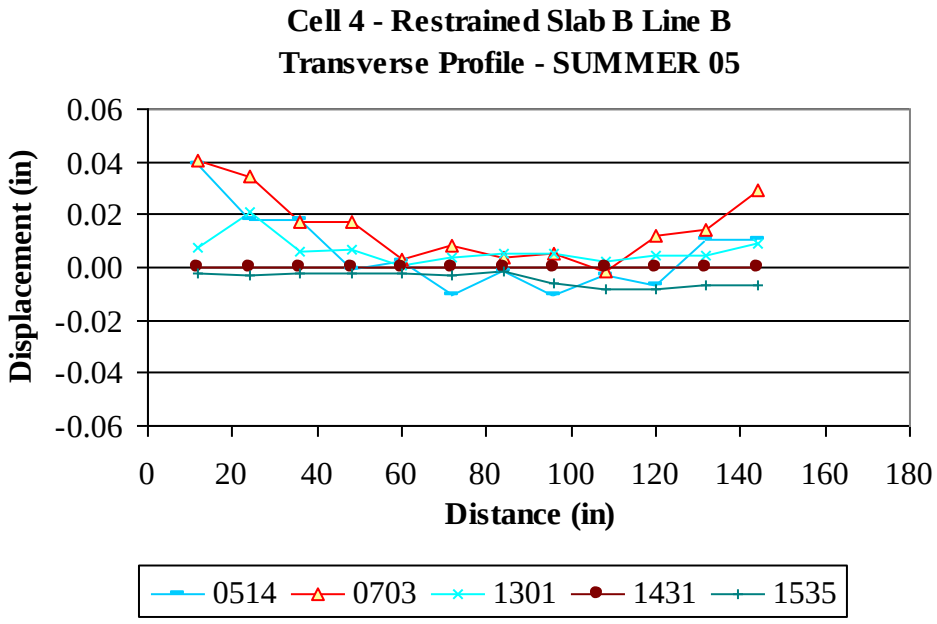

Figure C59. Restrained Slab B Line B transverse surface profiles for the summer of 2005.

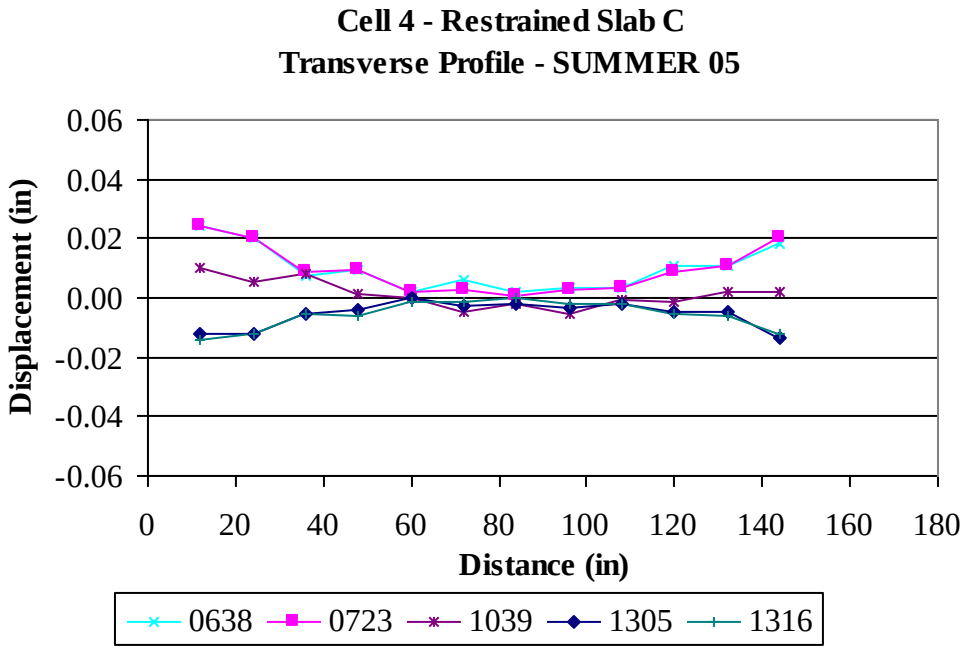

Figure C60. Restrained Slab C Line B transverse surface profiles for the summer of 2005.

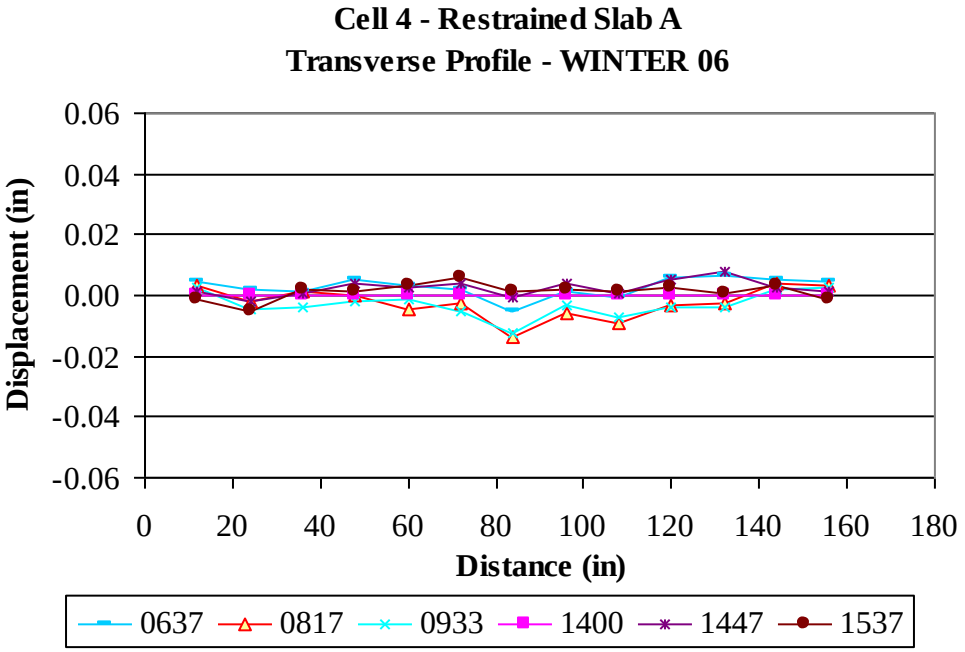

Figure C61. Restrained Slab A Line A transverse surface profiles for the winter of 2006.

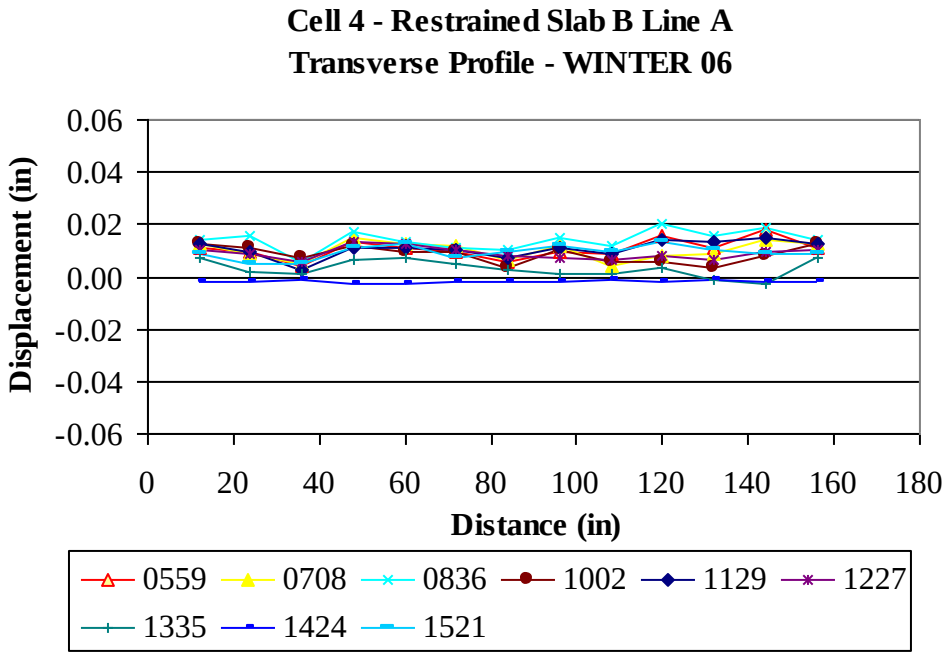

Figure C62. Restrained Slab B Line A transverse surface profiles for the winter of 2006.

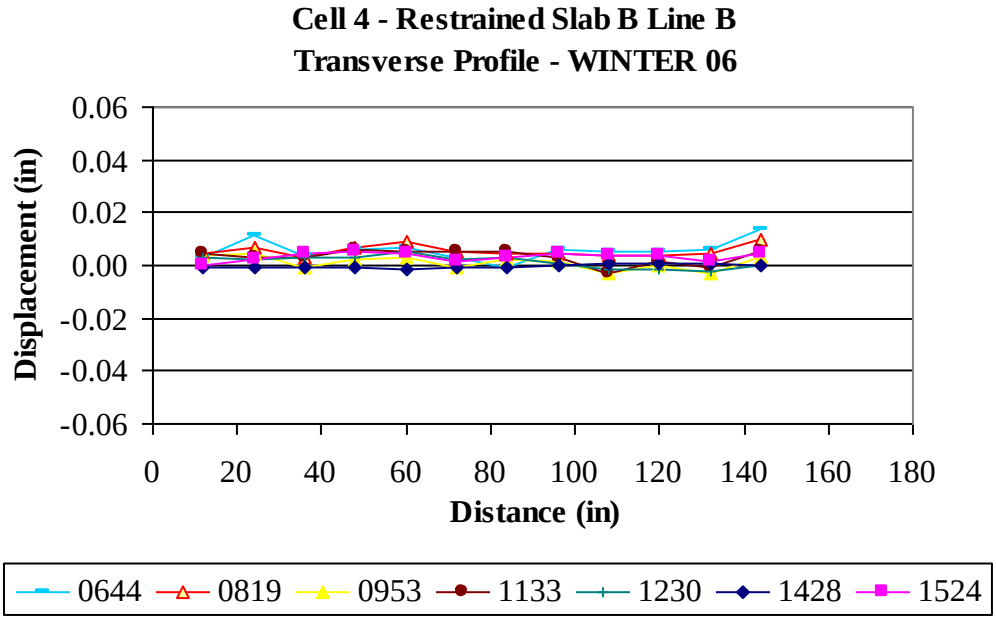

Figure C63. Restrained Slab B Line B transverse surface profiles for the winter of 2006.

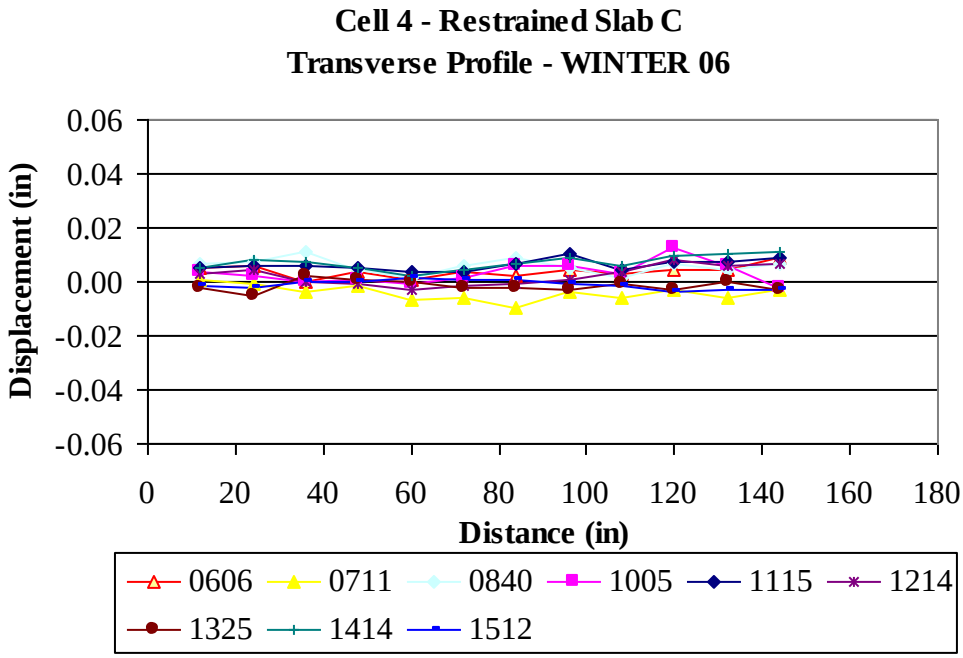

Figure C64. Restrained Slab C Line B transverse surface profiles for the winter of 2006.

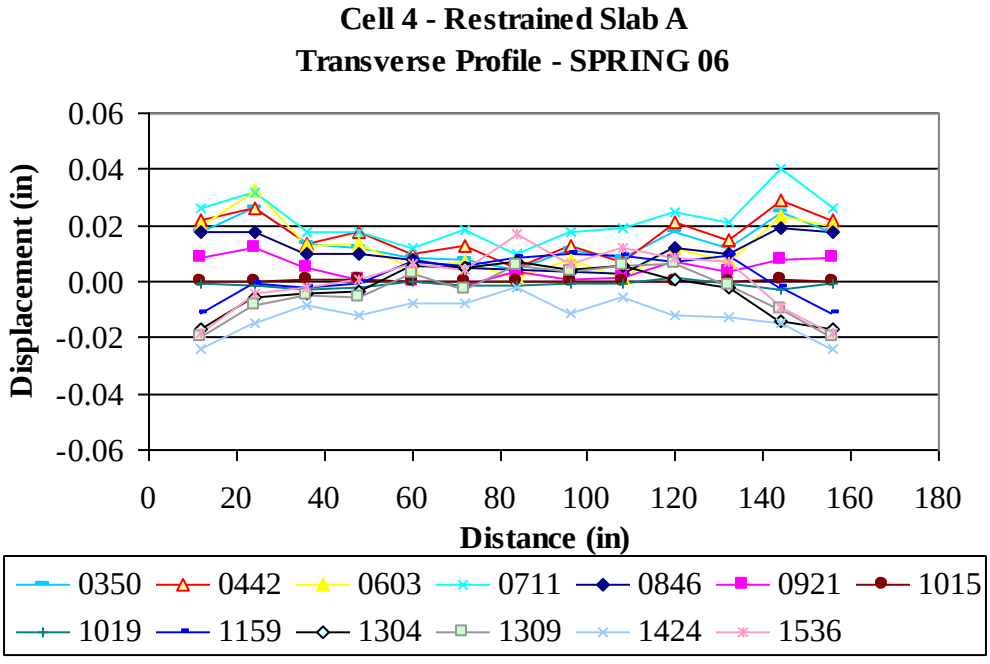

Figure C65. Restrained Slab A Line A transverse surface profiles for the spring of 2006.

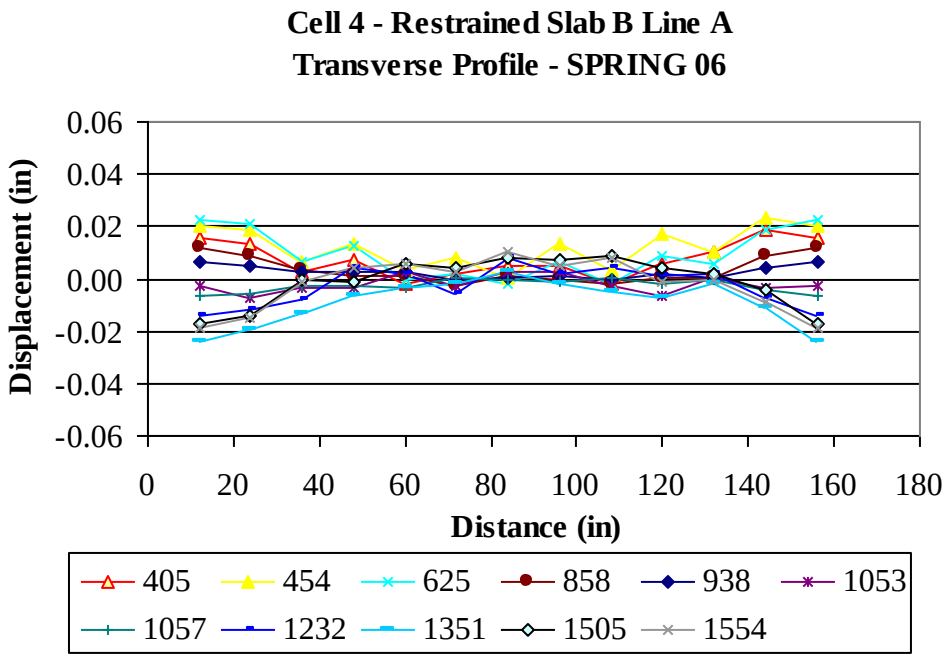

Figure C66. Restrained Slab B Line A transverse surface profiles for the spring of 2006.

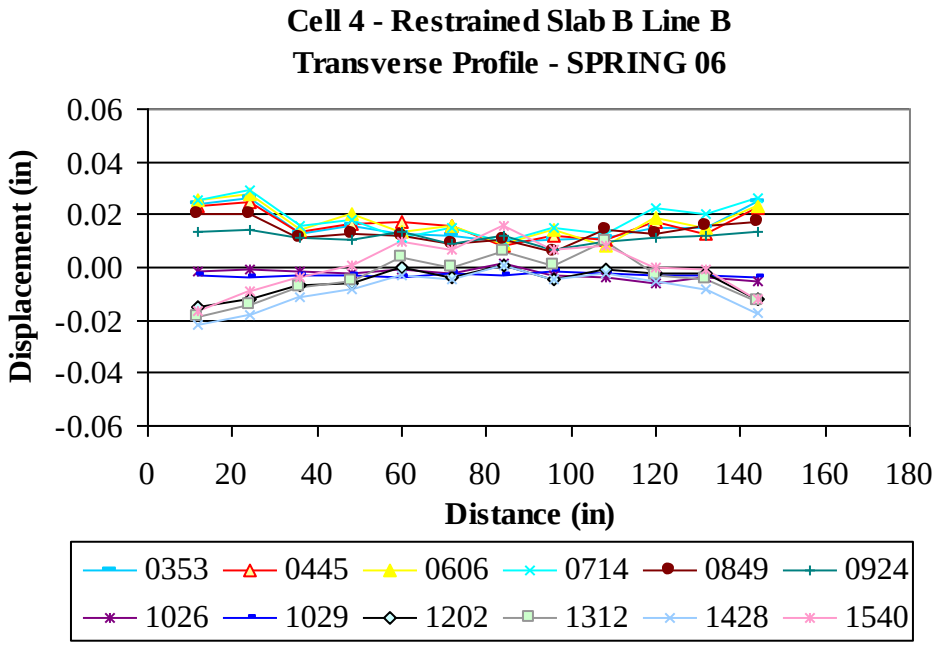

Figure C67. Restrained Slab B Line B transverse surface profiles for the spring of 2006.

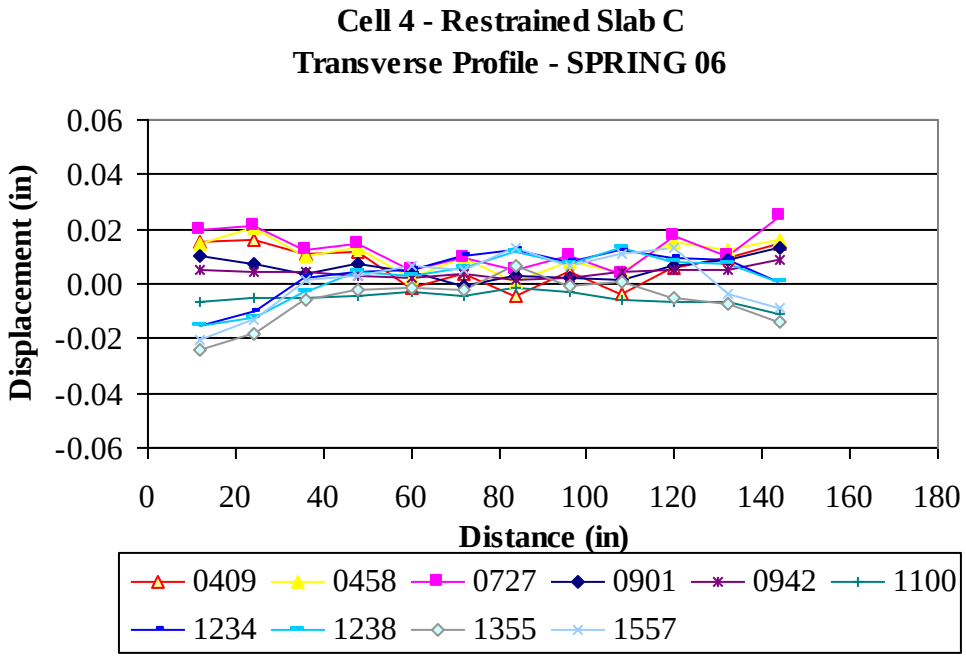

Figure C68. Restrained Slab C Line B transverse surface profiles for the spring of 2006.

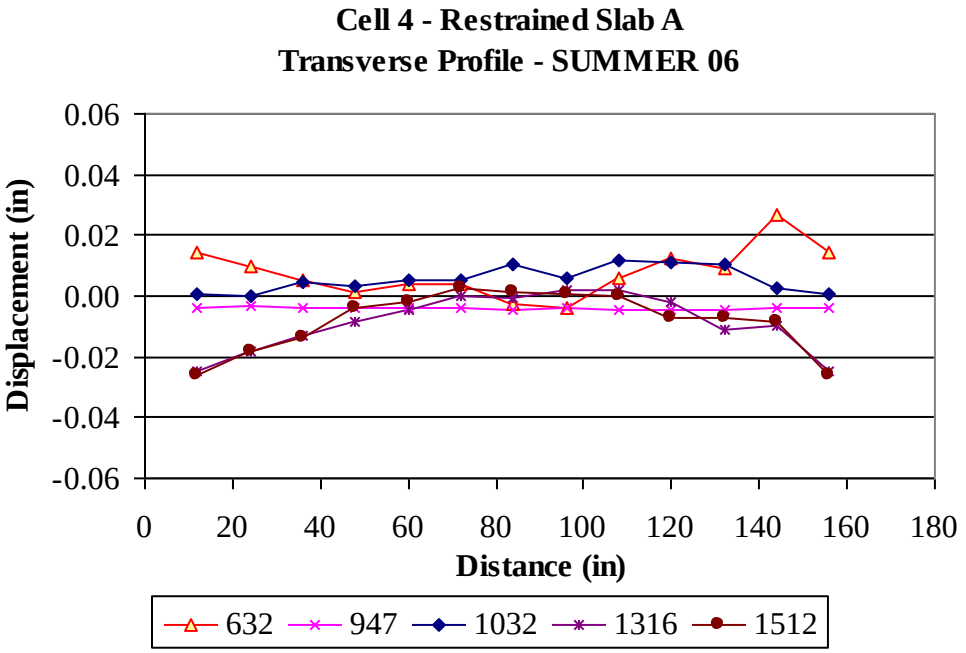

Figure C69. Restrained Slab A Line A transverse surface profiles for the summer of 2006.

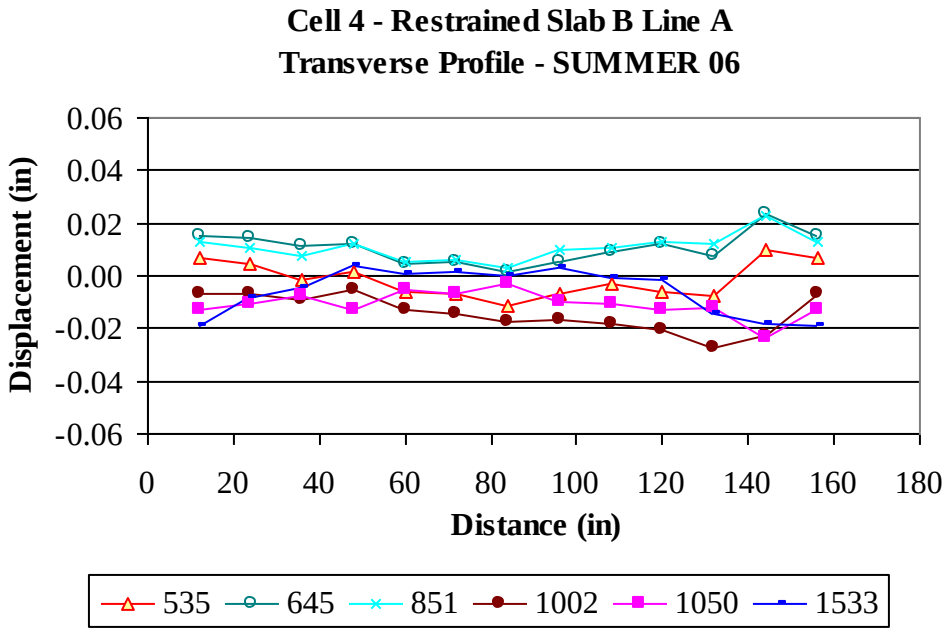

Figure C70. Restrained Slab B Line A transverse surface profiles for the summer of 2006.

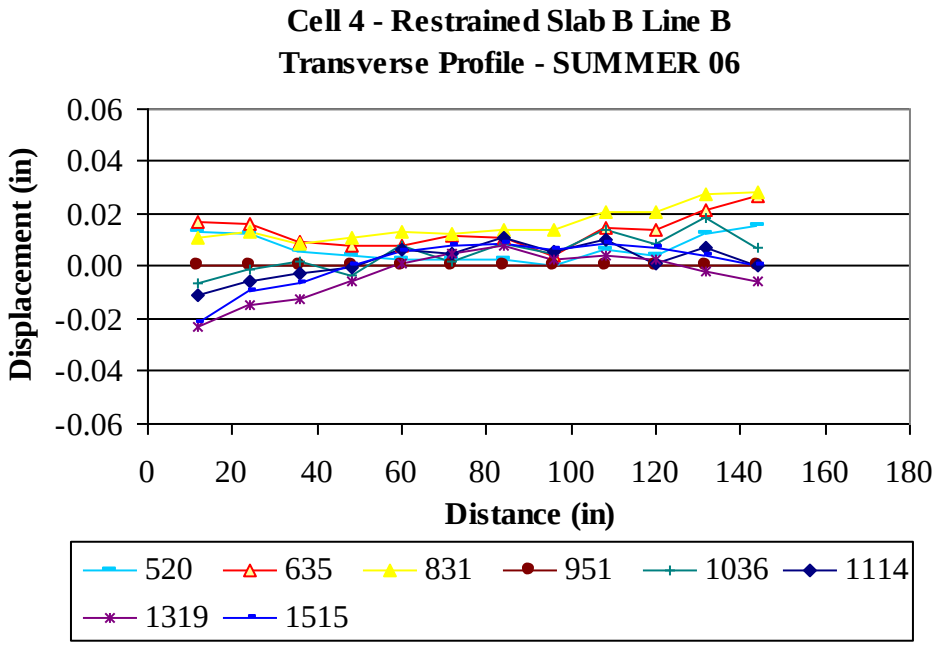

Figure C71. Restrained Slab B Line B transverse surface profiles for the summer of 2006.

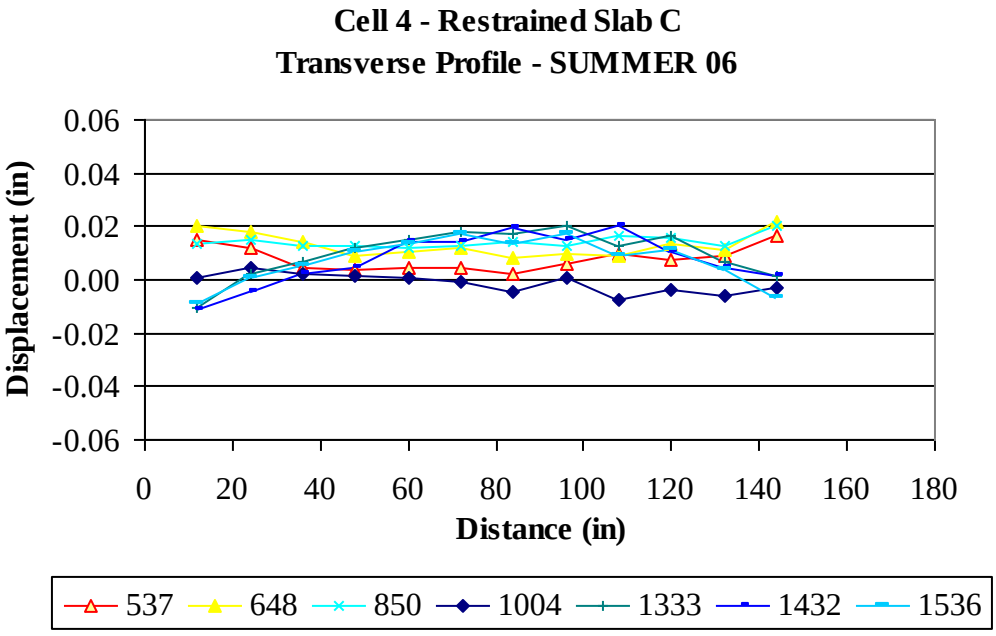

Figure C72. Restrained Slab C Line B transverse surface profiles for the summer of 2006.

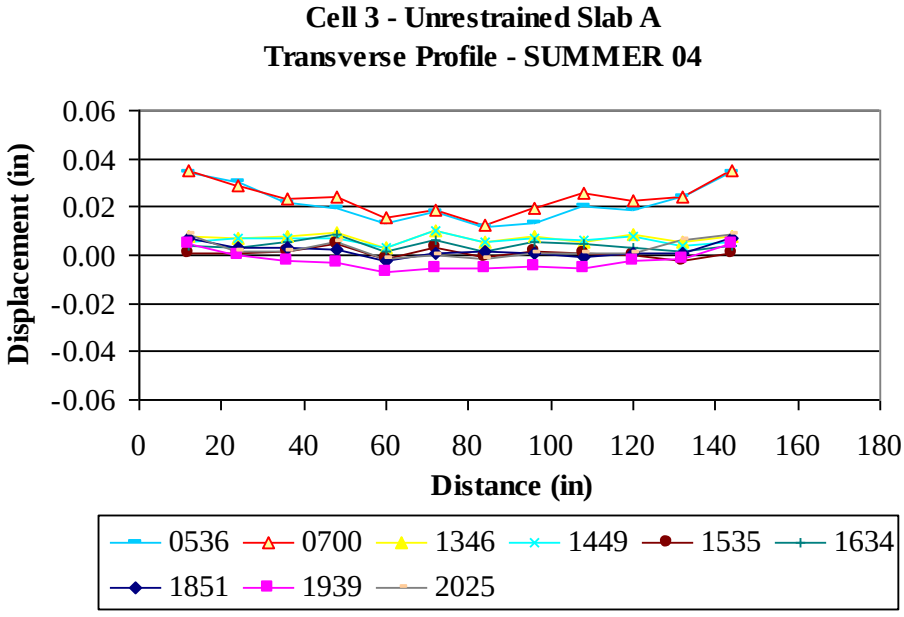

Figure C73. Unrestrained Slab A Line A transverse surface profiles for the summer of 2004.

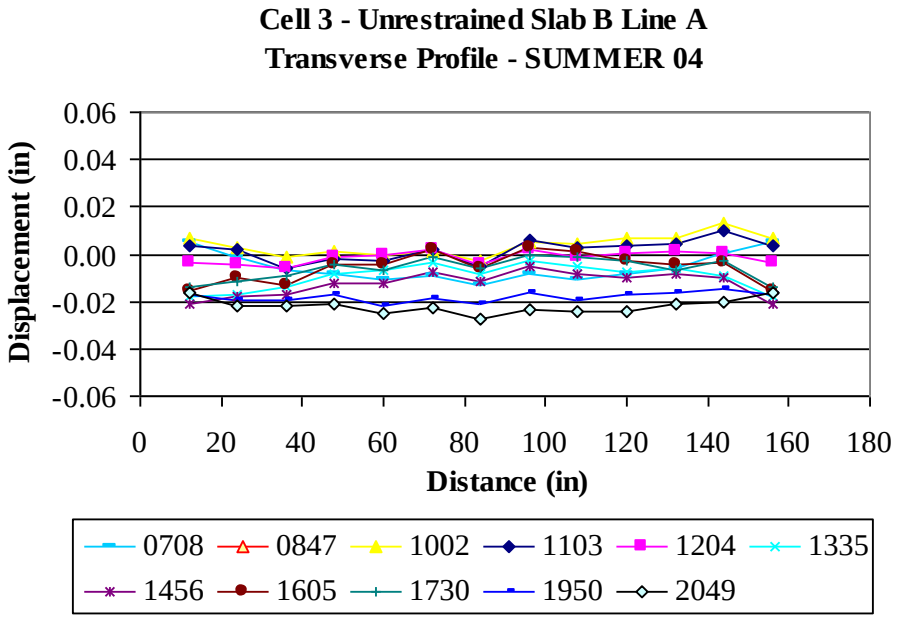

Figure C74. Unrestrained Slab B Line A transverse surface profiles for the summer of 2004.

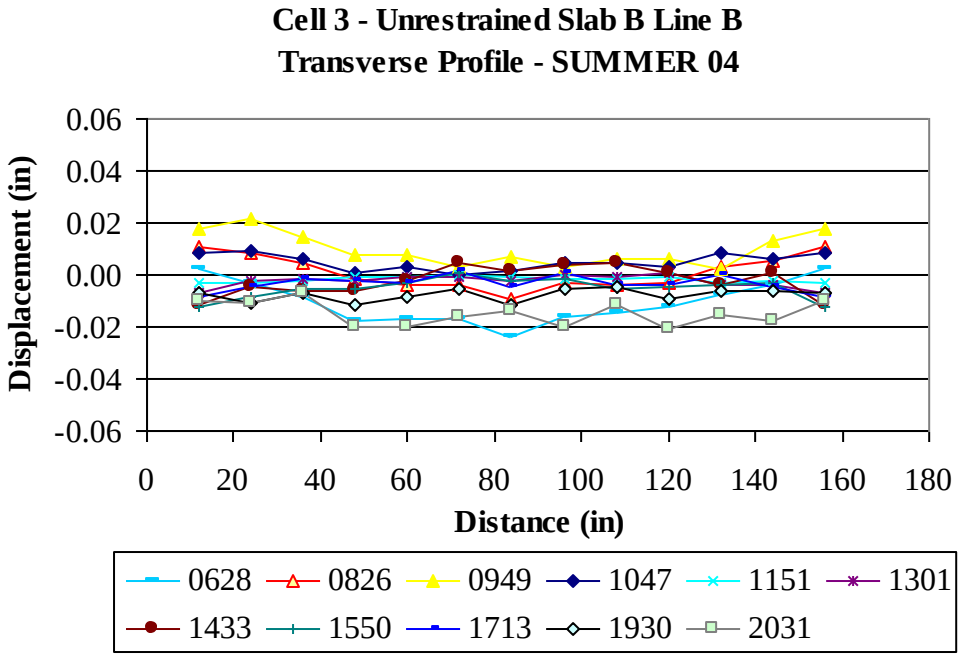

Figure C75. Unrestrained Slab B Line B transverse surface profiles for the summer of 2004.

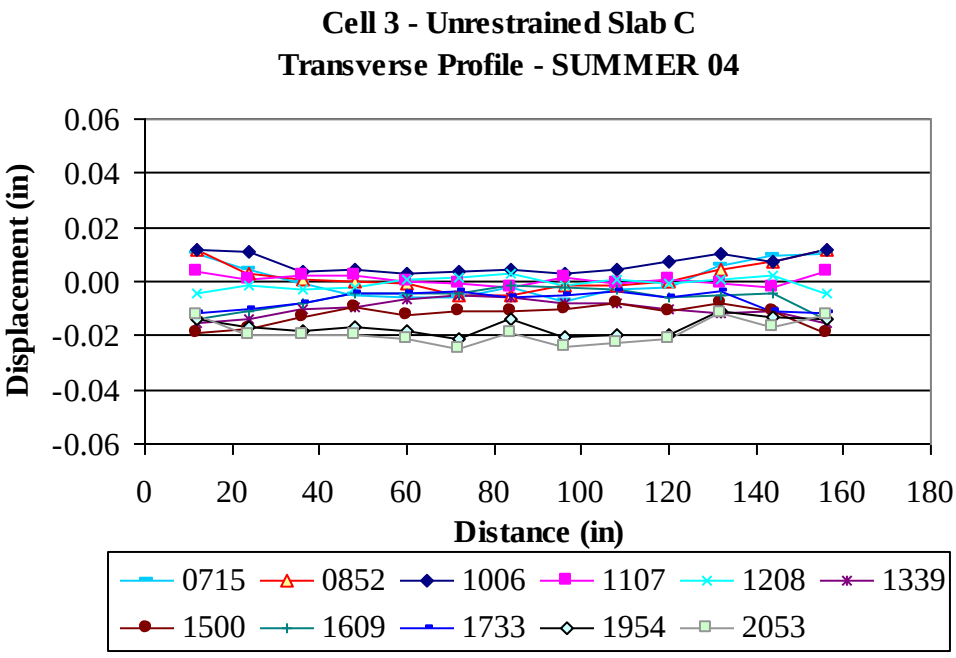

Figure C76. Unrestrained Slab C Line B transverse surface profiles for the summer of 2004.

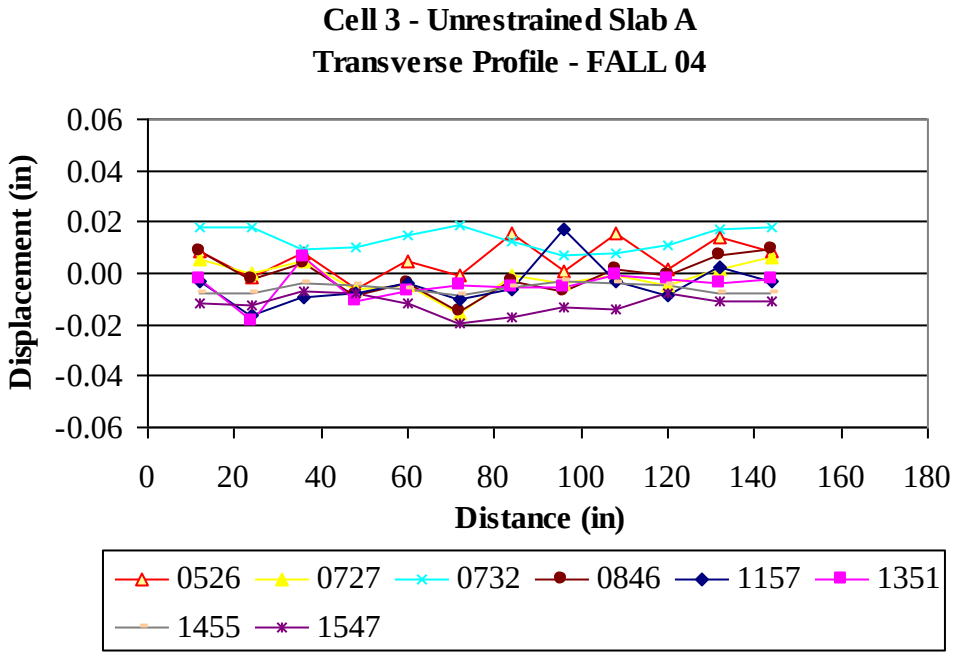

Figure C77. Unrestrained Slab A Line A transverse surface profiles for the fall of 2004.

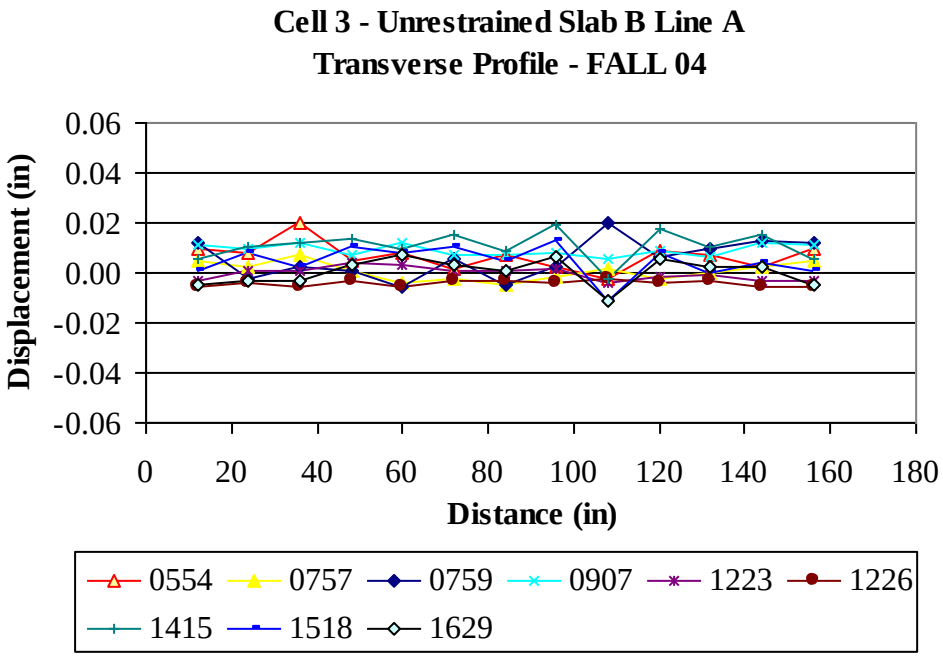

Figure C78. Unrestrained Slab B Line A transverse surface profiles for the fall of 2004.

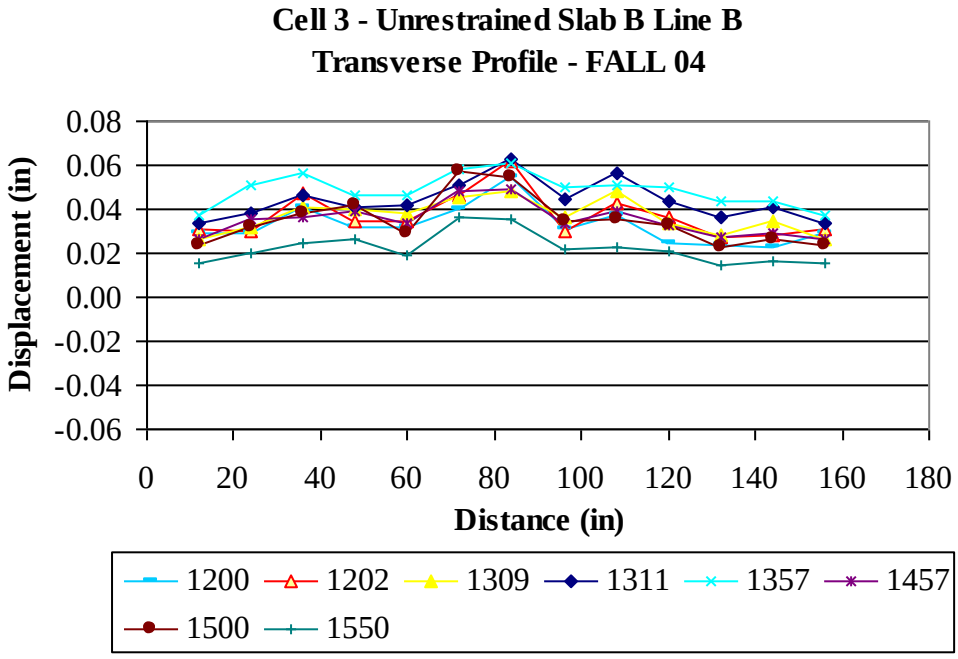

Figure C79. Unrestrained Slab B Line B transverse surface profiles for the fall of 2004.

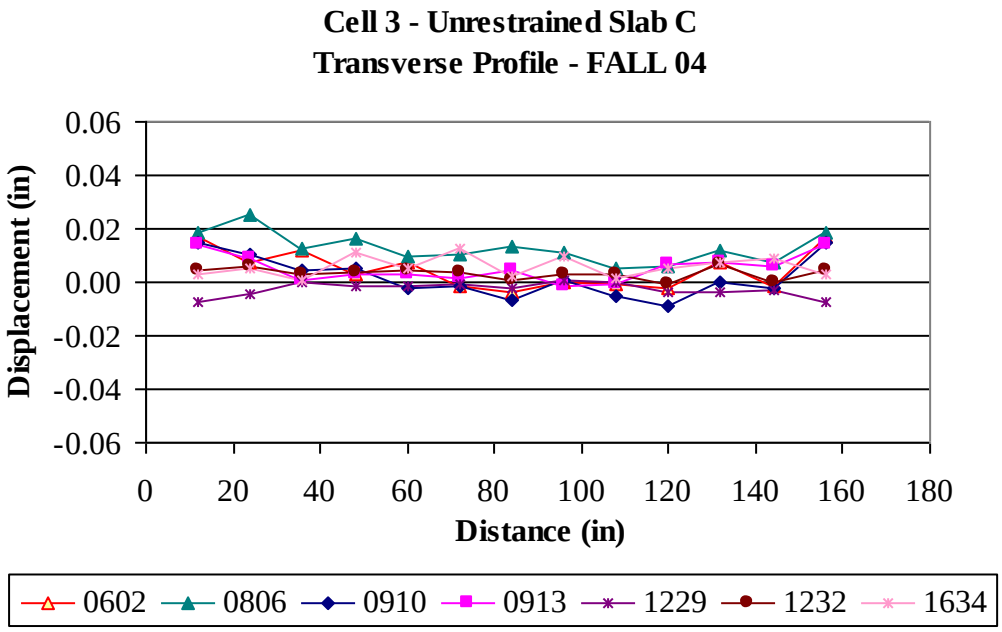

Figure C80. Unrestrained Slab C Line B transverse surface profiles for the fall of 2004.

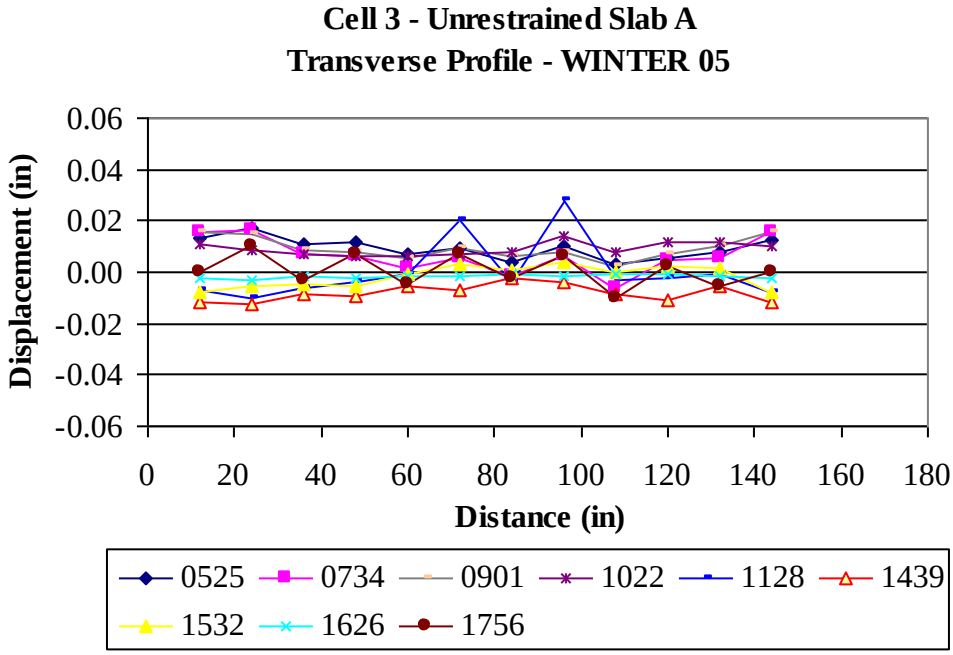

Figure C81. Unrestrained Slab A Line A transverse surface profiles for the winter of 2005.

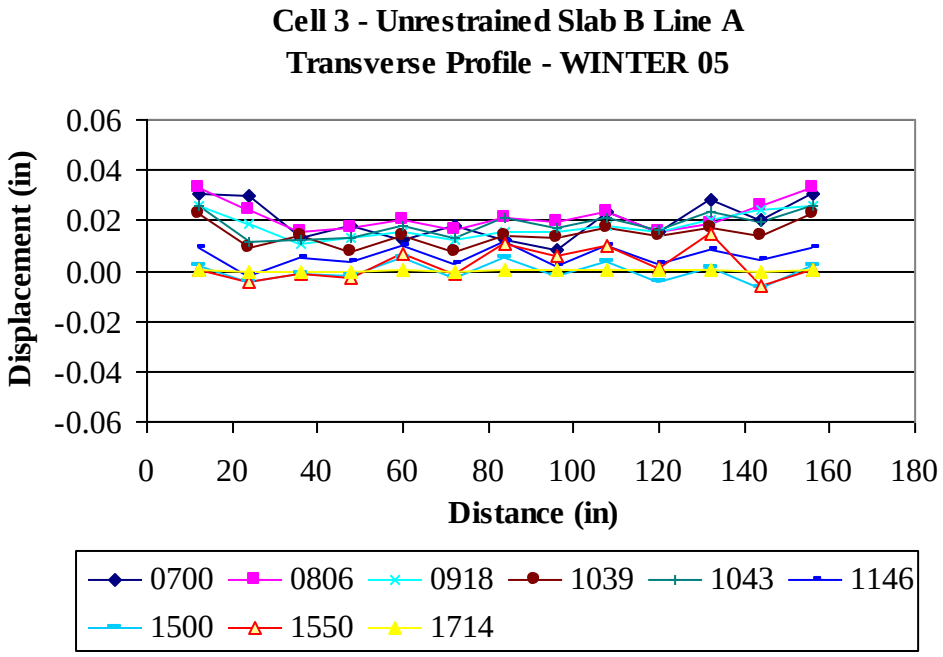

Figure C82. Unrestrained Slab B Line A transverse surface profiles for the winter of 2005.

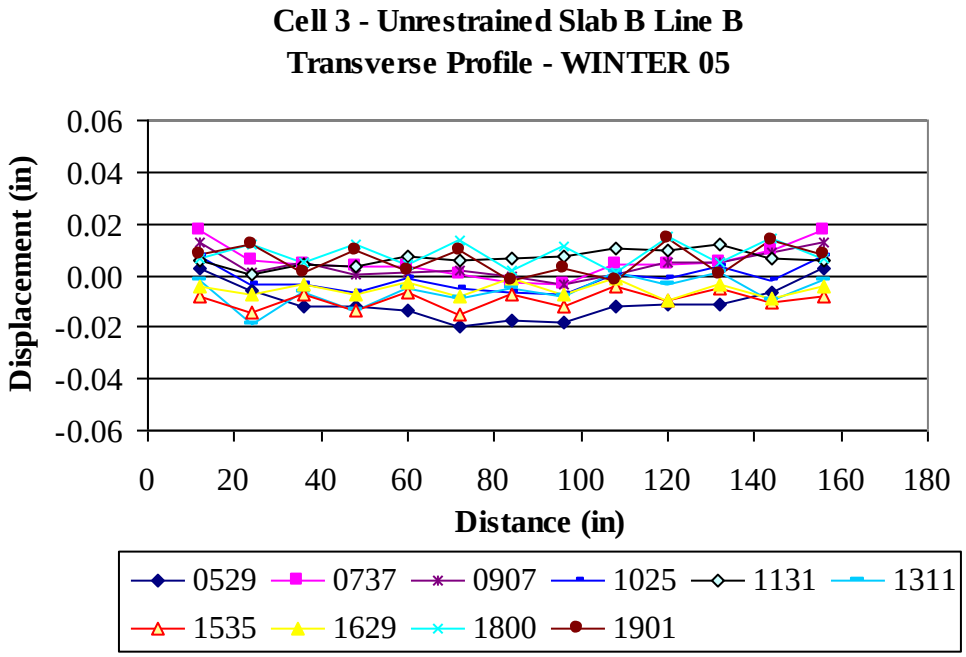

Figure C83. Unrestrained Slab B Line B transverse surface profiles for the winter of 2005.

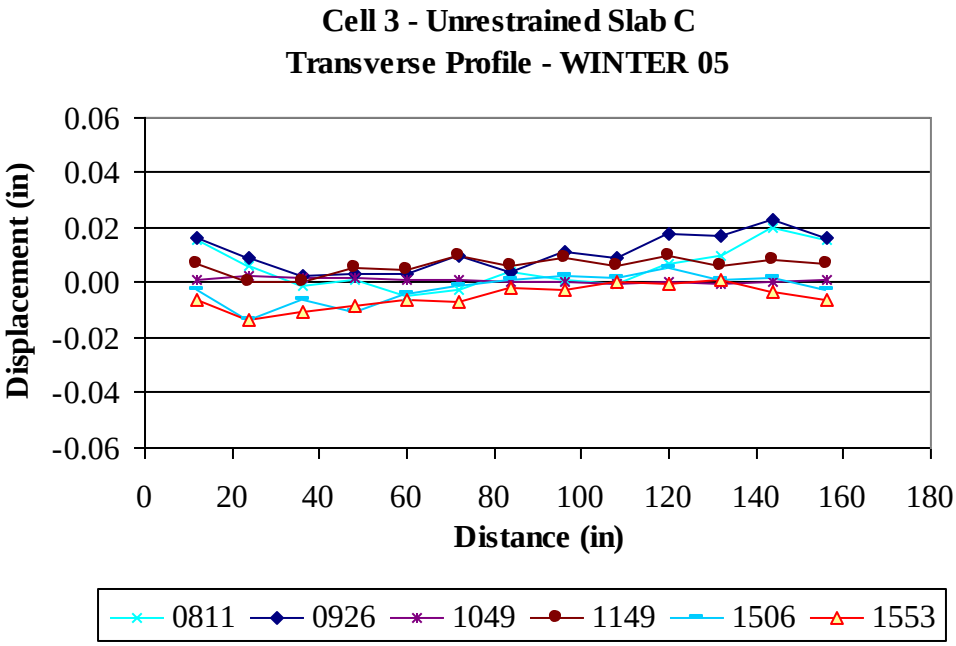

Figure C84. Unrestrained Slab C Line B transverse surface profiles for the winter of 2005.

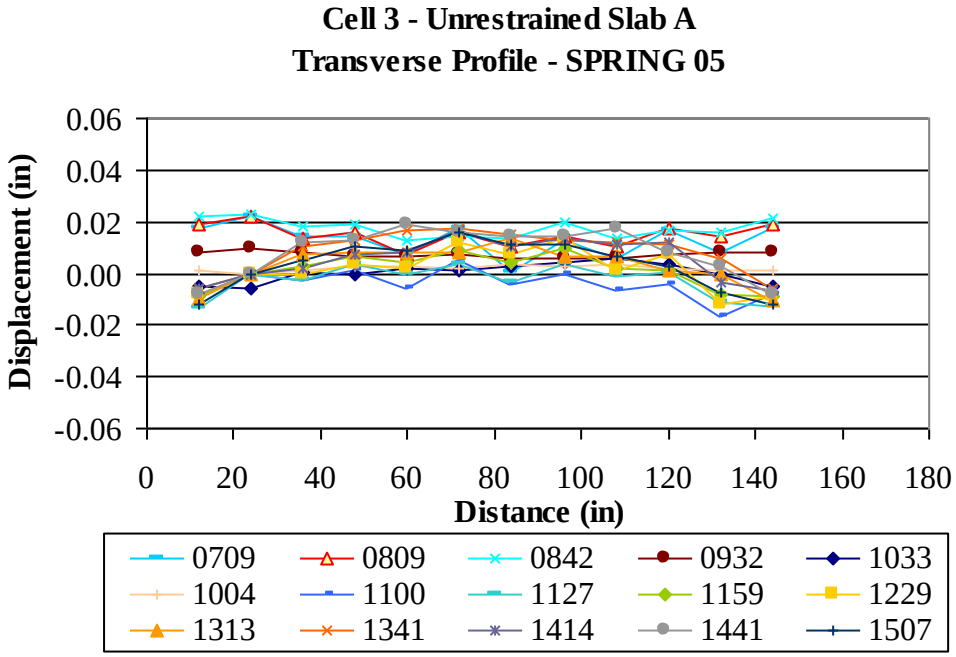

Figure C85. Unrestrained Slab A Line A transverse surface profiles for the spring of 2005.

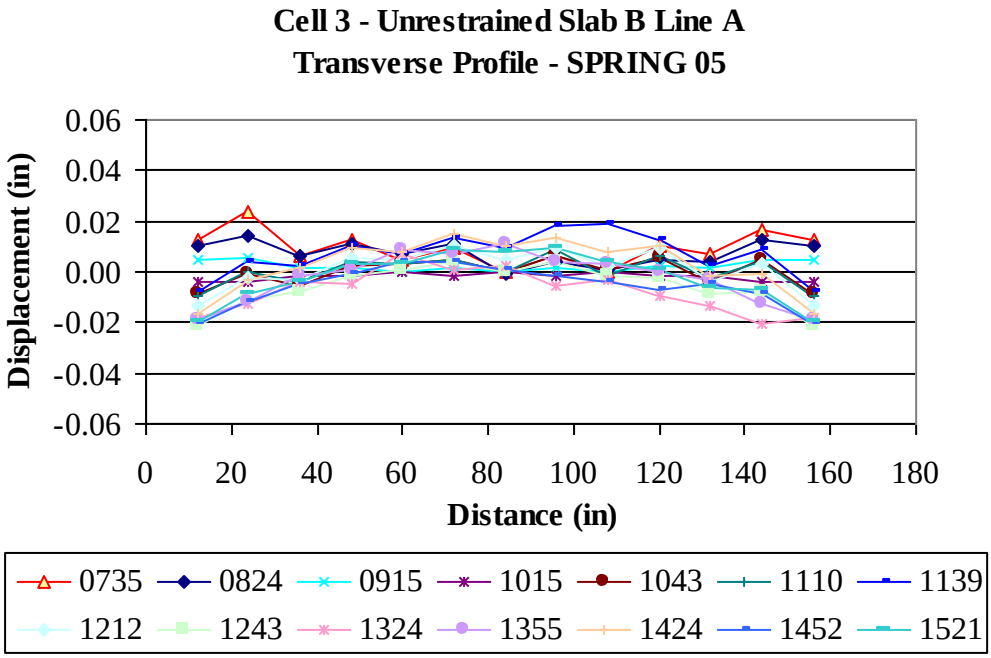

Figure C86. Unrestrained Slab B Line A transverse surface profiles for the spring of 2005.

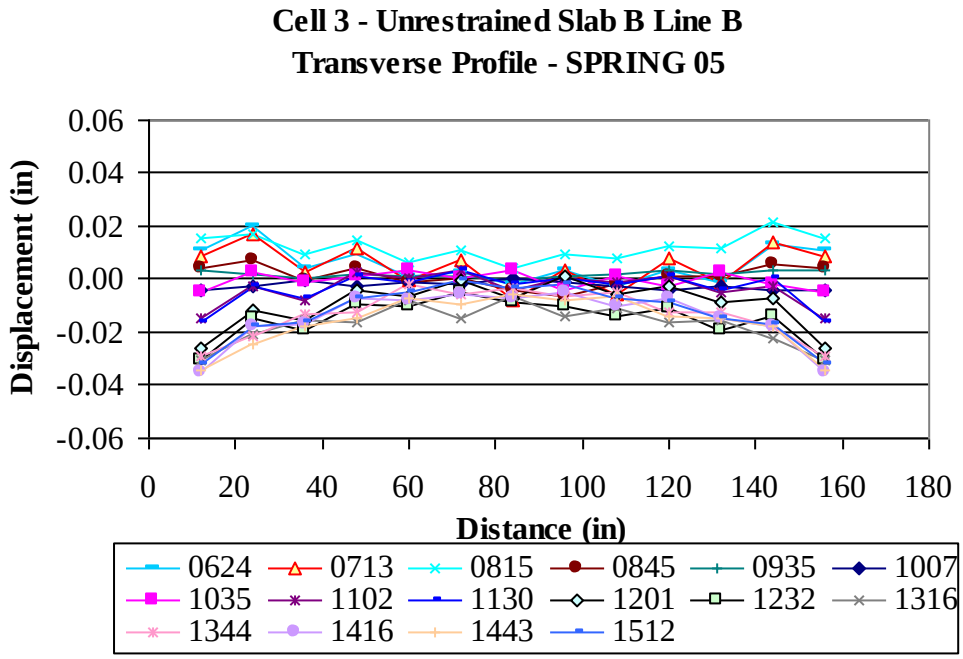

Figure C87. Unrestrained Slab B Line B transverse surface profiles for the spring of 2005.

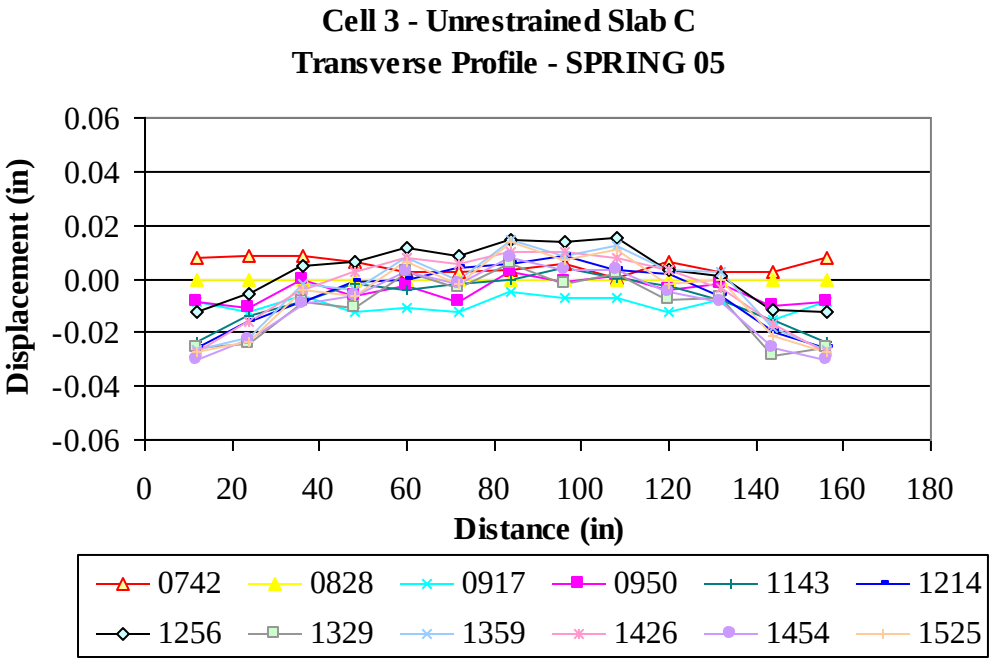

Figure C88. Unrestrained Slab C Line B transverse surface profiles for the spring of 2005.

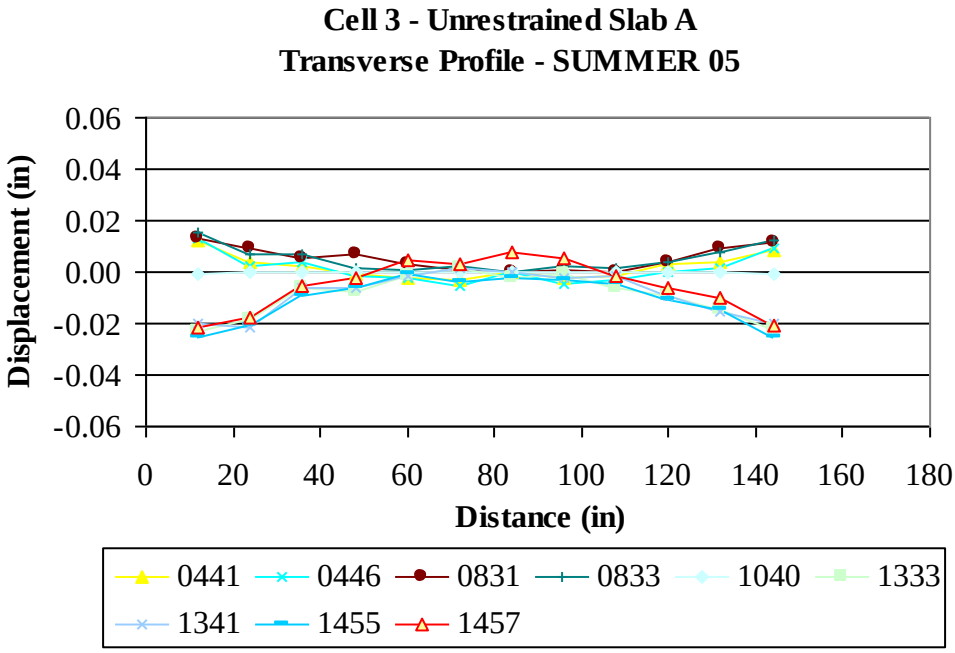

Figure C89. Unrestrained Slab A Line A transverse surface profiles for the summer of 2005.

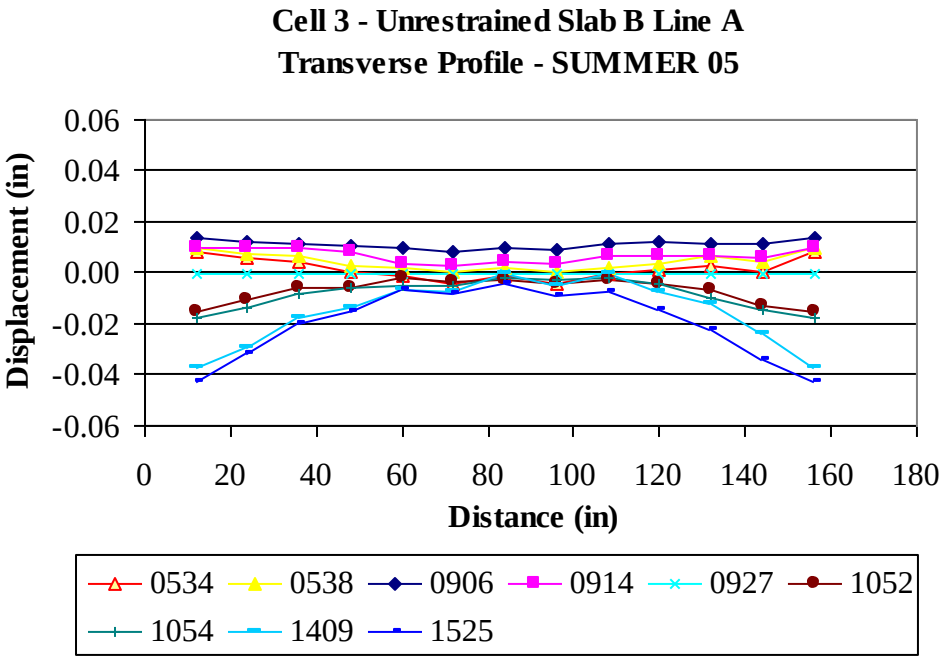

Figure C90. Unrestrained Slab B Line A transverse surface profiles for the summer of 2005.

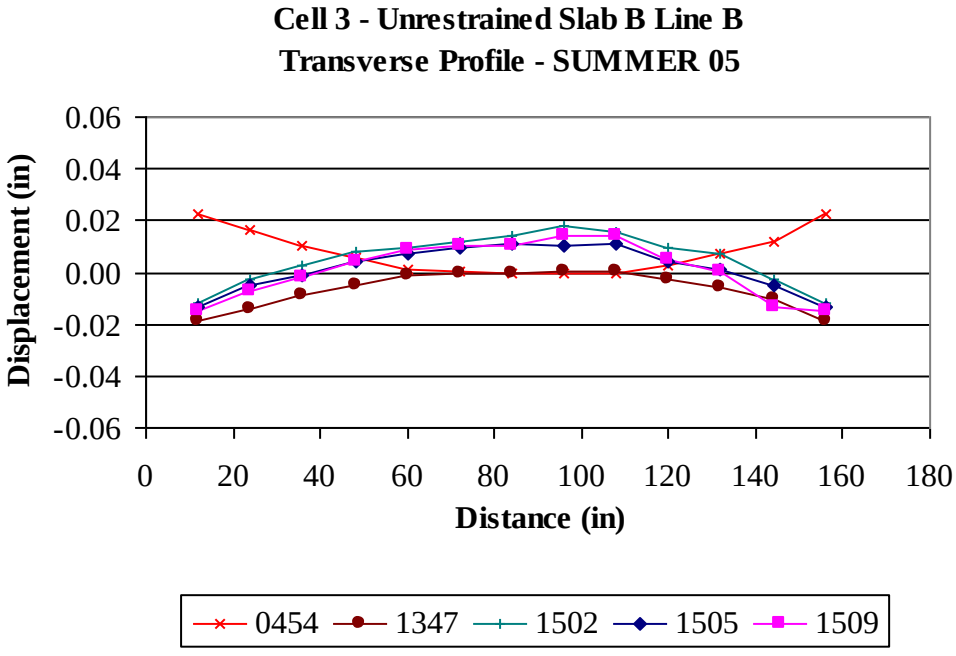

Figure C91. Unrestrained Slab B Line B transverse surface profiles for the summer of 2005.

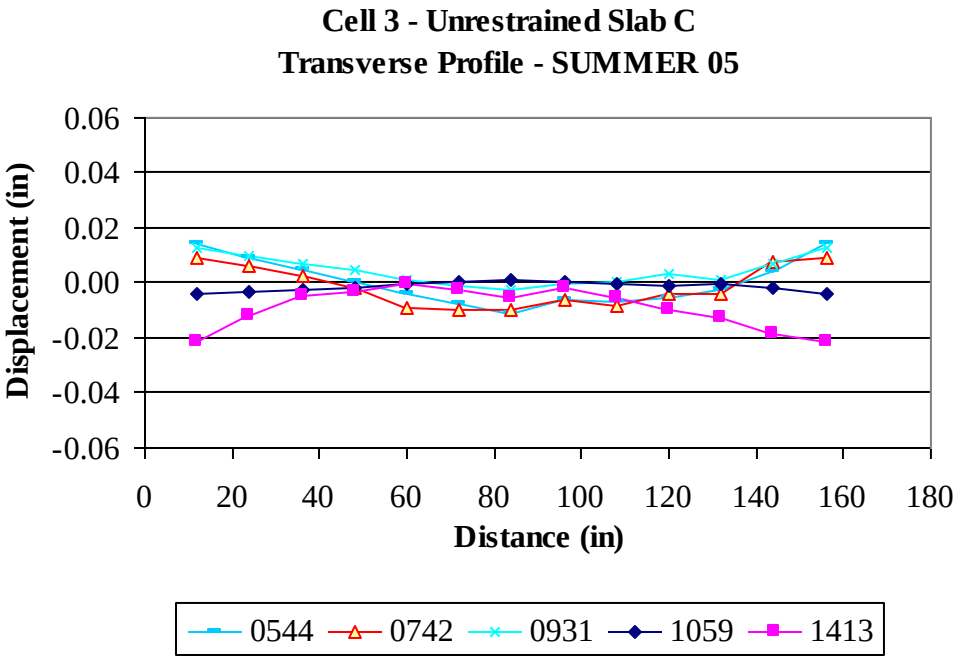

Figure C92. Unrestrained Slab C Line B transverse surface profiles for the summer of 2005.

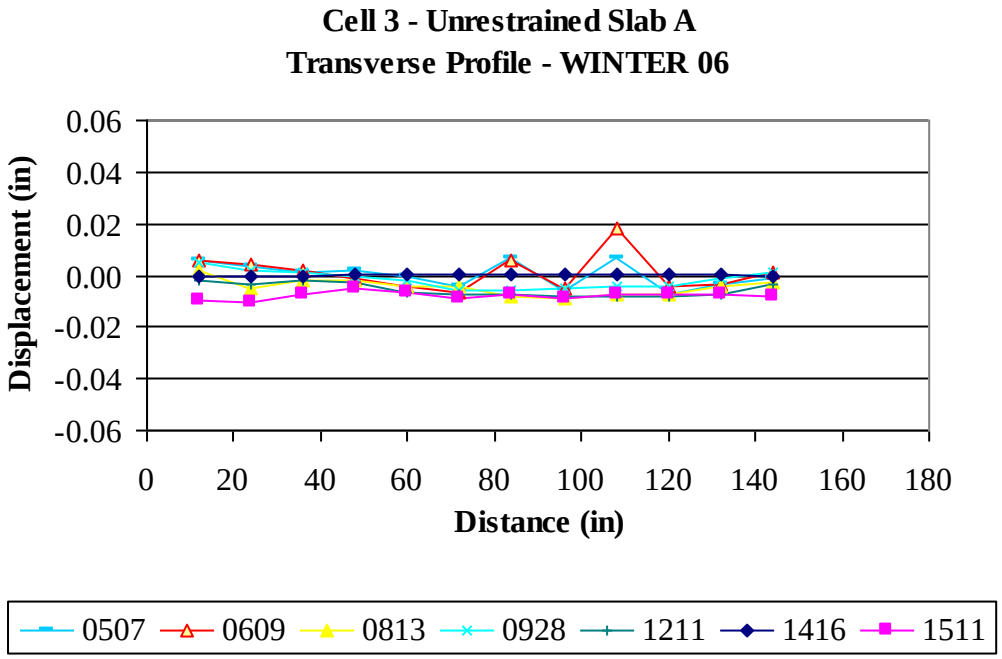

Figure C93. Unrestrained Slab A Line A transverse surface profiles for the winter of 2006.

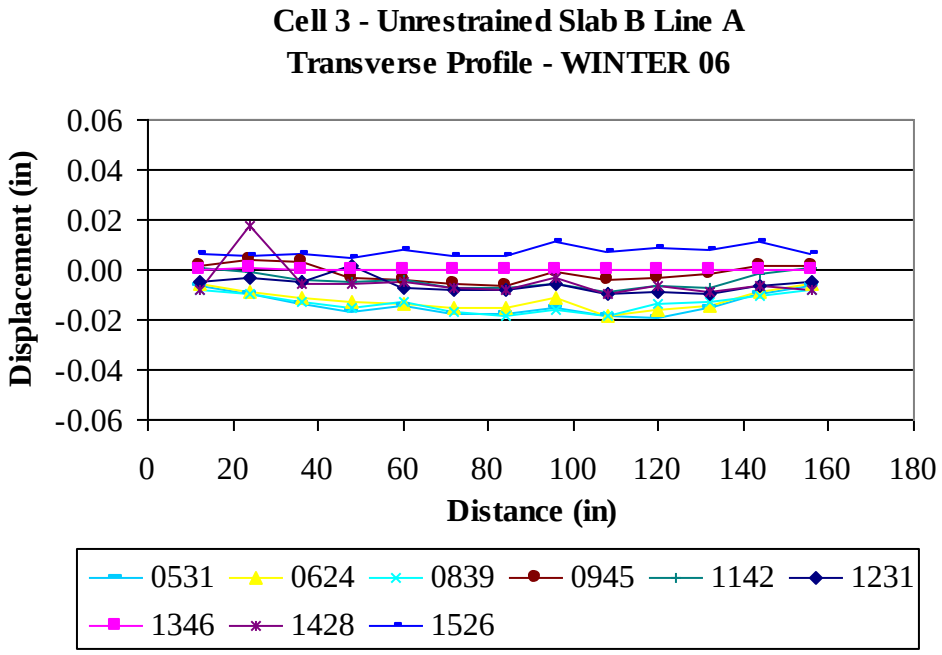

Figure C94. Unrestrained Slab B Line A transverse surface profiles for the winter of 2006.

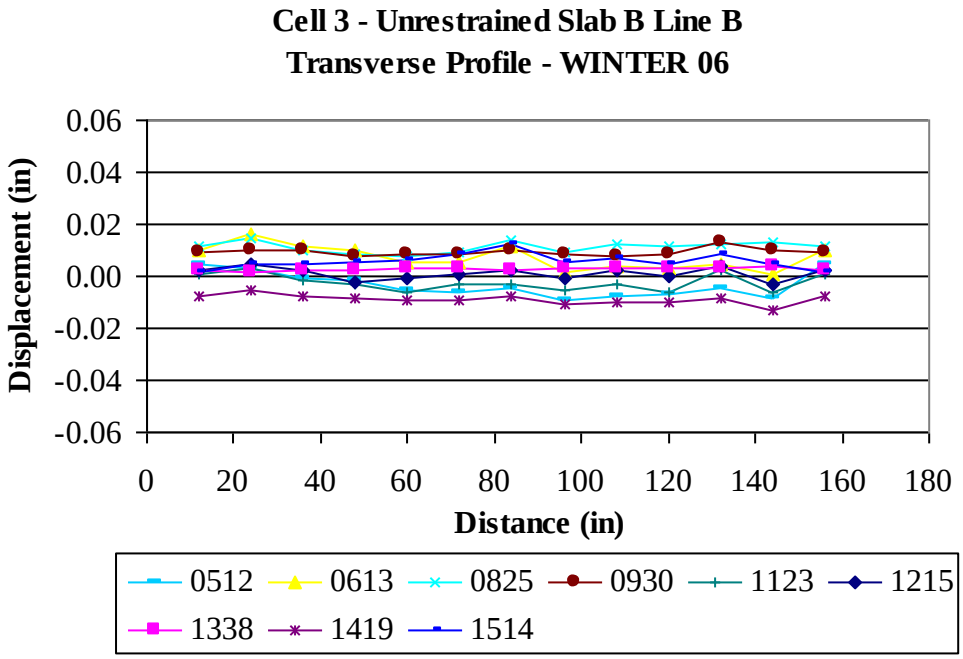

Figure C95. Unrestrained Slab B Line B transverse surface profiles for the winter of 2006.

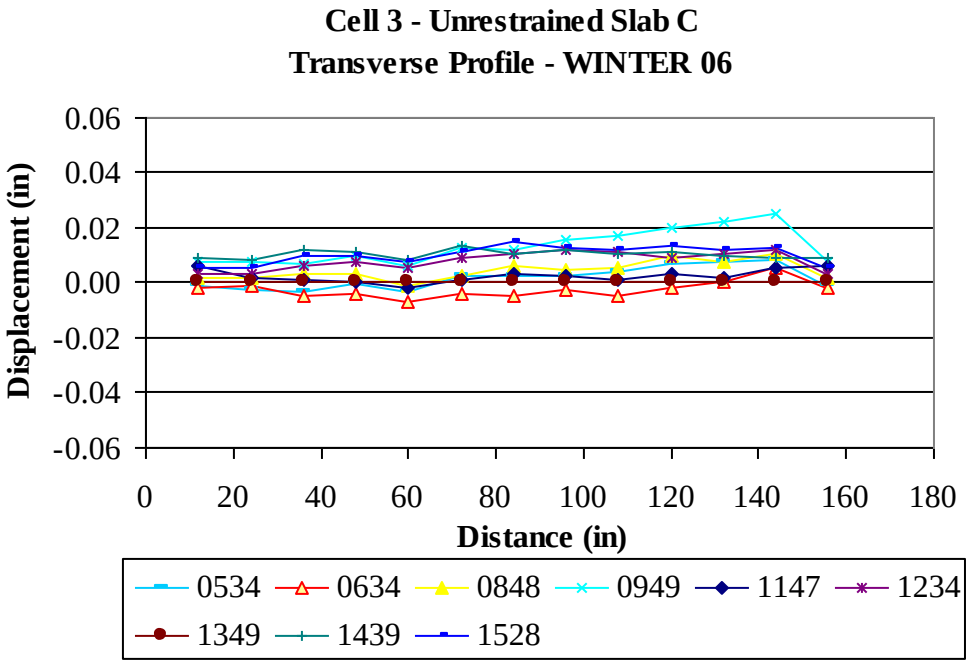

Figure C96. Unrestrained Slab C Line B transverse surface profiles for the winter of 2006.

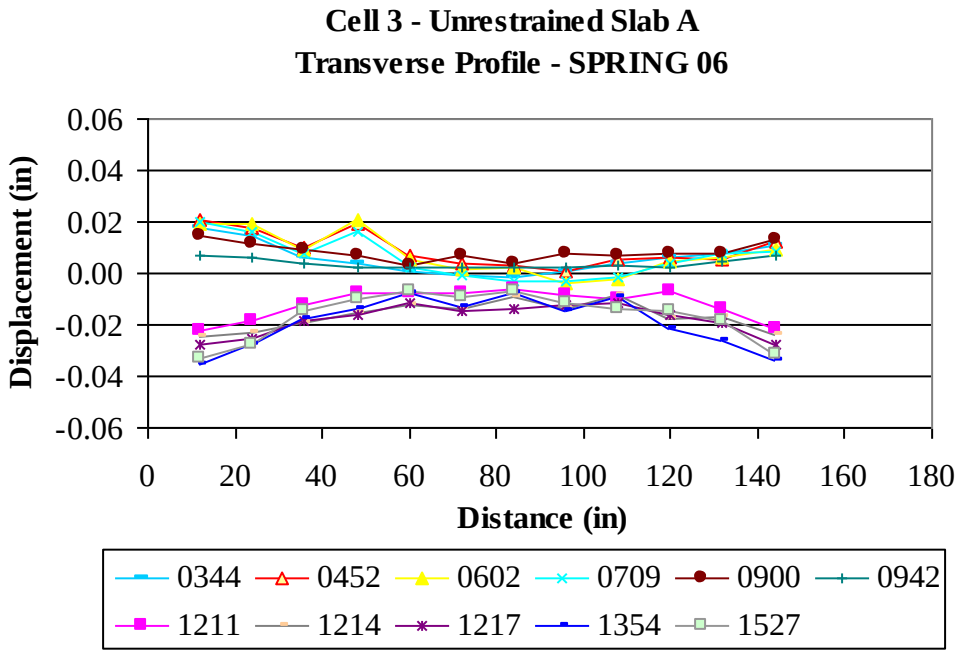

Figure C97. Unrestrained Slab A Line A transverse surface profiles for the spring of 2006.

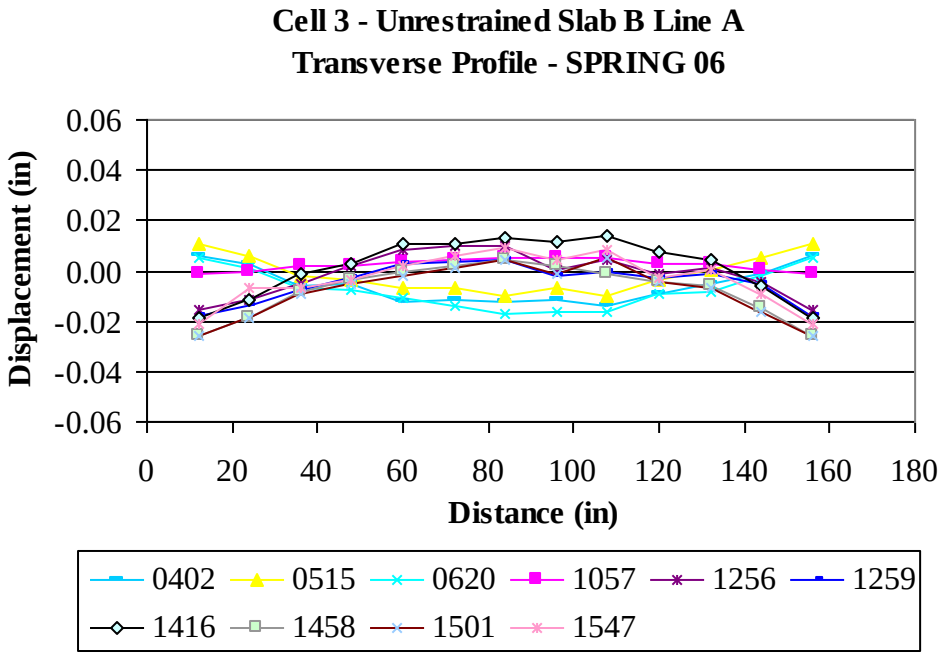

Figure C98. Unrestrained Slab B Line A transverse surface profiles for the spring of 2006.

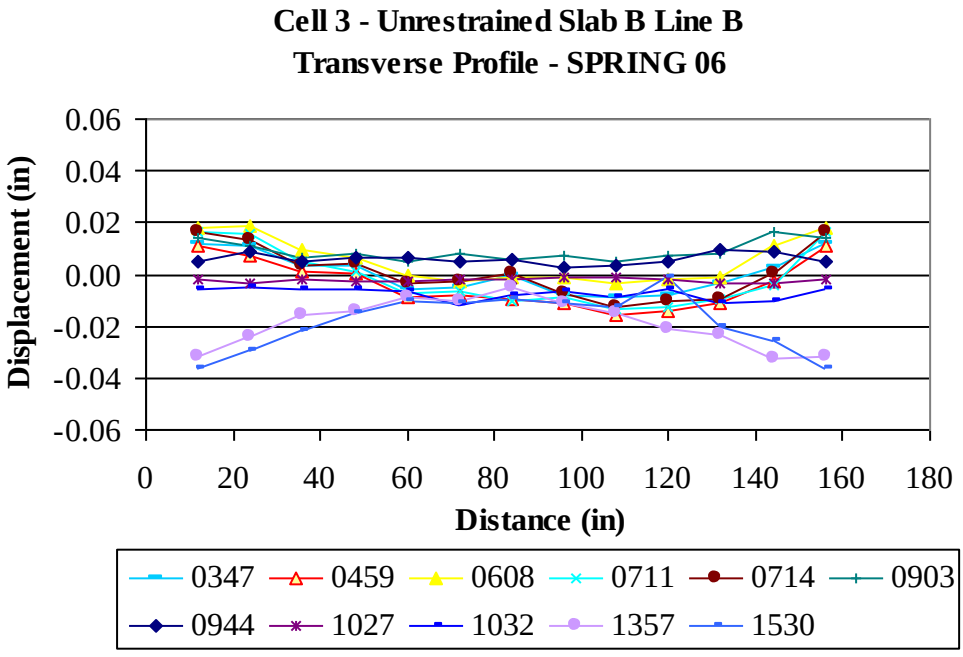

Figure C99. Unrestrained Slab B Line B transverse surface profiles for the spring of 2006.

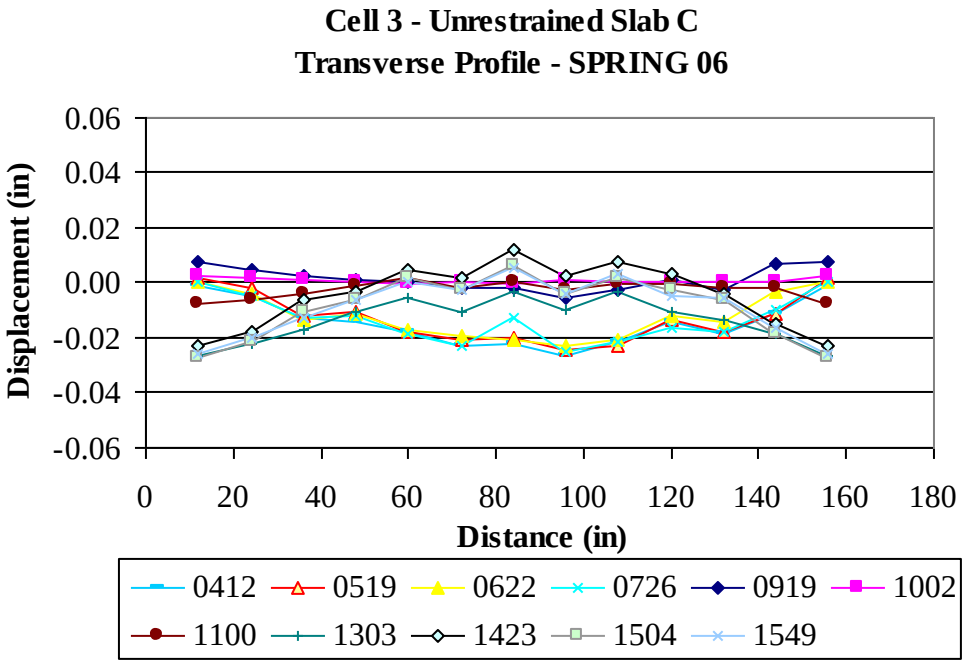

Figure C100. Unrestrained Slab C Line B transverse surface profiles for the spring of 2006.

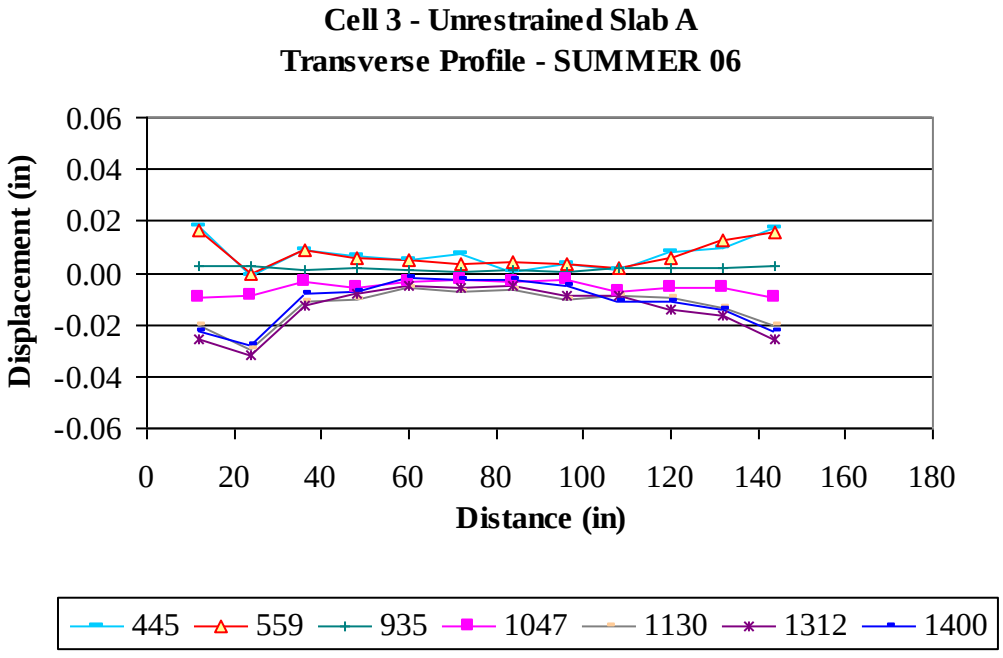

Figure C101. Unrestrained Slab A Line A transverse surface profiles for the summer of 2006.

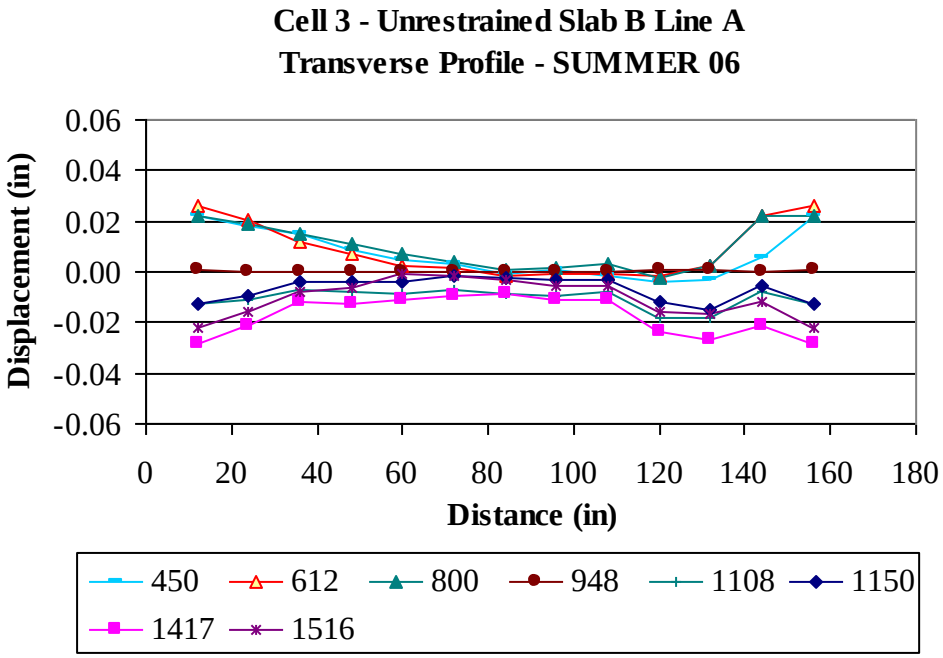

Figure C102. Unrestrained Slab B Line A transverse surface profiles for the summer of 2006.

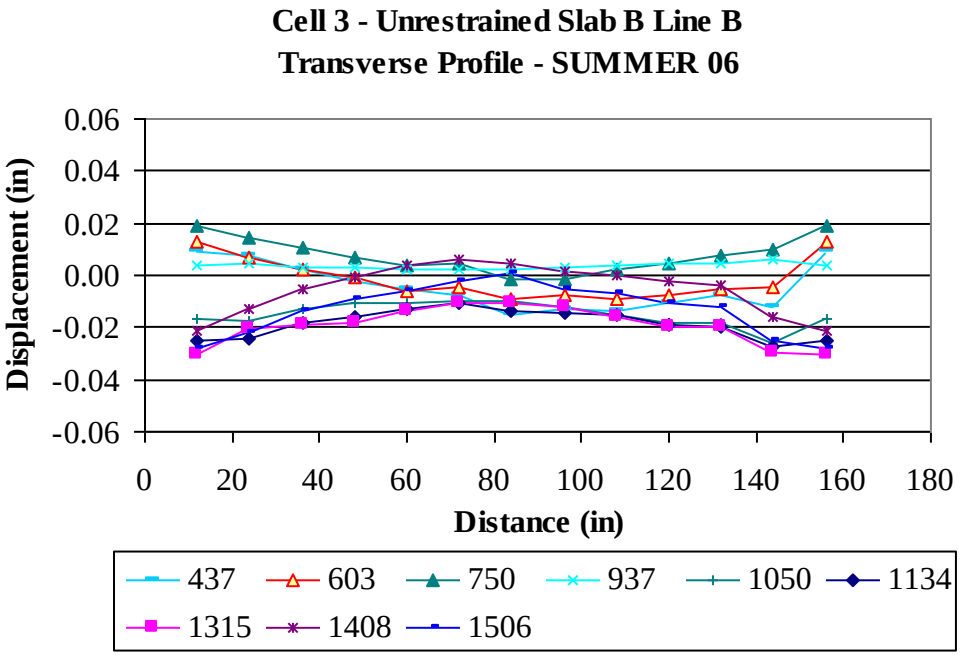

Figure C103. Unrestrained Slab B Line B transverse surface profiles for the summer of 2006.

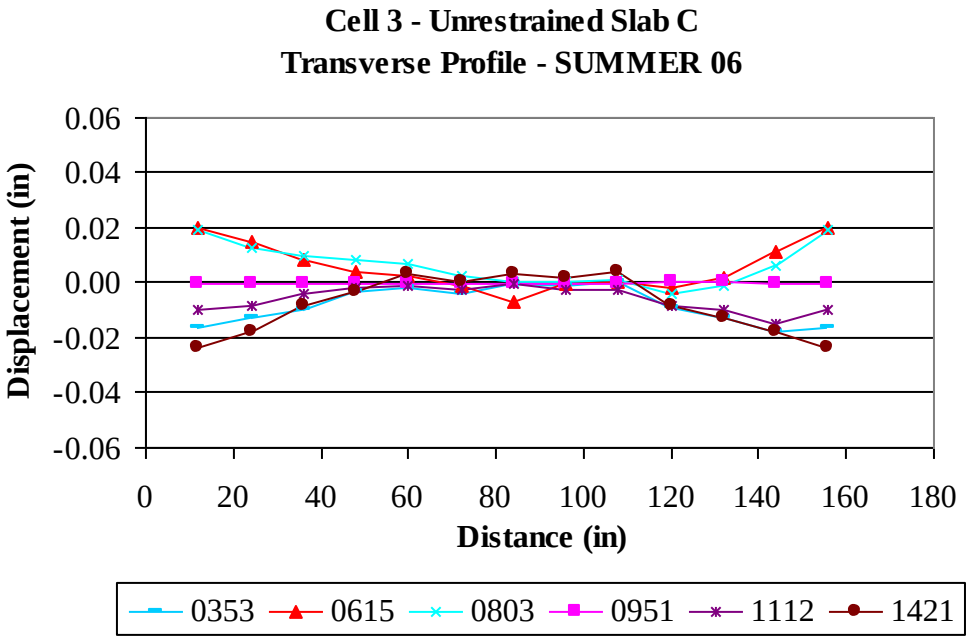

Figure C104. Unrestrained Slab C Line B transverse surface profiles for the summer of 2006.

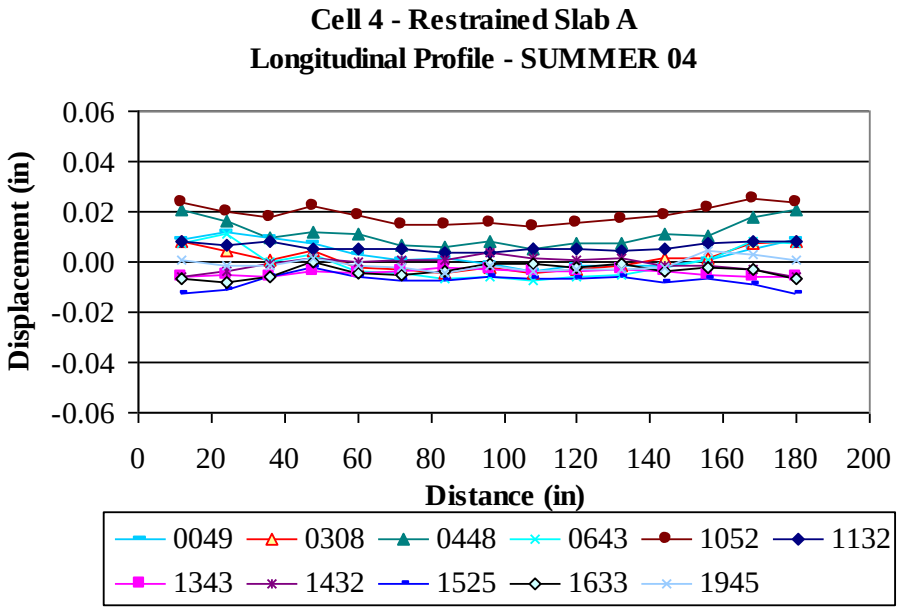

Figure C105. Restrained Slab A longitudinal surface profiles for the summer of 2004.

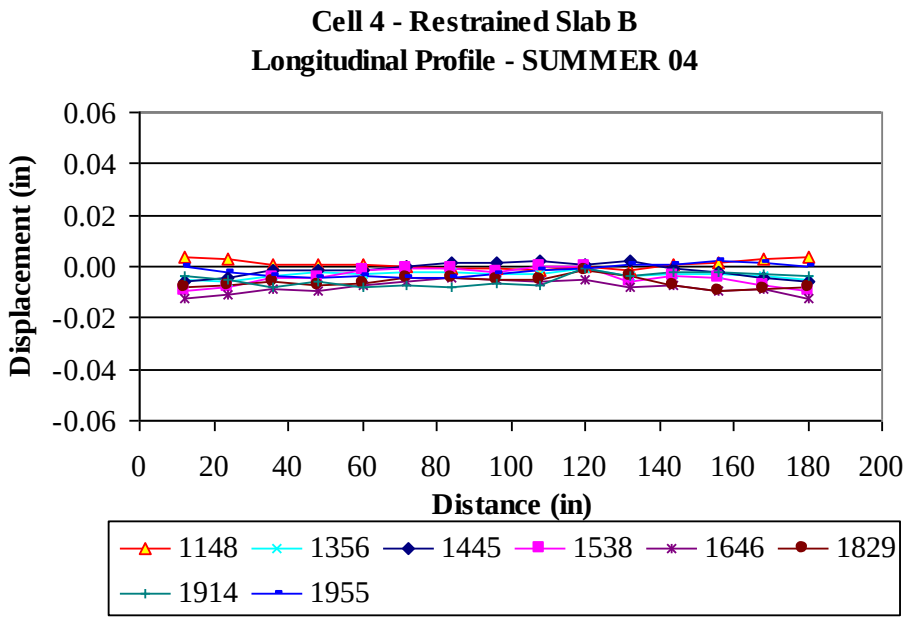

Figure C106. Restrained Slab B longitudinal surface profiles for the summer of 2004.

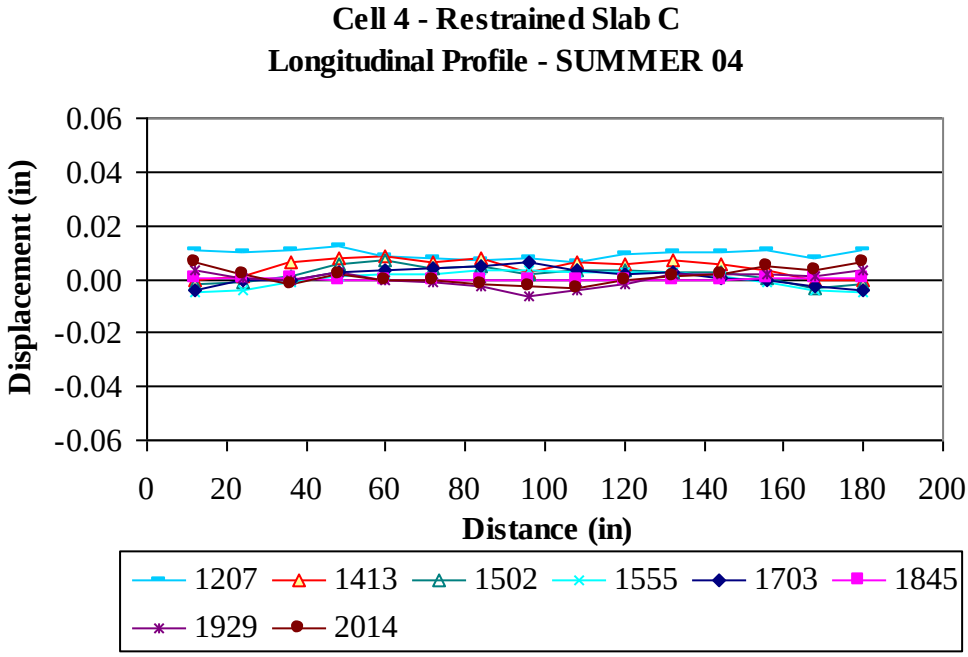

Figure C107. Restrained Slab C longitudinal surface profiles for the summer of 2004.

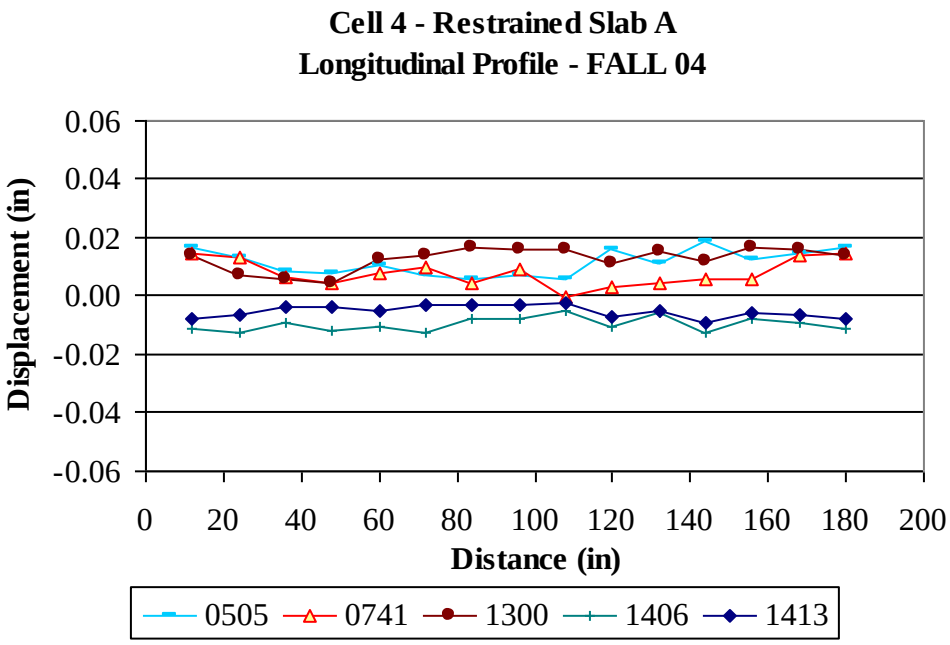

Figure C108. Restrained Slab A longitudinal surface profiles for the fall of 2004.

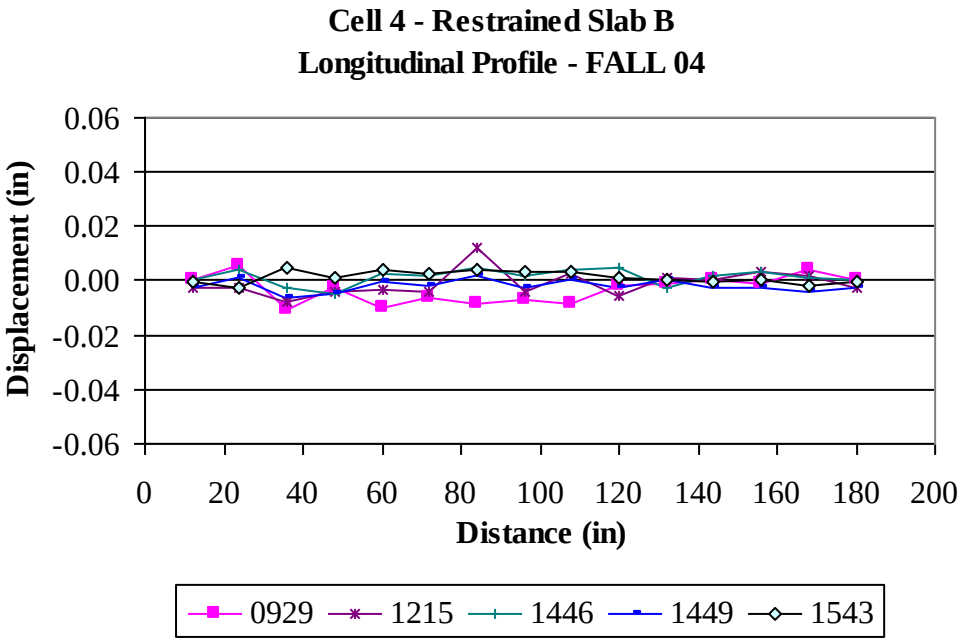

Figure C109. Restrained Slab B longitudinal surface profiles for the fall of 2004.

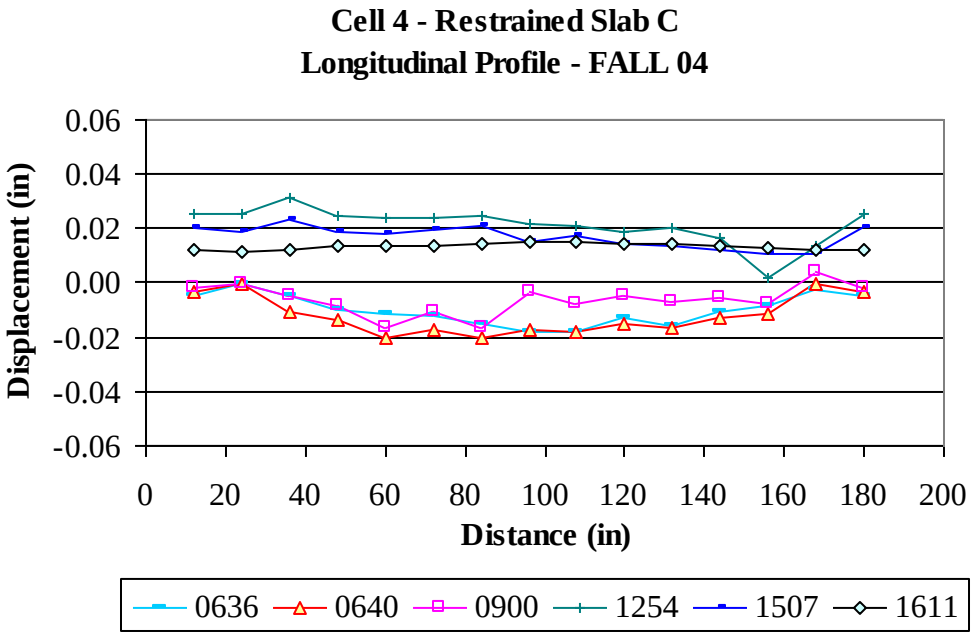

Figure C110. Restrained Slab C longitudinal surface profiles for the fall of 2004.

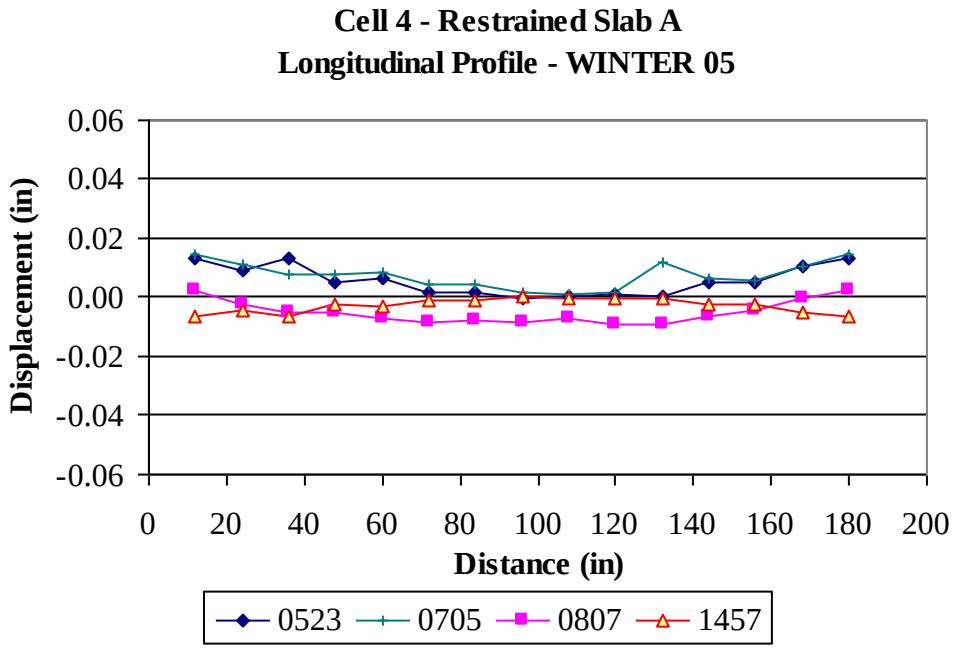

Figure C111. Restrained Slab A longitudinal surface profiles for the winter of 2005.

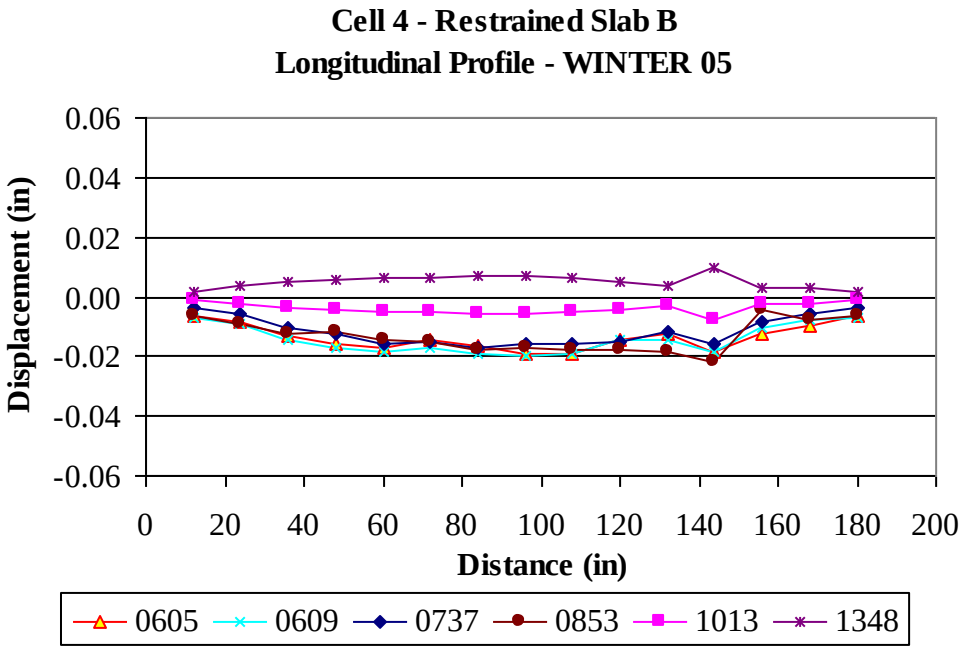

Figure C112. Restrained Slab B longitudinal surface profiles for the winter of 2005.

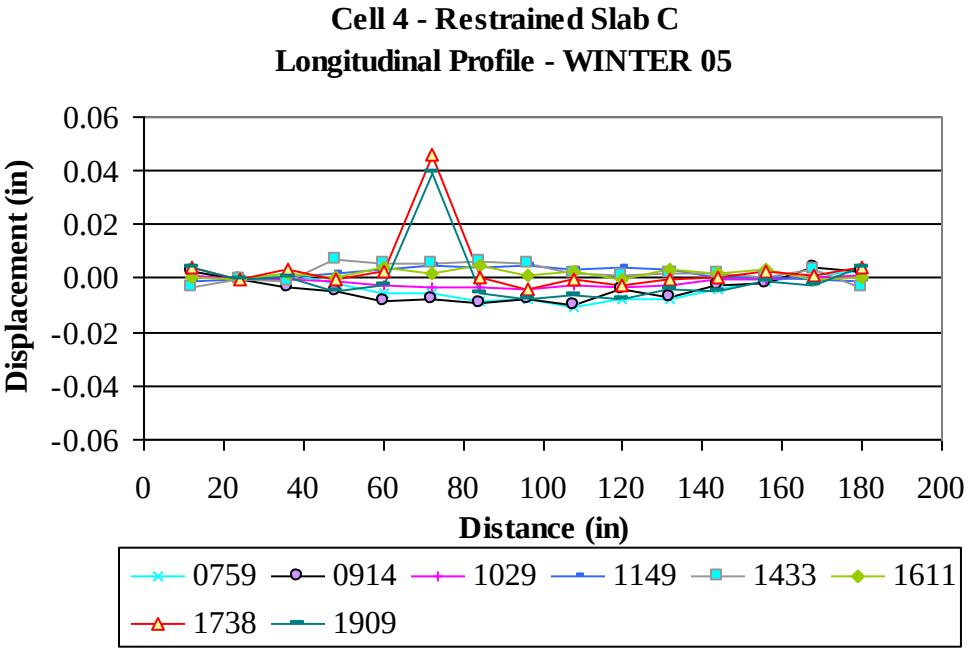

Figure C113. Restrained Slab C longitudinal surface profiles for the winter of 2005.

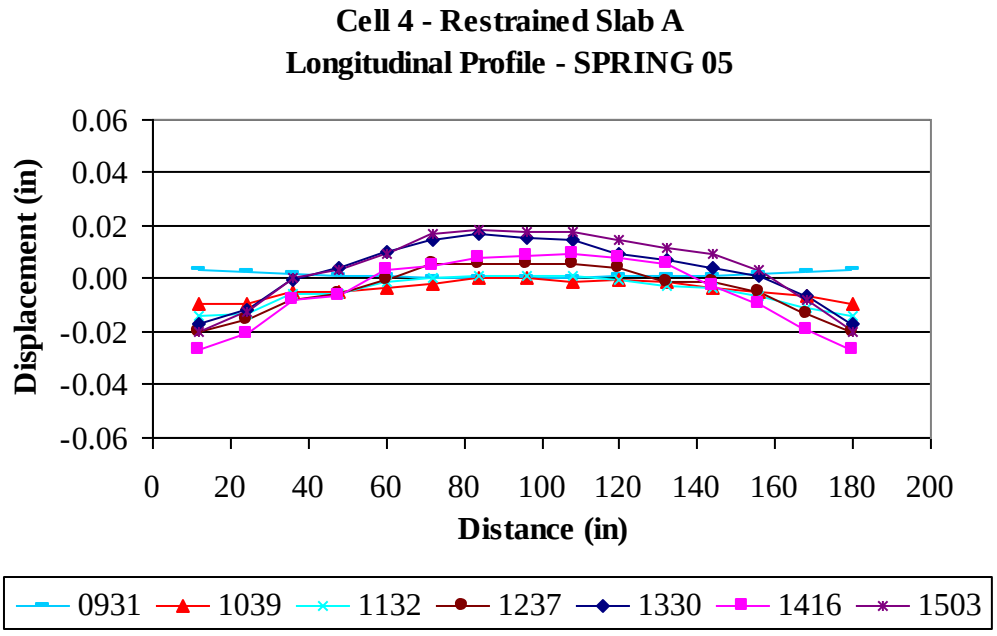

Figure C114. Restrained Slab A longitudinal surface profiles for the spring of 2005.

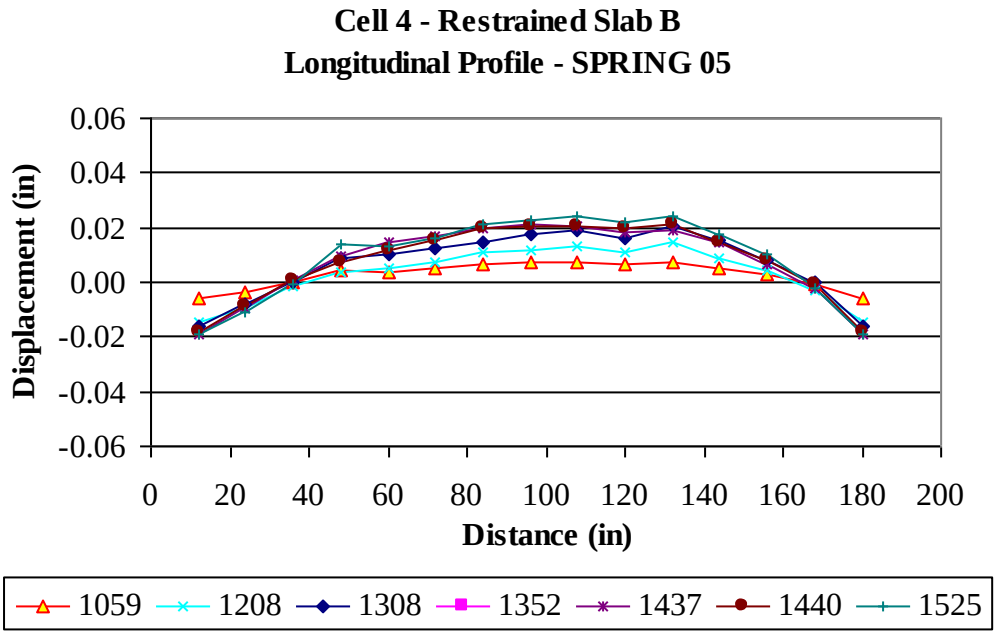

Figure C115. Restrained Slab B longitudinal surface profiles for the spring of 2005.

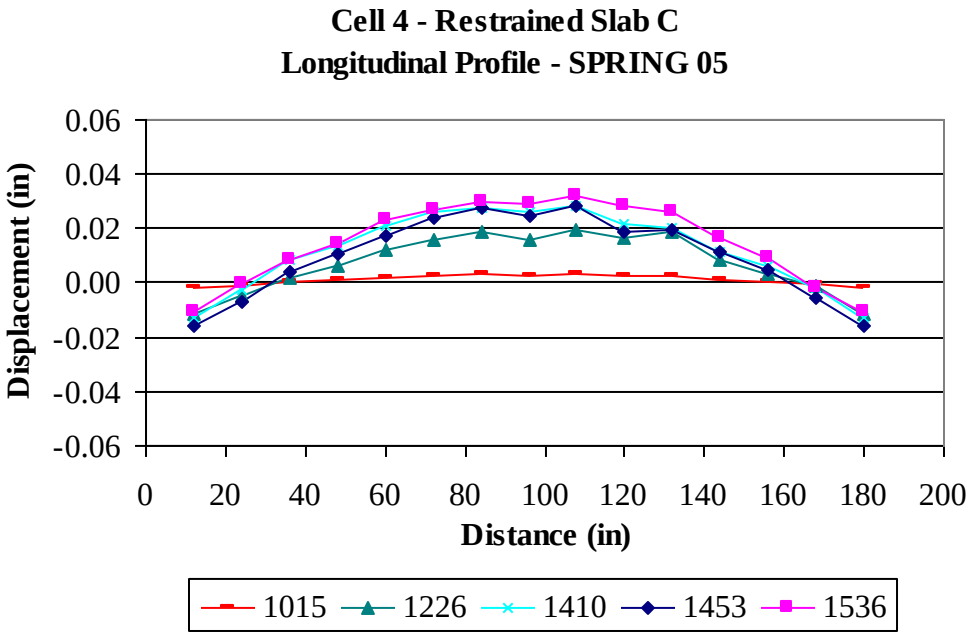

Figure C116. Restrained Slab C longitudinal surface profiles for the spring of 2005.

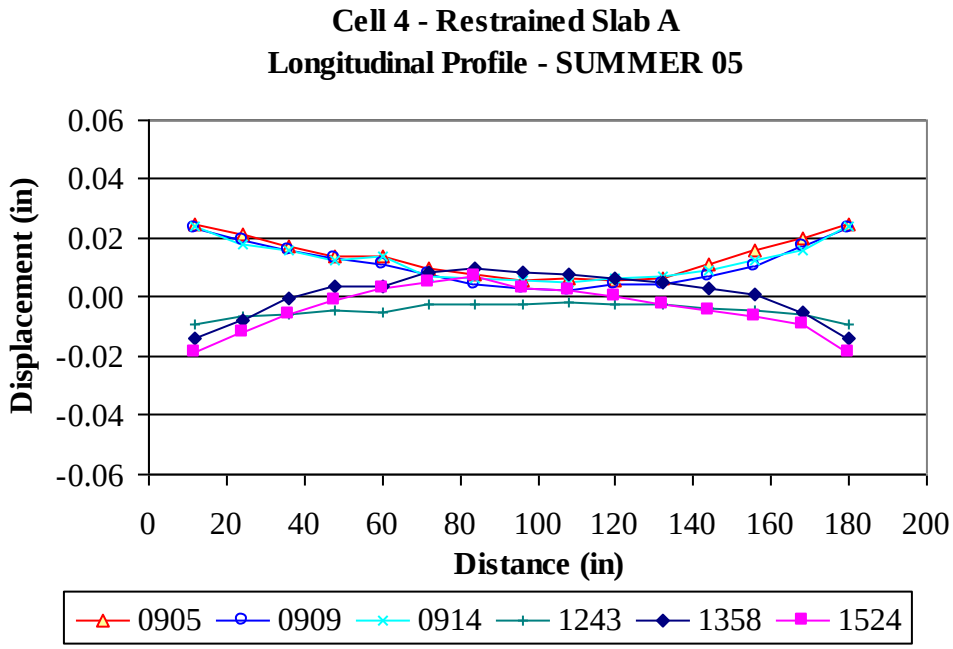

Figure C117. Restrained Slab A longitudinal surface profiles for the summer of 2005.

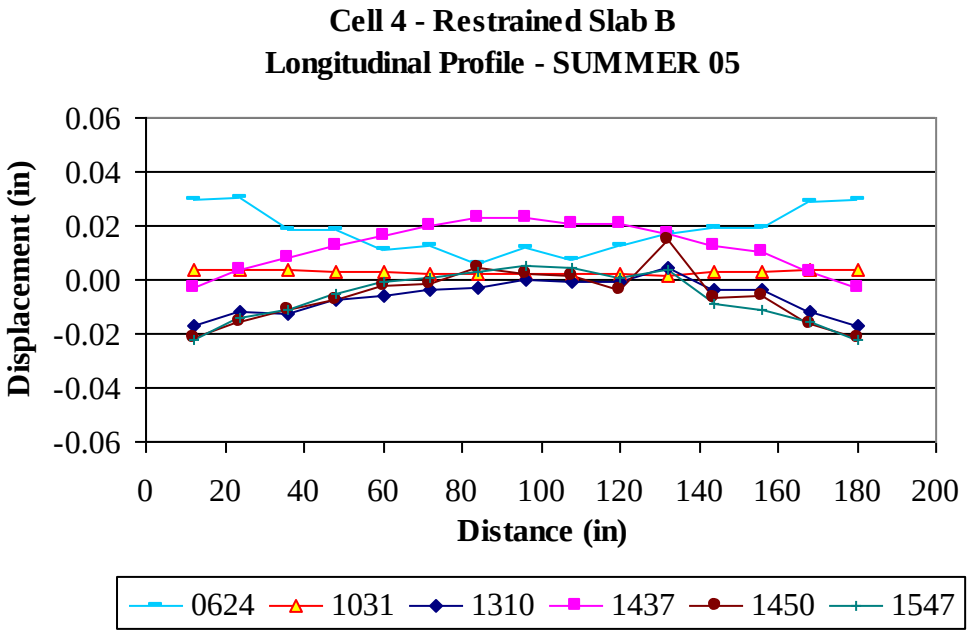

Figure C118. Restrained Slab B longitudinal surface profiles for the summer of 2005.

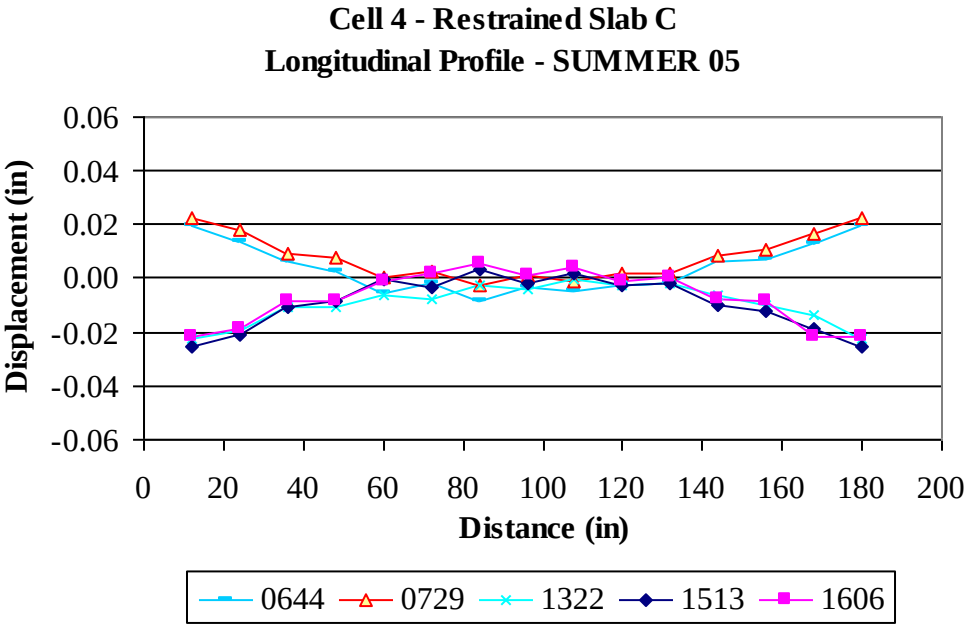

Figure C119. Restrained Slab C longitudinal surface profiles for the summer of 2005.

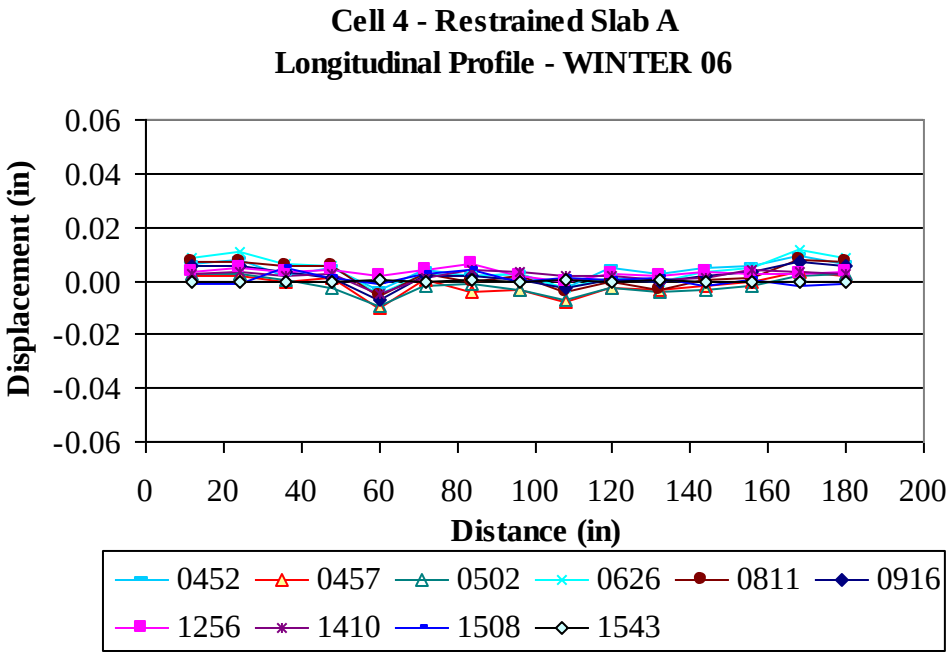

Figure C120. Restrained Slab A longitudinal surface profiles for the winter of 2006.

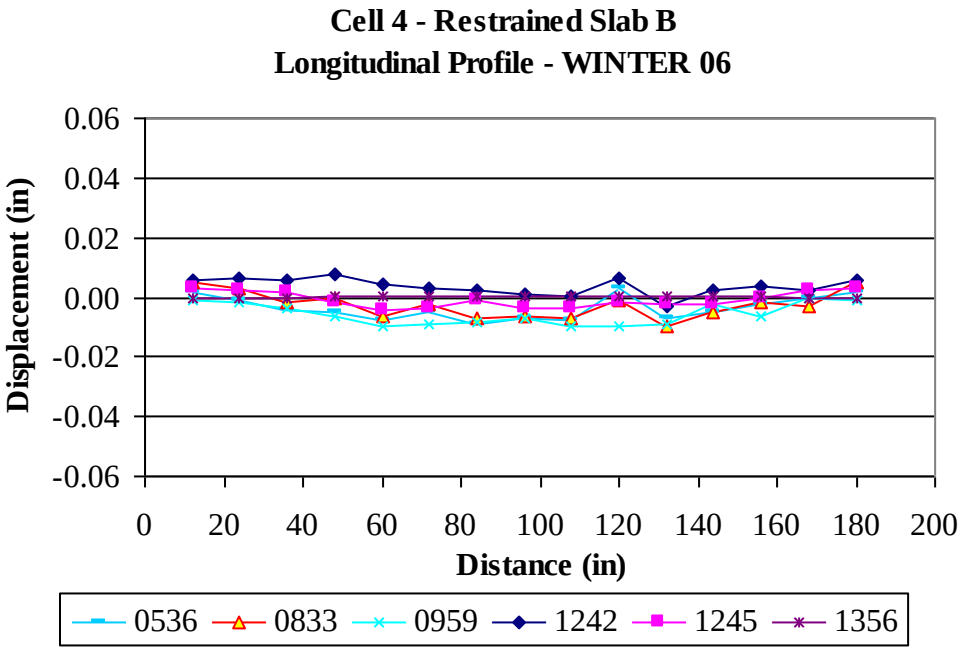

Figure C121. Restrained Slab B longitudinal surface profiles for the winter of 2006.

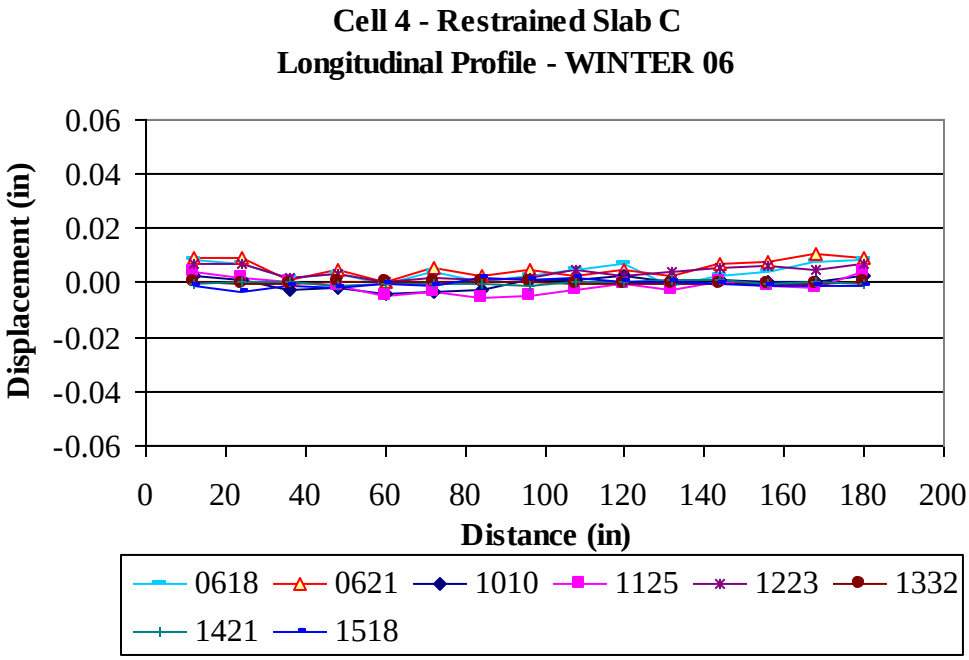

Figure C122. Restrained Slab C longitudinal surface profiles for the winter of 2006.

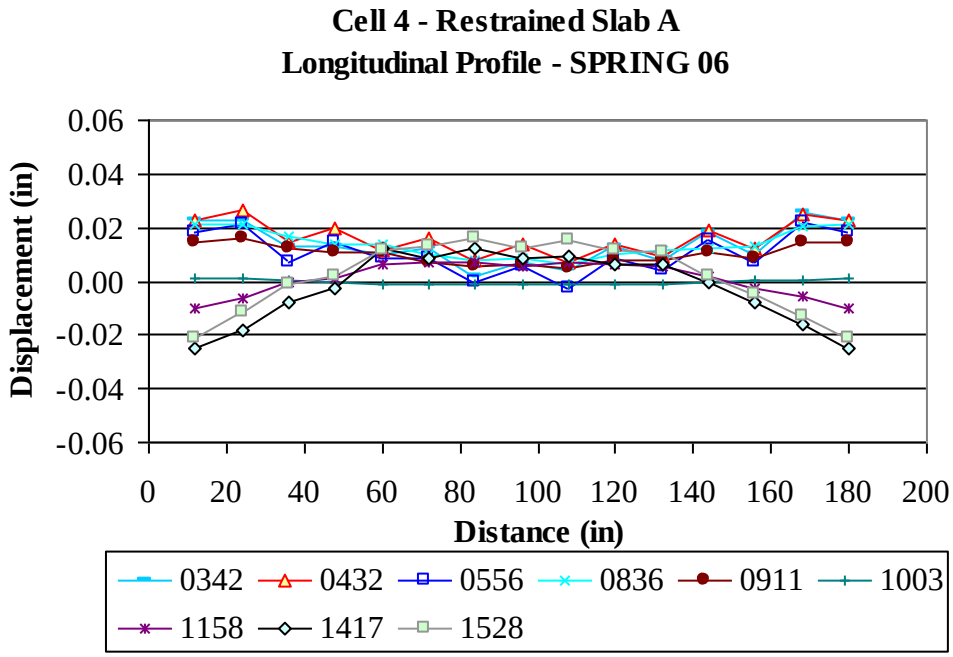

Figure C123. Restrained Slab A longitudinal surface profiles for the spring of 2006.

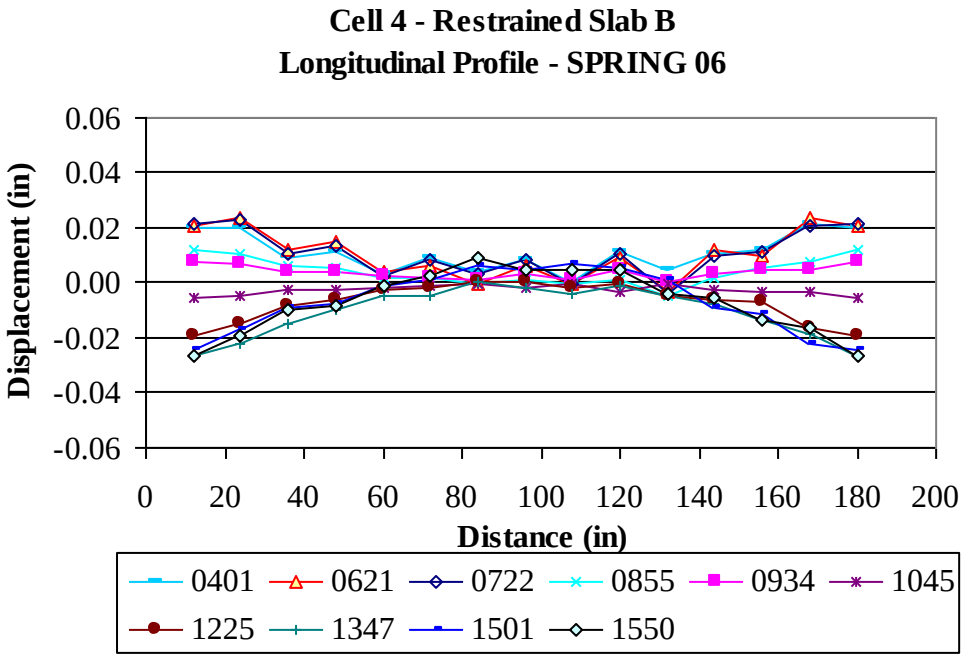

Figure C124. Restrained Slab B longitudinal surface profiles for the spring of 2006.

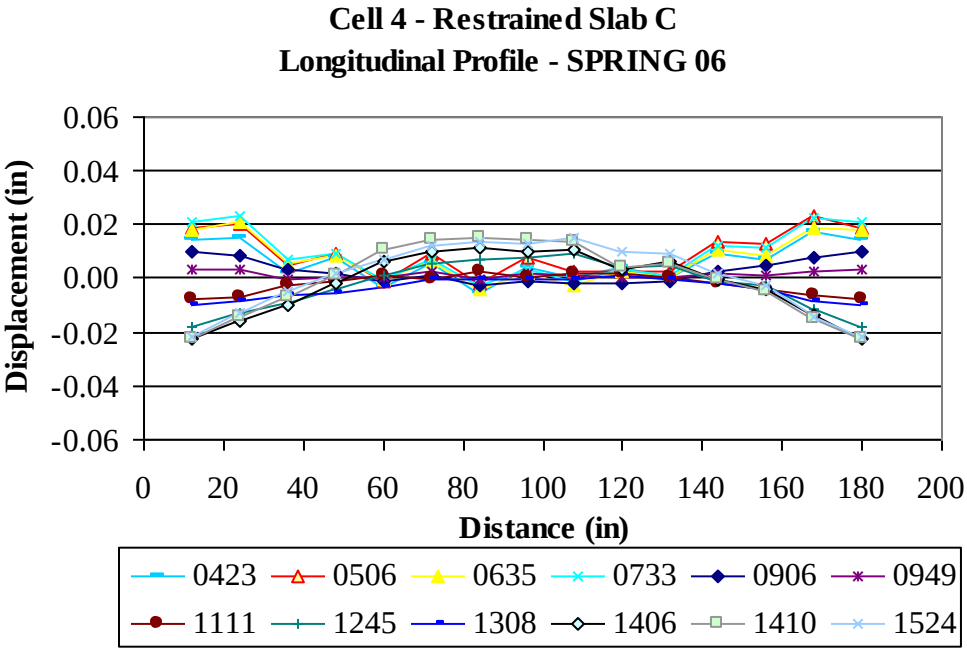

Figure C125. Slab C longitudinal surface profiles for the spring of 2006.

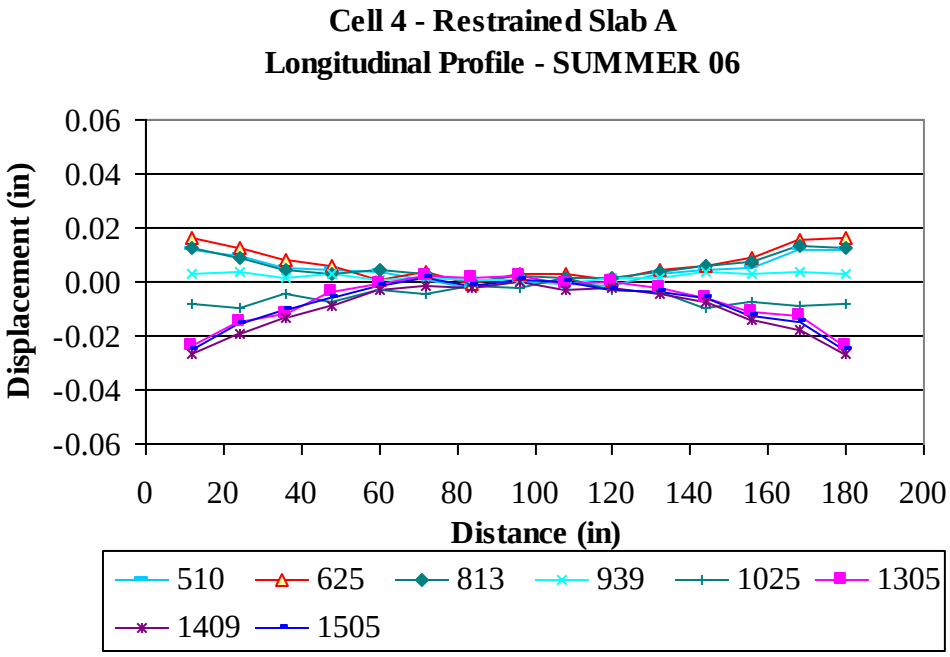

Figure C126. Restrained Slab A longitudinal surface profiles for the summer of 2006.

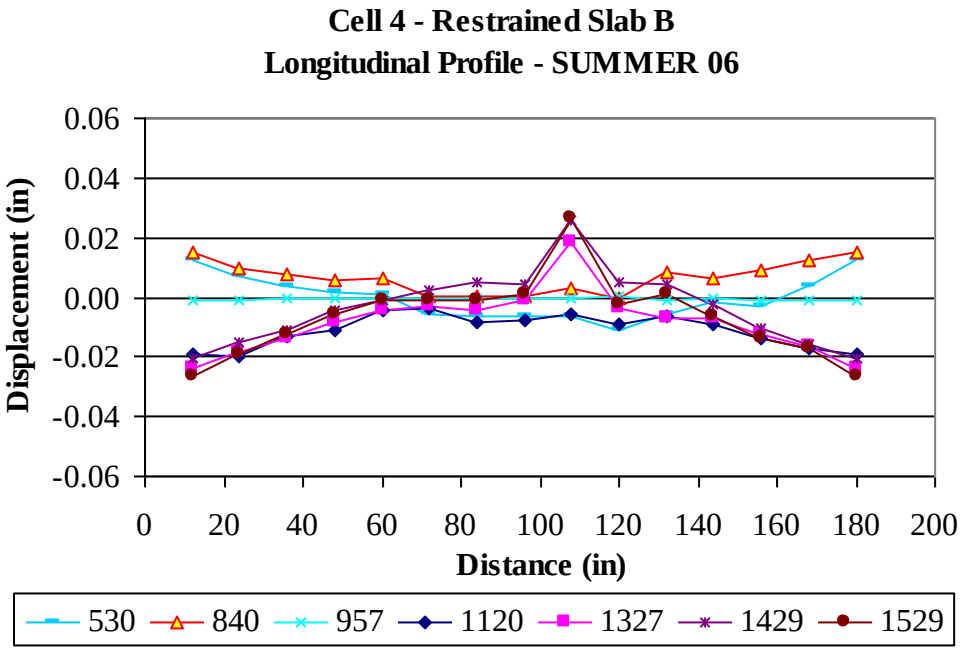

Figure C127. Restrained Slab B longitudinal surface profiles for the summer of 2006.

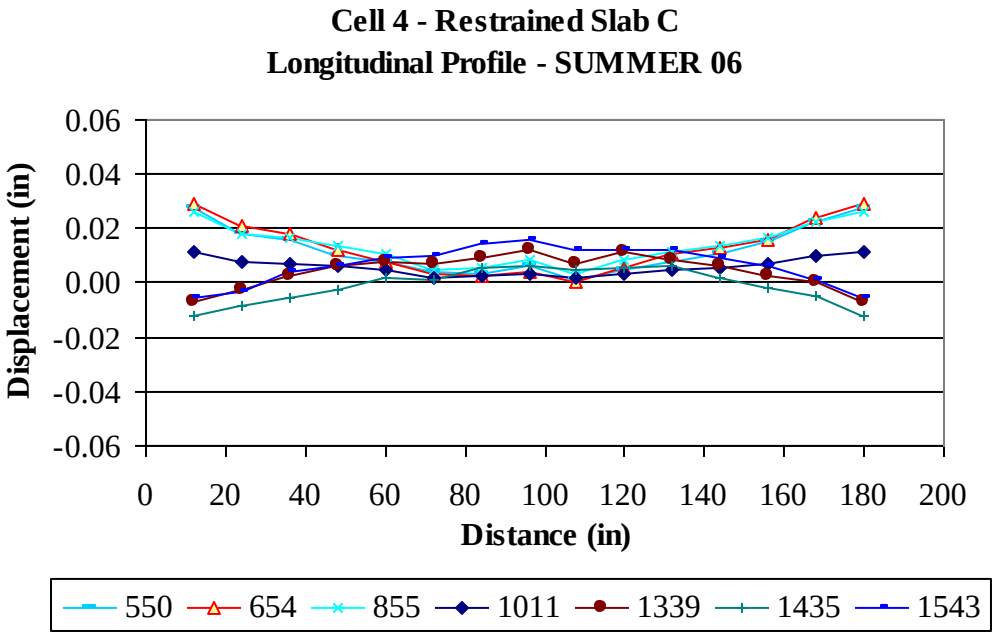

Figure C128. Restrained Slab C longitudinal surface profiles for the summer of 2006.

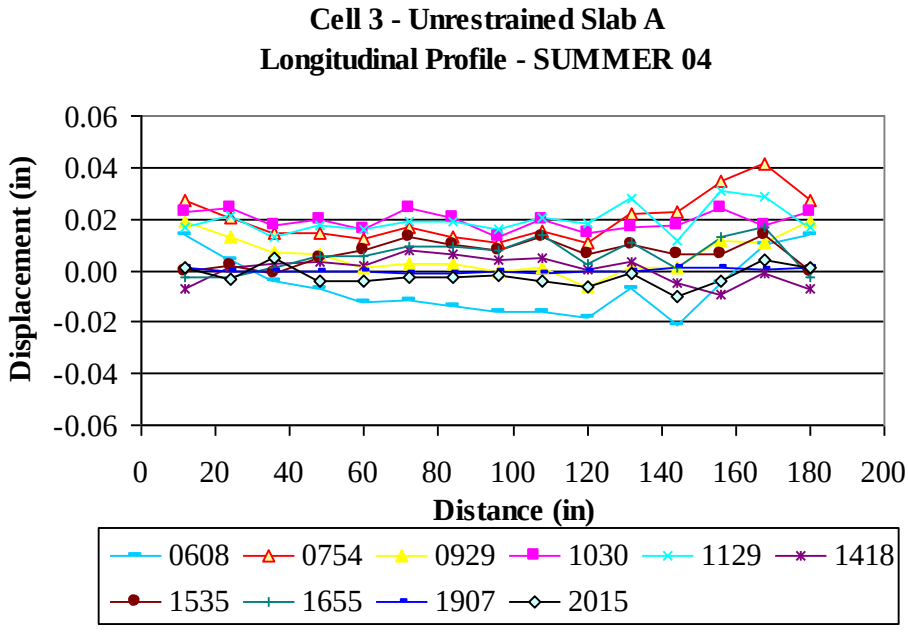

Figure C129. Unrestrained Slab A longitudinal surface profiles for the summer of 2004.

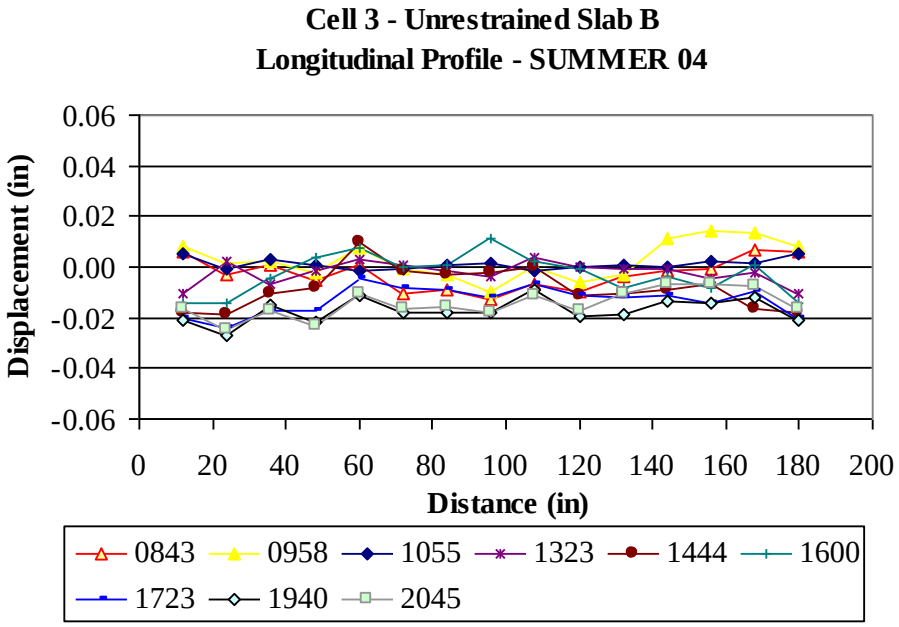

Figure C130. Unrestrained Slab B longitudinal surface profiles for the summer of 2004.

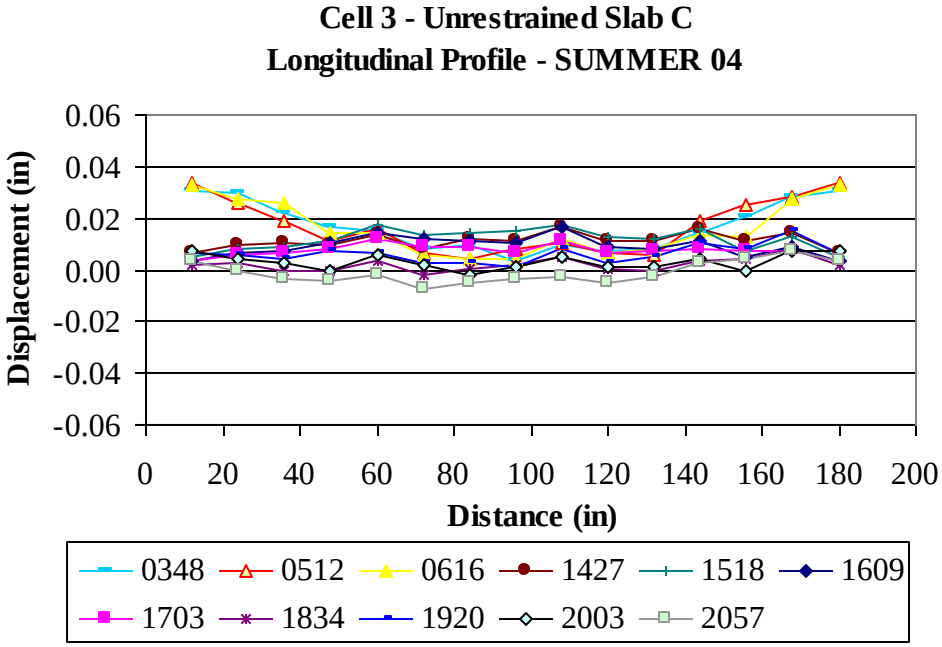

Figure C131. Unrestrained Slab C longitudinal surface profiles for the summer of 2004.

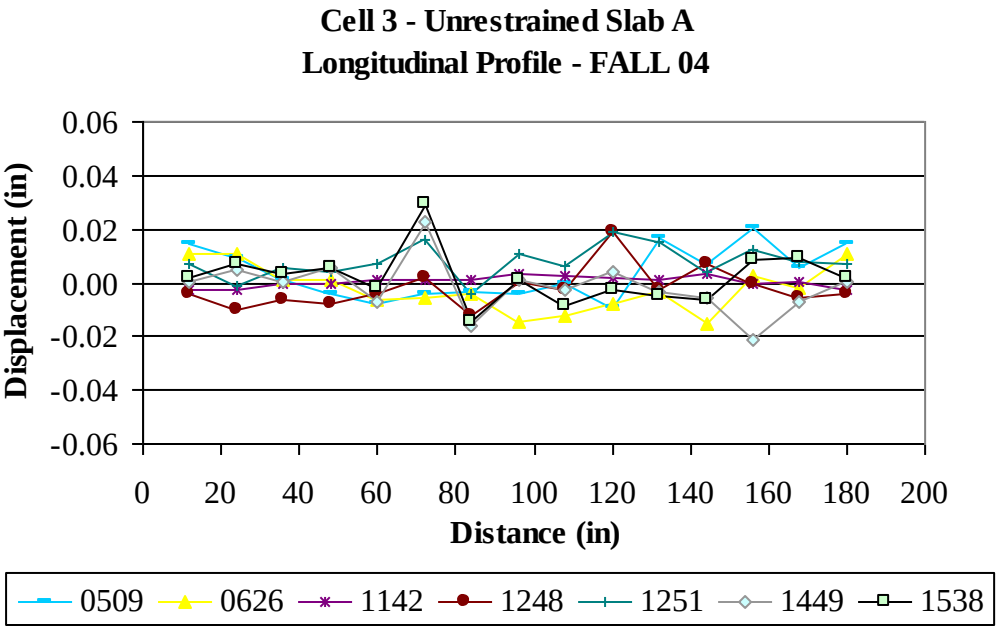

Figure C132. Unrestrained Slab A longitudinal surface profiles for the fall of 2004.

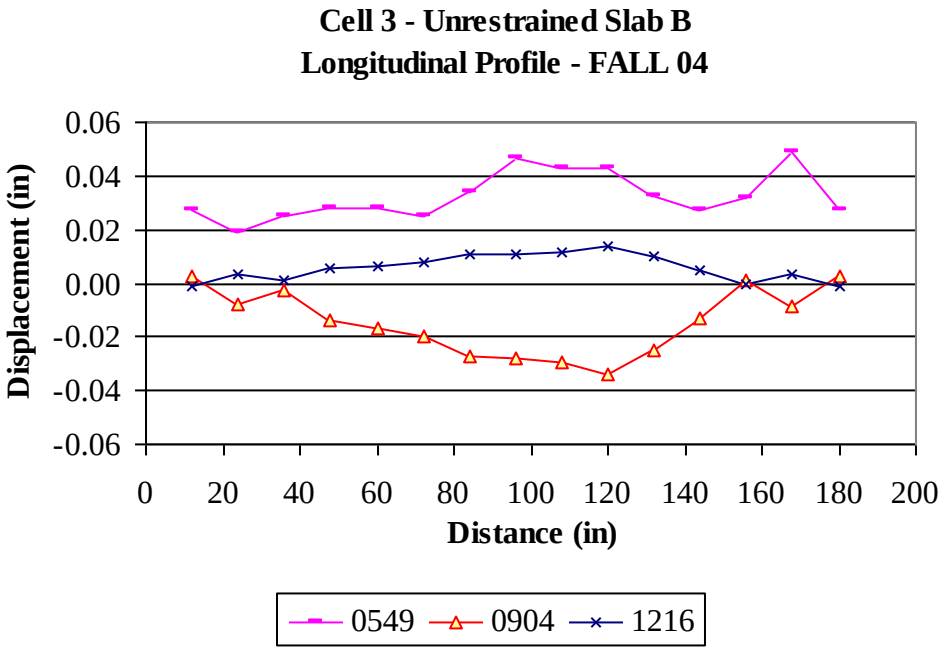

Figure C133. Unrestrained Slab B longitudinal surface profiles for the fall of 2004.

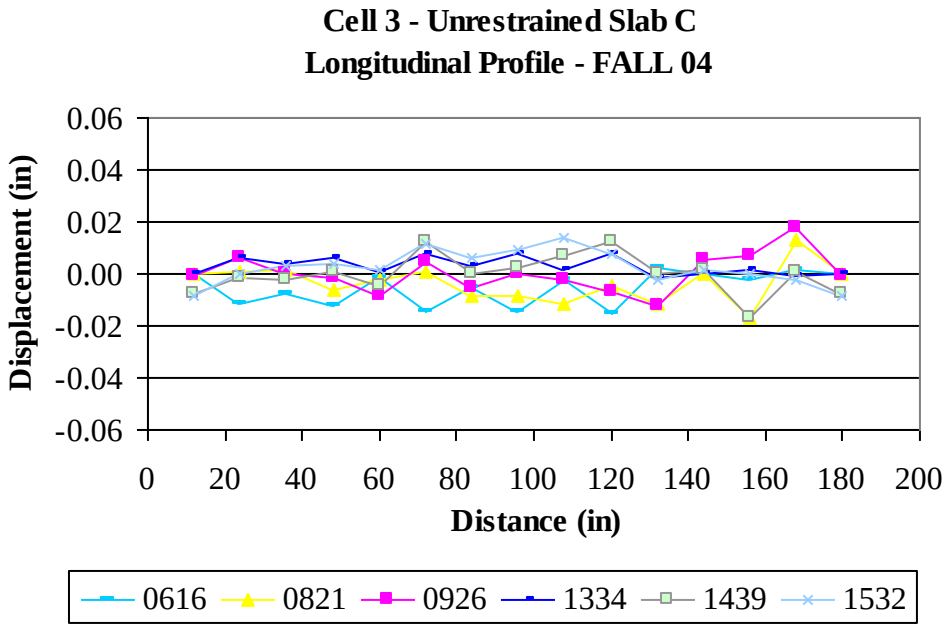

Figure C134. Unrestrained Slab C longitudinal surface profiles for the fall of 2004.

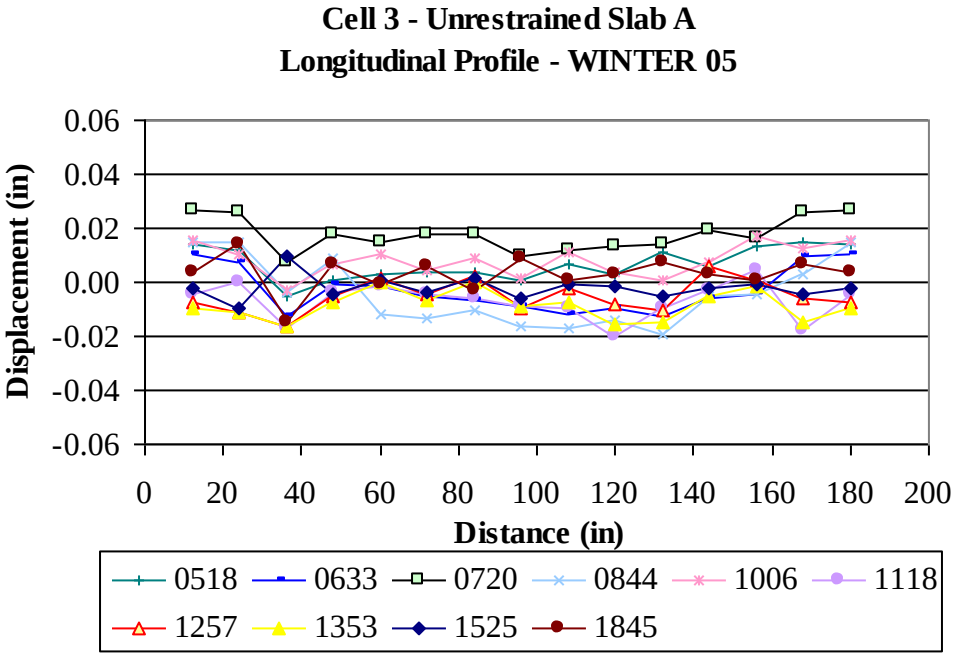

Figure C135. Unrestrained Slab A longitudinal surface profiles for the winter of 2005.

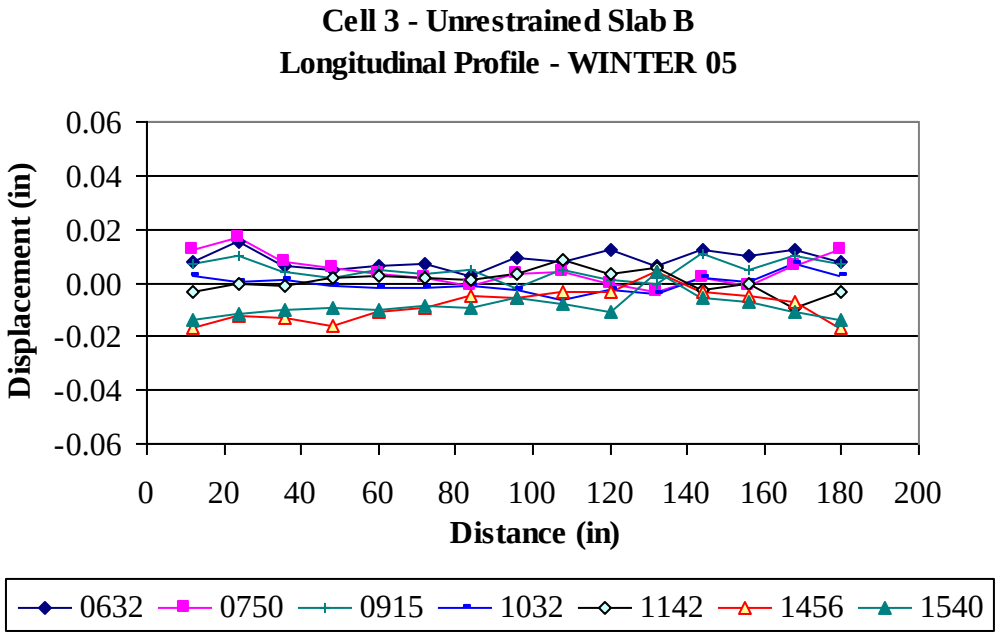

Figure C136. Unrestrained Slab B longitudinal surface profiles for the winter of 2005.

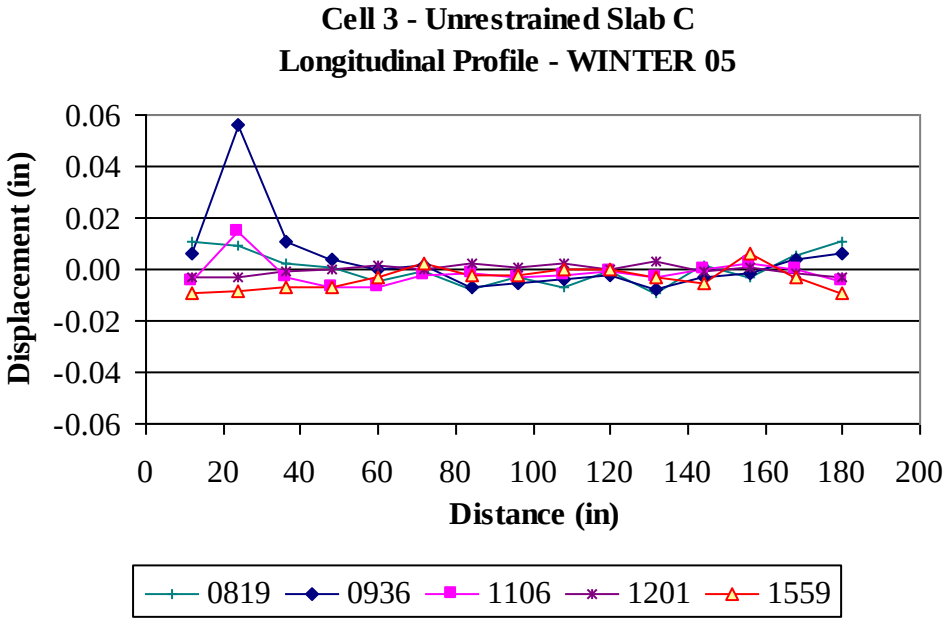

Figure C137. Unrestrained Slab C longitudinal surface profiles for the winter of 2005.

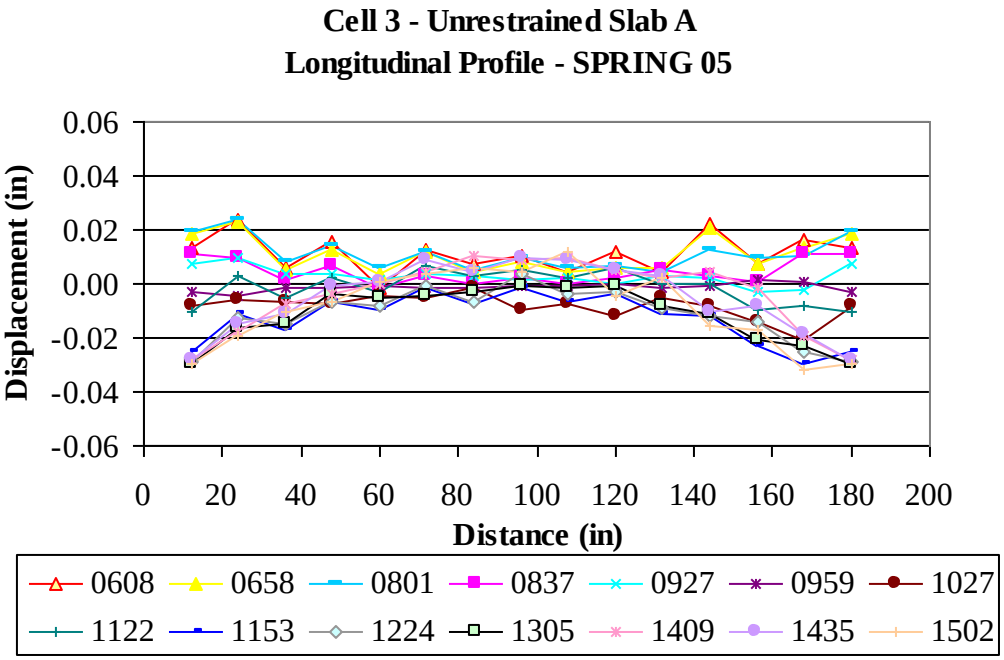

Figure C138. Unrestrained Slab A longitudinal surface profiles for the spring of 2005.

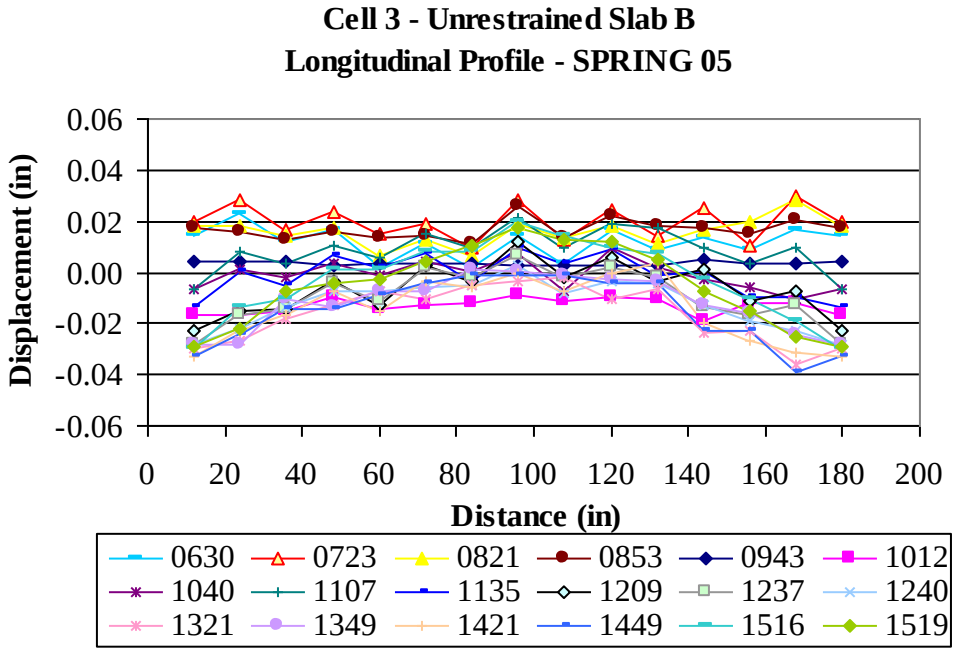

Figure C139. Unrestrained Slab B longitudinal surface profiles for the spring of 2005.

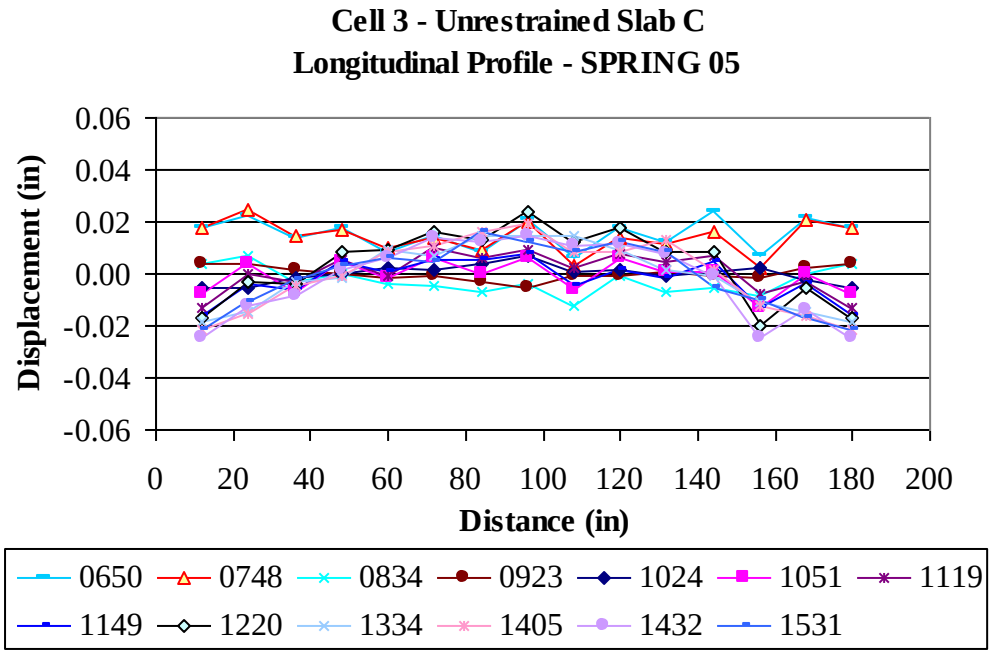

Figure C140. Unrestrained Slab C longitudinal surface profiles for the spring of 2005.

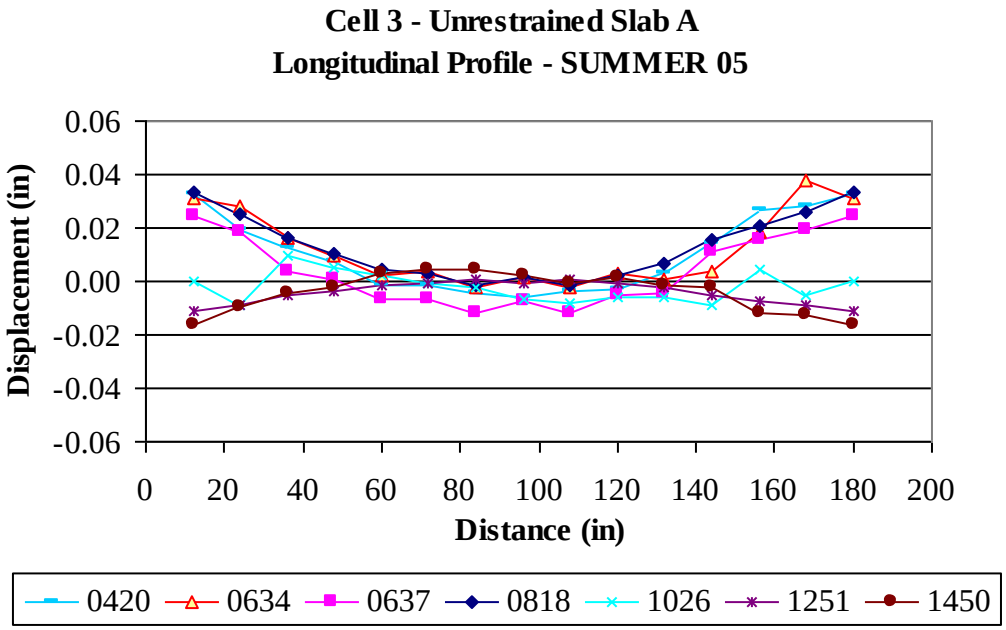

Figure C141. Unrestrained Slab A longitudinal surface profiles for the summer of 2005.

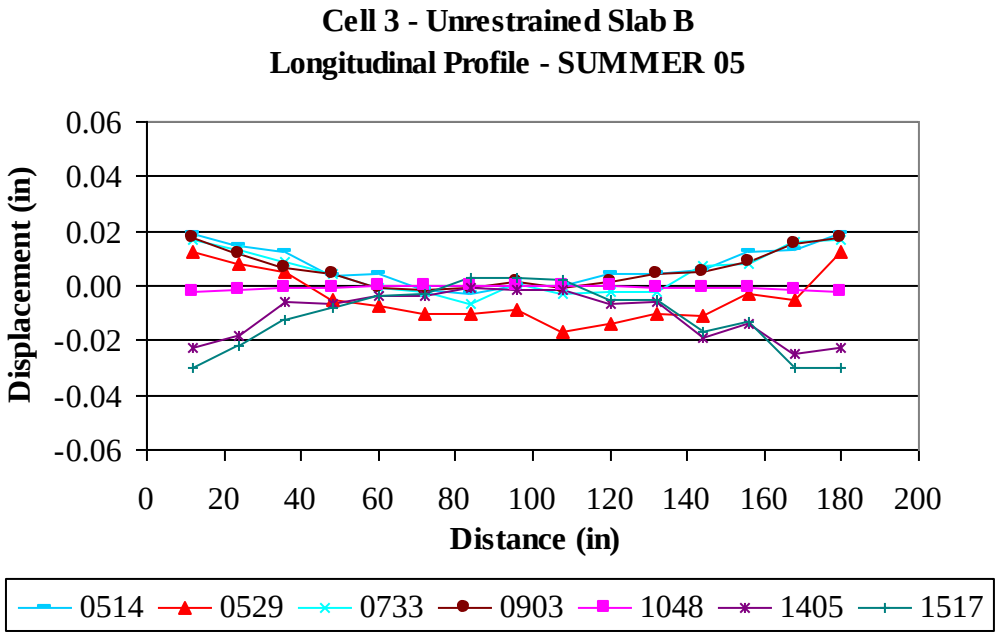

Figure C142. Unrestrained Slab B longitudinal surface profiles for the summer of 2005.

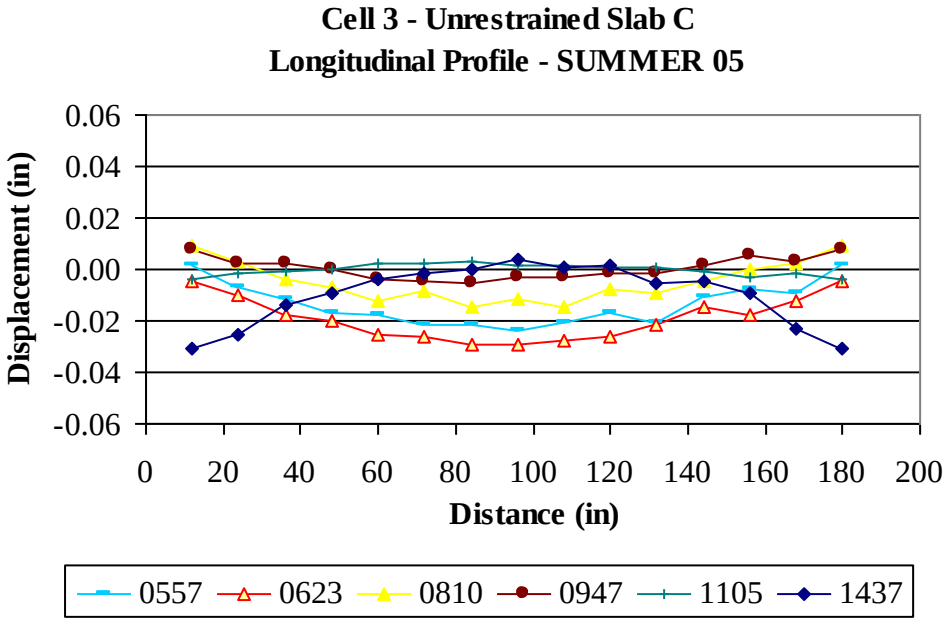

Figure C143. Unrestrained Slab C longitudinal surface profiles for the summer of 2005.

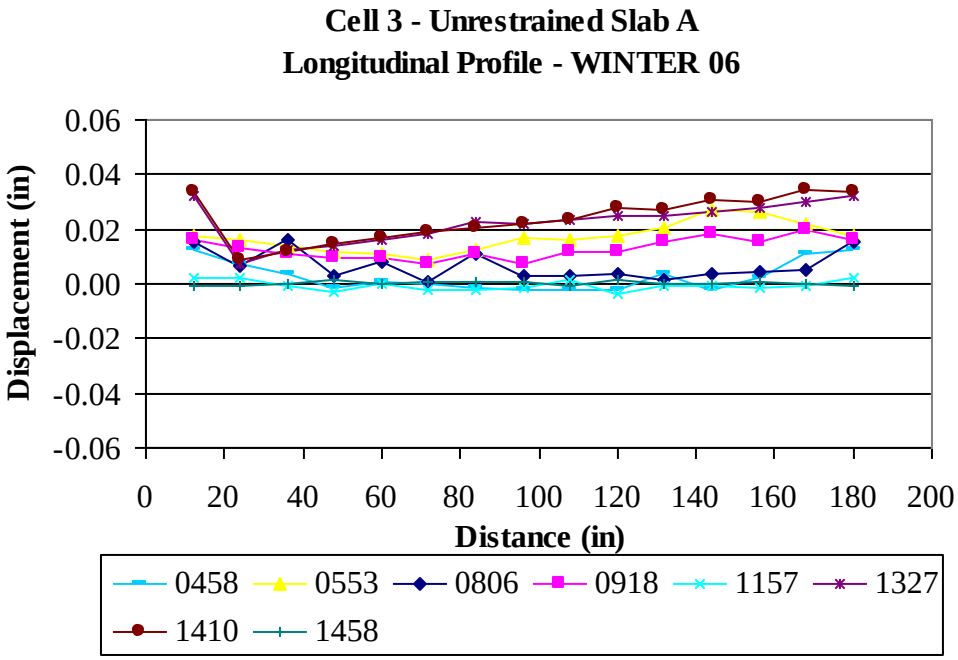

Figure C144. Unrestrained Slab A longitudinal surface profiles for the winter of 2006.

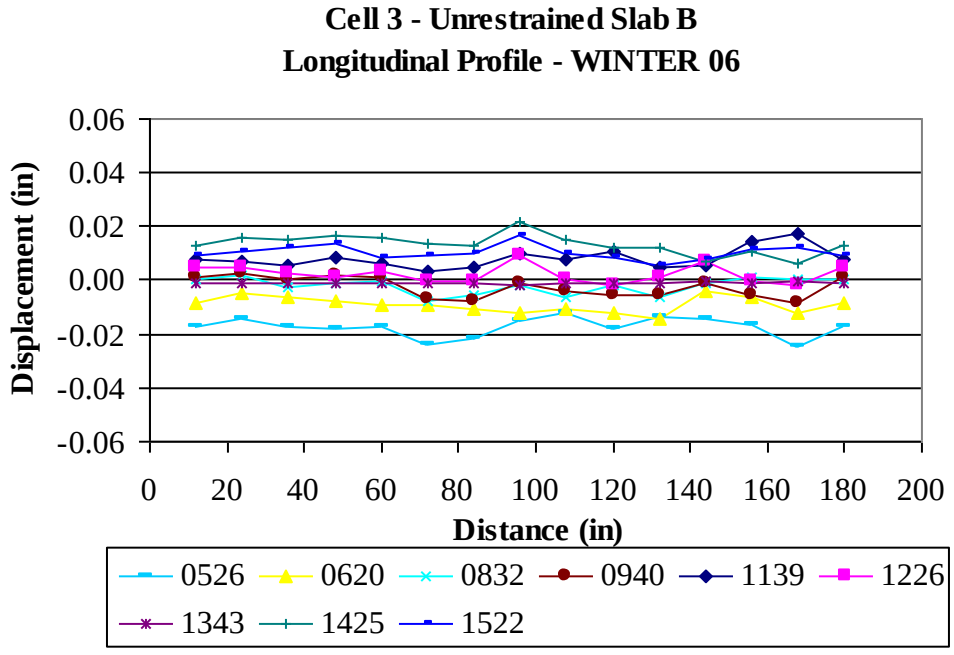

Figure C145. Unrestrained Slab B longitudinal surface profiles for the winter of 2006.

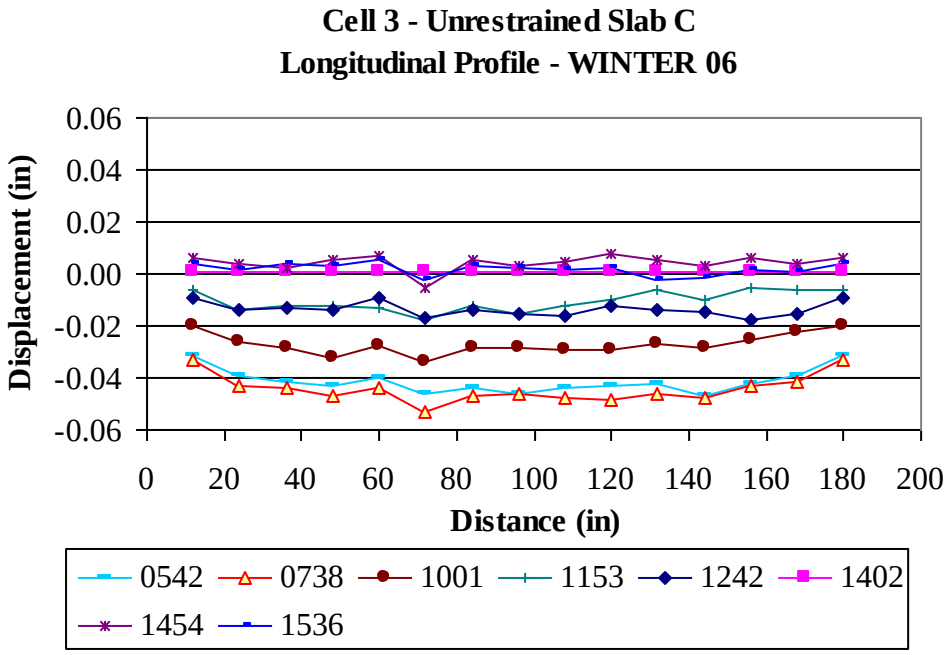

Figure C146. Unrestrained Slab C longitudinal surface profiles for the winter of 2006.

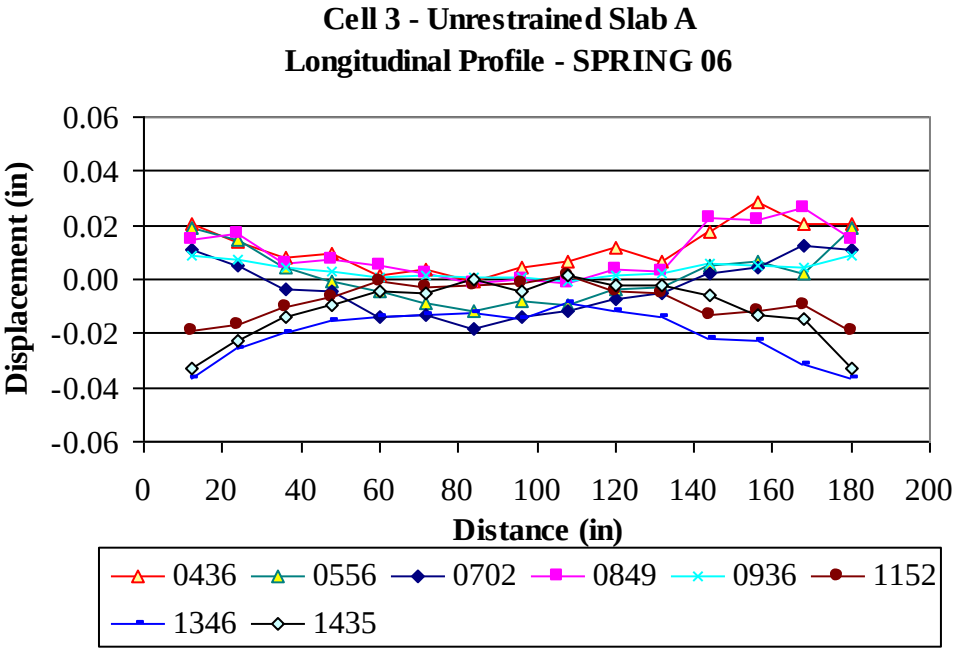

Figure C147. Unrestrained Slab A longitudinal surface profiles for the spring of 2006.

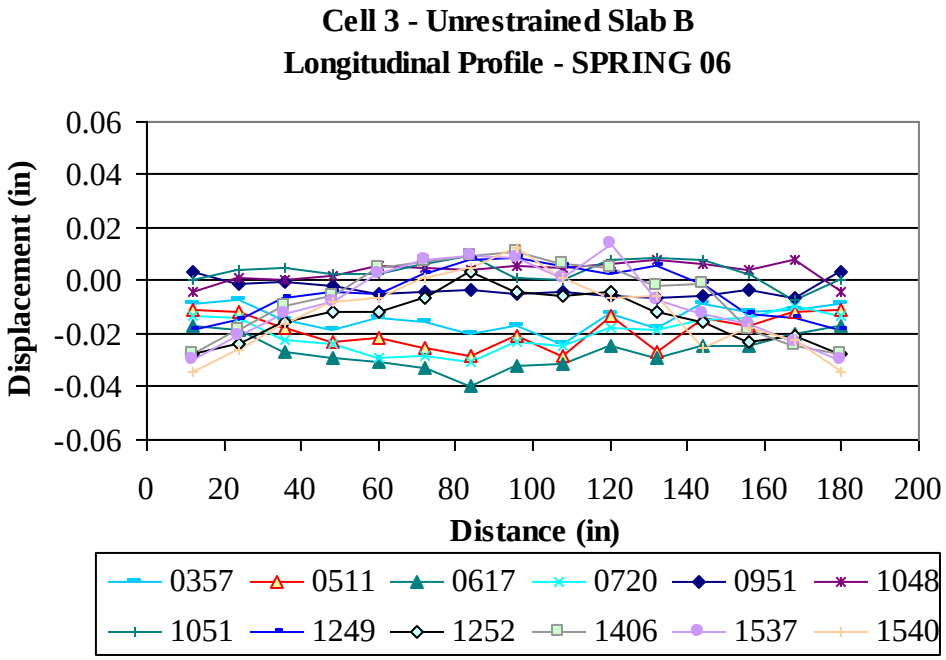

Figure C148. Unrestrained Slab B longitudinal surface profiles for the spring of 2006.

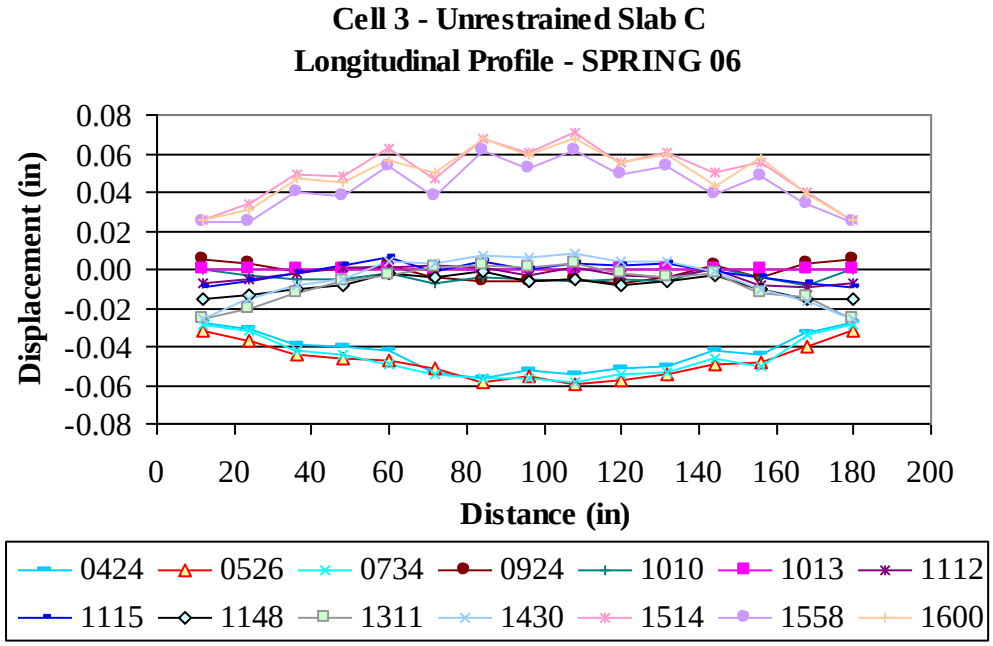

Figure C149. Unrestrained Slab C longitudinal surface profiles for the spring of 2006.

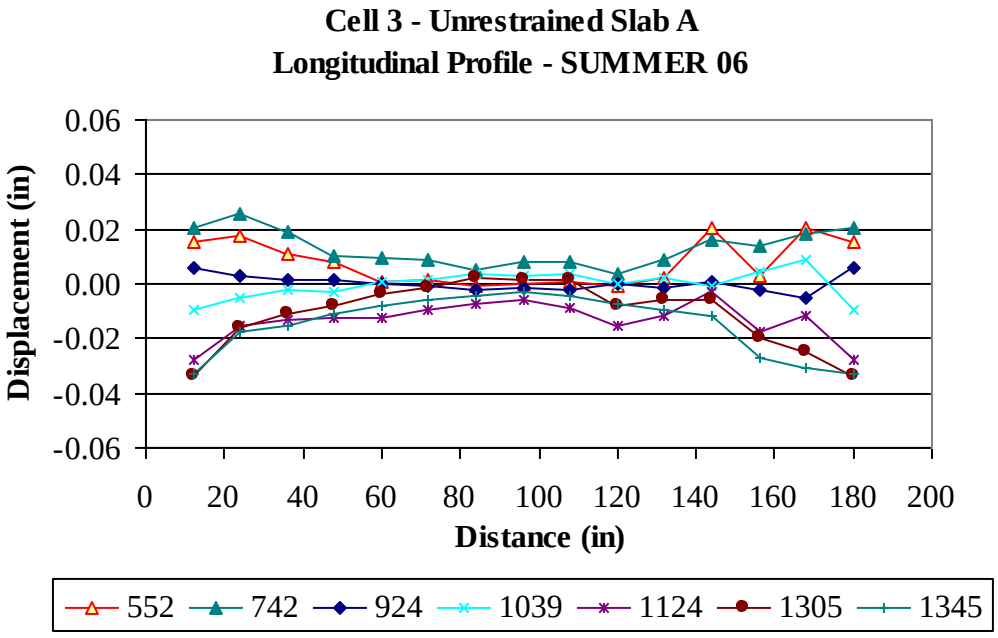

Figure C150. Unrestrained Slab A longitudinal surface profiles for the summer of 2006.

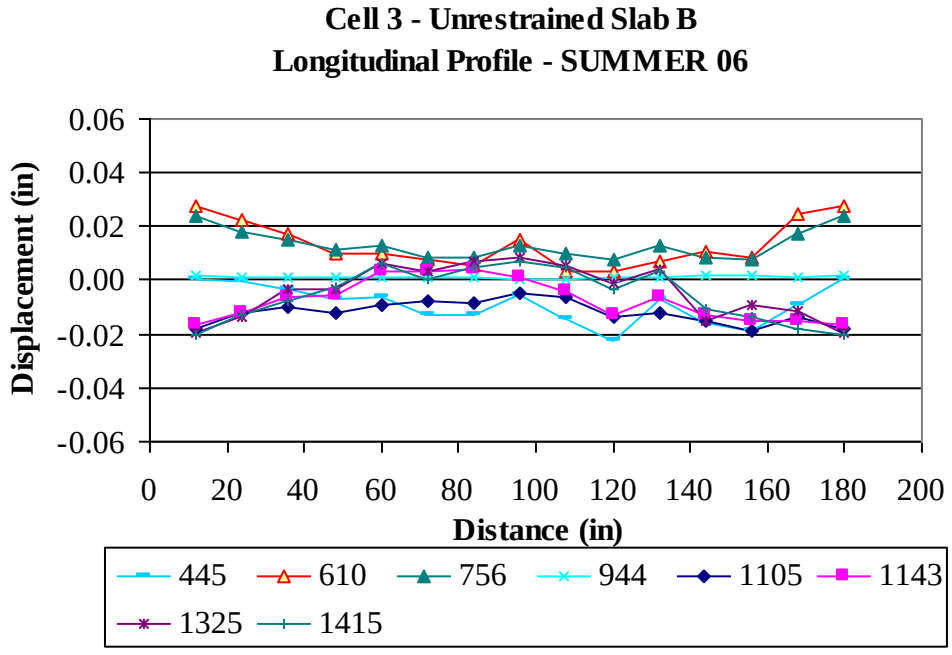

Figure C151. Unrestrained Slab B longitudinal surface profiles for the summer of 2006.

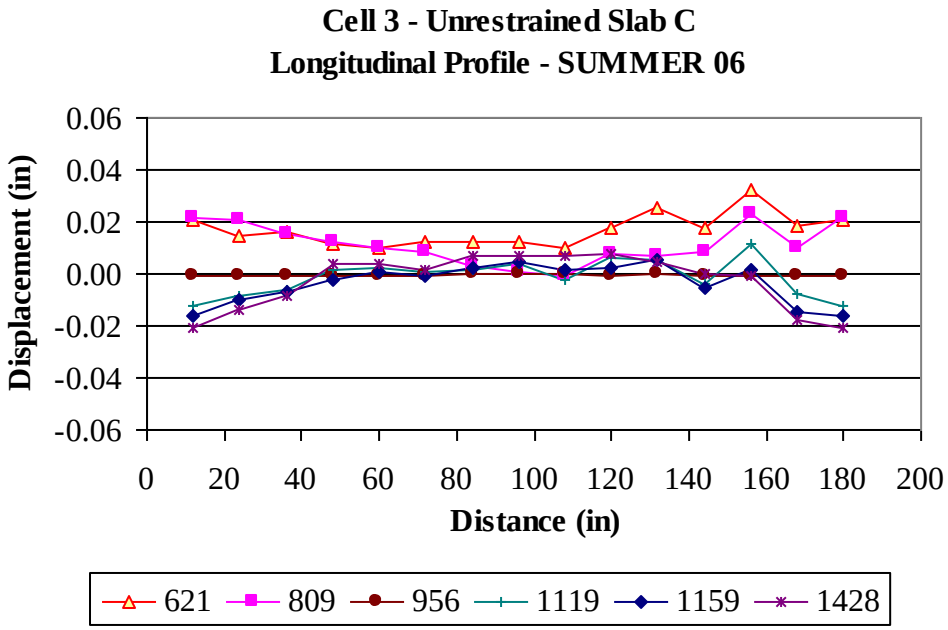

Figure C152. Unrestrained Slab C longitudinal surface profiles for the summer of 2006.

APPENDIX D

SLAB CURVATURE

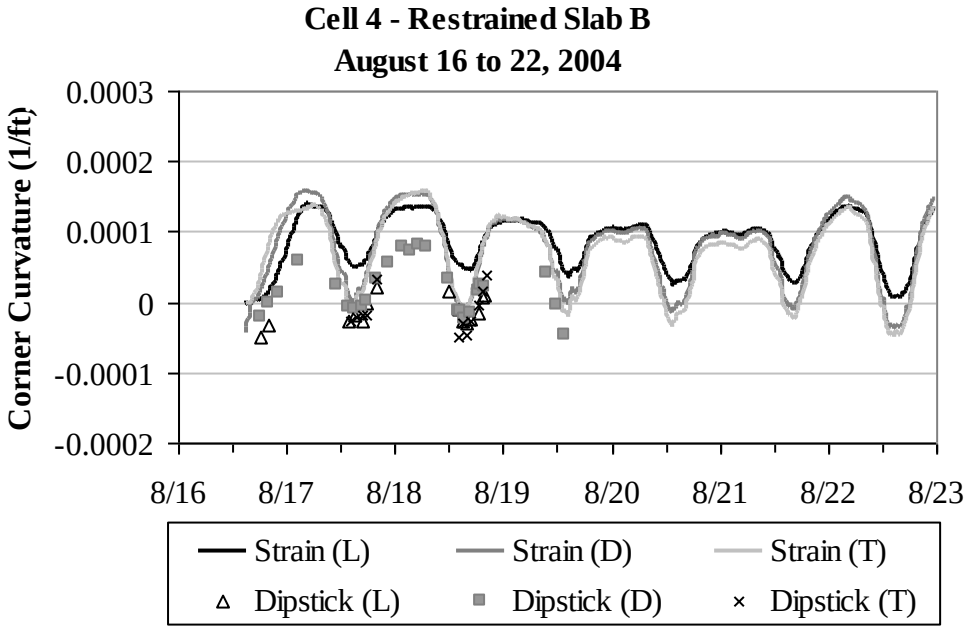

Figure D1. Curvature estimated from surface profiles and vibrating wire gages for restrained Slab B during the summer of 2004.

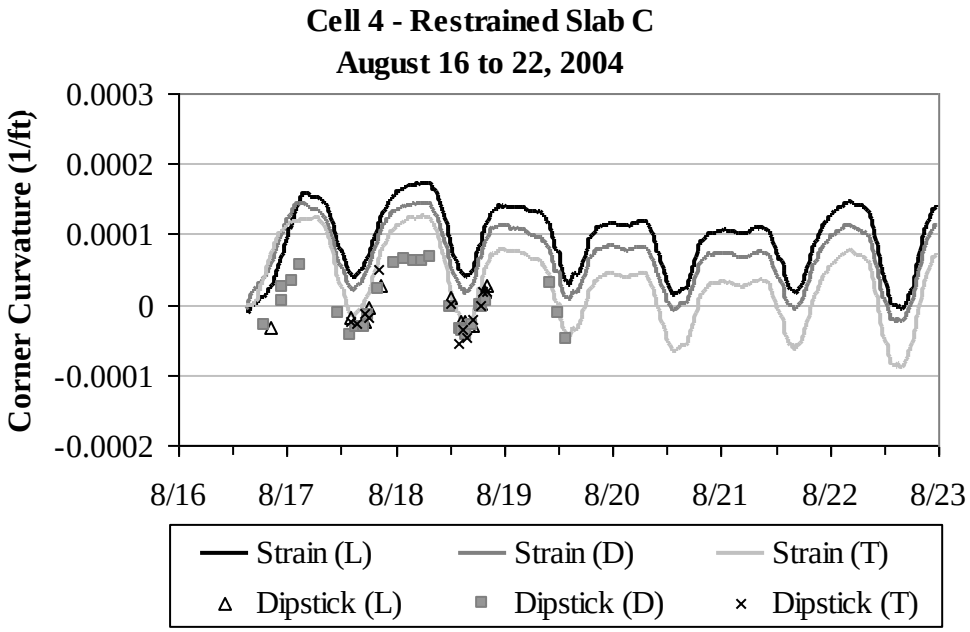

Figure D2. Curvature estimated from surface profiles and vibrating wire gages for restrained Slab C during the summer of 2004.

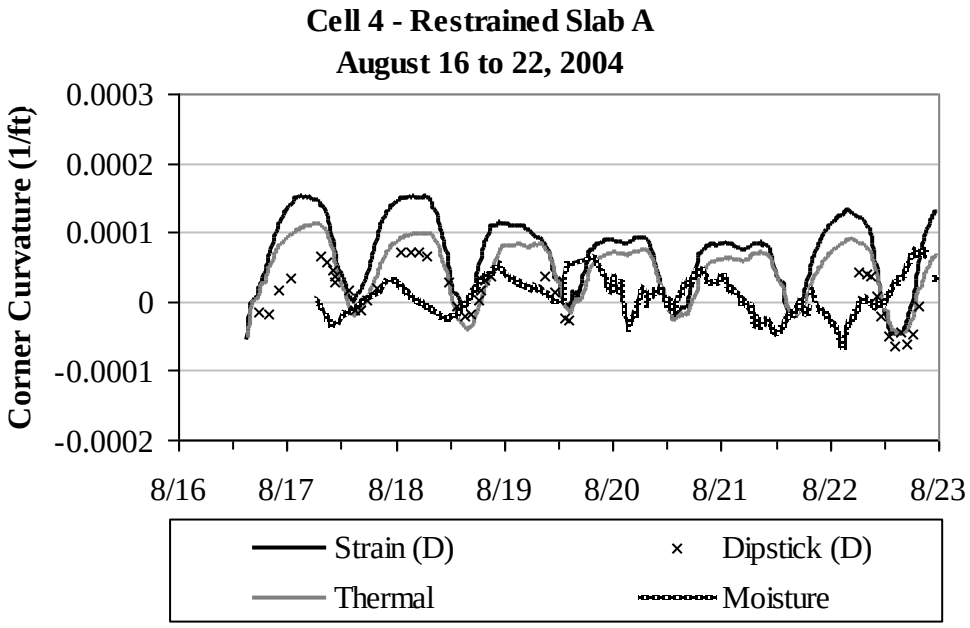

Figure D3. Comparison between curvatures estimated from the three types of data for restrained Slab A during the summer of 2004.

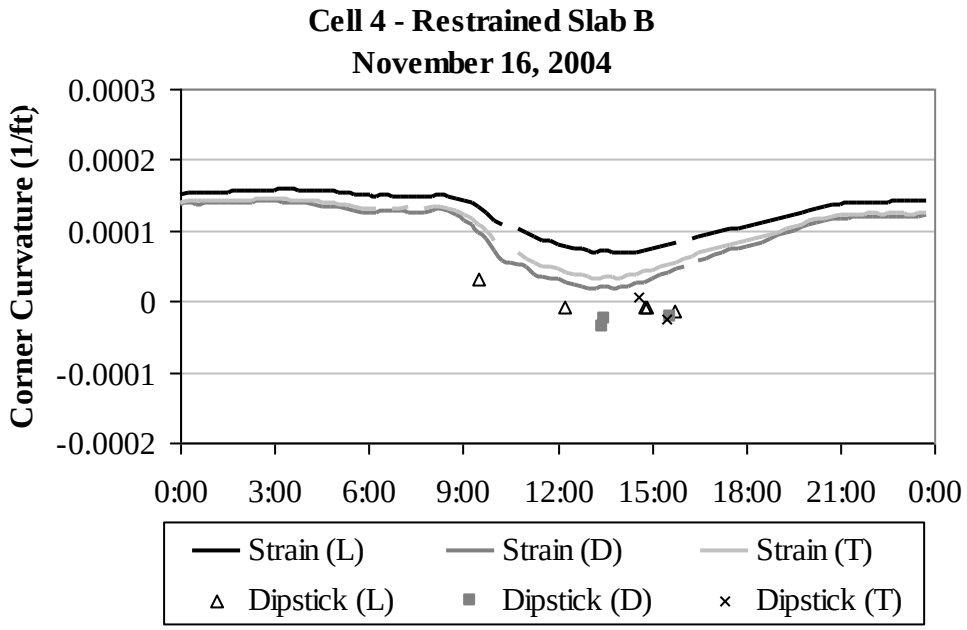

Figure D4. Curvature estimated from surface profiles and vibrating wire gages for restrained Slab B during the fall of 2004.

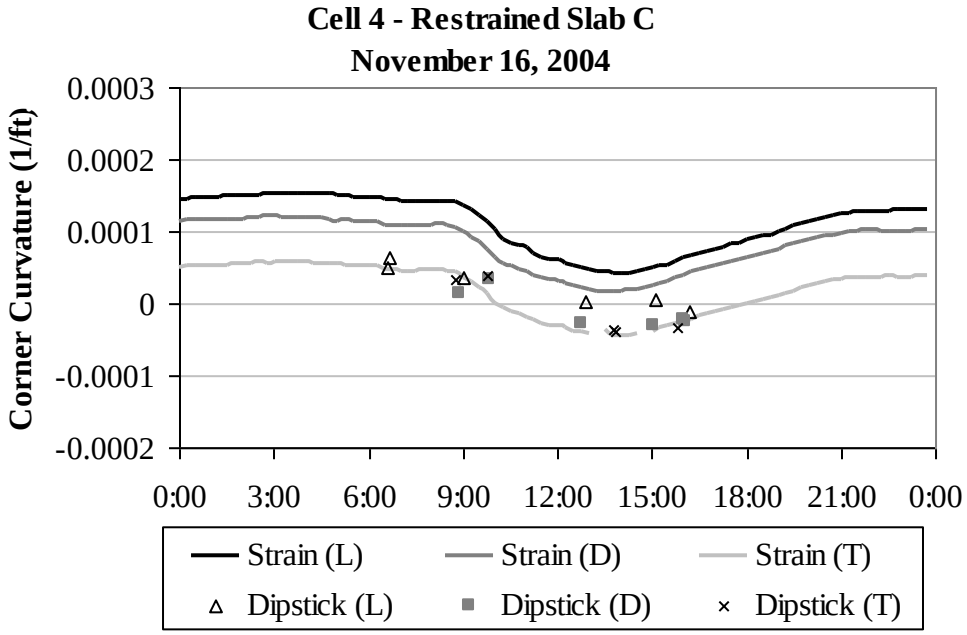

Figure D5. Curvature estimated from surface profiles and vibrating wire gages for restrained Slab C during the fall of 2004.

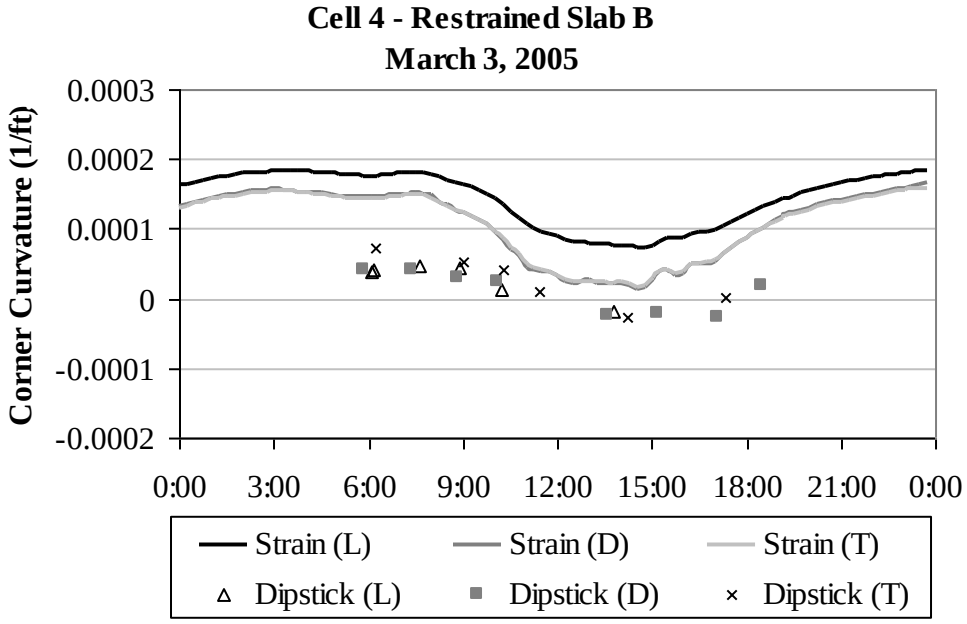

Figure D6. Curvature estimated from surface profiles and vibrating wire gages for restrained Slab B during the winter of 2005.

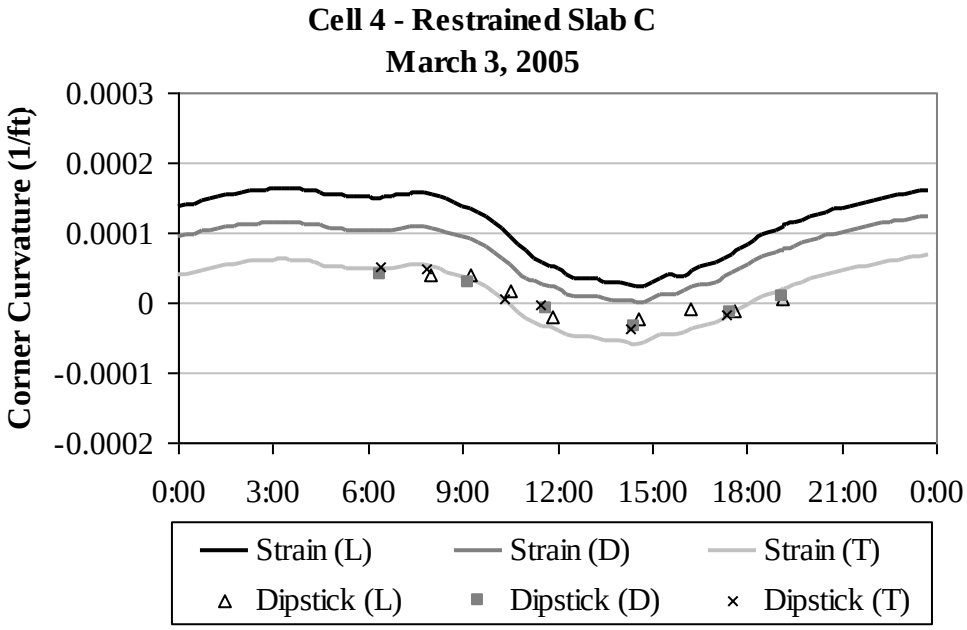

Figure D7. Curvature estimated from surface profiles and vibrating wire gages for restrained Slab C during the winter of 2005.

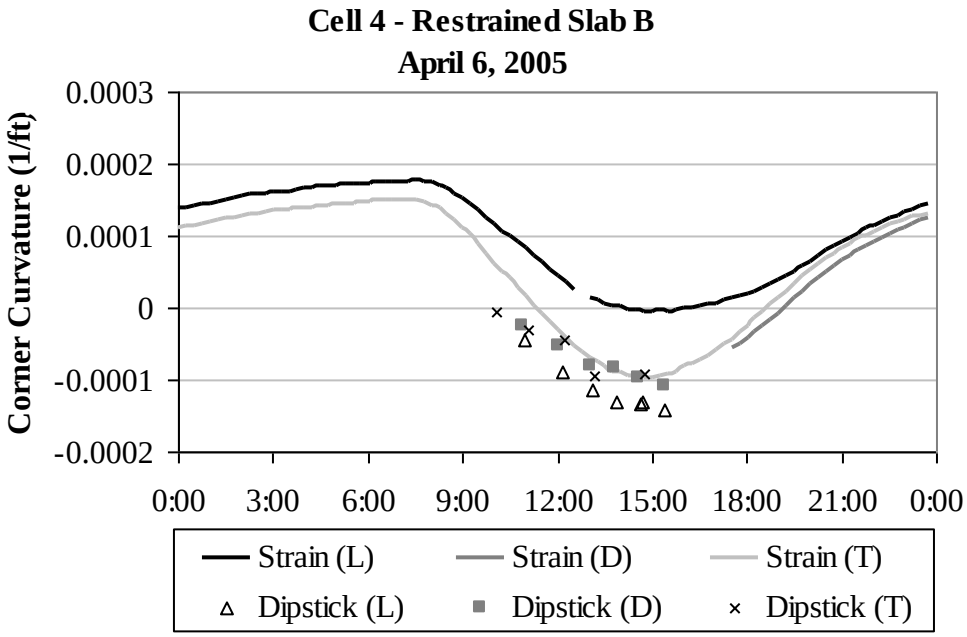

Figure D8. Curvature estimated from surface profiles and vibrating wire gages for restrained Slab B during the spring of 2005.

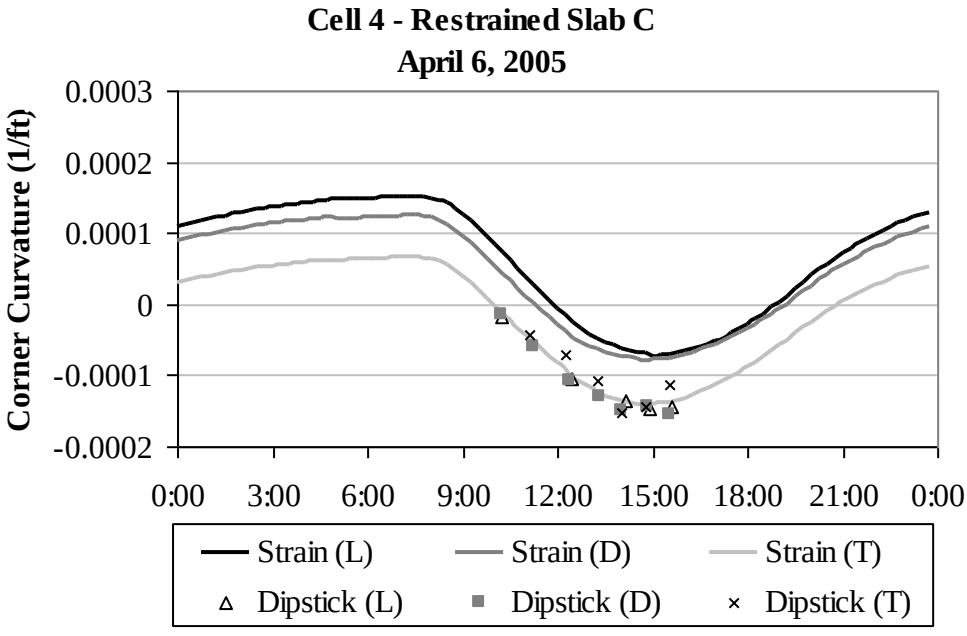

Figure D9. Curvature estimated from surface profiles and vibrating wire gages for restrained Slab C during the spring of 2005.

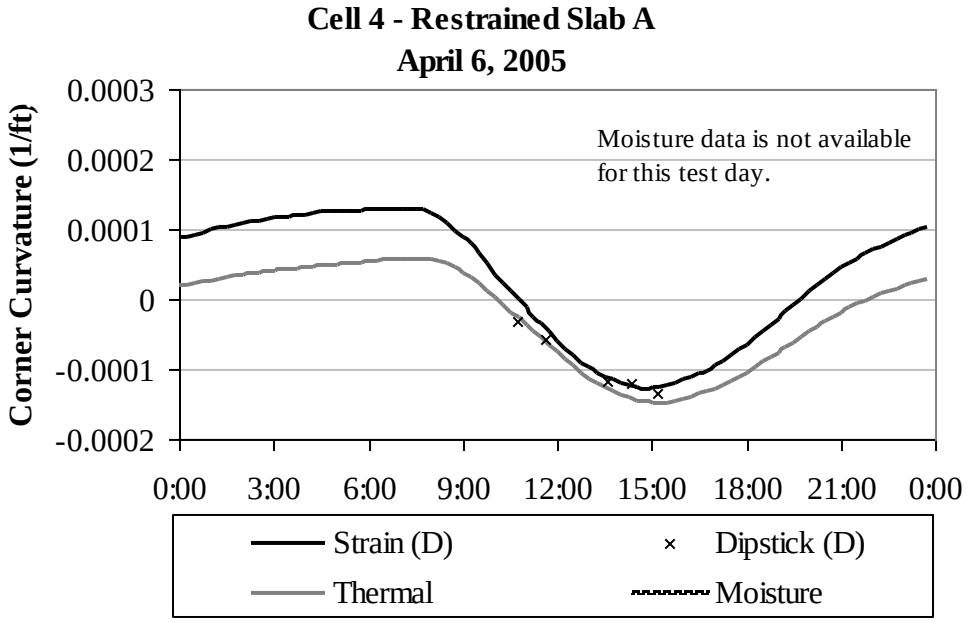

Figure D10. Comparison between curvatures estimated from the three types of data for restrained Slab A during the spring of 2005.

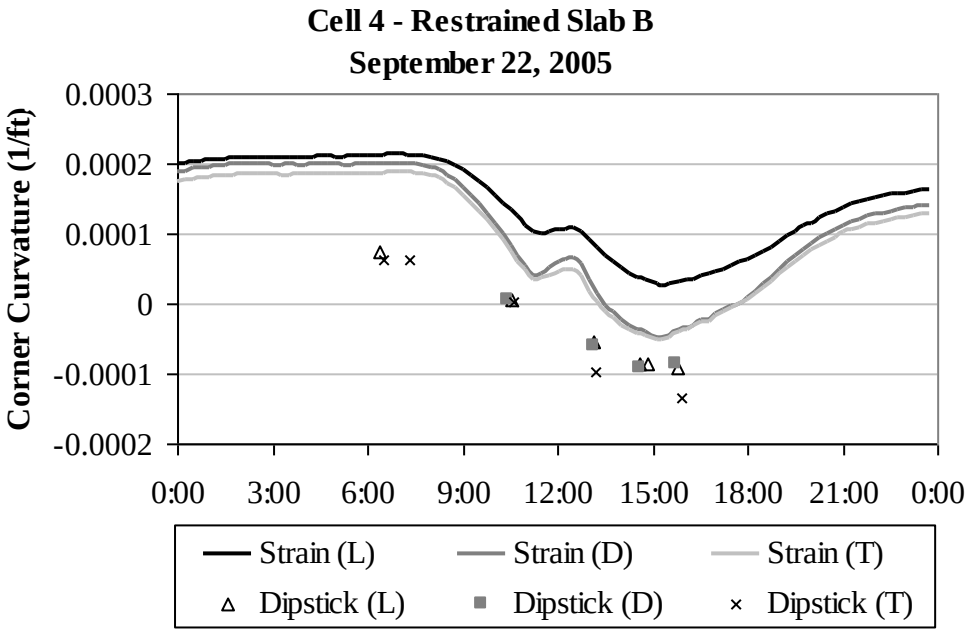

Figure D11. Curvature estimated from surface profiles and vibrating wire gages for restrained Slab B during the summer of 2005.

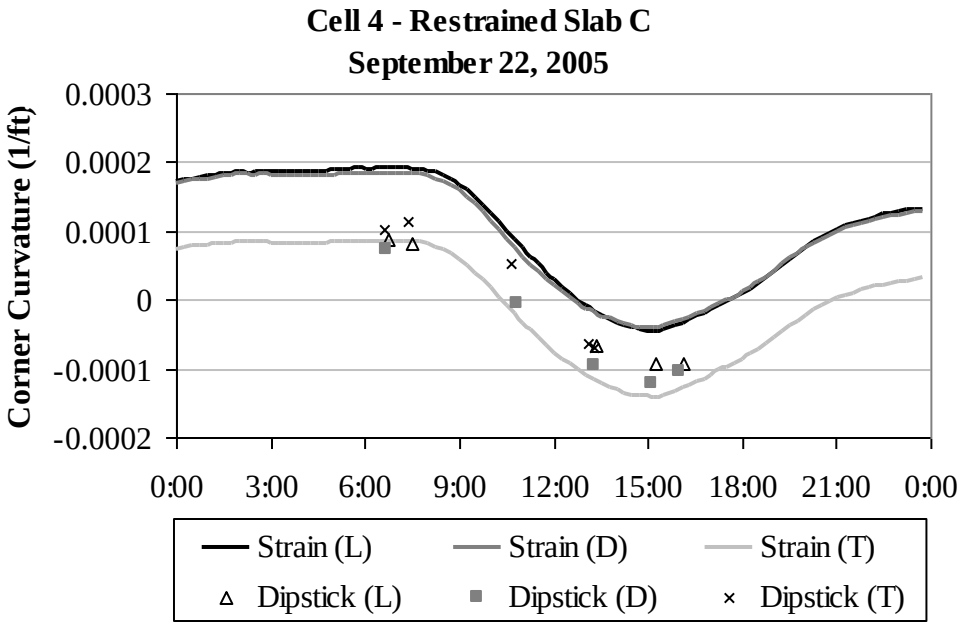

Figure D12. Curvature estimated from surface profiles and vibrating wire gages for restrained Slab C during the summer of 2005.

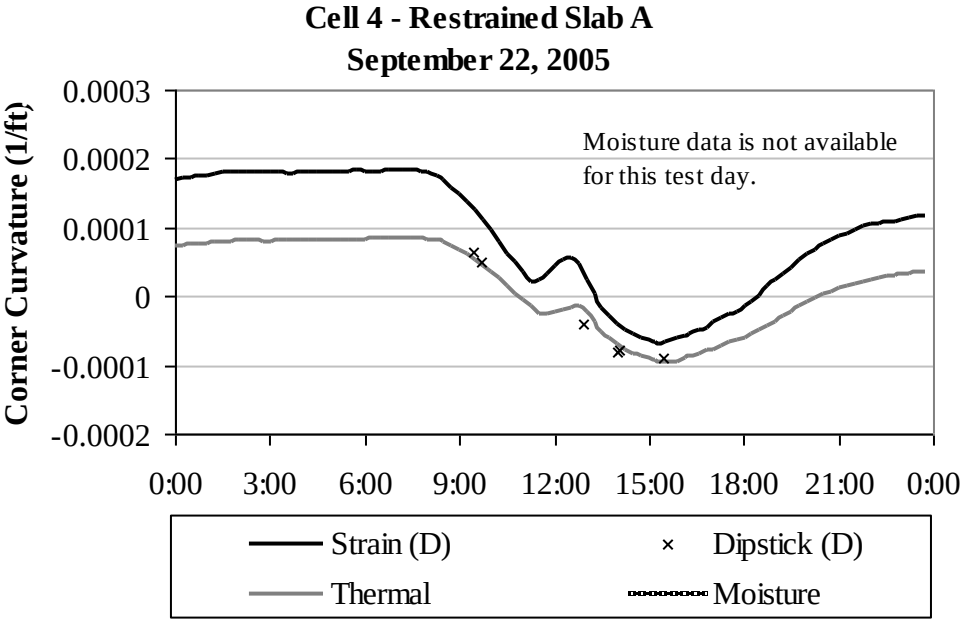

Figure D13. Comparison between curvatures estimated from the three types of data for restrained Slab A during the summer of 2005.

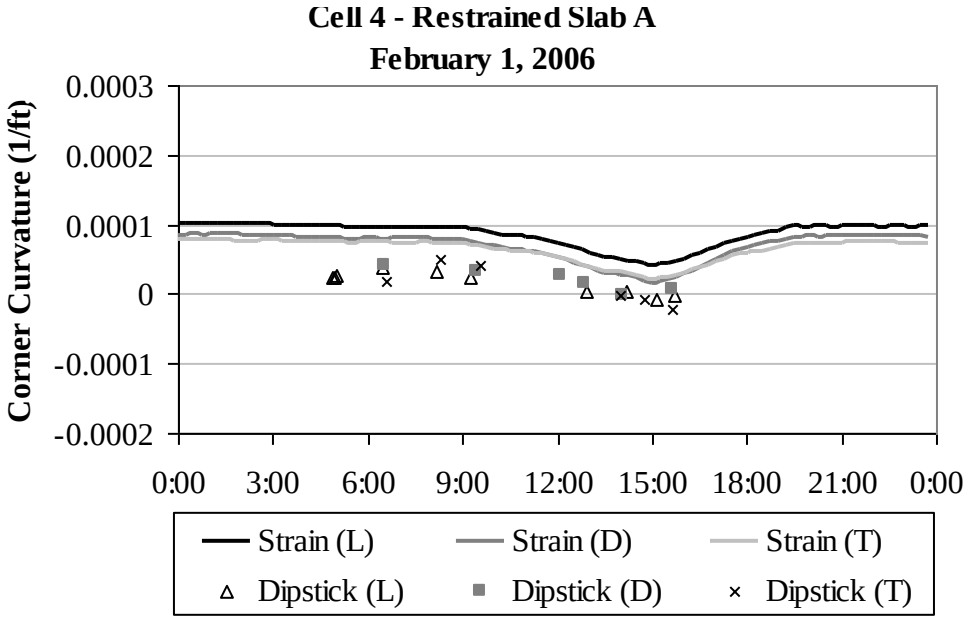

Figure D14. Curvature estimated from surface profiles and vibrating wire gages for restrained Slab A during the winter of 2006.

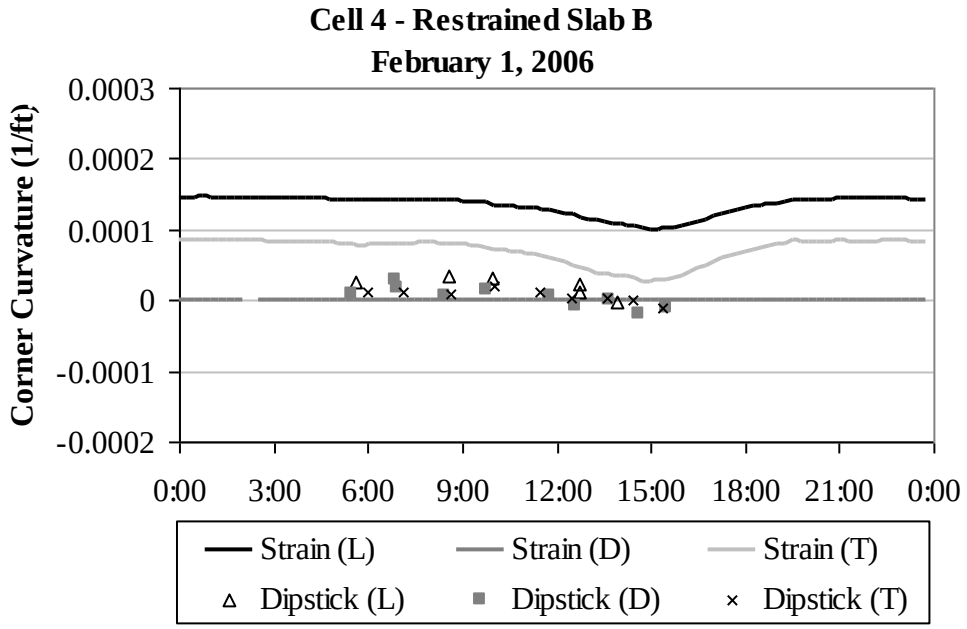

Figure D15. Curvature estimated from surface profiles and vibrating wire gages for restrained Slab B during the winter of 2006.

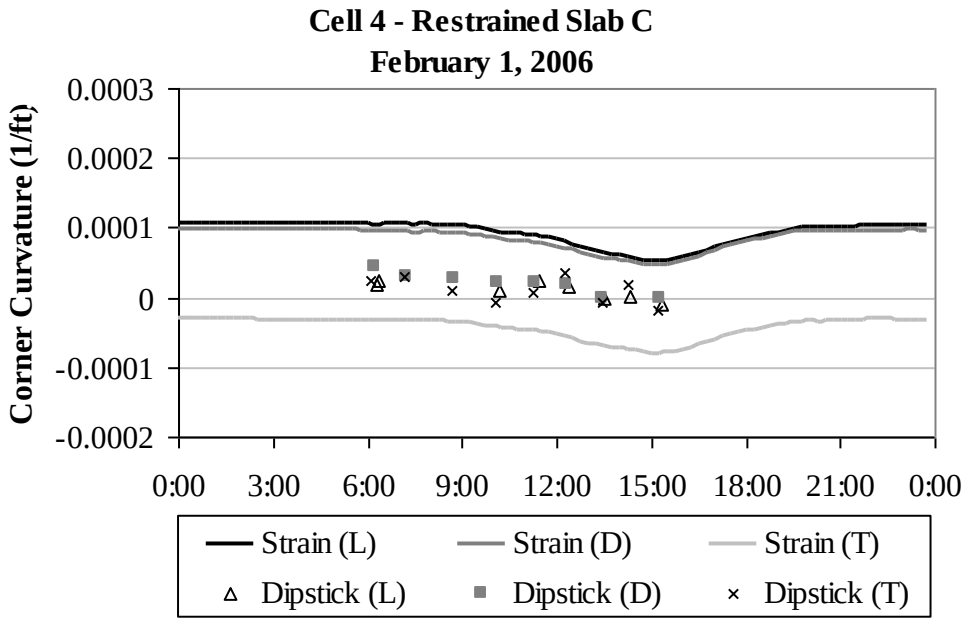

Figure D16. Curvature estimated from surface profiles and vibrating wire gages for restrained Slab C during the winter of 2006.

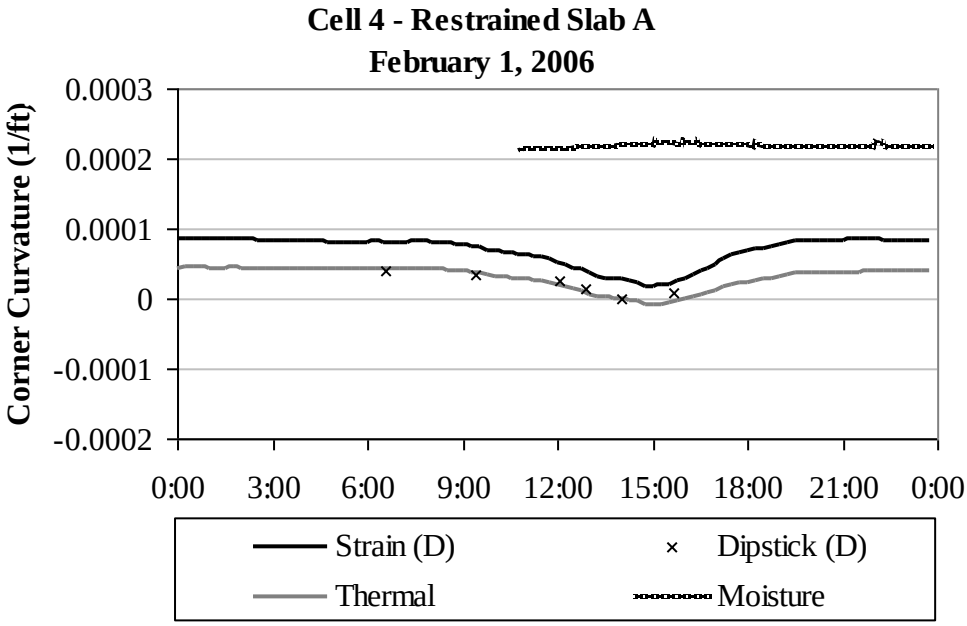

Figure D17. Comparison between curvatures estimated from the three types of data for restrained Slab A during the winter of 2006.

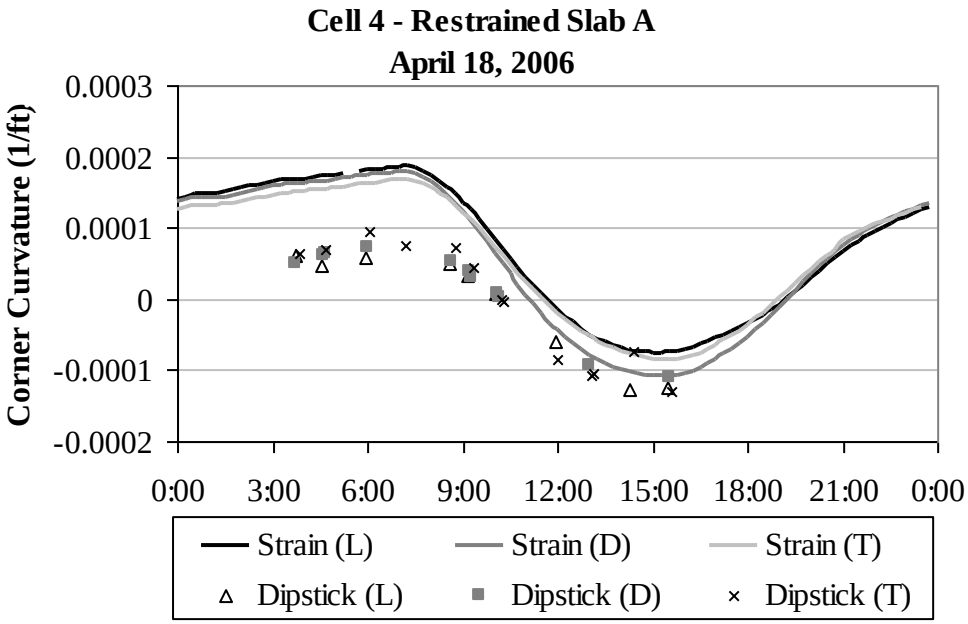

Figure D18. Curvature estimated from surface profiles and vibrating wire gages for restrained Slab A during the spring of 2006.

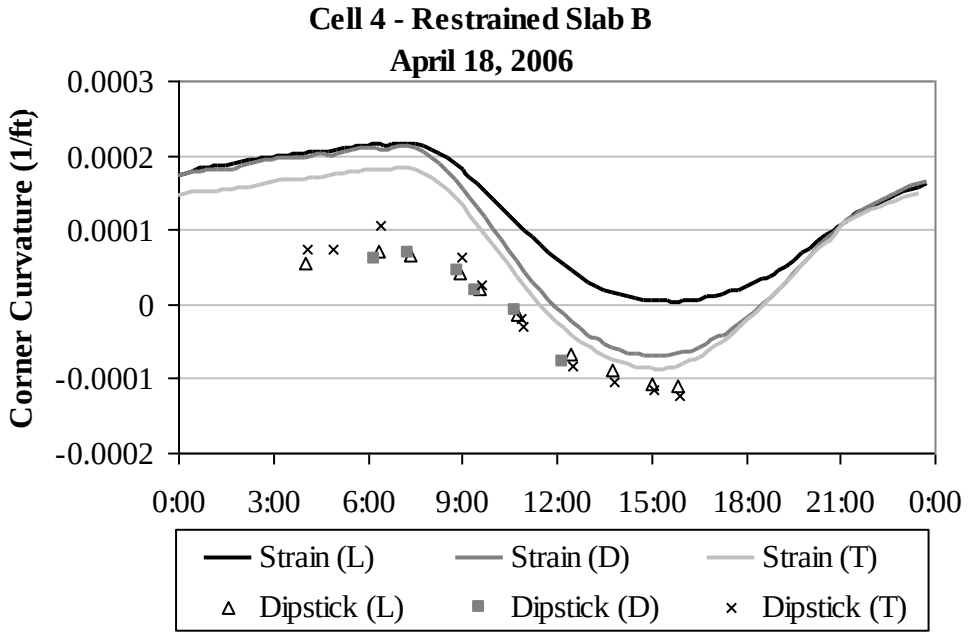

Figure D19. Curvature estimated from surface profiles and vibrating wire gages for restrained Slab B during the spring of 2006.

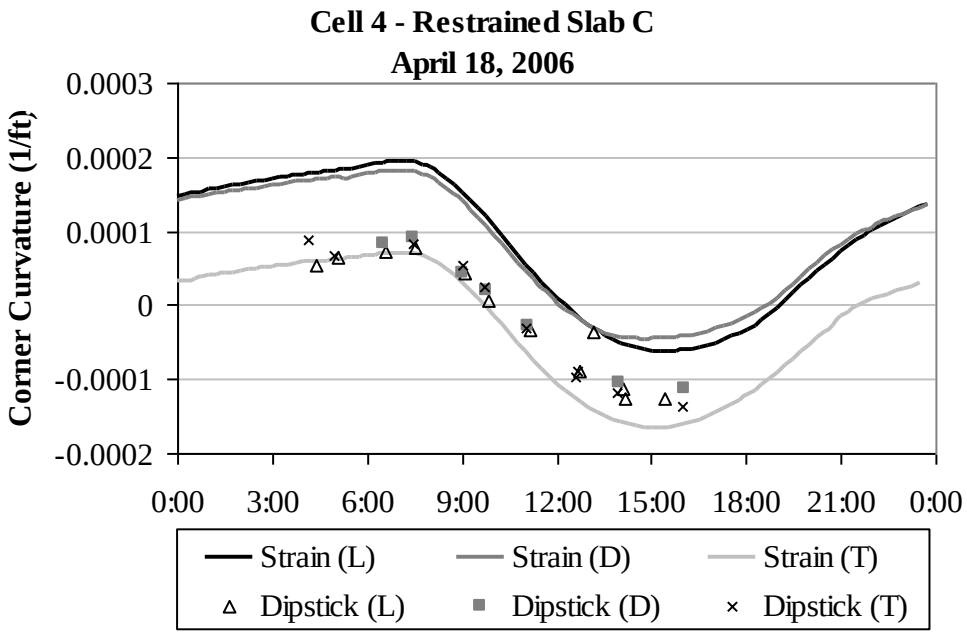

Figure D20. Curvature estimated from surface profiles and vibrating wire gages for restrained Slab C during the spring of 2006.

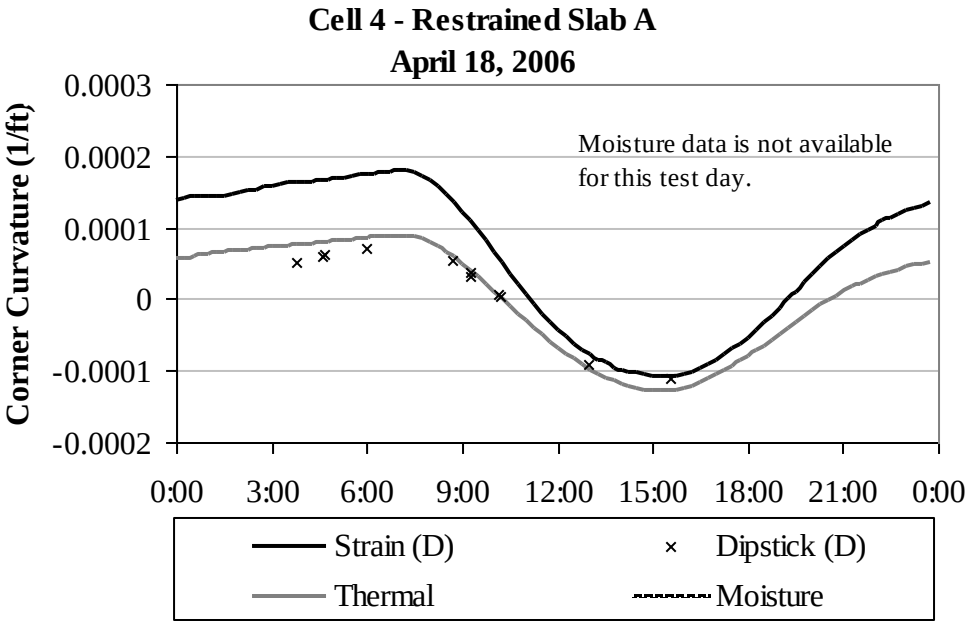

Figure D21. Comparison between curvatures estimated from the three types of data for restrained Slab A during the spring of 2006.

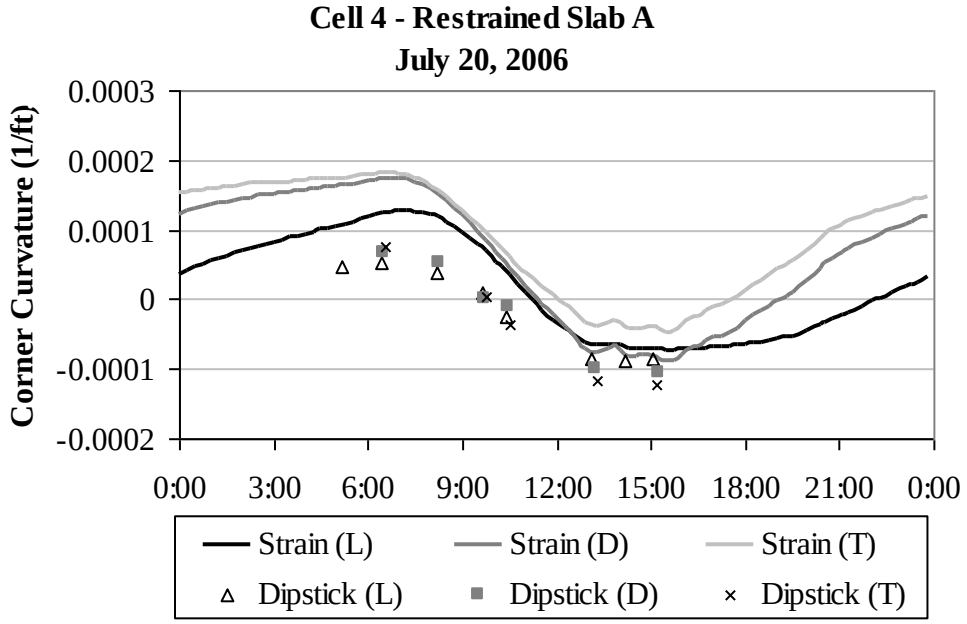

Figure D22. Curvature estimated from surface profiles and vibrating wire gages for restrained Slab A during the summer of 2006.

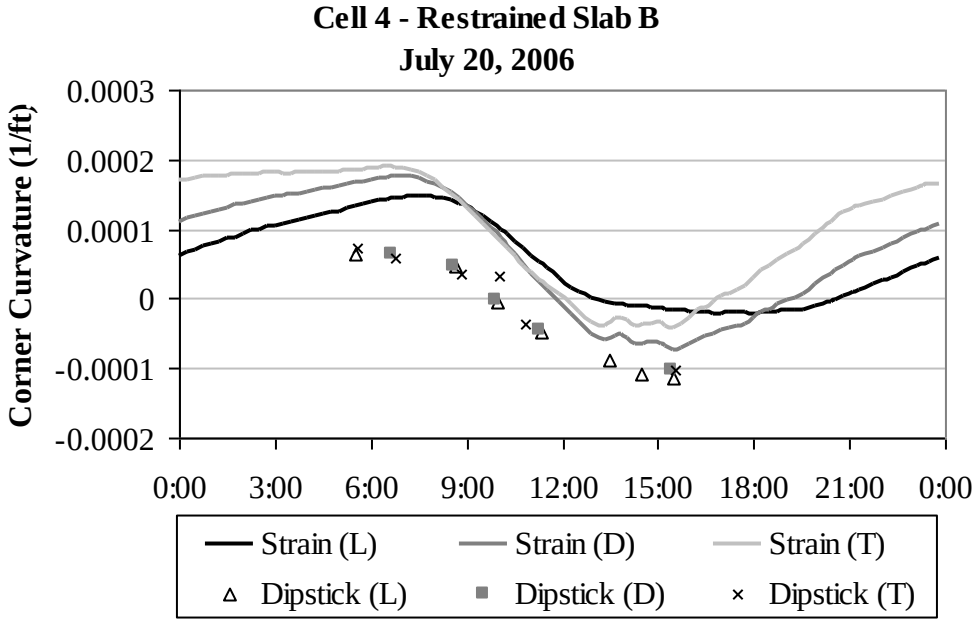

Figure D23. Curvature estimated from surface profiles and vibrating wire gages for restrained Slab B during the summer of 2006.

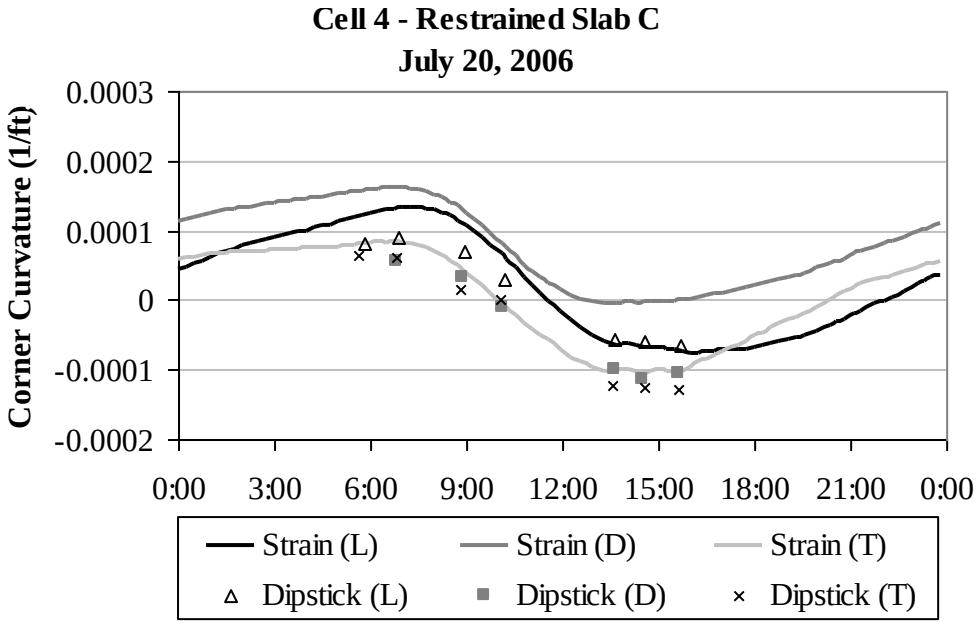

Figure D24. Curvature estimated from surface profiles and vibrating wire gages for restrained Slab C during the summer of 2006.

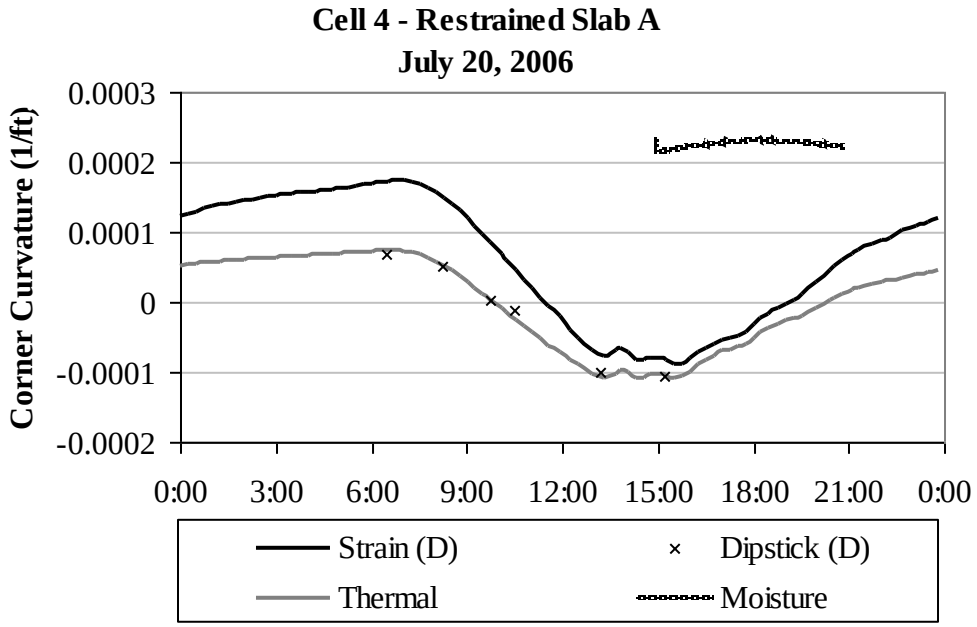

Figure D25. Comparison between curvatures estimated from the three types of data for restrained Slab A during the summer of 2006.

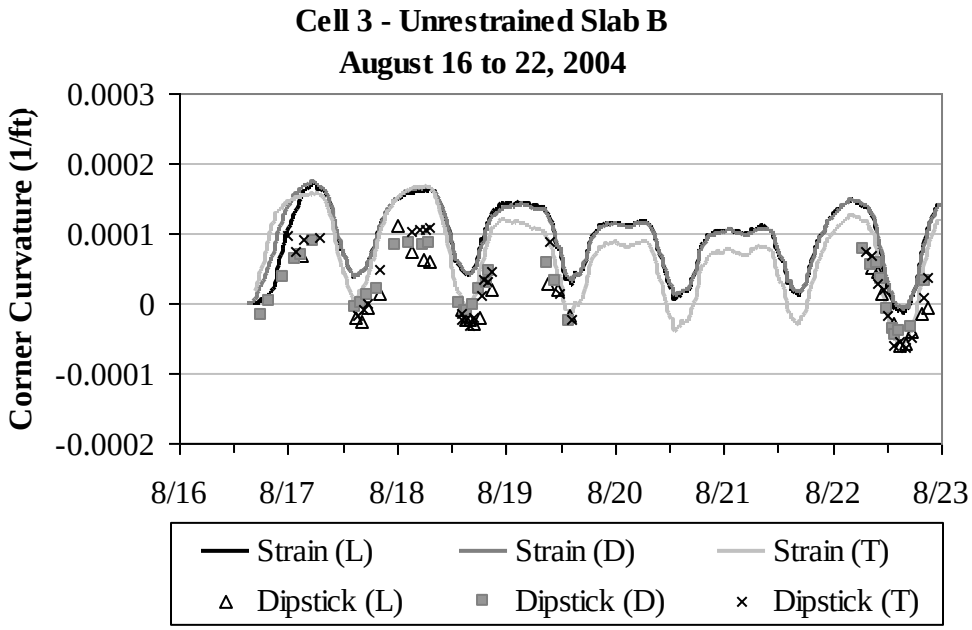

Figure D26. Curvature estimated from surface profiles and vibrating wire gages for unrestrained Slab B during the summer of 2004.

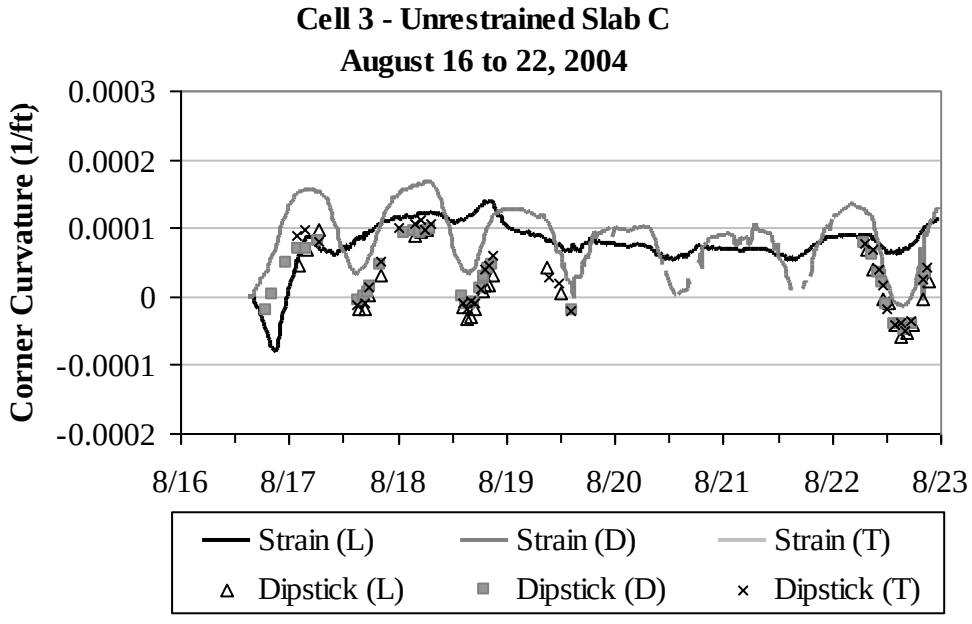

Figure D27. Curvature estimated from surface profiles and vibrating wire gages for unrestrained Slab C during the summer of 2004.

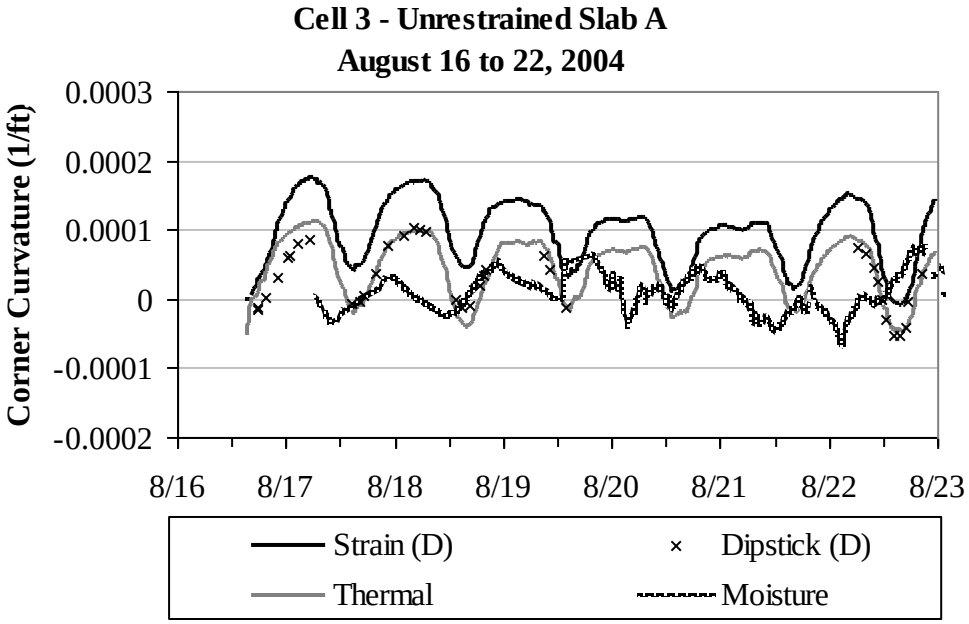

Figure D28. Comparison between curvatures estimated from the three types of data for restrained Slab A during the summer of 2004.

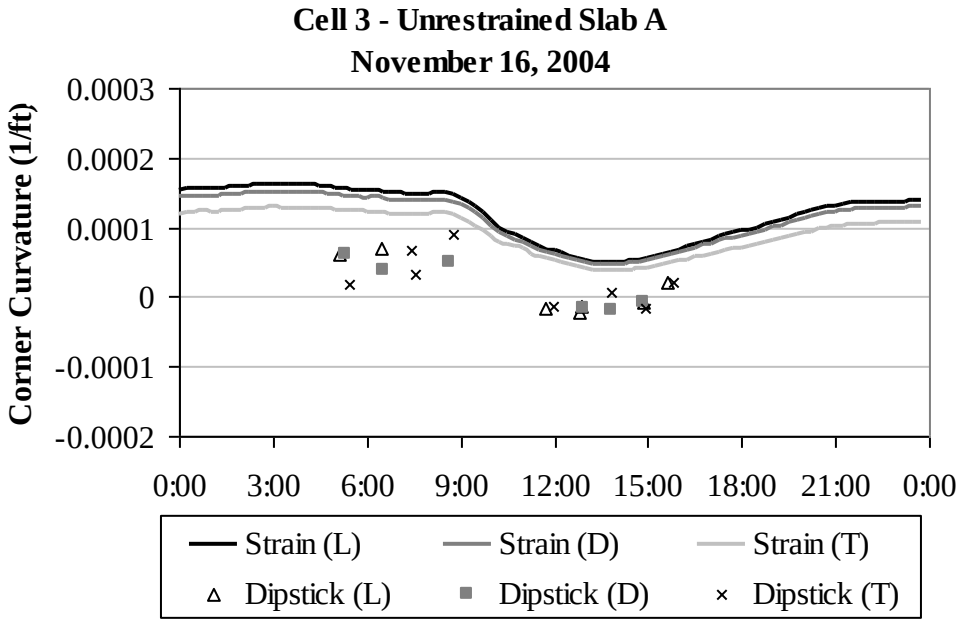

Figure D29. Curvature estimated from surface profiles and vibrating wire gages for unrestrained Slab A during the fall of 2004.

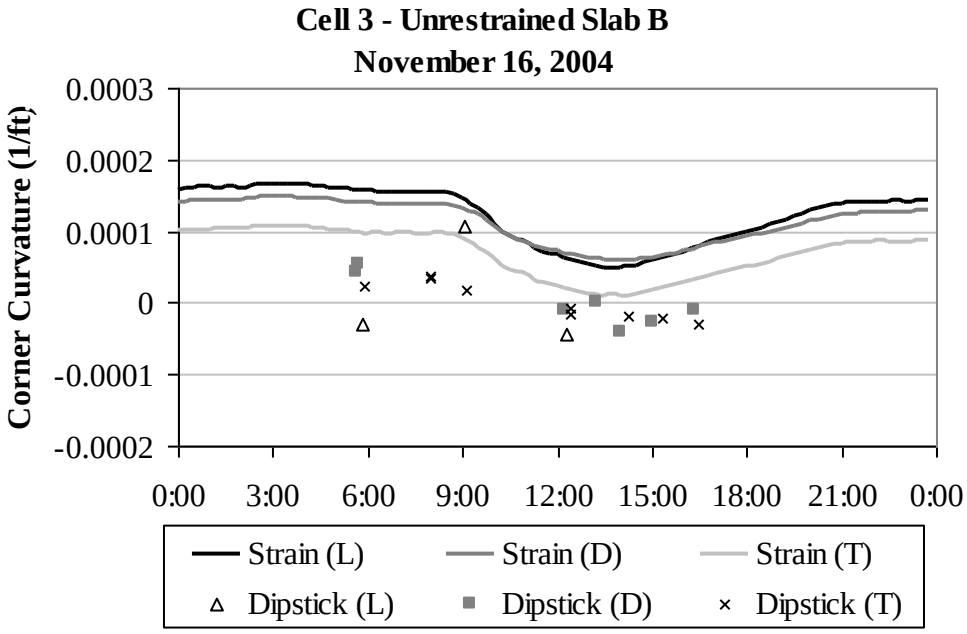

Figure D30. Curvature estimated from surface profiles and vibrating wire gages for unrestrained Slab B during the fall of 2004.

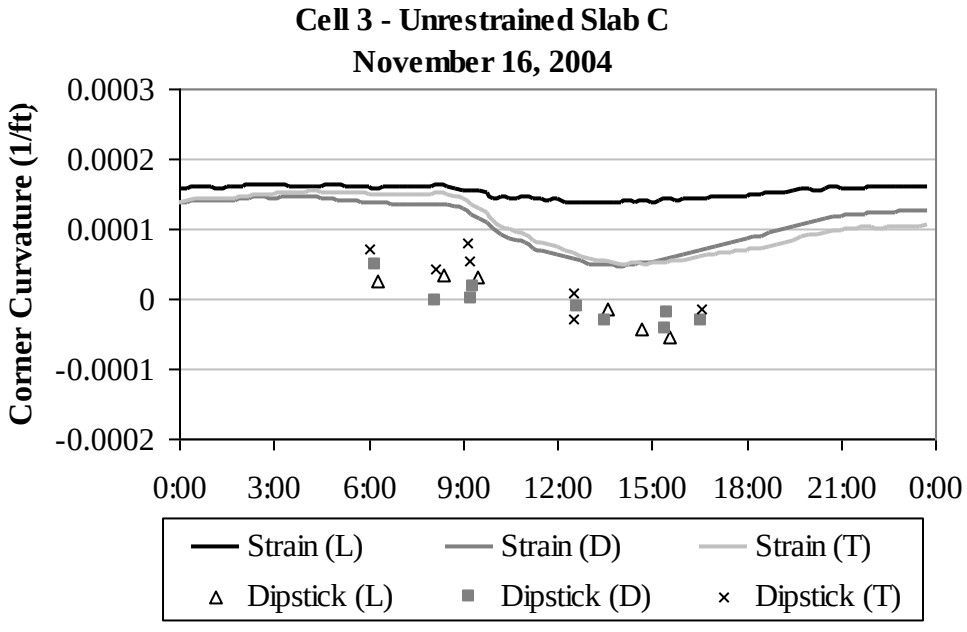

Figure D31. Curvature estimated from surface profiles and vibrating wire gages for unrestrained Slab C during the fall of 2004.

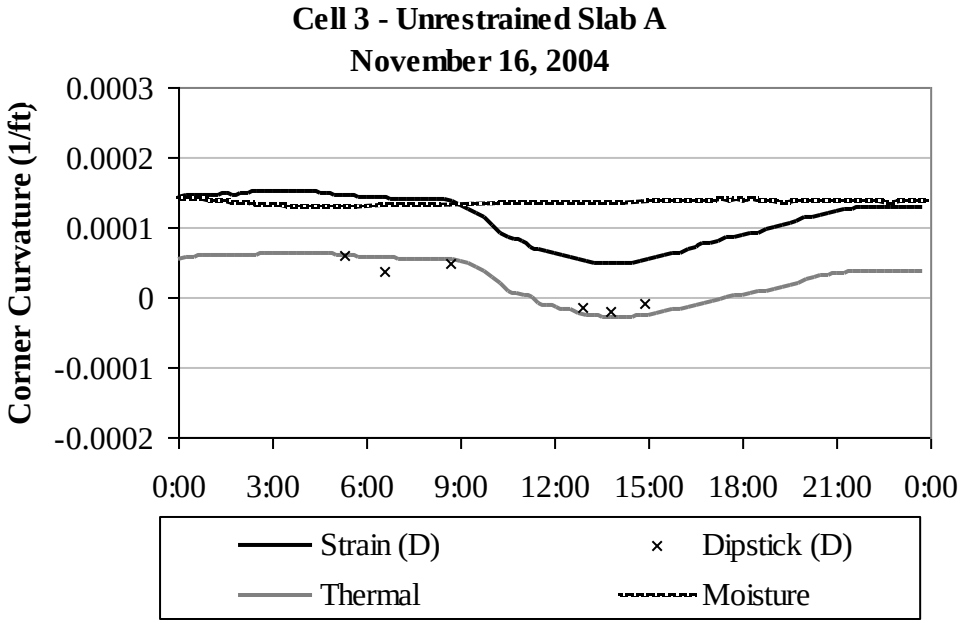

Figure D32. Comparison between curvatures estimated from the three types of data for restrained Slab A during the fall of 2004.

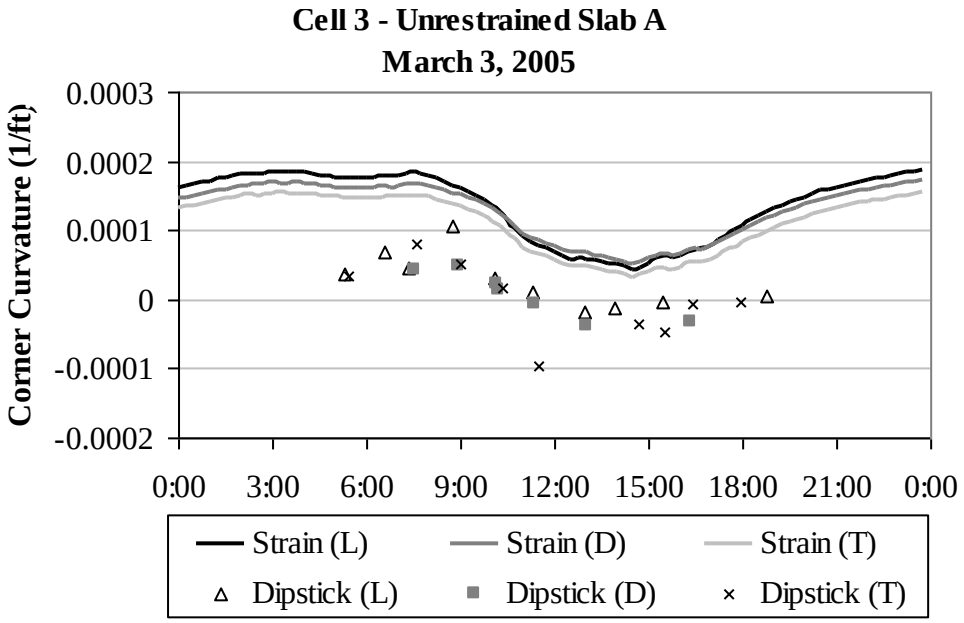

Figure D33. Curvature estimated from surface profiles and vibrating wire gages for unrestrained Slab A during the winter of 2005.

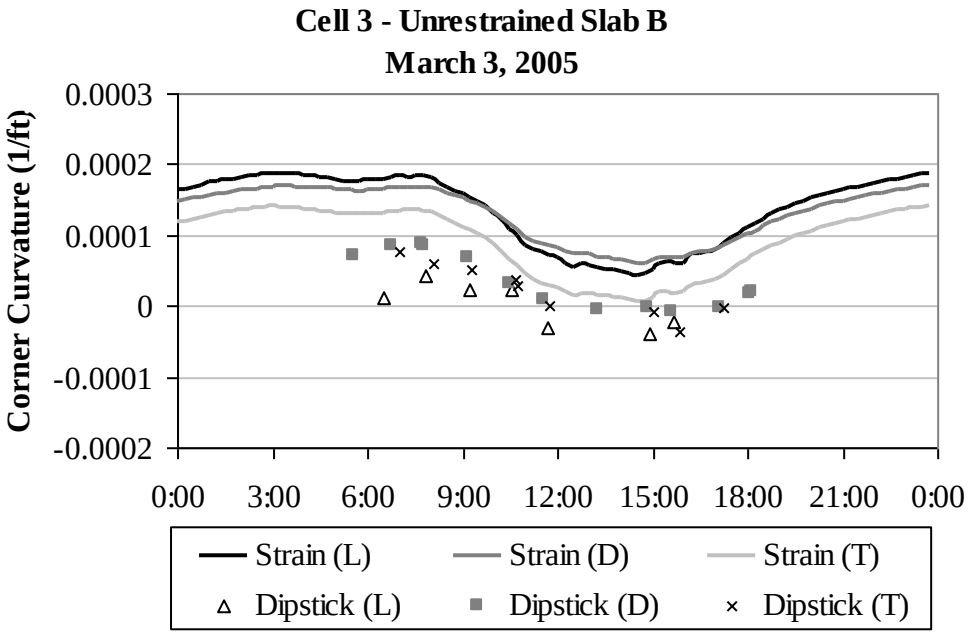

Figure D34. Curvature estimated from surface profiles and vibrating wire gages for unrestrained Slab B during the winter of 2005.

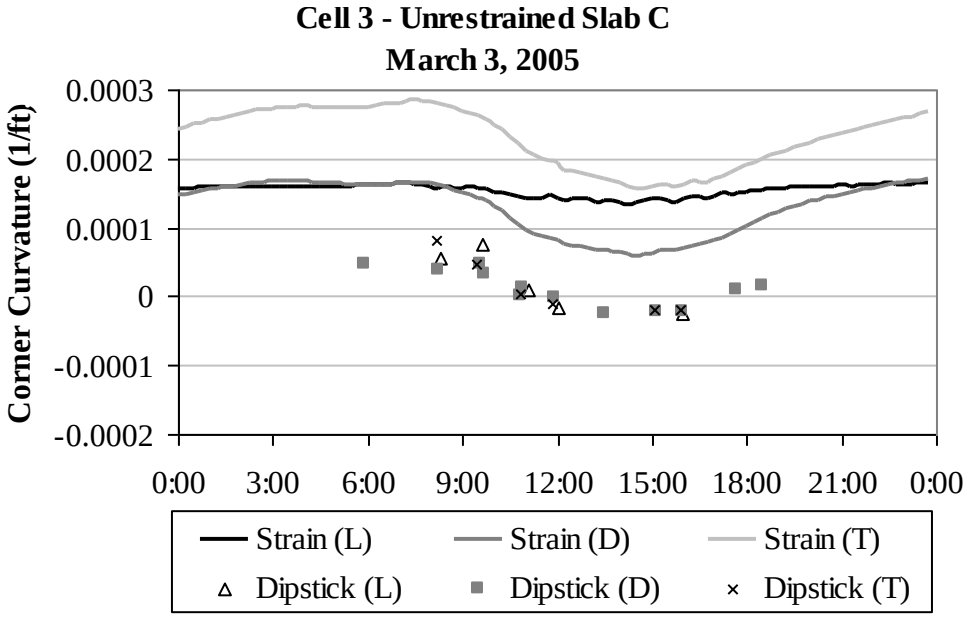

Figure D35. Curvature estimated from surface profiles and vibrating wire gages for unrestrained Slab C during the winter of 2005.

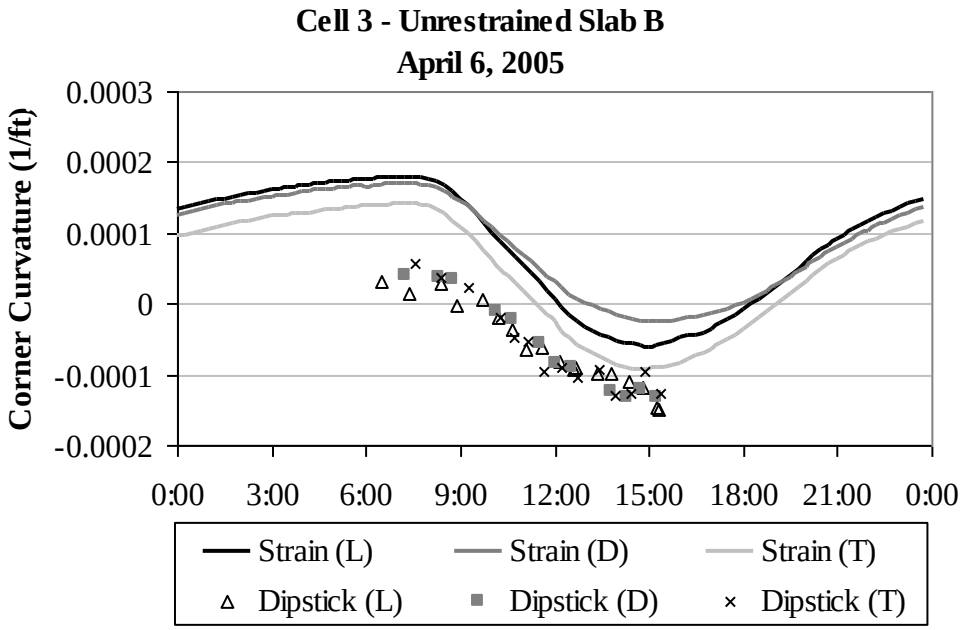

Figure D36. Curvature estimated from surface profiles and vibrating wire gages for unrestrained Slab B during the spring of 2005.

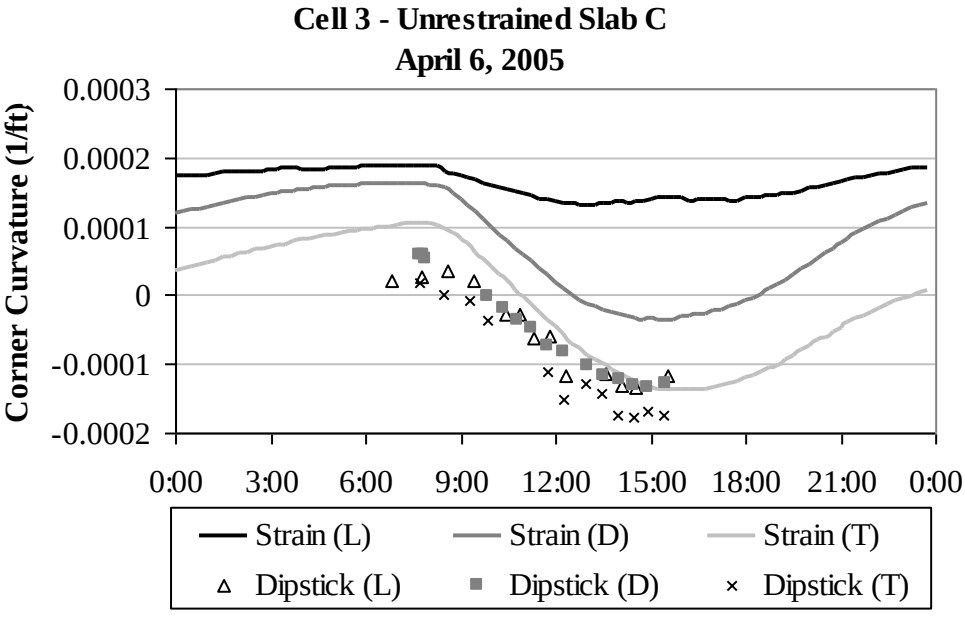

Figure D37. Curvature estimated from surface profiles and vibrating wire gages for unrestrained Slab C during the spring of 2005.

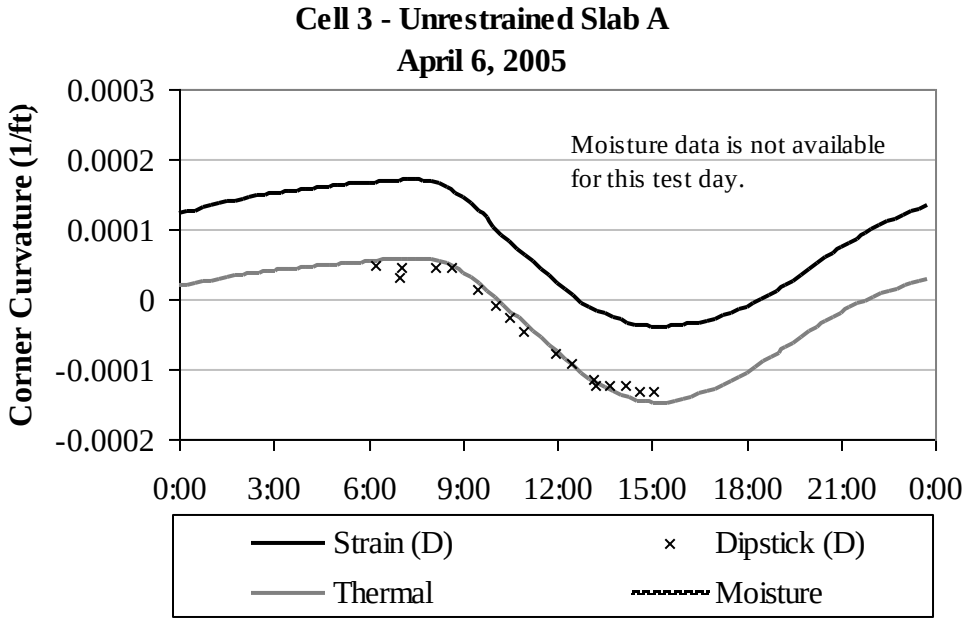

Figure D38. Comparison between curvatures estimated from the three types of data for restrained Slab A during the spring of 2005.

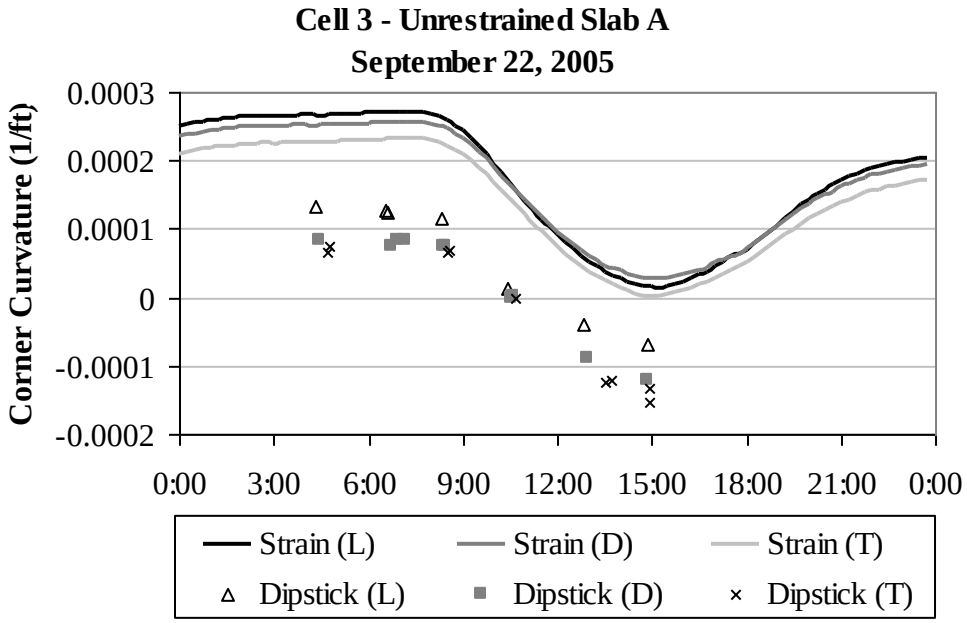

Figure D39. Curvature estimated from surface profiles and vibrating wire gages for unrestrained Slab A during the summer of 2005.

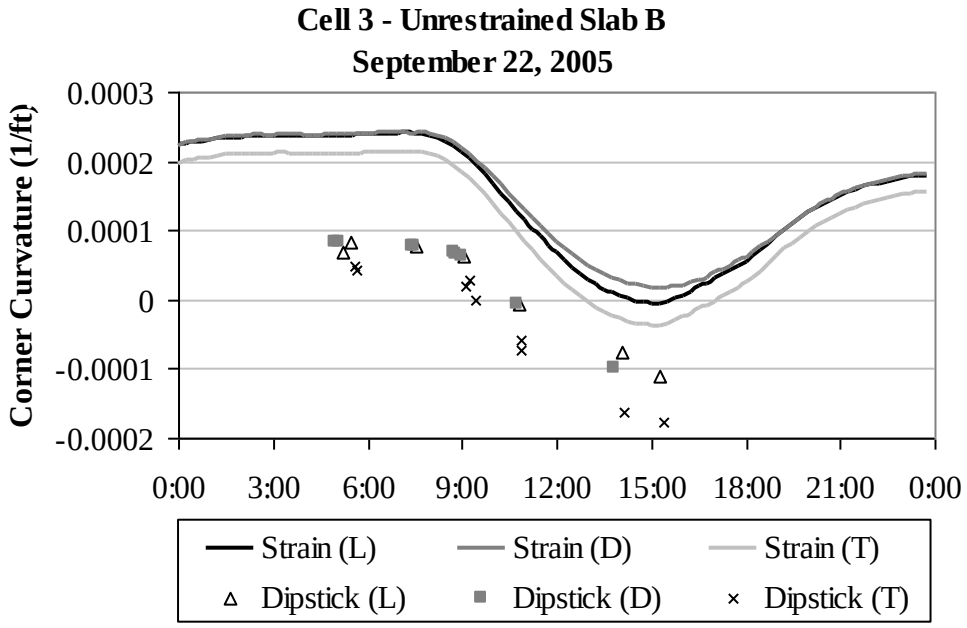

Figure D40. Curvature estimated from surface profiles and vibrating wire gages for unrestrained Slab B during the summer of 2005.

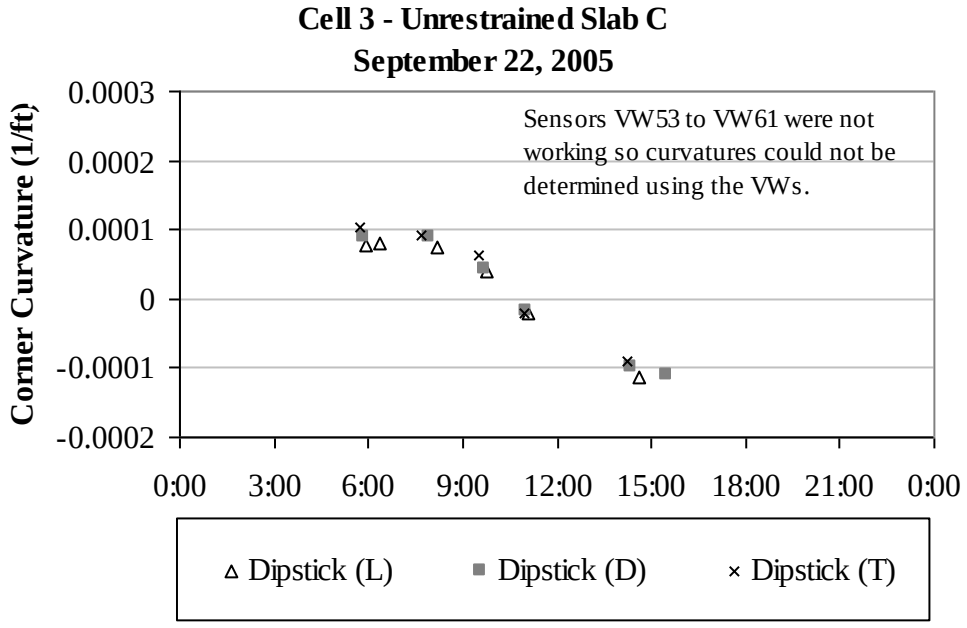

Figure D41. Curvature estimated from surface profiles and vibrating wire gages for unrestrained Slab C during the summer of 2005 (No vibrating wire data is available from the strain sensors).

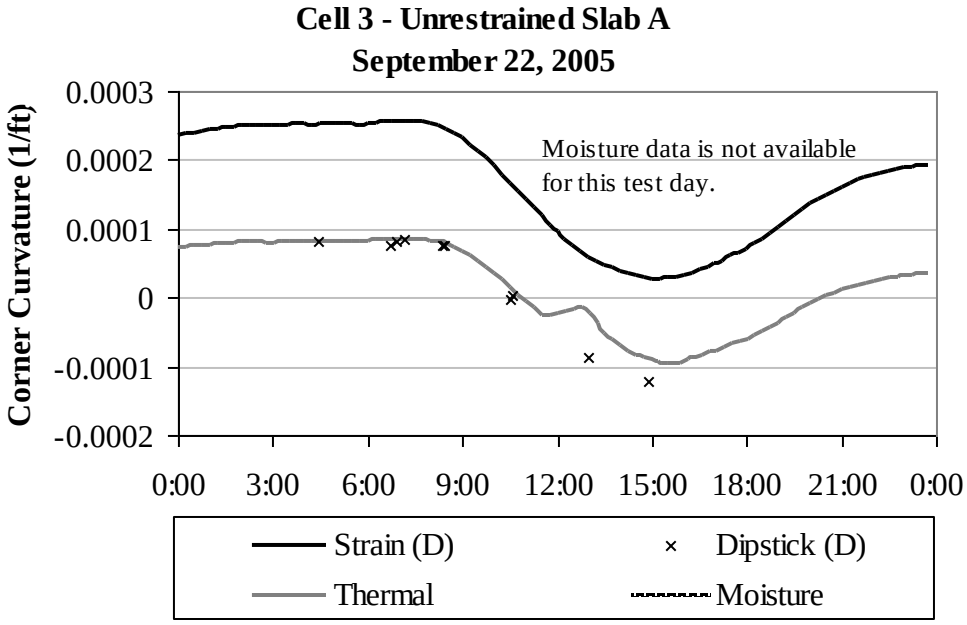

Figure D42. Comparison between curvatures estimated from the three types of data for restrained Slab A during the summer of 2005.

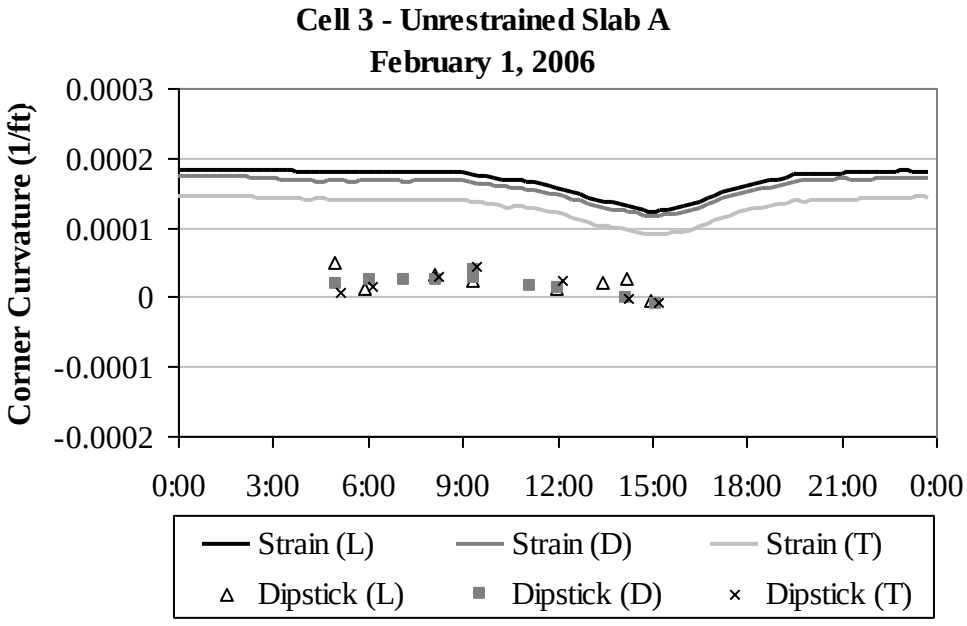

Figure D43. Curvature estimated from surface profiles and vibrating wire gages for unrestrained Slab A during the winter of 2006.

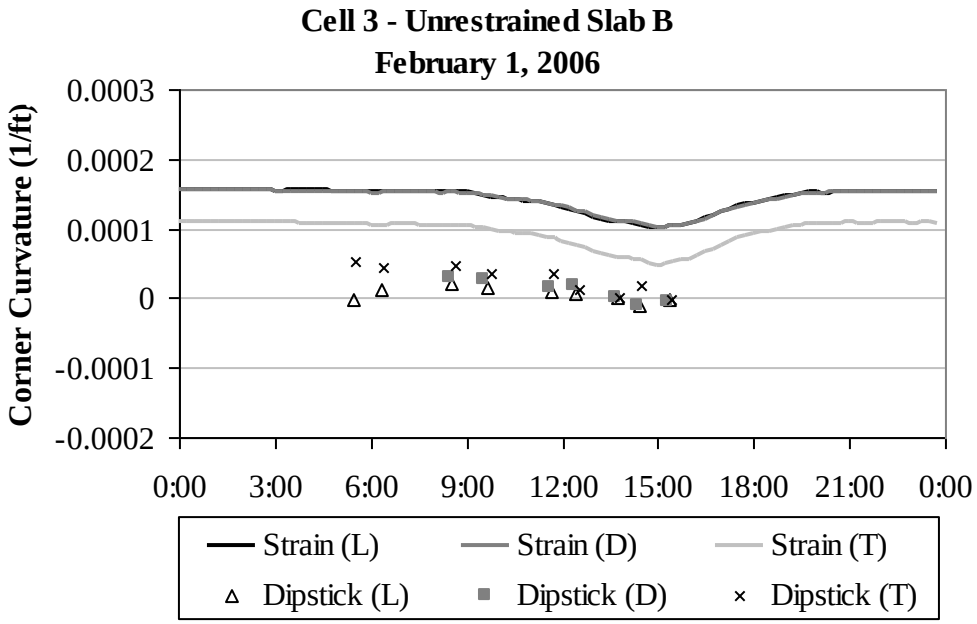

Figure D44. Curvature estimated from surface profiles and vibrating wire gages for unrestrained Slab B during the winter of 2006.

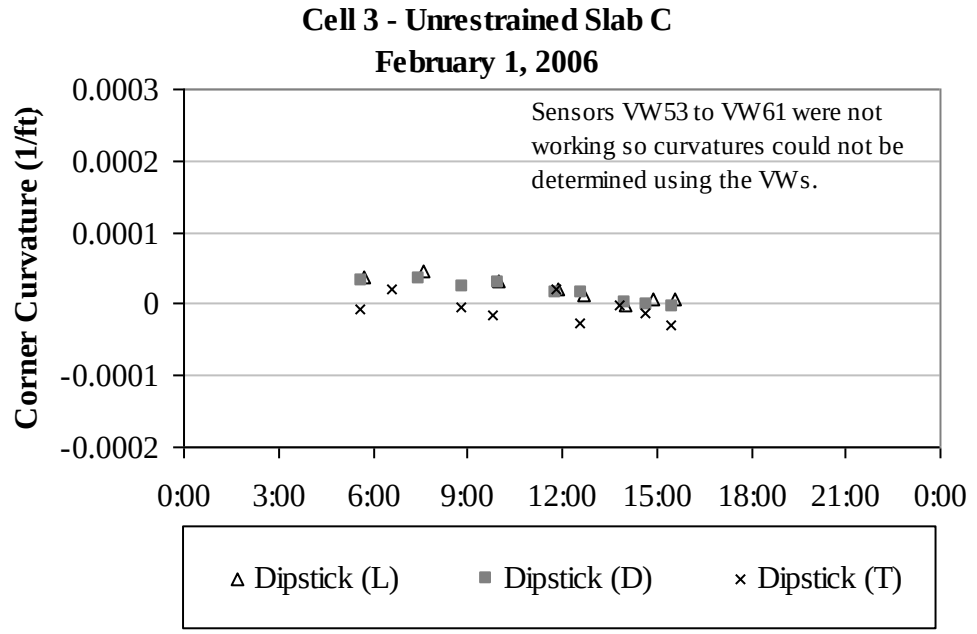

Figure D45. Curvature estimated from surface profiles and vibrating wire gages for unrestrained Slab C during the winter of 2006 (No vibrating wire data is available from the strain sensors).

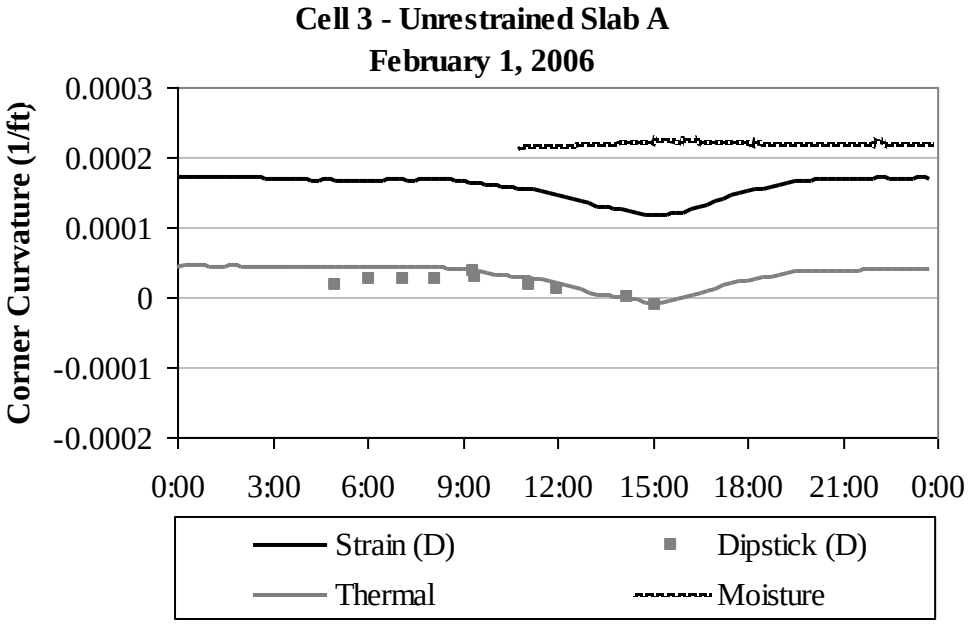

Figure D46. Comparison between curvatures estimated from the three types of data for restrained Slab A during the winter of 2006.

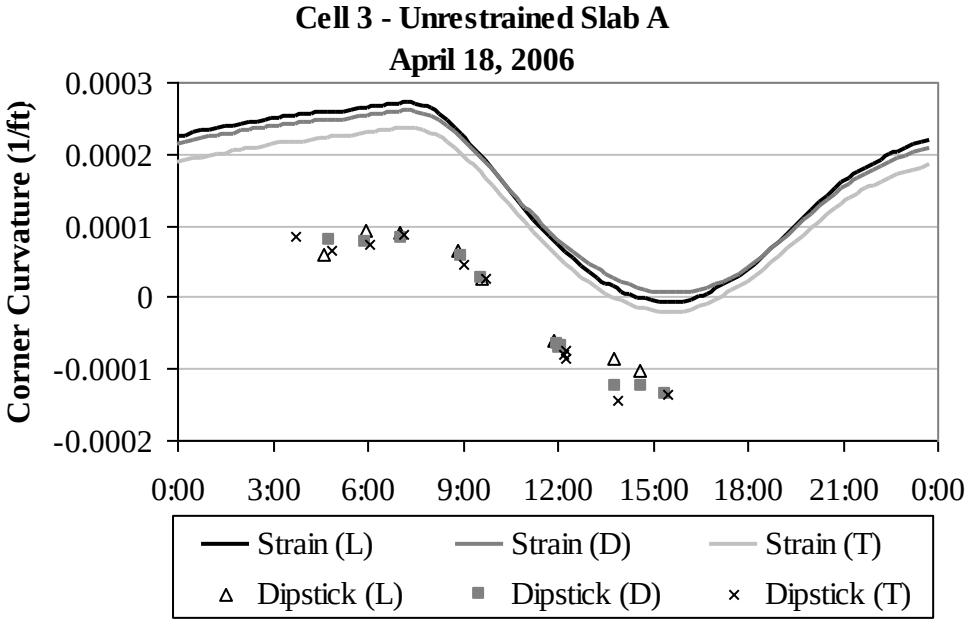

Figure D47. Curvature estimated from surface profiles and vibrating wire gages for unrestrained Slab A during the spring of 2006.

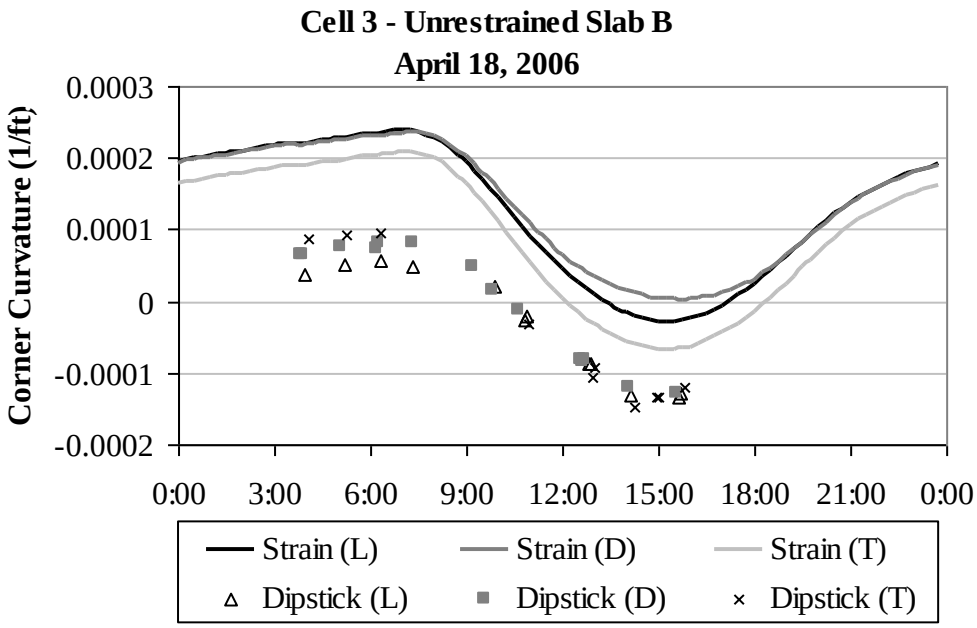

Figure D48. Curvature estimated from surface profiles and vibrating wire gages for unrestrained Slab B during the spring of 2006.

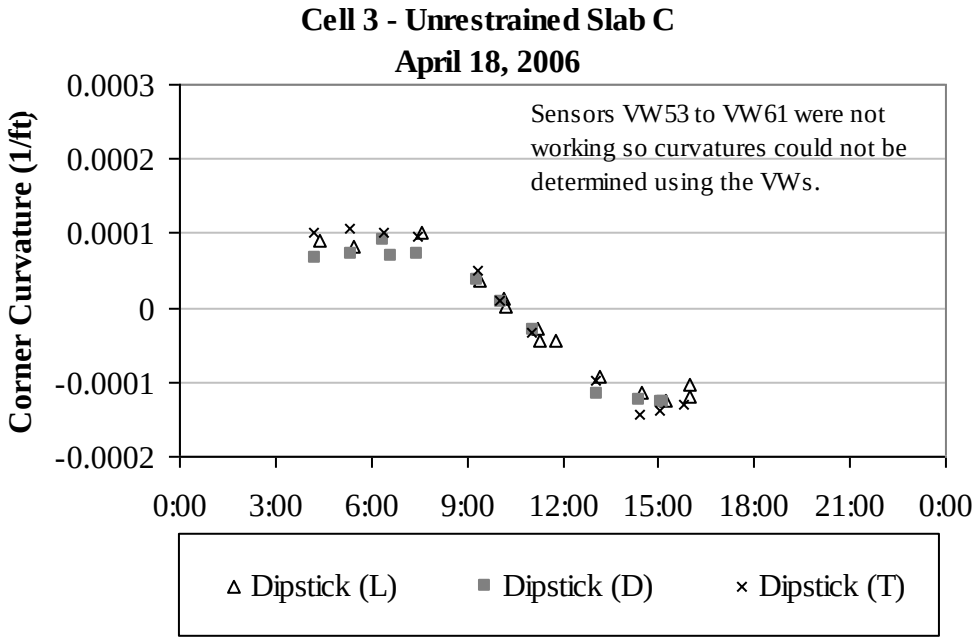

Figure D49. Curvature estimated from surface profiles and vibrating wire gages for unrestrained Slab C during the spring of 2006 (No vibrating wire data is available from the strain sensors).

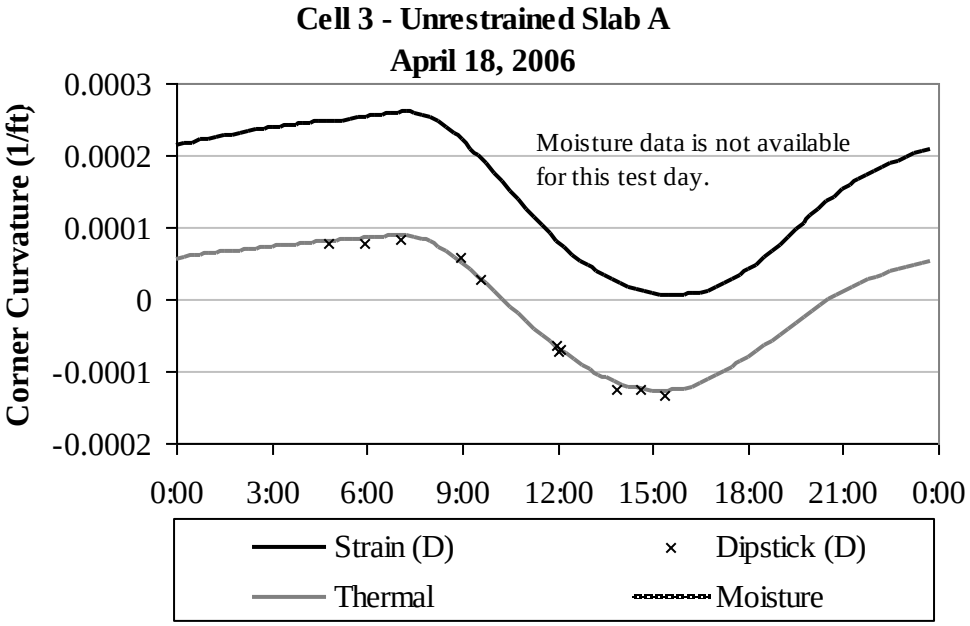

Figure D50. Comparison between curvatures estimated from the three types of data for restrained Slab A during the spring of 2006.

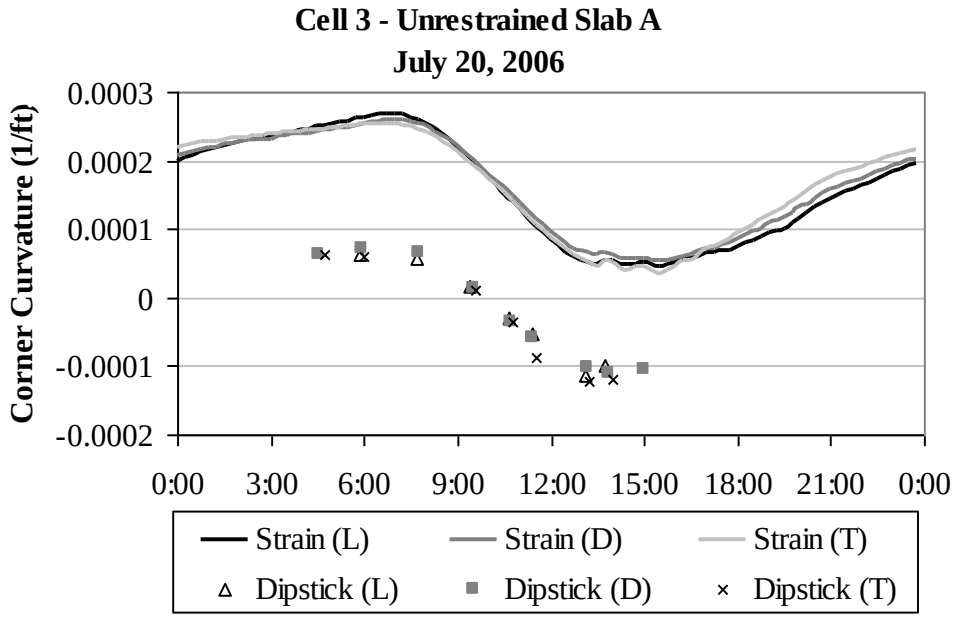

Figure D51. Curvature estimated from surface profiles and vibrating wire gages for unrestrained Slab A during the summer of 2006.

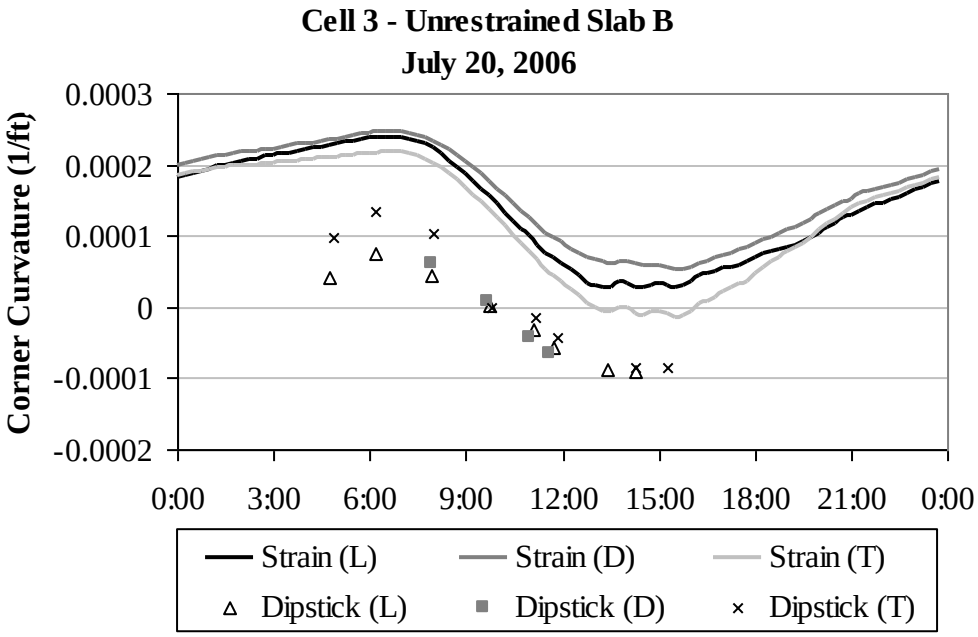

Figure D52. Curvature estimated from surface profiles and vibrating wire gages for unrestrained Slab B during the summer of 2006.

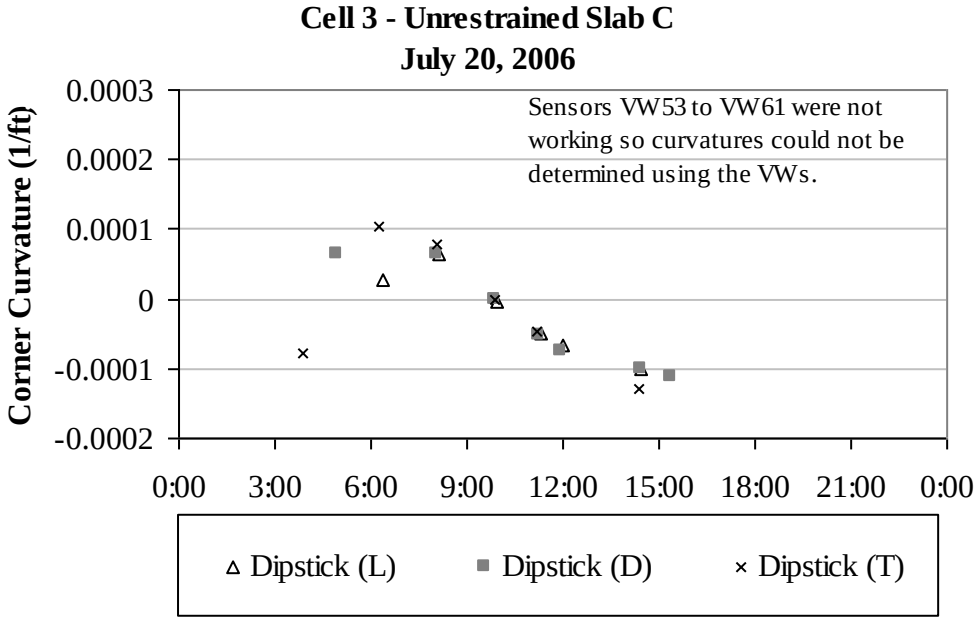

Figure D53. Curvature estimated from surface profiles and vibrating wire gages for unrestrained Slab C during the summer of 2006 (No vibrating wire data is available from the strain sensors).

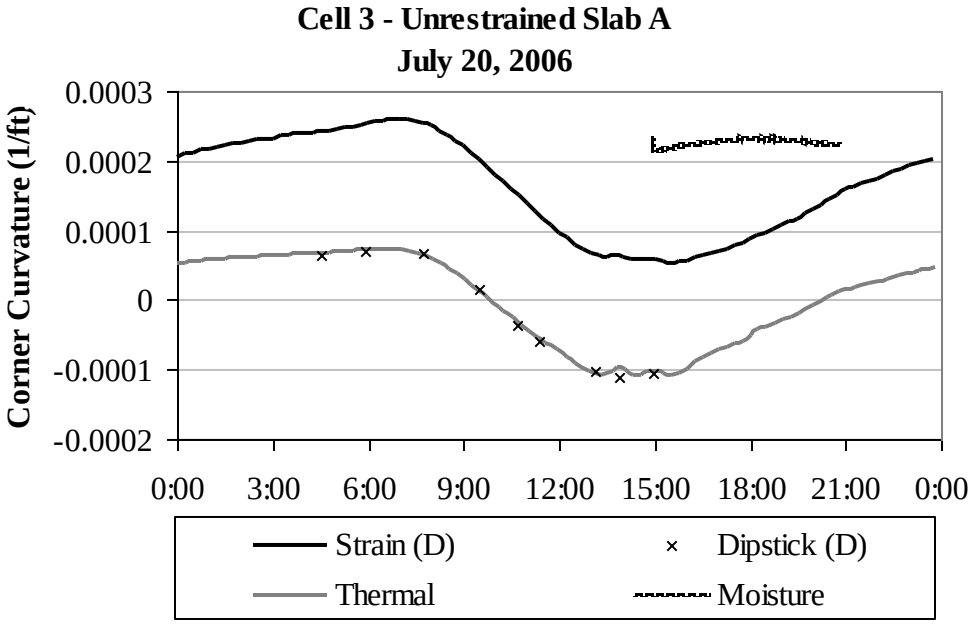

Figure D54. Comparison between curvatures estimated from the three types of data for restrained Slab A during the summer of 2006.

BIBLIOGRAPHY

Ahmed, Z., Marukic, I., Zaghloul, S., and Vitillo, N. 2005. "Validation of Enhanced Integrated Climatic Model Predictions Using New Jersey Seasonal Monitoring Data." Paper presented at 84th Annual Meeting, Transportation Research Board, Washington D.C.

American Association of State Highway and Transportation Officials (AASHTO). 1993. *Guide for Design of Pavement Structures*. Washington, D.C.

ARA, Inc., ERES Consultants Division. March 2004. *Guide for Mechanistic-Empirical Design of New and Rehabilitated Pavement Structures. Final Report*. National Cooperative Highway Research Program. Transportation Research Board, National Research Council. Champaign, Illinois.

Armaghani, J.M., T.J. Larsen, and L.L. Smith. 1987. Temperature Response of Concrete Pavement. Transportation Research Record 1121. Washington, DC: Transportation Research Board (TRB), National Research Council, pp. 23–33.

Asbahan, R. E., McCracken, J. K. and Vandenbossche, J. M. November 2006. *S.R.-22 Smart Pavement Phase II: One-Year Material Properties and Pavement Response Characteristics for Jointed Plain Concrete Pavements*. Submitted to the Pennsylvania Department of Transportation and the Federal Highway Administration, University of Pittsburgh, Department of Civil and Environmental Engineering. Pittsburgh, Pennsylvania.

ASTM. 1999a. "Standard Test Method for Slump of Hydraulic Cement Concrete." *ASTM C143, Annual Book of ASTM Standards*, West Conshohocken, Pa. ASTM.

ASTM. 1999b. "Standard Test Method for Air Content of Freshly Mixed Concrete by the Pressure Method." *ASTM C231, Annual Book of ASTM Standards*.

Beckemeyer, C. A., Khazanovich, L., and Yu, H. T. 2002. Determining amount of built-in curling in jointed plain concrete pavement: Case study of Pennsylvania I-80. *Transportation Research Record 1809*. Transportation Research Board. Washington, D.C. pp. 85–92.

Bergstrom, S.G. 1950. "Temperature stresses in concrete pavements". *Proceedings, Handlingar*, Swedish Cement and Concrete Research Institute, N:R 14, Sweden.

Bradbury, R. D. 1938. *Reinforced Concrete Pavements*. Wire Reinforcement Institute. Washington, D.C.

Byrum, C. R. 2000. Analysis by high-speed profile of jointed concrete pavement slab curvatures. *Transportation Research Record 1730*. Transportation Research Board. Washington, D.C. pp. 1–9.

Campbell Scientific, Inc. (September 2005). "TDR100 Instruction Manual". *Campbell Scientific, Inc.*, Logan, Utah.

Choubane, B., and M. Tia. (1992). Nonlinear Temperature Gradient Effect on Maximum Warping Stresses in Rigid Pavements. *Transportation Research Record No. 1370*, Transportation Research Board, National Research Council, Washington DC, pp. 11-19.

Davids, W.G. 2000. "Effect of Dowel Looseness on Response of Jointed Concrete Pavements." *Journal of Transportation Engineering*, ASCE, 126(1):50-57.

Dempsey, B.J. (1969). *A Heat-Transfer Model for Evaluating Frost Action and Temperature Related Effects in Multilayered Pavements Systems*. Thesis presented to the University of Illinois, at Urbana, IL, in partial fulfillment of the requirements for the degree of Doctor of Philosophy.

Dempsey, B. J., W. A. Herlach, and A. J. Patel, (1985), *The Climatic-Material-Structural Pavement Analysis Program*, FHWA/RD-84/115, Vol.3., Final Report, Federal Highway Administration, Washington D.C.

Eisenmann, J. and G. Leykauf, 1990. Simplified Calculation Method of Slab Curling Caused by Surface Shrinkage. *Proceedings, 2nd International Workshop on Theoretical Design of Concrete Pavements*: 185-197. Madrid, Spain.

Face Construction Technologies, Inc. 2004. *Dipfloor 6.1. User's Guide*. Face Construction Technologies, Inc.

Fredlund, D. G., A. Xing, and S. Huang. 1994. "Predicting the Permeability Function for Unsaturated Soils Using the Soil-Water Characteristic Curve", Canadian Geotechnical Journal, Vol 3., No. 4, pp. 533 - 546.

Fredlund, D. G., A. Xing, M. Fredlund, and S. L. Barbour. 1995. "The Relationship of the Unsaturated Shear Strength to the Soil-Water Characteristic Curve*",* Canadian Geotechnical Journal, Vol. 32, pp. 440-448.

GEOKON, (2006), "Earth Pressure Cells Technical Sheet Rev. E 09/06," Geokon Incorporated, NH, USA.

Grasley, Z.C. and Lange, D.A. 2002. "Modeling Drying Shrinkage Stress Gradients in Concrete." *Journal of Testing and Evaluation*, ASTM.

Grasley, Z.C., Lange, D.A. and D'Ambrosia, M.D. 2003. "Internal relative humidity and drying stress gradients in concrete." *Proceedings of Engineering Conferences International, Advances in Cement and Concrete IX*, Copper Mountain, CO.

Grasley, Z.C., and D.A. Lange. 2004. Modeling Drying Shrinkage Stress Gradients in Concrete. *Cement, Concrete and Aggregates* (ASTM). 26: (2) pp. 115 22.

Guymon, G. L., R. L. Berg, and T. C. Johnson, (1986), *Mathematical Model of Frost Heave and Thaw Settlement in Pavement*, Report: U. S. Army Cold Region Research and Engineering Laboratory, Hanover, New Hampshire.

Hall, K.T., M.I. Darter, T.E. Hoerner, and L. Khazanovich. (1997). *LTPP Data Analysis – Phase I: Validation of Guidelines for k-Value Selection and Concrete Pavement Performance Prediction*. Technical Report FHWA-RD-96-198.

Hammons, M.I. 1997. *Development of an Analysis System for Discontinuities in Rigid Airfield Pavements,* Tech. Report GL-97-3, U.S. Army Corps of Engineers.

Hansen, W., Wei, Y., Smiley, D.L., Peng, Y. and Jansen, E.A. December 2006. Effects of Paving Conditions on Built-In Curling and Pavement Performance. *International Journal of Pavement Engineering*. 7: (4) pp. 291-296.

Harik, I. E., P. Jianping, H. Southgate, and D. Allen. 1994. Temperature Effects on Rigid Pavements. *Journal of Transportation Engineering*. 120: (1) pp. 127–143.

Heath, A. C., Roesler, J. R. and Harvey, J. T. March 2003. Modeling Longitudinal, Corner and Transverse Cracking in Jointed Concrete Pavements. *The International Journal of Pavement Engineering*. 4 (1) pp. 51-58.

Huang, Yang H. 2004. *Pavement Analysis and Design*. Prentice Hall Inc. Englewood Cliffs, New Jersey.

Ioannides A.M. and Hammons, M.I. August 1996. "Developments in Rigid pavement Response Modeling". Technical Report, US Army Corps of Engineers.

Iwama, S. 1964. *Experimental Studies on the Structural Design of Concrete Pavement*, Pavement Laboratory Public works Research Institute, Ministry of Construction, Japan.

Janssen, D. J. 1987. Moisture in Portland Cement Concrete. *Transportation Research Record 1121*. National Research Council, Washington DC.

Janssen, D. J. and M. B. Snyder. June 2000. Temperature-Moment Concept for Evaluating Pavement Temperature Data. Technical Note No. 19948. *Journal of Infrastructure Systems.* American Society of Civil Engineers. Reston, VA, 6: (2) pp. 81-83.

Jeong, J.H. and Zollinger, D.G. 2004. "Early-age curling and warping behavior: insights from a fully instrumented test-slab system." Journal of the Transportation Research Board 1896, Transportation Research Record, Washington, DC, 66–74.

Jeong, Jin-Hoon and Zollinger, Dan G. 2005. Environmental effects on the behavior of jointed plain concrete pavements. *Journal of Transportation Engineering*. 131: (2) pp. 140-148.

Kelleher, K., and R.M. Larson. *The Design of Plain Doweled Jointed Concrete Pavement*. Proceedings of the Fourth International Conference on Concrete Pavement Design and Rehabilitation. Purdue University, West Lafayette, Indiana, April 18-20, 1989.

Khazanovich, L. July 2003. "Finite Element Analysis of Curling of Slabs on Pasternak Foundation". *16th ASCE Engineering Mechanics Conference,* University of Washington, Seattle.

Khazanovich, L., H. T. Yu, S. Rao, K. Galasova, E. Shats, and R. Jones. 2000. *ISLAB2000 - Finite Element Analysis Program for Rigid and Composite Pavements, User's Guide.* ERES Division of ARA, Inc. Champaign, IL.

Khazanovich, L., Tayabji, S.D. and Darter M.I. 2001. "Backcalculation of Layer Parameters for LTPP Test Sections, Volume I: Slab on Elastic Solid and Slab on Dense-Liquid Foundation Analysis of Rigid Pavements." Report No. FHWA-RD-00-086, Federal Highway Administration, McLean, VA.

Larson, G., and Dempsey, B.J. 1997. "*Enhanced Integrated Climatic Model, Version 2.0, Final Report",* Contract DTFA MN/DOT 72114, Department of Civil Engineering, University of Illinois at Urbana-Champaign, Urbana, IL.

Lytton, R. L., D. E. Pufahl, C. H. Michalak, H. S. Liang, and B. J. Dempsey, (1990), *An Integrated Model of the Climatic Effects on Pavement,* Texas Transportation Institute, Texas A&M University, Report No. FHWA-RD-90-033, Federal Highway Administration, McLean, VA.

McCarter, W.J., Watson, D.W., Chrisp, T.M., 2001, "Surface Zone Concrete: Drying, Absorption, and Moisture Distribution," *Journal of Materials in Civil Engineering,* Jan/Feb, pp. 49-57.

McCracken, J.K., 2008. "Seasonal Analysis of the Response of Jointed Plain Concrete Pavements to FWD and Truck Loads," Masters Thesis, University of Pittsburgh School of Engineering, Pittsburgh, PA.

McCracken, J., Asbahan, R. and Vandenbossche, J. 2008. *S.R.-22 Smart Pavement Phase II Final Report: Pavement Response Characteristics for Jointed Plain Concrete Pavements.* Submitted to the Pennsylvania Department of Transportation and the Federal Highway Administration. University of Pittsburgh, Department of Civil and Environmental Engineering, Pittsburgh, Pennsylvania.

Mindess, S., Young, J.F. and Darwin, D. 2003. "Concrete." Second Edition, Prentice Hall Pearson Education, Inc., Upper Saddle River, NJ,.

Miner, M. A. 1945. Cumulative Damage in Fatigue. *Transactions.* American Society of Mechanical Engineers, 67 pp. A159-A164.

Mirambell, E. (1990). Temperature and Stress Distributions in Plain Concrete Pavements Under Thermal and Mechanical Loads. *Proceedings,* Second International Workshop on the Design and Rehabilitation of Concrete Pavements, Sigüenza, Spain.

Mohamed, A. R. and Hansen, W. 1997. Effect of Nonlinear Temperature Gradient on Curling Stress in Concrete Pavements. *Transportation Research Record 1568*. TRB, National Research Council. Washington, D.C. pp. 65-71.

Nishizawa, T., Shimeno, S., Komatsubara, A. and Koyanagawa, M. 1998. Study on thermal stresses in continuously reinforced concrete pavement, *Transp. Res. Rec.*, 1629, 99–107.

National Oceanic and Atmospheric Administration Satellite and Information Service and the National Climatic Data Center. www.ncdc.noaa.gov. October 2006.

Powers, T.C., "Causes and Control of Volume Change." *Journal of the PCA Research and Development Laboratories*, Vol. 1, No. 1, pp. 29-39, 1959.

Rao, C., E. J. Barenberg, M. B. Snyder, and S. Schmidt. 2001. Effects of Temperature and Moisture on the Response of Jointed Concrete Pavements. *Proceedings, 7th International Conference on Concrete Pavements*. Orlando, Florida.

Rao, S. and Roesler, R. R. April 2005. Characterizing Effective Built-In Curling From Concrete Pavement Field Measurements. *Journal of Transportation Engineering*. American Society of Civil Engineers. 131: (4) pp. 320-327.

Richardson, J. M., and Armaghani, J. M. 1987. Stress caused by temperature gradient in Portland cement concrete pavements. *Transportation Research Record 1121*. Transportation Research Board, National Academy Press. Washington, D.C. pp. 7–13.

Ruiz J.M, Kim P.J., Schindler A.K., and, Rasmussen R.O. 2001. Validation of HIPERPAV for prediction of early-age jointed concrete pavement behavior. *Journal of the Transportation Research Board, TRR No. 1778*. Washington, D.C. pp. 17-25.

Siddique Z.Q., Hossain, M. and Meggers, D. 2005. "Temperature and Curling Measurements on Concrete Pavement." *Proceedings of the 2005 Mid-Continent Transportation Research Symposium*, Ames, Iowa, August 2005.

Schmidt, S. 2000. "Built-in curling and warping in PCC pavements." M.S. thesis, Univ. of Minnesota, Minneapolis.

Shoukry, S.N. 2000. Backcalculation of thermally deformed concrete pavements. *Journal of Transportation Research Record No. 1716*. National Research Council. Washington, D.C. pp 64–72.

Shoukry, S. N., William, G. W., and Riad, M. _2003. "Nonlinear temperature gradient effects in dowel jointed concrete slabs." *Int. J. Pavement Eng.*, 4:3, pp. 131–142.

Shoukry, S. N., William, G. W., and Riad, M. _2004. “Validation of 3DFE Model of Jointed Concrete Pavement Response to Temperature Variations.” *Int. J. Pavement Eng.*, 5:3, pp. 123–136.

Suprenant, B. A. 2002. “Why slabs curl - Part I and Part II.” *Concrete International*, 23:3, pp. 57–61.

Teller, L.W. and Sutherland, E.C. 1936. “The structural design of Concrete Pavements, Public Roads: Part II, Observed effects of variations in temperature and moisture on the size, shape and stress resistance of concrete pavement slabs”, Vol. 16, November, pp. 169-197.

Thomlinson, J. 1940. “Temperature variation and consequent stresses produced by daily and seasonal temperature cycles in concrete slabs”. *Concrete and Constructional Engineering*, Vol. 36, No. 6, pp. 298-307 and No. 7, pp. 352-360.

Thompson, M. R., B. J. Dempsey, H. Hill, and J. Vogel. 1987. Characterizing Temperature Effects for Pavement Analysis and Design. *Transportation Research Record 1121*, TRB, National Research Council. Washington, D.C. pp. 14–22.

Topp, G. C., Davis, J. L. and Annan, A. P. (1980). “Electromagnetic Determination of Soil Water Content: Measurements in Coaxial Transmission Lines”. *Water Resources Research*, Vol. 16, No. 3, pp. 574-582.

Vandenbossche, J. M. 2003. “*Interpreting Falling Weight Deflectometer Results for Curled and Warped Portland Cement Concrete Pavements”* Civil Engineering, University of Minnesota, Doctor of Philosophy Dissertation.

Wells, S. A., 2005. “Early Age Response of Jointed Plain Concrete Pavements to Environmental Loads,” Masters Thesis, University of Pittsburgh School of Engineering, Pittsburgh, PA.

Wells, S. A., Phillips, B. M. and Vandenbossche, J. M. June 2005. *S.R.-22 Smart Pavement Phase I: Early-Age Material Properties and Pavement Response Characteristics for Jointed Plain Concrete Pavements; 28-Day Report Final Revision*. Submitted to the Pennsylvania Department of Transportation and the Federal Highway Administration. University of Pittsburgh, Department of Civil and Environmental Engineering, Pittsburgh, Pennsylvania.

Wells, S.A., Phillips, B. M. and Vandenbossche, J. M. December 2006. Quantifying Built-In Construction Gradients and Early-Age Slab Deformation Caused by Environmental Loads in a Jointed Plain Concrete Pavement. *International Journal of Pavement Engineering*. 7: (4) pp. 275-289.

Westergaard, H. M. 1926. Analysis of Stresses in Concrete Pavement Due to Variations of Temperature. *Proc*., *Highway Research Board*, Washington, D.C. Vol. 6, pp. 201-215.

Westergaard, H. M. 1927. Theory of concrete pavement design. *Proc.*,*Highway Research Board, Part I*. Washington, D.C. pp. 175–181.

William, G. W. and Shoukry, S. N. 2001. 3D Finite Element Analysis of Temperature-Induced Stresses in Dowel Jointed Concrete Pavements. *International Journal of Geomechanics*. 1: (3) pp. 291-308.

Yang, Q. 1999. "Inner Relative Humidity and Degree of Saturation in High-Performance Concrete Stored in Water or Salt Solution for 2 Years," *Cement and Concrete Research*, Vol. 29, pp. 45-53.

Yu, H.T. and Khazanovich, L. September 2001. Effects of Construction Curling on Concrete Pavement Behavior. *Proceedings 7th International Conference on Concrete Pavements*. Orlando, FL. pp. 55-67.

Yu, H. T., K. D. Smith, M. I. Darter, J. Jiang and L. Khazanovich. 1998. *Performance of Concrete Pavements Volume III - Improving Concrete Pavement Performance*. Final Report, FHWA-RD-95-111, Federal Highway Administration. McLean, VA.

Zaghloul, S., Ayed, A., Abd El Halim A., Vitillo, N. and Sauber, R. (2006). "Investigations of Environmental and Traffic Impacts on MEPDG Predictions", Paper presented at the Transportation Research Board 85th Annual Meeting, Washington, DC.

Zhang, J., T.W. Fwa, K.H. Tan, and X.P. Shi. 2003. Model for Nonlinear Thermal Effect on Pavement Warping Stresses. Journal of Transportation *Engineering*, ASCE 129.6, pp. 695–702.